University of Trento

Doctoral Thesis

Torsion Pendulum Testing of the LISA Charge Management System

Author:
Davide Dal Bosco

Supervisor:
Prof. Rita Dolesi

A thesis submitted in fulfillment of the requirements for the degree of Doctor of Philosophy

in the

Experimental Gravitation Laboratory
Department of Physics

April 20, 2023

"*If science teaches us anything, it teaches us to accept our failures, as well as our successes, with quiet dignity and grace.*"

Dr. Frederick Frankenstein

UNIVERSITY OF TRENTO

Abstract

Department of Physics

Doctor of Philosophy

Torsion Pendulum Testing of the LISA Charge Management System

by Davide Dal Bosco

The Laser Interferometer Space Antenna (LISA) will be the first gravitational wave detector in space. The European Space Agency has selected LISA as a large mission scheduled to launch in the mid-2030s.

The sensitivity of LISA to gravitational waves is limited at low frequencies by force disturbances acting on the otherwise free-falling test masses. Among the stray forces relevant to the LISA noise budget, we find the ones that arise from the electrostatic interaction between the test masses and the surrounding capacitive sensor. Most of such electrostatic forces scale with the electric charge deposited on the test masses. This problem is aggravated by the fact that isolated objects in space, such as the floating LISA test masses, accumulate electric charge due to the constant bombardment of cosmic rays and solar energetic particles. We, therefore, understand that if the test masses were not discharged, the electrostatic disturbances could spoil the performance of the whole mission at low frequency.

The precursor LISA Pathfinder (LPF) mission proved that the test mass charge could be successfully managed with a contactless system based on photoelectric charge transfer. The light sources required for photoemission in LISA Pathfinder were mercury-vapor lamps emitting photons in the UV range.

In this thesis, we will present our on-ground testing campaign of a prototype Charge Management System for LISA, which relies on UV-LEDs as light sources. LEDs, compared to mercury-vapor lamps, can emit short pulses of UV light ($\sim 10\,\mathrm{ns}$), which can be synchronized with the time-varying electrostatic fields around the test mass. For this reason, we studied new discharge strategies made possible by adopting UV-LEDs characterized by pulsed illumination synced with the capacitive sensing injection bias. Our measurements indicate that UV-LEDs offer significant advantages regarding the flexibility and robustness of the Charge Management System. Moreover, the new illumination patterns offered by UV-LEDs allow fine-tuning the TM equilibrium potential without introducing local DC fields, easing the implementation of the continuous discharge mode to manage the TM potential. Finally, we investigated the charge noise introduced by the continuous discharge mode and verified that it could be kept within the LISA requirements.

We will present hereafter the outline of the thesis.

- In the first chapter, we present a mandatory introduction to gravitational waves and the LISA mission.

- In the second chapter, we present the instrument used for our experimental campaign, namely the four-test-masses torsion pendulum at the University of Trento. We also present the electrostatic model and the measurement techniques used to evaluate the electric charge on the pendulum test mass.
- In the third chapter, we introduce the concept of apparent yield, which is a figure of merit of the charge management system performance. We also present our experimental measurement, which encompasses tests on several UV-LEDs in different illumination patterns.
- In the fourth chapter, we derive a simple photoemission model, which is useful for interpreting the apparent yield data acquired. We will also use the model to fit the experimental data and extract estimates of the microscopic parameters that affect the photoemission from metallic surfaces, e.g. *work function* or *quantum yield*.
- In the fifth chapter, we present a model and our torsion pendulum measurements for the charge noise induced on the test masses when continuously illuminated with UV light. Such noise arises from the discrete and intrinsically stochastic nature of photoelectric charge transfer.
- Finally, in the last chapter, we will wrap up by presenting the problems encountered and the "lessons learned" during the years-long experimental endeavor.

Acknowledgements

The time has come to condense the work of these long four years into a thesis. I am not going to lie, this journey into real-world experimental physics has not always been easy, but hopefully, it was worth it. I would not be here without the help of many people. The following lines are dedicated to them.

Firstly, I would like to express my gratitude to my supervisor Prof. Rita Dolesi for all the opportunities and the trust. Thank you for always lifting my spirit when nothing seemed to work.

Secondly, I would like to thank my fellow lab companions. I am indebted to Antonella Cavalleri for sharing the long days spent in the laboratory and for her generosity. In addition, I want to praise Giuliana Russano for teaching me that an experimental physicist must be rigorous even in the most tedious tasks and for introducing me to the quirks of the codebase of our laboratory. "Gracias" also to Francisco Rivas Garcia for being a wonderful person to collaborate with and almost making me a Real Madrid FC supporter.

I owe a lot of gratitude to Renato Mezzena, the person you want to have on your side both in a research lab and on an excursion in the mountains. Thank you for your friendship and for always reserving some time to help me!

Let me thank Vittorio Chiavegato, one of the most brilliant people I know! Your passion for physics is unparalleled. I am sure you have an extraordinary future ahead of you. Thank you also for the dank memes (especially on Wednesdays).

A famous saying goes, "If you are the smartest person in the room, you are in the wrong room". If this maxim holds a grain of truth, I always felt in the right place when Prof. Stefano Vitale and Prof. William Joseph Weber were around! Thank you for your intuitions and unparalleled knowledge of the LISA mission.

I would express my gratitude to Dr. Mauro Hueller for the handy suggestions and the remarkably well-written legacy code he produced when he was a member of our laboratory.

I thank Karine Laurence Frisinghelli for the administrative support and the friendly conversations during the coffee breaks. A big "Thank you!" to Lorenzo Sala, Valerio Ferroni, Daniel Vetrugno, Davide Vignotto, and all the other members of the LISA group for the exciting discussions. Here I would also like to acknowledge the former members of our group, Martina Muratore and Eleonora Castelli.

I am also grateful to the lab members working on low-temperature physics: thanks to Paolo Falferi for his kindness, Andrea Vinante for his unique humor and understanding of physics, and Federica and Felix for the enjoyable talks during the lunch. Your experiment may be pretty cold, but you are the coolest to me!

Let me express my gratitude to the administrative staff of the Ph.D. program in Physics at the University of Trento, especially to Micaela Paoli, for her hard work and constant help. I want to commend the front desk personnel of the physics building for their unmatched dedication to enforcing every internal rule, no matter how pointless it may seem. Their professionalism made the access to the laboratory outside the working hours extra "interesting".

Finally, I would like to express all my gratitude to my family for their unlimited support during these years: they were the only ones who never lost faith in my qualities, even when I was the first to question them. Thank you for your love. Vi voglio bene!

Contents

List of Tables

List of Abbreviations

LISA	**L**aser **I**nterferometer **S**pace **A**ntenna
LPF	**L**ISA **P**ath**f**inder
ESA	**E**uropean **S**pace **A**gency
GRS	**G**ravitational **R**eference **S**ensor
EH	**E**lectrode **H**ousing
TM	**T**est **M**ass
STC	**St**iffness **C**ompensator
UV	**U**ltra**v**iolet
CMD	**C**harge **M**anagement **D**evice
CMS	**C**harge **M**anagement **S**ystem
ULU	**U**ltraviolet **L**ight **U**nit
FMR	**F**light **M**odel **R**eplica
ISUK	**I**nertial **S**ensor **U**V **K**it
GPRM	**G**rabbing **P**ositioning and **R**elease **M**echanism
SNR	**S**ignal to **N**oise **R**atio
FEM	**F**inite-**E**lement **M**odel
DOF	**D**egree **O**f **F**reedom
ASD	**A**mplitude **S**pectral **D**ensity
CSD	**C**ross **S**pectral **D**ensity
PSD	**P**ower **S**pectral **D**ensity
OB	**O**ptical **B**ench
ADC	**A**nalog to **D**igital **C**onverter
AC	**A**uto**c**ollimator
TRL	**T**echnology **R**ediness **L**evel
MOSA	**M**oving **O**ptical **S**ub-**A**ssembly
DFACS	**D**rag-**F**ree **A**ttitude **C**ontrol **S**ystem
GW	**G**ravitaional **W**ave
MBHB	**M**assive **B**lack **H**ole **B**inary
FEE	**F**ront-**E**nd **E**lectronics
AY	**A**pparent **Y**ield
QY	**Q**uantum **Y**ield
PMT	**P**hoto-**M**ultiplier **T**ube
PHD	**Ph**oto **D**iode

Parameters

TM mass	$M_{TM} = 1.9282\,\mathrm{kg}$
TM side	$l_{TM} = 4.6\,\mathrm{cm}$
4TM pendulum arm	$l_{arm} = 10.565\,\mathrm{cm}$
4TM pendulum moment of inertia	$I = 3.7 \cdot 10^{-3}\,\mathrm{kg\,m^2}$
4TM pendulum total TM capacitance	$C_{tot} = 36.40\,\mathrm{pF}$
LISA total TM capactitance	$C_{tot}^{LISA} = 34.40\,\mathrm{pF}$
x-electrode capactitance	$C_x = 1.18\,\mathrm{pF}$
x-electrode capactitance with respect to EH	$C_{x,h} = 5.94\,\mathrm{pF}$
y-electrode capactitance	$C_y = 0.95\,\mathrm{pF}$
z-electrode capactitance	$C_z = 0.70\,\mathrm{pF}$
Injection electrodes capactitance	$C_{inj} = 4.22\,\mathrm{pF}$
Derivative of C_x	$\frac{\partial C_x}{\partial x} = 299\,\mathrm{pF\,m^{-1}}$
Derivative of $C_{x,h}$	$\frac{\partial C_{x,h}}{\partial x} = -70.1\,\mathrm{pF\,m^{-1}}$
Second derivative of C_{tot}	$\frac{\partial^2 C_{tot}}{\partial x^2} = 1.18\,\mathrm{\mu F\,m^{-2}}$
Second derivative of C_x	$\frac{\partial^2 C_x}{\partial x^2} = 0.144\,\mathrm{\mu F\,m^{-2}}$
Second derivative of $C_{x,h}$	$\frac{\partial^2 C_{x,h}}{\partial x^2} = 8.71\,\mathrm{nF\,m^{-2}}$

Chapter 1

Introduction

Gravity is the engine that shaped our Universe. All the large scale structures that we see today, e.g. stars, galaxies and clusters of galaxies, came together because of gravity. In some sense, also the fact that you are reading these words right now has been made possible by gravity, which formed a planet that for some twist of fate had the right parameters to allow intelligent life to develop.

Moreover, we know that 95% of the energy content of the Universe is dark, i.e. it does not interact with electromagnetic radiation, but it definitely feels the gravitational interaction. If we want to understand our Universe, it is, therefore, fundamental to understand gravity.

We are living in very exciting times for science and gravitational physics in particular, because we are now able to measure gravitational waves, which are the messengers of gravitation, as light is for the electromagnetic interaction.

In 2015, almost one hundred years after the publication of the theory of General Relativity by Albert Einstein, the first direct detection of gravitational waves [1] by the LIGO/Virgo collaboration inaugurated the era of gravitational wave astronomy. The observed gravitational wave signal was in spectacular agreement with Einstein's theory of General Relativity.

A couple of years later, the even more important (we dare to say!) observation of the first binary neutron star merger with an electromagnetic counterpart [2] opened the era of multi-messenger astrophysics: we now have a new window to observe the universe and probe its mysteries.

In addition to the ground-interferometer measurements of gravitational waves, another historic feat of modern science has been achieved in 2019 by the Event Horizon Telescope collaboration, who announced the first direct image of a super massive black hole [3]: the strongest evidence to date for the existence of supermassive black holes. Once again Einstein's theory did not flinch: the observed image is consistent with expectations for the shadow of a Kerr black hole as predicted by General Relativity.

The observations and technological breakthroughs of the recent years are just the tip of the iceberg. The renaissance of gravitational wave physics will continue over the next decades, as new experiments are proposed and planned.

In this regard, one of the most mature future gravitational wave experiments is the Laser Interferometer Space Antenna. LISA will be the first detector of gravitational wave from space. Indeed, at the time of writing the technology to build a gravitational wave observatory in space is ready, as demonstrated with great success by the LISA Pathfinder mission.

LISA could potentially unravel some of the deepest mysteries of the Universe, and, on the other hand, find new and unexpected phenomena, whose interpretation challenges our current understanding of physics.

FIGURE 1.1: The image of the black hole at the center of galaxy M87 by the Event Horizon Telescope. The bright ring corresponds to the closed orbits of photons that bend in the stong gravitational field of the black hole (which is itself not visible at the center of the dark spot). The size of the light ring gives an estimate of the black hole mass $M \simeq 6.5 \cdot 10^9 \, M_\odot$ [4].

Before getting too ahead of ourselves, let us provide the reader with some context. Let us start from the idea gave birth to the field of gravitational waves physics: the theory of General Relativity.

1.1 General Relativity and gravitational waves

In 1915, Albert Einstein published a theory that rethinks the previously established conception of gravitation. Gravity is not considered anymore a force, but a geometry of spacetime. Massive bodies, or local concentrations of energy, bend the fabric of spacetime. Test particles, e.g. a planet, are deviated from uniform linear motion when they approach a massive body, e.g. a star, not because they feel a force, but rather they still move freely in a spacetime which is no more flat but curved. This equivalence between gravitational force and geometry of spacetime descends from the *equivalence principle*: the equality between gravitational mass and inertial mass makes so that it is impossible to distinguish the effect of gravitation from the effect of fictitious forces due to the acceleration of the frame of reference.

The geometry of spacetime is described by the metric tensor $g_{\mu\nu}$, which is related to the stress-energy tensor $T_{\mu\nu}$, i.e. a quantity which tells how much momentum and energy (or mass, which is a just form of energy) is present in a given point of the spacetime, through the Einstein field equations[1]

$$R_{\mu\nu} - \frac{1}{2} g_{\mu\nu} R = -\frac{8\pi G}{c^4} T_{\mu\nu} \tag{1.1}$$

where $R_{\mu\nu}$ is the Ricci tensor and R the Ricci scalar, obtained from a contraction of the Ricci tensor with the metric, i.e. $R = g^{\mu\nu} R_{\mu\nu}$. For the scope of this work, let us just say that the Ricci tensor is a very complicated differential operator that "measures" the curvature of spacetime. The meaning of these equations can be summarized by the potent words of physicist John Archibald Wheeler

[1] Here we use the sign convention of [5].

Matter tells spacetime how to curve, and curved spacetime tells matter how to move.

The solution of Einstein field equations is typically quite challenging and generally possible only with numerical methods. A special case, which can be solved analytically, is when the metric tensor is a small perturbation from the flat[2], or Minkowski, spacetime $\eta_{\mu\nu}$

$$g_{\mu\nu} = \eta_{\mu\nu} + h_{\mu\nu} \qquad \text{where} \qquad |h_{\mu\nu}| \ll 1 \tag{1.2}$$

In such weak-field limit it is possible to prove that the Einstein equations (1.1) reduce, to [5]

$$\left(\frac{1}{c^2}\frac{\partial^2}{\partial t^2} - \boldsymbol{\nabla}^2\right)\bar{h}_{\mu\nu} = \frac{16\pi G}{c^4}T_{\mu\nu} \tag{1.3}$$

where the quantity $\bar{h}$ is the trace-reversed metric perturbation[3] obtained by

$$\bar{h}_{\mu\nu} = h_{\mu\nu} - \frac{1}{2}\eta_{\mu\nu}h. \tag{1.4}$$

The (1.3) are the field equations in the linearized theory, which correspond to keeping only the terms linear in the metric perturbation $h_{\mu\nu}$.

If we assume to be outside the source, i.e. in vacuum, the stress energy tensor vanishes, i.e. $T_{\mu\nu} = 0$, and the equation (1.3) becomes

$$\left(\frac{1}{c^2}\frac{\partial^2}{\partial t^2} - \boldsymbol{\nabla}^2\right)\bar{h}_{\mu\nu} = 0 \tag{1.5}$$

In (1.5) we recognize a *wave equation*, similar to Maxwell's equation for electromagnetic waves. General Relativity, therefore, predicts the existence of gravitational waves that propagate at the speed of light. A possible solution of the previous equation is

$$\bar{h}_{\mu\nu} = A_{\mu\nu}\exp\left(\mathrm{i}k_\alpha x^\alpha\right) \qquad \text{where} \qquad k_\alpha = \left(k_0 = \frac{\omega}{c}, -\boldsymbol{k}\right) \tag{1.6}$$

which corresponds to a plane-wave with wave-vector $\boldsymbol{k}$ and angular frequency ω. As in electromagnetic waves in vacuum, the dispersion relation is $\omega = c|\boldsymbol{k}|$ and can be obtained plugging (1.6) into the wave-equation[4].

If we choose a specific gauge, which is called traceless-transverse (TT) gauge, is it possible to prove that the solution (1.6), can be

$$h^{TT}_{\mu\nu}(t,z) = \begin{bmatrix} 0 & 0 & 0 & 0 \\ 0 & h_+ & h_\times & 0 \\ 0 & h_\times & -h_+ & 0 \\ 0 & 0 & 0 & 0 \end{bmatrix} \exp\left[\mathrm{i}(\omega t - kz)\right] \tag{1.8}$$

[2] We chose the convention $\eta_{\mu\nu} = \mathrm{diag}(1,-1,-1,-1)$.

[3] In order for the (1.3), we also had to assume to be in the *Lorentz gauge*, i.e. $\partial_\mu \bar{h}^{\mu\nu} = 0$.

[4] Indeed we have $k^\alpha = (k_0, \boldsymbol{k})$, wich contracting with the flat metric gives $k_\alpha = \eta_{\alpha\nu}k^\nu = (k_0, -\boldsymbol{k})$. If we plug the solution (1.6) into the wave equation we have

$$0 = A_{\mu\nu}\left(\frac{1}{c^2}\frac{\partial^2}{\partial t^2} - \boldsymbol{\nabla}^2\right)e^{\mathrm{i}(k_0 ct - k_1 x - k_2 y - k_3 z)} = \underbrace{\left(-\frac{c^2k_0^2}{c^2} + k_1^2 + k_2^2 + k_3^2\right)}_{0}\bar{h}_{\mu\nu} \tag{1.7}$$

From which we must have $k_0^2 = k_1^2 + k_2^2 + k_3^2 = |\boldsymbol{k}|^2$. If we define $k_0 = c\omega$, we have the dispersion relation $\omega = c|\boldsymbol{k}|$.

which corresponds to a plane gravitational wave propagating in the z-direction, i.e. $\boldsymbol{k} = (0, 0, k)$. The terms h_+ and $h_\times$ are the two possible polarization of gravitational waves, which are called plus and cross polarization. By theorems of Fourier analysis, any solution of (1.5), can be written as a suitable superposition of plane waves.

We notice that the metric is real, hence, as usual also for electromagnetic waves, at the end of the calculations one has to take the real part of the complex solutions, i.e. the equation (1.8) actually is intended to be

$$\begin{aligned} h^{TT}_{\mu\nu}(t,z) &= \begin{bmatrix} 0 & 0 & 0 & 0 \\ 0 & h_+ & h_\times & 0 \\ 0 & h_\times & -h_+ & 0 \\ 0 & 0 & 0 & 0 \end{bmatrix} \cos(\omega t - kz) \\ &= \begin{bmatrix} 0 & 0 & 0 & 0 \\ 0 & h_+ & h_\times & 0 \\ 0 & h_\times & -h_+ & 0 \\ 0 & 0 & 0 & 0 \end{bmatrix} \cos\left[\omega\left(t - \frac{z}{c}\right)\right] \end{aligned} \tag{1.9}$$

where we also used the dispersion relation $k = \boldsymbol{k} = \omega/c$ for waves propagating along the z-direction.

1.1.1 Effect of GW on particles

Let us consider two test particles both at rest, one located at the origin, the other in the location $x = L_0$, $y = 0$, and $z = 0$, with L_0 small compared to the spatial distances at which the metric $g_{\mu\nu} = \eta_{\mu\nu} + h_{\mu\nu}$ changes significantly. If a gravitational wave of the form (1.9) impinges on them, their proper distance will be

$$L = \int \sqrt{\mathrm{d}s^2} = \int \sqrt{g_{\mu\nu}\,\mathrm{d}x^\mu \mathrm{d}x^\nu} = \int_0^{L_0} \sqrt{g_{11}}\,\mathrm{d}x \simeq \sqrt{g_{11}(x=0)}\,L_0 \tag{1.10}$$

where we used $\mathrm{d}x^\mu = 0$ for $\mu \neq 1$ and the fact that the metric is almost constant in $x = (0, L_0)$. If we consider now that the metric perturbation is small, we can expand the square root of g_{11} in a Taylor series

$$\sqrt{g_{11}(x=0)} = \sqrt{1 + h^{TT}_{11}(x=0)} \simeq 1 + \frac{1}{2} h^{TT}_{11}(x=0) \tag{1.11}$$

Hence

$$L = L_0 \left[1 + \frac{1}{2} h^{TT}_{11}(x=0)\right] = L_0 \left[1 + \frac{1}{2} h_+ \cos(\omega t)\right] \tag{1.12}$$

The proper distance between the particles changes with time as the gravitational wave impinges on the system. From this equation we also see that the relative variation of the proper distance $\Delta L = L - L_0$ is proportional to the gravitational wave amplitude

$$\frac{\Delta L}{L_0} \sim \frac{h}{2} \sim h. \tag{1.13}$$

The observable quantity $\Delta L/L_0$ is called the *strain* and can be used as a direct way to measure the amplitude of gravitational waves. We also see that the change of distance between the particles is proportional to their initial separation: the effect of gravitational waves is larger for bigger detectors.

In Figure 1.2 we show the effect of the cross and plus polarization on a ring of particles.

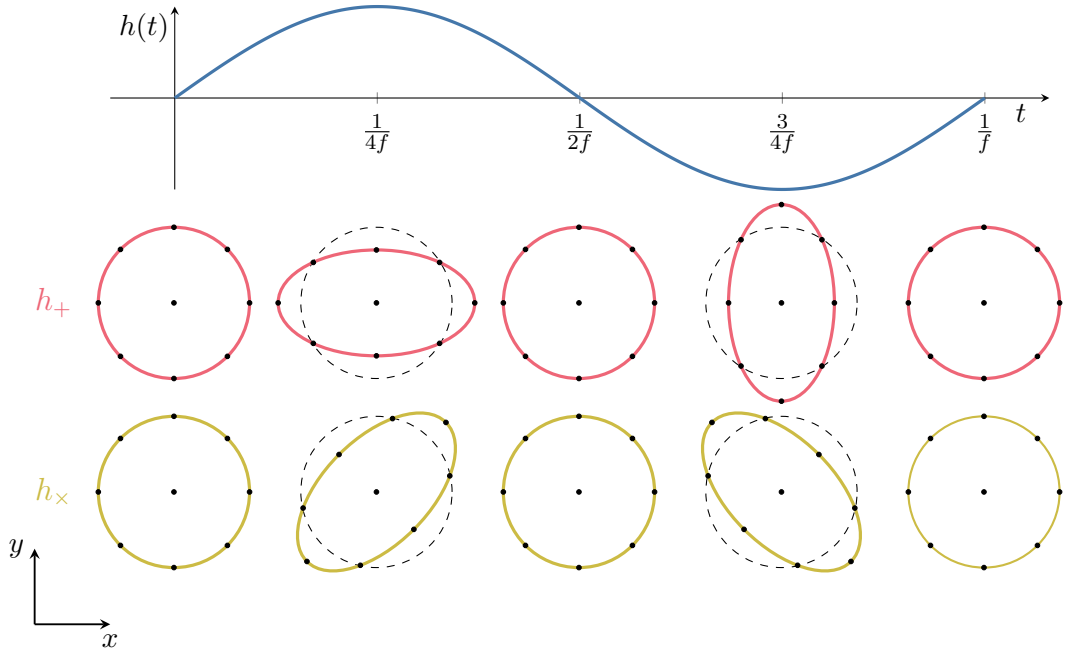

FIGURE 1.2: Effect a plane gravitational wave propagating in the z-direction on a ring of particles in the xy-plane.

1.1.2 Detecting of GW with light

In this section we will show how light can be used to measure the amplitude of gravitational waves, the principle at the core of all GW detectors based on laser interferometry. For this calculation we will follow reference [6].

Let us consider a gravitational wave traveling in the z-direction with pure plus-polarization for simplicity ($h_\times = 0$). The metric element is given by

$$\begin{aligned} \mathrm{d}s^2 &= g_{\mu\nu}\,\mathrm{d}x^\mu\,\mathrm{d}x^\nu \\ &= (\eta_{\mu\nu} + h^{TT}_{\mu\nu})\,\mathrm{d}x^\mu\,\mathrm{d}x^\nu \\ &= c^2\mathrm{d}t^2 - [1 + h_+(t - z/c)]\,\mathrm{d}x^2 - [1 + -h_+(t - z/c)]\,\mathrm{d}y^2 - \mathrm{d}z^2 \end{aligned} \tag{1.14}$$

Suppose again that we have two test particles: one at the origin, the other at $x = L$ (as in Figure 1.3). The first particle sends a photon towards the second particle at $x = L$, which recieves and sends it back. We can compute the proper time elapsed for the first particle from the time t_{em} at which the photon is emitted and the instant t_{return} at which the photon returns to the first particle.

Note that photons travel on null geodesics, i.e. $\mathrm{d}s^2 = 0$. Let us also assume for simplicity that the problem is one-dimensional, i.e. $\mathrm{d}y = \mathrm{d}z = 0$. Under such hypotheses the previous equation reduces to

$$0 = c^2\mathrm{d}t^2 - [1 + h_+(t - z/c)]\,\mathrm{d}x^2 \qquad \longrightarrow \qquad \left(\frac{\mathrm{d}x}{\mathrm{d}t}\right)^2 = \frac{c^2}{1 + h_+(t)} \tag{1.15}$$

We would like to notice that the effective speed $\mathrm{d}x/\mathrm{d}t$ may not be c because that is only a coordinate speed. A photon emitted at t_{em} will reach the coordinate location x at the time $t(x)$ obtained integrating the second of (1.15). In our case we want to

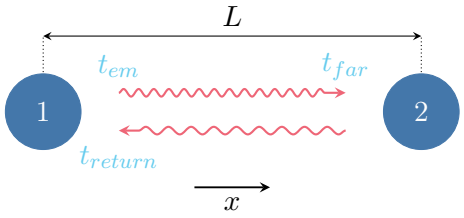

FIGURE 1.3: Two particles exchanging a photon in a perturbed spacetime $g_{\mu\nu} = \eta_{\mu\nu} + h_{\mu\nu}$.

compute the time at which $x = L$, that is

$$t_{far} = t(x = L) = t_{em} + \int_0^L \frac{\mathrm{d}x}{\mathrm{d}t}\,\mathrm{d}x = t_{em} + \underbrace{\frac{1}{c}\int_0^L \sqrt{1 + h_+(t(x))}\,\mathrm{d}x}_{t_{1\to 2}} \tag{1.16}$$

Now this equation is not as simple as it seems because the time t appears also inside the integral (h_+ is a function of time). However, as the metric perturbation h_+ is small, we can brutally approximate that the time inside the integral is the one that we would have in the flat spacetime, i.e $t(x) = t_{em} + x/c$ (the error due to this simplification is higher order in h_+ and thus negligible in the *linearized* treatment). Let us also expand the square root in a Taylor series at first order

$$\sqrt{1 + h_+(t(x))} \simeq 1 + \frac{1}{2}h_+(t(x)) \simeq 1 + \frac{1}{2}h_+\left(t_{em} + \frac{x}{c}\right) \tag{1.17}$$

If we plug this expression into the (1.16), we have

$$\begin{aligned} t_{far} &\simeq t_{em} + \frac{1}{c}\int_0^L \left[1 + \frac{1}{2}h_+\left(t_{em} + \frac{x}{c}\right)\right]\mathrm{d}x \\ &\simeq t_{em} + \frac{L}{c} + \frac{1}{2c}\int_0^L h_+\left(t_{em} + \frac{x}{c}\right)\mathrm{d}x \end{aligned} \tag{1.18}$$

Similar arguments allow us to determine the time $t_{2\to 1}$ that the photon need for the return trip once it is reflected by the second particle

$$\begin{aligned} t_{2\to 1} &\simeq \frac{L}{c} + \frac{1}{2c}\int_L^0 h_+\left(t_{em} + \frac{L}{c} - \frac{x}{c}\right)\mathrm{d}x \\ &\simeq \frac{L}{c} + \frac{1}{2c}\int_0^L h_+\left(t_{em} + \frac{L}{c} + \frac{x}{c}\right)\mathrm{d}x \end{aligned} \tag{1.19}$$

where in the last passage we did the change of variables $x \to -x$. Therefore, the time at which the photon returns to the first particle is

$$\begin{aligned} t_{return} &\simeq t_{em} + t_{1\to 2} + t_{2\to 1} \\ &\simeq t_{em} + \frac{2L}{c} + \frac{\int_0^L h_+\left(t_{em} + \frac{x}{c}\right)\mathrm{d}x}{2c} + \frac{\int_0^L h_+\left(t_{em} + \frac{L}{c} + \frac{x}{c}\right)\mathrm{d}x}{2c} \end{aligned} \tag{1.20}$$

If we derive t_{return} in terms of t_{em}, we have

$$\frac{\mathrm{d}t_{return}}{\mathrm{d}t_{em}} \simeq 1 + \frac{1}{2c}\int_0^L \frac{\mathrm{d}h_+\left(t_{em} + \frac{x}{c}\right)}{\mathrm{d}t_{em}}\,\mathrm{d}x + \frac{1}{2c}\int_0^L \frac{\mathrm{d}h_+\left(t_{em} + \frac{L}{c} + \frac{x}{c}\right)}{\mathrm{d}t_{em}}\,\mathrm{d}x \tag{1.21}$$

From (1.15), we have that

$$\frac{\mathrm{d}x}{\mathrm{d}t} = \frac{c}{\sqrt{1+h_+(t)}} \simeq c \qquad \text{for} \qquad h_+(t) \ll 1 \tag{1.22}$$

so that the integrands can be rephrased as

$$\frac{\mathrm{d}h_+}{\mathrm{d}t_{em}}\,\mathrm{d}x = \mathrm{d}h_+\,\frac{\mathrm{d}x}{\mathrm{d}t_{em}} \simeq \mathrm{d}h_+ \cdot c \tag{1.23}$$

In this way the (1.21), reduces to a trivial integration

$$\begin{aligned}\frac{\mathrm{d}t_{return}}{\mathrm{d}t_{em}} &\simeq 1 + \frac{1}{2}\int_0^L \mathrm{d}h_+\left(t_{em}+\frac{x}{c}\right) + \frac{1}{2}\int_0^L \mathrm{d}h_+\left(t_{em}+\frac{L}{c}+\frac{x}{c}\right)\\ &\simeq 1 + \frac{1}{2}\left[h_+\left(t_{em}+\frac{2L}{c}\right) - h_+\left(t_{em}\right)\right]\end{aligned} \tag{1.24}$$

This result is very important: it tells us that the rate of change in the return time depends only on the perturbation of the metric due to the gravitational wave at the time the photon was emitted and at the time it was received back at the origin. The GW amplitude when the photon is received by the distant particle cancels out at first order and, hence, plays no role.

Instead of focusing on single photons it is convenient to think in terms of electromagnetic waves: a specific phase of an EM waves, such as a "crest" propagates at the speed of light and hence behaves basically like a photon. As we are in $x = 0$, the phase is simply given by $\phi(t) = 2\pi\nu_{em}t$, where ν_{em} is the frequency of the emitted wave.

The phase of the returning wave after the round trip its the same at which it started, i.e.

$$\phi_{return} = \phi(t_{em}) = 2\pi\nu_{em}t_{em}, \tag{1.25}$$

which must be compared to the phase of the light emitted by the first particle at the time when the initial phase returns to the origin

$$\phi(t_{return}) = 2\pi\nu_{em}t_{return} \tag{1.26}$$

The phase difference between emitted and received light at $t = t_{return}$ is

$$\begin{aligned}\Delta\phi(t_{return}) &= \phi(t_{return}) - \phi(t_{em})\\ &= 2\pi\nu_{em}(t_{return} - t_{em})\\ &\simeq \omega_{em}\left[\frac{2L}{c} + \frac{\int_0^L h_+\left(t_{em}+\frac{x}{c}\right)\,\mathrm{d}x}{2c} + \frac{\int_0^L h_+\left(t_{em}+\frac{L}{c}+\frac{x}{c}\right)\,\mathrm{d}x}{2c}\right]\end{aligned} \tag{1.27}$$

where the (1.20) was used. We, therefore, see that the gravitational wave has the effect of introducing a phase shift between emitted and received laser light. This is actually how real experiments work because interferometers measure naturally phase shifts instead of photons travel times (or distances). If we define the new frequency

$$\nu_{return} = \frac{1}{2\pi}\frac{\mathrm{d}\phi(t_{return})}{\mathrm{d}t_{em}} = \nu_{em}\frac{\mathrm{d}t_{return}}{\mathrm{d}t_{em}} \tag{1.28}$$

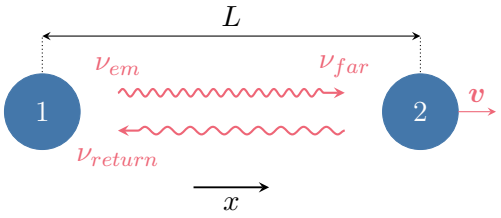

FIGURE 1.4: Doppler frequency shift for particles which have a non-zero relative velocity.

From the (1.24), we have

$$\frac{\nu_{return}}{\nu_{em}} = \frac{\mathrm{d}t_{return}}{\mathrm{d}t_{em}} \simeq 1 + \frac{1}{2}\left[h_+\left(t_{em} + \frac{2L}{c}\right) - h_+\left(t_{em}\right)\right] \tag{1.29}$$

A similar relation holds for the frequency shift between received and emitted light

$$\frac{\Delta\nu}{\nu_{em}} = \frac{\mathrm{d}t_{return}}{\mathrm{d}t_{em}} - 1 \simeq \frac{1}{2}\left[h_+\left(t_{em} + \frac{2L}{c}\right) - h_+\left(t_{em}\right)\right] \tag{1.30}$$

where we defined $\Delta\nu = \nu_{return} - \nu_{em}$.

Effects that mimic GW

Not only graviational waves are may induce a frequency shift in the electromagnetic radiation exchanged between two free-falling particles.

Let us consider the configuration depicted in Figure 1.4. Assuming to be in a perfectly flat spacetime, if the second particle has a relative velocity with respect to the first particle equal to $\boldsymbol{v} = v\hat{\boldsymbol{e}}_x$ with $|v| \ll c$ (so to neglect relativistic corrections), the classical *Doppler effect* will introduce a frequency shift the emitted and received frequencies which is indistinguishable from GWs. Indeed the classical Doppler effect predicts that frequency of light received by the second particle is

$$\nu_{far} = \left[1 - \frac{v(t_{em} + L/c)}{c}\right]\nu_{em} \tag{1.31}$$

where $v(t_{em} + L/c)$ is the velocity of the second particle when the arrive to it. At this point the second particle reflects instantaneously the wave that it receives at frequency ν_{far} towards the first particle. Also for the return trip there is a Doppler effect because the source (particle two) is moving away from the receiver (particle one). Hence, the frequency of the wave as it returns to the first particle is

$$\nu_{return} = \left[1 - \frac{v(t_{em} + L/c)}{c}\right]\nu_{far} \tag{1.32}$$

The velocity in the Doppler effect formula is always evaluated at $t = t_{em} + L/c$, because we assumed that the wave is reflected as soon as it reached the second particle. Using (1.31) and expanding at first order in v/c, we have

$$\nu_{return} = \left[1 - \frac{v(t_{em} + L/c)}{c}\right]^2 \nu_{em} \simeq \left[1 - 2\frac{v(t_{em} + L/c)}{c}\right]\nu_{em} \tag{1.33}$$

or in a more polished form

$$\frac{\Delta\nu}{\nu_{em}} \simeq -2\frac{v(t_{em} + L/c)}{c} \tag{1.34}$$

where as usual $\Delta\nu = \nu_{return} - \nu_{em}$.

We have shown that a relative velocity between the particles exchanging the laser beam will produce the same effect as a curved spacetime (1.30). As we are considering gravitational waves, i.e. a curvature that changes with time, the previous sentence can be rephrases as the fact that a variation in the relative velocity between the particles mimic a GW as they both produce a time-depending Doppler frequency shift in the emitted and received light.

In a real physical system fluctuations in the relative velocity between the particles may arise for two reasons:

- The presence of non-gravitational stray forces which accelerate the particles.
- Noise in the interferometric measurement of the distance between the particles (which can be back-converted into an apparent relative velocity of the particles).

1.1.3 Sources of GW

In reasonable hypotheses that the source of the gravitational waves is very far away from the observer (*compact source approximation*) and that the typical velocity of the source is much smaller than the speed of light, the *quadruple formula*[5] [5] can be used to estimate the amplitude of the emitted gravitational waves at leading order

$$\bar{h}^{ij}(t, r) = \frac{2G}{c^4 r}\ddot{I}^{ij}(t - r/c) \tag{1.35}$$

where r is the distance between source and observer, $\bar{h}^{ij}$ spatial part of the trace reversed perturbation of the metric (1.4), i.e. practically the gravitational wave, and $\ddot{I}(t - r/c)$ is the second derivative of the mass quadrupole moment evaluated at the retarded time. The mass quadrupole moment is defined as

$$I^{ij}(t) = \int \rho(t, \boldsymbol{x}) x^i x^j \, \mathrm{d}^3 x \tag{1.36}$$

where ρ is the distribution of the mass density of the source.

The amplitude of the gravitational waves decreases $\propto 1/r$ as we would expect form conservation energy.

We, therefore, see that every accelerating mass with non-zero quadrupole mass moment emits gravitational waves. The quadrupole formula, tells us that in order to generate gravitational waves with a relatively large amplitude, we need a lot of mass which is moving very fast and in an asymmetrical fashion. It also tells us that the measured GW amplitude decreases with the distance r from the source.

For instance, also rotating a pen in your hands radiates gravitational waves. How come that we never experience GWs in our everyday life? The problem lies in the fact that GW are absurdly tiny, because in the Einstein field equations (1.1) the proportionality constant between curvature and stress-energy tensor is $8\pi G/c^4 \sim 10^{-43}\,\mathrm{s}^2\,\mathrm{kg}^{-1}\,\mathrm{m}^{-1}$! Hence, spacetime is immensely rigid: is requires a lot of mass and energy to be curved even a little bit.

[5] See Appendix A for justification of the quadrupole formula with the principle of dimensional analysis.

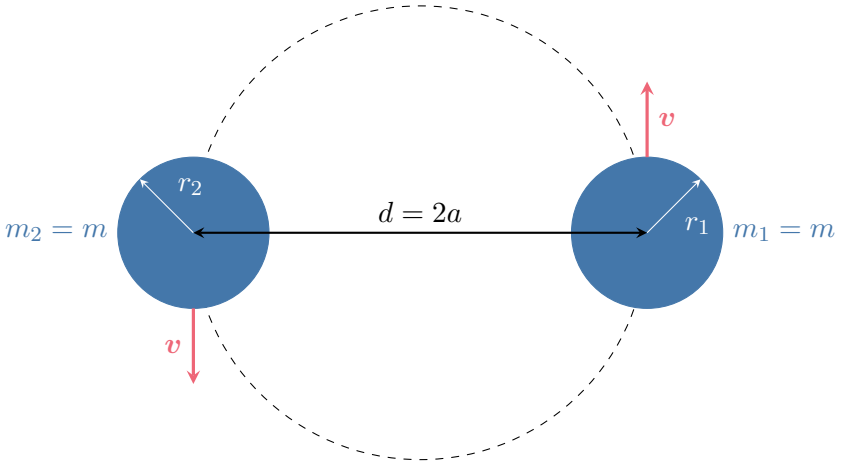

FIGURE 1.5: Equal mass binary in a circular orbit.

In the universe, the main systems that pack enough mass moving asymmetrically into a confined space to produce GW with a reasonable amplitude are binary systems of compact objects (e.g. white dwarfs, neutron stars and black holes).

Heuristic scaling for binary sources

In this section we will use hand-waving arguments to compute the expected amplitude and frequency of the gravitational waves emitted by astrophysical compact binary systems, which as explained previously are the favored sources of GWs.

GW frequency at merger In binary systems, an order of magnitude estimate for the emitted GW frequency can be found with a classical calculation. Consider the binary system of Figure 1.5, from Newton's Law of gravitation we have that the equation of motion for either mass is

$$G\frac{m_1 m_2}{(2a)^2} = m_i\frac{v^2}{a} \qquad \text{where} \qquad i = 1, 2. \tag{1.37}$$

Since the orbit is circular, we can write the orbital period as $T_{orb} = 2\pi a/v$. We also chose $m_1 = m_2 = m$. With this simplifications, the previous equation, solved for the orbital period, is

$$T_{orb} = 4\pi\sqrt{\frac{a^3}{Gm}} \tag{1.38}$$

which is just Kepler's Third Law. By symmetry arguments, we have that the frequency at which gravitational waves are emitted is twice the orbital frequency[6], we have that

$$f_{GW} = \frac{2}{T_{orb}} = \frac{1}{2\pi}\sqrt{\frac{Gm}{a^3}} \tag{1.39}$$

Let us estimate the frequency of gravitational waves at the merger (where the emission is more intense). We can assume that the merge happens when the surface of the two bodies touch, that is when $d = 2a = r_1 + r_2$. If the two bodies are Schwarzschild black

[6]Indeed, the system is the same if the position of m_1 and m_2 is flipped, hence the period of the GW signal must be half the orbital period. This holds also for asymmetric binaries, if the source is far away from the observer.

holes, their radius is directly proportional to their mass

$$r_1 = r_2 = r_s = \frac{2Gm}{c^2} \tag{1.40}$$

If we plug this expression into (1.39), using $d = 2r_s$, i.e. $a = r_s$, we have that the frequency of gravitational waves emitted at merger is

$$f_{GW}^{merger} \sim \frac{c^3}{GM_{tot}} \sim \left(10^4\,\mathrm{Hz}\right) \cdot \frac{M_\odot}{M_{tot}} \tag{1.41}$$

where we introduced $M_{tot} = 2m$ as the total mass of the binary and neglected the numerical factors. Even if this calculation is utterly simplified, it gives the correct scaling between GW frequency at merger and mass of the binary. The main message is that more massive binaries merge at lower frequencies.

GW amplitude during inspiral The amplitude of GW emitted by a binary can be found with the quadrupole formula (1.35). Here we will informally derive an estimate considering the simple case of equal mass binary in a circular orbit of radius a. We will also consider the two bodies to be point-like particles, i.e. the radius of the orbit is much larger than their spatial dimension. In such case, a rough estimate of the mass quadrupole moment will be[7]

$$I \sim 2ma^2 \tag{1.44}$$

From the quadrupole formula, we need to take the second derivative of I. We can roughly estimate it to be

$$\ddot{I} \sim \frac{I}{T_{orb}^2} \sim \frac{2ma^2}{T_{orb}^2} = \frac{M_{tot}a^2}{T_{orb}^2} \tag{1.45}$$

where we introduced the total binary mass $M_{tot} = 2m$ and T_{orb} is the orbital period of the binary, which form Kepler Third Law is of the order

$$T_{orb} \sim \sqrt{\frac{a^3}{GM_{tot}}} \tag{1.46}$$

Therefore, the expected amplitude of GW from the quadrupole formula (1.35) is

$$h \sim \frac{G^2}{c^4}\frac{M_{tot}^2}{a}\frac{1}{r} \sim 10^{-22}\left(\frac{M_{tot}}{10\,M_\odot}\right)^2\left(\frac{10^3\,\mathrm{km}}{a}\right)\left(\frac{100\,\mathrm{Mpc}}{r}\right) \tag{1.47}$$

[7] Indeed, assuming that the orbit takes place in the xy-plane and to be at a fixed time in which the bodies are located in $x_1 = a$ and $x_2 = -a$, we can write the density distribution of the source as

$$\rho(x,y,z) = \rho_1(x,y,z) + \rho_2(x,y,z) = m\delta(x-a)\delta(y)\delta(z) + m\delta(x+a)\delta(y)\delta(z) \tag{1.42}$$

where used the Dirac's delta for the density distribution of each body, because we assumed that they are point-like. If we plug this expression in the definition of the quadrupole moment (1.36), we have for example (choosing $i = j = 1$)

$$I^{xx} = \int \rho(x,y,z)x^2\,\mathrm{d}^3x = ma^2 + m(-a)^2 = 2ma^2 \tag{1.43}$$

This is a very important result. It tells us that the amplitude of GW grows with the compactness of the source: if we want to produce a large GW amplitudes, we have to pack a lot of mass into a small volume.

A similar scaling relation can be obtained from (1.45), remembering that the period is related to the orbital velocity v via the $T_{orb} = 2\pi a/v$, and then plugging everything into the quadrupole formula (neglecting numerical constants)

$$h \sim \frac{G}{c^4}\frac{M_{tot}v^2}{r} \sim 10^{-21}\left(\frac{M_{tot}}{10\,M_\odot}\right)\left(\frac{v}{c}\right)^2\left(\frac{100\,\mathrm{Mpc}}{r}\right) \tag{1.48}$$

which suggests that the amplitude of gravitational waves scales with the total binary mass and the orbital velocity. Only compact binaries can reach large orbital velocities (up to $v \lesssim c$ for BHs in the final moments before merger).

This confirms that the likely sources of GW can be astrophysical system of compact objects, such as black holes and neutron stars.

1.2 LISA

The Laser Interferometer Space Antenna (LISA) will be the first gravitational waves observatory in space. LISA has been officially selected by the European Space Agency (ESA) as a large scale mission with expected launch date in the mid-2030s. The nominal duration of the LISA mission is four years, with the possibility to extend it to ten years.

The motivation to build a gravitational wave observatory in space comes from the fact that gravitational waves in the low-frequency band (below $\sim 10\,\mathrm{Hz}$), are likely inaccessible from ground, because of the rise of the seismic[8] and Newtonian noise[9] [7]. Moreover, in space there is, as the name suggests, a lot of space to build a extremely large detector, which is convenient because the effect of gravitational waves on the test masses scales with the distance among them as we showed in (1.13), thus a large baseline helps in enhancing the GW signal.

1.2.1 Mission concept

LISA will be a constellation of three satellites at a distance of 2.5 million kilometers in the shape of an almost equilateral triangle. Each spacecraft is connected to the other two by laser beams, to form a huge interferometer. See Figure 1.6 to get an intuition of the sheer size of LISA.

LISA will perform an heliocentric orbit, trialing the Earth around the Sun (see Figure 1.7).

Inside each spacecraft there are two test masses, which acts as inertial frame of reference. The spacecraft follows the TMs and protect their geodesic free-fall from external forces along the science axis, which is directed towards the opposing spacecraft on the same interferometer arm. The spacecrafts act both as receivers and as transponders: each one emits a laser beam towards the opposing spacecrafts, which detect it and compare the phase of the light with the local interferometer. At the same time, the spacecrafts send back a phase locked laser signal to the first one. In Figure 1.8, we display a conceptual rendering of the spacecraft payload and the LISA constellation.

[8] That is noise due to the motion of the ground on the site of the experiment, due to, for example, earthquakes, wind, ocean waves, or human activities.

[9] That is noise related to the local fluctuations of the gravitational field.

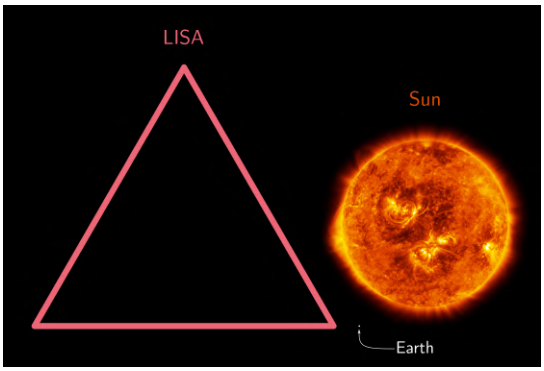

FIGURE 1.6: Size comparison between LISA and our Sun. the white dot close to the bottom right corner of LISA is not a speckle of dust on your monitor, but the relative size of the Earth.

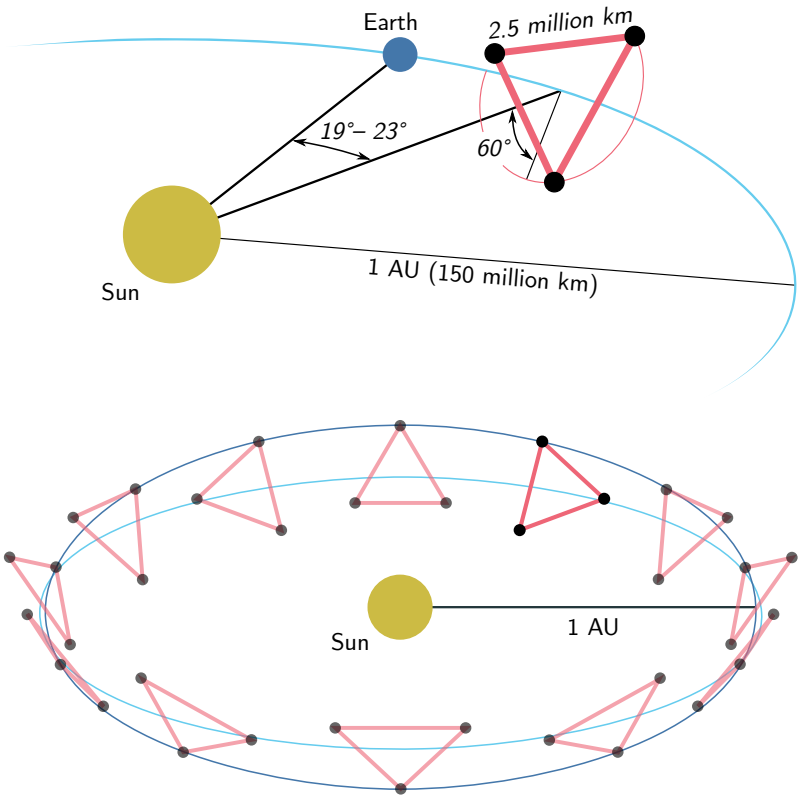

FIGURE 1.7: Orbit for the LISA constellation (not to scale). Adapted from [8].

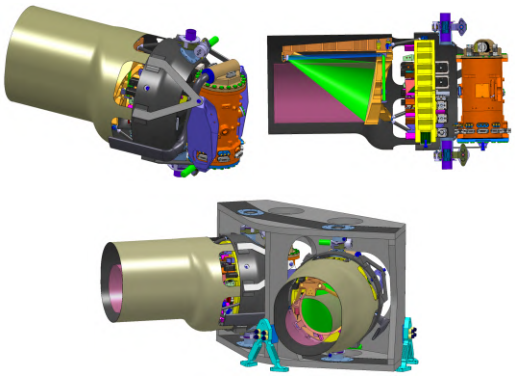

(A) Industrial rendering of the payload of the LISA spacecrafts [8]

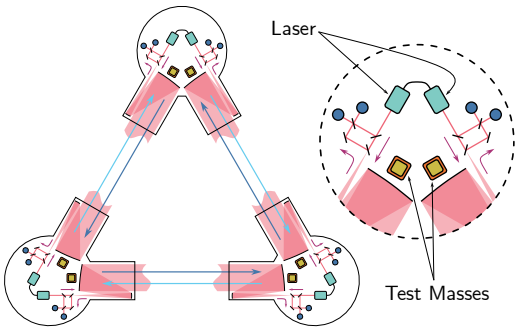

(B) Schematic representation of the LISA constellation [9]

FIGURE 1.8: The LISA mission. *Left*: straw-man payload conceptual design. One can see the telescope (*green*) capturing the laser beam from the distant spacecraft, the optical bench (*yellow*) and behind the gravitational reference sensor (*orange*) hosting the TM. All this instrumentation is integrated in a mobile optical sub-assembly (MOSA), which rotates to maintain the interferometer link with the opposing spacecraft at all times (a small angular *breathing* motion is expected due to the orbit dynamics in the solar system). *Right*: scheme of the LISA constellation with the three spacecrafts exchanging laser beams to synthesize a large triangular interferometer.

Gravitational waves induce a tidal acceleration on the distant test masses and are detected by the Doppler shift between the frequency of the emitted and the received laser light.

As argued in Section 1.1.2, the effect of gravitational waves is indistinguishable from disturbances in the interferometric measurement or from stray forces acting on the test mass. The LISA design sensitivity plotted in Figure 1.9 can be reached only if the acceleration noise on the single TM and the interferometer readout noise are under control.

The current top-level mission requirements for the single TM acceleration noise with respect to an inertial reference frame in the science direction is [12]

$$S_g(f) < \left(2.4\,\mathrm{fm/s^2/\sqrt{Hz}}\right)^2 \left[1+\left(\frac{0.4\,\mathrm{mHz}}{f}\right)^2\right]\left[1+\left(\frac{f}{8\,\mathrm{mHz}}\right)^4\right] \tag{1.49}$$

and the requirement for the one-way TM-to-TM displacement noise is

$$S_x(f) < \left(10\,\mathrm{pm/\sqrt{Hz}}\right)^2 \left[1+\left(\frac{2\,\mathrm{mHz}}{f}\right)^4\right] \tag{1.50}$$

The LISA sensitivity is limited at low-frequency by the stray forces that act on the TM, by the interferometric position readout at the minimum and by the signal transfer function of the instrument at high frequency (when the wavelength of gravitational waves becomes smaller than the interferometer arm-length).

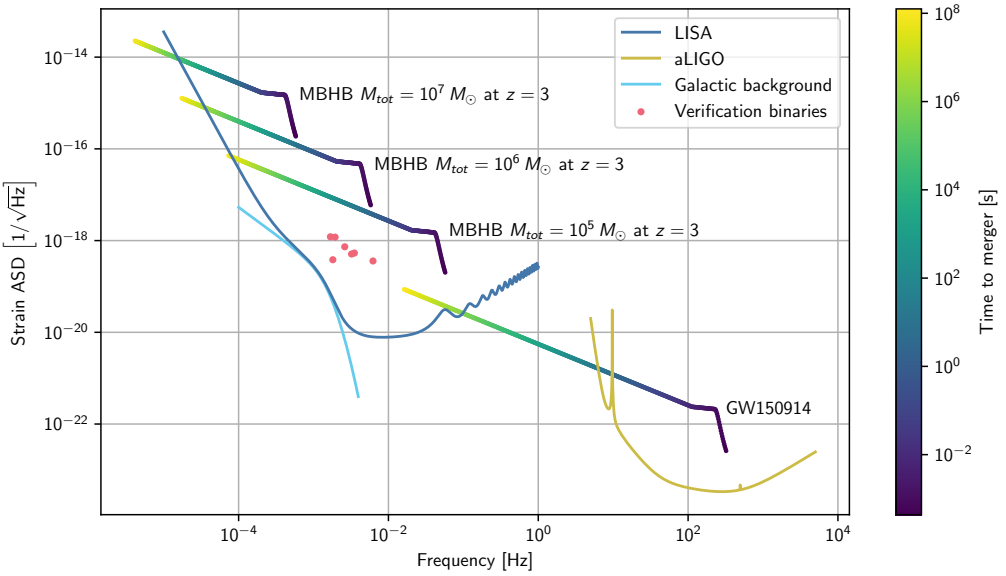

FIGURE 1.9: LISA and Advanced LIGO design sensitivity curves. The signal of some typical LISA sources is also plotted with the color corresponding to the time to merger. We can see that a source similar to GW150914 [1], would be in the LISA band years prior to entering the LIGO band fractions of second before merger. Obtained with the method described in [10]. The verification binaries data is from [11].

Gravitational Reference Sensor

The core of the LISA instrument is the so called Gravitational Reference Sensor (GRS), which host the free falling test masses. The GRS is composed of the following elements [13]

- The Test Mass (TM) itself, which is a cube of side 46 mm and weighting approximately 2 kg made of an gold-platinum alloy with very low magnetic susceptibility.
- An Electrode Housing (EH), which surrounds the test mass and provides, via dedicated electrodes, nm-level capacitive sensing of the TM position and nN-level actuation in all degrees of freedom. The role of the EH is also to shield the TM from external electrostatic fields and, due to its large thermal conductivity, temperature gradients. The EH is designed to provide an environment around the TM that limits all stray forces to the fN level.
- An ultra-high vacuum chamber with the possibility of venting to space once in orbit.
- A caging system to keep the TM locked during launch vibrations.
- The Grabbing Positioning and Release Mechanism (GPRM), which allows to delicately set the TM into free fall with very small residual velocity once in orbit.

The six GRS for LISA will be provided by the Italian Space Agency. LISA Pathfinder successfully verified in light the performance of the GRS for LISA (see Section 1.3).

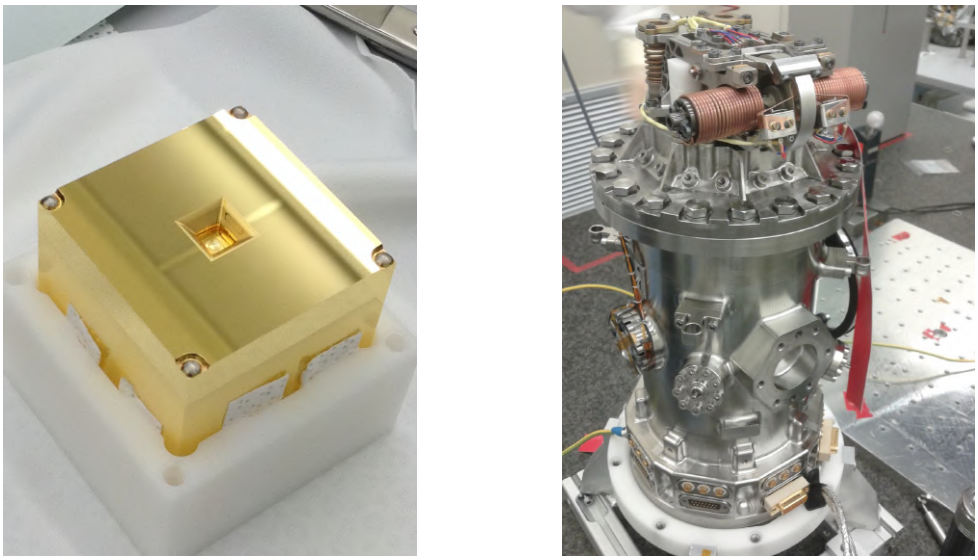

(A) LISA Pathfinder TM (B) LISA Pathfinder GRS

FIGURE 1.10: Elements of the LISA Pathfinder Gravitational Reference Sensor [14].

1.2.2 Science objectives

The milli-hertz region of the gravitational wave spectrum is rich in sources and very interesting physics. The LISA top-level requirements has been purposely chosen to have the sensitivity needed to reach the science objectives that will be listed here.

Among the most important science goals of LISA we list [8]

- LISA will be able to trace the origin, growth and merger of massive BHs across all cosmic ages, possibly enabling to reconstruct how the structure of the Universe has evolved. The supermassive black holes that we find in today's galaxies, have probably formed by coalescence of smaller black holes with masses in the range $10^4 - 10^8\, M_\odot$. Such binary systems will merge in the LISA band as indicated by (1.41). LISA will have a very large signal-to-noise ratio for massive BH binaries, as evident from Figure 1.11.

- Study of the evolution of compact binary stars[10] in our galaxy. LISA is expected to observe a number so high of such systems, that the ones at low SNR will be indistinguishable, creating a background noise in the sensitivity curves (see Figure 1.9). Several verification binaries, i.e. sources that are well constrained by astrophysical observations and have large SNR, have been identified [11] and their signal can be used to check that the instrument is working properly. The observation of GW from galactic binaries would allow to probe the structure of the Milky Way.

- Study of extreme-mass-ratio inspirals (EMRIs), that is the long-lasting signal of binary system in which one of the body is a stellar mass BH ($m \sim 10\, M_\odot$) and the other is a super-massive BH ($m \sim 10^6\, M_\odot$). EMRIs are expected to be a unique way to test General Relativity in the strong-field regime.

- Understand the astrophysics of stellar-origin BHs. LISA would be able to detect binary system of BHs in the range of masses $10 - 30\, M_\odot$ months or years prior

[10] Mainly white dwarf systems, but also composed by neutron stars and stellar black holes in any combination.

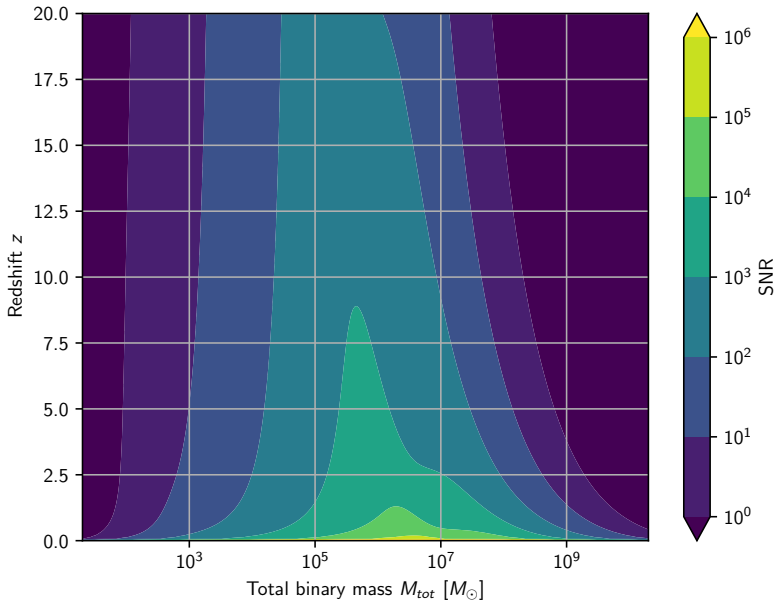

FIGURE 1.11: Four-years sky averaged SNR contour plot for equal mass BH binaries mergers as a function of the total mass and redshift. Do not be fooled by the colors: already a bluish shade of green corresponds to large SNRs. For total binary masses in the range $10^5 - 10^6\, M_\odot$, the SNR ratio is high up to redshift $z \sim 20$, which corresponds to detecting any such merger in the observable Universe. Adapted form [8].

to the coalescence. These are the type of black holes mergers observed by the LIGO/Virgo collaboration. It is therefore possible a joint observation of the same black hole binary first with LISA and then, close to the merger, with LIGO (*multi-band event*).

- Use gravitational wave signals to measure the Hubble parameter independently from the current (incompatible) values obtained either from the cosmic microwave background or from local universe standard candles (type Ia supernovae).

- Possibly measuring the stochastic GW background of cosmological origin. It is the gravitational equivalent of what the cosmic microwave background is for electromagnetic interaction. The possibility of detecting the stochastic GW background is still under debate[11], but if proved possible, would allow us to peer into the first moments of the early Universe after the Big Bang.

Just from this limited list of science goals, we understand that discovery potential of LISA could be ground-breaking. That is why the astrophysical and cosmological communities are very excited for the project.

As anticipated in LISA, contrary to LIGO, a large number of GW sources will overlap at all times. As in a "cocktail party" problem, extracting and singling out the

[11]The problem lies in the fact that in LISA it would not be easy to characterize the instrumental noise, because many GW signals will be present at all times. Therefore, it would be hard to disentangle what is the noise of the instrument from a (presumably) faint stochastic GW signal from the early Universe.

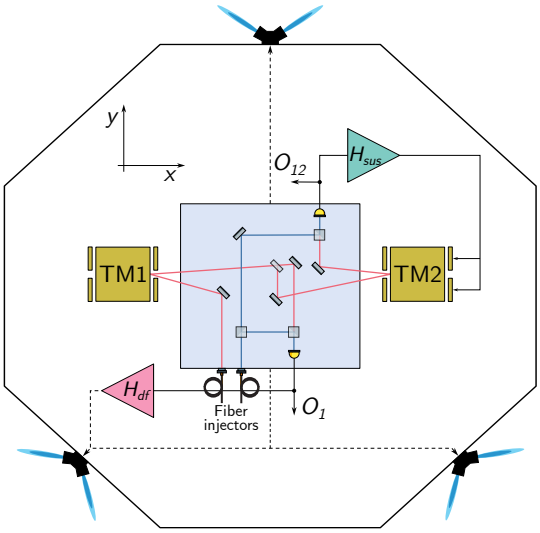

FIGURE 1.12: Schematic diagram of the LPF mission. The two TMs are hosted in their Electrode Housings (EH) and an interferometer measures not only their relative position, but also the position of TM1 with respect to the spacecraft along the drag-free sensitive x-axis. A drag-free control loop actuated by µN-thrusters keeps the spacecraft centered on TM1. Adapted from [9].

individual signals will be quite challenging from a technical and theoretical point of view.

1.3 LISA Pathfinder

LISA Pathfinder (LPF) was an ESA mission launched in 2015 and decommissioned in 2017. LPF was envisioned as a dress rehearsal for LISA: it aimed at demonstrating that the technology for future space-borne gravitational wave detectors is ready [15]. Indeed, no previous space mission (let alone experiment on ground) has ever demonstrated that the LISA top-level requirements regarding the metrology and residual TM acceleration could be achieved. Space missions for geodesy, such as GRACE and GOCE, which are somewhat comparable to LISA in the sense that they fly test masses which acts as highly precise accelerometers, have performance more than two orders of magnitude worse than what is required for LISA [16, 13].

The LPF spacecraft contains an equivalent LISA arm shrunk to just $\sim 38\,\mathrm{cm}$. As shown in Figure 1.12, LISA Pathfinder host two identical Gravitational Reference Senosors test masses each surrounded by an electrode housing for capacitive actuation and sensing in all degrees of freedom. The distance between the test masses along the science x-axis is monitored by a heterodyne interferometer. The GRS instrumentation and the drag-free attitude control of LPF accurately reflects the needs of LISA.

The LPF spacecraft follows one the test masses, which is in pure free fall and acts as an inertial reference system. On the other hand, small forces are imparted to the second test mass by control loops to keep its position fixed with respect to the first one. In Figure 1.13, we show some pictures of LISA Pathfinder.

The main goal of LISA Pathfinder was to verify that two test masses can be set into free fall with parasitic acceleration disturbances within the LISA requirements. In Figure 1.14, we plot the amplitude spectral density of the measured relative acceleration between the LPF test masses, after the subtraction of the forces commanded by

(A) Spacecraft before launch

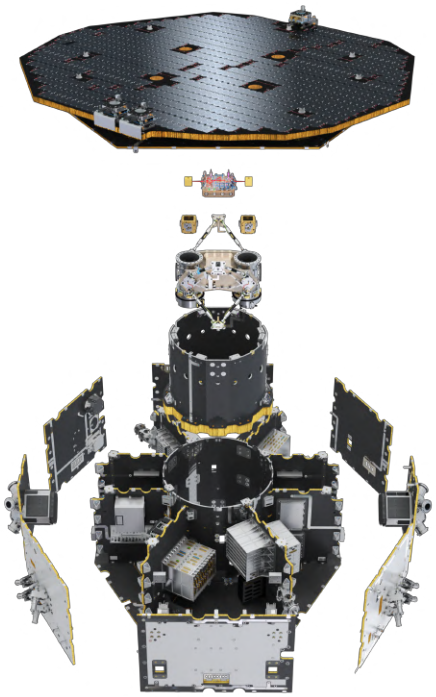

(B) Exploded view of LPF

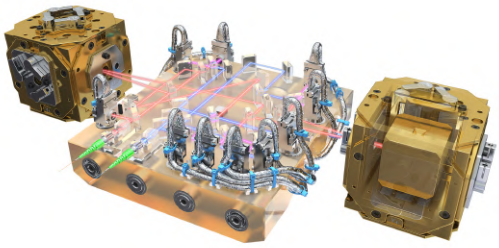

(C) Optical bench and interferometer

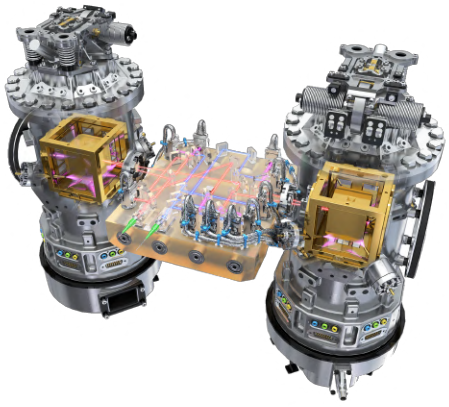

(D) View of the LISA technology package

FIGURE 1.13: LISA Pathfinder. Credits ESA/ATG medialab [14].

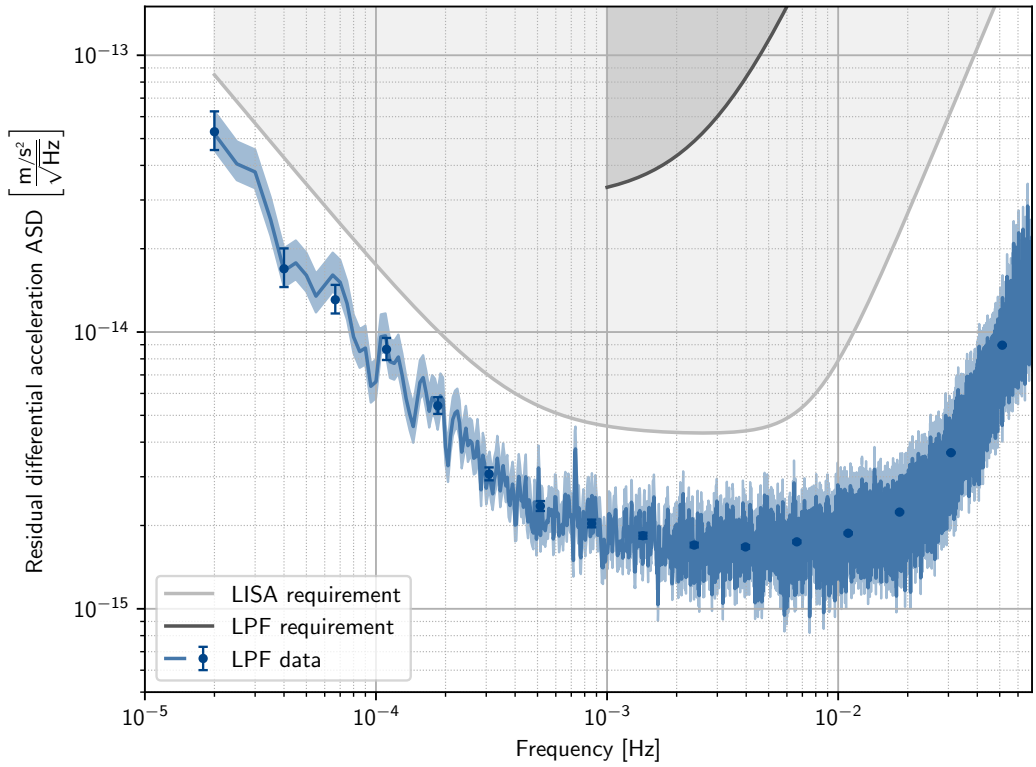

FIGURE 1.14: Amplitude spectral density of the residual differential acceleration of the LPF test masses. The data are below the LISA requirements at all frequencies [17].

the control loop on the second test mass and other known contributions (e.g. fictitious forces due to the rotation of the spacecraft, such as Euler and centrifugal force, and the stiffness due to the coupling of the TMs with the nearby sensor). We see that the ASD of the differential spurious acceleration between the LPF test masses is below the (old[12]) LISA requirement[13] at all frequencies. This is the experimental proof that the LISA acceleration requirement (1.49) can be attained.

LISA Pathfinder also tested several subsystem that would be needed for LISA, such as

- Caging system for the test masses during launch.
- Grabbing Positioning and Release Mechanism (GPRM), needed for TM release and re-grabbing in orbit.
- Drag-free attitude control system of the spacecraft based on µN-cold-gas thrusters to keep the spacecraft centered on one TM.
- Charge Management System bases on UV-light from mercury-vapor lamps to neutralize the TM charge due to cosmic rays and solar energetic particles.

[12]The LISA requirement for the single TM acceleration at the time of LPF was

$$S_g(f) < \left(3\,\mathrm{fm/s^2/\sqrt{Hz}}\right)^2 \left[1+\left(\frac{0.4\,\mathrm{mHz}}{f}\right)^2\right]\left[1+\left(\frac{f}{8\,\mathrm{mHz}}\right)^4\right]. \tag{1.51}$$

[13]The LISA requirement has been multiplied by a factor $\sqrt{2}$ because we are considering the relative TM accelerations between two (uncorrelated) test masses instead of the single TM acceleration.

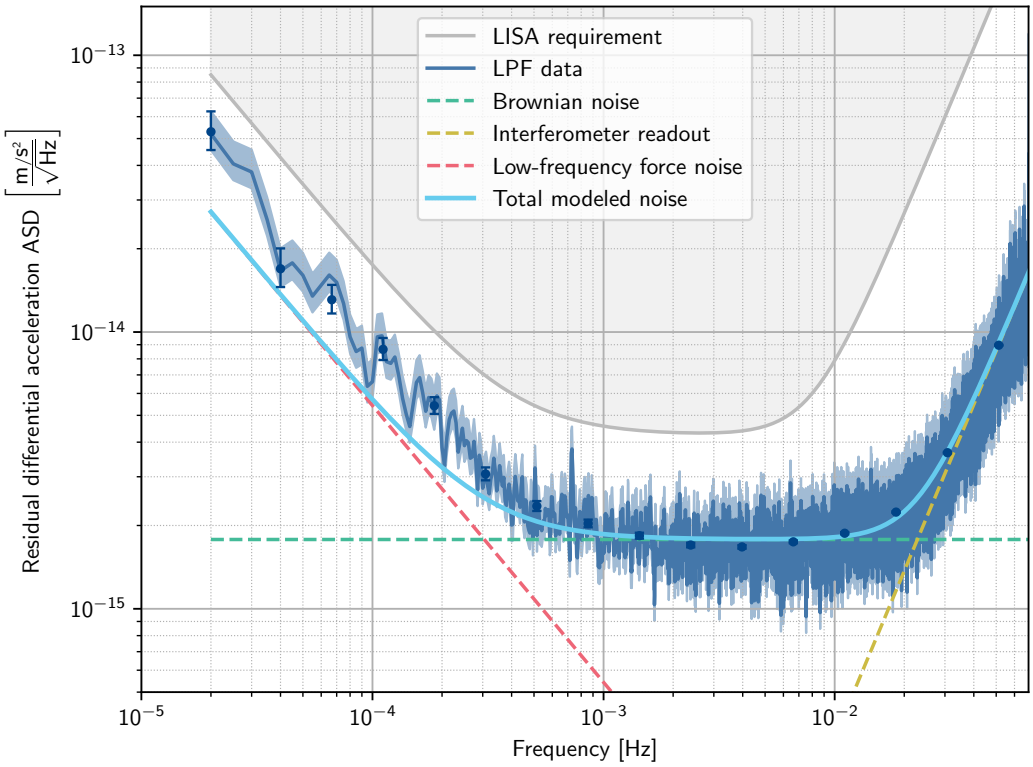

FIGURE 1.15: LPF estimate of the dominant noise contributions. At low-frequency there is an excess of about a factor two in amplitude over the budgeted noise sources. Adapted from [9].

The LISA Pathfinder mission was a great success and paved the way for LISA. Still there are some aspects that are still not completely understood, i.e.

- The presence of spurious transient acceleration events, known as glitches [18].
- An excess noise at low-frequency of unknown origin which exceeds the current noise model by approximately a factor two in amplitude (see Figure 1.15).

Both these issues are still being investigated to make sure that they will not be a problem for LISA.

Given the overall success of LISA Pathfinder and the fact that the LPF hardware was tested in space, makes so that the design of the Gravitational Reference Sensor for LISA is practically frozen to the one of LPF. There are still a few areas, where modifications are planned: one of them regards the use of UV-LEDs instead of mercury-vapor lamps as light sources for the Charge Management System. The on-ground test of the performance of UV-LEDs to discharge the test masses is the main topic of this thesis.

Chapter 2

Small-force measurements with 4TM torsion pendulum

Torsion pendulums are unique tools to measure small forces acting on macroscopic systems. The principle that makes them so special is that they naturally dispose themselves orthogonal to the local gravitational field. In this way, rotations in the plane orthogonal to the suspending fiber are almost free, saved for the elastic constant of the fiber, which could be in principle very small.

In this way forces acting on the "soft" rotational-degree of freedom, easily set the pendulum into motion. On the other hand, small forces acting on the other "hard" degrees of freedom are not detectable because they have to fight against gravity which is many order of magnitudes more intense than the forces we aim to detect.

For this reason, torsion pendulums have been used by physicists for many years. Charles-Augustin de Coulomb is generally credited as the inventor of torsion pendulums, which he used to measure the electrostatic force between charges and establish the law that bears his name [19]. Another, probably even more famous, experimental application of torsion pendulums was due to the British scientist Henry Cavendish at the end of the eighteenth century [20]. The Cavendish experiment is commonly regarded as the first measurement of the gravitational constant G, but some recent review [21] argue that Cavendish's aim was to measure the average density of the Earth. Indeed, at the time of Cavendish work, the determination of G was not even recognized as an open problem, contrary to the determination of the mean density of our planet. Nevertheless, a modern analysis of Cavendish data, would lead to the first accurate measurement of the gravitational constant.

In more recent times, torsion pendulums have been used to test the *equivalence principle* [22], starting from the acclaimed Eötvös experiment, which placed stringent upper limits for the violation of the equality between inertial and gravitational mass; and to test the inverse-square law of gravitation [23].

Focusing on LISA, torsion pendulums have been key instruments to drive the design of the Gravitational Reference Sensor and to test its performance before the flight of LISA Pathfinder.

Even after the launch and huge success of LISA Pathfinder, torsion pendulums remain relevant. Indeed, we can use them to investigate some aspects of LPF that remain unclear (such as glitches [18] and the excess-noise at low-frequency) or to verify if proposed modifications to the LISA Pathfinder design are viable.

This is exactly the idea upon which this thesis has been built: in this chapter we will introduce the reader to our four-test-masses (4TM) torsion pendulum, which is the primary testbed for the LISA Gravitational Reference Sensor on ground. We would like to notice that a similar facility has been developed at the University of Florida [24] to test the performance of ultra-precise inertial sensors for space-based gravitational wave observatories, including LISA, and geodesy missions.

Later, in Chapter 3, we will present how we tested with the 4TM torsion pendulum the performance of a prototype charge management system for LISA based on photoelectric emission from UV-LEDs. Indeed, one of the few planned design changes moving from LPF to LISA is to employ UV-LEDs, instead of UV-lamps as light sources for the CMS. Moreover, in Chapter 5 we will show how we used our torsion pendulum to evaluate for the charge noise induced by the *continuous discharge* strategy to keep the TM charge under control, which was not routinely implemented in LPF.

In addition, as an example on how torsion pendulums can help to understand features in the LISA Pathfinder data which are still unexplained, we will present in Section 2.1.5 an estimation of the 4TM pendulum sensitivity to LPF glitches.

2.1 4TM torsion pendulum

The four-test masses torsion pendulum, 4TM pendulum for brevity, has been designed to reproduce as closely as possible the environment around the LISA Pathfinder test masses [25]. The name of the game is *representativity* in terms of geometry, hardware and and environment conditions.

Indeed, in a space mission as LISA Pathfinder or LISA, it is fundamental to test on ground the performance of all subsystems prior to the flight in an environment as representative as possible, because there is usually no possibility to fix a malfunctioning, once the instrument is in space. The 4TM torsion pendulum is the primary testbed for the GRS subsystem on ground.

For this reason, the 4TM pendulum needs to be directly sensitive to forces, and not just to torques. The only way to detect forces is suspending the test mass not directly below the fiber, as in the single-mass torsion pendulum [26], but to mount it off-center. In this way any force acting on the TM with non-zero component in the direction orthogonal to both the fiber and the pendulum arm (the science axis), produces a torque that sets the pendulum into motion. The 4TM pendulum arm-length l_{arm} is approximately 10.6 cm.

As the inertial member must lie horizontally (orthogonal to the local gravitational field), at least another test mass on the opposite side with respect to the one used for testing is required to balance out the pendulum. The minimal configuration for the inertial member is a linear shaft with two test masses at its ends and suspended by its center of mass. Such configuration is, however, quite sensitive to fluctuations of the local gravity, especially as the arm-length of the pendulum increases. In order to reduce the coupling with local gravitational field variations, we need to increase the symmetry of the inertial member[1]. The inertial member of the 4TM pendulum is therefore cross shaped, with four identical hollow test masses at the ends. The symmetry of the inertial member nullifies the mass-quadrupole moment and, hence, reduces the coupling of the pendulum with local gravity fluctuations. In Figure 2.1, we show a schematic diagram of the 4TM torsion pendulum.

[1] So to minimize the multipole expansion of the mass distributions of the system at increasing orders.

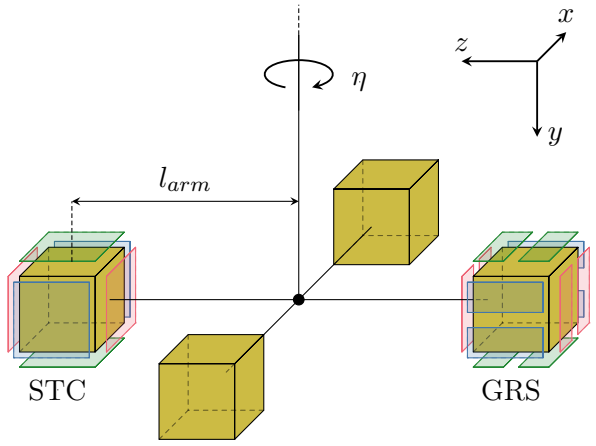

FIGURE 2.1: Geometry of the 4TM torsion pendulum. The four test masses are mounted at the ends of a cross shaped inertial member. One of the test masses is hosted in the flight model replica of the LISA Pathfinder Gravitational Reference Sensor (GRS), whereas the opposite is contained in a simplified capacitive sensor, called Stiffness Compensator (STC). See Section 2.1.2 for more details.

2.1.1 Measurement concept

As shown in Figure 2.2, the torque on the torsion pendulum along the y-axis due to a collection of forces $\boldsymbol{F}_i$ acting on the test mass can be computed as

$$\begin{aligned} N_y &= \boldsymbol{N} \cdot \hat{\boldsymbol{e}}_y \\ &= \left(\sum_i \boldsymbol{R}_i \times \boldsymbol{F}_i \right) \cdot \hat{\boldsymbol{e}}_y \\ &= \left(\sum_i \boldsymbol{b} \times \boldsymbol{F}_i \right) \cdot \hat{\boldsymbol{e}}_y + \left(\sum_i \boldsymbol{r}_i \times \boldsymbol{F}_i \right) \cdot \hat{\boldsymbol{e}}_y \end{aligned} \tag{2.1}$$

where we used $\boldsymbol{R}_i = \boldsymbol{b} + \boldsymbol{r}_i$ with $\boldsymbol{b}$ the vector along the pendulum arm connecting the fiber with the center of the TM. If we use in the first term the *triple product* vector identity[2], we have

$$\begin{aligned} N_y &= \left(\sum_i \boldsymbol{F}_i \right) \cdot \underbrace{\hat{\boldsymbol{e}}_y \times \boldsymbol{b}}_{-b\hat{\boldsymbol{e}}_x} + \underbrace{\left(\sum_i \boldsymbol{r}_i \times \boldsymbol{F}_i \right)}_{\boldsymbol{N}_{TM}} \cdot \hat{\boldsymbol{e}}_y \\ &= -b \sum_i \boldsymbol{F}_i \cdot \hat{\boldsymbol{e}}_x + \boldsymbol{N}_{TM} \cdot \hat{\boldsymbol{e}}_y \\ &= l_{arm} \sum_i F_{i,x} + N_{TM,y} \end{aligned} \tag{2.2}$$

where we used the fact that $b = l_{arm}$. From this equation we can see that our torsion pendulum is sensitive to both forces along the x-axis and to pure torques along the y-axis (which are induced by unbalanced couples of forces in the x or z-direction). However, the sensitivity to pure torques is significantly lower than forces. Indeed, the average arm of forces acting on the TM in the x-direction is the pendulum arm-length $b = l_{arm}$, whereas the typical arm of the forces that produce only a torque on the TM

[2] That is $(\boldsymbol{a} \times \boldsymbol{b}) \cdot \boldsymbol{c} = (\boldsymbol{c} \times \boldsymbol{a}) \cdot \boldsymbol{b} = (\boldsymbol{b} \times \boldsymbol{c}) \cdot \boldsymbol{a}$.

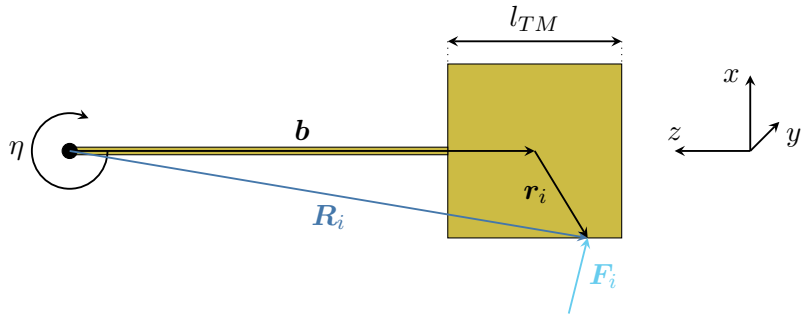

FIGURE 2.2: Diagram illustrating the principle that makes torsion pendulums directly sensitive to forces: suspending the TM off-center with respect to the fiber via a rigid connection would allow detection of forces acting along the x-axis. The black dot is the position of the suspending fiber. Roughly to scale with our 4TM torsion pendulum. Adapted from [25].

is $l_{TM}/2$. Hence the suppression factor of pure torques with respect to forces in the x-direction is

$$\frac{l_{TM}}{2l_{arm}} \simeq \frac{1}{5} \tag{2.3}$$

for our geometry ($l_{arm} \simeq 10.6\,\text{cm}$ and $l_{TM} \simeq 4.6\,\text{cm}$). This quick back-of-the-envelope calculation convinces us that the 4TM torsion pendulum is mostly sensitive to forces acting on the TM along the x-direction.

2.1.2 Instrumentation

Not only in terms of geometry, but also hardware, the 4TM pendulum resembles as closely as possible LISA Pathfinder and, consequently, LISA.

As anticipated the inertial member is cross-shaped with four test masses at its ends. The four test masses are hollow, to reduce the pendulum weight, as it is crucial for better noise performance (see Section 2.1.3).

One of the test masses has the same surface finish and features (e.g. domes for the caging fingers and pyramidal grooves for the GPRM) as the LPF test masses. It is hosted in a flight-model replica of the LISA Pathfinder electrode housing, which is fully representative in terms of materials and surface finish. Identical copies of the unmodified LPF Inertial Sensor UV-Kit (IUSK) are mounted on the electrode housing. The ISUKs carry the UV-light for charge management inside the GRS. In our setup we have two IUSKs: one is pointed directly towards the TM and the other towards the EH (see Appendix B for more details). The main difference between our setup and LISA Pathfinder is that we do not have the iridium fingers for TM locking during launch. Otherwise our apparatus resembles closely LPF in terms of geometry, materials and surface finish.

The test mass on the opposite side of the inertial member with respect to the FRM, is hosted in a simplified capacitive sensor called the Stiffness Compensator (STC), which has just one electrode per face. The STC has large gaps ($\sim 8\,\text{mm}$) to minimize the electrostatic disturbances induced on its TM. The STC can be used to compensate for the electrostatic stiffness (hence its name), but we mainly use it in combination with the replica GRS to achieve a more sensitive measurement of the rotation angle of the pendulum. Indeed the rotation angle of the pendulum can be

obtained as

$$\eta = \frac{x_{STC} - x_{GRS}}{2l_{arm}} \tag{2.4}$$

This is currently the most sensitive measurement of the pendulum rotational degree of freedom at low-frequency.

The capacitive readout of the flight-model replica of the EH is carried out by an engineering model of the LISA Pathfinder front-end electronics (FEE), called ELM-light, which is representative in terms of design, sensing performance and actuation patterns (both AC and DC) on all degrees of freedom.

An Elcomat Vario optical autocollimator produced by the company Möller-Wedel is pointed towards a mirror mounted on the inertial member and provides us with an independent measurement of the rotational degrees of freedom η and ϕ. As shown in Figure 2.4b, the autocollimator has better high-frequency readout noise, but at low-frequency the combination of GRS and STC capacitive sensing (2.4) provides the more sensitive reading of the pendulum rotation angle.

Naturally, the whole setup is installed into a high-vacuum vessel and kept at low pressures ($\sim 10^{-5}$ Pa). Around the vacuum vessel there is a thermal chamber (with the possibility of having active thermal control) which helps stabilizing the temperature around the 4TM pendulum.

In Figure 2.3, we show some pictures of the 4TM torsion pendulum facility.

2.1.3 Thermal noise

The main factor that drives the design of torsion pendulums in high-vacuum condition is the thermal noise floor due to intrinsic damping of the suspending fiber [27].

As the restoring torque exerted by the suspending fiber is given by

$$N_f = -k\eta \tag{2.5}$$

where k is the torsional spring constant and η is the pendulum angular coordinate, the equation of motion of a torsion pendulum in the domains of time and frequency are

$$I\ddot{\eta}(t) = N(t) - k\eta(t) \qquad \xrightarrow{\mathcal{F}} \qquad \tilde{\eta}(\omega) = \frac{\tilde{N}(\omega)}{\tilde{k} - I\omega^2} \tag{2.6}$$

where I is the moment of inertia of the inertial member. The period of the pendulum can be found in analogy with the equation of an harmonic oscillator[3] as

$$T_0 = \frac{2\pi}{\omega_0} = 2\pi\sqrt{\frac{I}{k}} \tag{2.7}$$

In the previous equation, we intentionally neglected the dissipation term proportional to the angular velocity $\dot{\eta}$, because in the case of intrinsic damping of the fiber the dissipation can be modeled introducing an imaginary part in the torsional spring constant in the frequency domain.

$$\tilde{k} \longrightarrow k(1 + \mathrm{i}\delta) \qquad \text{for intrinsic damping} \tag{2.8}$$

[3] The equation of a simple harmonic oscillator is $\ddot{x}(t) + \frac{k}{m}x(t) = 0$ whose solution has the form $x(t) = A\sin(\omega_0 t + \phi)$ with $\omega_0 = \sqrt{k/m}$.

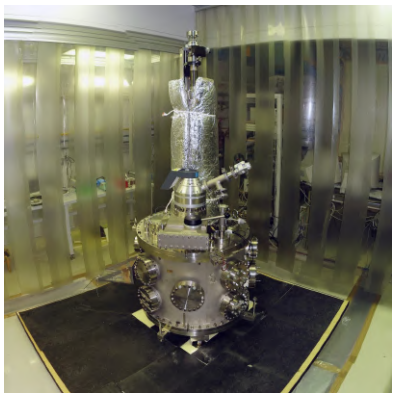

(A) Full view of the vacuum chamber

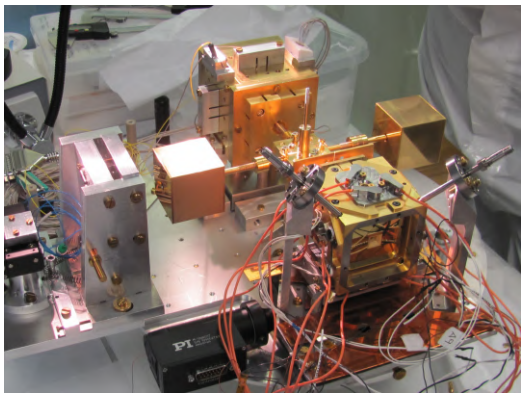

(B) Inertial member

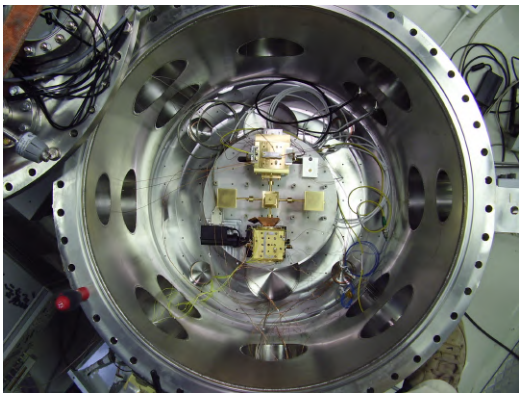

(C) Inertial member inside the vacuum chamber

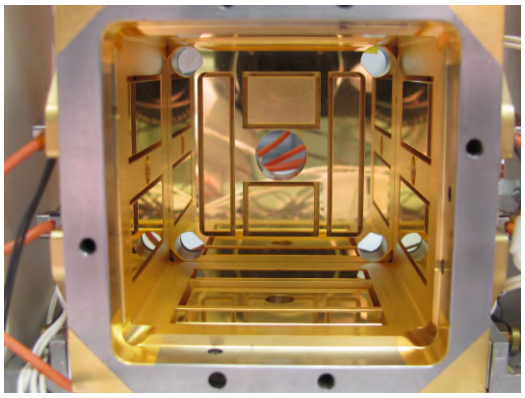

(D) New electrode housing identical to LPF

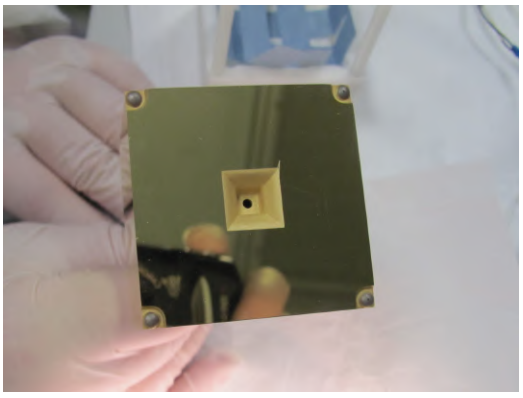

(E) Hollow TM with uncoated domes

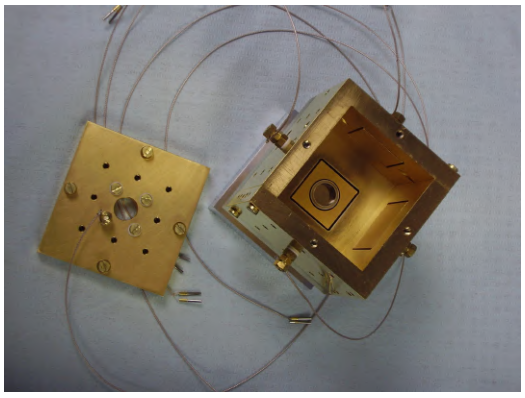

(F) Stiffness Compensator

FIGURE 2.3: Pictures of the 4TM torsion pendulum.

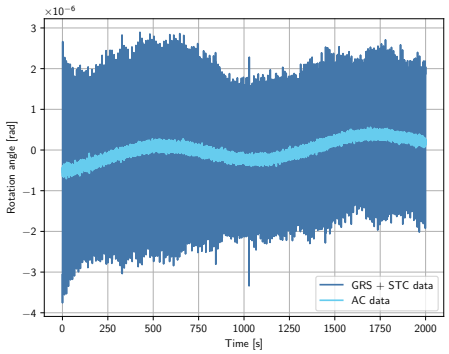

(A) Timeseries of the pendulum rotation angle

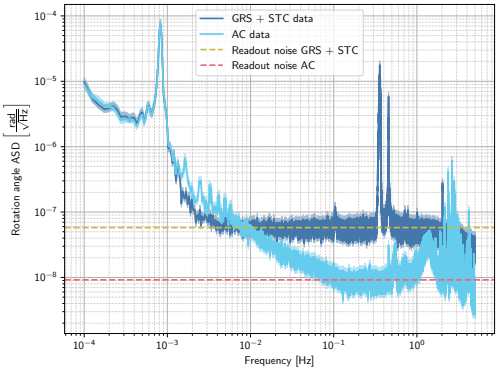

(B) ASD of the pendulum rotation angle

FIGURE 2.4: Comparison between the timeseries and amplitude spectral density of the torsion pendulum rotation angle obtained with the autocollimator (AC) or combining of GRS and STC readings. The peaks in the autocollimator data at high frequency are likely due to vibrations of its mechanical support. The high-frequency spikes in the capacitive readout are due to cross-talks between the STC and GRS injection bias and other electrical interferences.

The quantity δ is the loss-angle which can be considered independent of frequency and it is related to the quality factor Q of the pendulum as

$$\delta = \frac{1}{Q} \tag{2.9}$$

Therefore the transfer function of the torsion pendulum can be written as

$$H(\omega) = \frac{\tilde{\eta}(\omega)}{\tilde{N}(\omega)} = \frac{1}{k\left(1 + \frac{\mathrm{i}}{Q}\right) - I\omega^2} = \frac{1}{k\left(1 - \frac{\omega^2}{\omega_0^2} + \frac{\mathrm{i}}{Q}\right)} \tag{2.10}$$

The quality factor of the pendulum Q depends on the losses of the fiber material and can be measured from the damping time τ of the pendulum

$$Q = \pi \frac{\tau}{T_0} \tag{2.11}$$

Indeed, the damping time τ can be directly measured from the decaying of the amplitude of oscillations which is proportional to $e^{-t/\tau}$ (see Figure 2.5). The quality factor of our torsion pendulum suspended by a tungsten fiber is ~ 3200, which, considering the free period of $T_0 \simeq 1220\,\mathrm{s}$, corresponds to a damping time of approximately 14 days.

The *fluctuation-dissipation theorem* tells us that whenever a process dissipates energy in a physical system, turning into heat, there will be a reverse process related to thermodynamic fluctuations that will induce noise in the observable physical quantity related to the dissipation process. In the case of our torsion pendulum, the losses in the fiber induce noise in the torque. The expression for the one-sided power spectral density of thermal noise in torque is

$$S_N^{therm}(\omega) = 4k_B T \frac{k}{Q\omega} \tag{2.12}$$

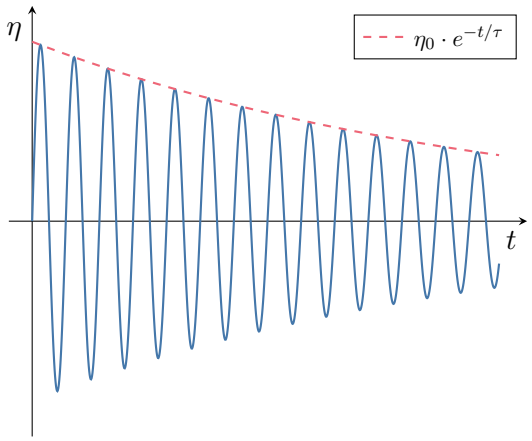

FIGURE 2.5: Illustrative plot for the measurement of the pendulum decay time.

where k_B is the Boltzmann constant and T is the pendulum temperature. The torsional elastic constant of the fiber k can be modeled as [25]

$$k = \frac{\pi r_f^4}{2L_f}\left(E_f + \frac{mg}{\pi r_f^2}\right) \tag{2.13}$$

where L_f is the length of the fiber, r_f its section radius and E_f the Young's modulus of its material. From the previous expression, we understand that to reduce the thermal noise and reach competitive pendulum sensitivity, we need either to have a very long or a very thin fiber. As the scaling of the torsional constant k is linear in the length of the fiber ($k \propto 1/L_f$), but it is at least quadratic in the fiber radius ($k \propto r_f^2$), we see that for reducing the noise it is more convenient to minimize the section of the fiber rather than having a very long fiber. As a thin fiber cannot support a lot of weight (the maximum load scales with the section of the fiber[4], hence with r_f^2), we need to reduce the mass of the inertial member as much as possible. This is the reason why our test masses are hollow[5]. The fiber mounted in our apparatus is made of tungsten, has a length of approximately one meter, and a diameter of 50 µm.

From (2.7), we can estimate precisely the spring constant of the pendulum as a function of directly measurable quantities

$$k = (2\pi T_0)^2 I \tag{2.14}$$

If we plug this expression in the thermal noise (2.12), we have

$$S_N^{therm}(\omega) = 16\pi^2 k_B T \frac{I}{T_0^2 Q \omega} \tag{2.15}$$

The torsion pendulum noise floor can be obtained summing the thermal noise with the readout noise for η converted via the transfer function (2.10) into an equivalent

[4]The maximum load that a fiber can carry is given by $F_{max} = \pi r_f^2 Y$ where Y is the ultimate tensile strength of the fiber material. Hence, the radius of the fiber must be $r_f \geq \sqrt{\frac{mg}{\pi Y}}$ to sustain an inertial member of mass m.

[5]This is not a huge problem for the representativeness of our setup, as most of the disturbances are generated on the surfaces, rather than from the bulk of TM.

torque noise, i.e.

$$S_N^{min}(\omega) = S_N^{therm}(\omega) + \frac{S_\eta^{read}(\omega)}{|H(\omega)|^2} \tag{2.16}$$

where $S_\eta^{read}(\omega)$ is the readout noise of the angular degree of freedom.

2.1.4 Torque estimation

Once the timeseries of the rotation angle of the torsion pendulum $\eta[t_i = i\Delta t]$ has been acquired, the preferred method to recover the external torque acting on the torsion pendulum is inverting the equation of motion in the time domain

$$\begin{aligned} N[t_i] &= I\ddot{\eta}[t_i] + \beta\dot{\eta}[t_i] + k\eta[t_i] \\ &= I\ddot{\eta}[t_i] + \frac{I}{Q}\left(\frac{2\pi}{T_0}\right)\dot{\eta}[t_i] + I\left(\frac{2\pi}{T_0}\right)^2\eta[t_i] \end{aligned} \tag{2.17}$$

where the dot indicates the time derivative. The careful reader will recognize that we just used the equation of motion for an harmonic oscillator subjected to viscous damping, whereas our experiment is ideally limited by intrinsic structural damping of the fiber. We notice, however, that the effect of this approximation turns to be negligible[6] [25]. The first and second derivative of $\eta[t_i]$ are computed by a sliding least-squares fit of a second order polynomial[7] over five consecutive samples as described in [28].

In Figure 2.6, we plot the 4TM torsion pendulum force noise at low frequency compared to the LISA acceleration requirement converted into force. Naturally the readout noise at frequencies close to the pendulum natural frequency is very small because even small torques produce a large angular displacement if their frequency resonates with the one of the pendulum.

Our setup is a factor ~ 8 in noise amplitude above the thermal noise at 1 mHz and a factor ~ 150 above the LISA requirement at the same frequency.

Even if the noise performance of the 4TM torsion pendulum is worse than the LISA requirement, our facility can still place stringent upper limits on the force noise introduced by the inertial sensor surrounding the TM. Moreover, it is possible to measure the force noise induced on the TM by fluctuations of environmental physical quantities (such as temperature) by modulating the source of disturbance itself and then observing the coherent response of the pendulum. In this regard, an estimate of the sensitivity of the 4TM torsion pendulum to a long-lasting sinusoidal force signal of frequency f_{mod} is

$$\sigma_A \simeq \sqrt{\frac{S_F(f_{mod})}{\Delta t}} \tag{2.18}$$

[6] The transfer function (2.10) and the one we obtain from (2.17) are very close at all frequencies.

[7] The fit function is $\eta_{fit}(t) = a_k t^2 + b_k t + c_k$, where the fit coefficients depend on the index k of the central point in the five-point stencil used for the fit (we fitted the set $\{\eta(t_{k-2}), \eta(t_{k-1}), \eta(t_k), \eta(t_{k+1}), \eta(t_{k+2})\}$). At this point the first derivative at the time t_k can be estimate as

$$\dot{\eta}[t_k] = \left.\frac{\mathrm{d}\eta_{fit}}{\mathrm{d}t}\right|_{t=t_k} = 2a_k t_k + b_k.$$

Analogously, the assessment of the second order derivative reads

$$\ddot{\eta}[t_k] = \left.\frac{\mathrm{d}^2\eta_{fit}}{\mathrm{d}t^2}\right|_{t=t_k} = 2a_k.$$

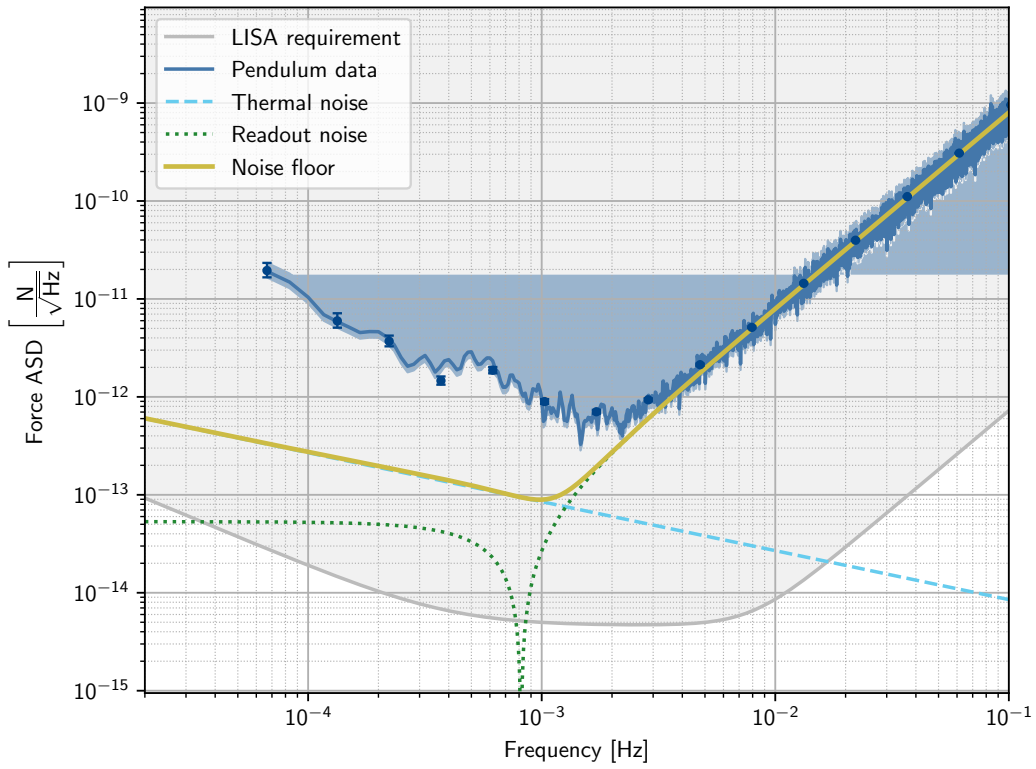

FIGURE 2.6: Amplitude spectral density of the force noise on the torsion pendulum. The data here refer to the most sensitive channel at low-frequency, which combines the capacitive readings of GRS and STC. The darker points with errobars are Bayesian estimates of the force ASD at independent frequencies. The gray line is the LISA acceleration requirement converted into force.

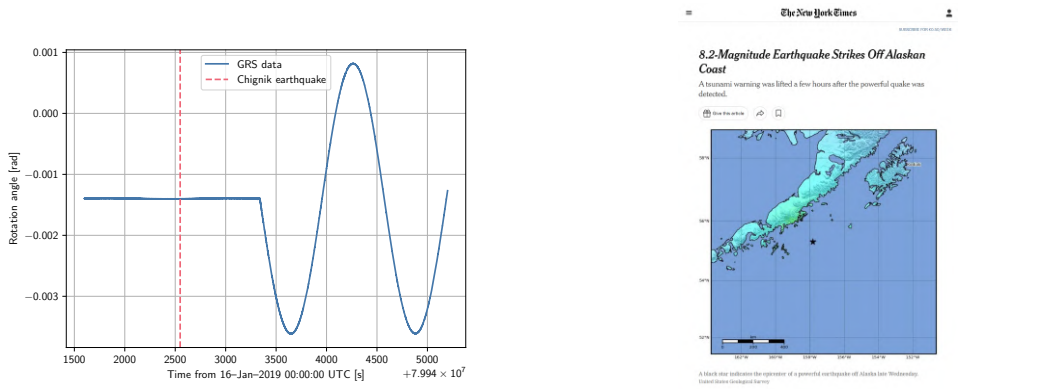

(A) Effect on the pendulum rotation angle (B) Newspaper article on the earthquake

FIGURE 2.7: Effect of the Chignik earthquake (Alaska) on the 4TM torsion pendulum in 2021. The seismic waves traveled for ~ 12 minutes before reaching our apparatus at a distance of 8600 km.

where Δt is the observation time and $S_F(f_{mod})$ is the one-sided PSD of the force noise on the pendulum at the modulation frequency. At the current performance the 4TM, the minimum detectable amplitude of a sinusoidal signal at 2 mHz is ~ 10 fN for an observation time of one hour.

The realistic maximum duration of an interrupted measurement with the torsion pendulum is limited by environmental factors, such as earthquakes happening somewhere on the Earth, which may cause the oscillation amplitude of the torsion pendulum to increase significantly (for an example, see Figure 2.7).

2.1.5 Detection of LPF glitches on-ground

An example of a possible application of the 4TM torsion pendulum to help investigating aspects of LISA Pathfinder that are still not understood is the search for spurious transient acceleration events, known as glitches [18].

Here we present a sensitivity analysis to the LISA Pathfinder impulse carrying glitches obtained with the technique of Wiener optimal filtering.

The LPF glitches are divided into

- *Impulse carrying glitches* of unknown origin;
- *Fast, low-impulse carrying glitches*, which are likely due to anomalies in the interferometer.

Here we focus on the impulse carrying glitches. Most of them (89%) are fitted by the template

$$h(t) = \Delta v \underbrace{\frac{t - t_0}{\tau^2} \exp\left(-\frac{t - t_0}{\tau}\right) \Theta(t - t_0)}_{f(t)} \tag{2.19}$$

where τ is a characteristic time, t_0 is the glitch arrival time, and Δv is the total impulse per unit mass transferred to the TM and $\Theta(\cdot)$ is the Heaviside step function. We can define the duration parameter Δ as the time interval that contains 99% of the glitch energy, that is

$$\frac{\int_{t_0}^{t_0+\Delta} h^2(t)\,\mathrm{d}t}{\int_{-\infty}^{+\infty} h^2(t)\,\mathrm{d}t} = 0.99 \tag{2.20}$$

Numerically we find $\Delta \simeq 4.2\tau$.

Assume that we would like to search for a signal of unknown amplitude but described by the template (2.19) in a noisy timeseries

$$g(t) = \Delta v \cdot f(t) + n(t) \tag{2.21}$$

where $f(t)$ is the normalized template, Δv is the unknown signal amplitude and $n(t)$ is a zero-mean noise. Assuming that the measured timeseries $g(t)$ is much longer than the duration of the signal, the *Wiener optimal filter* to detect $f(t)$ is

$$\mathcal{H}_{opt}(\omega) = \sigma^2_{\Delta v} \frac{\tilde{f}(\omega)}{S_{nn}(\omega)} \tag{2.22}$$

where $\tilde{f}(\omega)$ is the Fourier transform of the glitch template normalized so that is carries unitary impulse per unit mass and $S_n(\omega)$ is the acceleration power spectral density of the instrument that aims at detecting the signal $f(t)$, in our case the 4TM torsion pendulum. The constant $\sigma^2_{\Delta v}$ corresponds to the standard deviation of the filtered data and it is given by

$$\sigma_{\Delta v} = \left(\frac{1}{2\pi} \int \frac{|f(\omega)|^2}{S_n(\omega)} \, \mathrm{d}\omega \right)^{-\frac{1}{2}} \tag{2.23}$$

The $\sigma_{\Delta v}$ corresponds to the minimum detectable signal amplitude[8] , i.e. the amplitude of a glitch that would be measured with 100% relative error (SNR = 1).

In Figure 2.8, we show the sensitivity curves of the 4TM torsion pendulum to glitch-like signals obtained with (2.23) as a function of the duration parameter Δ. We see that a fraction of the LPF glitches would be detectable, although with limited SNR, with the torsion pendulum at the current noise performance.

2.2 Electrostatic model

The core of our experimental work entails the precise estimation of the charge deposited on our replica of the LISA test mass via small-force measurements with our 4TM torsion pendulum. Therefore, it is fundamental to present the theory that underlies such measurements and tells us how to convert a force into an assessment of the TM charge.

In this section, we will present a general model for the electrostatic forces generated in the LISA gravitational reference sensor, which can be applied to several types of experiments, such as the aforementioned charge measurement, or to the estimation of the stray biases on the sensing electrodes.

[8] In the case of multiple detection channels, the expression of the minimum detectable signal amplitude is generalized to

$$\sigma_{\Delta v} = \left(\frac{1}{2\pi} \int \boldsymbol{f}^\dagger(\omega) \boldsymbol{S}^{-1}(\omega) \boldsymbol{f}(\omega) \, \mathrm{d}\omega \right)^{-\frac{1}{2}} \tag{2.24}$$

where $\boldsymbol{f}(\omega) = [f_1(\omega), f_2(\omega), \ldots, f_n(\omega)]^T$ is a vector of templates (one for each channel) and $\boldsymbol{S}^{-1}$ is the inverse of the cross-spectral-density matrix at each frequency

$$\boldsymbol{S}(\omega) = \begin{bmatrix} S_{11}(\omega) & S_{12}(\omega) & \ldots & S_{1n}(\omega) \\ S_{21}(\omega) & S_{22}(\omega) & \ldots & S_{2n}(\omega) \\ \vdots & \vdots & \ddots & \vdots \\ S_{n1}(\omega) & S_{n2}(\omega) & \ldots & S_{nn}(\omega) \end{bmatrix} \tag{2.25}$$

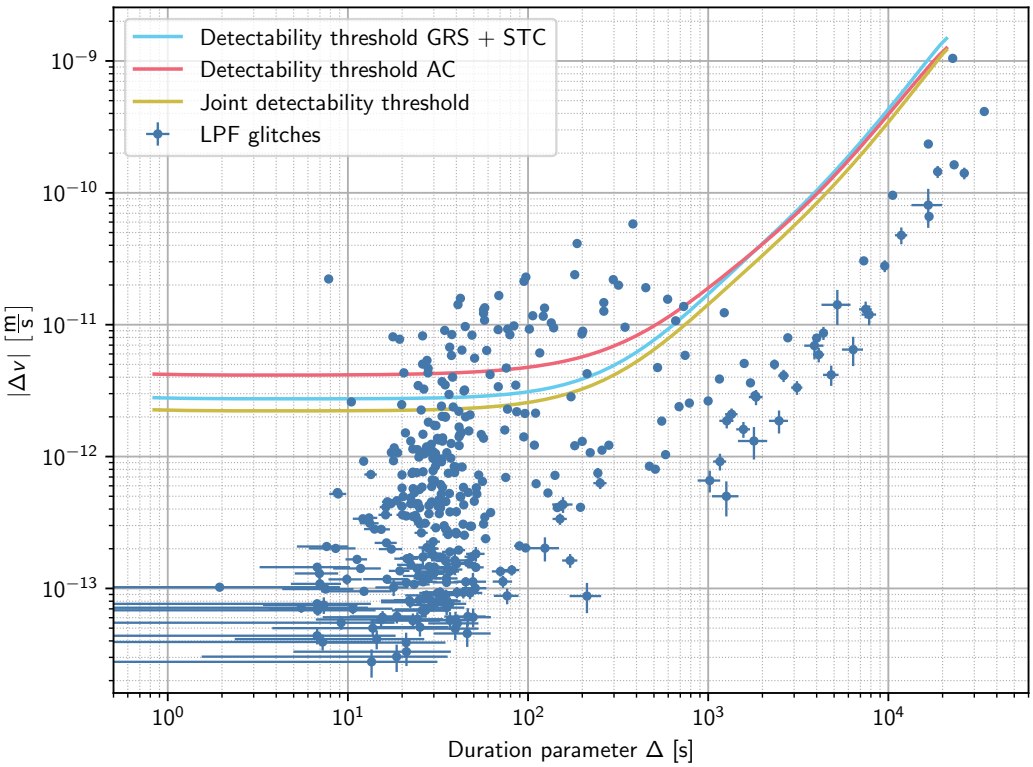

FIGURE 2.8: Sensitivity of the 4TM torsion pendulum to glitch-like signals for SNR = 1. The cyan curve corresponds to the sensitivity of the combined GRS + STC capacitive readout, whereas the red one to the AC sensitivity. The red curve is the sensitivity for a joint detection in both channels. The glitches data are from [18].

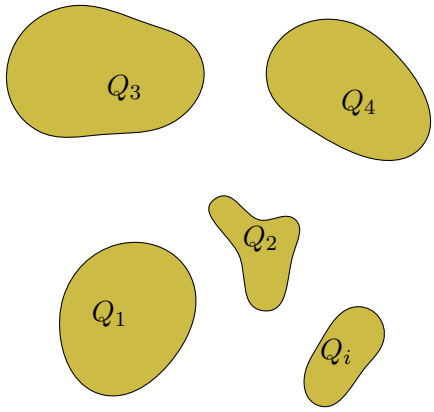

FIGURE 2.9: A system of isolated conductors.

2.2.1 System of conductors

The LISA sensor is basically a system of conductors. We recall in this section a few notions that will be useful in the remainder of the chapter.

Let us consider a system of N isolated conductors, each one with electric charge Q_i, as the one displayed in Figure 2.9

The linearity of Electrostatics ensures that the potential on any conductor can be obtained as

$$V_i = \sum_{j=1}^{N} p_{ij} Q_j \qquad \text{for} \qquad i = 1, \dots, N \tag{2.26}$$

where p_{ij} are the *coefficients of potentials*, which depend solely on the system geometry. The previous linear system can be inverted, leading to

$$Q_i = \sum_{j=1}^{N} c_{ij} V_j \qquad \text{where} \qquad \boldsymbol{c} = \{c_{ij}\} = \{p_{ij}\}^{-1} = \boldsymbol{p}^{-1} \tag{2.27}$$

The matrix $\{c_{ij}\}$ is the capacitive matrix, obtained inverting the matrix of the coefficient of potentials. From the symmetry of the Laplace equation in electrostatics, one can prove that the capacitive matrix is symmetrical, i.e. $c_{ij} = c_{ji}$ [29]. If we define now the new coefficients C_{ij} such that [30]

$$\begin{cases} c_{ij} = -C_{ij}, & \text{for } i \neq j \\ c_{ii} = \sum_{k \neq i} C_{ik}, & \text{otherwise} \end{cases} \tag{2.28}$$

We notice that the matrix of the C_{ij} is also symmetrical, as it is defined just inverting the sign of c_{ij} for $i \neq j$. If we substitute the newly defined C_{ij} into the (2.27), we have

$$Q_i = c_{ii} V_i - \sum_{j \neq i} c_{ij} V_j = \sum_{j \neq i} C_{ij} V_i - \sum_{j \neq i} C_{ij} V_j = \sum_{j \neq i} C_{ij} (V_i - V_j) \tag{2.29}$$

In this way we wrote the charge on the ith conductor as it were the armor of a capacitor. In other words, we converted the system of conductors into a system of capacitors. We can interpret C_{ij} as the capacitance between the ith and jth conductor. As expected the capacitances C_{ij} depend only on the system geometry, as they are defined from the potentials coefficients p_{ij}.

From the definition of potential, we can now write the internal energy U of the system as

$$U = U(\boldsymbol{r}_1, \dots, \boldsymbol{r}_N; \boldsymbol{\vartheta}_1, \dots, \boldsymbol{\vartheta}_N) = \frac{1}{2} \sum_{i=1}^{N} Q_i V(\boldsymbol{r}_i) \tag{2.30}$$

where the factor of one half accounts for the "double counting" of charge pairs and $V(\boldsymbol{r}_i)$ is the electrostatic potential due to all conductors except the one at $\boldsymbol{r}_i$. We explicitly wrote that the internal energy depends on the positions $\{\boldsymbol{r}_i\}$ and orientation $\{\boldsymbol{\vartheta}_i\}$ of all conductors in the system. As the conductors are equipotential surfaces, we must have $V(\boldsymbol{r}_i) = V_i$, hence

$$U(\boldsymbol{r}_1, \dots, \boldsymbol{r}_N; \boldsymbol{\vartheta}_1, \dots, \boldsymbol{\vartheta}_N) = \frac{1}{2} \sum_{i=1}^{N} Q_i V_i = \frac{1}{2} \sum_{i=1}^{N} \sum_{j}^{N} c_{ij} V_j V_i \tag{2.31}$$

where in the last passage we used (2.27). We can rephrase now the expression for the internal energy just derived in terms of the capacitances C_{ij} defined in (2.28)

$$\begin{aligned} U(\boldsymbol{r}_1, \dots, \boldsymbol{r}_N; \boldsymbol{\vartheta}_1, \dots, \boldsymbol{\vartheta}_N) &= \frac{1}{2} \sum_{i=1}^{N} \sum_{j \neq i} c_{ij} V_j V_i + \frac{1}{2} \sum_{i=1}^{N} c_{ii} V_i^2 \\ &= -\frac{1}{2} \sum_{i=1}^{N} \sum_{j \neq i} C_{ij} V_j V_i + \frac{1}{2} \sum_{i=1}^{N} \sum_{j \neq i} C_{ij} V_i^2 \end{aligned} \tag{2.32}$$

We notice that the last term on the right-hand side of the last equation can be written as

$$\begin{aligned} \sum_{i=1}^{N} \sum_{j \neq i} C_{ij} V_i^2 &= \frac{1}{2} \sum_{i=1}^{N} \sum_{j \neq i} C_{ij} V_i^2 + \frac{1}{2} \sum_{j}^{N} \sum_{i \neq j} C_{ji} V_j^2 \\ &= \frac{1}{2} \sum_{i=1}^{N} \sum_{j \neq i} C_{ij} V_i^2 + \frac{1}{2} \sum_{j}^{N} \sum_{i \neq j} C_{ij} V_j^2 \\ &= \frac{1}{2} \sum_{i=1}^{N} \sum_{j \neq i} C_{ij} \left(V_i^2 + V_j^2 \right) \end{aligned} \tag{2.33}$$

where we used the symmetry of the capacitances $C_{ij} = C_{ji}$ and the fact that the order of summation can be flipped. If we plug this expression into the internal energy (2.32), we obtain

$$\begin{aligned} U(\boldsymbol{r}_1, \dots, \boldsymbol{r}_N; \boldsymbol{\vartheta}_1, \dots, \boldsymbol{\vartheta}_N) &= \frac{1}{4} \sum_{i=1}^{N} \sum_{j \neq i} C_{ij} \left(V_i^2 + V_j^2 - 2 V_j V_i \right) \\ &= \frac{1}{4} \sum_{i=1}^{N} \sum_{j \neq i} C_{ij} \left(V_i - V_j \right)^2 \\ &= \frac{1}{2} \sum_{i=1}^{N} \sum_{j < i} C_{ij} \left(V_i - V_j \right)^2 \end{aligned} \tag{2.34}$$

where, in the last passage, we restricted $j < i$ to avoid double counting.

From the internal energy for a system of isolated conductors, we can obtain the force acting on the ith conductor $\boldsymbol{F}_i$ using the *principle of virtual works*

$$\boldsymbol{F}_i \cdot \mathrm{d}\boldsymbol{r}_i = \delta W = -\mathrm{d}U \qquad \Longrightarrow \qquad \boldsymbol{F}_i = -\boldsymbol{\nabla}_i U \tag{2.35}$$

where $\mathrm{d}\boldsymbol{r}_i$ is the infinitesimal translation of the ith conductor and $\boldsymbol{\nabla}_i$ is the gradient with respect to the coordinates of the ith particle[9]. If we restrict to compute the force acting along a general direction, that we shall call x, we have that the component of the force on the ith conductor along the x-axis is

$$\boldsymbol{F}_i \cdot \hat{\boldsymbol{e}}_x = F_{i,x} = -\frac{\partial U}{\partial x_i} \tag{2.37}$$

where x_i is the coordinate of the ith conductor on the x-axis. A similar expression is also true for the torques[10]

$$\boldsymbol{N}_i \cdot \hat{\boldsymbol{e}}_\vartheta = N_{i,\vartheta} = -\frac{\partial U}{\partial \vartheta_i} \tag{2.41}$$

Comment for conductors at fixed potential The derivation above assumes that all conductors in the system are isolated, hence the internal energy is given by the total electrostatic energy of the conductors.

In the case that the conductors are kept at a constant potential due to the presence of generators, the formula above is not true anymore, if we do not include the work done by the generators on the system [31]. Therefore, the principle of virtual work must include not only the mechanical work, but also the electric work done by the generators

$$-\mathrm{d}U = \delta W_{tot} = \boldsymbol{F}_i \cdot \mathrm{d}\boldsymbol{r}_i + \delta W_{gen} \tag{2.42}$$

Hence

$$\boldsymbol{F}_i \cdot \mathrm{d}\boldsymbol{r}_i = -\mathrm{d}U - \delta W_{gen} = -\mathrm{d}U + \mathrm{d}U_{gen} = -\mathrm{d}\left(U - U_{gen}\right) \tag{2.43}$$

We finally have that in the presence of generators that keep the conductors potential fixed, we must modify (2.35) as

$$\boldsymbol{F}_i = -\boldsymbol{\nabla}_i \left(U - U_{gen}\right) = -\boldsymbol{\nabla}_i U_{tot}. \tag{2.44}$$

[9] That is, assuming Cartesian coordinates

$$\boldsymbol{\nabla}_i = \frac{\partial}{\partial x_i}\hat{\boldsymbol{e}}_x + \frac{\partial}{\partial y_i}\hat{\boldsymbol{e}}_y + \frac{\partial}{\partial z_i}\hat{\boldsymbol{e}}_z \tag{2.36}$$

[10] One can prove the expression below from the infinitesimal work in terms of the torque

$$\delta W = \boldsymbol{N} \cdot \mathrm{d}\boldsymbol{\vartheta} \tag{2.38}$$

which itself arises from the definition of work

$$\delta W = \boldsymbol{F} \cdot \mathrm{d}\boldsymbol{s} = \boldsymbol{F} \cdot (\mathrm{d}\boldsymbol{\vartheta} \times \boldsymbol{R}) = (\boldsymbol{R} \times \boldsymbol{F}) \cdot \mathrm{d}\boldsymbol{\vartheta} = \boldsymbol{N} \cdot \mathrm{d}\boldsymbol{\vartheta}. \tag{2.39}$$

where we used the fact that a general infinitesimal displacement $\mathrm{d}\boldsymbol{s}$ can be written as the cross product of the corresponding angular displacement $\mathrm{d}\boldsymbol{\vartheta}$ and the radius vector $\boldsymbol{R}$. Moreover we used the vector identity $\boldsymbol{a} \cdot (\boldsymbol{b} \times \boldsymbol{c}) = (\boldsymbol{c} \times \boldsymbol{a}) \cdot \boldsymbol{b}$. From the principle of virtual work (restricting to torques along a specific rotation axis), we have

$$-\mathrm{d}U = \delta W = N_\vartheta \, \mathrm{d}\vartheta \tag{2.40}$$

which is what we wanted to prove.

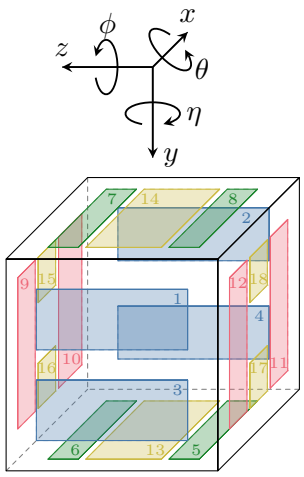

FIGURE 2.10: Electrode configuration of the gravitational reference sensor. The colors differentiate the various families of electrodes: blue for x, green for y, red for z, and yellow for the injection electrodes. We use here a slightly different convention for the numbering of the x-electrodes with respect to our reference [32].

Hence, the generic expression for a force (or torque) along a generic q-direction (or angular coordinate) acting on the ith conductor is

$$F_{i,q} = -\frac{\partial U_{tot}}{\partial q_i} = -\frac{\partial U}{\partial q_i} + \frac{\partial U_{gen}}{\partial q_i} \tag{2.45}$$

We notice that $F_{q,i}$ can be interpreted as either a force or a torque, depending if q is a linear or angular coordinate.

2.2.2 Electrostatic force model

In this section we will present the electrostatic model for LISA. The main reference will be the technical note [32]. As anticipated, the LISA sensor can be modeled as collection of conductors, which may be grouped into four categories

- Sensing and actuation electrodes;
- Injection electrodes;
- Rest of electrode housing;
- Test mass;

In Figure 2.10, we show a diagram of the various electrodes in the LISA sensor, accompanied by a numbering convention.

We will now derive the expression for the electrostatic forces acting on the test mass. As the electrode housing is a rigid body, the only element of the system that can move is the test mass. The expression for the generic force or torque (2.45), can be simplified as

$$F_q(\boldsymbol{r}, \boldsymbol{\vartheta}) = -\frac{\partial U_{tot}(\boldsymbol{r}, \boldsymbol{\vartheta})}{\partial q} = -\frac{\partial U(\boldsymbol{r}, \boldsymbol{\vartheta})}{\partial q} + \frac{\partial U_{gen}(\boldsymbol{r}, \boldsymbol{\vartheta})}{\partial q} \tag{2.46}$$

TABLE 2.1: Conversion between numbering and naming for the sensing/actuation electrodes.

Number	Name
1	x_1^-
2	x_1^+
3	x_2^-
4	x_2^+
5	y_1^+
6	y_2^+
7	y_2^-
8	y_1^-
9	z_1^+
10	z_2^+
11	z_2^-
12	z_1^-

where $\boldsymbol{r}$ is a vector specifying the test mass position and $\boldsymbol{\vartheta}$ a vector of angles defining its orientation[11]. The generic degree of freedom q can be either a position, for which F_q is to be interpreted a force, or an angle, which would make F_q a torque. The electrostatic energy of the capacitors can found from (2.34), but before we must explain what is the meaning the capacitances pairs C_{ij} in the context of the LISA sensor. As the EH is a rigid body, only the test mass is free to move: the capacitances will depend solely on the test mass position and rotation

$$C_{ij} = C_{ij}(\boldsymbol{r}, \boldsymbol{\vartheta}) \tag{2.47}$$

As we divided the GRS into actuation/sensing electrodes, injection electrodes, rest of EH, and test mass, the C_{ij} can be grouped in following classes[12]

- Capacitances between electrodes (both actuation/sensing and injection) and the TM, that we shall call C_i, where $i = 1, 2, \ldots, 18$ (indeed we have 12 actuation/sensing electrodes and 6 injection electrodes).
- Capacitances between electrodes (both actuation/sensing and injection) and the rest of the electrode housing, that we shall call $C_{i,h}$. As before $i = 1, 2, \ldots, 18$.
- Capacitance between TM and rest of the housing (not including the electrodes), which we call $C_{TM,h}$.

The scheme in Figure 2.11 is an useful visual aid to understand how we are modeling the GRS as a capacitive circuit.

Thus, the internal electrostatic energy for the capacitors (2.34), can be written summing over the capacitances just listed

$$U = \frac{1}{2}\sum_{i=1}^{18} C_i \left(V_i - V_{TM}\right)^2 + \frac{1}{2}\sum_{i=1}^{18} C_{i,h} V_i^2 + \frac{1}{2} C_{TM,h} V_{TM}^2 \tag{2.48}$$

where V_i are the voltages on the electrodes and V_{TM} is the test mass potential. We used the fact that the potential of the housing is always zero, because it is grounded.

[11] In Cartesian coordinates $\boldsymbol{r} = (x, y, z)$ and $\boldsymbol{\vartheta} = (\theta, \eta, \phi)$

[12] In this list we neglect the intra-electrode capacitances, which are two or three orders of magnitude lower and thus negligible [33].

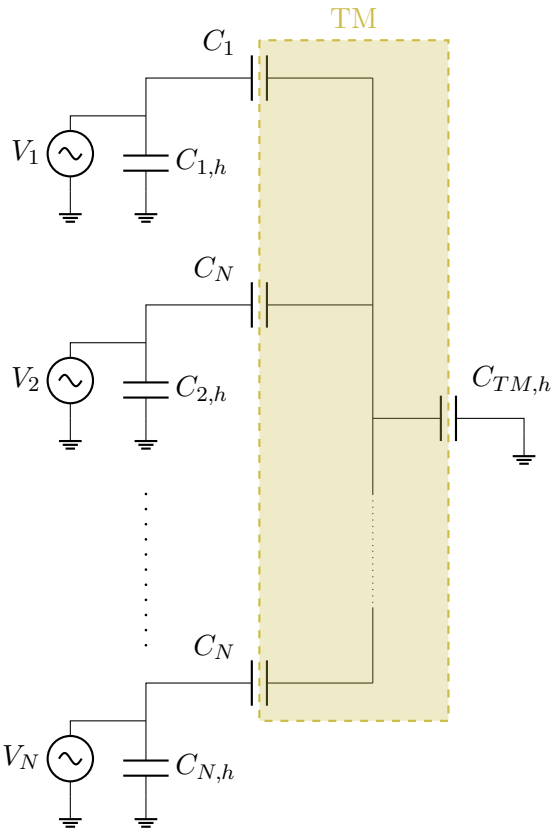

FIGURE 2.11: Schematic representation of the LISA sensor as a circuit. Indicated are the main capacitances connecting the various elements. Adapted from [32].

We notice that the test mass is of course floating, but we have FEE generators working to keep the potential of all injection and sensing electrodes at the desired values independently of the test mass position. We need therefore now to compute the energy provided by such generators, which is given by[13]

$$U_{gen} = \sum_{i=1}^{18} Q_{tot,i} V_i \tag{2.49}$$

where $Q_{tot,i}$ is the total charge deposited on the ith electrode, which is composed of two terms because each electrode is practically formed by two capacitors (see Figure 2.11). One capacitor is the one between electrode and TM (C_i) and the other is the capacitor between electrode and rest of the grounded housing $C_{i,h}$). Hence, we can write

$$Q_{tot,i} = Q_i + Q_{i,h} = C_i(V_i - V_{TM}) + C_{i,h} V_i \tag{2.50}$$

If we substitute this expression into the (2.49), we have that the energy provided by the generators is

$$U_{gen} = \sum_{i=1}^{18} \left[(C_i + C_{i,h}) V_i^2 - C_i V_{TM} V_i \right] \tag{2.51}$$

Consequently, combining (2.51) and (2.48), total internal energy assumes the form

$$\begin{aligned} U_{tot} &= U - U_{gen} \\ &= -\frac{1}{2} \sum_{i=1}^{18} (C_i + C_{i,h}) V_i^2 + \frac{1}{2} \left(C_{TM,h} + \sum_{i=1}^{18} C_i \right) V_{TM}^2 \\ &= -\frac{1}{2} \sum_{i=1}^{18} (C_i + C_{i,h}) V_i^2 + \frac{1}{2} C_{tot} V_{TM}^2 \end{aligned} \tag{2.52}$$

where we defined the total test mass capacitance as $C_{tot} = C_{TM,h} + \sum_{i=1}^{18} C_i$. As in the scheme of Figure 2.11, we can consider the test mass as an armor of a capacitor. Hence the TM charge can be found as

$$Q_{TM} = \sum_{i=1}^{18} C_i (V_{TM} - V_i) + C_{TM,h} V_{TM} \tag{2.53}$$

which solving for V_{TM} gives

$$V_{TM} = \frac{Q_{TM} + \sum_{i=1}^{18} C_i V_i}{C_{TM,h} + \sum_{i=1}^{18} C_i} = \frac{Q_{TM} + \sum_{i=1}^{18} C_i V_i}{C_{tot}} \tag{2.54}$$

This is the familiar expression for the test mass voltage, which includes the TM charge and the polarization that the electrodes induce on the test mass.

[13] In this case we do not have the prefactor one-half because we are counting just over the electrodes capacitances towards the TM (and not also over the symmetrical capacitances of the TM towards the electrodes).

At this point, we can write the expression for the general force (or torque) acting on the test mass (2.46) as

$$\begin{aligned} F_q &= \frac{1}{2}\frac{\partial}{\partial q}\left[\sum_{i=1}^{18}\left(C_i + C_{i,h}\right)V_i^2 - C_{tot}V_{TM}^2\right] \\ &= \frac{1}{2}\left(\sum_{i=1}^{18}\frac{\partial C_i}{\partial q}V_i^2 + \sum_{i=1}^{18}\frac{\partial C_{i,h}}{\partial q}V_i^2 - V_{TM}^2\frac{\partial C_{tot}}{\partial q} - 2C_{tot}V_{TM}\frac{\partial V_{TM}}{\partial q}\right) \end{aligned} \tag{2.55}$$

where we used the fact, due to the presence of the generators, V_i are constant and do not depend on the coordinate q. Let us compute the partial derivative of the test mass potential in the coordinate q

$$\begin{aligned} \frac{\partial V_{TM}}{\partial q} &= \frac{\partial}{\partial q}\left(\frac{Q_{TM} + \sum_{i=1}^{18} C_i V_i}{C_{tot}}\right) \\ &= \frac{1}{C_{tot}}\frac{\partial Q_{TM}}{\partial q} + \frac{1}{C_{tot}}\sum_{i=1}^{18} V_i\frac{\partial C_i}{\partial q} - \frac{Q_{TM} + \sum_{i=1}^{18} C_i V_i}{C_{tot}^2}\frac{\partial C_{tot}}{\partial q} \\ &= \frac{1}{C_{tot}}\sum_{i=1}^{18} V_i\frac{\partial C_i}{\partial q} - \frac{V_{TM}}{C_{tot}}\frac{\partial C_{tot}}{\partial q} \end{aligned} \tag{2.56}$$

where we used $\frac{\partial Q_{TM}}{\partial q} = 0$ since the test mass is electrically isolated. Plugging this expression into (2.55) leads us to

$$\begin{aligned} F_q &= \frac{1}{2}\left(\sum_{i=1}^{18}\frac{\partial C_i}{\partial q}V_i^2 + \sum_{i=1}^{18}\frac{\partial C_{i,h}}{\partial q}V_i^2 + V_{TM}^2\frac{\partial C_{tot}}{\partial q} - 2V_{TM}\sum_{i=1}^{18} V_i\frac{\partial C_i}{\partial q}\right) \\ &= \frac{1}{2}\left[\sum_{i=1}^{18}\left(\frac{\partial C_i}{\partial q} + \frac{\partial C_{i,h}}{\partial q}\right)V_i^2 + \right. \\ &\quad \left. + V_{TM}^2\left(\frac{\partial C_{TM,h}}{\partial q} + \sum_{i=1}^{18}\frac{\partial C_i}{\partial q}\right) - 2V_{TM}\sum_{i=1}^{18} V_i\frac{\partial C_i}{\partial q}\right] \\ &= \frac{1}{2}\left[\sum_{i=1}^{18}\frac{\partial C_i}{\partial q}(V_i - V_{TM})^2 + \sum_{i=1}^{18}\frac{\partial C_{i,h}}{\partial q}V_i^2 + V_{TM}^2\frac{\partial C_{TM,h}}{\partial q}\right] \end{aligned} \tag{2.57}$$

where, in the second passage, we decomposed $C_{tot} = C_{TM,h} + \sum_{i=1}^{18} C_i$. This is the general expression for the electrostatic force (or torque) on the LISA test mass along the general direction (or angle) q.

More general formulation The result (2.57) is consistent with the actuation model in [30], where the force along a general q coordinate is given by

$$F_q = \frac{1}{2}\sum_i\sum_{j<i}\frac{\partial C_{ij}}{\partial q}\left(V_i - V_j\right)^2 \tag{2.58}$$

Equivalently, the formula for the torque around a general angle β is

$$N_\beta = \frac{1}{2}\sum_i\sum_{j<i}\frac{\partial C_{ij}}{\partial \beta}\left(V_i - V_j\right)^2 \tag{2.59}$$

where the summations span in general over all the sensor and test mass surfaces. Analogously, the test mass potential is given by

$$V_{TM} = \frac{Q_{TM}}{C_{tot}} + \frac{\sum_{i(S)} C_{i(S)} V_{i(S)}}{C_{tot}} \tag{2.60}$$

where the summation index $i(S)$ runs over all the sensor surfaces, excluding the ones belonging to the test mass. In this way $C_{i(S)}$ represent the capacitance between the ith surface of the sensor and the TM and $V_{i(S)}$ represent the potential of this surface with respect to ground. Dealing with the most general form of equations (2.58) and (2.59) is pretty difficult. Usually, instead of referring to single surface elements, one makes the assumption that coherent and uninterrupted areas if the sensor, such as a given sensing electrode or the TM, are associated with a mean potential, as we did previously, following the model of reference [32].

2.2.3 Capacitance model

We would like to highlight that the capacitances and their derivatives in the previous equations dependent upon the TM displacement and rotation. In the general case the test mass is not necessarily centered, hence we need to known the value of the capacitance and their derivatives at the specific test mass position. As we are usually dealing with very small displacements and rotations from a centered test mass, a first order Taylor expansion provides with enough accuracy. The reference [32] presents a second order model for the capacitances. Here we focus only on the expansion of the x-electrodes capacitance and the total capacitance along the x-direction, which, as we shall see, are the quantities of interest for our analysis.

***x*-electrodes capacitance** We are mainly interested in the expression for the capacitance of x-electrodes because that is the sensitive axis of LISA and our torsion pendulum. The Taylor expansion of the x-electrodes capacitance at second order reads

$$\begin{aligned} C_1(x,y,z,\phi,\eta,\theta) \simeq C_x &- \left|\frac{\partial C_x}{\partial x}\right| x - \left|\frac{\partial C_x}{\partial \phi}\right| \phi + \\ &+ \frac{1}{2}\left|\frac{\partial^2 C_x}{\partial x^2}\right| x^2 + \frac{1}{2}\left|\frac{\partial^2 C_x}{\partial \phi^2}\right| \phi^2 + \frac{1}{2}\left|\frac{\partial^2 C_x}{\partial \eta^2}\right| \eta^2 + \\ &+ \left|\frac{\partial^2 C_x}{\partial \phi \partial x}\right| x\phi - \left|\frac{\partial^2 C_x}{\partial \phi \partial y}\right| y\phi + \left|\frac{\partial^2 C_x}{\partial \eta \partial z}\right| z\eta \end{aligned} \tag{2.61}$$

$$\begin{aligned} C_2(x,y,z,\phi,\eta,\theta) \simeq C_x &+ \left|\frac{\partial C_x}{\partial x}\right| x + \left|\frac{\partial C_x}{\partial \phi}\right| \phi + \\ &+ \frac{1}{2}\left|\frac{\partial^2 C_x}{\partial x^2}\right| x^2 + \frac{1}{2}\left|\frac{\partial^2 C_x}{\partial \phi^2}\right| \phi^2 + \frac{1}{2}\left|\frac{\partial^2 C_x}{\partial \eta^2}\right| \eta^2 + \\ &+ \left|\frac{\partial^2 C_x}{\partial \phi \partial x}\right| x\phi + \left|\frac{\partial^2 C_x}{\partial \phi \partial y}\right| y\phi - \left|\frac{\partial^2 C_x}{\partial \eta \partial z}\right| z\eta \end{aligned} \tag{2.62}$$

$$C_3(x,y,z,\phi,\eta,\theta) \simeq C_x - \left|\frac{\partial C_x}{\partial x}\right| x + \left|\frac{\partial C_x}{\partial \phi}\right| \phi + \\ + \frac{1}{2}\left|\frac{\partial^2 C_x}{\partial x^2}\right| x^2 + \frac{1}{2}\left|\frac{\partial^2 C_x}{\partial \phi^2}\right| \phi^2 + \frac{1}{2}\left|\frac{\partial^2 C_x}{\partial \eta^2}\right| \eta^2 - \\ - \left|\frac{\partial^2 C_x}{\partial \phi \partial x}\right| x\phi - \left|\frac{\partial^2 C_x}{\partial \phi \partial y}\right| y\phi + \left|\frac{\partial^2 C_x}{\partial \eta \partial z}\right| z\eta \quad (2.63)$$

and

$$C_4(x,y,z,\phi,\eta,\theta) \simeq C_x + \left|\frac{\partial C_x}{\partial x}\right| x - \left|\frac{\partial C_x}{\partial \phi}\right| \phi + \\ + \frac{1}{2}\left|\frac{\partial^2 C_x}{\partial x^2}\right| x^2 + \frac{1}{2}\left|\frac{\partial^2 C_x}{\partial \phi^2}\right| \phi^2 + \frac{1}{2}\left|\frac{\partial^2 C_x}{\partial \eta^2}\right| \eta^2 - \\ - \left|\frac{\partial^2 C_x}{\partial \phi \partial x}\right| x\phi + \left|\frac{\partial^2 C_x}{\partial \phi \partial y}\right| y\phi - \left|\frac{\partial^2 C_x}{\partial \eta \partial z}\right| z\eta \quad (2.64)$$

where the values the C_x and its derivatives have been computed for a centered TM in [33] with a FEM model of the GRS. Similar relations hold also for the $C_{i,h}$ capacitances for $i = 1, 2, 3, 4$.

At this point we would like to make a couple of observations:

- The sign of the capacitance first derivative in the direction x is positive for the electrodes on the x^+ face of the test mass and negative for the electrodes on the x^- face
$$\left.\frac{\partial C_1}{\partial x}\right|_{x=0} = \left.\frac{\partial C_3}{\partial x}\right|_{x=0} = -\left|\frac{\partial C_x}{\partial x}\right| \quad (2.65)$$
and
$$\left.\frac{\partial C_2}{\partial x}\right|_{x=0} = \left.\frac{\partial C_4}{\partial x}\right|_{x=0} = +\left|\frac{\partial C_x}{\partial x}\right| \quad (2.66)$$
The reason for this behavior is simple: if the TM moves from $x = 0$ to $x = \mathrm{d}x$, we have that it will be closer to the electrodes on the face x^+ face than to the ones on the x^- face. As the capacitance is expected to scale with the inverse of the distance between the armors, this causes the C_2 and C_4 capacitance to increase and, conversely, the C_1 and C_3 to decrease. See Figure 2.12 for a visual aid.

- We would like to point out that, at first order, the capacitance of the x-electrodes does not depend on the rotation angle η (see Figure 2.13 for a simple explanation)
$$\left.\frac{\partial C_i}{\partial \eta}\right|_{\eta=0} = 0 \qquad \text{for} \qquad i = 1, 2, 3, 4 \quad (2.67)$$
Consequently, if the test mass is centered in η, and some potentials are applied to the x-electrodes, there will be no pure torque acting on the pendulum but just a force along the x-direction (this is important for our charge measurement technique that will be discussed in Section 2.3).

Notice also that here we used a slight different numbering of the x-electrodes with respect to [32]. We did this trick, in order to write the capacitance of a general x-electrode when we are centered all DOF except for x, as

$$C_i(x) = C_x + (-1)^i \left|\frac{\partial C_x}{\partial x}\right| x + \frac{1}{2}\left|\frac{\partial^2 C_x}{\partial x^2}\right| x^2 + \mathcal{O}(x^2) \quad (2.68)$$

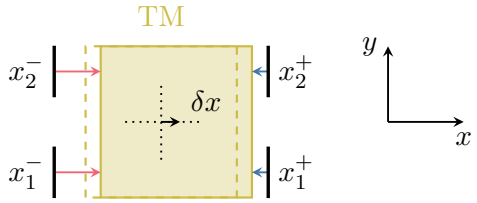

FIGURE 2.12: The capacitance of the electrodes on the x^+ face increase for a displacement δx of the TM from its centered position. The opposite is true for the electrodes on the x^- face.

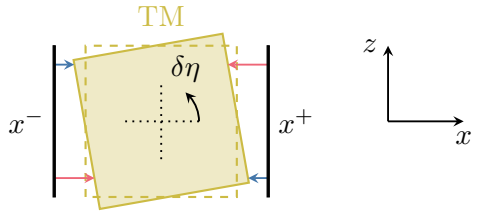

FIGURE 2.13: The capacitance of the x-electrodes does not change for small rotations $\delta\eta$, because the distance of the TM from one side of the electrodes increases, whereas on the other side, it decreases, giving, at first order, no contribution.

where $i = 1, 2, 3, 4$. A similar relation holds for the $C_{i,h}$ electrodes, but with the sign of derivative inverted. This arises from the fact that, if the test mass approaches one of the x-electrodes, a larger fraction of the electrostatic field lines would connect to the TM, rather than fall back to the EH region around the electrodes, i.e.

$$C_{i,h}(x) = C_{x,h} + (-1)^{i+1} \left|\frac{\partial C_{x,h}}{\partial x}\right| x - \frac{1}{2}\left|\frac{\partial^2 C_{x,h}}{\partial x^2}\right| x^2 + \mathcal{O}(x^2) \tag{2.69}$$

Total TM capacitance From symmetry reasons we can see that the first derivative of the total capacitance in all DOF is zero. Indeed starting from a centered TM, the symmetry of the electrode housing makes so that a displacement in any direction or angle will produce a variation of the total capacitance equal to a displacement in the opposite direction or angle

$$C_{tot}(\delta q) = C_{tot}(-\delta q), \tag{2.70}$$

which means that the value of the total capacitance for a centered test mass $q = 0$ is a stationary point

$$\left.\frac{\partial C_{tot}}{\partial q}\right|_{q=0} = 0 \qquad \Longrightarrow \qquad \left.\frac{\partial C_{tot}}{\partial x}\right|_{x=0} = 0 \tag{2.71}$$

Hence, the expansion of the total TM capacitance along the x-coordinate is

$$C_{tot}(x) = C_{tot}(x = 0) + \frac{1}{2}\left.\frac{\partial^2 C_{tot}}{\partial x^2}\right|_{x=0} x^2 + \mathcal{O}(x^2) \tag{2.72}$$

We notice that the second order derivative are not zero.

The numerical values for the capacitances and their derivatives have been computed for a centered test mass in [33] with a FEM model including the exact geometry of LISA Pathfinder GRS.

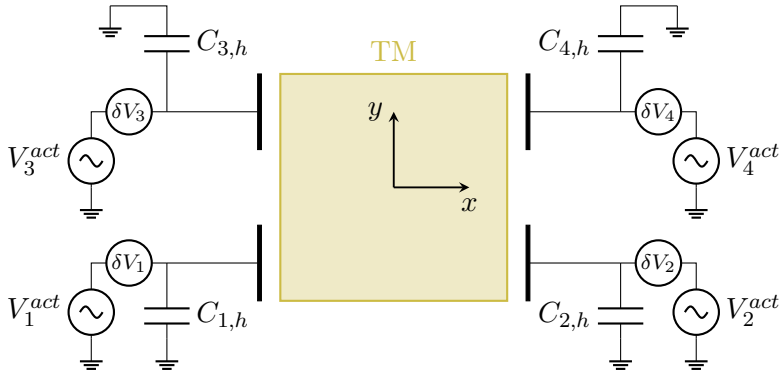

FIGURE 2.14: Schematic representation the capacitances needed to compute the electrostatic force the x-direction. The commanded actuation potentials are indicated with V_i^{act} and the stray biases as δV_i.

2.2.4 Force along the science axis

In LPF and in LISA the main sensitive direction is the x-axis, along which the test masses are free falling and no actuation is applied. For this reason, let us compute the expression for the electrostatic force acting on the TM along the x-direction. The scheme in Figure 2.14 shows the quantities relevant for calculations throughout the section.

In an ideal sensor[14], the only the electrodes on the x-faces have a non-vanishing capacitance derivative in the test mass x-position, i.e.

$$\frac{\partial C_i}{\partial x} = \frac{\partial C_{i,h}}{\partial x} = 0 \qquad \text{for} \qquad i \neq 1,2,3,4 \tag{2.73}$$

where we used the numbering of Figure 2.10. Therefore, the expression for the force (2.57) in the x-direction, reduces to

$$F_x = \frac{1}{2}\left[\sum_{i=1}^{4}\left(\frac{\partial C_i}{\partial x} + \frac{\partial C_{i,h}}{\partial x}\right)V_i^2 + V_{TM}^2\frac{\partial C_{tot}}{\partial x} - 2V_{TM}\sum_{i=1}^{4}V_i\frac{\partial C_i}{\partial x}\right] \tag{2.74}$$

If we assume that no potentials are applied to any of the electrodes except for the unavoidable stray biases δV_i, the previous equation would reduce to

$$F_{x,noise} = \frac{1}{2}\sum_{i=1}^{4}\left(\frac{\partial C_i}{\partial x} + \frac{\partial C_{i,h}}{\partial x}\right)\delta V_i^2 + \frac{1}{2}V_{TM}^2\frac{\partial C_{tot}}{\partial x} - V_{TM}\sum_{i=1}^{4}\delta V_i\frac{\partial C_i}{\partial x} \tag{2.75}$$

From this expression we can find all the possible electrostatic disturbances on the test mass that are listed in the LISA noise budget [12]. Let us notice that if the test mass is centered, the term proportional to V_{TM}^2 is negligible because of the (2.71).

Let us introduce the very important quantity Δ_x as

$$\Delta_x = \frac{\sum_{i=1}^{4}\delta V_i\frac{\partial C_i}{\partial x}}{\left|\frac{\partial C_x}{\partial x}\right|} \tag{2.76}$$

The Δ_x is often referred as *DC stray bias* and it is an effective potential on a single x-electrode that would explain the entire average residual electrostatic field felt by

[14]Here, with *ideal* we mean a sensor with perfect geometry and a test mass which is perfectly equipotential.

the TM in the x-direction [12, 30]. Actually the definition just given, reduces to $\Delta_x = -\delta V_1 + \delta V_2 - \delta V_3 + \delta V_4$ for a centered TM[15], i.e. Δ_x is the difference between the stray potentials on the x^+ face on the x^- face. On the other hand, the definition (2.76) in the less ideal case that the GRS geometry is not perfect and that the TM is a patchwork of different potentials, according to (2.58), must be generalized to

$$\Delta_x = \frac{1}{\left|\frac{\partial C_x}{\partial x}\right|} \sum_{i(TM)} \sum_{j(S)} (V_j - \delta V_i) \frac{\partial C_{ij}}{\partial x} \tag{2.77}$$

If we plug the definition of Δ_x (2.76) and the expression for V_{TM} (2.54) into (2.75), we have

$$\begin{aligned} F_{x,noise} = & \frac{1}{2} \sum_{i=1}^{4} \left(\frac{\partial C_i}{\partial x} + \frac{\partial C_{i,h}}{\partial x} \right) \delta V_i^2 + \\ & + \frac{1}{2} \left(\frac{Q_{TM} + \sum_{i=1}^{18} C_i V_i}{C_{tot}} \right)^2 \frac{\partial C_{tot}}{\partial x} - \left(\frac{Q_{TM} + \sum_{i=1}^{18} C_i V_i}{C_{tot}} \right) \left| \frac{\partial C_x}{\partial x} \right| \Delta_x \end{aligned} \tag{2.78}$$

From this expression we see that the leading term of the force noise in the charge for a centered[16] test mass is

$$F_{x,noise}^{Q_{TM}} = -\frac{Q_{TM}}{C_{tot}} \left| \frac{\partial C_x}{\partial x} \right| \Delta_x \tag{2.79}$$

This equation shows that the force scales with the TM charge: any noise on the stray potentials is translated into a noisy force with coupling coefficient proportional to the TM charge. We, therefore, understand that it is important to keep the TM charge as close to neutrality as possible, otherwise significant sources of force noise may arise.

2.3 Charge measurement technique

In this section we will explain how we can measure the test mass charge by applying modulation voltages to the x-electrodes.

We would like to make a few assumptions to simplify the calculation

- The test mass is centered in all degrees of freedom, except for the x-position. Consequently, according to the observation in Section 2.2.3, a potential applied to the x-electrodes generates a pure force F_x and no pure torque on the test mass around the angle η. In this way the signal induced on our torsion pendulum is due to only the electrostatic forces acting on the TM.

- The amplitude of the modulation is equal to the commanded value on all x-electrodes. Measurement with our FEE in [34], seem to suggest that the stability of the actuation amplitudes is remarkable (relative variations $\sim 1000\,\text{ppm}$).

For the 4TM torsion pendulum we decided to apply a modulation only to the x_2^+ and x_2^- electrodes (number 3 and 4 in Figure 2.10), which are the farther from the region illuminated by the ISUKs bringing UV-light into the GRS for charge management.

[15] From now on, in this section, we will assume that the test mass is centered if not otherwise specified.

[16] If the test mass is centered from (2.71) we have that $\frac{\partial C_{tot}}{\partial x}\big|_{x=0} = 0$.

We make this choice because we did not want to alter the photoelectron trajectories and, hence, the GRS discharge characteristics by applying local time-varying potentials of amplitude $\sim 1\,\mathrm{V}$ close to the area illuminated with the UV light.

The actuation pattern applied to the x-electrodes during our charge management reads

$$\begin{cases} V_1 = \delta V_1 \\ V_2 = \delta V_2 \\ V_3 = \delta V_2 - V_{mod}\sin(2\pi f_{mod} t) \\ V_4 = \delta V_2 + V_{mod}\sin(2\pi f_{mod} t) \end{cases} \tag{2.80}$$

The modulation frequency f_{mod} is chosen to be $\sim$ mHz to exploit the band where our torsion pendulum is most sensitive (see Figure 2.6). The modulation amplitude V_{mod} is chosen to be either 1 V for the apparent yield measurements (for which the charge signal is large) or 5 V for the continuous discharge measurements (for which we need to enhance the sensitivity).

The potential on all other EH sensing/actuation electrodes is supposed to be zero[17]. We notice that the modulation applied has opposite sign on electrode 3 with respect to electrode 4, in order not to polarize significantly the test mass (at least when it is centered). Indeed, from (2.54), considering the actuation pattern (2.80), we have

$$V_{TM}(x) = \frac{Q_{TM}}{C_{tot}(x)} + \frac{1}{C_{tot}(x)}\sum_{i=1}^{4} C_i(x)\delta V_i - \\ - \frac{C_3(x)V_{mod}}{C_{tot}(x)}\sin(2\pi f_{mod}t) + \frac{C_4(x)V_{mod}}{C_{tot}(x)}\sin(2\pi f_{mod}t) \tag{2.81}$$

Notice that in general V_{TM} depends on the x-position because the capacitances C_i and C_{tot} are function of the x-coordinate. However, if the test mass is centered in x, from (2.68) we have $C_3(x=0) = C_4(x=0) = C_x$ and the test mass potential reduces to

$$V_{TM}(x=0) = \frac{Q_{TM} + \sum_{i=1}^{4} C_x \delta V_i}{C_{tot}(x=0)} \tag{2.82}$$

If we plug the actuation pattern (2.80) and the corresponding test mass potential (2.81), into the general expression for the force along the x-direction (2.74) and we expand the result[18] at first order in the x coordinate, remembering equations for the expansion of the capacitances (2.68), (2.69) and (2.72), we obtain that the in-phase

[17] We do not consider in this calculation the potential on the injection electrodes, because it is modulated at frequencies completely different from the one of charge measurement (100 kHz versus $\sim$ mHz).

[18] We let Mathematica [35] the pleasure of performing the calculation because, given the large number of terms, the probability of making an error in an hand-made calculation is practically unity.

(I) force component at the modulation frequency is

$$F_{x,I}^{f_{mod}} = -2V_{mod}\left\{\left[\frac{Q_{TM}+C_x(\delta V_1+\delta V_2+\delta V_3+\delta V_4)}{C_{tot}}-\frac{\delta V_3+\delta V_4}{2}\right]\left|\frac{\partial C_x}{\partial x}\right|+\right.$$
$$\left.+\frac{\delta V_3+\delta V_4}{2}\left|\frac{\partial C_{x,h}}{\partial x}\right|\right\}+$$
$$+V_{mod}\left[\frac{4(\delta V_1-\delta V_2+\delta V_3-\delta V_4)}{C_{tot}}\left|\frac{\partial C_x}{\partial x}\right|^2+\right.$$
$$\left.+(\delta V_4-\delta V_3)\left(\left|\frac{\partial^2 C_x}{\partial x^2}\right|-\left|\frac{\partial^2 C_{x,h}}{\partial x^2}\right|\right)\right](x-x_0)+$$
$$+\mathcal{O}\left[(x-x_0)^2\right] \quad (2.83)$$

Another relevant force term that comes out of the expansion is

$$F_x^{DC,2f_{mod}} = K(x-x_0)\cdot\sin^2(2\pi f_{mod}t)+\mathcal{O}\left[(x-x_0)^2\right] \quad (2.84)$$

where

$$K=\frac{V_{mod}^2}{C_{tot}}\left[C_{tot}\left(\left|\frac{\partial^2 C_x}{\partial x^2}\right|-\left|\frac{\partial^2 C_{x,h}}{\partial x^2}\right|\right)-4\left|\frac{\partial C_x}{\partial x}\right|^2\right]. \quad (2.85)$$

Using the trigonometric duplication formula $2\sin^2(\alpha)=1-\cos(2\alpha)$, we can rephrase (2.84) as

$$F_x^{DC,2f_{mod}} = \frac{K}{2}(x-x_0)-\frac{K(x-x_0)}{2}\cos(4\pi f_{mod}t)+\mathcal{O}\left[(x-x_0)^2\right]. \quad (2.86)$$

Therefore, we can see that the force $F_x^{DC,2f_{mod}}$ gives rise to a quadrature (Q) force component at twice the modulation frequency

$$F_{x,Q}^{2f_{mod}} = -\frac{K}{2}(x-x_0)+\mathcal{O}\left[(x-x_0)^2\right] \quad (2.87)$$

and to a DC force

$$F_x^{DC} = \frac{K}{2}(x-x_0)+\mathcal{O}\left[(x-x_0)^2\right] \quad (2.88)$$

The forces in (2.87) and (2.88) can be interpreted as an AC and DC stiffness term because they produce a force that is proportional to the TM displacement. Both terms scale with the square of the modulation voltage V_{mod}, hence they can become quickly relevant if larger V_{mod} are chosen.

In the previous equations, we introduced x_0 as the zero-force point, that where the first derivatives of the capacitances of the x-electrodes on the plus side to the TM are exactly opposite to the ones on the minus side[19]

$$-\left.\frac{\partial C_1}{\partial x}\right|_{x=x_0} = -\left.\frac{\partial C_3}{\partial x}\right|_{x=x_0} = \left.\frac{\partial C_2}{\partial x}\right|_{x=x_0} = \left.\frac{\partial C_4}{\partial x}\right|_{x=x_0} \quad (2.89)$$

From (2.65) and (2.66), we would expect $x_0=0$. However, in general, the sensing zero position $x=0$ does not necessarily coincides with the zero-force point $x=x_0$ because of imperfections in the geometry of the GRS.

[19] Similar relations hold for the derivative of the capacitance $C_{i,h}$ of the electrodes with respect to the housing.

Even if we are theoretically expanding around $x = x_0$ in the previous equations, we still use the numerical values for the capacitances and their derivatives from the FEM model [33] which assumes a perfect geometry, i.e. $x_0 = 0$ (anyhow a correction is not needed because it would be second, or higher, order).

Estimation of zero-force point We can use the quadrature component at twice the modulation frequency as a clean measure of the distance from the zero-force point x_0. Indeed it does not depend on the unknown stray potentials δV_i on the electrodes. From (2.87), we have

$$\begin{aligned} x - x_0 &= -\frac{2F_{x,Q}^{2f_{mod}}}{K} \\ &= -\frac{2F_{x,Q}^{2f_{mod}}}{\frac{V_{mod}^2}{C_{tot}}\left[C_{tot}\left(\left|\frac{\partial^2 C_x}{\partial x^2}\right| - \left|\frac{\partial^2 C_{x,h}}{\partial x^2}\right|\right) - 4\left|\frac{\partial C_x}{\partial x}\right|^2\right]} \end{aligned} \tag{2.90}$$

In general, if we adjust the x-position of the TM in the EH so to null the force component at $2f_{mod}$, we are sure to be in $x = x_0$.

During the charge measurements with our torsion pendulum we took care to be approximately centered in $x \simeq x_0$. This configuration was, however, possible only for a limited amount of time, as the unwinding of the suspending fiber, causes an unavoidable secular drift in the equilibrium point of the pendulum.

Simplification for negligible stray biases If we assume that the stray biases on the x-electrodes are small ($\delta V_i \simeq 0$ for $i = 1, 2, 3, 4$), the previous equations can be simplified. Let us introduce the number of electrodes used for the x-modulation (either 2 or all 4) with the symbol N_{el}. The in-phase force component (2.83) for negligible stray biases becomes

$$F_{x,I}^{f_{mod}} = -N_{el} V_{mod} \left|\frac{\partial C_x}{\partial x}\right| \frac{Q_{TM}}{C_{tot}} + \mathcal{O}\left[(x - x_0)^2\right]. \tag{2.91}$$

In the 4TM torsion pendulum, the estimated force along the x-direction is obtained from the torque

$$F_x = -\frac{N}{l_{arm}} \tag{2.92}$$

where the minus comes from the sign convention in the coordinate system of the torsion pendulum (a positive x-forces produces a negative torque). Hence from (2.91), we have that demodulating the amplitude of the in-phase torque at f_{mod} gives an estimate of the test mass potential

$$V_{TM} = \frac{Q_{TM}}{C_{tot}} = \frac{N_{x,I}^{f_{mod}}}{l_{arm} N_{el} V_{mod} \left|\frac{\partial C_x}{\partial x}\right|} \tag{2.93}$$

The quadrature force component at twice the modulation frequency (2.87) and the DC force (2.88) do not depend on the stray potentials. Let us just rephrase the stiffness K including explicitly the number of modulation electrodes

$$K = \frac{N_{el}^2 V_{mod}^2}{4C_{tot}}\left[C_{tot}\left(\left|\frac{\partial^2 C_x}{\partial x^2}\right| - \left|\frac{\partial^2 C_{x,h}}{\partial x^2}\right|\right) - 4\left|\frac{\partial C_x}{\partial x}\right|^2\right]. \tag{2.94}$$

These are the equations actually employed in the torsion pendulum for the charge measurement. The hypothesis of negligible stray bias on the electrodes has to be checked with dedicated DC stray bias measurements, which are presented in the next section.

Subtraction of AC and DC stiffness In our torsion pendulum the DC force (2.88) acts as an extra stiffness that opposes to the fiber restoring torque, causing the period of the pendulum to increase. On the other hand, the AC stiffness (2.87) produces a peak in the torque spectrum at $2f_{mod}$, which could potentially spoil our charge signal at the modulation frequency (due to, for example, spectral leakage).

In order to have a cleaner charge measurement when we are not perfectly centered[20] on x_0, we subtracted the contributions of the AC and DC stiffness terms in (2.84) from the total torque.

In Figure 2.15 we show the effect of the stiffness subtraction on the torsion pendulum torque spectra during a charge management. The procedure is quite effective: the peaks at twice the modulation frequency due to (2.87) (an its beatings with the pendulum natural frequency) are significant lower. We also suppress the low-frequency peak, which is caused by the fact that the DC stiffness (2.88) reduces the natural frequency of the pendulum.

Observations Now that we derived all important equations for the charge measurements, let us make a couple of observations:

- Even if we are in the zero-force point ($x = x_0$), the in-phase force component at f_{mod} (2.83) does not give a measurement of just the test mass potential, but includes a term proportional to the stray biases on the electrodes used for modulation

$$V_{TM}^{meas} = -\frac{F_{x,I}^{f_{mod}}}{2V_{mod}\left|\frac{\partial C_x}{\partial x}\right|} = V_{TM}(x_0) - \frac{\delta V_3 + \delta V_4}{2}\left(1 - \frac{\left|\frac{\partial C_{x,h}}{\partial x}\right|}{\left|\frac{\partial C_x}{\partial x}\right|}\right) \tag{2.95}$$

  where

$$V_{TM}(x_0) = \frac{Q_{TM} + C_x(\delta V_1 + \delta V_2 + \delta V_3 + \delta V_4)}{C_{tot}} \tag{2.96}$$

  is the TM potential when centered on the zero-force point x_0.

- From the second term in (2.83), we see that, if the x-coordinate changes with time, we will observe a change in the amplitude of the in-phase force component at the modulation frequency, which is in turn directly converted into a drift of the measured TM potential.

2.4 DC stray bias measurements

As argued in the previous sections, the presence of a large, uncompensated, DC stray bias Δ_x may introduce complications and excess noise in our charge measurements. This is particularly critical for the *continuous discharge campaign* (see Chapter 5), that is focused on estimating charge noise induced by the UV-illumination. We,

[20] This is, to some extent, unavoidable due to the unwinding of the fiber, which causes a slow drift of the pendulum x-coordinate.

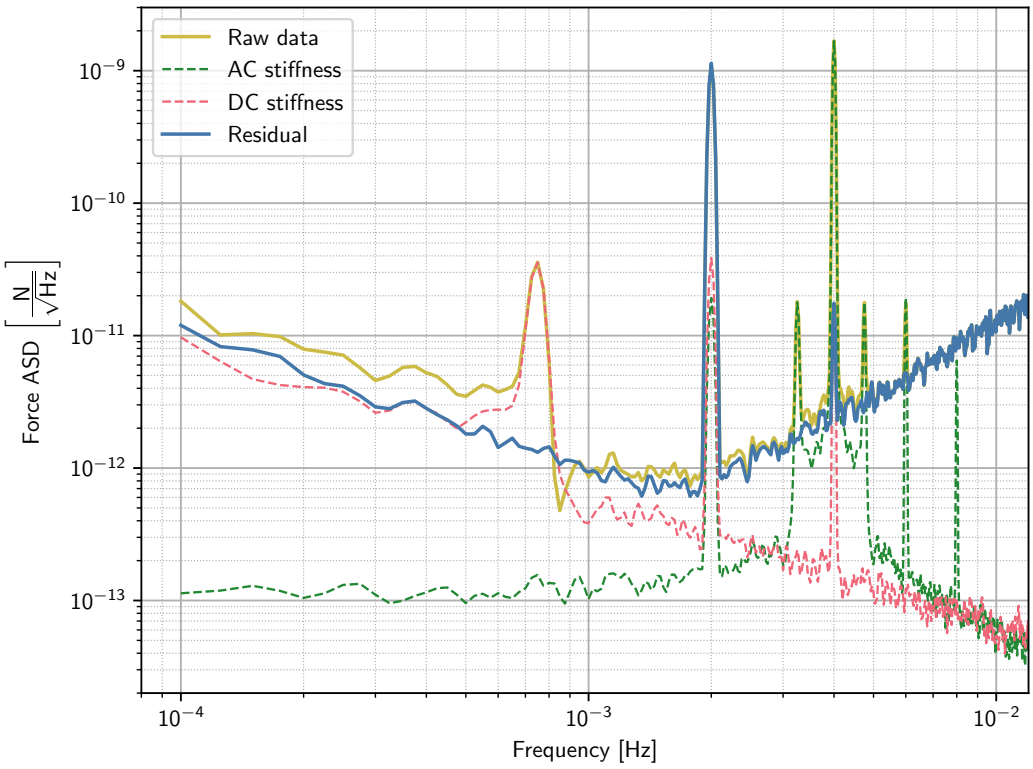

FIGURE 2.15: Subtraction of DC and AC stiffness terms. In *yellow* we have the force spectrum of the 4TM torsion pendulum data during a charge measurement ($N_{el} = 2$, $V_{mod} = 5\,\mathrm{V}$, and $f_{mod} = 2\,\mathrm{mHz}$) computed with the free pendulum period and in *blue* we see the residual force ASD after the stiffness subtraction. The residual force spectrum shows levels comparable to the instrumental noise floor (see Figure 2.6), except for the peak at the modulation frequency.

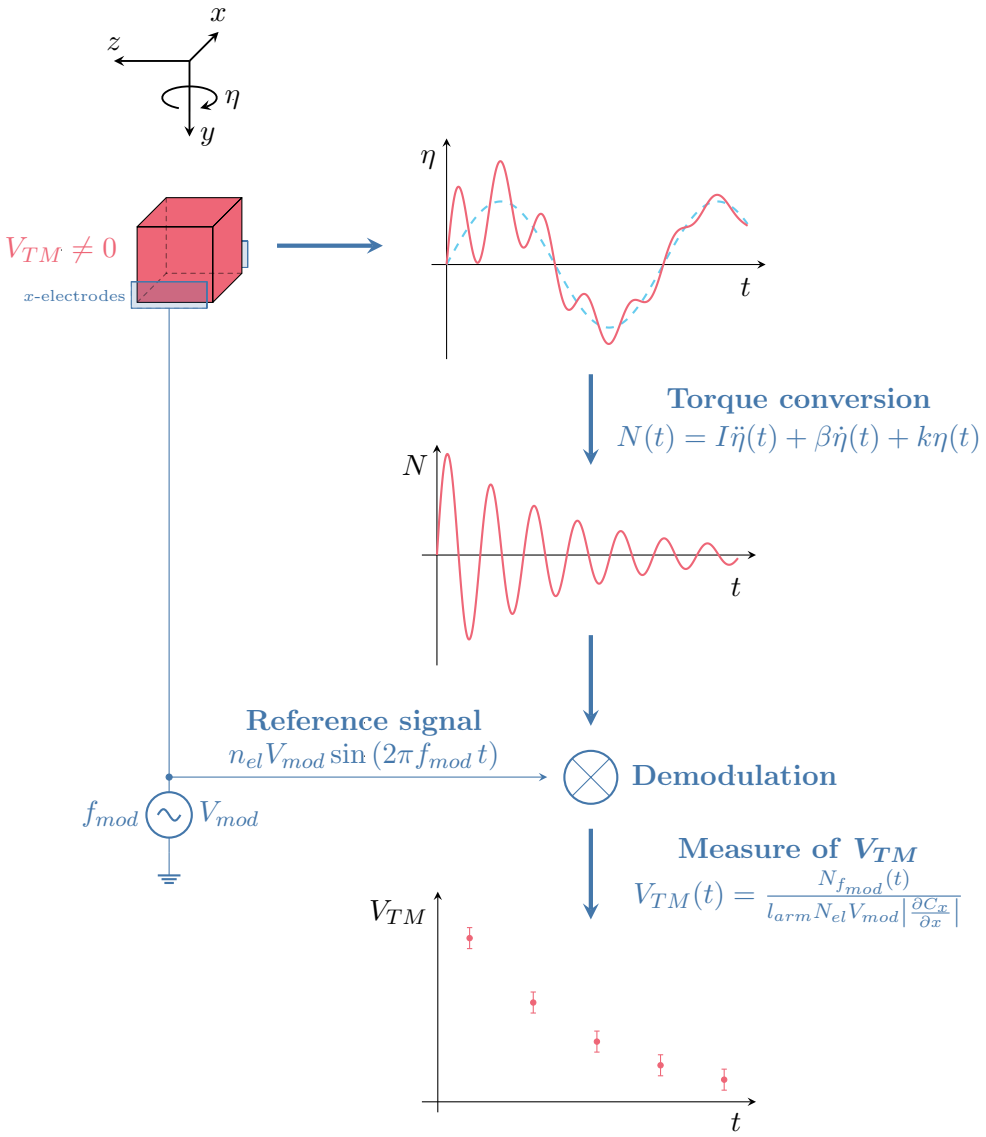

FIGURE 2.16: Flowchart illustrating the charge measurement procedure: once the timeseries of the pendulum rotation angle has been acquired, it is converted into torque and subsequently demodulated to recover the in-phase component at the modulation frequency. The test mass potential is then computed with (2.93).

therefore, decided to estimate the stray DC bias of our flight model replica GRS with two different methods, namely

- Test mass potential modulation technique;
- Charge burst technique.

which will be presented in the next sections.

2.4.1 TM potential modulation technique

The idea of this measurement is to simulate a time-varying charge by polarizing the test mass with the y-electrodes.

A sinusoidal potential with amplitude V_{mod} and frequency f_{mod} is applied coherently to $n \leq 4$ electrodes on the y-faces of the EH. Assuming that the test mass is geometrically centered in the y- and θ-coordinates[21] and that no potentials are present on all other electrodes, except for the stray bias on the x-electrodes[22], from (2.54), we have that

$$\begin{aligned} V_{TM}(t) &= \frac{Q_{TM}}{C_{tot}(x)} + \sum_{i=5}^{8} \frac{C_i}{C_{tot}(x)} V_i(t) + \sum_{k=1}^{4} \frac{C_k(x)}{C_{tot}(x)} \delta V_k \\ &= \frac{Q_{TM}}{C_{tot}(x)} + \sum_{j=1}^{n} \frac{C_y}{C_{tot}(x)} V_{mod} \sin(2\pi f_{mod} t) + \sum_{k=1}^{4} \frac{C_k(x)}{C_{tot}(x)} \delta V_k \\ &= \frac{Q_{TM}}{C_{tot}} + \underbrace{n V_{mod} \frac{C_y}{C_{tot}(x)}}_{A_{mod}} \sin(2\pi f_{mod} t) + \sum_{k=1}^{4} \frac{C_k(x)}{C_{tot}(x)} \delta V_k \end{aligned} \tag{2.97}$$

The force along the sensitive x-axis is given by the equation (2.74). If we expand this equation at first order in $x - x_0$, remembering that in the zero-force point the derivative of the capacitances on opposite sides of the test mass have flipped sign, it is possible to prove that the in-phase component of the force at the modulation frequency is

$$\begin{aligned} F_{x,I}^{f_{mod}} = &\frac{A_{mod}}{C_{tot}} (\delta V_1 - \delta V_2 + \delta V_3 - \delta V_4) \left| \frac{\partial C_x}{\partial x} \right| + \\ &+ \frac{A_{mod}}{C_{tot}^2} (x - x_0) \left[\left(C_x \left| \frac{\partial^2 C_{tot}}{\partial x^2} \right| - C_{tot} \left| \frac{\partial^2 C_x}{\partial x^2} \right| \right) \sum_{i=1}^{4} \delta V_i + Q_{TM} \left| \frac{\partial^2 C_{tot}}{\partial x^2} \right| \right] + \\ &+ \mathcal{O}\left[(x - x_0)^2 \right] \end{aligned} \tag{2.98}$$

The quadrature component of the force at twice the modulation frequency is

$$F_{x,Q}^{2f_{mod}} = -\frac{A_{mod}^2}{4C_{tot}^2} \left| \frac{\partial^2 C_{tot}}{\partial x^2} \right| (x - x_0) + \mathcal{O}\left[(x - x_0)^2 \right] \tag{2.99}$$

and can be again used as an estimate of the distance from the zero-force point x_0. If we are reasonably close ($\sim 10\,\mu m$) to x_0, we see that the second term in (2.98) is

[21] In this way, we can simply use the nominal value C_y for the y-electrode capacitance, without the need of expanding it in a Taylor series.

[22] That is $V_i = \delta V_i$ for $i = 1, 2, 3, 4$.

negligible, hence

$$\begin{aligned} F_{x,I}^{f_{mod}} &\simeq \frac{A_{mod}}{C_{tot}} \left| \frac{\partial C_x}{\partial x} \right| (\delta V_1 - \delta V_2 + \delta V_3 - \delta V_4) \\ &\simeq -\frac{A_{mod}}{C_{tot}} \left| \frac{\partial C_x}{\partial x} \right| \Delta_x \end{aligned} \tag{2.100}$$

where we recognized the definition of DC stray bias Δ_x. If we solve for Δ_x, we have

$$\Delta_x \simeq -\frac{F_{x,I}^{f_{mod}}}{\frac{A_{mod}}{C_{tot}} \left| \frac{\partial C_x}{\partial x} \right|} \tag{2.101}$$

This equation gives a way to estimate the Δ_x from the in-phase component of force acting on the pendulum at the modulation frequency[23].

It is convenient to repeat the measurement of Δ_x applying some artificial compensating potentials on the x-electrodes in the pattern

$$V_1^{act} = V_3^{act} = -V_{comp} \qquad \text{and} \qquad V_2^{act} = V_4^{act} = V_{comp} \tag{2.103}$$

so that in equation (2.101), we would measure

$$\Delta_x^{meas}(V_{comp}) = \Delta_x + 4V_{comp} \tag{2.104}$$

In this way we can obtain a series of measured DC stray biases as a function of the compensating voltage. Given the linear dependence of the measured Δ_x^{meas} on the V_{comp}, the intercept of a linear fit gives an estimate the true DC stray bias Δ_x of the sensor in absence of any compensation voltage. We present the data acquired with our torsion pendulum for several combination of the y-electrodes used for the modulation in Figure 2.17.

This procedure, although convenient from an experimental point of view, is intrinsically flawed by the presence of shear forces that arise when you consider a non-equipotential TM model [30], or due to the misalignment of the TM in the GRS (especially with respect to the y-electrodes used for the modulation).

The error due to the presence of such shear forces can be naively estimated by repeating the same procedure with different combinations of the y-electrodes used for modulation.

Previous experimental campaigns showed that the systematic errors on Δ_x with the TM potential modulation technique can be as large as the DC stray bias itself. Our data, obtained by modulating five different combinations of the y-electrodes, seem to confirm this fear. We observe completely different estimates of the DC stray bias in the range $-10\,\mathrm{mV}$ to $+10\,\mathrm{mV}$. The weighted mean of all measurements lead to the following estimate of the DC stray bias for our sensor

$$\Delta_x = (-2 \pm 2)\,\mathrm{mV} \qquad \text{for } y\text{-electrodes modulation technique} \tag{2.105}$$

[23] Notice that, for the choice of coordinates in the torsion pendulum, a force with positive x-component produces a negative torque, hence when converting the torque into a force along the x-direction a minus sign must be applied

$$F_x = -\frac{N}{l_{arm}}. \tag{2.102}$$

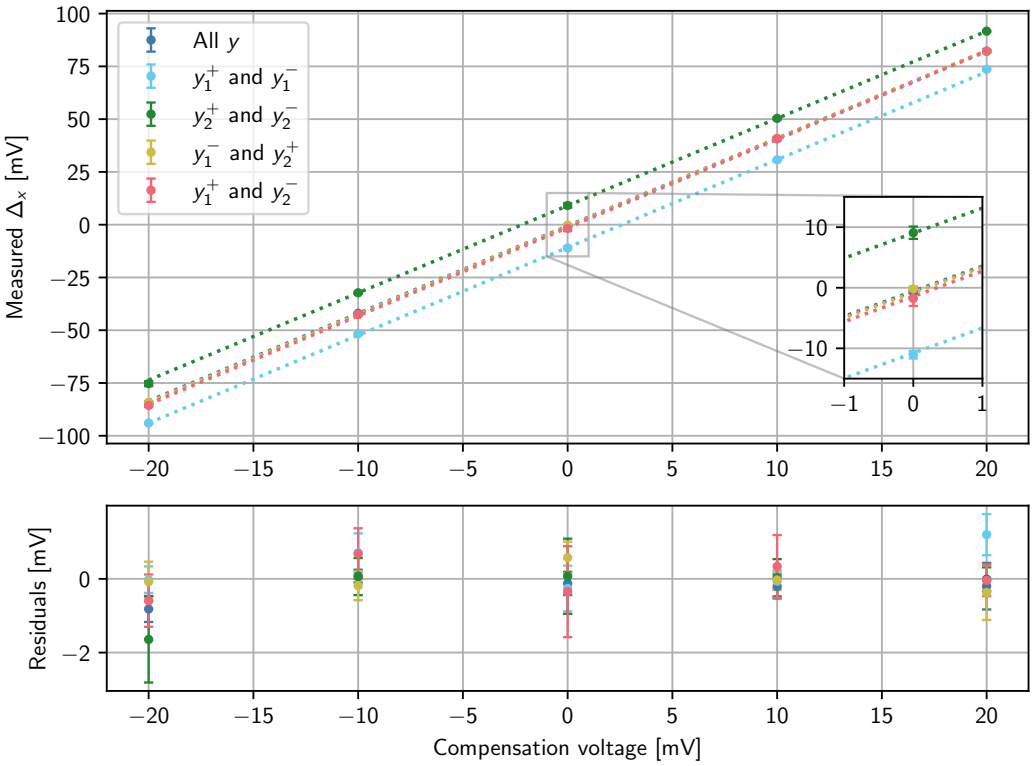

FIGURE 2.17: Measured DC stray bias as a function of the compensation voltage applied to the x-electrodes for several combinations of the y-electrodes used for the modulation. The dotted lines are least-squares linear fits on the experimental data with the same color coding.

The considerations above regarding the unreliability of this measurement technique, pushed us to try the *charge-burst method* to measure the DC stray bias, which should be immune to the aforementioned systematic errors.

2.4.2 Charge burst technique

The charge burst technique allows for a more direct measurement of the stray DC bias and is not affected by the systematic error related the shear forces. The idea is to measure the force step associated with a rapid change in the test mass charge induced by UV-illumination.

The measurement is less convenient then the method described in the previous section because it requires to estimate variations in the DC level of the force acting on the torsion pendulum, instead of demodulating a signal.

Assuming, as previously, that there are no potentials applied to the electrodes, except for the stray biases δV_i on the x-electrodes, and that we are centered in all DOF, except for x, we have that the test mass potential is

$$V_{TM}(x) = \frac{Q_{TM} + \sum_{i=1}^{4} C_i(x)\delta V_i}{C_{tot}(x)} \tag{2.106}$$

If we expand at linear order in $x - x_0$ the expression for the general force in the x-direction (2.74), we obtain

$$\begin{aligned} F_x(Q_{TM}) = \mathcal{C} + Q_{TM} \Bigg[& \frac{\delta V_1 - \delta V_2 + \delta V_3 - \delta V_4}{C_{tot}} \left| \frac{\partial C_x}{\partial x} \right| + \\ & + \frac{x - x_0}{C_{tot}} \left(\frac{C_x}{C_{tot}} \left| \frac{\partial^2 C_{tot}}{\partial x^2} \right| - \left| \frac{\partial^2 C_x}{\partial x^2} \right| \right) \sum_{i=1}^{4} \delta V_i \Bigg] + \\ & + \frac{Q_{TM}^2}{2C_{tot}^2} \left| \frac{\partial^2 C_{tot}}{\partial x^2} \right| (x - x_0) + \mathcal{O}\left[(x - x_0)^2\right] \end{aligned} \tag{2.107}$$

where $\mathcal{C}$ is a constant term that does not depend on the test mass charge. If we are reasonably close to x_0, we can ignore the term proportional to $\sum_{i=1}^{4} \delta V_i$. Hence

$$F_x(Q_{TM}) \simeq \mathcal{C} - Q_{TM} \frac{\Delta_x}{C_{tot}} \left| \frac{\partial C_x}{\partial x} \right| + \frac{Q_{TM}^2}{2C_{tot}^2} \left| \frac{\partial^2 C_{tot}}{\partial x^2} \right| (x - x_0) \tag{2.108}$$

where we recognized the definition of the DC stray bias, i.e.

$$\Delta_x = -\delta V_1 + \delta V_2 - \delta V_3 + \delta V_4 \tag{2.109}$$

The expression of the derivative of the force in the TM charge is

$$\frac{\mathrm{d}F_x}{\mathrm{d}Q_{TM}} \simeq -\frac{\Delta_x}{C_{tot}} \left| \frac{\partial C_x}{\partial x} \right| + \frac{Q_{TM}}{C_{tot}^2} \left| \frac{\partial^2 C_{tot}}{\partial x^2} \right| (x - x_0) \tag{2.110}$$

If we estimate the value of the derivative of the force in the charge for several values of Q_{TM}, we can obtain the Δ_x as the intercept of the linear fit on the data.

Experimental procedure Induce with UV illumination a rapid change in the test mass charge and measure the associated force step.

1. Perform a charge measurement to estimate the charge V_{TM}^{init} before the illumination;

2. Switch off the charge measurement and leave the pendulum oscillate freely (with small amplitude);

3. Switch on the UV illumination to rapidly change the test mass charge;

4. Leave the pendulum oscillate for some time, in order to have the force step ΔF_x associated with the illumination in the middle of a stretch of data where the pendulum is quiet;

5. Perform a charge measurement to estimate the charge V_{TM}^{fin} after the illumination;

6. The derivative of the force in the test mass voltage can be estimated as

$$\frac{\mathrm{d}F_x}{\mathrm{d}Q_{TM}} \simeq \frac{\Delta F_x}{\left(V_{TM}^{fin} - V_{TM}^{init}\right) C_{tot}} \tag{2.111}$$

7. Repeat for several values of the test mass potential.

In Figure 2.18, we plot a force step due to the rapid change in the test mass charge as measured by the sensitive channels of the 4TM torsion pendulum. A low-pass Blackman-Harris filter with cutoff-frequency $f_c = 8\,\mathrm{mHz}$ has been applied to the force timeseries in order to make the steps stand out.

The amplitude of the step ΔF_x has been reconstructed from a linear piecewise fit of the data before and after the illumination time window.

As we have two channels to estimate the force on the pendulum, i.e. the autocollimator and the combined capacitive readings of GRS and STC, we actually estimate the force step ΔF_x as the mean of signal measured by the AC and GRS + STC channels. The same holds for the error on ΔF_x, which is found as the standard deviation of the force step amplitude by the two channels.

In Figure 2.19, we plot the derivative of the force in the test mass potential. A least squares fit is performed on the data. The value of the DC stray bias is estimated from (2.110) as

$$\begin{aligned} \Delta_x &= -\frac{C_{tot}}{\left|\frac{\partial C_x}{\partial x}\right|} \left.\frac{\mathrm{d}F_x}{\mathrm{d}Q_{TM}}\right|_{Q_{TM}=0} \\ &= -\frac{1}{\left|\frac{\partial C_x}{\partial x}\right|} \left.\frac{\mathrm{d}F_x}{\mathrm{d}V_{TM}}\right|_{V_{TM}=0} \\ &= (23 \pm 6)\,\mathrm{mV} \end{aligned} \tag{2.112}$$

where $\left.\frac{\mathrm{d}F_x}{\mathrm{d}V_{TM}}\right|_{V_{TM}=0}$ is the intercept of the linear fit in Figure 2.19.

Limitations This was the first time we measured the stray DC bias with the charge burst technique. We would line to make a few observations to improve the experimental procedure for future measurements

- It would have been advisable to repeat the measurement applying a compensation voltages as in the Section 2.4.1. In this way a more accurate determination of Δ_x could be obtained from a linear fit over multiple sets of charge burst measurements.

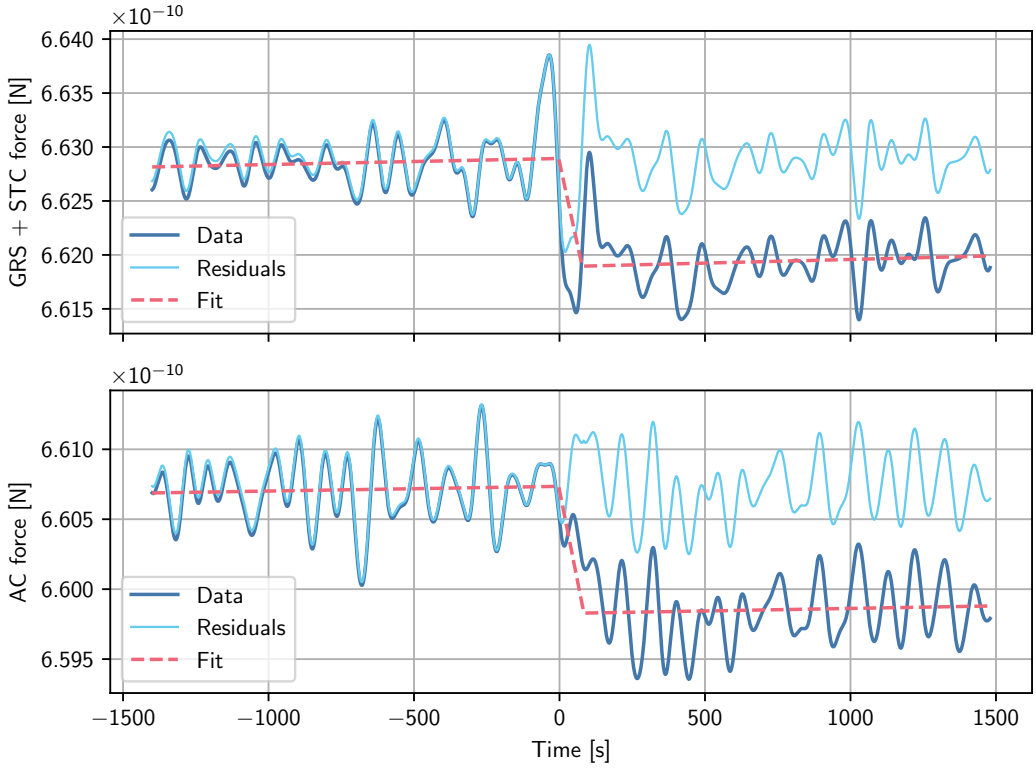

FIGURE 2.18: Example of a force step induced by a quick variation of the test mass charge. In the top panel we see the force time series measured with the combination of the STC and GRS capacitive sensing, whereas the bottom panel shows the force data obtained from the autocollimator. An equal low-pass filter with cutoff frequency 8 mHz has been applied to the data.

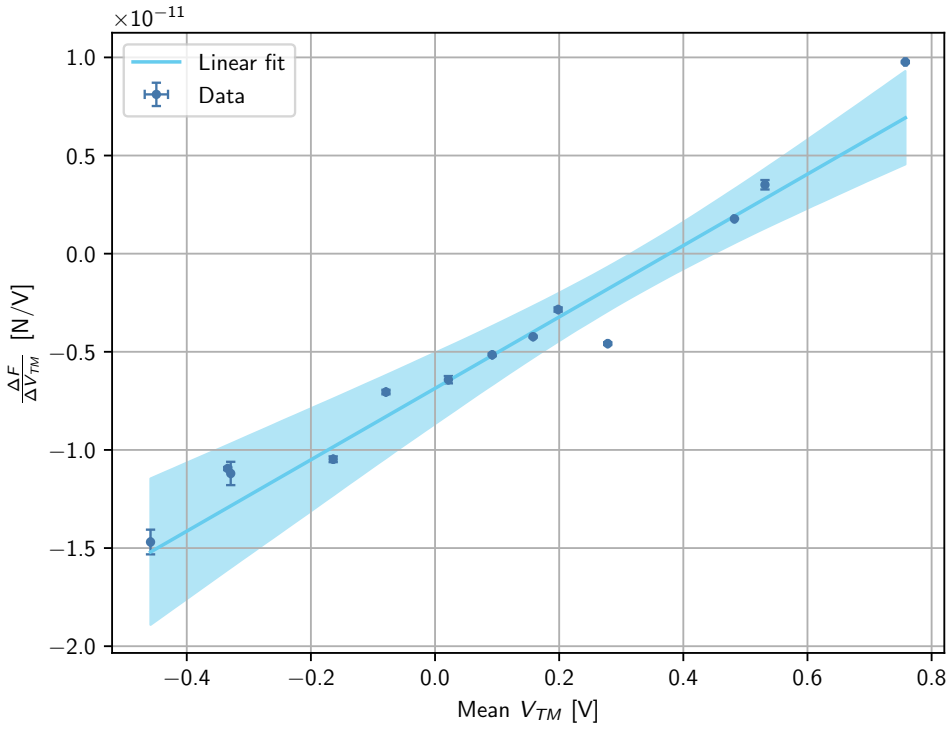

FIGURE 2.19: Estimated derivative of the force in the test mass voltage as a function of the mean V_{TM} during the charge step. The uncertainty region on the linear fit corresponds to 1σ-confidence.

- The amplitude of the charge steps was probably too large ($\sim 250\,\mathrm{mV}$): ideally in order to estimate correctly the derivative we would need infinitesimal charge variations, but that would produce a force step which is not detectable. Given the 4TM pendulum sensitivity, we advise variations of the test mass potential in the range of $50 - 100\,\mathrm{mV}$.
- The infamous and unavoidable low-frequency drift of the x-position of the test mass in the pendulum (due to *unwinding* of the suspending fiber), spoils a bit the measurement, as the derivative of the force (2.110) depends on $x - x_0$. The only solution would be to perform the measurement in a relatively short amount of time to limit the x-drift amplitude.
- The data analysis could be improved with an optimal filter to detect steps in the force timeseries.

2.4.3 Conclusions

The more charge-burst technique grants a more reliable measurement of the DC stray bias, which reads

$$\Delta_x = (23 \pm 6)\,\mathrm{mV} \qquad \text{for charge-burst method.} \tag{2.113}$$

The estimated stray DC bias for our GRS is comparable to the values measured on LISA Pathfinder[24] [36]. The value measured for Δ_x is expected not to hinder the charge measurements with the 4TM pendulum.

[24]The sensors that flew in LPF are nominally identical copies of the one installed in our torsion pendulum, as they are produced by the same company.

Chapter 3

Charge Management System testing for LISA

A known issue in astronautics is that isolated objects in space tend to accumulate electrical charge over time due to the constant bombardment of cosmic rays and solar energetic particles. The free-floating LISA test masses are no exception: an average net charging of around $+25\,e/\mathrm{s}$ is expected [36].

Already in the mid-nineties the team of the space mission Gravity Probe B was aware of the environmental charging problem and proposed solutions to measure and manage the charge build-up on their gyroscopes based on UV photoelectric emission [37].

Space mission for geodesy [38], such as GRACE[1], implement a spectacularly simpler solution to keep the charge on their test masses under control: a grounding wire.

This solution is not feasible for LISA, as the thermal acceleration noise induced by the mechanical damping from the wire would exceed the noise budget by orders of magnitude. As shown in [39], the *fluctuation-dissipation theorem* allows to compute the expected one-sided PSD of the thermal acceleration noise due to the grounding wire

$$S_g^{wire}(\omega) = 2 \cdot \frac{2k_B T}{M_{TM}} \frac{k_W}{Q(\omega)} \frac{1}{\omega}, \tag{3.1}$$

where k_W and $Q(\omega)$ are, respectively, the elastic constant and the quality factor of the wire. If we model the wire as a cylindrical cantilever subjected to a shear force perpendicular to its principal axis and applied at its free end, we can estimate the elastic constant k_W as

$$k_W = 3\pi \frac{E r^4}{l^3}, \tag{3.2}$$

where r is the wire radius, l its length, and E is the Young's modulus of the wire material. Even in the very optimistic case that the wire is made of gold ($E \simeq 80\,\mathrm{GPa}$) with a radius of just $5\,\mu\mathrm{m}$, a length of $1\,\mathrm{cm}$, and with quality factor of 100 at all frequencies, we have that the thermal noise due to the grounding wire (3.1) at $1\,\mathrm{mHz}$ for $T = 300\,\mathrm{K}$ is almost three orders of magnitude in amplitude above the LISA acceleration requirement at the same frequency

$$S_g^{wire}(f) \simeq \left(1.8\,\mathrm{pm/s^2/\sqrt{Hz}}\right)^2 \left(\frac{2\,\mathrm{kg}}{M_{TM}}\right) \left(\frac{T}{300\,\mathrm{K}}\right) \left(\frac{100}{Q}\right) \left(\frac{E}{80\,\mathrm{GPa}}\right) \cdot \\ \cdot \left(\frac{r}{5\,\mu\mathrm{m}}\right)^4 \left(\frac{1\,\mathrm{cm}}{l}\right)^3 \left(\frac{1\,\mathrm{mHz}}{f}\right) \tag{3.3}$$

[1] Others are GRACE-FO, CHAMP, GOCE and MICROSCOPE (which aims at testing the *Equivalence Principle*).

For this reason, LISA needs a contactless system to keep the test mass charge under control.

In this chapter, we will present an experimental campaign to explore the performance of a prototype Charge Management System for LISA based on photoelectric emission induced by the UV-light generated by light-emitting diodes (LEDs).

3.1 Electrostatic noise

In this section we will explain the reason why a non-neutral TM is a problem for LISA.

If the charge build-up on from cosmic rays and solar energetic particles on the LISA test masses were not counteracted, sources of force noise would start to become relevant. Indeed, in Section 2.2.4 we showed that the electrostatic force along the science axis is

$$F_{x,noise} = \frac{1}{2}\sum_{i=1}^{4}\left(\frac{\partial C_i}{\partial x}+\frac{\partial C_{i,h}}{\partial x}\right)\delta V_i^2 + \\ + \frac{1}{2}\left(\frac{Q_{TM}+\sum_{i=1}^{18}C_iV_i}{C_{tot}}\right)^2\frac{\partial C_{tot}}{\partial x} - \left(\frac{Q_{TM}+\sum_{i=1}^{18}C_iV_i}{C_{tot}}\right)\left|\frac{\partial C_x}{\partial x}\right|\Delta_x \quad (3.4)$$

This expression clearly depends on the test mass charge Q_{TM}. If the TM is centered, so that $\partial C_{tot}/\partial x = 0$, the leading force term in Q_{TM} is

$$F_{x,noise}^{Q_{TM}} = -\frac{Q_{TM}}{C_{tot}}\left|\frac{\partial C_x}{\partial x}\right|\Delta_x \quad (3.5)$$

As described in the following, once the TM charge overcomes the threshold of $1.5{\cdot}10^7\,e$, it is expected that the electrostatic force disturbances would exceed their allocation in the LISA noise budget, potentially spoiling the performance of the whole observatory.

3.1.1 Electrostatic budget

As anticipated in Section 1.2, the top-level requirements that must be met to achieve the design LISA sensitivity are:

- Overall single TM acceleration noise requirement along the science axis

$$S_g(f) < \left(2.4\,\mathrm{fm/s^2/\sqrt{Hz}}\right)^2\left[1+\left(\frac{0.4\,\mathrm{mHz}}{f}\right)^2\right]\left[1+\left(\frac{f}{8\,\mathrm{mHz}}\right)^4\right] \quad (3.6)$$

- Overall one-way displacement sensitivity requirement along the science axis

$$S_x(f) < \left(10\,\mathrm{pm/\sqrt{Hz}}\right)^2\left[1+\left(\frac{2\,\mathrm{mHz}}{f}\right)^4\right] \quad (3.7)$$

In the LISA noise budget [12], the current allocation for the acceleration noise on the TM due to all electrostatic force noise sources is

$$S_g^{ES}(f) \leq \left(3\,\mathrm{fm/s^2/\sqrt{Hz}}\right)^2\left(\frac{0.1\,\mathrm{mHz}}{f}\right)+\left(0.3\,\mathrm{fm/s^2/\sqrt{Hz}}\right)^2 \quad (3.8)$$

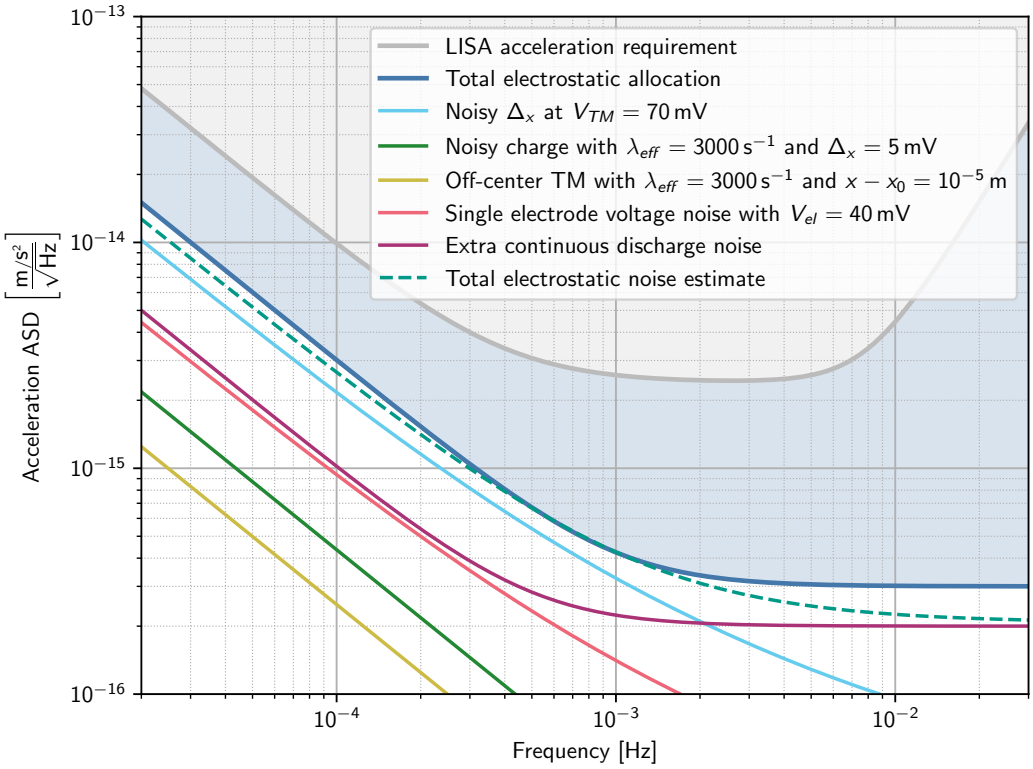

FIGURE 3.1: Power spectral density of the dominant sources of the electrostatic noise budget. Note that the two random charging effects are fully correlated and have been summed coherently [12].

The breakdown of such allocation into the relevant individual noise sources is described hereafter and visually displayed in Figure 3.1. For a more complete list of disturbances, which includes other (very) minor contributions to the electrostatic noise budget, see [12]. Most of the noise terms can be directly obtained[2] from the equation for a general electrostatic force along the x-axis (3.5), or its simplification for a centered test mass (3.4).

Noisy stray electric fields The allocated acceleration noise due to the interaction of a charged TM with noisy stray bias reads

$$\begin{aligned} S_g^{\Delta_x}(f) &\simeq \left[\frac{1}{M_{TM}}\frac{\partial C_x}{\partial x}\frac{Q_{TM}}{C_{tot}}\right]^2 S_{\Delta_x}(f) \\ &\simeq \left(2\,\mathrm{fm/s^2/\sqrt{Hz}}\right)^2 \left(\frac{Q_{TM}}{1.5\cdot 10^7\, e}\right)^2 \frac{S_{\Delta_x}(f)}{\left(0.2\,\mathrm{mV/\sqrt{Hz}}\right)^2} \end{aligned} \tag{3.11}$$

[2] Remembering that for linear systems the power spectral density at the output depends from the PSD at the input as

$$S_{out}(f) = |H(f)|^2 S_{in} \tag{3.9}$$

where $h(f)$ is the transfer function of the linear system. In our case the transfer function for the various force noise contributions can be obtained linearizing the electrostatic force (3.4) in the relevant quantity, i.e.

$$S_{F_x}^{\mathcal{I}} = \left|\frac{\partial F_x}{\partial q}\right|^2 S_{\mathcal{I}} \tag{3.10}$$

where $\mathcal{I}$ is a generic noisy quantity at the input.

where the allocation for noise in the stray bias Δ_x is

$$S_{\Delta_x}(f) = \left(4.5\,\mu\text{V}/\sqrt{\text{Hz}}\right)^2 + \left(75\,\mu\text{V}/\sqrt{\text{Hz}}\right)^2 \left(\frac{0.1\,\text{mHz}}{f}\right) + \\ + \left(190\,\mu\text{V}/\sqrt{\text{Hz}}\right)^2 \left(\frac{0.1\,\text{mHz}}{f}\right)^2 \quad (3.12)$$

which is comparable to the level measured by LPF [36].

Random TM charging The allocated acceleration noise due to the interaction of TM charge fluctuations with the DC stray bias is

$$\begin{aligned} S_g^{Q_{TM}}(f) &\simeq \left[\frac{1}{M_{TM}}\frac{\partial C_x}{\partial x}\frac{\Delta_x}{C_{tot}}\right]^2 S_{Q_{TM}}(f) \\ &\simeq \left[\frac{1}{M_{TM}}\frac{\partial C_x}{\partial x}\frac{\Delta_x}{C_{tot}}\right]^2 \frac{2e^2\lambda_{eff}}{2\pi f} \\ &\simeq \left(0.3\,\text{fm/s}^2/\sqrt{\text{Hz}}\right)^2 \left(\frac{\Delta_x}{5\,\text{mV}}\right)^2 \left(\frac{\lambda_{eff}}{1300\,\text{s}^{-1}}\right) \left(\frac{0.1\,\text{mHz}}{f}\right)^2 \end{aligned} \quad (3.13)$$

In the second passage, we assumed that the charge accumulation on he test mass can be described by a *Poisson process* with effective rate λ_{eff}, to which corresponds to the power spectral density[3]

$$S_{Q_{TM}}(f) = \frac{2e^2\lambda_{eff}}{2\pi f} \quad (3.14)$$

where λ_{eff} is effective charging rate, for which a value comparable to LPF measurement has been chosen (see Table 3.1).

Random charge noise with charged, off-center TM The allocated acceleration noise due to a non-centered charged TM reads

$$\begin{aligned} S_g^{OC}(f) &\simeq \left[\frac{1}{M_{TM}}\frac{\frac{\partial^2 C_{tot}}{\partial x^2}}{C_{tot}}(x-x_0)\right]^2 \left(\frac{Q_{TM}}{C_{tot}}\right)^2 S_{Q_{TM}}(f) \\ &\simeq \left[\frac{1}{M_{TM}}\frac{\frac{\partial^2 C_{tot}}{\partial x^2}}{C_{tot}}(x-x_0)\right]^2 \left(\frac{Q_{TM}}{C_{tot}}\right)^2 \frac{2e^2\lambda_{eff}}{2\pi f} \\ &\simeq \left(0.2\,\text{fm/s}^2/\sqrt{\text{Hz}}\right)^2 \left(\frac{x-x_0}{10\,\mu\text{m}}\right)^2 \left(\frac{\lambda_{eff}}{1300\,\text{s}^{-1}}\right) \left(\frac{0.1\,\text{mHz}}{f}\right)^2 \end{aligned} \quad (3.15)$$

This noise contribution can be obtained expanding the second term in (3.4) for small displacements from the *zero-force* point x_0. Here we also assumed that the charging of the TM can be modeled as a Poisson process. LPF showed that the test mass displacement from x_0 can be measured and corrected with accuracy better than 10 µm. For the plot in Figure 3.1, we considered $x - x_0 \simeq 10\,\mu\text{m}$ and $Q_{TM} \simeq 1.5 \cdot 10^7\,e$.

Individual electrode actuation fluctuations The allocated acceleration noise due to individual electrode potential fluctuations coupled with residual electrode DC

[3] See Appendix F for the detailed derivation of the power spectrum of a Poisson process.

biases

$$S_g^{V_{el}}(f) \simeq 4V_{el}^2 \left[\frac{1}{M_{TM}}\left(\frac{\partial C_x}{\partial x}+\frac{\partial C_{x,h}}{\partial x}\right)\right]^2 S_{V_{el}}(f)$$
$$\simeq \left(0.9\,\mathrm{fm/s^2/\sqrt{Hz}}\right)^2 \left(\frac{V_{el}}{40\,\mathrm{mV}}\right)^2 \frac{S_{V_{el}}(f)}{\left(0.1\,\mathrm{mV/\sqrt{Hz}}\right)^2} \tag{3.16}$$

This noise contribution arises directly from the first term of (3.4). For the plot in Figure 3.1, we considered $V_{el} \simeq 40\,\mathrm{mV}$ and

$$S_{V_{el}}(f) = \frac{S_{\Delta_x}(f)}{4} \tag{3.17}$$

Extra continuous discharge noise In the electrostatic budget includes an allocation for an unmodeled TM acceleration noise caused by continuous discharge (see Section 3.2.2) with power spectral density

$$S_g^{CD} = \left(1\,\mathrm{fm/s^2/\sqrt{Hz}}\right)^2 \left(\frac{0.1\,\mathrm{mHz}}{f}\right)^2 + \left(0.2\,\mathrm{fm/s^2/\sqrt{Hz}}\right)^2 \tag{3.18}$$

3.2 LPF heritage

The precursor mission LISA Pathfinder successfully demonstrated that effective charge management could be achieved with a system that relies on photoelectric charge transfer between the TM and EH surfaces under illumination by UV light[4]. Mercury-vapor lamps were the UV-light sources chosen for LISA Pathfinder.

3.2.1 TM charging processes

If the test masses are captured by the Grabbing, Positioning and Release Mechanism (GPRM), they are electrically grounded via the spacecraft. However, once the TMs are released, they are electrically floating and subjected to the environmental charging.

First of all we must notice that the release itself of the test mass deposits a significant charge on the test mass (in the range $-10\,\mathrm{mV}$ to $-500\,\mathrm{mV}$ for LISA Pathfinder data) as reported in [40]. The current explanation for the large TM charge induced by the release is the triboelectric charging due to breaking of the adhesion between the GPRM fingers and the test mass at release.

Once the test masses are released the expected dominant sources of charging are [41]

- A permanent background of *cosmic rays* of galactic origin (mainly protons and light nuclei). The flux of cosmic rays is modulated by the 11-years-long solar cycle: when the solar activity is at its minimum, the interplanetary magnetic field, which acts as a shield, is at its weakest and, hence, the flux of cosmic rays is expected to increase. In other words, the cosmic ray flux in the inner solar system is anti-correlated with the solar activity [42].

[4] It is remarkable to notice that in order to build a working gravitational wave observatory in space to test the so-far-glorious theory of General Relativity devised by Albert Einstein, we need to exploit the photoelectric effect, which is completely unrelated to General Relativity apart for the fact that Einstein himself gave its theoretical explanation, which granted him the physics Nobel prize in 1921.

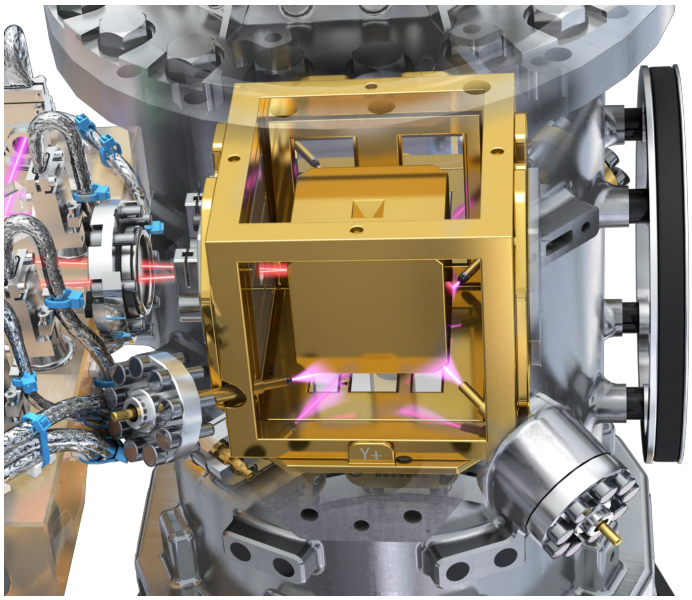

FIGURE 3.2: Rendering of a LISA Pathfinder GRS. It is possible to see the optical fiber vacuum feedthroughs (ISUK) that shine UV-light into the GRS for charge management. Adapted from [14].

- *Solar energetic particles* (SEP) events: temporary increases in the flux of high-energy particles (primary protons) originating from solar eruptions. The number of SEP events is correlated with the solar activity. The number of typical SEP events is estimated to be $10-20$ per year. The effect of such events is increasing momentarily, but significantly, the charging rate on the LISA test masses. Extraordinary[5], although rare (one every 60 years), SEP events are possible and expected to cause the charging rate on the TM to increase by several orders of magnitude with respect to that induced by cosmic rays [41, 43].

The detailed models behind the TM charging require as inputs precise estimates of the galactic cosmic rays and SEP fluxes, together with a realistic geometric model of the LISA spacecraft. Moreover the physics of the interaction of high-energy particles with the spacecraft materials is quite complicated. Indeed, as high-energy particles hit the spacecraft a shower of low-energy secondary particles is produced. Several production channels for secondaries particles have been identified and investigated, among them the dominant ones are expected to be ionization by the incident particles and kinetic electron emission [44]. The role of low-energy particles ($E \lesssim 100\,\mathrm{eV}$) is thought to be relevant. The only way to precisely model the environmental charging process is via dedicated numerical simulations.

LISA Pathfinder also measured accurately the properties of the environmental charging process, in the assumption that it has a Poissonian nature. Let us introduce two quantities, which are useful to characterize the properties of environmental charging, namely the *net charging rate* and the *effective charging rate*[6], which are defined as

$$\lambda_{net}^{env} = \sum_j j\lambda_j \qquad \text{and} \qquad \lambda_{eff}^{env} = \sum_j j^2\lambda_j. \tag{3.19}$$

[5]The most extreme may cause malfunctioning of electronic equipment also on the surface of the Earth.

[6]The effective charging rate is important because it determines PSD of the noise on the physical quantity that is described as a Poisson process.

TABLE 3.1: Net and effective charging rates at neutral TM measured by LPF [36].

Quantity	Symbol	TM1	TM2	Units
Net charging rate	λ_{net}^{env}	$+22.9$	$+24.5$	s^{-1}
Effective charging rate	λ_{eff}^{env}	1060 ± 90	1360 ± 130	s^{-1}

The index j runs over all integer numbers and represents the *multiplicity*, i.e. the number of elementary charges carried by each charging event. LPF measured (at neutral TM) the values reported in Table 3.1. Net and effective charging rate do not coincide because the environmental charging is composed by a positive and a negative current, which oppose one another, and because events with multiplicity larger than unity are possible.

Detailed simulations to estimate the TM charging rate have been performed for LPF [45] and showed a good estimate for the net charging rate, but underestimated the effective charging rate of about a factor three. The mismatch between measured and expected λ_{eff}^{env} is still under investigation with more refined simulations that trace subatomic particles (in particular electrons) down to energies lower than 100 eV [43], which are the suspected culprits for the measured excess in LPF.

3.2.2 Discharge strategies

Two alternative strategies have been envisioned to keep the test masses charge under control during the LISA mission. The first one is known as the *intermittent*, or *fast discharge* and it entails letting the test mass accumulate environmental charge until a threshold is reached (currently this limit is $1.5 \cdot 10^7\, e$, or 70 mV, which corresponds to approximately a couple of weeks of science operation under the reasonable cosmic ray charging rate of $25\, e/s$), and then discharging it quickly ($\sim$ minutes) with UV-light. In LISA Pathfinder the intermittent discharge was the default strategy to control the test mass charge. However, in LISA one would like to keep the gaps[7] in the science data at a minimum. Indeed, during the fast discharge the LPF data are polluted by transients[8] and extra noise[9], causing an unavoidable degradation of the instrument performance.

To solve this issue a second charge management strategy, namely the *continuous discharge*, was proposed. As the name suggests, in continuous discharge scheme UV-light is shone at all times on the test masses. The illumination pattern is accurately chosen to have an equilibrium potential close to neutrality. As the environmental net charging rate λ_{net}^{env} due to cosmic rays and solar energetic particles is positive, we need a negative photocurrent at neutral TM to ensure an effective charge management.

The LISA noise budget [12] allocates a maximum TM acceleration noise due to electrostatic forces and charge management in the *continuous discharge mode*. During the *fast discharge* procedure we may violate the mission requirements (3.6) and (3.7), causing a temporary interruption in the science data taking. On the other hand, the

[7] Or, rather, the time windows in which the data quality is degraded.

[8] From (3.5), a rapid variation in the TM potential from the threshold value $+70$ mV to -70 mV would cause a force step of approximately 0.2 pN if $\Delta_x \simeq 5$ mV, which corresponds to an acceleration step of $\sim 0.1\, pm\, s^{-2}$ (clearly detectable in LISA).

[9] An illumination with high UV power induces Poissonian charge fluctuations, which is converted into force noise with the (3.5). This is related to the discrete nature of charge transfer (see Chapter 5 for the full details).

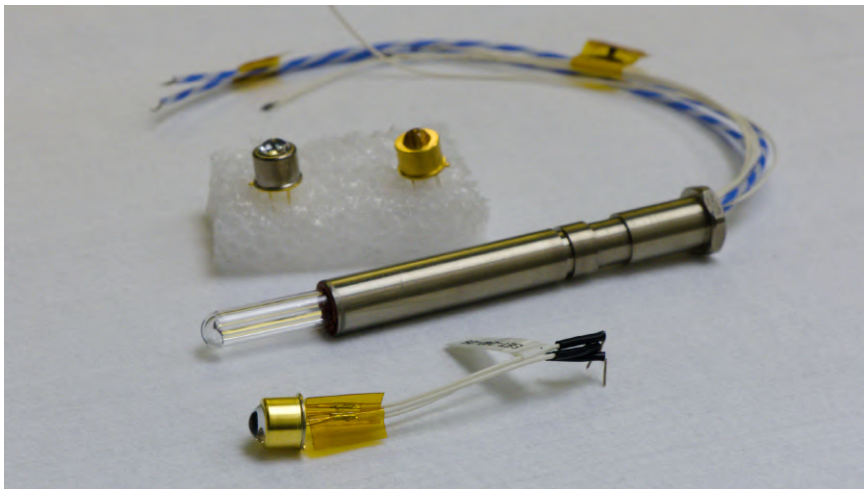

FIGURE 3.3: Form factor comparison between a mercury-vapor lamp used in LISA Pathfinder and the UV-LEDs currently tested for LISA.

continuous discharge mode must be compatible with the previous top level mission requirements.

3.2.3 New UV-sources for LISA

LPF proved that mercury-vapor lamps are valid light sources for the management of the test mass charge. However, for LISA, it is currently envisioned to use UV-LEDs, since they are expected provide great advantages in terms of weight, volume, and power saving without compromising on the reliability[10].

More importantly, the photon emission from UV-LEDs follows quasi instantaneously to the driving current, allowing them to produce pulses of light that can be synchronized with the 100 kHz-polarization voltage which biases the TM for capacitive sensing [49, 50, 51].

In this way, one can choose to illuminate the GRS surfaces when it is most favorable in terms of TM polarization and configuration of the surrounding electrostatic fields due to both injection and (possibly) actuation.

The possibility of choosing the phase of the illumination provides with flexibility in the discharge strategy, allows to tune finely the equilibrium voltage and, finally, makes the Charge Management System overall more robust[11].

Finally, we would like to comment on the feasibility of continuously discharging the test masses. Although the continuous discharge strategy is, in principle, possible[12]

[10] A mass lifetime testing of candidate UV-LEDs for LISA has been conducted at the University of Florida [46]. The results indicate that UV-LEDs can fulfill all requirements of the LISA UV-light sources. Previous studies on a smaller sample size reached the same conclusion [47] and suggest that UV-LEDs can withstand high levels of ionizing radiation typical of the space environment [48].

[11] With the pulsed illumination the only condition we need to discharge the TM is that the EH emits some photo-electrons. Adjusting phase of the illumination or the DC fields, we can block the photo-electrons emitted form the TM and thus achieve a net negative current. A more robust CMS means that the requirements for the emission properties of the GRS surfaces can be relaxed and still be able to obtain a negative UV equilibrium potential.

[12] As stated previously the continuous discharge strategy can work only if the equilibrium potential of the illumination is negative to ensure a current opposing to cosmic rays at neutrality. This depends on the emission properties of the TM and inner surfaces of EH. Such properties cannot be kept entirely under control during manufacturing and storage of the sensor and they could be quite different from expected: in LPF the continuous discharge experiment could be performed only with one of the two GRSs.

with UV lamps, as showed in LPF [52], it is greatly eased by the adoption of LEDs as the LISA UV-sources for the reasons stated previously.

3.3 Apparent yield measurements

3.3.1 Qualitative behavior of the LISA Charge Management System

The LISA sensor can be seen as a capacitor with two plates: the test mass and the electrode housing. The illumination with UV-light generates a charge transfer, i.e. a current, via the photoelectric effect. We consider the photo-current to be positive when elementary charges reach the test mass (i.e. when electrons leave the TM) and negative when elementary charges leave the TM (i.e. when electrons reach the TM).

In LISA we expect the cosmic rays to charge the test masses positively, so the Charge Management System needs to generate a net negative current at neutral test mass.

As shown in Figure 3.4, a net negative current can be achieved by illuminating the electrode housing with the corresponding ISUK: in this way photo-electrons are emitted from the EH and propagate towards the TM. Even if the majority of UV-photons is absorbed by the electrode housing when we illuminate with the EH ISUK, a fraction is inevitably reflected towards the TM, where such photons are absorbed and may extract photoelectrons. Therefore, even if we illuminate the electrode housing, we still have a (typically smaller) photo-current with opposing sign (from the TM to the EH).

A similar reasoning holds for TM illumination, albeit the dominant current this time is from the TM towards the EH, as we depict in Figure 3.5.

From the Einstein equation for the photoelectric effect, we expect that the maximum kinetic energy of the emitted photoelectrons is equal to the energy of the incoming photons minus the work function of the emitter

$$E_{max} = \frac{hc}{\lambda_{UV}} - W \tag{3.20}$$

As the work function of the gold surfaces is of the order $\sim 5\,\mathrm{eV}$ and the energy of the UV-light sources is also in the same ballpark, we expect that the maximum kinetic energy of the emitted electrons to be $\sim 1\,\mathrm{eV}$. This means that a potential barrier of the order $\sim 1\,\mathrm{V}$ between the surface emitting and the one collecting the electrons may have a critical impact on the magnitude of the photo-currents described previously. Such potential barrier arises not only from the DC and AC actuation voltages that may be applied locally to the actuation/sensing electrodes, but also from the overall test mass potential itself (EH is grounded), i.e.

$$V_{TM}(t) = \frac{Q_{TM}(t)}{C_{tot}} + \frac{C_{inj}V_{inj}}{C_{tot}} \sin\left(2\pi f_{inj} t\right) + \frac{1}{C_{tot}} \sum_i C_i V_i(t) \tag{3.21}$$

where the summation runs over all EH electrodes that with their potential may polarize the TM apart from the injection electrodes, whose effect has been explicitly isolated in the second term. We have to notice that the actuation scheme for LISA, inherited from LPF, does not polarize significantly the TM, hence the last term is usually negligible.

In order to understand the qualitative behavior of the net photocurrent as a function of the TM potential, let us consider two extreme cases

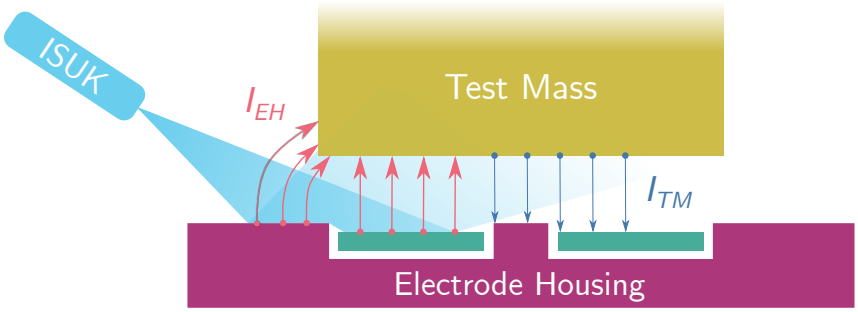

(A) Qualitative scheme showing the UV-light injected into the GRS and the photo-electron trajectories for EH illumination

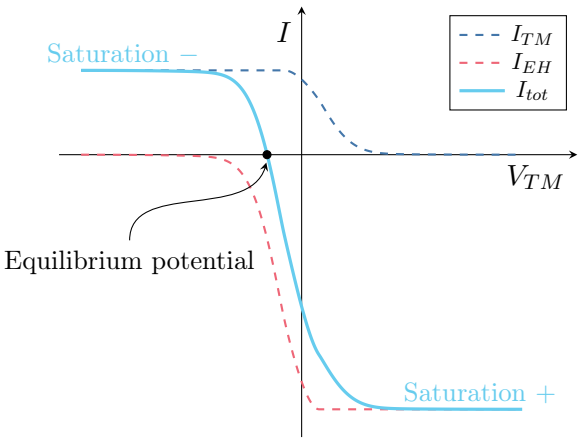

(B) Expected qualitative functional dependence of the photocurrents from the test mass potential for EH illumination

FIGURE 3.4: Qualitative behavior of the photocurrents for illumination with the ISUK pointing towards the EH.

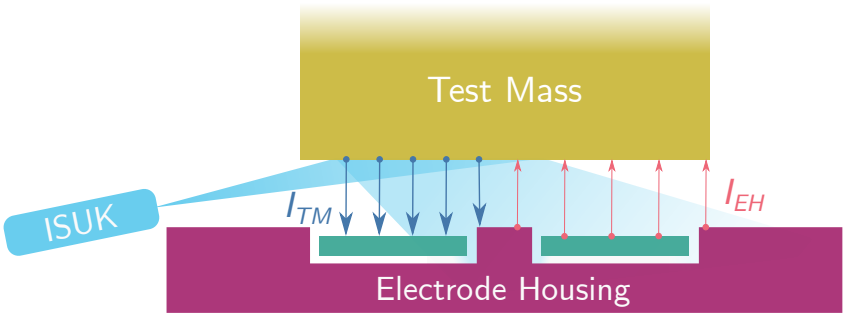

(A) Qualitative scheme showing the UV-light injected into the GRS and the photo-electron trajectories for TM illumination

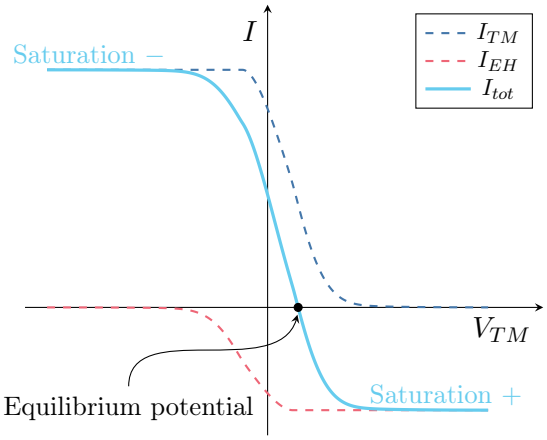

(B) Expected qualitative functional dependence of the photocurrents from the test mass potential for TM illumination

FIGURE 3.5: Qualitative behavior of the photocurrents for illumination with the ISUK pointing towards the TM.

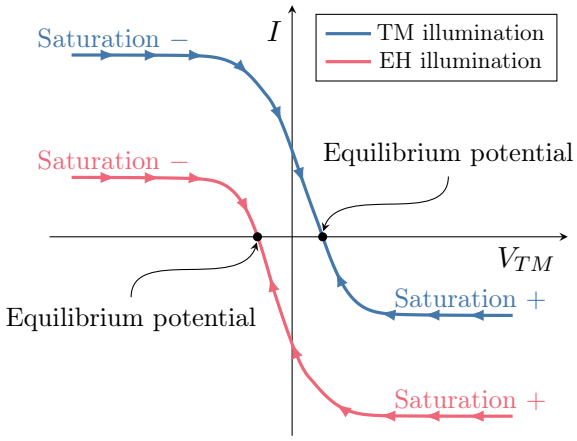

FIGURE 3.6: Comparison of the expected photocurrent for EH and TM illuminations as a function of the test mass voltage.

- If the test mass potential tends to very large positive values ($V_{TM} \to +\infty$), we have that all photo-electrons emitted from the TM encounter a very large potential barrier and do not reach the EH, whereas all photo-electrons emitted from the EH are attracted by the electrostatic field of the TM, where they are collected. This case is defined *positive saturation* as the EH current saturates to its maximum value and the TM current is completely suppressed.

- On the other hand, if the test mass potential assumes very large negative values ($V_{TM} \to -\infty$), we have that all photo-electrons emitted from the TM are pushed towards the EH, whilst the electrons emitted from the EH are blocked by the large potential barrier. This situation is called *negative saturation* since the TM photo-current reaches it maximum value and the EH current vanishes.

For intermediate TM potentials, we expect to have a mixture of the opposing photocurrents. See the bottom panels of Figures 3.4 and 3.4, where we plot the qualitative behavior of the TM and EH photocurrents.

No matter which is the TM charge at the start of the UV illumination, it will evolve with time under the effect of the photocurrents, until a steady state is reached: the potential at which this happens is called *equilibrium potential*, because it realizes the equilibrium between the opposing EH and TM currents.

From equation (3.21), we see the test mass potential is modulated by the polarization effect of injection bias. If we manage to shine UV-light with a specific delay with respect to the zero-crossing of the injection, the discharge behavior will be altered because the photocurrents critically depend on the instantaneous TM potential, as argued previously. Therefore, the effect of a synchronized illumination with the injection bias is a critical aspect to be experimentally investigated.

3.3.2 Charge management instrumentation

In this section we will briefly describe the specific hardware used for the apparent yield measurements in our laboratory. See Figure 3.7b for a general scheme of the experimental apparatus.

In our torsion pendulum it is installed a flight model replica of the LISA Pathfinder electrode housing which is fully representative in terms of geometry and surface finishing. The test mass hosted inside the EH and connected to the torsion pendulum inertial member has also the same geometry and surface finishing of the LISA Pathfinder TM, but it is hollow.

Two ISUKs identical to the baseline[13] one in LPF are mounted on the torsion pendulum: one points the TM corner and the other the EH. They are mounted with the same inclination angle as in LPF (see Figure 3.8).

Our setup differs from LPF because the iridium fingers of the caging mechanism are not installed. This difference is expected not to be critical, because iridium seems to have very low emissivity, as showed by direct measurements at the University of Modena [53].

The capacitive readout and actuation of our GRS is provided by the ELM-light unit, an engineering model of the LPF front-end electronics. This unit is a realistic copy of the LPF-FEE in terms of noise and performance. Moreover, it provides the same DC and AC actuation patterns on the electrodes.

Here we will not discuss the Charge Management System currently being developed for LISA, as it is quite more complicated as it requires a high level of redundancy,

[13] One of the EH ISUK designed for LPF was modified with a small mirror-like optical element.

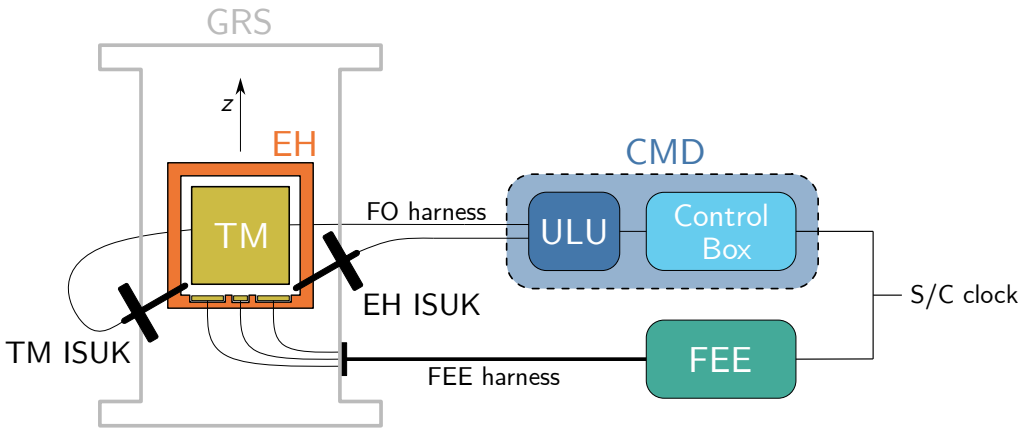

(A) GRS hardware relevant to charge management in LISA

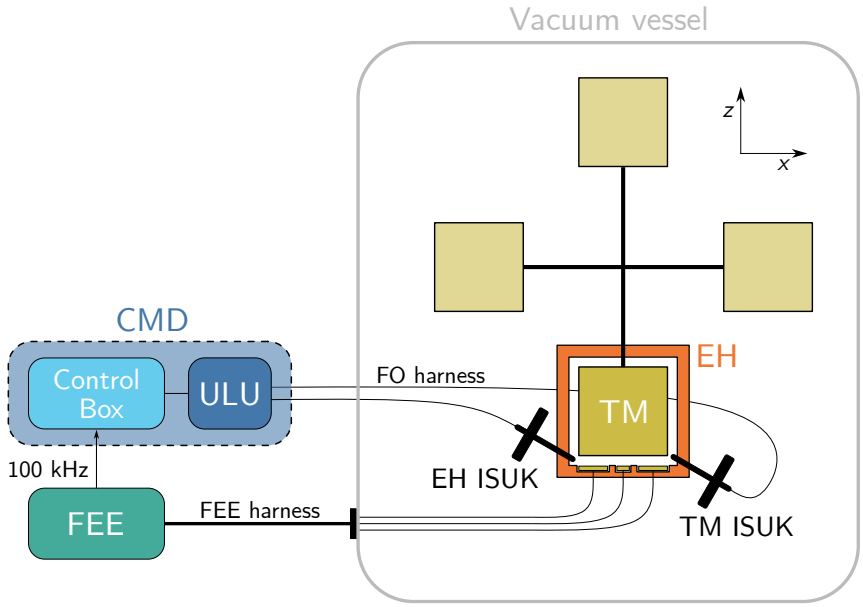

(B) Hardware relevant for the Charge Management System testing campaign with the 4TM torsion pendulum

FIGURE 3.7: Comparison between the Charge Management System hardware for LISA and the one used for our experimental testing campaign with the 4TM torsion pendulum.

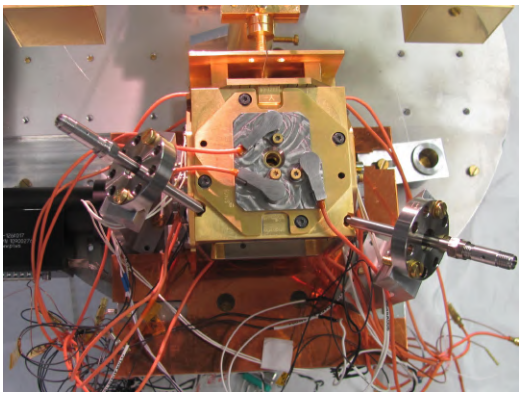

(A) ISUKs positioning from y^- face

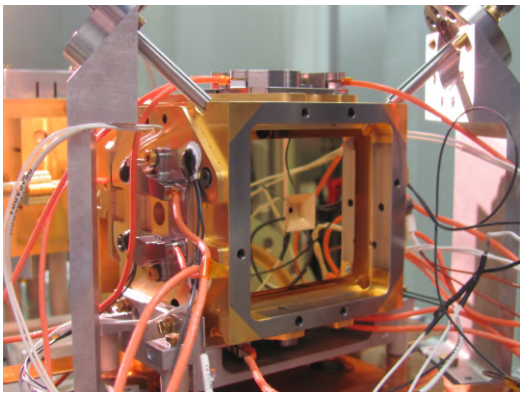

(B) ISUKs positioning from z^- face

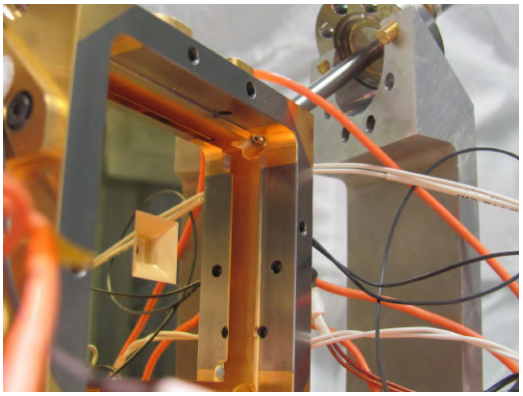

(C) Detail of the TM ISUK

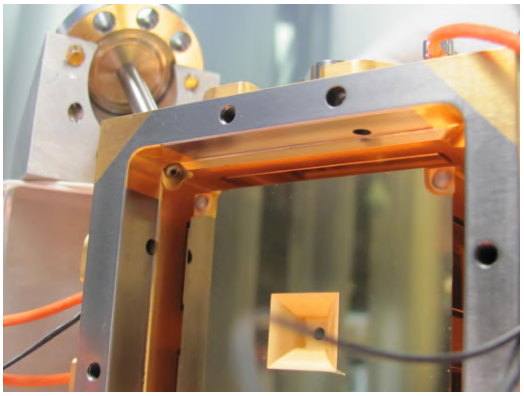

(D) Detail of the EH ISUK

FIGURE 3.8: ISUK positioning in the 4TM torsion pendulum.

but rather we will discuss the setup specific for our experimental campaign. We will state, however, where our apparatus differs from what is currently planned for LISA.

Charge Management Device

The central component of the Charge Management System (CMS) is the Charge Management Device (CMD), that is the unit that controls and generates the UV light needed for the photoelectric charge transfer between EH and TM. It is composed by a programmable control box and by the UV light sources themselves, contained in the UV-Light Unit (ULU).

The charge management device (CMD) used for this work is a prototype manufactured by the INFN/Roma Tor Vergata group (see Figure 3.9). The prototype CMD is composed of a control box and several separated UV units, each containing a LED. In this way with just one electronics, we can control several light sources. The control box contains an FPGA, programmable via a software interface and the electronics needed to drive one LED at the time (single output). The prototype CMD has two modes

- *Continuous light mode*: a programmable DC current is sent to the LED. The light power emitted by the LEDs scales with the current.
- *Pulsed light mode*: bursts of current are sent to the LEDs, which as a result produce pulses of light. As shown in Figure 3.10, the user can control the duration and delay of the pulsed with respect to an input reference (which is in

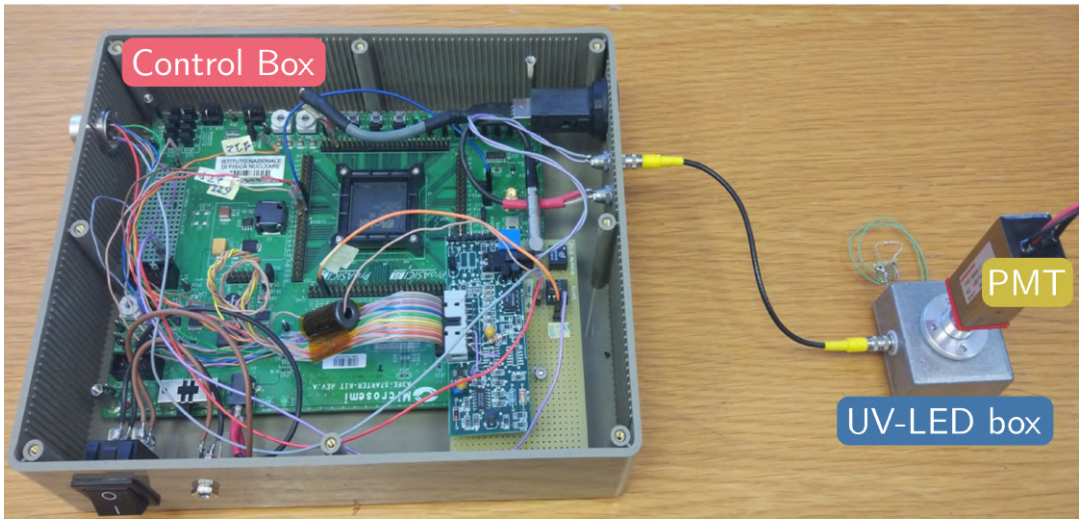

FIGURE 3.9: Prototype charge management device provided by the INFN/Roma Tor Vergata group. The control box contains a FPGA to program the duration, delay and decimation of the light pulses. Separate units contain each a UV-LED and can be connected to the control box with a LEMO cable. In this picture a PMT is directly connected to the LED, but this configuration is never used in our measurements: we always connected LEDs and power sensitive device through the short optical fiber.

our case is the FEE injection bias). Moreover, one can set a decimation, that is the number of cycles of the reference in which the illumination is skipped between a light pulse and the subsequent. In the pulsed mode it is not possible to control the current flowing through the LED during the pulses due to limitations of the electronics[14]: the current is always the maximum allowed, that is approximately 32 mA.

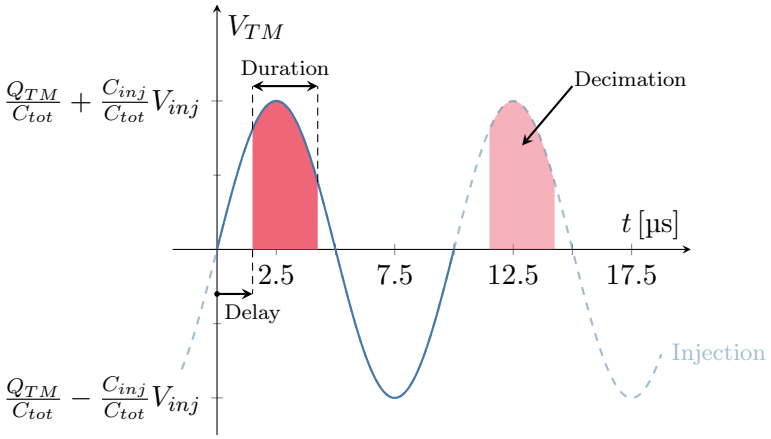

FIGURE 3.10: Parameters that can be controlled for the illumination with UV-LEDs.

The University of Florida provided us with the TRL4 prototype CMD with similar (or better) features [54]. We conducted only few and preliminary tests with this unit,

[14] An updated version of the prototype INFN/Roma Tor Vergata CMD added the possibility of setting a specific current across the LEDs also in the pulsed light mode.

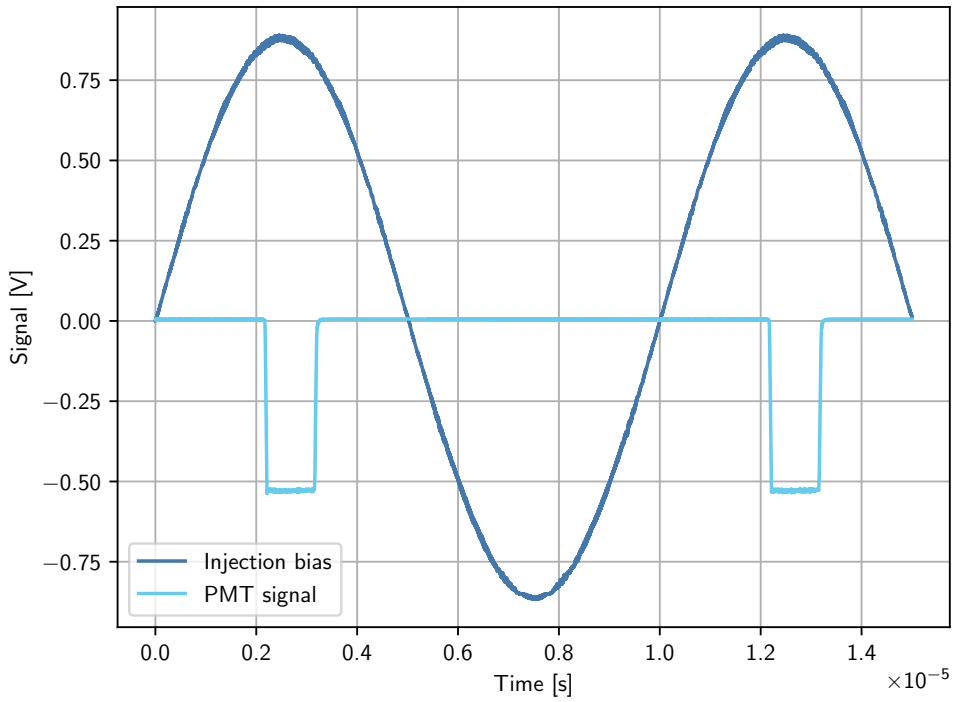

FIGURE 3.11: Oscilloscope measurement of the light pulses for the UV-LED Crystal 250. The cyan data is the UV-light intensity measured by a calibrated PMT (whose signal is negative if some light is detected). In this case the chosen illumination pattern has a duration of 1 µs and a nominal delay of 2 µs (one can observe however a further systematic delay of about 0.2 µs). To obtain a cleaner signal the oscilloscope is operated in the waveform averaging mode.

TABLE 3.2: Peak wavelength and full width at half maximum (FWHM) of the UV-sources spectra.

UV-source	Peak wavelength [nm]	FWHM [nm]
Hg-lamp	253.64	0.04
Crystal 250	249.97	10.43
SETi 255	258.71	9.88
SETi 240	247.15	10.28
UVphotonics 230	233.78	11.04

because of some problems in measuring accurately the UV power in the pulsed setting mode when the number of pulses per second was reduced[15].

Our current prototypes of CMD connect directly to the front-end electronics (through the "plunger") to get the 100 kHz-injection bias that they use as a reference for the pulsed-light mode.

This will not be the case for LISA, since it is not advisable to connect directly FEE and CMD from a noise and risk mitigation perspective. Therefore, as shown in Figure 3.7a, the LISA charge management device will receive a clock signal common for all spacecraft instruments (including FEE), which may be either a pulse per second (PPS) or a signal in the MHz-frequency band (this aspect is still being discussed). Systematic phase-delays may be arise due to the fact that both FEE and CMD have to generate their own 100 kHz-injection bias signal.

Light sources

In the experimental campaign we focused on UV-LEDs as light sources for the CMD. Four different models of UV-LEDs are available in our laboratory

- OPTAN-250J-BL, which we will call Crystal 250 from now on, produced by Crystal IS, Inc.
- SETi 255 produced by Sensor Electronic Technology, Inc.
- SETi 240 produced by Sensor Electronic Technology, Inc.
- UVphotonics 230 produced by the German company UVphotonics.

A heritage engineering model of the LISA Pathfinder UV-light unit (ULU) based on Hg-lamps was also employed for some preliminary and testing measurements, but the data quality is not particularly good (we wanted to repeat some of the measurements but, after some years of disuse, the Hg-lamps failed to emit any light).

The spectra of our UV-light sources obtained with our AvaSpec-ULS2048XL-EVO spectrometer are displayed in Figure 3.12.

The LEDs spectra over a wider range of wavelengths have also been acquired by our INFN/Roma Tor Vergata colleagues and there are hints that at low driving

[15]Indeed with the TRL4 unit of the University of Florida it is possible to control the number of pulses per second instead of the decimation: the maximum number of pulses is, of course, $10^5\,s^{-1}$, which corresponds to no decimation (a light pulse every cycle of the 100 kHz-injection bias). If the number of pulses per second is reduced, the pulses are produced at every cycle of the injection until the desired value is reached, and then the LED stays off for the rest of the time until the full second is reached. As our way to measure the UV power consists of making the difference between the DC signal when the light is on and off ("darks & lights"), we do not have a clean light signal because the LED keeps switching on and off with a period of one second, which for us is a pretty short timescale with respect to sampling rate of our facility, i.e. 10 Hz.

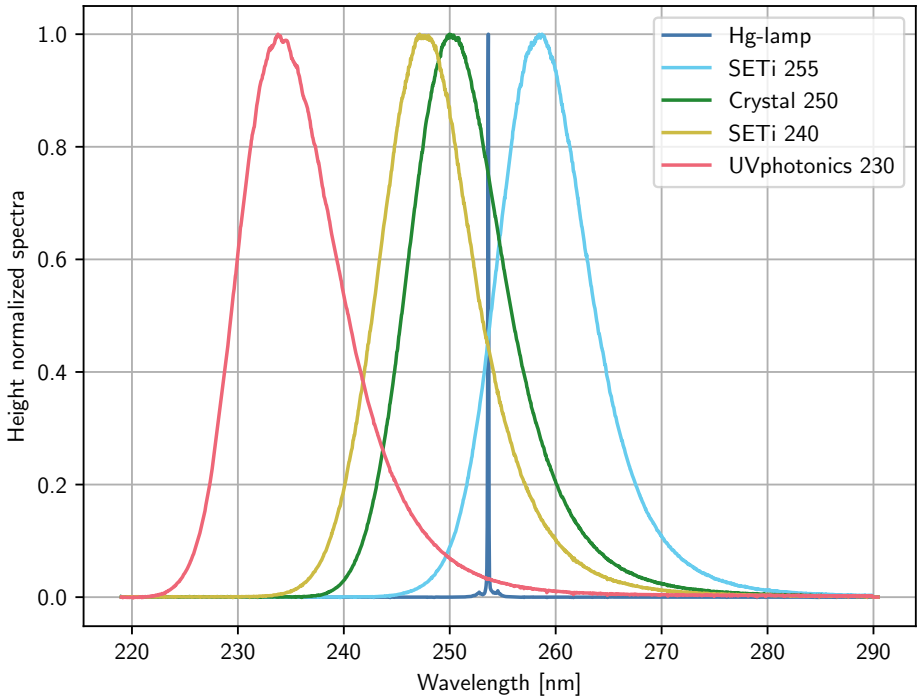

FIGURE 3.12: Spectra of the UV-light sources normalized to have unit height for an easier comparison.

currents, the LEDs may emit a fraction of their light at larger wavelengths. This effect is particularly evident for the SETi 255 LED as shown in Figure 3.13 and it may be due to the fact that at low currents the LEDs may be operating outside their optimal range (i.e. on the "knee" of its current voltage characteristics instead of the linear region). This may have minor consequences in the apparent yield estimate, as a fraction of the measured UV power lies at photon energies that are too low to extract photoelectrons[16].

UV-power measurement devices

The assessment of the UV-light power during the illuminations is critical for the apparent yield measurements, that will be presented in the remainder of the chapter.

In our laboratory we have three instruments to measure the light power:

- *Hamamatsu S1337-1010BQ*: uncalibrated photodiode (PHD) with in-house readout circuit. The photodiode is the heritage power measuring device used in our laboratory since 2014.
- *Hamamatsu H6780-03*: uncalibrated PMT module with integrated power supply. We paired it with the Hamamatsu C6438-01 amplifier. It is characterized by a fast response to follow the time evolution of the light pulses.

[16]This fact should not impact excessively our apparent yield measurements, as they were all taken in the pulsed mode (to control the power, we used mainly the decimation). Indeed, in the pulsed mode the current across the LEDs due to limitations of the CMD prototype cannot be controlled and it is the maximum possible, that is 32 mA. The LED emission at longer wavelengths may have an impact on the continuous-light measurements performed at low driving current, i.e. low power (mainly calibration measurements of the photodiode or measurements of the optical fibers transmission).

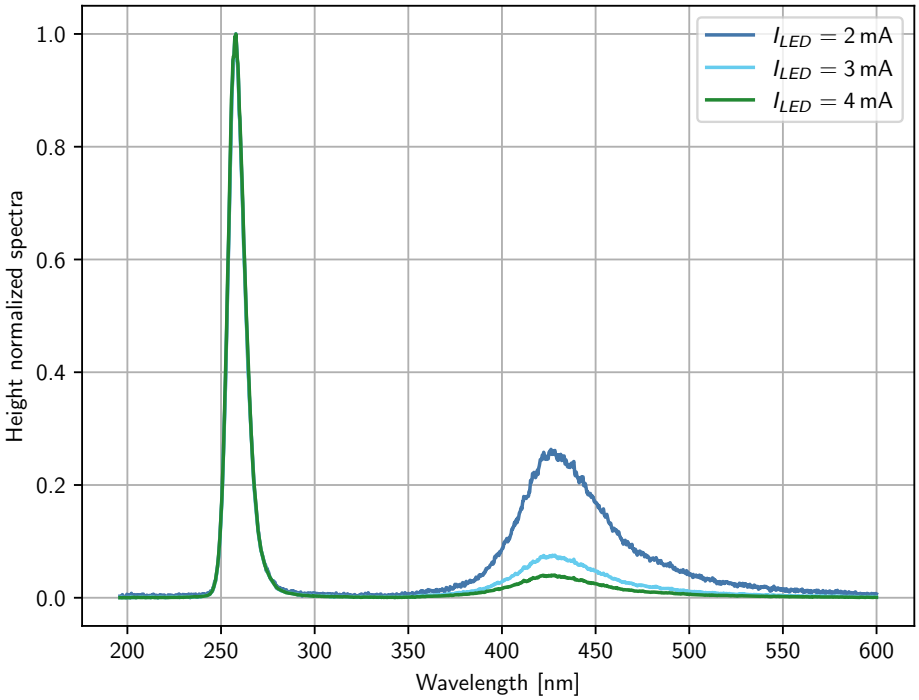

FIGURE 3.13: Spectra of the SETi 255 LED at low driving current. A secondary peak at $\sim 425\,\mathrm{nm}$ is visible. Credits to the INFN team at Roma Tor Vergata.

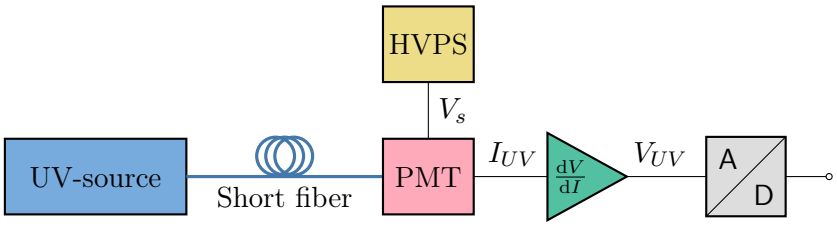

FIGURE 3.14: The Hamamatsu R9875U PMT system: the gain is controlled by the V_s provided by a high-voltage power supply. The anode current I_{UV} is converted by the amplifier into a voltage signal V_{UV}, which is acquired with our ADC.

- *Hamamatsu R9875U*: calibrated PMT. It is paired with the Hamamatsu E13643 PMT socket, the Hamamatsu C12789 high-voltage power supply, and the Hamamatsu C6438 amplifier. The time resolution of the system is $\lesssim 7\,\text{ns}$. We acquired this PMT at the beginning of 2021. A scheme of the full PMT setup is depicted in Figure 3.14.

The preferred instrument to measure the UV light power is the Hamamatsu R9875U, as it is factory calibrated. The measured anode radiant sensitivity for our device is

$$s_{cal} = \frac{\mathrm{d}I}{\mathrm{d}P}(\lambda_{cal}, V_{cal}) = 2.11 \cdot 10^4\,\mathrm{A\,W^{-1}} \tag{3.22}$$

The calibration was performed at a wavelength of 253.7 nm with a total potential difference between the dynodes (supply voltage) of $V_{cal} = 1000\,\text{V}$. However, for the power range of interest for our experiments ($0.1 - 100\,\text{nW}$), we needed to lower the potential drop across the dynodes to 600 V, otherwise we would saturate the output amplifier during the measurements at the maximum LED power. The Hamamatsu PMT handbook [55] reports the following formula to rescale the PMT radiant sensitivity as a function of the supply voltage

$$s(V_s) = s_{cal} \cdot \left(\frac{V_s}{V_{cal}}\right)^{kn} \tag{3.23}$$

where n is the number of dynodes (in our PMT model $n = 10$) and k is a parameter depending on the their material and typically has values between 0.7 and 0.8. A power law fit of the form

$$s(V_s) = s_0 \cdot \left(\frac{V_s}{1000\,\text{V}}\right)^{10k} \tag{3.24}$$

on the PMT output as a function of the supply voltage for a constant UV-power, returns the optimal parameters $s_0 = (2.14 \pm 0.13) \cdot 10^4\,\text{A/W}$ and $k = 0.787 \pm 0.004$ (see Figure 3.15a). Using this relation we could scale the PMT anode radiant sensitivity for a supply voltage of 600 V.

Secondly, we applied a correction to the radiant anode sensitivity due to the non-monochromatic spectrum of our LEDs. Indeed, as one can see in Figure 3.15b, the nominal radiant anode sensitivity of the PMT is not constant in the wavelength range of interest. In order to find the correct radiant anode sensitivity, we need to average it over the spectra of our LEDs

$$\langle s \rangle = \frac{s_{cal}}{s_{DS}(\lambda_{cal})} \frac{\int s_{DS}(\lambda) \cdot f_{UV}(\lambda)\,\mathrm{d}\lambda}{\int f_{UV}(\lambda)\,\mathrm{d}\lambda} \tag{3.25}$$

where $s_{DS}(\lambda)$ is the radiant anode sensitivity interpolated from the data sheet and $f_{UV}(\lambda)$ is the emission spectrum of the UV-source considered.

The prefactor $s_{cal}/s_{DS}(\lambda_{cal})$ is there to rescale the data sheet sensitivity at the wavelength $\lambda_{cal} = 253.7\,\text{nm}$ to the number actually measured at calibration.

Finally, in order to find the average response function, we need to include the role of the amplifier Hamamatsu C6438, which is basically a current-to-voltage converter with a bandwidth from DC to 50 MHz, with a conversion factor $\frac{\mathrm{d}V}{\mathrm{d}I} = 1000\,\text{V A}^{-1}$ if connected high-impedance load (as our ADC is).

Putting all together, we have that the transfer function from signal to UV-power of the PMT can be found as

$$\begin{aligned} H_{V\to P}(\lambda, V_s) &= \frac{\mathrm{d}P}{\mathrm{d}V}(\lambda, V_s) \\ &= \frac{\mathrm{d}I}{\mathrm{d}V} \cdot \frac{\mathrm{d}P}{\mathrm{d}I}(\lambda, V_s) \\ &= \left(\frac{\mathrm{d}V}{\mathrm{d}I}\right)^{-1} \left[\frac{s_{cal}\cdot s_{DS}(\lambda)}{s_{DS}(\lambda_{cal})} \left(\frac{V_s}{V_{cal}}\right)^{kn}\right]^{-1} \end{aligned} \tag{3.26}$$

Or, when averaging over the UV-sources spectra

$$\begin{aligned} \langle H_{V\to P}(V_s)\rangle &= \left\langle \frac{\mathrm{d}P}{\mathrm{d}V}(V_s) \right\rangle \\ &= \frac{\mathrm{d}I}{\mathrm{d}V} \cdot \left\langle \frac{\mathrm{d}P}{\mathrm{d}I}(V_s) \right\rangle \\ &= \frac{\left(\frac{\mathrm{d}V}{\mathrm{d}I}\right)^{-1}}{\langle s\rangle \left(\frac{V_s}{V_{cal}}\right)^{kn}} \end{aligned} \tag{3.27}$$

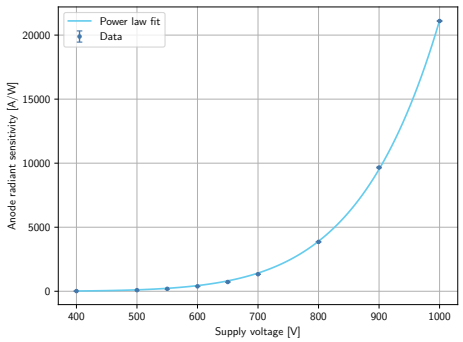

(A) Measured radiant anode sensitivity as a function of the supply voltage across the dynodes. Superimposed to the data is a power law fit.

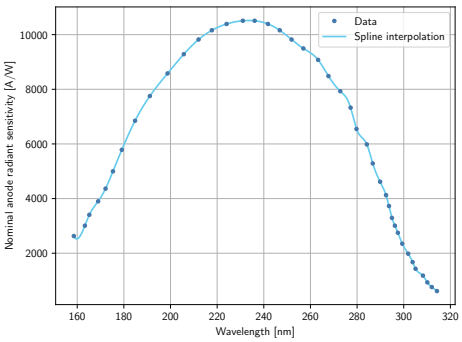

(B) Nominal radiant anode sensitivity as a function of the wavelength of the incident light. Data have been extracted and then interpolated from the PMT data sheet.

FIGURE 3.15: Spectral response and measured gain of the calibrated Hamamatsu R9875U PMT.

For the first part of the experimental campaign, only the photodiode was available, as we acquired the calibrated PMT only at the beginning of 2021. We re-calibrated *a posteriori* the photodiode with respect to the PMT R9875U.

The photodiode and its in-house readout circuit, are not an ideal measurement device, because its sensitivity is not great and the output signal shows trends and

TABLE 3.3: Calibration coefficients of PMT and photodiode.

UV-source	Calibrated PMT [V/W]	Photodiode [V/W]
Hg-lamp	$(3.80 \pm 0.04) \cdot 10^5$	$(9.3 \pm 0.4) \cdot 10^4$
Crystal 250	$(3.84 \pm 0.04) \cdot 10^5$	$(1.08 \pm 0.05) \cdot 10^5$
SETi 255	$(3.62 \pm 0.04) \cdot 10^5$	$(7.60 \pm 0.18) \cdot 10^4$
SETi 240	$(3.91 \pm 0.04) \cdot 10^5$	$(9.0 \pm 0.3) \cdot 10^4$
UVphotonics 230	$(4.08 \pm 0.04) \cdot 10^5$	$(1.87 \pm 0.09) \cdot 10^5$

instabilities[17]. Moreover, as shown in Figure 3.16, the ADC resolution itself limits our sensitivity as the photodiode signal is centered around approximately $-0.8\,\mathrm{V}$ and the typical signal induced by UV-light is $\sim$ mV (we could not lower the ADC full-scale to appreciate better the small variations over the background).

The calibrated PMT proved to be a much more reliable choice, saved for a small hysteresis [55] when measuring high light intensity.

Power measurements The experimental procedure for the power measurements consists in exposing periodically the power sensitive device either to the UV-light source or to a dark cavity. Such procedure is informally called "darks & lights". Samples of the UV-power signal V_{UV} are obtained as the difference between consecutive light and dark levels. There are two modalities for executing the "darks & lights"

- *On-off method*: the light and dark level are obtained by switching on and off the LED, without removing the short fiber.
- *Attach-detach method*: the LED is kept on at all times and we intermittently connect the short fiber either to the light source or to a distinct dark cavity.

As argued in Section 3.4.3, the loose machining of in-house SMA connectors on the LED housing, caused a variability of $\sim 8\%$ on average in the light injected in the fiber, whenever it was detached and re-attached to the LED. Hence, the on-off method tends to underestimate the uncertainty on the UV-power as it does not sample the effect of detaching the fiber to the LED housing. Sadly, for convenience the on-off method was used for most apparent yield measurements in 2019 and 2021, because we did not realize the issues related to the unreliability of the connections until mid 2020.

Spectrometer We also have a compact spectrometer AvaSpec-ULS2048XL-EVO produced by the company Avantes B.V. to measure the emission spectra of the LEDs in the range $220 - 290\,\mathrm{nm}$. The measurements of the spectra of our specific light sources proved to be very useful.

Fiber optic harness

The optical fibers and vacuum feedthroughs installed in our facility have been supplied by the company MDC Vacuum Limited EU, now MDC Precision. The fibers used are designed to be used with UV light (wavelength range $180 - 1200\,\mathrm{nm}$) and have single core made of high purity silica with a diameter of $600\,\mu\mathrm{m}$. The nominal attenuation coefficient at 248 nm is less than $< 1.2\,\mathrm{dB\,m^{-1}}$). The fibers are rated for optical powers way higher than our application (up to $100\,\mathrm{kW\,m^{-2}}$).The outer fibers are

[17] Such instabilities may be related to temperature fluctuations or to loose electrical connections.

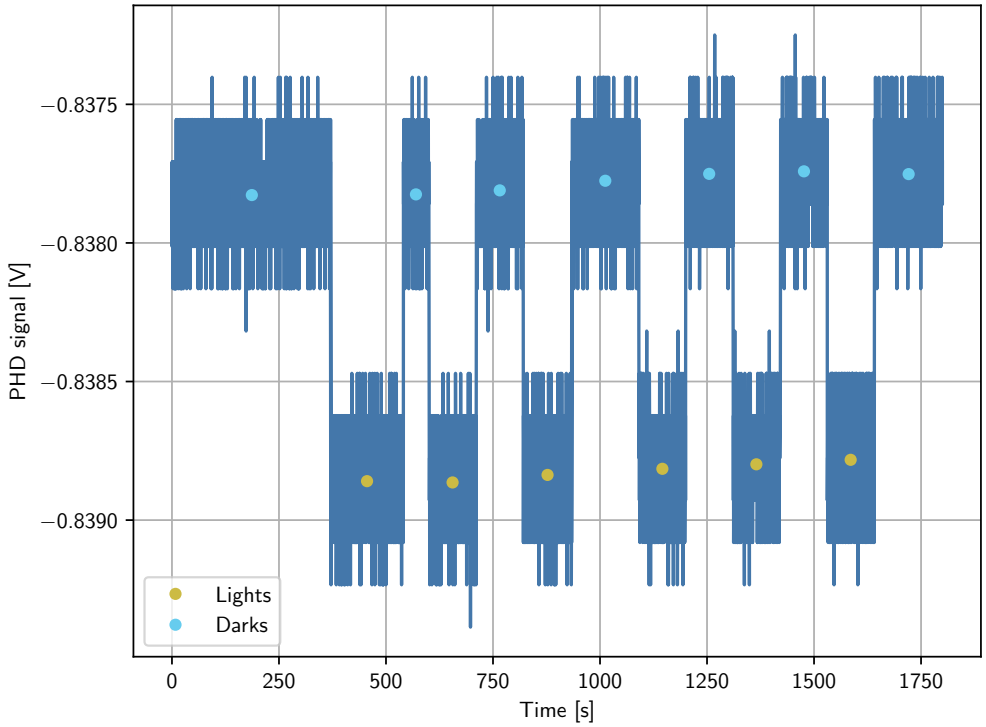

FIGURE 3.16: Example of a set of "darks & lights" with the photodiode. The UV-power signal samples are obtained by the difference of the dark and light levels, which in turn are estimated averaging the signal over stretches of $\sim 100\,\mathrm{s}$ duration. Subsequently the UV-power signal samples are obtained by the difference of the dark and light. The accuracy of the low-power measurements with the photodiode are limited by the ADC resolution.

(A) Short fiber configuration for the power measurements

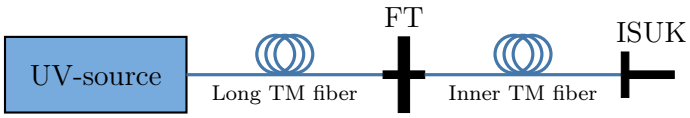

(B) Optical chain for TM illuminations

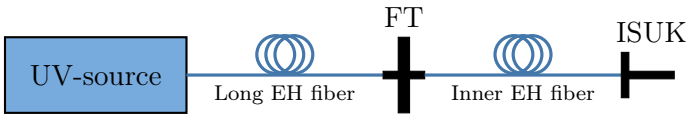

(C) Optical chain for EH illuminations

FIGURE 3.17: Optical fiber configurations in our experimental setup.

armored for extra durability. At the flange of the vacuum vessel we have ultra-high-vacuum optical feedthroughs always supplied by MDC Vacuum and equipped with SMA-905 connectors. The inner optical fiber terminates into an exact replica of the LISA Pathfinder ISUK, which is also in the same geometric position as LPF ISUK JF01 (*TM illumination*) and ISUK JF02 (*EH illumination*). A scheme of the TM and EH optical chains is depicted in Figure 3.17.

As we shall see, the apparent yield measurements presented later in this chapter require to know the optical power injected into the GRS. Therefore, we need to estimate the transmission coefficient of the optical fiber chain. Such characterization can be performed in the following way. Assume that the UV source emits a constant, but unknown, power P_{source}. When the short fiber is connected between source and a photosensitive device, such as a photodiode or a PMT, we would measure

$$P_{SF}^{meas} = \alpha_{SF} \cdot P_{source}, \tag{3.28}$$

where $0 \leq \alpha_{SF} \leq 1$ is the transmission coefficient of the short fiber. This is the configuration for the power measurements (see Figure 3.17). If the whole TM optical chain is now connected to the photosensitive device (of course the same applies for the EH chain as well) while the source power is kept constant, we would measure

$$P_{TM}^{meas} = \underbrace{\alpha_{TM,out} \cdot \alpha_{FT} \cdot \alpha_{TM,in} \cdot \alpha_{ISUK}}_{\alpha_{TM}} \cdot P_{source}. \tag{3.29}$$

If we combine the previous equations, we can estimate the transmission coefficients ratio directly from the ratio of the measured powers

$$a_{TM} = \frac{\alpha_{TM}}{\alpha_{SF}} = \frac{P_{TM}^{meas}}{P_{SF}^{meas}} \tag{3.30}$$

Once the transmission coefficients have been obtained with dedicated measurements, we can estimate the power at the GRS as

$$P_{TM} = \alpha_{TM} \cdot P_{source} = \frac{\alpha_{TM}}{\alpha_{SF}} P_{SF} = a_{TM} \cdot P_{SF} \tag{3.31}$$

Obviously a similar relation hold for EH illuminations as well

$$P_{EH} = a_{EH} \cdot P_{SF} \qquad \text{where} \qquad a_{EH} = \frac{\alpha_{EH}}{\alpha_{SF}} \tag{3.32}$$

We have to notice that we assumed that the absorption coefficient of the fibers is independent of the wavelength, at least in the range of emission of our UV sources ($220 - 280\,\text{nm}$).

The transmission of the complete TM and EH optical fiber chains, has been quickly measured at integration in 2014 (more careful measurements would have been preferable).

The fiber setup is not entirely representative for LISA. It is currently planned to use fiber bundles for LISA to carry the UV-light from the nominal and redundant LEDs to the corresponding ISUK. We recently acquired a representative fiber bundle built by the company Molex/Fiberguide but we still have to integrate it on the torsion pendulum.

Comment for outer fiber substitution During our years-long experimental campaign the external fibers have been substituted. Here we will explain how the transmission coefficients can be corrected for the new fibers without having to re-characterize the whole optical chain (which would require to open the vacuum vessel). See Table 3.4 for a list of the recent transmission coefficients.

If, for example, the long external TM fiber and the short fiber have been substituted, we just need to estimate the new transmission ratio between the new short fiber and the new TM long fiber[18]

$$\begin{cases} \tilde{P}^{meas}_{SF} = \tilde{\alpha}_{SF} \cdot P_{source} \\ \tilde{P}^{meas}_{TM,out} = \tilde{\alpha}_{TM,out} \cdot P_{source} \end{cases} \longrightarrow \quad \frac{\tilde{\alpha}_{TM,out}}{\tilde{\alpha}_{SF}} = \frac{\tilde{P}^{meas}_{TM,out}}{\tilde{P}^{meas}_{SF}} \tag{3.33}$$

The new absorption ratio can be found re-scaling the old absorption ratio by the characteristics of the new fibers

$$\tilde{a}_{TM} = \frac{\tilde{\alpha}_{TM,out} \cdot \alpha_{FT} \cdot \alpha_{TM,in} \cdot \alpha_{ISUK}}{\tilde{\alpha}_{SF}} = \frac{\tilde{\alpha}_{TM,out}}{\tilde{\alpha}_{SF}} \frac{\alpha_{SF}}{\alpha_{TM,out}} a_{TM} \tag{3.34}$$

where used the fact that the transmission ratio of the original short and outer TM fiber $\alpha_{SF}/\alpha_{TM,out}$ has been measured at integration in a similar way as described in (3.33). Of course an equivalent relation may be applied if the EH fiber is substituted as well

$$\tilde{a}_{EH} = \frac{\tilde{\alpha}_{EH,out} \cdot \alpha_{FT} \cdot \alpha_{EH,in} \cdot \alpha_{ISUK}}{\tilde{\alpha}_{SF}} = \frac{\tilde{\alpha}_{EH,out}}{\tilde{\alpha}_{SF}} \frac{\alpha_{SF}}{\alpha_{EH,out}} a_{EH} \tag{3.35}$$

3.3.3 Definition of apparent yield

As the number of photo-electrons extracted scales with the number of photons that are absorbed by the emitting surface, if we normalize the observed photo-currents by the UV power during the illumination, we obtain a quantity that it is independent of the light power itself. This is the idea behind the definition of the quantity known as *apparent yield*.

The apparent yield $\mathcal{Y}$ is defined as the net number of elementary charges that are deposited on the TM per photon injected in the GRS. Obviously, the definition does

[18] We indicate with a superscript tilde the quantities relative to the new fibers.

TABLE 3.4: Transmission coefficients of the TM and EH optical chains over the years.

Quantity	2014	2019	2021	2023
a_{TM}	0.218 ± 0.003	0.203 ± 0.006	0.171 ± 0.003	0.253 ± 0.005
a_{EH}	0.211 ± 0.004	0.179 ± 0.009	0.209 ± 0.006	0.407 ± 0.010
$\frac{\alpha_{TM,out}}{\alpha_{SF}}$	0.977 ± 0.010	0.91 ± 0.02	0.765 ± 0.008	1.133 ± 0.009
$\frac{\alpha_{EH,out}}{\alpha_{SF}}$	0.721 ± 0.010	0.61 ± 0.03	0.714 ± 0.007	1.387 ± 0.004

not change if we consider both of these quantities per unit time

$$\mathcal{Y} = \frac{\#\text{ charges}}{\#\text{ photons}} = \frac{\#\text{ charges/s}}{\#\text{ photons/s}} \tag{3.36}$$

The apparent yield is a photo-electron current normalized by light power and, naturally, is an useful quantity to estimate the performance of a Charge Management System based on photo-emission.

The charge rate can be rephrased as

$$\#\text{ charges/s} = \frac{1}{e}\frac{\mathrm{d}Q_{TM}}{\mathrm{d}t} = \frac{C_{tot}}{e}\frac{\mathrm{d}V_{TM}}{\mathrm{d}t}. \tag{3.37}$$

If we consider, for the moment, that the light is *monochromatic*, the number of photons injected into the GRS per unit time is

$$\#\text{ photons/s} = \frac{P_{UV}}{E_{UV}} = \frac{P_{UV}}{\frac{hc}{\lambda_{UV}}} \tag{3.38}$$

where P_{UV} is the true power of the UV light at the ISUK output and E_{UV} is the single photon energy. As we will explain more accurately in the next sections, the measurement of P_{UV} is absolutely crucial to determine the apparent yield.

The power P_{UV} at the GRS can be estimated from the signal of a calibrated photosensitive device V_{UV}, such as a photodiode or a PMT, considering also that a fraction of the light from the source is lost due to absorption in the optical chain. In a formula

$$P_{UV} = a \cdot H_{V\to P}(\lambda = \lambda_{UV}) \cdot V_{UV} \tag{3.39}$$

where $H_{V\to P_{UV}}(\lambda)$ is the spectral response of the photosensitive device (which is in general a function of the photons wavelength), a is the fiber optic harness transmission coefficient[19] from the UV light source to the GRS, and V_{UV} is the output signal of the photosensitive device. Once again, in the case of *monochromatic light* the function $H_{V\to P_{UV}}(\lambda)$ reduces to just a constant calibration factor, which can be indicated as

$$H_{V\to P}(\lambda = \lambda_{UV}) = \left.\frac{\mathrm{d}P}{\mathrm{d}V}\right|_{\lambda=\lambda_{UV}} = \text{const.} \tag{3.40}$$

[19] In general also the transmission coefficient depends on the light wavelength $a = a(\lambda)$. We do not have the spectral dependence of the transmission for our optical fibers, so we consider it to be constant in the range of wavelength of interest. This assumption is reasonable because the transmission coefficients are a smooth function of the wavelength, unless close to absorption edges of the fiber core material.

Therefore, we have that the photon rate (3.38) can be expressed as

$$\begin{aligned} \#\ \text{photons/s} &= \frac{\lambda_{UV}}{hc} \cdot \left(a \left.\frac{\mathrm{d}P}{\mathrm{d}V}\right|_{\lambda=\lambda_{UV}} \right) \cdot V_{UV} \\ &= E_{UV} \cdot \left(a \left.\frac{\mathrm{d}P}{\mathrm{d}V}\right|_{\lambda=\lambda_{UV}} \right) \cdot V_{UV} \end{aligned} \tag{3.41}$$

If we plug (3.37) and (3.41) into the definition of apparent yield (3.36), we get

$$\mathcal{Y} = E_{UV} \frac{C_{tot}}{e} \cdot \frac{\frac{\mathrm{d}V_{TM}}{\mathrm{d}t}}{\left(a \left.\frac{\mathrm{d}P}{\mathrm{d}V}\right|_{\lambda=\lambda_{UV}} \right) \cdot V_{UV}} \tag{3.42}$$

Generalization for non-monochromatic light

If the light sources of the Charge Management System are not monochromatic, as it is for the UV-LEDs that we considered in our experimental campaign, the previous equation must be slightly modified.

Let $f_{UV}(\lambda)$ be the spectrum of the light emitted by the UV source considered[20]. As the spectral response of the photosensitive device is in general not constant, the true light power injected into the GRS is

$$\begin{aligned} P_{UV} &= a \cdot \frac{\int H_{V\to P}(\lambda) f_{UV}(\lambda)\,\mathrm{d}\lambda}{\int f_{UV}(\lambda)\,\mathrm{d}\lambda} \cdot V_{UV} \\ &= a \left\langle H_{V\to P} \right\rangle \cdot V_{UV} \\ &= a \left\langle \frac{\mathrm{d}P}{\mathrm{d}V} \right\rangle \cdot V_{UV} \end{aligned} \tag{3.43}$$

where with $\langle\cdot\rangle$ we denoted the average over the light spectrum. Here we assumed again that the transmission coefficient of the optical fibers a does not depend on the light wavelength, at least in the spectral range of our sources. We also introduced a notation similar to (3.40) for the average spectral response of the photo-detector.

On the other hand, the power injected P_{UV} can be obtained as simply the time derivative of the number of photons N entering the GRS multiplied their mean energy

$$\begin{aligned} P_{UV} &= \frac{\mathrm{d}}{\mathrm{d}t} \left[N \cdot \frac{\int \frac{hc}{\lambda} \cdot f_{UV}(\lambda)\,\mathrm{d}\lambda}{\int f_{UV}(\lambda)\,\mathrm{d}\lambda} \right] \\ &= \frac{\mathrm{d}N}{\mathrm{d}t} \cdot \left\langle \frac{hc}{\lambda} \right\rangle \\ &= \frac{\mathrm{d}N}{\mathrm{d}t} \cdot \langle E_{UV} \rangle \end{aligned} \tag{3.44}$$

where $\mathrm{d}N/\mathrm{d}t$ is the rate of injected photons and $\langle E_{UV} \rangle$ is the average energy of a photon in the spectrum. If we compare (3.43) and (3.44), we have that

$$\frac{\mathrm{d}N}{\mathrm{d}t} = \#\ \text{photons/s} = \frac{a \left\langle \frac{\mathrm{d}P}{\mathrm{d}V} \right\rangle \cdot V_{UV}}{\langle E_{UV} \rangle} \tag{3.45}$$

[20] We do not consider any specific *normalization* for $f_{UV}(\lambda)$.

Unsurprisingly, if we want to estimate correctly the number of photons injected into the GRS per unit time, we have to average both the response of the instrument used to estimate the light power and the energy of the photons emitted by the light source.

Therefore, the expression for the apparent yield (3.42) in the case of a light source which cannot be treated as monochromatic becomes

$$\mathcal{Y} = \langle E_{UV} \rangle \frac{C_{tot}}{e} \cdot \frac{\frac{\mathrm{d}V_{TM}}{\mathrm{d}t}}{a \left\langle \frac{\mathrm{d}P}{\mathrm{d}V} \right\rangle \cdot V_{UV}} \tag{3.46}$$

Parameters that affect the apparent yield

With the geometry of the system fixed to the LISA gravitational reference sensor (in our case), the apparent yield may depend on

- The microscopic photoemission properties of the illuminated surfaces, such as the Fermi energy, work-function, or the quantum yield.
- The photon spectrum of the light source.
- The instantaneous test mass potential during the illumination, which depends not only on the charge deposited on it, but also on the 100 kHz-injection bias, needed for the capacitive sensing

  $$V_{TM} = \frac{Q_{TM}}{C_{tot}} + \frac{C_{inj}}{C_{tot}} V_{inj} \sin(2\pi f_{inj} \cdot t) \tag{3.47}$$

  In this sense, the delay and duration of the synchronized illumination affect the apparent yield just because we shine light when the TM potential is shifted with respect to the pure charge term Q_{TM}/C_{tot} due to the injection-electrodes polarization. In other words, the behavior of the apparent yield does not depend on the TM charge, but only on the difference of potential between TM and EH.
- The configuration of constant and time-varying actuation potentials around the TM.

A very simple photoemission model, which nevertheless proved to be quite accurate in interpreting our data, will be described in Chapter 4.

3.3.4 Experimental procedure

The experimental procedure for a typical apparent yield measurement is described hereafter.

1. Bring the TM potential to large positive or negative values by illuminating in the presence of DC bias to polarize the TM;
2. Turn on the charge measurements by coherently modulating the chosen combination of x-electrodes (see 2.3);
3. Estimate the UV power before the apparent yield measurement with the photodiode or the PMT;
4. Start illuminating either the TM or the EH with the charge measurement on;
5. Stop illuminating when the TM potential is reasonably close to the equilibrium potential;

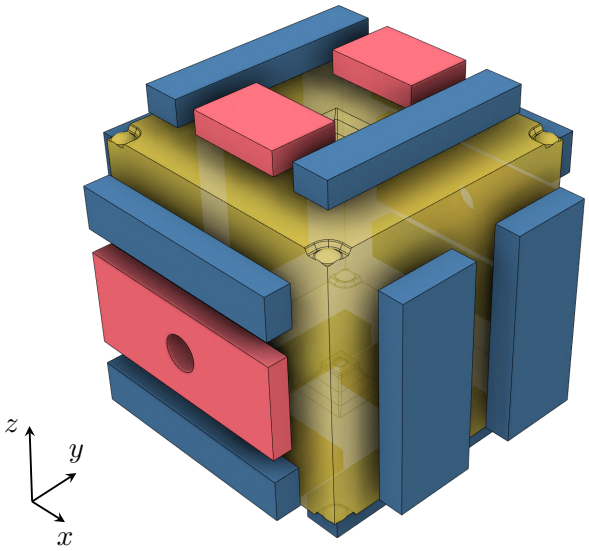

FIGURE 3.18: Scheme of LISA test mass surrounded by the actuation/sensing electrodes (*blue*) and the injection electrodes (*red*).

6. Measure again the UV power after the apparent yield measurement.

Such procedure is repeated for each branch composing an apparent yield measurement, that is from large positive TM potentials (*positive branch*) to the equilibrium and from large negative TM potentials to the equilibrium (*negative branch*).

3.3.5 Data analysis

Once the timeseries of test mass potential has been obtained by coherently demodulating the torque induced by the modulation potentials applied to the x-electrodes. We decided to modulate the x_2^+ and x_2^- electrodes because they are the farthest away from the region where the ISUKs illuminate the GRS (only a small fraction of the UV-photons is absorbed by the x_2^+ and x_2^- electrodes[21]. See Appendix B for the table of the absorption coefficients considered for the torsion pendulum. The charge measurement modulation has a frequency of 5.3 mHz and an amplitude of of 1 V. Even if the frequency of the modulations was significantly above the resonance of the torsion pendulum (whose free period is ~ 1215 s), the instrumental noise was not a limiting factor for our AY measurements, because the charge signal is quite large ($V_{TM} \sim$ V).

As depicted in Figure 3.19, the derivative of the TM potential has been computed by linear fitting non-overlapping sets of n consecutive points[22] of the TM potential timeseries: the slope parameter of the linear fit (and its error) gives a direct estimate of the derivative (and its random uncertainty).

The errorbars in Figure 3.19a include not only the random error due to the pendulum noise at the modulation frequency f_{mod} of the charge measurement, but also systematic uncertainties due to the conversion factors needed to estimate the TM potential from the in-phase torque component at f_{mod} (see Section 2.3). More precisely, the random error due to the pendulum torque noise is set equal to the standard deviation of the quadrature component at f_{mod}. Such way to estimate the random

[21] And so even if the photocurrent emitted from these electrodes is altered by the potentials applied for the charge measurement, it is still small compared to all other sensor surfaces.

[22] The number n, always odd, ranged from 3 to 15 approximately, depending on the duration of the measurement.

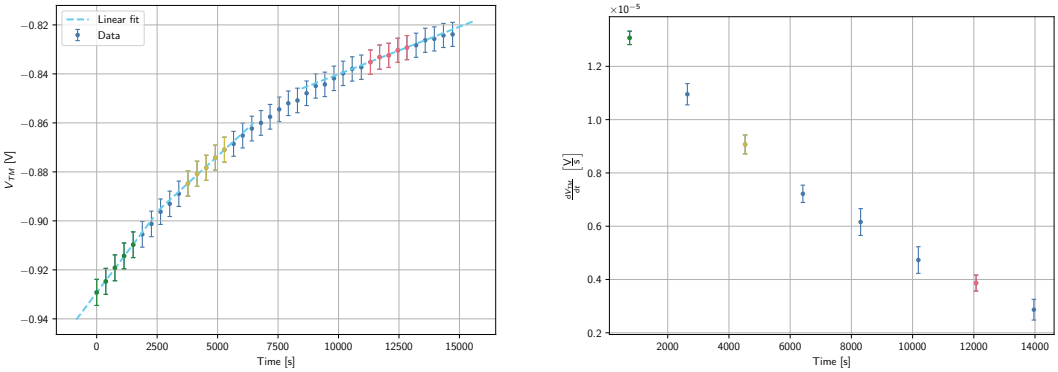

(A) Timeseries of the TM potential V_{TM}

(B) Timeseries of the derivative of V_{TM}

FIGURE 3.19: Visualization of the data analysis procedure to estimate the time derivative of the TM potential: the data is split into non-overlapping stretches of n points ($n = 5$ in the case depicted), and fitted with a linear dependence to estimate the time derivative and its uncertainty from the slope of the fit.

uncertainty is entirely correct only if we are measuring a signal whose amplitude is constant. On the other hand, if the signal amplitude varies with time, it could lead to an overestimate of the actual uncertainty, because some of the signal may leak into the quadrature component (this is especially true if V_{TM} changes rapidly). Anyhow, such possible overestimate does not impact the error on the derivative of the test mass potential, because in the linear fit[23] the data are not weighted by their uncertainty and the error on the parameters is computed from the covariance matrix of the fit. Hence, the errors on the single TM potential points $V_{TM,i}$ do not play any role to determine the uncertainty[24] on the time derivative $\mathrm{d}V_{TM,i}/\mathrm{d}t$.

Once the timeseries of the time derivative of the test mass potential has been obtained, we normalize it by the UV power measured by either the PHD or PMT to compute the apparent yield. In the figures it is customary to plot the apparent yield as a function of the test mass voltage, to give a sort of current-voltage characteristics of the LISA sensor.

The measure of the UV power for each illumination is obtained averaging the dark and light samples.

We remember that the formula for the apparent yield for non-monochromatic light (3.46) is

$$\mathcal{Y}_i = \langle E_{UV} \rangle \frac{C_{tot}}{e} \cdot \frac{\frac{\mathrm{d}V_{TM,i}}{\mathrm{d}t}}{a \left\langle \frac{\mathrm{d}P}{\mathrm{d}V} \right\rangle \cdot \bar{V}_{UV}} \tag{3.48}$$

where we introduced the average signal from the photosensitive device as the arithmetic mean of the dark and lights

$$\bar{V}_{UV} = \frac{1}{N} \sum_{j=1}^{N} V_{UV,j}. \tag{3.49}$$

[23] Provided by the MATLAB function `polyfit` [56].

[24] Only the scatter of the $V_{TM,i}$ points from the "true" slope matters.

The statistical, or random, error on the apparent yield measurements is due to the error on the estimate of the test mass derivative and can be found as

$$\sigma_{stat}\left(\mathcal{Y}_i\right) = \left| \langle E_{UV} \rangle \frac{C_{tot}}{e} \cdot \frac{1}{a \left\langle \frac{\mathrm{d}P}{\mathrm{d}V} \right\rangle \cdot \bar{V}_{UV}} \right| \cdot \sigma \left(\frac{\mathrm{d}V_{TM,i}}{\mathrm{d}t} \right), \tag{3.50}$$

where $\sigma\left(\frac{dV_{TM,i}}{dt}\right)$ indicates the error on the slope parameter of the linear fit. On the other hand, the systematic error is related to the uncertainty in the power measurement

$$\sigma_{syst}\left(\mathcal{Y}_i\right) = |\mathcal{Y}_i| \sqrt{\left[\frac{\sigma(a)}{a}\right]^2 + \left[\frac{\sigma\left(\left\langle \frac{\mathrm{d}P}{\mathrm{d}V} \right\rangle\right)}{\left\langle \frac{\mathrm{d}P}{\mathrm{d}V} \right\rangle}\right]^2 + \left[\frac{\sigma\left(V_{UV}\right)}{\bar{V}_{UV}}\right]^2} \tag{3.51}$$

The uncertainty $\sigma\left(V_{UV}\right)$ can be found as the standard deviation of the dark and light samples

$$\sigma\left(V_{UV}\right) = \sqrt{\frac{1}{N-1} \sum_{j=1}^{N} \left(V_{UV,j} - \bar{V}_{UV}\right)^2} \tag{3.52}$$

We did not use the uncertainty on mean of the dark and light samples, because for each discharge curve, in the moment we connect the long TM or EH fiber, we extract only one possible power from the distribution sampled with the dark and lights (we do not average repeated discharge curves taken at the same illumination setting).

We observe that the systematic uncertainty is proportional to the apparent yield itself, hence it tends to zero as we approach the equilibrium voltage. This is not the case for the random uncertainty, which depends on the noise of the charge measurement and hence it is more or less independent of the test mass voltage.

3.3.6 Experimental data

As one can notice from Figure 3.20, the apparent yield experimental campaign has been truly an endeavor lasting almost four years. As anticipated, we considered four different types of LEDs and for each one we acquired data for several illumination patterns. Moreover, we had to withstand and overcome two hardware failures of the Electric Ground Support Equipment (EGSE), i.e. the computer controlling our FEE, and an infamous global pandemic. The effort of such an extensive experimental work has been shared with Giuliana Russano, Antonella Cavalleri and Francisco Rivas.

In the following plots we show the apparent yield curves as a function of the measured TM voltage[25]. The statistical uncertainty on the data is represented by the errorbars (which is usually quite small), whereas the systematic uncertainty is represented by the shaded area.

For each UV-LED and in the case of both TM and EH illumination, we generally acquired apparent yield curves in the following settings

- Duration 10 µs and no delay (100%-duty cycle) with low injection voltage ($V_{inj} = 0.54\,\mathrm{V}$);

[25] Actually, as evident from (2.95), we measure not just the potential on the TM due to charge, but also terms related to the stay biases on the electrodes. There may be, therefore, a systematic offset on the x-axis of all plots. As the DC bias in our sensor are quite small, we expect this offset to be of the order $\sim 10 - 50\,\mathrm{mV}$.

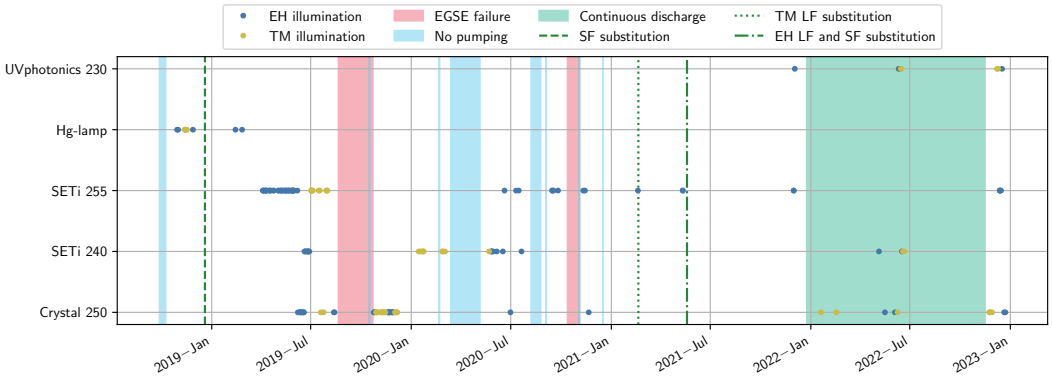

FIGURE 3.20: Timeline of the apparent yield experimental campaign: the red and cyan bands corresponds to periods where we could not acquire data because either the FFE was inoperative, or because the pumping of the vacuum vessel was interrupted (we never vented to atmosphere, just closed the gate valve between pump and vacuum vessel). The green band corresponds to the time dedicated to the *continuous discharge* measurement campaign (see Section 5).

- Duration 10 µs and no delay (100%-duty cycle) with nominal injection voltage[26] ($V_{inj} = 5.4\,\mathrm{V}$);
- Duration 1 µs and delay 2 µs (10%-duty cycle, *in-phase*) with nominal injection voltage ($V_{inj} = 5.4\,\mathrm{V}$);
- Duration 1 µs and delay 7 µs (10%-duty cycle, *out-of-phase*) with nominal injection voltage ($V_{inj} = 5.4\,\mathrm{V}$);

The first setting is meant to represent the cleanest measurement: minimal electrostatic fields around the TM and small excursion of the TM voltage due to injection polarization. We did not set the injection voltage to zero, because we still wanted use the combined capacitive sensing of STC and GRS to read the rotation angle of the pendulum during the charge measurements, which grants better noise performance than the autocollimator.

The measurements with pulse duration of 10 µs and nominal 5.4 V injection are aimed at evaluating the smearing effect of illuminating during the whole cycle of the injection.

The measurements with delay 2 µs and 7 µs are meant to evaluate two extreme cases of synchronization with the injection bias: they correspond, respectively, to illuminations almost centered on at the maximum and minimum of the injection potential. As the TM voltage oscillates of $\pm\frac{C_{inj}}{C_{tot}}V_{inj} \simeq \pm 0.6\,\mathrm{V}$ if $V_{inj} = 5.4\,\mathrm{V}$ during the injection cycle, we expect that the apparent yield curves at delays equal to 2 µs and 7 µs to resemble the apparent yield curve at low-injection, but shifted of approximately

[26] In the 4TM torsion pendulum the injection voltage is slightly larger than in LISA Pathfinder ($V_{inj}^{LPF} = 4.88\,\mathrm{V}$) to compensate the extra capacitance due to the pendulum shaft. In this way the potential induced on the TM by the injection bias is approximately the same, i.e.

$$V_{inj}\frac{C_{inj}}{C_{tot}} \simeq V_{inj}^{LPF}\frac{C_{inj}}{C_{tot}^{LISA}} \simeq 0.6\,\mathrm{V}. \tag{3.53}$$

$\pm 0.6\,\mathrm{V}$ respectively[27]. In Figure 3.21, we show the equilibrium voltage as a function of the delay for pulses of $1\,\mu\mathrm{s}$ duration for the Crystal 250 LED. The equilibrium potential does not depend on the power of the UV light, but just on the illumination pattern, and the properties of the surfaces.

We notice that by controlling the phase of the illumination, we can achieve a bipolar discharge (negative equilibrium potential for TM illumination and positive for EH illumination), with clear advantages in terms of the robustness of the Charge Management System. Indeed, as the net environmental charging is expected to be positive, it is important that we can achieve a negative photocurrent at $V_{TM} = 0\,\mathrm{V}$ for the TM illumination channel as well, in the (very unlikely) case that both EH illumination channels[28] fail during the mission. In this way we add a further level of redundancy to the CMS.

The Figures from 3.22 to 3.24 show the apparent yield data in the case of TM and EH illumination for the LEDs considered in the first part (2019-2021) of the testing campaign.

Overall the data in the case of EH illumination do not seem to reach complete saturation for high test mass voltages: this may be due to geometry effect. Indeed, the geometry of the GRS is such that the electrode housing surrounds completely the TM, hence, at neutral TM, most of the electrons emitted by the TM will reach the EH. On the other hand, only a fraction of the electrons emitted from the EH will ballistically reach the TM at $V_{TM} \simeq 0\,\mathrm{V}$. However, if V_{TM} increases, a larger fraction of the electrons emitted will land on the test mass, because their trajectories will be deviated by the electrostatic field due to the TM charge.

In Figure 3.25 we compare the apparent yield curves for TM illumination with a pulse duration of $1\,\mu\mathrm{s}$ and a delay of $2\,\mu\mathrm{s}$ for three LEDs discussed up to now. We see that the saturation levels increase when considering light sources with higher mean photon energy. We notice that not all data series follow this expected behavior, because our UV-power measurements is not always very reliable (for more details in Section 3.4).

We acquired the UVphotonics 230 LED at the end of 2021 and we did only few measurements. It is the LED with the highest average photon energy available. The power measurements for the AY data of UVphotonics 230 have been performed with the new PMT. For the data with UVphotonics 230 LED, it is not possible to compare directly the apparent yield at saturation with the other light sources, because the measurements were taken in 2022, around two years after the other measurements presented so far. Indeed in 2020-2021, we noticed a change in the saturation levels for all light sources (see Section 3.4.2 for more details and a possible explanation). Taken this into account, the UVphotonics 230 still gives the largest apparent yield, which is expected as it has the highest mean photon energy.

[27] The shift of exactly $\pm 0.6\,\mathrm{V}$ is an upper limit and would be possible if we illuminated with pulses of very small duration centered on precisely the maximum or minimum of the injection voltage. As the considered light pulses have a duration of $1\,\mu\mathrm{s}$, we expect the shift to be smaller than $\pm 0.6\,\mathrm{V}$. Other factors, that make the data deviate from the ideal case, are:

- There is a contribution to the photocurrent from the injection electrodes (especially true for the case of EH illumination);
- Geometry and border effects.

[28] As in LPF, the LISA GRS will be equipped with a nominal and redundant ISUK pointing towards the EH. On the other hand, there will only be one ISUK pointing towards the TM.

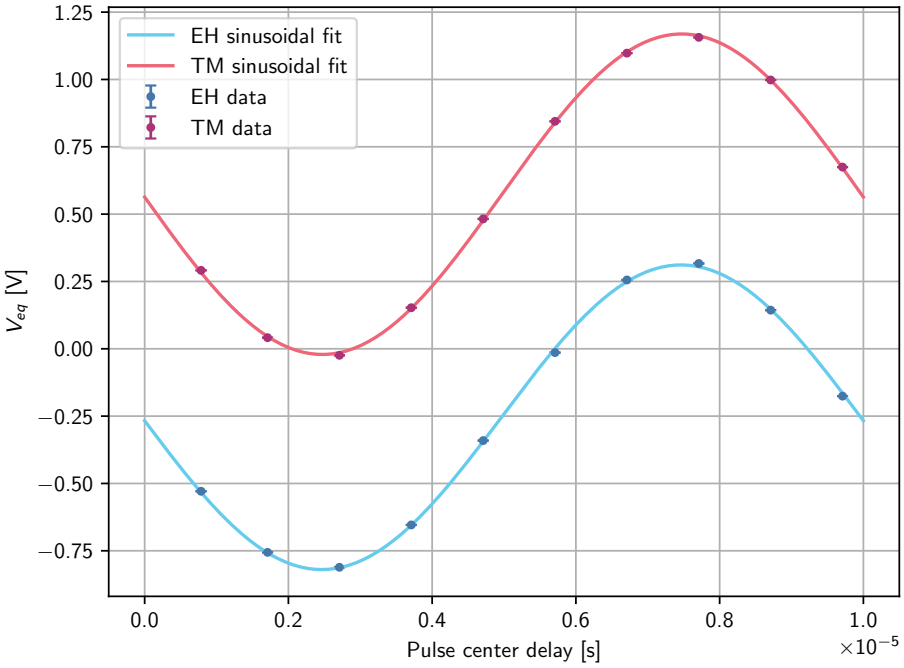

FIGURE 3.21: Dependence of the equilibrium voltage on the phase of the illumination with the Crystal 250 for light pulses of 1 µs duration. An empirical sinusoidal fit has been performed on the data and the resulting amplitude is (0.566 ± 0.004) V for EH illumination and (0.595 ± 0.003) V for TM illumination.

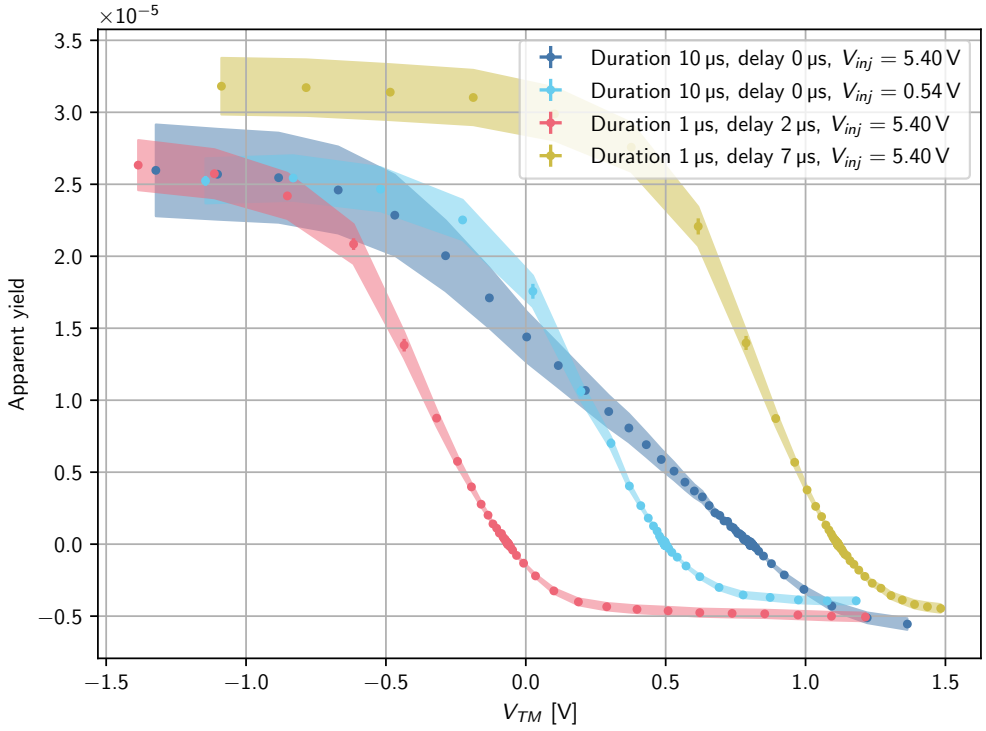

(A) TM illumination

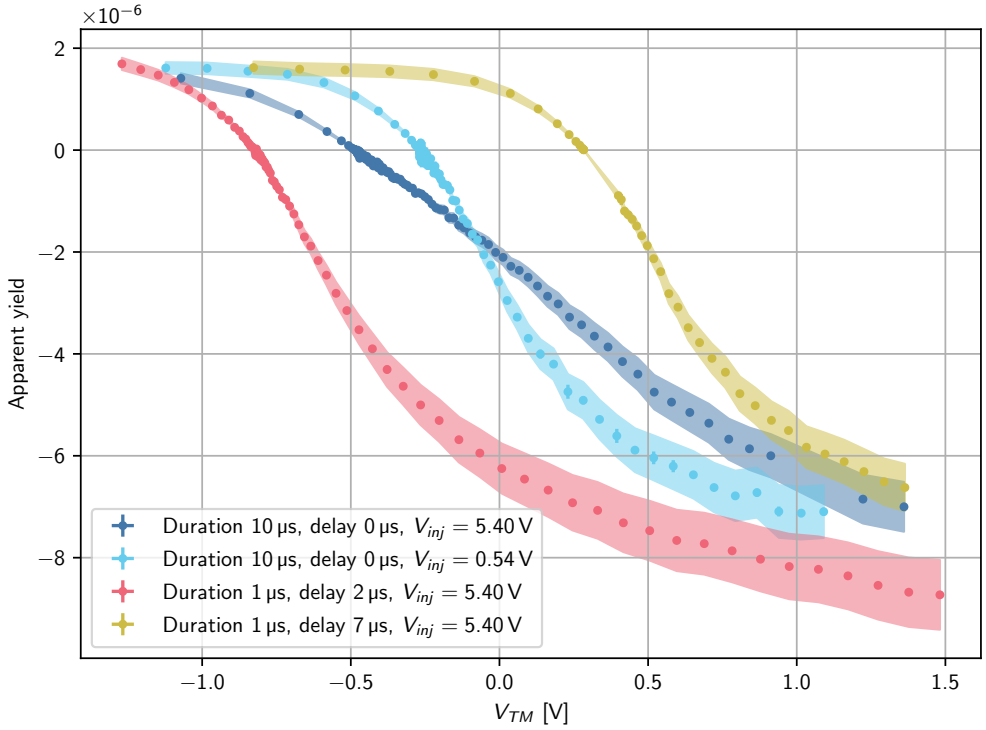

(B) EH illumination

FIGURE 3.22: Crystal 250 apparent yield data.

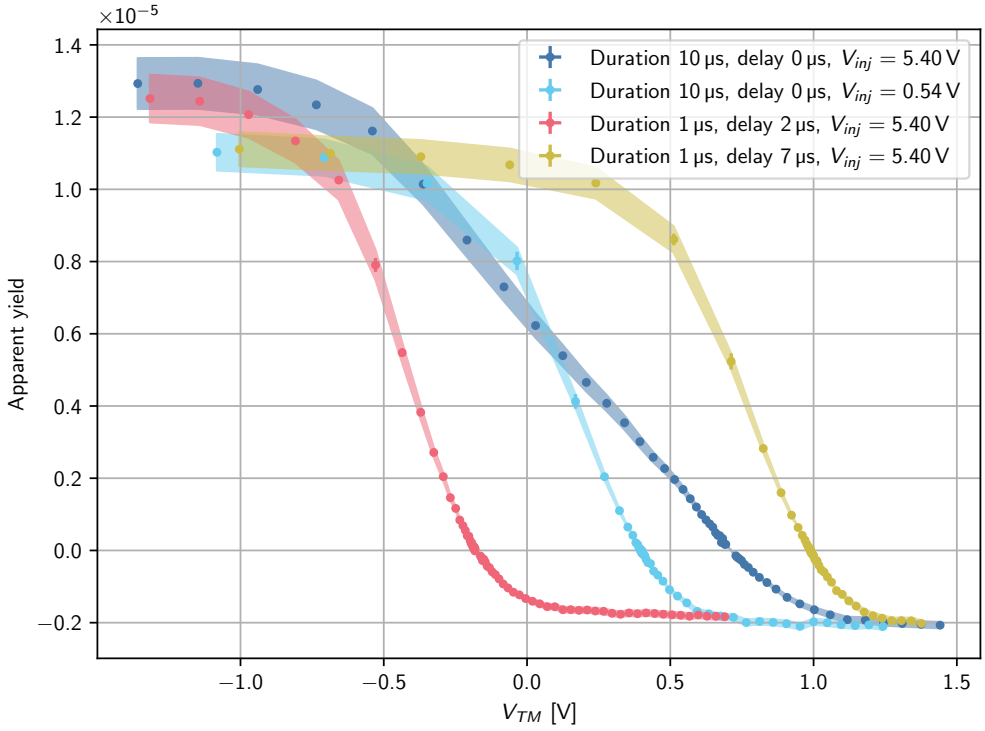

(A) TM illumination

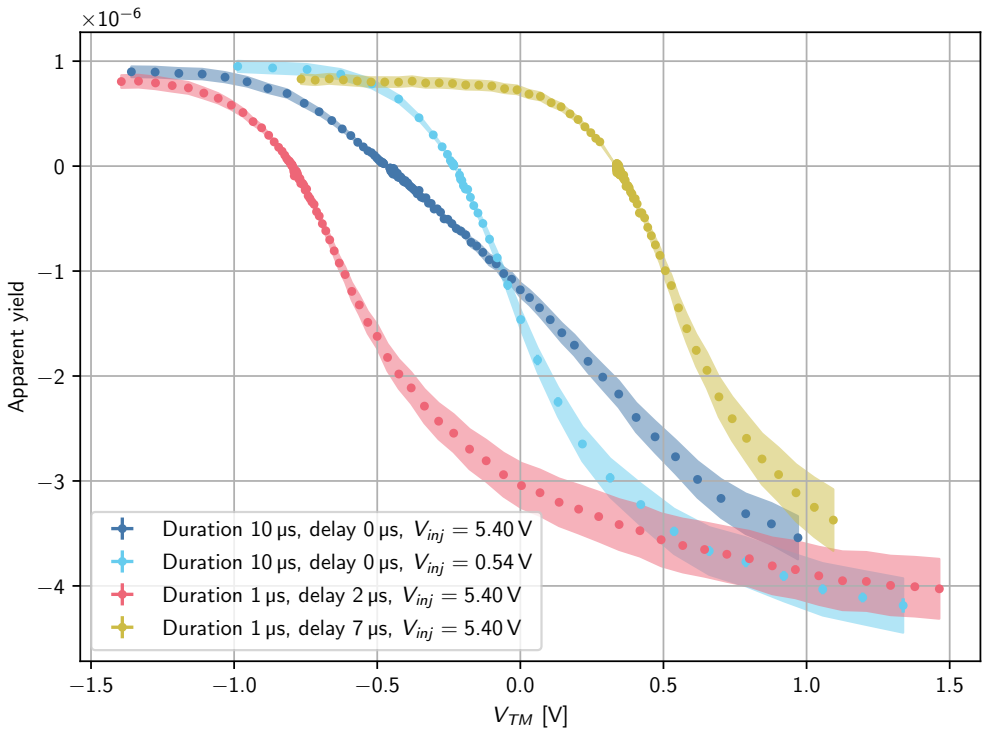

(B) EH illumination

FIGURE 3.23: SETi 255 apparent yield data.

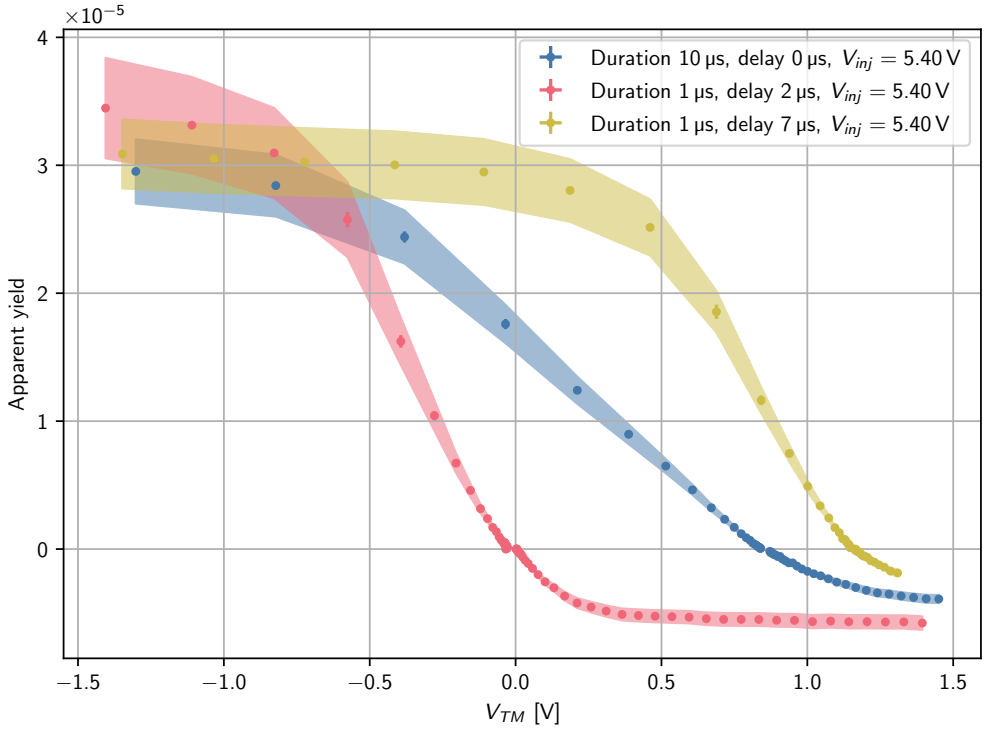

(A) TM illumination

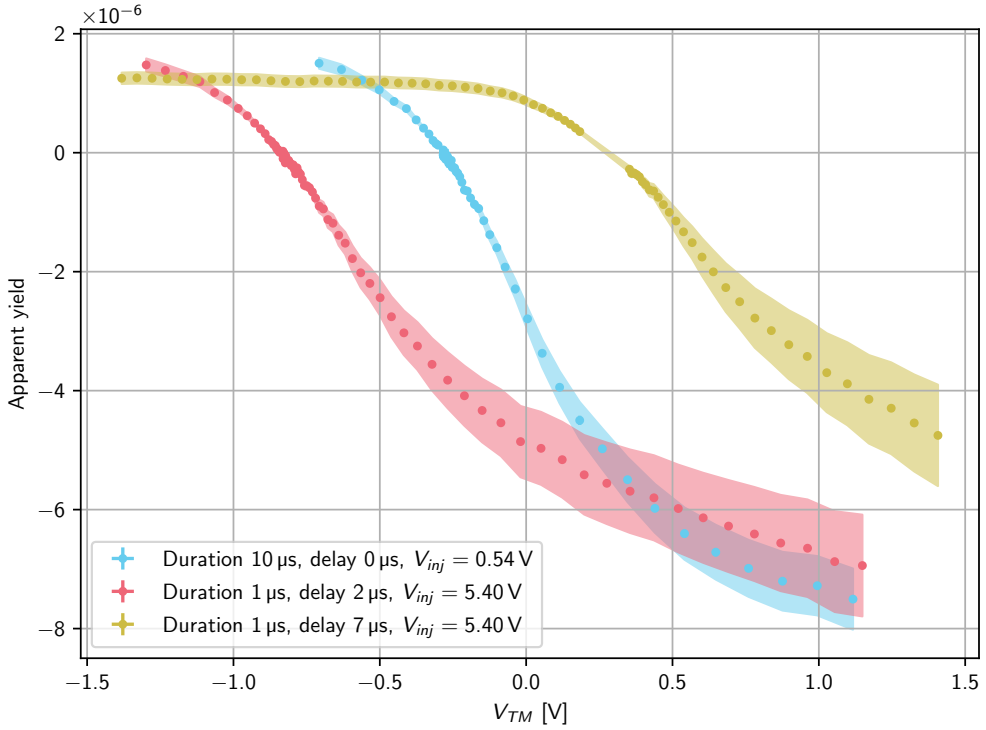

(B) EH illumination

FIGURE 3.24: SETi 240 apparent yield data.

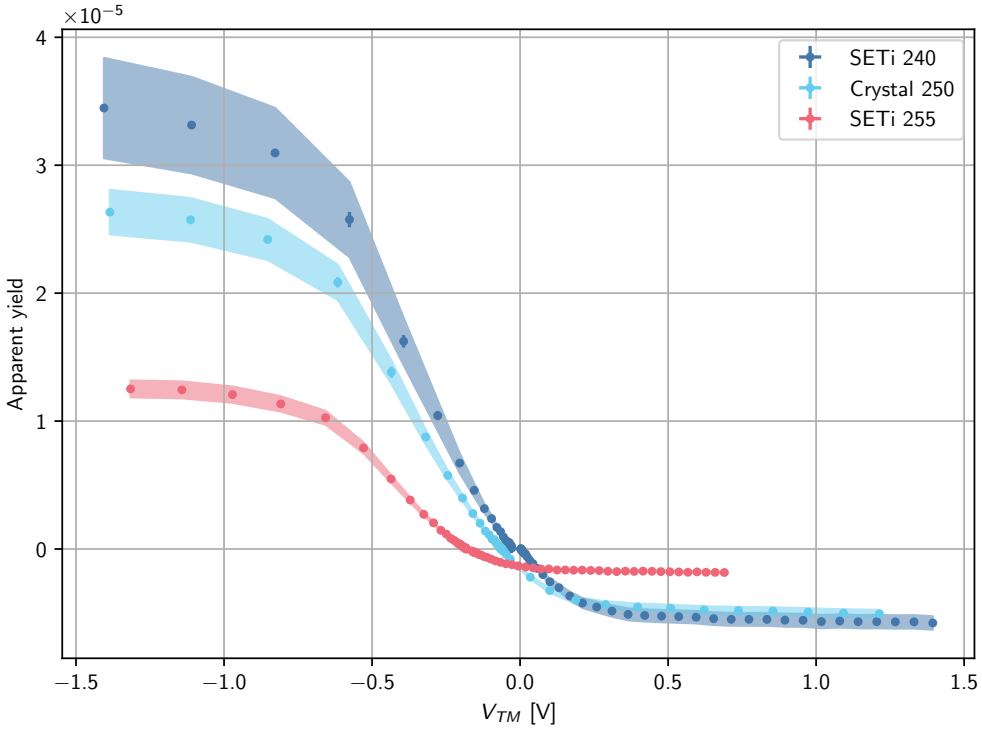

FIGURE 3.25: Comparison of the apparent yield curves for different light sources (TM illumination with duration of 1 µs and delay of 2 µs).

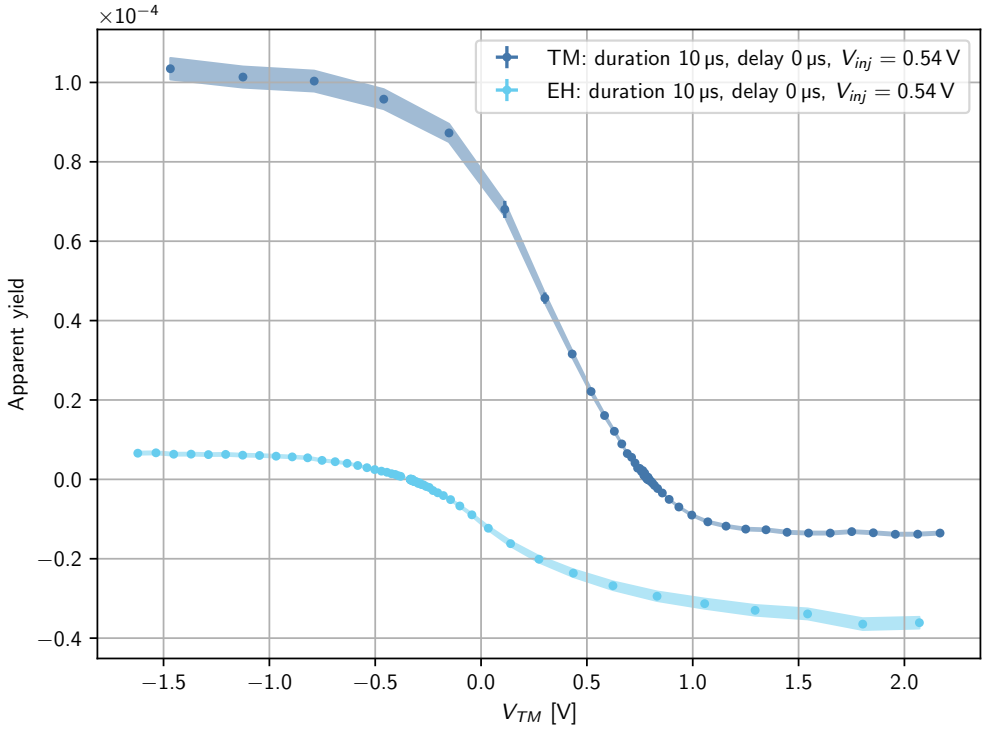

FIGURE 3.26: UVphotonics 230 apparent yield data

Effect of DC and AC actuations

It is important to evaluate how the apparent yield curves depends on the actuation voltages applied to the electrodes. Indeed, in LISA actuation potentials will be applied on all degrees of freedom, except the science axis, to keep the test masses centered in their electrode housings.

We decided to apply DC and AC actuations on the z-electrodes because, as evident from the light absorption coefficients of Appendix B, are the ones that collect most light (besides the x-electrodes, that we prefer not to use, apart for the charge measurement itself, because they lie on the sensitive axis of the pendulum).

In all cases the actuation pattern was chosen so that the TM was not polarized.

DC actuation To evaluate the effect of actuation in an extreme case, we applied equal $\pm 5\,\mathrm{V}$ DC to $z^-_{1,2}$ electrodes and an opposing $\mp 5\,\mathrm{V}$ DC to $z^+_{1,2}$ electrodes. In this way the polarization on the TM is negligible.

As shown in Figure 3.27, we acquired two sets of measurements with DC actuation, one with nominal and one with low injection ($V_{inj} = 0.54\,\mathrm{V}$). All the data were taken within one month time.

From the absorption coefficients in Appendix B, we see that, in the case of EH illumination, only the electrode z^-_1 absorbs a significant fraction of the total light injected ($\sim 5.6\%$). The other z-electrodes absorb only tiny amount of light. It is, therefore, reasonable to focus only on the z^-_1 to explain the effect of DC actuation. As expected we have that

- If $+5\,\mathrm{V}$ are applied to the $z^-_{1,2}$, the photoelectrons emitted from the corresponding region of the electrode housing encounter a large potential barrier. This causes a suppression of the EH photo-current.
- If $-5\,\mathrm{V}$ are applied to the $z^-_{1,2}$, the photo-electrons emitted from the corresponding region of the test mass encounter a large potential barrier. This causes a suppression of the TM photo-current.

Overall DC actuations have a significant but not dramatic effect on the apparent yield curves: at neutral TM we still have a negative current, although reduced when $+5\,\mathrm{V}$ are applied to the electrodes on the z^- face.

AC actuation For the case of AC actuation we still focused on the patterns that affect the z-electrodes only, i.e. V_{1z}, V_{2z}, $V_{1\eta}$, and $V_{2\eta}$. The amplitude chosen for the AC actuation is always $3\,\mathrm{V}$. We always applied the actuations in a way that they cancel each other out. Hence, the TM polarization was negligible even at the audio-frequency of the AC voltages.

We have observed that in our version of the front-end electronics AC actuations seem not to be synchronized with the injection voltage and consequently with the CMD light pulses.

As evident form the Figures 3.28 – 3.30, the effect of AC actuation is smearing the apparent yield curves. The change in the equilibrium voltage is limited.

Our data show that there is a dependence of the apparent yield curves form the AC actuation, hence we suggest for LISA to develop illumination strategies that take into account also the potential applied instantaneously to the sensing electrodes. A possibility would be to illuminate only when the actuation potential of the relevant[29] electrodes is reasonably close to zero.

[29] Namely the electrodes close to the regions where a significant fraction of the UV-photons is absorbed.

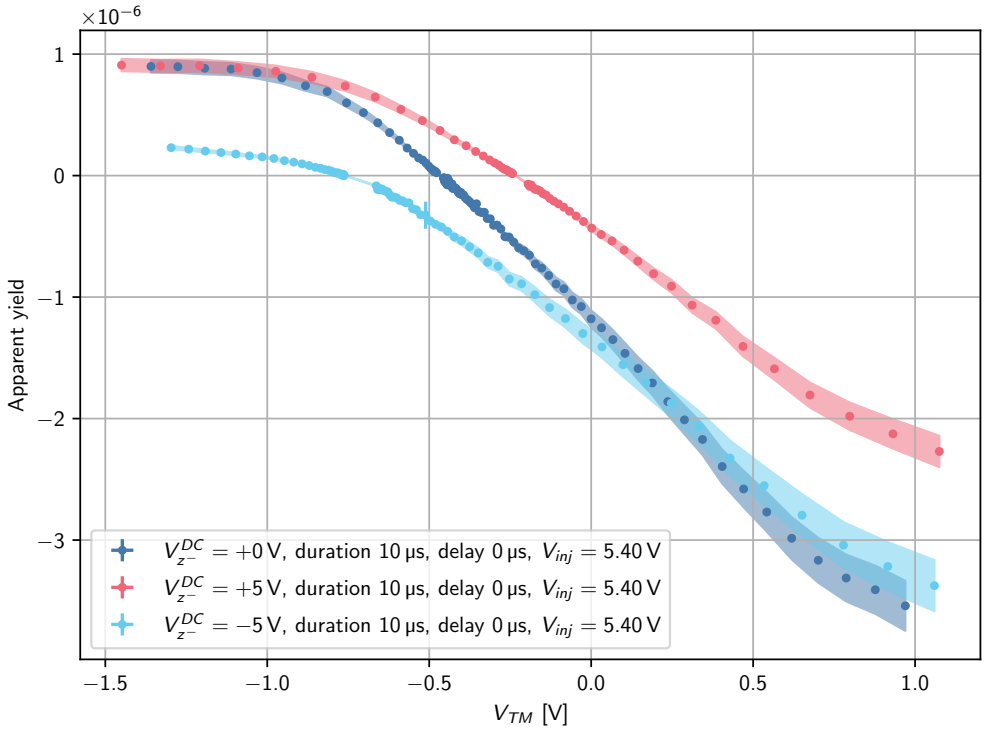

(A) Data for $V_{inj} = 5.4\,\mathrm{V}$

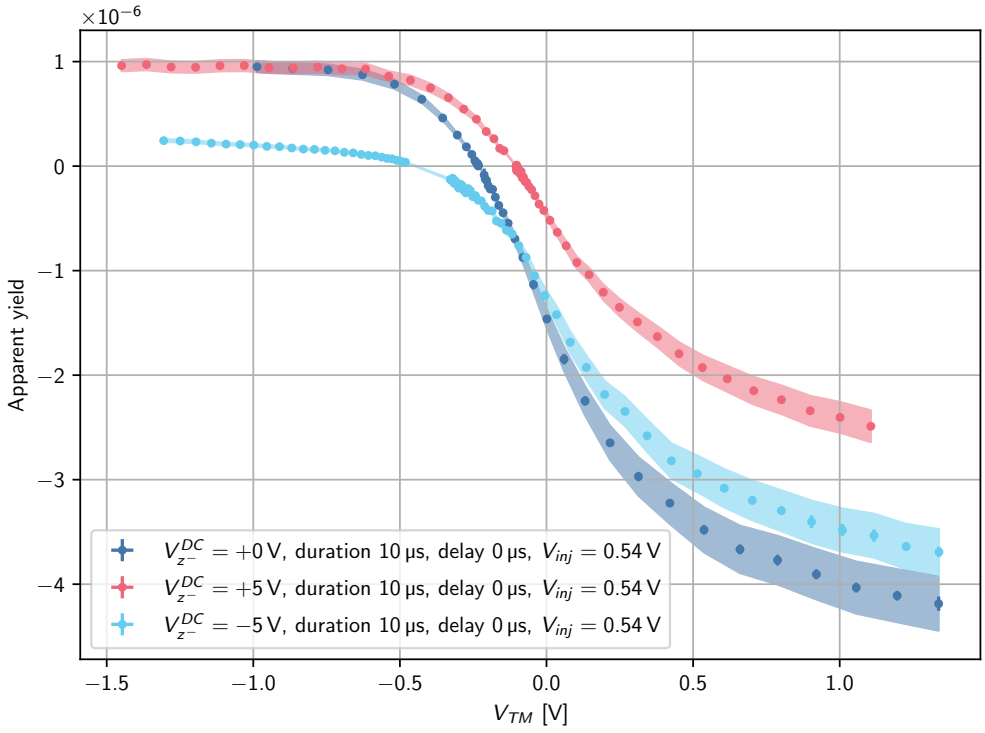

(B) Data for $V_{inj} = 0.54\,\mathrm{V}$

FIGURE 3.27: Apparent yield data for EH illumination with SETi 255 in the presence of DC actuation on the z-electrodes.

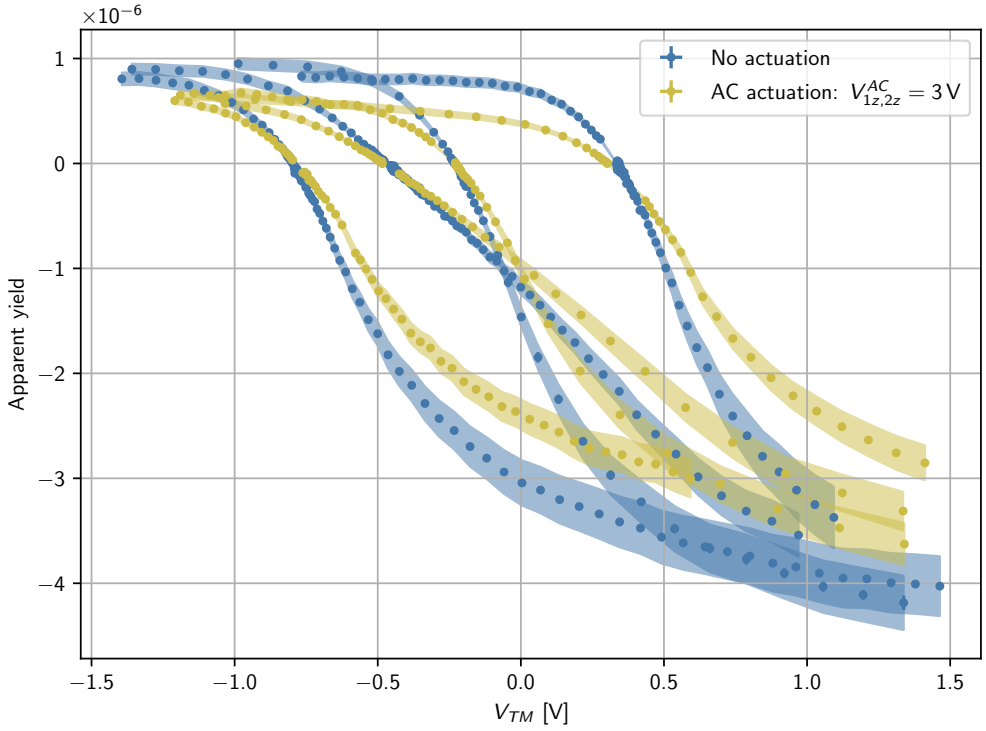

FIGURE 3.28: Apparent yield curve for EH illumination with SETi 255 in the presence of AC actuation on z-electrodes. The illumination patterns are the same as in Figure 3.23b.

In Figure 3.29 we compare the effect of AC actuation on the apparent yield data in the patterns V_{1z} and V_{2z} (cyan curve) and when also the patterns $V_{1\eta}$ and $V_{2\eta}$ were applied (red curve). Surprisingly the data show no significant difference between the two settings. This is likely related to the fact that, as stated previously, only z_1^- electrode absorbs a significant fraction of the UV-light among all electrodes activated by the actuation pattern.

3.4 Experimental problems

During the experimental campaign some unexpected problems arose. Such issues mainly affect our ability to measure the UV power injected into the GRS.

3.4.1 Degradation of the optical fibers

The testing campaign subjected the optical fibers to an intensive use. Indeed, for each apparent yield measurement, we needed to connect and disconnect the optical fibers several times to measure the light power and to bring the UV light to either the TM or EH ISUK. Over time the wear and tear caused damages and dirt build-up at the termination of the optical fibers and, consequently, a reduction of their transmission coefficient. The timescale of such degradation is several months. In Figure 3.31, we show the condition of one of the fibers after a couple of years of use.

A change in the optical properties of the fibers affects the accuracy of our power measurements, as they are based on a transmission coefficient measured at the beginning of the experimental campaign. This induces an unmodeled systematic error

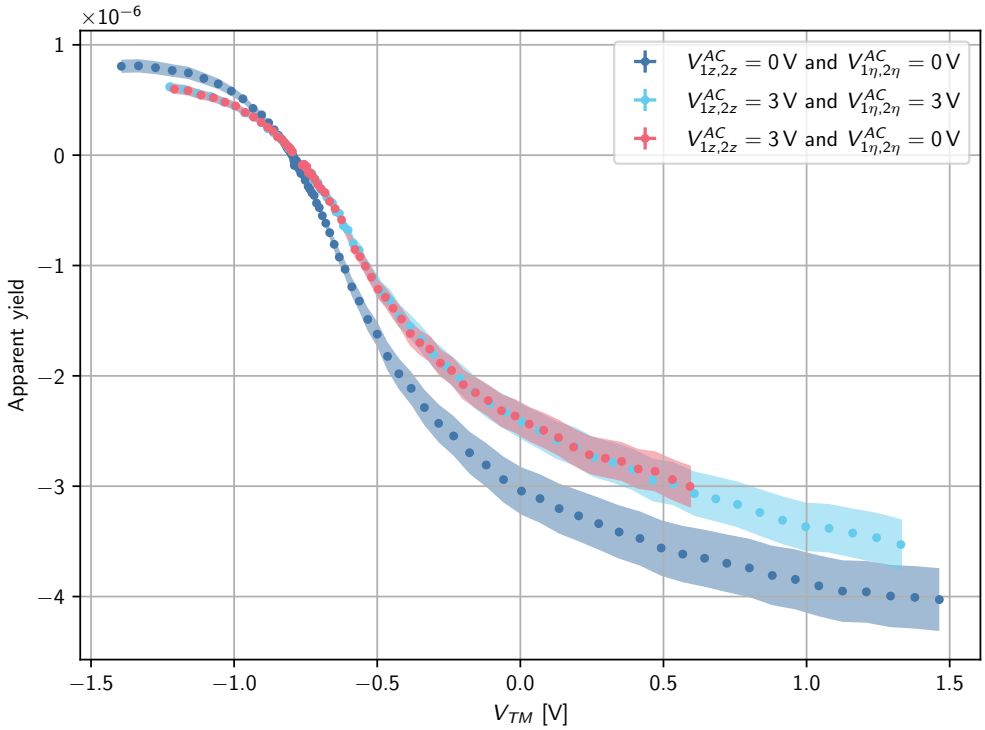

FIGURE 3.29: Apparent yield curve for EH illumination with SETi 255: we observe no difference between the data with AC actuation in the scheme V_{1z} and V_{2z} with respect to the data with AC actuation also on $V_{1\eta}$ and $V_{2\eta}$. All curves have been obtained with a light-pulse duration of 1 µs and delay 2 µs.

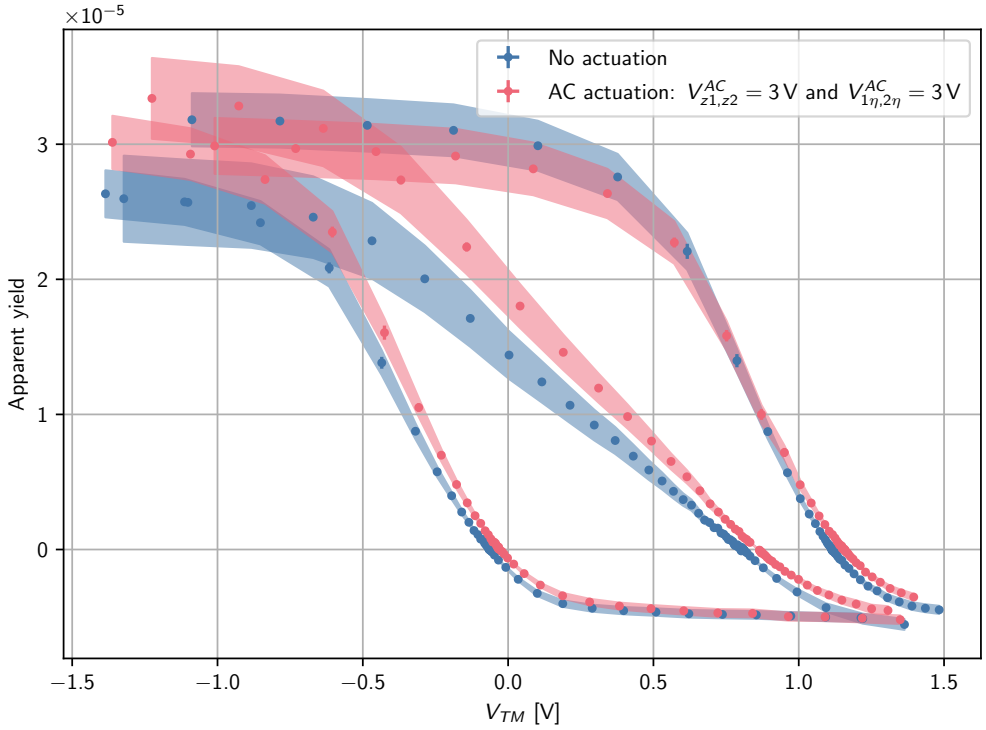

(A) TM illumination

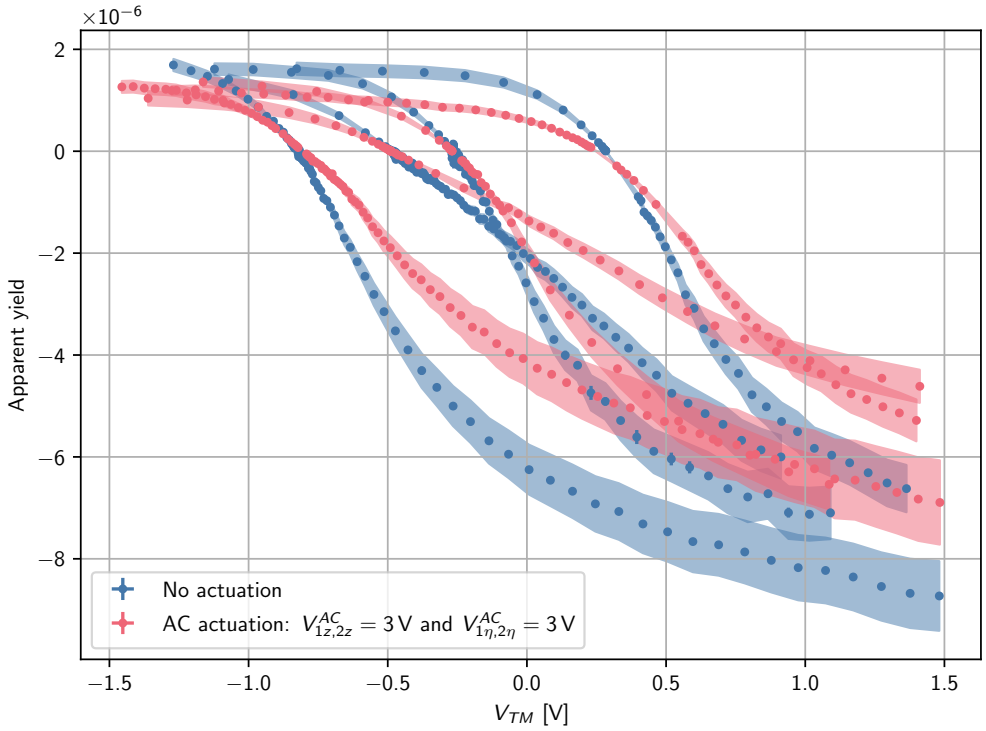

(B) EH illumination

FIGURE 3.30: Apparent yield data for illuminations with Crystal 250 in the presence of AC actuation on the z-electrodes. The illumination patterns are the same as in Figure 3.22.

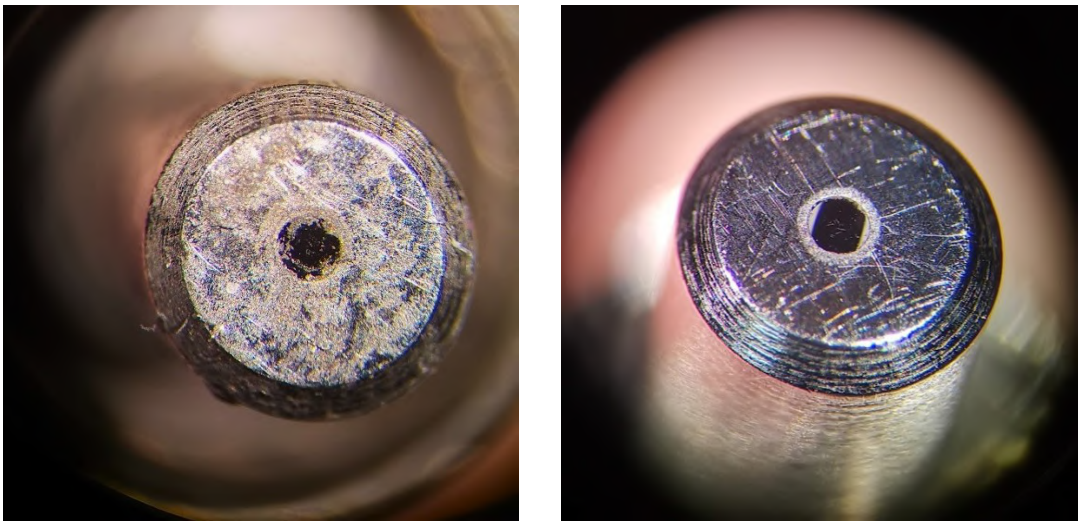

(A) TM long fiber before cleaning (B) TM long fiber after cleaning

FIGURE 3.31: Status of the TM long fiber before and after cleaning with optical paper.

in the apparent yield measurements, that cannot be distinguished from a *coherent* change of the emission properties of TM and EH over time.

In addition, two of the six fibers used during these years failed completely[30].

The environment in our laboratory is quite dusty and no specific care has been put in keeping the LED housing and connectors clean. They just have been closed after use with some rubber caps. Later these caps have been substituted with metal ones to avoid the dispersion of rubber fragments.

We advise to maintain a high level of cleanliness while working with the optical fibers and the light sources. Ideally one should keep the optical equipment in a clean environment, or at least, clean[31] it at regular intervals. Indeed, after cleaning the fibers we observed a significant increase in their transmission coefficient (+80% and +50% for respectively the EH and TM fiber and only +11% for the short fiber[32]). Still, the transmission coefficients did not reach the values measured at the beginning of the experimental campaign due to the presence of some scratches and permanent damage on the ends of the fibers. For this reason we decided to substitute and re-characterize all external optical fibers in the spring of 2021. Naturally also the freshly installed fibers, especially the short and most used one, accumulated dirt and damage over the years (see Table 3.6).

3.4.2 Variation in the measured apparent yield over time

Repeating the same measurements after years resulted in a general increase of the apparent yield. As an example, see Figure 3.32, where we plot some apparent yield curves for the Crystal 250 which have been repeated after a couple of years. Another example is depicted in Figure 3.33, where we plot the time evolution of the apparent

[30] One of the fiber used was not armored and, hence, less resistant to mechanical stress.

[31] At first we just dusted the terminations of the fibers and the LED housing with a flux of helium. This non-aggressive method was not super effective, as some of the grime was firmly attached to the surfaces. We then used optical paper and ethanol which proved more adequate to remove the dirt.

[32] The scarce increase of the transmission coefficient in the short fiber after cleaning, despite being by far the one subjected to the most use, is probably due to a some permanent damage, i.e. some scratches, on the dielectric interface of the short fiber.

TABLE 3.5: Transmission coefficients of the TM and EH optical chains before and after cleaning the external fibers in 2021.

Quantity	Before cleaning	After cleaning	Variation
a_{TM}	0.158 ± 0.003	0.189 ± 0.003	+19%
a_{EH}	0.100 ± 0.003	0.157 ± 0.004	+57%
$\frac{\alpha_{TM,out}}{\alpha_{SF}}$	0.708 ± 0.004	0.845 ± 0.006	+19%
$\frac{\alpha_{EH,out}}{\alpha_{SF}}$	0.339 ± 0.002	0.534 ± 0.003	+57%

TABLE 3.6: Comparison between the transmission coefficient of the optical fibers installed in 2021 when new and after two years of use.

Quantity	New (2021)	Used (2023)	Variation
a_{TM}	0.171 ± 0.003	0.253 ± 0.005	+48%
a_{EH}	0.209 ± 0.006	0.407 ± 0.010	+95%
$\frac{\alpha_{TM,out}}{\alpha_{SF}}$	0.765 ± 0.008	1.133 ± 0.009	+48%
$\frac{\alpha_{EH,out}}{\alpha_{SF}}$	0.714 ± 0.007	1.387 ± 0.004	+95%

yield at positive saturation for a measurement which has been repeated several times over the years. Comparable increases in the saturation levels have been observed across the board for all LEDs.

As we measure the transmission coefficient of the fibers only rarely, we cannot determine with certainty if the change in the apparent yield saturation levels are due to a change in the emission properties of the surfaces, or, to the aforementioned deterioration of the optical fibers (which cause to systematically underestimate the UV-power injected into the GRS).

We also observe that the equilibrium voltages are almost constant over the years, which indicates that the change in the saturation may be due to a wrong estimate of the UV-power injected in the GRS, or to the (unlikely) possibility that the modification of the emissivity of TM and EH surfaces is symmetrical. If we pair this observation with the fact that the discrepancy in the apparent yield at saturation is reduced when we consider an updated fiber transmission coefficient, we have strong evidence that the culprit of our inconsistencies may be an inaccurate assessment of the UV-power due to the progressive degradation of the optical fibers.

It should also be noted that no significant variation in the surface emission properties (i.e. apparent yield) was observed during the LISA Pathfinder mission [52].

Anyhow, even in the unlikely case that the change in the apparent yield were completely due to a modification of the emission properties of the sensor surfaces, this would no be dramatic because we dealing with "just" a factor two[33]. It would have been bad news if after years the emissivity of either TM or EH would have dropped to zero, which is not the case from our data.

[33]Comparable variations of the apparent yield from gold surfaces have been observed in dedicated experiments with the same class UV-LEDs as light sources [57].

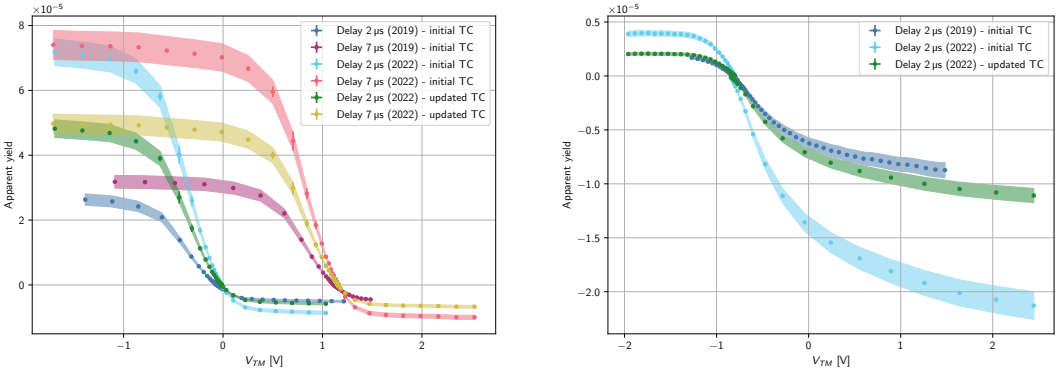

(A) TM illumination (B) EH illumination

FIGURE 3.32: Apparent yield curves with Crystal 250 obtained in 2019 and in 2022. We see a pretty large change in the saturation levels. If we analyze the latest data with an updated fiber transmission coefficient measured few weeks afterwards (last column of Table 3.4), we obtain saturation levels closer to the original data acquired in 2019.

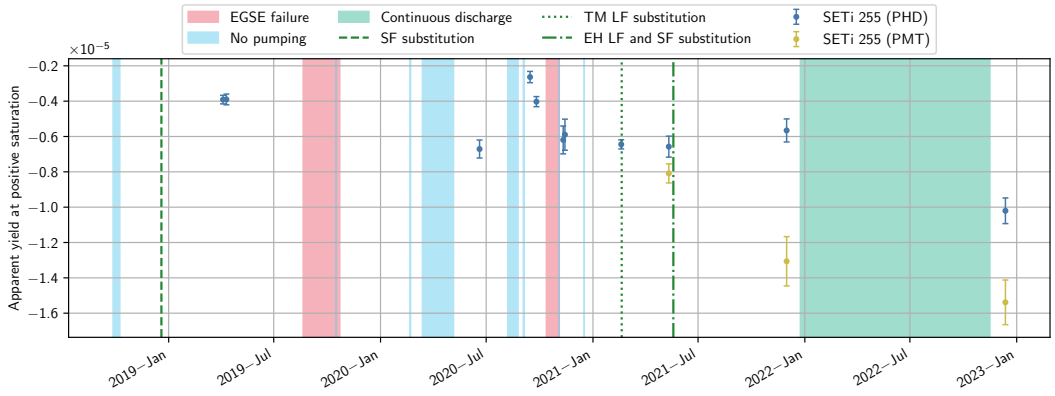

FIGURE 3.33: Measured apparent yield value at positive saturation for EH illumination with the SETi 255 LED (duration 1 µs, delay 2 µs and $V_{inj} = 5.4\,\text{V}$). The blue data points correspond to apparent yield measurements with the UV power estimated via the photodiode, the yellow one are the few data for which a power measurement with the calibrated PMT was also available. We observe an increase in the last year of about a factor two in the saturation levels. Unfortunately, we also see that the saturation levels for the same measure may vary significantly if the power measurement is performed with the photodiode or the calibrated PMT. This is probably due an improper calibration or to the insufficient sensitivity of the photodiode at low UV-power

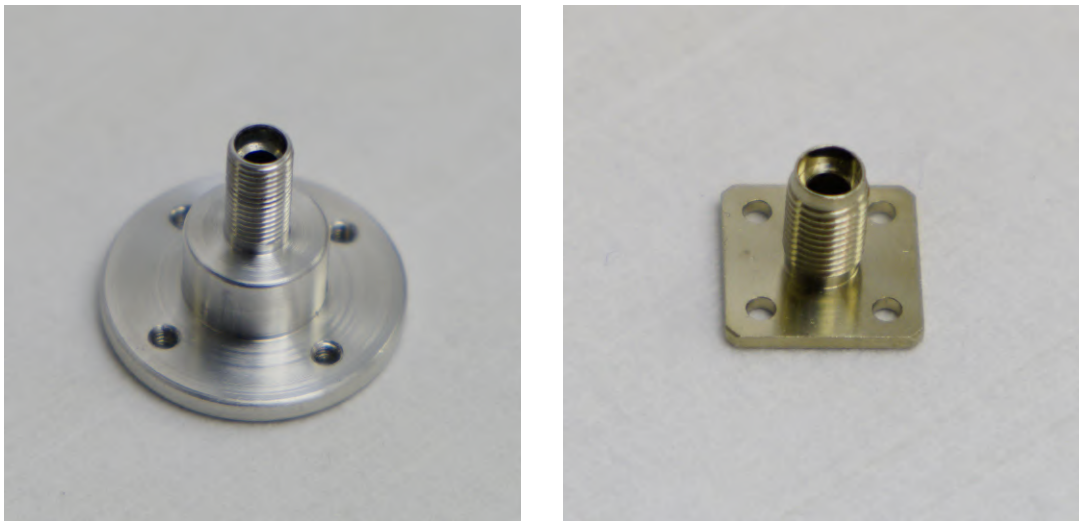

(A) Old SMA connector (B) New SMA connector

FIGURE 3.34: SMA connectors that couple the optical fibers with the UV light source.

3.4.3 SMA connector between LED and optical fiber

The CMD prototype provided was equipped with SMA-905 connectors to couple the UV-LEDs with the optical fibers. Such connectors were manufactured in house and lacked the mechanical precision to provide a reliable fitting with the fibers. We observed typical variations of $\sim 8\%$ (with upper limit around 30%) in the light power whenever the fiber was removed and reconnected. This represents, again, a problem in correctly estimating the UV power during the illumination. Indeed, in an apparent yield measurement the UV power is estimated with the short fiber connecting the LED to the power measuring device (either photodiode or PMT). Afterwards the short fiber is removed and the LED is connected to either the TM or the EH optical chain. As there is this disconnection, it may happen that the measured power does not reflect the real value that is injected into the GRS, as the fiber coupling through the connector is different.

As shown in Figure 3.35, we did not realize the severity of this problem until summer 2020. Indeed in the first part of the experimental campaign, we estimated the light power just by switching on and off the LEDs via the software interface (*on-off method*) without disconnecting the short fiber between the LED and the power measuring device. This caused an underestimation of the systematic uncertainty in the power measurement.

Afterwards, we performed the power measurements by keeping the LED on at all times and by switching periodically between the light source and a dark cavity (*detach-attach method*). In this way we were able to sample the effect of attaching and detaching the fiber.

In the month of November 2022, we installed new SMA-905 connectors produced by Diamond SA, a company specialized in optical fiber assemblies, which ensured a typical coupling error of the order 2% (with a maximum measured value of 4%). We have to point out that we performed only a handful of measurements with the new connectors, hence the statistics is pretty low, but the data available indicate that the new connector provide a more reliable coupling between the light sources and the optical fiber.

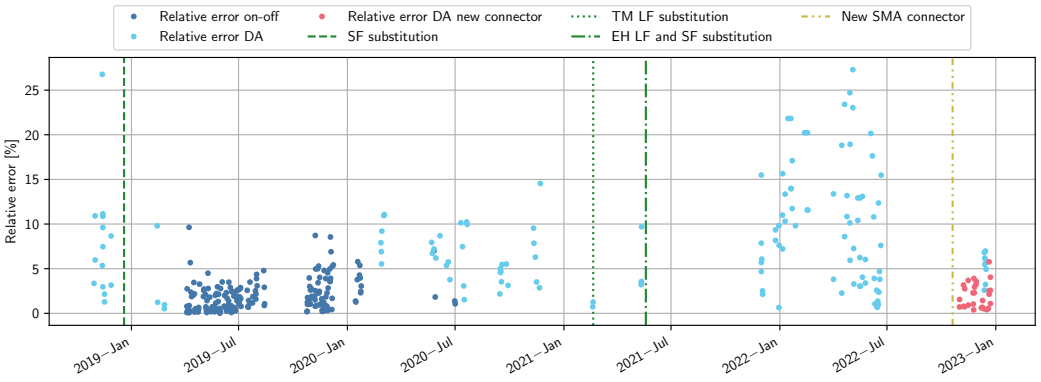

FIGURE 3.35: Timeline of the "darks & lights" measurements: the data in 2018 obtained with the detach-attach method refer to the Hg-lamp, which could not be switched on and off rapidly, hence we were forced to unknowingly use the more correct detach-attach procedure.

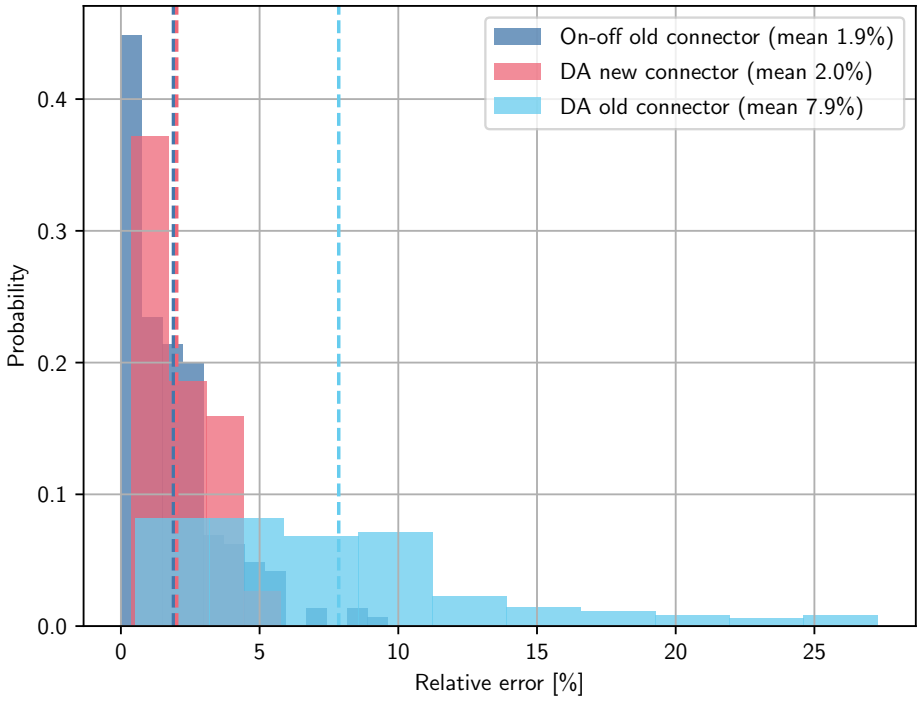

FIGURE 3.36: Histogram of the relative error for the various "dark & light" modalities: we see that the on-off method underestimates the uncertainty compared to the detach-attach procedure. The new SMA connectors provide superior reproducibility in the mechanical connection between optical fiber and LED housing.

The mounting of the LEDs in the UV-light Unit is not recognized as significant problem for the reproducibility of the power measurements. Indeed, the LED is inserted into a recess[34] of the metal base rigidly coupled to the SMA connector for the optical fibers. Supposedly the mounting pressure does not allow significant residual motion, once the LED is integrated. Moreover, we basically never removed the LEDs from their housing, except when we needed to mount the new SMA connectors.

3.5 Conclusions

The most important takeaway of our experimental testing is that the flight-model replica of the LISA electrode housing integrated in our torsion pendulum allows to achieve a net negative photocurrent for both EH and TM illuminations, just by controlling the phase of the UV-light pulses without the need of adding local DC fields. In Section 4.5, we will use the photoemission model developed in Chapter 4 to argue why we think that this would have been possible also for the inertial sensors that flew in LISA Pathfinder, if we had had the potentiality of pulsed illumination.

The possibility of realizing a bipolar discharge of the test masses made possible by the pulsed illumination scheme, increases greatly the robustness of the Charge Management System for the LISA mission. Indeed, we would still be able to discharge the TM in the case that the optical channel supplying UV-light to the EH ISUK failed.

Furthermore, being able to set the duration and delay of the illumination with respect to the injection bias, allows us to tune finely the equilibrium voltage, which eases the implementation of the continuous discharge mode.

We also investigated the role of DC and AC actuations on the apparent yield curves. This is particularly important because in LISA actuation potentials will be imparted on all degrees of freedom, except that on the science x-axis, to keep the TM centered inside the EH. Our measurements indicate that volt-level actuation potentials have an impact on the apparent yield curves, especially in the case of EH illumination (for which a larger fraction of the UV-light is absorbed by sensing/actuation electrodes).

Unfortunately the apparent yield values at saturation are not very reliable also because of the problems in estimating the UV power (especially with the photodiode) and because, for the first part of the experimental campaign, we were not sampling correctly the effect of detaching and re-attaching the optical fibers, when we used the on-off method for the "darks & lights".

We would like to wrap up with a comment on the change of apparent yield observed over time: a systematic increase of the apparent yield at saturation of approximately a factor two may be either due to an increment of the emissivity of the surfaces, or due to a progressive degradation of the optical fibers, whose transmission properties decreases with time. This second explanation is favored at the moment.

The observed increase of approximately a factor two in the apparent yield data at saturation, although not optimal, is, in itself, not terribly bad news, as it does not compromise the capability of the Charge Management System, even if it were entirely due to a change in the microscopic properties of the surfaces.

[34] The recess is approximately fitted to the outer dimension of the LED casing.

Chapter 4

Photoemission model

In this chapter we will present a simple photo-emission model that could be useful to interpret the experimental apparent yield data presented in Chapter 3.

We would like to remember that our photo-emission model, remains a model and, hence, a simplification of the reality, which is way more complex. Every model is an imperfect description of reality, but if they are appropriate, they can be helpful in highlighting the most important aspects of the physical system under study.

This work has been inspired by the research of Dr. Daniel Hollington for the Pathfinder data [58, 59]. We somehow approached the photo-emission process in a different way, as we developed also a small theory for the photo-electron emission spectra instead of using the semi-empirical model that assumes a triangular distribution for the spectrum of the emitted photo-electrons. Our approach has been inspired by [60].

Moreover, previous research always considered photo-emission from metallic surfaces for monochromatic light sources (single energy photons). This was the case for LISA Pathfinder, as the photons emitted from the mercury-vapor lamps can be reasonably treated as monochromatic. UV-LEDs, contrary to mercury lamps whose spectrum is practically a line, emit photons with a broader energy distribution.

Finally, we applied the photo-emission model developed to fit the experimental apparent yield data, in an attempt to extract an estimate of the microscopic properties of the GRS surfaces.

4.1 Free-electron model for metals

Electrons in metal, as all Fermions, obey *Pauli exclusion principle*, hence they follow the Fermi-Dirac distribution

$$F(\varepsilon) = \frac{1}{\exp\left(\frac{\varepsilon-\mu}{k_B T}\right) + 1}, \tag{4.1}$$

which gives the probability of an energy level being occupied. In (4.1) we indicated with ε the energy and with μ the chemical potential.

In order to compute any property of the physical system under study, one has to combine the probability that an energy level is occupied, i.e. the Fermi-Dirac distribution, with the density of states $g(\varepsilon)$, i.e. the number of solutions of the Schrödinger equation for the physical system considered per unit volume and energy[1]. More precisely, the product of the Fermi-Dirac distribution (i.e. the probability of a state to be occupied) and the density of states

$$n(\varepsilon) = F(\varepsilon)g(\varepsilon) \tag{4.2}$$

[1] The quantity $g(\varepsilon)\,\mathrm{d}\varepsilon$ is the number density of single-particle states in the energy range $(\varepsilon, \varepsilon + \mathrm{d}\varepsilon)$.

gives the density of states actually populated by particles at each energy.

A trivial application is to find the numeric particle density in the system, which can be obtained by integrating[2] the density of occupied single-particle states $n(\varepsilon)$ over all energies

$$\frac{N}{V} = \int n(\varepsilon)\,\mathrm{d}\varepsilon = \int F(\varepsilon) g(\varepsilon)\,\mathrm{d}\varepsilon \tag{4.3}$$

A slightly more complicated example is the internal energy density u, i.e. the internal energy per unit volume $u = U/V$, which can be computed as

$$u = \int \varepsilon\, F(\varepsilon)\, g(\varepsilon)\,\mathrm{d}\varepsilon \tag{4.4}$$

which is the sum of the energy of all occupied single-particle states.

The expression of the density of states $g(\varepsilon)$ depends on the physical system considered.

In our case we want to derive the formula for the velocity distribution of electrons in a metal, considering them as free and non-interacting fermions (*independent electron approximation*). It is possible to find the following calculation in any solid state physics textbook, a personal favorite is Ashcroft-Mermin [61]. We will outline a sketch of the calculation in the remainder of this section.

Schrödinger equation for the free-electron gas Assume that we are considering a cubic sample of volume $V = L^3$. A single non-interacting electron can be described by a wave function $\psi(\boldsymbol{r})$, which obeys the following time-independent Schrödinger equation[3]

$$-\frac{\hbar^2}{2m} \underbrace{\left(\frac{\partial^2}{\partial x^2} + \frac{\partial^2}{\partial y^2} + \frac{\partial^2}{\partial z^2} \right)}_{\nabla^2} \psi(\boldsymbol{r}) = \varepsilon \psi(\boldsymbol{r}), \tag{4.5}$$

whose solution is the familiar plane-wave expression

$$\psi(\boldsymbol{r}) = \frac{1}{\sqrt{V}} e^{\mathrm{i}\boldsymbol{k}\cdot\boldsymbol{r}} \tag{4.6}$$

with energy eigenvalue

$$\varepsilon = \varepsilon(\boldsymbol{k}) = \frac{\hbar^2 \boldsymbol{k}^2}{2m}. \tag{4.7}$$

We have to notice that $\boldsymbol{k}$ is the position-independent wave vector and the prefactor $1/\sqrt{V}$ in (4.6) is related to the normalization of the wave function[4].

If we now impose the infamous *Born-von Karman* periodic boundary conditions

$$\begin{aligned} \psi(x + L, y, z) &= \psi(x, y, z) \\ \psi(x, y + L, z) &= \psi(x, y, z) \\ \psi(x, y, z + L) &= \psi(x, y, z) \end{aligned} \tag{4.8}$$

[2] In general the energy levels are quantized, hence it would be more formal to use a discrete sum instead of an integral. However, for typical solid state systems, the energy levels are so close to each other that they become, with excellent approximation, a continuum.

[3] There is no potential term because the sample can be considered as an infinite potential well where the electrons are free to move. Therefore, the potential in the cubic sample is a constant, which we can set to zero without loss of generality.

[4] Indeed we must have $\int_V |\psi(\boldsymbol{r})|^2 \mathrm{d}\boldsymbol{r} = 1$, which means that we have unit probability of finding the electron inside the volume V.

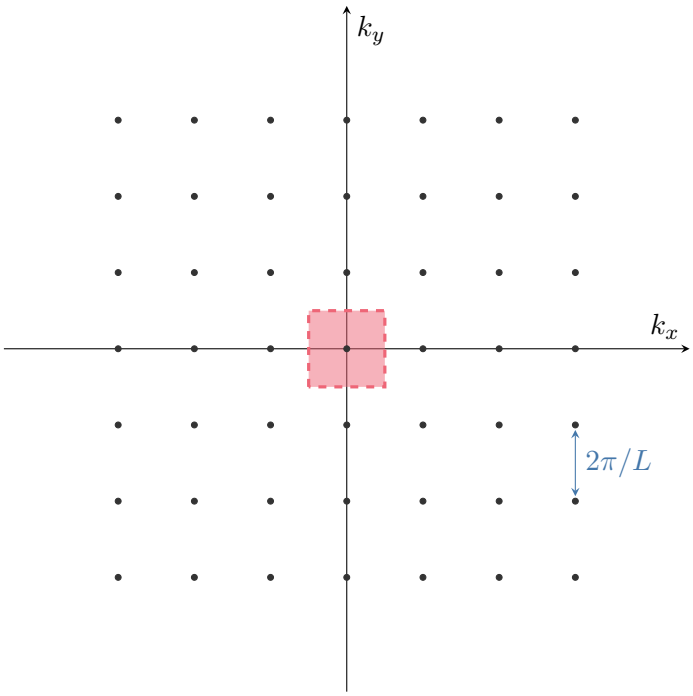

FIGURE 4.1: Allowed k-points in a two-dimensional space. The area per point, highlighted by the red dashed square, is $(2\pi/L)^2$. If the space were d-dimensional the generalized volume would be $(2\pi/L)^d$ per allowed point.

where L is the side of the cubic volume of the sample, to our family of solutions (4.6), we must have that

$$e^{ik_x L} = e^{ik_y L} = e^{ik_z L} = 1 \tag{4.9}$$

Therefore, only certain discrete values of the wave vector $\boldsymbol{k} = (k_x, k_y, k_z)$ are allowed, namely

$$k_x = \frac{2\pi}{L} n_x, \quad k_y = \frac{2\pi}{L} n_y, \quad k_z = \frac{2\pi}{L} n_z \quad \text{with} \quad n_x, n_y, n_z = 0, \pm 1, \pm 2, \dots \tag{4.10}$$

This means that the solutions of the (4.5), i.e. the allowed states (neglecting spin-degeneracy), can be labeled with the wave vectors $\boldsymbol{k}$ whose components are an integer multiple of $2\pi/L$. In Figure, 4.1 we represent the allowed k-states in two dimensions.

Now we can estimate the number of allowed $\boldsymbol{k}$-vectors, contained in a large[5] (3-dimensional) volume Ω in the k-space. If the volume is not too oddly shaped[6], we can approximate the number of points contained in Ω as the ratio of the volume and the volume per point

$$\mathcal{N} = \frac{\Omega}{(2\pi/L)^3} = \frac{\Omega V}{(2\pi)^3} \tag{4.11}$$

If we are considering particles with spin s, we have to multiply this value by the spin degeneracy $(2s+1)$ to account for all possible spin orientations of each solution.

[5] That is with linear extension much bigger than the length-scale $2\pi/L$.
[6] So that not too many points lie on the surface.

Therefore the overall *number of states*, including spin, can be found as:

$$N = (2s+1)\mathcal{N} = (2s+1)\frac{\Omega V}{(2\pi)^3} \tag{4.12}$$

The number density in the k-space of allowed stated for a given volume V in real space is

$$\rho_N = \frac{N}{\Omega} = (2s+1)\frac{V}{(2\pi)^3}. \tag{4.13}$$

Calculation of the velocity distribution of a free-electron gas Now we have all ingredients to sketch the computation for the velocity distribution of a free-electron gas.

1. Consider a sample of volume $V = L^3$ in real space. The number of free-electrons levels in the momentum space, or $\boldsymbol{k}$-space, about a point $\boldsymbol{k}$ of volume $\mathrm{d}\boldsymbol{k}$ for this sample is
$$\mathrm{d}N = \rho_N \,\mathrm{d}\boldsymbol{k} = 2\frac{V}{8\pi^3}\,\mathrm{d}\boldsymbol{k}, \tag{4.14}$$
where the 2 is due to the twofold spin degeneracy $(2s+1)$ of spin-1/2 particles.

2. The free-electron energy density in the $\boldsymbol{k}$-space, can be written as
$$g[\varepsilon(\boldsymbol{k})] = \frac{1}{V}\frac{\mathrm{d}N}{\mathrm{d}\boldsymbol{k}} = 2\frac{1}{8\pi^3} \tag{4.15}$$

3. Of course, for the free electron gas, the energy corresponds to the kinetic energy
$$\varepsilon(\boldsymbol{k}) = \frac{\hbar^2\boldsymbol{k}^2}{2m} \tag{4.16}$$

4. If we multiply the density of states $g[\varepsilon(\boldsymbol{k})]$ with the Fermi-Dirac distribution (i.e. the *probability of each level to be occupied*), we obtain the density of electrons with momentum in the volume element $\mathrm{d}\boldsymbol{k}$ per unit volume of real space
$$n(\boldsymbol{k}) = g[\varepsilon(\boldsymbol{k})]\cdot F[\varepsilon(\boldsymbol{k})] = 2\frac{1}{8\pi^3}\frac{1}{\exp\left(\frac{\frac{\hbar^2\boldsymbol{k}^2}{2m}-\mu}{k_BT}\right)+1} \tag{4.17}$$

5. As the number of particles must be conserved, we must have that the number of electrons in an element of volume $\mathrm{d}\boldsymbol{v}$ about $\boldsymbol{v}$ is the same as the number of electrons in an element of volume $\mathrm{d}\boldsymbol{k}$ about $\boldsymbol{k}$:
$$n(\boldsymbol{k})\,\mathrm{d}\boldsymbol{k} = n(\boldsymbol{v})\,\mathrm{d}\boldsymbol{v}, \tag{4.18}$$
where the velocity is given by $\boldsymbol{v} = \frac{\hbar\boldsymbol{k}}{m}$. In Cartesian coordinates the equation above becomes
$$n(\boldsymbol{k})\,\mathrm{d}k_x\,\mathrm{d}k_y\,\mathrm{d}k_z = n(\boldsymbol{v})\,\mathrm{d}v_x\,\mathrm{d}v_y\,\mathrm{d}v_z \tag{4.19}$$

From here we can easily find that

$$\begin{aligned} n(\boldsymbol{v}) &= n(\boldsymbol{k}) \frac{\mathrm{d}k_x}{\mathrm{d}v_x} \frac{\mathrm{d}k_y}{\mathrm{d}v_y} \frac{\mathrm{d}k_z}{\mathrm{d}v_z} \\ &= n(\boldsymbol{k}) \left(\frac{m}{\hbar}\right)^3 \\ &= 2\left(\frac{m}{2\pi\hbar}\right)^3 \frac{1}{\exp\left(\frac{\frac{\hbar^2\boldsymbol{k}^2}{2m}-\mu}{k_B T}\right)+1} \\ &= 2\left(\frac{m}{h}\right)^3 \frac{1}{\exp\left[\frac{\frac{m}{2}\left(v_x^2+v_y^2+v_z^2\right)-\mu}{k_B T}\right]+1} \end{aligned} \tag{4.20}$$

We just derived the expression for the velocity distribution of a free-electron gas.

Note on Fermi energy and chemical potential If we start building, according to Pauli's exclusion principle, the ground state (at $T = 0\,\mathrm{K}$) of N electrons, we will start by placing two electrons with opposite spin orientation in the state with zero momentum $\boldsymbol{k} = 0$, making our way up to a maximum wave vector $\boldsymbol{k}_F$, which is called the *Fermi wave vector*. If N is very big, the region in the momentum space occupied by the ground state will be essentially a sphere[7] centered around $\boldsymbol{k} = 0$. The volume $\Omega_F = \frac{4}{3}\pi k_F^3$ in the momentum space occupied by the ground state is known, due to its shape, as Fermi sphere.

As showed in (4.12), the number of states in the Fermi sphere is

$$N = (2s+1)\frac{\Omega_F V}{(2\pi)^3} = (2s+1)\frac{4}{3}\pi k_F^3 \frac{V}{(2\pi)^3} = \frac{k_F^3}{3\pi^2} V, \tag{4.21}$$

where, in the last passage, we used the fact that for electrons $s = 1/2$. It is convenient to divide the last expression for the volume V in the real space, so that we find the relation between the electron number density n and the Fermi wave vector

$$n = \frac{N}{V} = \frac{k_F^3}{3\pi^2}. \tag{4.22}$$

We can now define the Fermi energy E_F as

$$E_F = \frac{\hbar^2 k_F^2}{2m} = \frac{\hbar^2 (3\pi^2 n)^{2/3}}{2m}. \tag{4.23}$$

The Fermi energy can be computed from the density of free electrons per unit volume. We must notice that for us to correctly estimate the Fermi energy of metals, which will be our focus later, we need to consider only the density of the conduction electrons, rather than the overall density of all electrons. Indeed, in the metallic bounds, only a few electrons per atom can be realistically considered free.

We have debated that in the ground state only and all the states with energy $\varepsilon \leq E_F$ are occupied. We also know that in the low temperature limit ($T \to 0$), the Fermi-Dirac distribution (4.1), tells us that the states with energy lower than the chemical potential μ have occupation number equal to unity, whereas the states with

[7] Indeed, as the energy for the free electron case goes as $\varepsilon \propto k^2$, if there were states with the modulus of the momentum lower than $\hbar k_F$ unoccupied, we would not be in the ground state, as the total energy would not be minimized.

energy larger than μ have occupation number identical to zero.

$$\lim_{T\to 0} F(\varepsilon) = \Theta(\mu - \varepsilon), \tag{4.24}$$

where $\Theta(\cdot)$ is the Heaviside step function.

If we want to reconcile these two observations we must have that, at least in the ground state, the chemical potential μ is equal to the Fermi energy. Therefore, the following limit must hold

$$\lim_{T\to 0} \mu = E_F. \tag{4.25}$$

One can prove that the leading order expression for the dependence of the chemical potential from the temperature is [61, 62]

$$\mu(T) = E_F \left[1 - \frac{1}{3}\left(\frac{\pi k_B T}{2E_F}\right)^2 + \mathcal{O}\left(T^4\right)\right] \tag{4.26}$$

The temperature scale at which the chemical potential becomes quite different from the Fermi energy is

$$T_c = \frac{2\sqrt{3}E_F}{\pi k_B} \sim 6.5 \cdot 10^4\,\mathrm{K}\left(\frac{E_F}{5\,\mathrm{eV}}\right). \tag{4.27}$$

Typically the T_c is much larger than the typical temperature of the sample[8].

We notice that the Fermi energy is a constant defined at $T = 0\,\mathrm{K}$. As we have shown that the Fermi energy and the chemical potential for the metals have very close values up to high temperatures, we will fail to distinguish between the two. In precise calculations it is essential to take into account how much the chemical potential $\mu = \mu(T)$ differs from its value at zero temperature, i.e. the Fermi energy E_F.

4.2 Fowler's theory of photo-emission

R. H. Fowler assumed that electrons in a metal behave like a *free-electron gas*, following a Fermi-Dirac distribution [63, 64]. Therefore, each electron in the sample has a velocity which is randomly distributed in direction and modulus according to (4.20).

If photons are shone on the sample, they are absorbed by the free electrons. At this point Fowler assumed that an electron is emitted if the sum of its initial kinetic energy in the direction normal to the metal surface and of the photon energy is larger than the potential barrier to transit to the vacuum-state, which is equal to the sum work function and the chemical potential of the sample.

The crucial idea at the base of this model is reducing photo-emission to a one dimensional problem. This is reasonable if the interface between sample and vacuum can be approximated an infinite plane surface compared to the geometric scales of the photo-emission event.

4.2.1 Energy spectrum of the photo-electrons

In the previous section, we derived that the number of electrons per unit volume with velocity components in the ranges $(v_x, v_x + \mathrm{d}v_x)$, $(v_y, v_y + \mathrm{d}v_y)$ and $(v_z, v_z + \mathrm{d}v_z)$ is

$$n(v_x, v_y, v_z)\,\mathrm{d}v_x\,\mathrm{d}v_y\,\mathrm{d}v_z = 2\left(\frac{m}{h}\right)^3 \frac{\mathrm{d}v_x\,\mathrm{d}v_y\,\mathrm{d}v_z}{\exp\left[\frac{\frac{m}{2}\left(v_x^2+v_y^2+v_z^2\right)-\mu}{k_B T}\right] + 1}. \tag{4.28}$$

[8] This is particularly true for our torsion pendulum experiment which is at $\sim 300\,\mathrm{K}$.

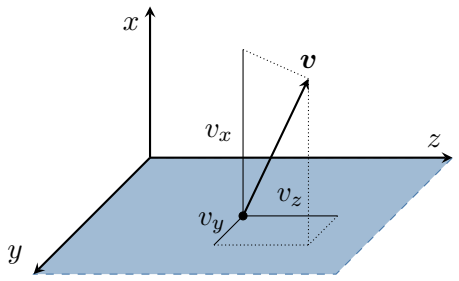

FIGURE 4.2: Coordinates system of the photo-emission model.

The factor two is, once again, due to the degeneracy of spin-1/2 particles and μ is as usual the chemical potential. We can choose, without loss of generality, that v_x is the velocity component normal to the surface (as shown in Figure 4.2).

If we integrate the number density $n(v_x, v_y, v_z)$ for all velocities parallel to the emission surface, that is in the y and z directions, we have[9]

$$\begin{aligned} n(v_x) &= \int_{-\infty}^{+\infty}\int_{-\infty}^{+\infty} n(v_x, v_y, v_z)\,\mathrm{d}v_y\,\mathrm{d}v_z \\ &= \frac{4\pi k_B T}{m}\left(\frac{m}{h}\right)^3 \log\left[1+\exp\left(-\frac{\frac{1}{2}mv_x^2-\mu}{k_B T}\right)\right]. \end{aligned} \tag{4.29}$$

We have found the expression for the number density of the electrons in the emitter, which have velocity v_x in the direction normal to the emission surface. For reasons that will be soon clear, it is convenient to go back to expressing $n(v_x)$ as a function of the energy. Considering that the energy of a free electron in the direction *normal*[10] to the surface is $E_n = \frac{1}{2}mv_x^2$, we have

$$v_x = \sqrt{\frac{2E_n}{m}} \quad \longrightarrow \quad \mathrm{d}v_x = \frac{1}{2}\left(\frac{2E_n}{m}\right)^{-1/2}\frac{2}{m}\,\mathrm{d}E_n = \frac{1}{\sqrt{2E_n m}}\,\mathrm{d}E_n. \tag{4.30}$$

The number of electrons with normal velocity in the range $(v_x, v_x+\mathrm{d}v_x)$ must be equal to the number of electrons whose longitudinal energy lies within $(E_n, E_n+\mathrm{d}E_n)$, i.e.

$$n\left(E_n\right)\mathrm{d}E_n = n\left(v_x\right)\mathrm{d}v_x, \tag{4.31}$$

which leads to

$$\begin{aligned} n\left(E_n\right)\,\mathrm{d}E_n &= \frac{4\pi k_B T}{m}\left(\frac{m}{h}\right)^3 \log\left[1+\exp\left(-\frac{E_n-\mu}{k_B T}\right)\right]\frac{1}{\sqrt{2E_n m}}\,\mathrm{d}E_n \\ &= \frac{4\pi k_B T}{\sqrt{2E_n m^3}}\left(\frac{m}{h}\right)^3 \log\left[1+\exp\left(-\frac{E_n-\mu}{k_B T}\right)\right]\mathrm{d}E_n. \end{aligned} \tag{4.32}$$

This is the expression for the distribution of the energy normal to the sample-vacuum interface in the free electron gas.

Let $h\nu$ be the energy of the photons shone on the sample. At this point Fowler assumed that there is photo-emission if the sum of the electron energy in the direction

[9] We verified this expression with Wolfram Mathematica [35].

[10] The expression kinetic energy in a particular direction would make any Physics 101 professor shiver. We will use this unfortunate name, because it is convenient to reason in term of energy instead of velocity. At the end this matter is just yak shaving, because our model is fundamentally one dimensional, hence the normal energy is simply "the energy" because that is the only direction that exists in our problem.

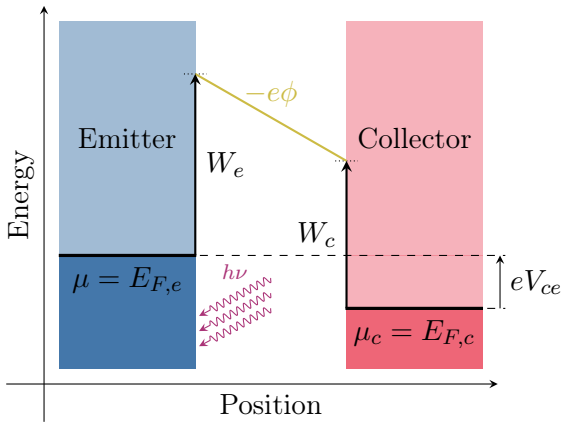

FIGURE 4.3: Visualization of the physical quantities relevant for photo-emission at low-temperatures, for which we have that the Fermi energy coincides with the chemical potential. We introduce here for later use the *contact*, or *Volta*, potential $\phi = \frac{E_{F,c}+W_c-E_{F,e}-W_e}{e}$.

normal to the sample-vacuum interface plus the energy of the absorbed photon $h\nu$ is larger than the sum of the chemical potential μ_e and the work function of the emitter W_e (the potential barrier to reach the vacuum-state). This can be expressed with the following condition

$$(E_n - \mu) + h\nu \geq W_e \qquad \Longrightarrow \qquad \text{Photo-emission} \tag{4.33}$$

See Figure 4.3 for an energetic scheme of the photoemission event.

In other words the transmission coefficient across the sample-vacuum surface is unity if (4.33) is verified, zero otherwise. In Section 4.2.2, we will propose a modification to this condition.

There are a couple of crucial assumptions behind such hypothesis:

- The entire photon energy is used to increase the normal energy of the electron. If we are close to threshold, i.e. if the energy of the incoming photons is just enough to overcome the work function and to create photo-electrons, this assumption is not as unreasonable as it may sound. Indeed close to threshold, the electrons are emitted, only if most of the photon energy is used to increase the kinetic energy in the direction normal to the emitting surface.

- The probability of absorbing a photon does not depend on the initial energy state of the electrons inside the emitter.

As discussed previously, at low temperatures the chemical potential is almost equal to the Fermi energy. From (4.23), it is possible to estimate easily the Fermi energy from the number density of electrons in the sample, which can be reasonably treated as non-interacting. For the relevant case of gold, which is the material chosen for the coating of the LISA GRS, the Fermi energy is approximately 5.53 eV.

If we model the sharp cutoff given by (4.33) as a *transmission coefficient*[11], whose functional expression is an Heaviside step function, we conclude that the emitted

[11] We will use the term transmission coefficient as synonym for transmission probability.

photo-electron spectrum[12] $\tilde{n}$ is

$$\tilde{n}\left(E_n\right)\,\mathrm{d}E_n = \frac{4\pi k_B T}{\sqrt{2E_n m^3}}\left(\frac{m}{h}\right)^3 \log\left[1+\exp\left(-\frac{E_n-\mu}{k_B T}\right)\right]\cdot \\ \cdot\,\Theta\left(E_n-\mu+h\nu-W_e\right)\,\mathrm{d}E_n. \quad (4.34)$$

We define now the new quantity ϵ as

$$\epsilon = E_n-\mu+h\nu-W_e \quad\longrightarrow\quad E_n=\epsilon+\mu-h\nu+W_e \quad\text{and}\quad \mathrm{d}E_n=\mathrm{d}\epsilon, \quad (4.35)$$

which can be physically interpreted as the (kinetic) energy of the emitted photo-electrons in the direction normal to the emitting surface. In this way, we can rephrase (4.34) as

$$\tilde{n}(\epsilon)\,\mathrm{d}\epsilon = \frac{4\pi k_B T}{\sqrt{2(\epsilon+\mu-h\nu+W_e)m^3}}\left(\frac{m}{h}\right)^3\cdot \\ \cdot\log\left[1+\exp\left(-\frac{\epsilon-h\nu+W_e}{k_B T}\right)\right]\Theta(\epsilon)\,\mathrm{d}\epsilon. \quad (4.36)$$

4.2.2 Transmission across the metal-vacuum interface

As mentioned before, in the Fowler's theory for the photoelectric effect, we consider that if an electron after absorbing a photon has an energy in the longitudinal direction larger than the potential barrier, it is automatically emitted form the material. In this way the transmission coefficient $\mathcal{T}$, is

$$\mathcal{T}=\Theta\left(E_n-\mu+h\nu-W_e\right)=\begin{cases}1, & \text{if } E_n-\mu+h\nu\geq W_e\\ 0, & \text{otherwise}\end{cases} \quad (4.37)$$

This is the expression for the transmission coefficient that we would expect from a classical theory. In the following we propose a modification to such transmission coefficient to take into account the quantum mechanical nature of electrons.

This is justified by the fact that if the electrons are treated quantum-mechanically when they are inside the emitter, a quantum mechanical approach should be preferable to a classical one when modeling their transition across the sample-vacuum interface.

Quantum mechanical transmission coefficient for a potential step

The safest approach is to consider the potential barrier between emitter and vacuum as a step. Indeed, more sophisticated models, would require extra (unknown) parameters.

The quantum mechanical transmission coefficient across a potential step can be found by solving the one-dimensional Schrödinger equation [65]

$$\left[-\frac{\hbar^2}{2m}\frac{\mathrm{d}^2}{\mathrm{d}x^2}+U(x)\right]\psi(x)=E\psi(x) \qquad \text{for} \qquad U(x)=\begin{cases}0, & \text{if } x\leq 0\\ U_0, & \text{if } x>0\end{cases} \quad (4.38)$$

[12] The quantities here have no strict normalization, we will address this thorny matter later. The expression for $\tilde{n}$ would be the number of emitter electrons if all free-electrons in the emitter would have absorbed a photon of energy $h\nu$. The calculation for the true flux of emitted electrons would require us to develop a significantly more complex model, which involves the cross-section of the photoelectric effect and the rate at which photons impinge on the target. Let us ignore this complicated physics, and consider from now on the quantity $\tilde{n}$ as the spectrum of the photoelectrons as a function of the normal energy E_n up to a normalization constant.

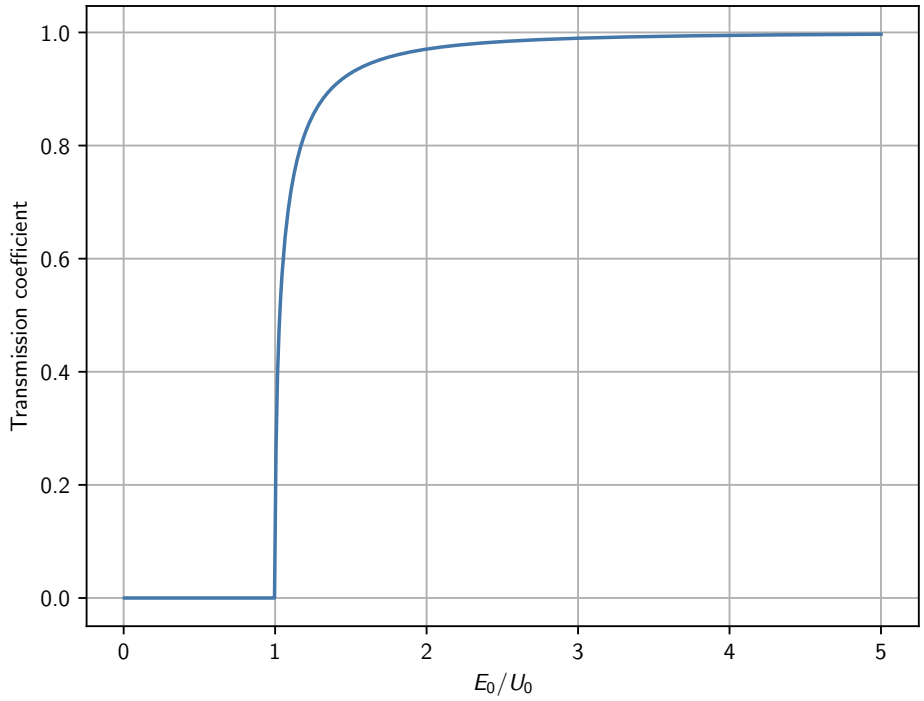

FIGURE 4.4: Example of the QM transmission coefficient for a potential step as a function of the ratio E_0/U_0.

The transmission coefficient, i.e. the probability of overcoming the potential step of height U_0, is a function of the energy of the incident particles E_0 and reads (see Appendix C for the calculations)

$$\mathcal{T}(E_0, U_0) = \begin{cases} \frac{4\sqrt{E_0(E_0-U_0)}}{\left(\sqrt{E_0}+\sqrt{E_0-U_0}\right)^2}, & \text{if } E_0 \geq U_0 \\ 0, & \text{otherwise} \end{cases} \tag{4.39}$$

Now we wish to apply the transmission coefficient just computed to the case of the *photoelectric effect*. The energy of the incoming particle E_0 corresponds to the normal energy of the photoelectron in the emitter plus the energy of the photon

$$E_0 = E_n + h\nu \tag{4.40}$$

and the height of the potential step U_0 is equal to the Fermi energy plus the work function of the emitter

$$U_0 = \mu + W_e. \tag{4.41}$$

Therefore, the transmission coefficient (C.17) for the photoelectric effect becomes

$$\begin{aligned} &\mathcal{T}(E_n + h\nu, W_e + \mu) = \\ &\qquad = \begin{cases} \frac{4\sqrt{(E_n+h\nu)(E_n+h\nu-W_e-\mu)}}{\left(\sqrt{E_n+h\nu}+\sqrt{E_n+h\nu-W_e-\mu}\right)^2}, & \text{if } E_n - \mu + h\nu \geq W_e \\ 0, & \text{otherwise} \end{cases} \end{aligned} \tag{4.42}$$

Comment on more complex models The interface between the crystal lattice of the metallic sample under consideration and the vacuum could be modeled with more sophisticated potentials, rather than the simple potential step. For now we decide not to investigate them, because a more complex functional dependence of the potential barrier would introduce more parameters. Probably with our experimental data we do not have the resolution necessary to distinguish between them[13].

In general, the QM transmission coefficient of more exotic potentials could be computed with standard techniques, such as the WKB approximation.

4.2.3 Fowler's theory including the QM transmission coefficient

Our photo-emission model is strongly based on Fowler's theory, with the modification that we consider that the emission of the exited electrons across the sample-vacuum interface to be regulated by the QM transmission coefficient for a step potential. In particular we assume, as Fowler did, that the whole energy of the absorbed photon goes to increase the velocity of the electron in the direction normal to the emitting surface.

From equation (4.32), we have that the energy spectrum of the electrons that have been excited by a photon of energy $h\nu$ is

$$\begin{aligned} n^*\left(E_n + h\nu\right) \mathrm{d}E_n &= n\left(E_n\right) \mathrm{d}E_n \\ &= \frac{4\pi k_B T}{\sqrt{2E_n m^3}} \left(\frac{m}{h}\right)^3 \log\left[1 + \exp\left(-\frac{E_n - \mu}{k_B T}\right)\right] \mathrm{d}E_n \end{aligned} \tag{4.43}$$

The excited electrons are emitted only if their normal energy is sufficient for them to cross the potential barrier of height $W_e + \mu$ that separate the internal states of the emitter and the vacuum-state. This means that the spectrum of the emitted photo-electrons is given by the product of the excited electron spectrum $n^*\left(E_n + h\nu\right)$ with the probability of crossing the sample-vacuum interface, i.e. the transmission coefficient

$$\begin{aligned} \tilde{n}(E_n + h\nu - W_e - \mu)\,\mathrm{d}E_n &= \mathcal{T}(E_n + h\nu, W_e + \mu)\, n^*\left(E_n + h\nu\right) \mathrm{d}E_n \\ &= \mathcal{T}(E_n + h\nu, W_e + \mu)\, n\left(E_n\right) \mathrm{d}E_n. \end{aligned} \tag{4.44}$$

where the transmission coefficient $\mathcal{T}$ in our model is given by (4.42). Introducing the energy of the emitted electrons ϵ as in (4.35), we have that the previous equation becomes

$$\begin{aligned} \tilde{n}(\epsilon)\,\mathrm{d}\epsilon &= \mathcal{T}(\epsilon + \mu + W_e, W_e + \mu)\, n^*\left(\epsilon + \mu + W_e\right) \mathrm{d}\epsilon \\ &= \mathcal{T}(\epsilon + \mu + W_e, W_e + \mu)\, n\left(\epsilon + \mu - h\nu + W_e\right) \mathrm{d}\epsilon \end{aligned} \tag{4.45}$$

In Figure 4.5 we plot the expected emitted photo-electron spectra $\tilde{n}(\epsilon)$ for several values of the incident photon energy (monochromatic). We observe that if the energy of the absorbed photons increases not only a larger fraction of the excited electrons in the emitter is able to reach the vacuum-state, but also their average emission energy is larger.

Normalization The quantities we introduced in this section have no strict normalization: all the spectra are meant to be interpreted up to a normalization constant

[13] For the same reason we do not consider a transport coefficient that model the propagation of the excited electrons from the bulk of the emitter to the surface, or the more refined three-step model for photoemission

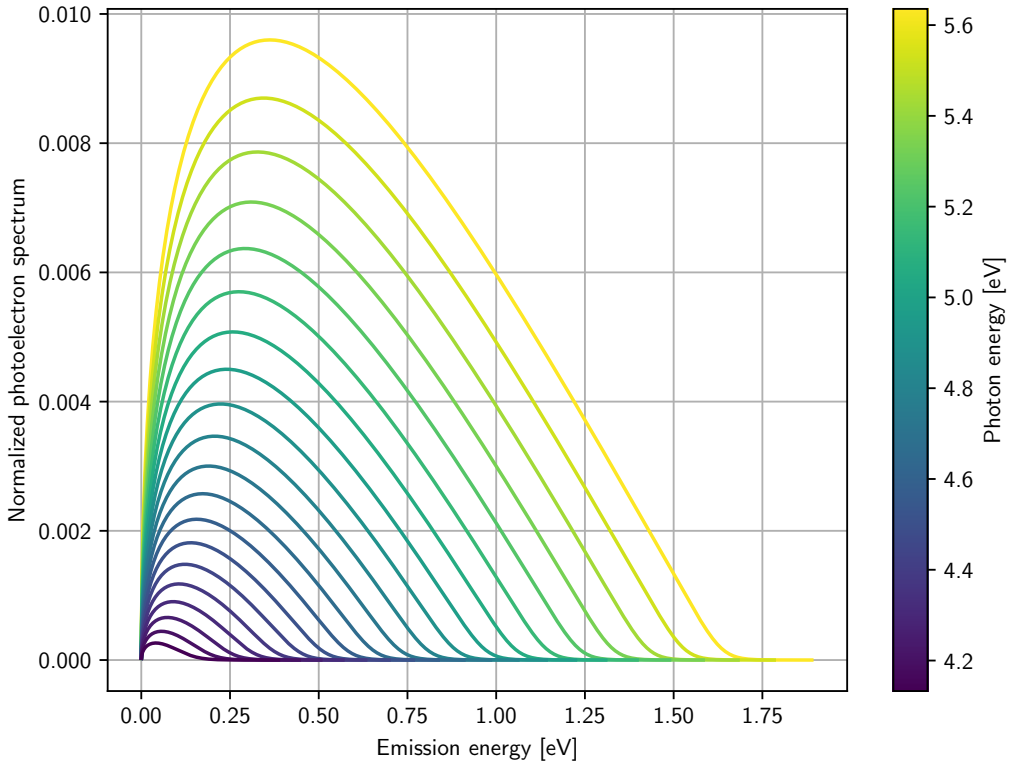

FIGURE 4.5: Photo-electron spectrum $\tilde{n}(\epsilon)$ as a function of the emission energy in the normal direction for several values of the incident photon energy (monochromatic). It has been normalized by the total number of free-electrons per unit volume of the sample. For this plot we set $\mu = 5.53\,\mathrm{eV}$ (nominal value for gold), $T = 300\,\mathrm{K}$, and $W_e = 4\,\mathrm{eV}$.

that hides all the complicated physics that we neglected (e.g. cross-section of the photoelectric effect).

The $n(E_n)$ is defined as the number density of free-electrons per unit volume of the emitter that have energy in the direction normal to the sample-vacuum interface in the range $(E_n, E_n + \mathrm{d}E_n)$.

The $n^*(E_n + h\nu)$ would be the spectrum of the exited electrons in the emitter if each one had absorbed a photon of energy $h\nu$.

The $\tilde{n}(\epsilon)$ would be the spectrum of the photoelectrons as a function of the emission energy if all free-electrons in the emitter absorbed a photon of energy $h\nu$ and impinged on the QM potential step at the emitter surface.

The total number of free-electrons per unit volume of the emitter is given by the integral of the Fermi function

$$\begin{aligned}\frac{N}{V} &= \int_{-\infty}^{+\infty}\int_{-\infty}^{+\infty}\int_{-\infty}^{+\infty} n(v_x, v_y, v_z)\,\mathrm{d}v_x\,\mathrm{d}v_y\,\mathrm{d}v_z \\ &= -4\sqrt{2}\pi^{3/2}\left(\frac{m}{h}\right)^3\left(\frac{k_B T}{m}\right)^{3/2}\mathrm{Li}_{3/2}\left(-e^{\frac{\mu}{K_B T}}\right)\end{aligned} \tag{4.46}$$

where $\mathrm{Li}_s(z)$ indicates the polylogarithm function. Computing the polylogarithm is quite unpleasant. Fortunately an excellent approximation [66] comes to the rescue

$$\lim_{\mathrm{Re}(z)\to\infty}\mathrm{Li}_s\left(\pm e^z\right) = -\frac{z^s}{\Gamma(s+1)} \qquad \text{for} \qquad s \neq -1, -2, -3, \ldots \tag{4.47}$$

where $\Gamma(\cdot)$ is the Gamma function. In our case $s = 3/2$ and, as we are in the low-temperature limit $T \ll E_F/k_B = \mu/k_B$, we have $z = \mu/(K_B T) \gg 1$. The approximation is legitimate. Hence

$$\frac{N}{V} \simeq \frac{4\sqrt{2}\pi^{3/2}}{\Gamma\left(5/2\right)}\left(\frac{m\,\mu}{h^2}\right)^{3/2} \tag{4.48}$$

If we normalize $\tilde{n}(\epsilon)$ with the number of free electron per unit volume N/V, we would obtain the energy spectrum of the fraction of all excited electrons that actually exit the emitter and reach the vacuum state. This quantity is plotted in Figure 4.5.

Generalization for non-monochromatic light

As the UV-LEDS are not monochromatic, we shall adapt (4.45) to account for the specific spectra of the incident photons.

In order to estimate the photo-electron energy distribution for broad-band UV-sources, we need to sum monochromatic emission spectra as the one in (4.45) over all photon energies and weighted by the source-specific probability of having a photon at the considered energy.

If the functional dependence of the photon spectrum as a function of energy $f_{UV}(h\nu)$ were completely known, the procedure described would reduce to computing the following integral

$$\begin{aligned}\tilde{n}_{f_{UV}}(\epsilon) &= \frac{\int f_{UV}(h\nu)\cdot\tilde{n}[\epsilon(\nu)]\,\mathrm{d}\nu}{\int f_{UV}(h\nu)\,\mathrm{d}\nu} \\ &= \frac{\int f_{UV}(h\nu)\cdot\mathcal{T}\left[\epsilon(\nu)+\mu+W_e, W_e+\mu\right] n\left[\epsilon(\nu)+\mu-h\nu+W_e\right]\,\mathrm{d}\nu}{\int f_{UV}(h\nu)\,\mathrm{d}\nu}\end{aligned} \tag{4.49}$$

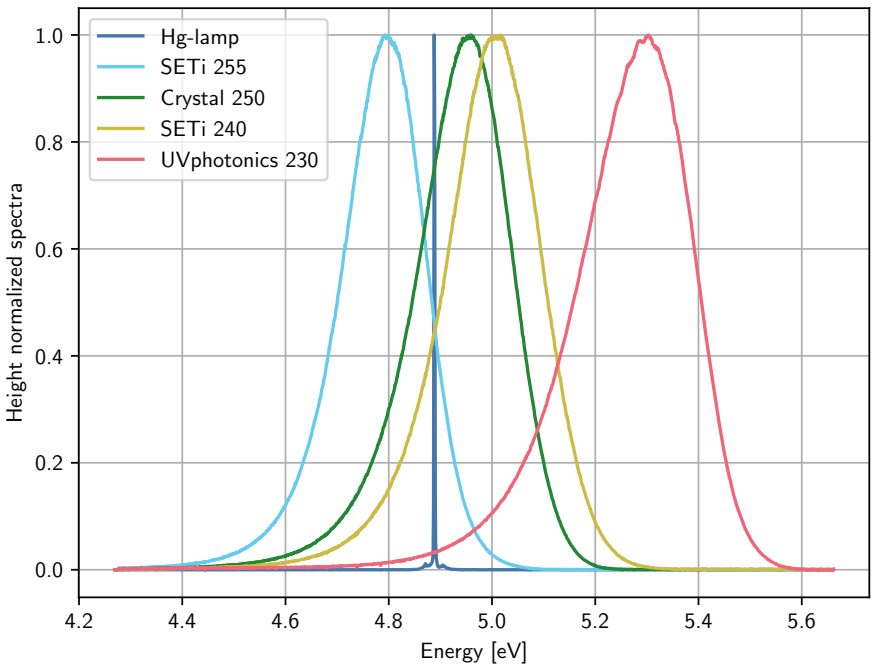

FIGURE 4.6: Spectra of the UV-light sources as a function of the energy and normalized to have unit height for an easier comparison.

where we indicated explicitly the dependence of the normal emission energy of the photo-electrons on the photon energy $\epsilon = \epsilon(\nu)$ as defined in (4.35).

In practice, our spectrometer samples the true photon spectrum f_{UV} over a discrete array of energies $(h\nu_0, h\nu_1, \dots, h\nu_N)$, i.e. it outputs a series of counts for each energy

$$c_i = f_{UV}(h\nu_i) \tag{4.50}$$

From the raw counts we can find the probability of having a photon at the energy $h\nu_i$ is given by

$$p_i = p(h\nu_i) = \frac{f_{UV}(h\nu_i)}{\sum_i f_{UV}(h\nu_i)} = \frac{c_i}{\sum_i c_i}. \tag{4.51}$$

At this point we can rephrase (4.49), as a discrete sum

$$\begin{aligned} \tilde{n}_{f_{UV}}(\epsilon) &= \sum_i p_i \cdot \mathcal{T}(\epsilon + \mu + W_e, W_e + \mu)\, n\left(\epsilon + \mu - h\nu_i + W_e\right) \\ &= \frac{\sum_i f_{UV}(h\nu_i) \cdot \mathcal{T}(\epsilon + \mu + W_e, W_e + \mu)\, n\left(\epsilon + \mu - h\nu_i + W_e\right)}{\sum_i f_{UV}(h\nu_i)} \end{aligned} \tag{4.52}$$

Given the LED spectra shown in Figure 4.6, choosing $\mu = 5.53\,\text{eV}$, $T = 300\,\text{K}$, $W_e = 4\,\text{eV}$, we obtain the effective spectra displayed in Figure 4.7.

4.2.4 Apparent yield and photocurrents

The final goal of our photo-emission model is to simulate the apparent yield curve for a user-defined set of microscopic parameters of the emitting surfaces (e.g. work-function, chemical potential), illumination pattern (e.g. delay and duration of the light

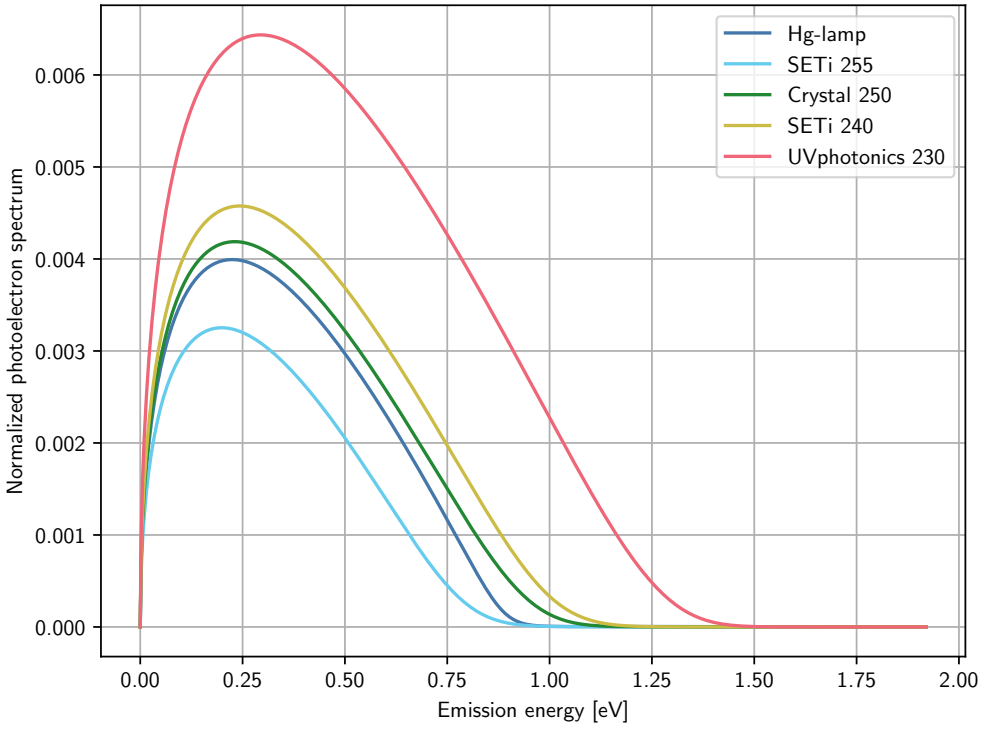

FIGURE 4.7: Photo-electron spectra $\tilde{n}_{f_{UV}}(\epsilon)$ for the UV-light sources available in our laboratory normalized by the total number of the electrons per unit volume of the sample. For this plot we set $\mu = 5.53\,\text{eV}$ (nominal value for gold), $T = 300\,\text{K}$, and $W_e = 4\,\text{eV}$.

pulses with respect to the injection bias), and spectrum of the incident photons. In order to achieve this goal we have to convert the spectrum of the photo-electrons into an electrical current flowing from the emitter to the collector.

Let us consider the simple one-dimensional model presented in Figure 4.8. Once a photon has been absorbed by an electron in the emitter, it is extracted only if the sum of its initial energy in the normal direction E_n and the photon energy is larger than the surface barrier given by the sum of the Fermi energy $\mu = E_{F,e}$ and the work-function W_e, as we can see from (4.42). If this condition is satisfied, the energy of the photo-electron in the direction normal to the emitter surface will be

$$\epsilon = E_n + h\nu - W_e - \mu \qquad \text{if} \qquad E_n + h\nu \geq \mu + W_e. \tag{4.53}$$

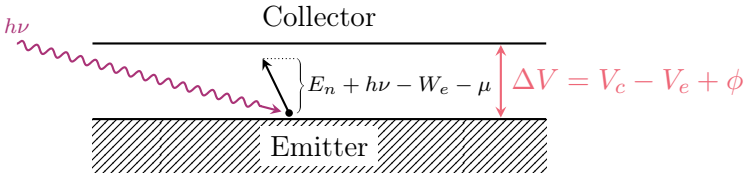

FIGURE 4.8: Photoemission in an idealized geometry. Scheme of the basic element of the model: an emitting surface with work function W_e is illuminated with a photon of energy $h\nu$, which may lead to the production of a photo-electron (black dot). ΔV is the potential difference between emitter and collector including the contribution of the contact potential ϕ.

Assuming that between emitter and collector there is a stopping potential

$$\Delta V = V_e - V_c + \phi, \tag{4.54}$$

where V_e and V_c are the electrostatic potential of, respectively, the emitter and the collector and ϕ is the *contact potential*[14] (see also Figure 4.3)

$$\phi = \frac{W_c + \mu_c - W_e - \mu}{e} = \frac{W_c + E_{F,c} - W_e - E_{F,e}}{e}, \tag{4.55}$$

we have that only those photoelectrons which have normal kinetic energy larger than $-e\Delta V$ (minus because the electric charge of electrons is negative) reach the collector and hence generate a photo-current. In a formula

$$\mathcal{P}(\Delta V) = \frac{\int_{-e\Delta V}^{\infty} \tilde{n}_{f_{UV}}(\epsilon)\,\mathrm{d}\epsilon}{\int \tilde{n}_{f_{UV}}(\epsilon)\,\mathrm{d}\epsilon}, \tag{4.56}$$

where we normalized by the total number of photo-electrons, so that $\mathcal{P}(\Delta V)$ can be interpreted as the probability of the emitted electrons to reach the collector and hence contribute to the photo-current.

At this point we can compute the observed number of electrons that reach the collector per photon shone on the emitter, i.e. the *apparent yield* of the emitter $\mathcal{Y}_e$, as

$$\mathcal{Y}_e(\Delta V) = A_e \cdot \mathcal{Q}_e \cdot \mathcal{P}(\Delta V) \tag{4.57}$$

where A_e is the fraction if the injected light absorbed by the emitter and $\mathcal{Q}_e$ is the (intrinsic) *quantum yield* of the emitter that is the number of photoelectrons per absorbed photon

$$\mathcal{Q}_e = \frac{\#\text{ charges emitted}}{\#\text{ photons absorbed}}. \tag{4.58}$$

The quantum yield is the rug under which we swept all the complex photoemission physics such as the cross-section of the photoelectric effect. It is a measurable quantity that depends on the microscopic properties of the emitter and of the incident light (energy, angle of incidence, etc.). We expect that the apparent yield grows as the wavelength of UV-light decreases, simply because a larger amount of photons has enough energy to extract an electron.

In order to compute a current, we have to multiply the apparent yield by the number of photons shone on the emitter per unit time

$$I_e(\Delta V) = e\mathcal{Y}_e(\Delta V) \underbrace{\frac{P_{UV}}{\langle E_{UV}\rangle}}_{\#\text{ photons/s}} \tag{4.59}$$

Comment on Schottky effect In principle we should take into account the *Schottky effect*, that is the lowering of the work function due to the presence of a DC electric field outside the metal sample. Indeed we have that the nominal work function W in the presence of external DC fields, has to be substituted by the effective work function

$$W_{eff} = W - \Delta W_{Shottky} \tag{4.60}$$

[14] As usual the chemical potential is equal to the Fermi energy in the low-temperature limit.

where $\Delta W_{Shottky}$ is of the order [67]

$$\Delta W_{Shottky} = \sqrt{\frac{e^3}{4\pi\varepsilon_0} E} \tag{4.61}$$

where E is the modulus of the external electric field. In the case of the LISA sensor we can reasonably assume that $E = \Delta V/d$, as in a plane parallel capacitor. A worst case scenario for LISA is $\Delta V \sim 5\,\mathrm{V}$ and $d \sim 2\,\mathrm{mm}$, so that $W_{Shottky} \sim 2 \cdot 10^{-3}\,\mathrm{eV}$, hence the Schottky effect is negligible.

4.3 Computational model for LISA

We now have all the elements to build a photo-emission model for the LISA sensor. Indeed, fixed the light source (i.e. spectrum of light) and the surface parameters (i.e. work function, chemical potential, temperature), we can compute the photoelectron spectrum with (4.52). Once the photoelectron spectrum is known, we can obtain the EH and TM photo-currents under the following assumptions:

- The LISA sensor is divided into pairs of overlooking surfaces, one belonging to the TM and one to the EH. The number of such surfaces can be arbitrary. Generally, we choose to use the minimum number of surface pairs needed to reproduce the senor configuration in terms of injection and actuation voltages. For example, if we consider the case where there is no injection bias and no actuation potential on the electrodes, we just need a surface pair to describe the system, namely the EH and the TM. On the other hand, if we add the injection bias, we would have to consider two surface pairs: a pair is composed of the injection electrodes and the part of the test mass facing the injection electrodes, the other surface pair encompasses of the rest of TM and EH. If we add, on top of the injection bias, AC or DC actuation on one or more sensing electrodes, we would have to add surface pairs to match the number of electrodes activated.

- Even if the geometry of these surfaces can be quite complex, they are treated as infinite plane parallel sheets.

- The amount of light absorbed by the sensor surfaces for the case of EH and TM illumination is considered fixed[15] and equal to the data provided by the Astrium simulation (see Appendix B).

- The quantum yield is assumed uniform over the surface element considered. As our model is one-dimensional, we do not consider a dependence of the apparent yield on the incident angle of the surfaces.

- The model considers that the DC and AC actuation one the electrodes is applied in pattern such that they do not induce a polarization of the TM. This is important to keep in mind, because the model do not check explicitly for the above to be true. If we apply an unbalanced potential to the electrodes the result of the model could be inaccurate.

- In the case of AC actuations, the model assumes that there is no fixed relative phase between the actuation voltage and the 100 kHz-injection bias.

[15] The absorption coefficients are obtained via ray-tracing simulation for a centered test mas. Therefore, motion of the TM in the sensor, would, in principle, make such coefficients vary with time. We assume that this effect is small.

- The transmission of the photoelectrons from emitter to collector is instantaneous, if they have enough energy to overcome the electrostatic stopping potential ΔV.

The basic building block of our photo-emission model for the LISA sensor is the one depicted in Figure 4.8. However, it is important to notice that, as the inner GRS surfaces are quite reflective, TM and EH both act at the same time emitters (and collectors), even if the illumination is conducted via only the TM or EH fiber.

Let us make an example for the sake of clarity. Considering, for simplicity, only one surface pair, namely an element of the EH and the overlooking TM area.

Case 1: EH is emitter and TM is collector The electrostatic stopping potential encountered by the electrons emitted from the EH to the TM is

$$\Delta V = \Delta V_{EH\to TM} = V_{TM} - V_{EH} + \phi_{EH} \tag{4.62}$$

where V_{TM} is the test mass potential

$$V_{TM}(t) = \frac{Q_{TM}}{C_{tot}} + \frac{C_{inj}V_{inj}}{C_{tot}}\sin\left(2\pi f_{inj}t\right) + \underbrace{\frac{1}{C_{tot}}\sum_i C_i V_i(t)}_{0}\,. \tag{4.63}$$

The last term is zero because we assume that the actuation pattern does not polarize significantly the TM. On the other hand V_{EH}, is the potential of the EH surface considered which is

$$V_{EH}(t) = \begin{cases} V_i(t), & \text{for sensing/actuation electrodes} \\ V_{inj}\sin(2\pi f_{inj}t), & \text{for injection electrodes} \\ 0, & \text{for rest of EH} \end{cases} \tag{4.64}$$

Finally, ϕ_{EH} is the EH contact potential[16]

$$\phi_{EH} = \frac{W_{TM} + \mu_{TM} - W_{EH} - \mu_{EH}}{e}. \tag{4.65}$$

As the TM and EH potentials are, in general, a function of time, we have that also the electrostatic barrier $\Delta V(t)$ will depend on time.

If we consider that the UV illumination has a delay t_{UV} with respect to the zero-crossing of the injection bias and a duration Δt_{UV}, we can write form (4.57), the apparent yield of solely the EH surface as

$$\mathcal{Y}_{EH}[\Delta V(t), t_{UV}, \Delta t_{UV}] = -A_{EH}\cdot\mathcal{Q}_{EH}\frac{\int_{t_{UV}}^{t_{UV}+\Delta t_{UV}}\mathcal{P}_{EH}[\Delta V(t)]\,\mathrm{d}t}{\int_0^{f_{inj}^{-1}}\mathcal{P}_{EH}[\Delta V(t)]\,\mathrm{d}t} \tag{4.66}$$

where, similarly to (4.56), $\mathcal{P}_{EH}$ is given by

$$\mathcal{P}_{EH}[\Delta V(t)] = \frac{\int_{-e\Delta V(t)}^{\infty}\tilde{n}_{f_{UV}}^{EH}(\epsilon)\,\mathrm{d}\epsilon}{\int\tilde{n}_{f_{UV}}^{EH}(\epsilon)\,\mathrm{d}\epsilon}, \tag{4.67}$$

[16]The contact potential acts as an additional potential term that can either aid or hinder the motion of the photoelectrons.

Here $\tilde{n}^{EH}_{f_{UV}}$ is the spectrum of the photoelectrons emitted from the EH, which depends on its microscopic properties (i.e. the work function W_{EH} and the chemical potential μ_{EH}).

In practice we averaged the probability of the photo-electrons emitted form the EH to reach the collector (in this case the TM) over the period of the illumination. The minus sign in front arises form the fact that conventionally apparent yield is *positive* when electrons *leave* the TM.

Case 2: TM is emitter and EH is collector At the same time, also the TM emits photo-electrons towards the EH. Since we swapped the surface that acts as emitter and collector with respect to the previous case, the stopping potential that electrons emitted from the TM encounter is the opposite

$$\begin{aligned}\Delta V_{TM\to EH} &= V_{EH} - V_{TM} + \phi_{TM} \\ &= V_{EH} - V_{TM} + \frac{W_{EH} + \mu_{EH} - W_{TM} - \mu_{TM}}{e} \\ &= -\Delta V\end{aligned} \tag{4.68}$$

From (4.66) considering the new electrostatic barrier, we have that the expression for the TM apparent yield[17] is

$$\mathcal{Y}_{TM}[\Delta V(t), t_{UV}, \Delta t_{UV}] = A_{TM} \cdot \mathcal{Q}_{TM} \frac{\int_{t_{UV}}^{t_{UV}+\Delta t_{UV}} \mathcal{P}_{TM}[\Delta V(t)]\,\mathrm{d}t}{\int_0^{f_{inj}^{-1}} \mathcal{P}_{TM}[\Delta V(t)]\,\mathrm{d}t} \tag{4.69}$$

where, similarly to before,

$$\mathcal{P}_{TM}[\Delta V(t)] = \frac{\int_{e\Delta V(t)}^{\infty} \tilde{n}^{TM}_{f_{UV}}(\epsilon)\,\mathrm{d}\epsilon}{\int \tilde{n}^{TM}_{f_{UV}}(\epsilon)\,\mathrm{d}\epsilon}, \tag{4.70}$$

In this case $\tilde{n}^{TM}_{f_{UV}}$ is the spectrum of the photoelectrons emitted from the TM, which is a function of the microscopic properties W_{TM} and μ_{TM}.

The total apparent yield is the sum of the individual apparent yields

$$\mathcal{Y}(\Delta V) = \mathcal{Y}_{EH}(\Delta V) + \mathcal{Y}_{TM}(\Delta V) \tag{4.71}$$

At this point we are able to simulate apparent yield curves with our model and compare them to the experimental data[18].

4.3.1 Parameters of the model

For a matter of clarity, we summarize in Table 4.1 the information or parameters that we need to provide to our photo-emission model, in order to generate the apparent yield curves. These parameters must be defined for each emitting surface. For example in the minimal model of just a surface pair, we have to define two sets of parameters: one for the EH element, the other for the TM.

[17] In the next equation there is no minus sign because the electron leaving the TM give rise to a positive apparent yield.

[18] Provided that we express the simulated $\mathcal{Y}$ as a function of the test mass voltage due to charge $V_{TM} = Q_{TM}/C_{tot}$.

TABLE 4.1: Parameters of our photo-emission model.

Name	Symbol	Known?	Comments
Quantum yield	$\mathcal{Q}_e$	No	Quantum yield of the surface element.
Work function	W_e	Partially	We have measurements for clean gold samples, but we expect the GRS surfaces to be contaminated.
Light-absorption coefficient	A_e	Mostly	We base our analysis on the Astrium ray-tracing data (see Appendix B), which are in agreement with the GEANT4 data by Dr. Hollington [59].
Chemical potential	μ	Partially	We can compute it theoretically from (4.26) for a given material, but it could vary from the ideal case if contamination is present. Anyhow, it is not critical, as the model depends very weakly on μ. We assume $\mu = 5.53\,\text{eV}$, i.e. the nominal value for gold [61].
Temperature	T	Yes	It is not a crucial parameter (no significant impact on the curves for $k_B T \ll E_F \simeq \mu$). We assume $T = 300\,\text{K}$.
Injection voltage	V_{inj}	Yes	Amplitude of injection bias for capacitive sensing.
Potential applied	$V_i(t)$	Yes	Potential applied to the electrode considered (DC or AC).
Delay	t_{UV}	Yes	Delay of the illumination from the zero-crossing of the injection bias.
Duration	Δt_{UV}	Yes	Duration of the illumination.
Spectrum	f_{UV}	Yes	Spectrum of the incident light.

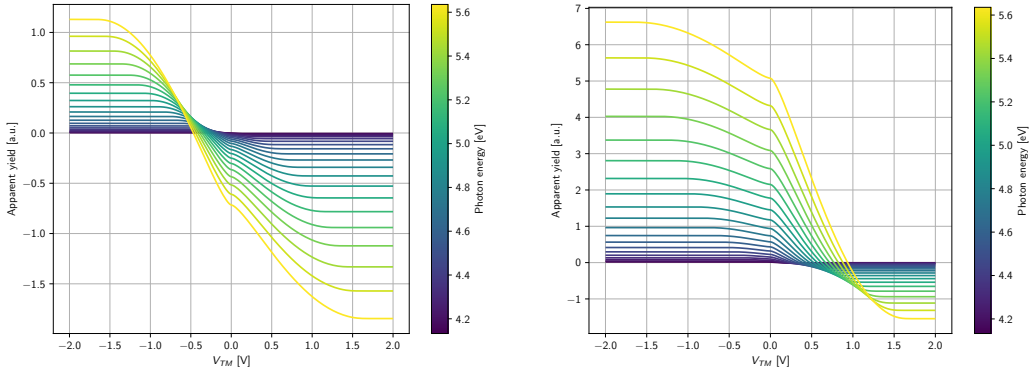

(A) EH illumination (B) TM illumination

FIGURE 4.9: Simulated apparent yield curves for monochromatic photons at various energies (see colormap). To produce the plots we assumed $\mu = 5.53\,\text{eV}$ and $W_{EH} = W_{TM} = 4\,\text{eV}$. The injection voltage is set to zero ($V_{inj} = 0\,\text{V}$). The y-axes of both plots have same arbitrary units that are intended to be proportional to the number of elementary charges transferred per injected photon.

4.3.2 Simulations with the photoemission model

We can apply the photoemission model to simulate the apparent yield curves in some relevant configurations, assuming the light absorption coefficients of Appendix B and reasonable values for the model parameters.

Effect of the photon energy

We can investigated how the photon peak energy affects the apparent yield curves. In Figure 4.9 we plot some simulated apparent yield data considering monochromatic incident light with photon energy ranging from 4.1 eV to 5.6 eV. In addition we fixed the workfunction of EH and TM to $W_{EH} = W_{TM} = 4\,\text{eV}$.

The quantum yield of TM and EH is the same and proportional to the integral of the total number of emitted photo-electrons

$$\mathcal{Q}_{EH} = \mathcal{Q}_{TM} \propto \int \tilde{n}(\epsilon)\,\mathrm{d}\epsilon, \tag{4.72}$$

where $\tilde{n}(\epsilon)$ is the photoelectron spectrum defined in (4.45). As we consider the same photon energies, the apparent yield curves of Figure 4.9 have the same color correspondence of the spectra in Figure 4.5.

As expected, we observe that the magnitude of the apparent yield increases with the incident photon energy: this is due to the fact that a larger pool of the electrons inside the emitter can reach an energy sufficient to overcome the potential barrier when a more energetic photon is absorbed. Moreover, we notice that the equilibrium voltage moves towards more negative or more positive values for EH and TM illumination respectively.

We notice that this simulation may be oversimplified because we assumed that the quantum yield scales proportionally to the number of emitted photoelectrons. In reality the physical quantities that underlie the photo-emission, such as the cross section of the photoelectric effect, may depend on the incident photon energy and hence influence the emission spectrum.

Effect of the injection bias

In the case that the injection bias is null ($V_{inj} = 0\,\mathrm{V}$), the current generated from the injection electrodes does not differ from the other areas of EH and TM. Indeed in this case, it was not even necessary to define the injection electrodes as a separate surface pair from the EH and TM: they could be included in the rest of TM and EH.

On the other hand, if the injection voltage is different from zero (in particular we focus on the case $V_{inj} = 5.4\,\mathrm{V}$ used for the torsion pendulum measurements), the current coming from the injection electrodes (and the area of the TM facing them) will be quite different from the rest of the sensor. This is due to the fact that close to the injection electrodes the electrostatic fields are quite intense ($\sim V_{inj}/d$, where $d \sim$ mm is the distance between injection electrodes and TM).

More precisely, from equations (4.62)–(4.65) the potential barrier between EH and TM in the region of the injection electrodes will be

$$\begin{aligned}\Delta V_{inj}(t) &= V_{TM}(t) - V_{inj}\sin(2\pi f_{inj}t) + \phi_{EH} \\ &= \frac{Q_{TM}}{C_{tot}} - V_{inj}\underbrace{\left(1 - \frac{C_{inj}}{C_{tot}}\right)}_{\simeq 1}\sin(2\pi f_{inj}t) + \phi_{EH}\end{aligned} \tag{4.73}$$

The approximation is valid because for the LISA sensor the total capacitance is approximately a factor 8 larger than the injection electrodes one, i.e. $C_{tot} \gg C_{inj}$. On the other hand, the rest of the EH is grounded, hence the potential barrier will just be

$$\begin{aligned}\Delta V_{rest}(t) &= V_{TM}(t) + \phi_{EH} \\ &= \frac{Q_{TM}}{C_{tot}} + V_{inj}\frac{C_{inj}}{C_{tot}}\sin(2\pi f_{inj}t) + \phi_{EH}.\end{aligned} \tag{4.74}$$

Considering that $C_{tot} \gg C_{inj}$ and the nominal $V_{inj} = 5.4\,\mathrm{V}$ for the 4TM torsion pendulum, we see that the electrostatic field in the region close to the injection electrodes is generally quite different[19] from the rest of the electrode housing and hence must be treated separately by the numerical model.

100%-duty cycle illuminations In Figure 4.10 we plot the predicted discharge curves for the Crystal 250 LED for EH illumination with 100%-duty cycle.

The effect of the 100 kHz-injection voltage on the apparent yield curve with illumination duty cycle equal to 100% is, as expected, also to smear out the discharge curves, because at each value of the test mass charge the resulting apparent yield is the average over an oscillating potential barrier[20] between EH and TM.

Out-of-phase and in-phase illuminations Next we evaluate the effect of the synchronization of the light pulses with the 100 kHz-injection bias. In Figure 4.11, we compare the apparent yield curve obtained at zero-injection with the curves obtained with a pulse delay of 2 µs and 7 µs (duration always 1 µs). Such configurations are also called in-phase and out-of-phase illumination because the pulse of light is centered on, respectively, the maximum and minimum of the injection bias.

The main effect of a pulsed illumination synchronized with the injection bias is to shift the apparent yield curve obtained at $V_{inj} = 0\,\mathrm{V}$ by an amount equal to the

[19] In particular when the sinusoidal injection bias approaches the maximum or minimum.

[20] This effect is enhanced in the areas close to the injection electrodes, where the amplitude of the applied potential is larger.

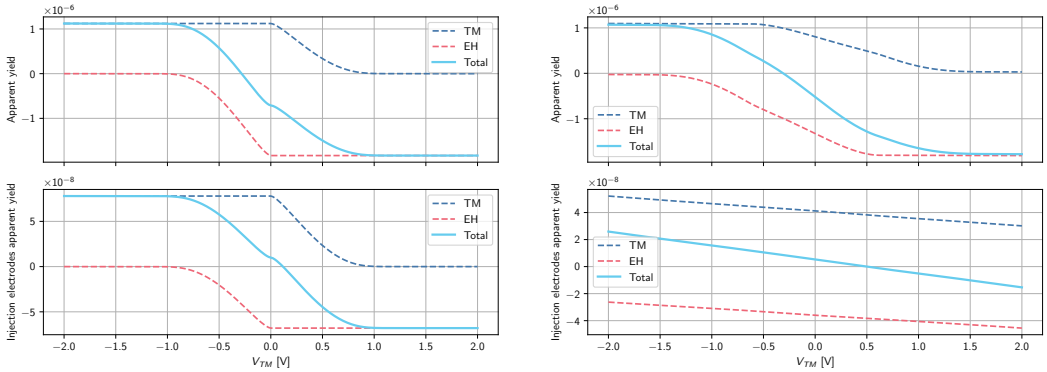

(A) Injection voltage $V_{inj} = 0\,\mathrm{V}$ (B) Injection voltage $V_{inj} = 5.4\,\mathrm{V}$

FIGURE 4.10: Predicted discharge curves for the Crystal 250 LED in the case of EH illumination for a light pulse duration of 10 µs. The value of other relevant parameters chosen for this plot are $\mu = 5.53\,\mathrm{eV}$, $W_{EH} = W_{TM} = 4\,\mathrm{eV}$, and $\mathcal{Q}_{EH} = \mathcal{Q}_{TM} = 10^{-5}$. In the bottom panel, we plot the contribution of just the injection electrodes.

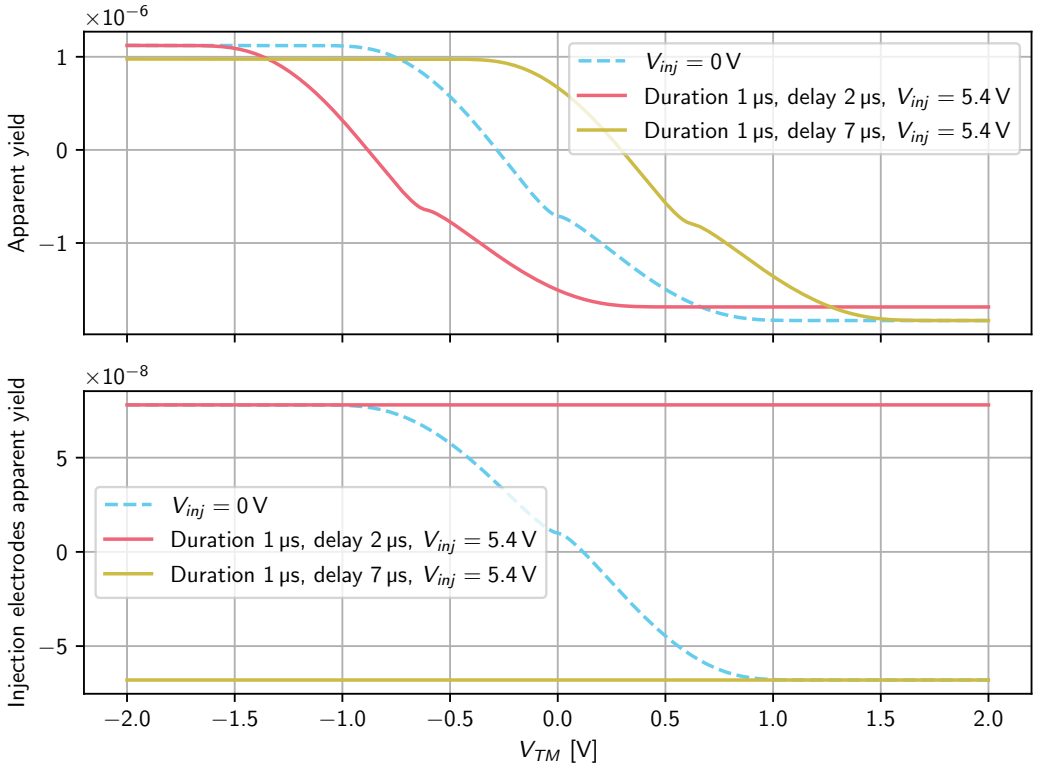

FIGURE 4.11: Predicted Crystal 250 discharge curves for EH illumination with duration 1 µs and delays 2 µs and (*red*) 7 µs (*yellow*) compared to the data zero-injection case (*cyan*). The model parameters are $\mu = 5.53\,\mathrm{eV}$, $W_{EH} = W_{TM} = 4\,\mathrm{eV}$, and $\mathcal{Q}_{EH} = \mathcal{Q}_{TM} = 10^{-5}$. In the bottom panel, we plot the contribution of just the injection electrodes.

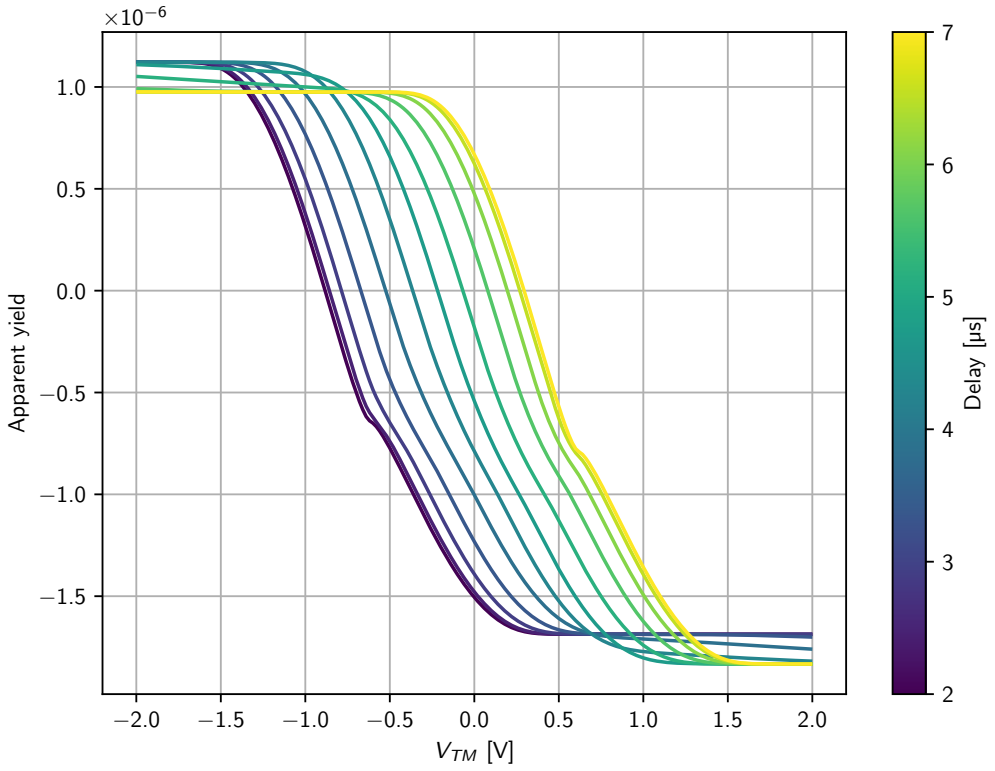

FIGURE 4.12: Simulated apparent yield curves for EH illumination with Crystal 250 with $V_{inj} = 5.4\,\mathrm{V}$. The duration of the light pulses is 1 µs and the delay varied in the range $2 - 7\,\mu\mathrm{s}$ (see colorbar). The vaues of the model parameters are $\mu = 5.53\,\mathrm{eV}$, $W_{EH} = W_{TM} = 4\,\mathrm{eV}$, and $\mathcal{Q}_{EH} = \mathcal{Q}_{TM} = 10^{-5}$.

polarization potential imparted by the injection electrodes during the illumination window (see also Figure 4.12). This is due to the fact that for the photocurrents, the only relevant quantity is the potential difference between EH and TM, and not the TM charge. The injection bias modulates this potential barrier with time.

A secondary effect is a change in the saturation levels, due to the contribution of the injection electrodes to the apparent yield. As we can see from the bottom panel of Figure 4.11, we have that the apparent yield from the injection electrodes is equal to its negative and positive saturation in the case of, respectively, the in-phase and out-of-phase illuminations. This effect is more severe for illumination of the EH compared to the TM because in the former case a larger fraction of the "useful" light is absorbed in the area of the injection electrodes.

We can explain the change in the saturation levels by observing that if we illuminate in phase with the injection bias, the potential barrier for electrons emitted from the injection electrodes from (4.73) will be

$$\Delta V\left(t = \frac{1+4k}{4f_{inj}}\right) = \frac{Q_{TM}}{C_{tot}} - V_{inj}\left(1 - \frac{C_{inj}}{C_{tot}}\right) + \phi_{EH} \ll 0 \qquad \text{(in-phase)} \qquad (4.75)$$

where $k = 0, \pm 1, \pm 2, \ldots$. The negative and large in magnitude potential barrier causes a suppression of the EH photocurrent. The opposite is true for out-of-phase

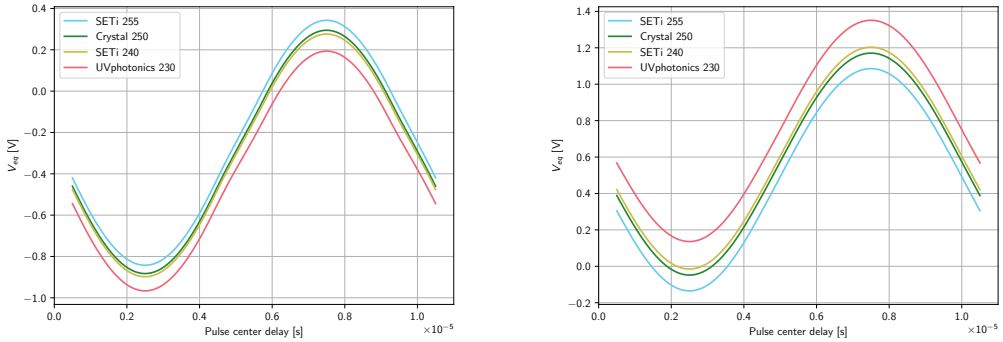

(A) EH illumination (B) TM illumination

FIGURE 4.13: Simulated equilibrium potentials in the case of EH and TM illuminations for light pulses of duration 1 µs and variable delay. The injection voltage is $V_{inj} = 5.4\,\mathrm{V}$. The model parameters chosen are $\mu = 5.53\,\mathrm{eV}$, $W_{EH} = W_{TM} = 4\,\mathrm{eV}$, and $\mathcal{Q}_{EH} = \mathcal{Q}_{TM}$.

illuminations: the potential barrier between EH and TM will be

$$\Delta V\left(t = \frac{3+4k}{4f_{inj}}\right) = \frac{Q_{TM}}{C_{tot}} + V_{inj}\left(1 - \frac{C_{inj}}{C_{tot}}\right) + \phi_{EH} \gg 0 \qquad \text{(out-of-phase)} \quad (4.76)$$

which causes a suppression of the TM photocurrent.

We would like to point out that this change in the saturation currents is apparent only because we can explore a limited range of possible TM potentials[21]: at $|Q_{TM}/C_{tot}| \gg V_{inj}\,(1 - C_{inj}/C_{tot}) \simeq V_{inj}$ we would observe the in-phase and out-of-phase saturation reach the ones of the zero-injection case, because the electric field due to the test mass charge will be much stronger than the local electric field close to the injection electrodes. The reference [68] confirms independently this supposition.

Quantitatively the true positive saturation is attained when no photoelectron generated anywhere on the TM (hence also in front of the injection electrodes) reaches the EH, which happens when they encounter a potential barrier larger than the maximum emission energy. Conversely, we are in complete negative saturation when the potential barrier is larger than the maximum emission energy of the photoelectrons emitted from any domain of the EH (including the injection electrodes).

Equilibrium potentials Of course our model is able to estimate the equilibrium potential, i.e. the value of V_{TM} at which the apparent yield vanishes $\mathcal{Y}(V_{TM} = V_{eq}) = 0$, for any illumination pattern. In Figure 4.13, we plot the equilibrium potential as a function of the pulse center delay for EH and TM illuminations with the LEDs at our disposal (duration of the pulses is 1 µs and $V_{inj} = 5.4\,\mathrm{V}$). The simulation confirms that with the phase of the illumination we can control the equilibrium voltage for both TM and EH illumination approximately[22] in the range

$$V_{eq} \in V_{eq}(V_{inj} = 0) \pm \frac{C_{inj}}{C_{tot}} V_{inj} \quad (4.77)$$

where $V_{eq}(V_{inj} = 0)$ is the equilibrium potential when the injection bias is null.

[21] Here we neglect the contact potential ϕ_{EH}, because it is expected to be small.

[22] Small deviations are expected due to the non-negligible pulse duration and from the contribution to the apparent yield from the injection electrodes.

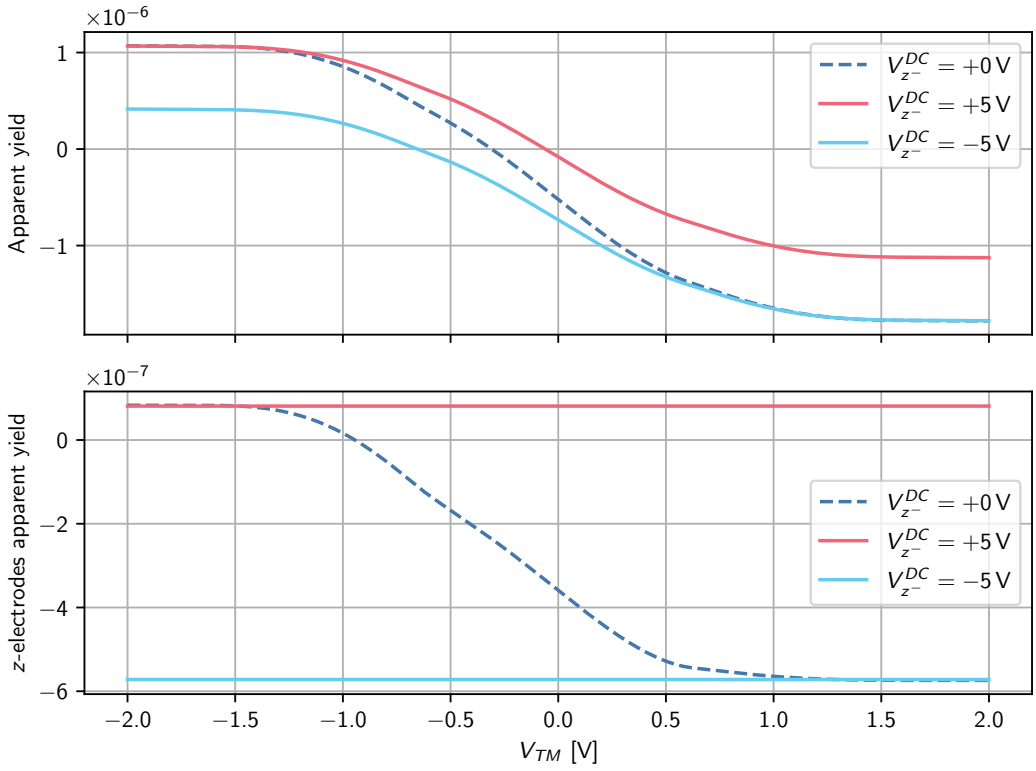

FIGURE 4.14: Discharge curves with DC actuation on the z-electrodes for the EH illumination of duration $10\,\mu$s with the Crystal 250 LED ($V_{inj} = 5.4\,\mathrm{V}$). In the legend we report the DC potential on both the z^--electrodes, but and equal and opposite potential is applied to the z^+-electrodes in order not to polarize the test mass. The model parameters are $\mu = 5.53\,\mathrm{eV}$, $W_{EH} = W_{TM} = 4\,\mathrm{eV}$, and $\mathcal{Q}_{EH} = \mathcal{Q}_{TM} = 10^{-5}$. In the bottom panel, we plot the contribution of just the z-electrodes.

Effect of DC and AC actuation

In this section we simulate the effect of the DC and AC actuation on the discharge curves. For all the results presented here, there is the fundamental assumption that the actuation does not polarize the TM.

The effect of DC actuation on the z-electrodes is displayed in Figure 4.14 for EH illumination with the Crystal 250 LED. From the table of the torsion pendulum absorption coefficients in Appendix B, we see that in the case of EH illumination only the z_1^- electrode receives a significant amount of light ($\sim 5.6\%$, which becomes $\sim 19\%$ if we consider only the fraction of "useful" light[23]). Hence we have that apparent yield curves will be mainly influenced by the potential applied to such electrode. If $V_{z_1^-} = -5\,\mathrm{V}$, the electrons emitted from the area of the TM in front of the electrode will be repelled, causing a suppression in the TM photocurrent. On the other hand, the EH photocurrent will be reduced if $V_{z_1^-} = +5\,\mathrm{V}$ This is confirmed by the simulated data.

Finally, we analyze the effect of AC actuation. We chose AC actuation in the V_{1z}, V_{2z}, $V_{1\eta}$ and $V_{2\eta}$ pattern, which activate the z-electrodes only. The waveform on the

[23] That is light which is not considered lost in Appendix B and can actually produce a photocurrent.

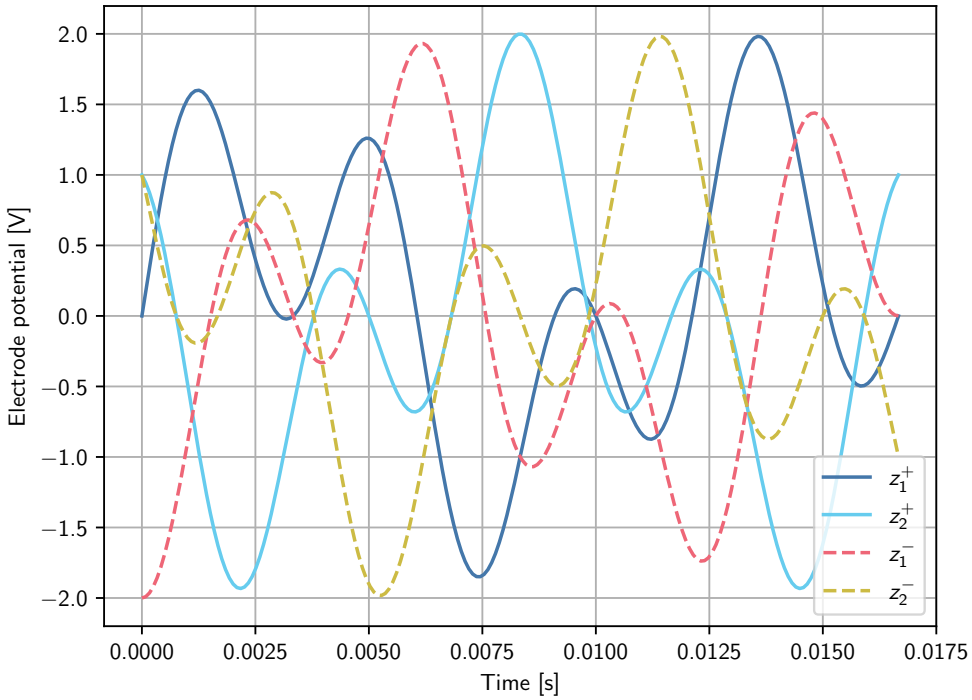

FIGURE 4.15: Example of the z-electrodes potential with AC actuation pattern $V_{1z} = V_{2z} = V_{1\eta} = V_{2\eta} = 1\,\mathrm{V}$.

individual electrodes[24] is [32]

$$\begin{cases} V_{z_1^+}(t) = +V_{1z}\sin(2\pi \cdot 90\,\mathrm{Hz} \cdot t) + V_{1\eta}\sin(2\pi \cdot 240\,\mathrm{Hz} \cdot t) + V_{z_1^+}^{DC} \\ V_{z_2^+}(t) = -V_{1z}\sin(2\pi \cdot 90\ \mathrm{Hz} \cdot t) + V_{2\eta}\cos(2\pi \cdot 240\ \mathrm{Hz} \cdot t) + V_{z_2^+}^{DC} \\ V_{z_1^-}(t) = -V_{2z}\cos(2\pi \cdot 90\ \mathrm{Hz} \cdot t) - V_{2\eta}\cos(2\pi \cdot 240\ \mathrm{Hz} \cdot t) + V_{z_1^-}^{DC} \\ V_{z_2^-}(t) = +V_{2z}\cos(2\pi \cdot 90\ \mathrm{Hz} \cdot t) - V_{1\eta}\sin(2\pi \cdot 240\ \mathrm{Hz} \cdot t) + V_{z_2^-}^{DC} \end{cases} \tag{4.78}$$

As mentioned before, we assume that there is no specific phase between the injection bias and the AC actuation voltages. We include this fact in our model averaging the estimated apparent yield for a given illumination pattern over an array of the electrode potentials sampled from its actuation waveform.

An example of the potential on z-electrodes as a function of time is shown in Figure 4.15.

The predicted effect of AC actuation on the apparent yield curved of the Crystal 250 LED are displayed in Figure 4.16.

The effect of AC actuation on the apparent yield curved for TM illumination is small because only a minor fraction of light is absorbed in the area close to the z-electrodes ($\sim 1.6\%$, or $\sim 2\%$ if we consider only the useful light) with respect to the case of EH illumination ($\sim 6.5\%$, or a significant $\sim 22\%$ of the useful light[25]), as one

[24] The frequency of the AC actuation is different from LPF, because in our torsion pendulum we use the FEE-electronics z-channels to read the EH y-electrodes and vice-versa. This swap caused us a few headaches.

[25] In the case of EH illumination most of the light is considered lost, whereas for TM illumination the fraction of light lost is minor.

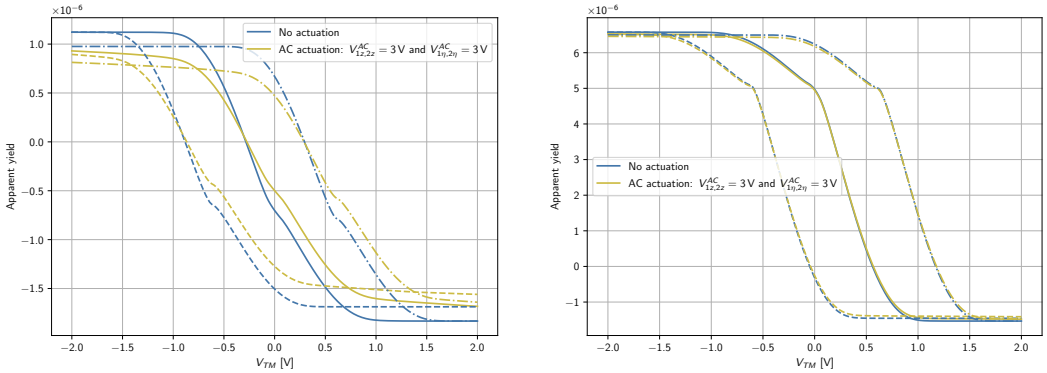

(A) EH illumination (B) TM illumination

FIGURE 4.16: Predicted discharge curves for the Crystal 250 LED in the case of EH illumination with AC actuation $V_{1z} = V_{2z} = V_{1\eta} = V_{2\eta} = 3\,\mathrm{V}$. The value of other relevant parameters chosen for this plot are $\mu = 5.53\,\mathrm{eV}$, $W_{EH} = W_{TM} = 4\,\mathrm{eV}$, and $\mathcal{Q}_{EH} = \mathcal{Q}_{TM} = 10^{-5}$. Here we simulate the apparent data for the illumination with duration $10\,\mu\mathrm{s}$ and $V_{inj} = 0.54\,\mathrm{V}$ (*continuous* lines) and the in-phase (*dashed* lines) and out-of-phase (*dash-dotted* lines) illumination with duration $1\,\mu\mathrm{s}$ and $V_{inj} = 5.4\,\mathrm{V}$.

can see from the absorption coefficients in Appendix B.

4.4 Fit of the experimental data

The examples presented in the previous section convinced us that the model has the potential to produce pretty accurate apparent yield curves. Therefore, we decided to try and fit the experimental apparent yield data with our model. A fit is technically feasible, because our simple photoemission model is not computationally intensive. The time required to generate an apparent yield curve is of the order of tens of milliseconds.

4.4.1 Likelihood for the fit

The apparent yield data acquired have two kind of uncertainty: the random error, due to the noise in the charge measurement with the torsion pendulum and the dominant systematic error, due to the UV-power measurement. We have to be careful when building a likelihood that accounts correctly for the systematic uncertainty.

Indeed, it would be not formally correct to add together systematic and random errors for each data point into a total uncertainty, which is then used in, say, a Gaussian likelihood to fit the data.

The statistically correct way to perform the fit requires to disentangle random and systematic uncertainty. In order to do so, we do not fit directly the experimental apparent yield data, but rather the photo-current, which can be modeled as

$$\hat{I}(V_{TM}) = C_{tot}\frac{\mathrm{d}\hat{V}_{TM}}{\mathrm{d}t} = e\frac{\hat{P}_{UV}}{\langle E_{UV}\rangle}\cdot\hat{\mathcal{Y}}(V_{TM};\boldsymbol{\theta}) \tag{4.79}$$

where the vector $\boldsymbol{\theta}$ includes all the parameters that are needed by our photoemission model to compute the apparent yield (e.g. workfunctions, quantum yields, etc.). The quantity $\hat{P}_{UV}$ is the fit estimate for the UV-power injected into the GRS can be

modeled as

$$\hat{P}_{UV} = \hat{\beta}\hat{V}_{UV} \tag{4.80}$$

where we introduced the conversion factor $\hat{\beta}$ that translates the fit estimate for the true signal in the photodetector $\hat{V}_{UV}$ into the power injected into the GRS. The conversion factor $\hat{\beta}$ includes both the optical fiber transmission and the calibration of the power sensitive device.

Therefore, the fit parameters are:

- The array of parameters $\boldsymbol{\theta}$ needed by our photoemission model to compute the apparent yield.
- The true signal $\hat{V}_{UV}$ at the output of the photosensitive device.
- The true conversion factor $\hat{\beta}$ between the photodetector signal and the power injected into the GRS.

Let us spend some words on the data that we are going to fit.

- A set of measurements of the discharge rate $\left\{\frac{\mathrm{d}V_{TM,i}}{\mathrm{d}t}\right\}_M$ with their associated causal error $\left\{\sigma\left(\frac{\mathrm{d}V_{TM,i}}{\mathrm{d}t}\right)\right\}_M$, which are primarily due to the noise in charge measurement with the torsion pendulum.
- A series of "darks & lights" $\{V_{UV,j}\}_N$, i.e. samples of the signal measured by the photodiode or PMT . The uncertainty is estimated as the standard deviation of the samples

$$\sigma(V_{UV}) = \sqrt{\frac{\sum_{j=1}^{N}\left(V_{UV,j} - \bar{V}_{UV}\right)^2}{N-1}} \qquad \text{where} \qquad \bar{V}_{UV} = \frac{\sum_{j=1}^{N} V_{UV,j}}{N} \tag{4.81}$$

- The measured value of the overall conversion factor β, which includes both the transmission of the optical fibers a and the calibration of the photosensitive device $\langle \mathrm{d}P/\mathrm{d}V \rangle$

$$\beta = a\left\langle \frac{\mathrm{d}P}{\mathrm{d}V} \right\rangle \tag{4.82}$$

with error

$$\sigma(\beta) = \sqrt{\left[\sigma(a)\cdot\left\langle \frac{\mathrm{d}P}{\mathrm{d}V} \right\rangle\right]^2 + \left[a\cdot\sigma\left(\left\langle \frac{\mathrm{d}P}{\mathrm{d}V} \right\rangle\right)\right]^2} \tag{4.83}$$

The value of $\langle \mathrm{d}P/\mathrm{d}V \rangle$ depends on the photodetector (PMT and photodiode have different calibration coefficients) and on the spectrum of the light-source (we averaged the response of the photodetector over the spectra of our light-sources). The value of the transmission coefficient a depends on the optical chain considered (EH illumination or TM) and on the year of the measurements (we characterized the optical fibers repeatedly).

Now we have all ingredients to cook up the likelihood for the fit. We decided to go for a safe choice and use a Gaussian log-likelihood (ignoring an additive constants which

play no role)

$$\mathcal{LL}\left(\boldsymbol{\theta}, \hat{V}_{UV}, \hat{\beta}\right) = -\overbrace{\frac{1}{2}\sum_{i=1}^{M}\left[\frac{C_{tot}\frac{\mathrm{d}V_{TM,i}}{\mathrm{d}t} - e\frac{\hat{\beta}\hat{V}_{UV}}{\langle E_{UV}\rangle}\hat{\mathcal{Y}}(V_{TM,i};\boldsymbol{\theta})}{C_{tot}\,\sigma\left(\frac{\mathrm{d}V_{TM,i}}{\mathrm{d}t}\right)}\right]^2}^{\text{Model for } \hat{I}(V_{TM};\boldsymbol{\theta})} - \underbrace{\frac{1}{2}\sum_{j=1}^{N}\left[\frac{V_{UV,j} - \hat{V}_{UV}}{\sigma(V_{UV})}\right]^2}_{\text{Model for } \hat{V}_{UV}} - \underbrace{\frac{1}{2}\left[\frac{\beta - \hat{\beta}}{\sigma(\beta)}\right]^2}_{\text{Model for } \hat{\beta}} \tag{4.84}$$

For each apparent yield measurement, we have just one true signal $\hat{V}_{UV}$ that we estimate from the "darks & lights" samples, associated with several charge rate measurements $\left\{\frac{\mathrm{d}V_{TM,i}}{\mathrm{d}t}\right\}_M$. We do not learn anything from the estimate of $\hat{\beta}$, as it is just a normalization constant equal to all data in the fit, we include it so to simulate the error in the power calibration and in the optical fiber transmission coefficient.

Actually for each apparent yield curve, we have generally two set of measurements (the negative and positive branches), each one characterized by its own UV-power. Hence in the typical case that an experimental apparent yield curve is composed of two branches, the total likelihood is

$$\mathcal{LL}_{tot}\left(\boldsymbol{\theta}, \hat{V}^{+}_{UV}, \hat{V}^{-}_{UV}, \hat{\beta}\right) = -\frac{1}{2}\sum_{\flat=+,-}\sum_{i=1}^{M_\flat}\left[\frac{C_{tot}\frac{\mathrm{d}V^{\flat}_{TM,i}}{\mathrm{d}t} - e\frac{\hat{\beta}\hat{V}^{\flat}_{UV}}{\langle E_{UV}\rangle}\hat{\mathcal{Y}}(V^{\flat}_{TM,i};\boldsymbol{\theta})}{C_{tot}\,\sigma\left(\frac{\mathrm{d}V^{\flat}_{TM,i}}{\mathrm{d}t}\right)}\right]^2 - \frac{1}{2}\sum_{\flat=+,-}\sum_{j=1}^{N_\flat}\left[\frac{V^{\flat}_{UV,j} - \hat{V}^{\flat}_{UV}}{\sigma(V^{\flat}_{UV})}\right]^2 - \frac{1}{2}\left[\frac{\beta - \hat{\beta}}{\sigma(\beta)}\right]^2 \tag{4.85}$$

where the index $\flat$ runs over the positive and negative branch. The likelihood above can be generalized immediately to any number of sub-measurements that compose the experimental apparent yield data at the cost of increasing the number of parameters.

We decided to consider a model with a reduced number of parameters. We assumed that the microscopic properties such as workfunction and quantum yield are uniform on all TM surfaces and on all EH surfaces, in order not to make the number of parameters explode. No matter the number of surface pairs that we consider to model the GRS, we assign to all surfaces belonging the EH same quantum yield and work function. The same holds for the TM surfaces, but of course with possibly different values for such properties. In this way the fit parameters are always the ones reported in Table 4.2.

4.4.2 Bayesian fit

We sampled the log-likelihood with the NUTS Hamiltonian Monte Carlo sampler [69] implemented in the PyMC probabilistic programming library for Python [70].

The advantages of using such a technique rely on the fact that it formally always converges and that it provides a posterior distribution (i.e. an assessment of the uncertainty) for the fit parameters. The disadvantages of a Bayesian fit are that it is more computational intensive than traditional methods, especially when the number of parameters grows.

TABLE 4.2: Parameters for the fit of the apparent yield data.

Name	Symbol	Comments
TM quantum yield	$\mathcal{Q}_{TM}$	Assumed uniform on all TM surfaces
EH quantum yield	$\mathcal{Q}_{EH}$	Assumed uniform on all TM surfaces
EH work-function	W_{EH}	Assumed uniform on all TM surfaces
Difference in EH and TM work-function	$\Delta W = W_{TM} - W_{EH}$	This gimmick reduces the correlation with W_{EH}
UV-signal for positive branch	$\hat{V}_{UV}^{+}$	True signal that we should have measured
UV-signal for negative branch	$\hat{V}_{UV}^{-}$	True signal that we should have measured
Conversion coefficient for UV-power	$\hat{\beta}$	Includes the power calibration of the power sensitive device and the fiber transmission coefficient

For what regards the priors of the fit parameters reported in Table 4.2, we chose broad Gaussian distributions centered on reasonable theoretical values for the quantities that we could not measure directly (e.g. the quantum yields and work functions). On the other hand, for the quantities that we did experimentally measure, that is the UV signal V_{UV} and the overall conversion factor β, we chose informative Gaussian distributions centered on the measured value and with standard deviation equal to the measurement uncertainty.

Once the MCMC algorithm has found the posterior distributions of the fit parameters $\boldsymbol{\theta}$, we could obtain an unbiased[26] estimate of the apparent yield as

$$\hat{\mathcal{Y}}(V_{TM}, \boldsymbol{\theta}) = \begin{cases} \frac{\langle E_{UV} \rangle}{e\beta \bar{V}_{UV}^{+}} \hat{I}(V_{TM}; \boldsymbol{\theta}), & \text{for positive branch } (\hat{I} \leq 0) \\ \frac{\langle E_{UV} \rangle}{e\beta \bar{V}_{UV}^{-}} \hat{I}(V_{TM}; \boldsymbol{\theta}), & \text{for negative branch } (\hat{I} > 0) \end{cases} \tag{4.86}$$

where β and $\bar{V}_{UV}^{\pm}$ are the experimentally measured quantities for each AY branch.

The MCMC algorithm samples the likelihood by finding candidate values for the model parameters at each iteration. The arrays of such values for each parameter are called *posteriors* of the model. If we plug the posteriors into the model, we obtain a collection of fits (*posterior predictive checks*), each characterized by a set of parameters. The posterior predictive checks are helpful to make sure that the model describes the observed data well. For an example, see Figure 4.17, where we show the posterior predictive checks for a fit of an apparent yield curve obtained illuminating the TM with the Crystal 250 LED with a duration of 10 µs and a delay of 0 µs ($V_{inj} = 5.4\,\mathrm{V}$).

The agreement between data and samples of the fit is quite good and we explored the whole uncertainty region due to systematic errors.

[26] Indeed the fit will always force $\hat{\beta}$ and $\hat{V}_{UV}$ towards values which are not exactly the ones measured.

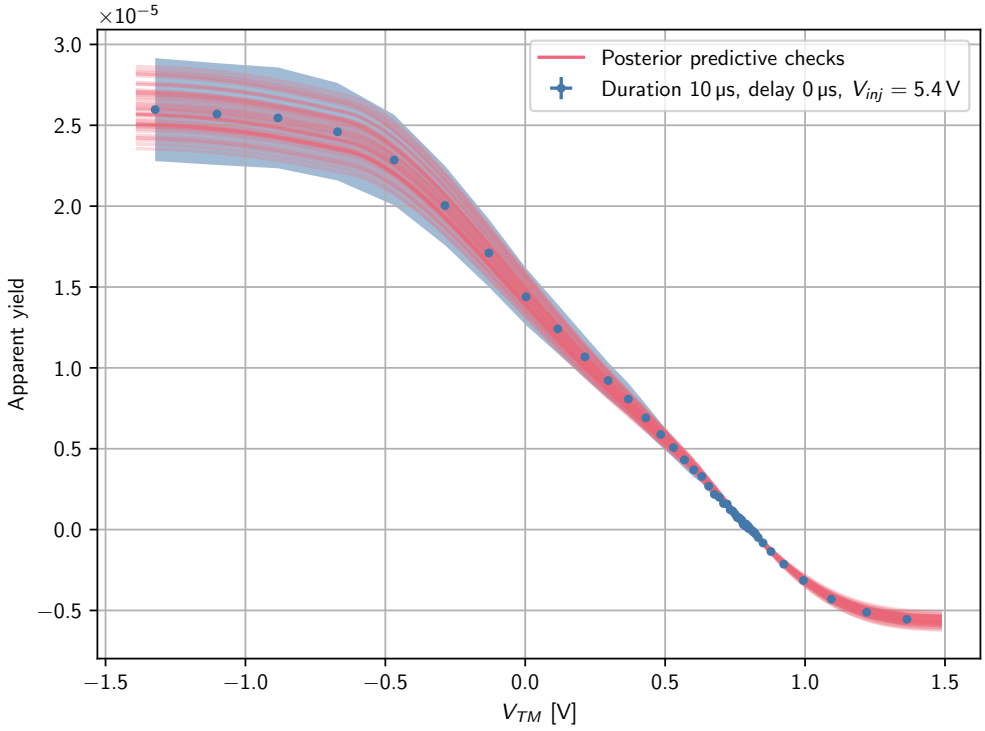

FIGURE 4.17: Posterior predictive checks for the Bayesian fit of an apparent yield curve obtained illuminating the TM with the Crystal 250 LED with a duration of 10 µs and a delay of 0 µs ($V_{inj} = 5.4$ V). We observe a nice agreement between data and fits.

In Figures 4.18 and 4.19, we display, respectively, the trace and the pair plot for the model parameters that characterize the microscopic properties of the surfaces.

The plots on the right-hand side of Figure 4.18 represent the MCMC values of the parameters as a function of the iteration of the fit. The four distinct lines correspond to different MCMC chains. The plots on the left-hand side represent the Gaussian kernel density estimates of the parameter traces (this conceptually similar to a smoothed histogram). The trace plot is useful to check the convergence of the MCMC algorithm: if we see that all chains provide similar estimate for the posterior distribution of the parameters, we are confident that the algorithm is exploring effectively the likelihood. Moreover, the posterior distributions give an indication of the uncertainty on the fit parameters.

The pair plot in Figure 4.19 is useful to evaluate the correlation between the model parameters.

In the Figures 4.20 – 4.26, we show the comparison between fit and experimental data for most of the apparent yield data acquires experimentally in our laboratory. In such plots we decide to plot the median of the fit samples with uncertainty band given by the area within the 15.9th- and the 84.1th-percentiles (which correspond to $\pm 1\sigma$-confidence intervals).

Moreover, we also plot the posterior distributions of selected parameters[27]. In Appendix D, we report the summary tables for the fit parameters that give information on the microscopic properties of the TM and EH surfaces.

For more detailed plots of each fit see Appendix E.

[27] Indeed the parameters we are interested to estimate are the ones that characterize the microscopic properties of the surfaces (e.g. quantum yield and workfunction)

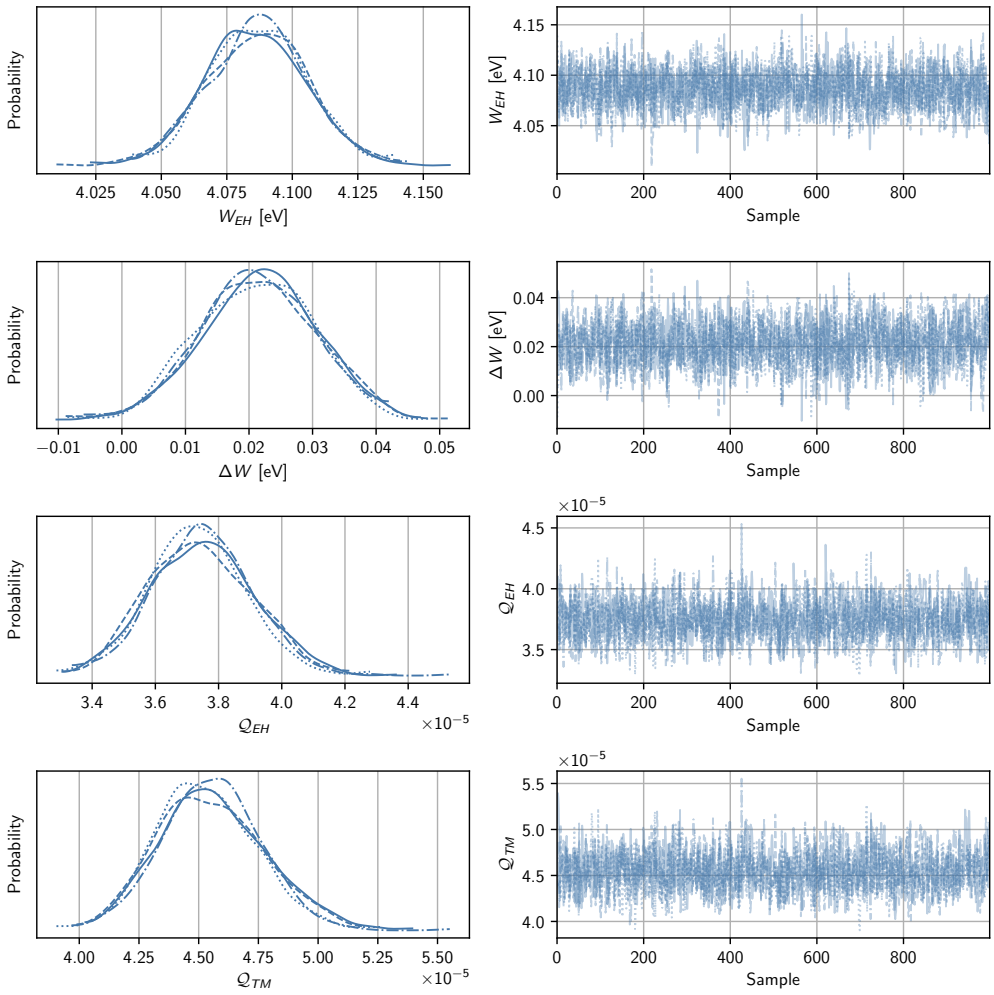

FIGURE 4.18: Traces of the MCMC samples of selected model parameters for the data in Figure 4.17. We observe a good convergence of the NUTS algorithm.

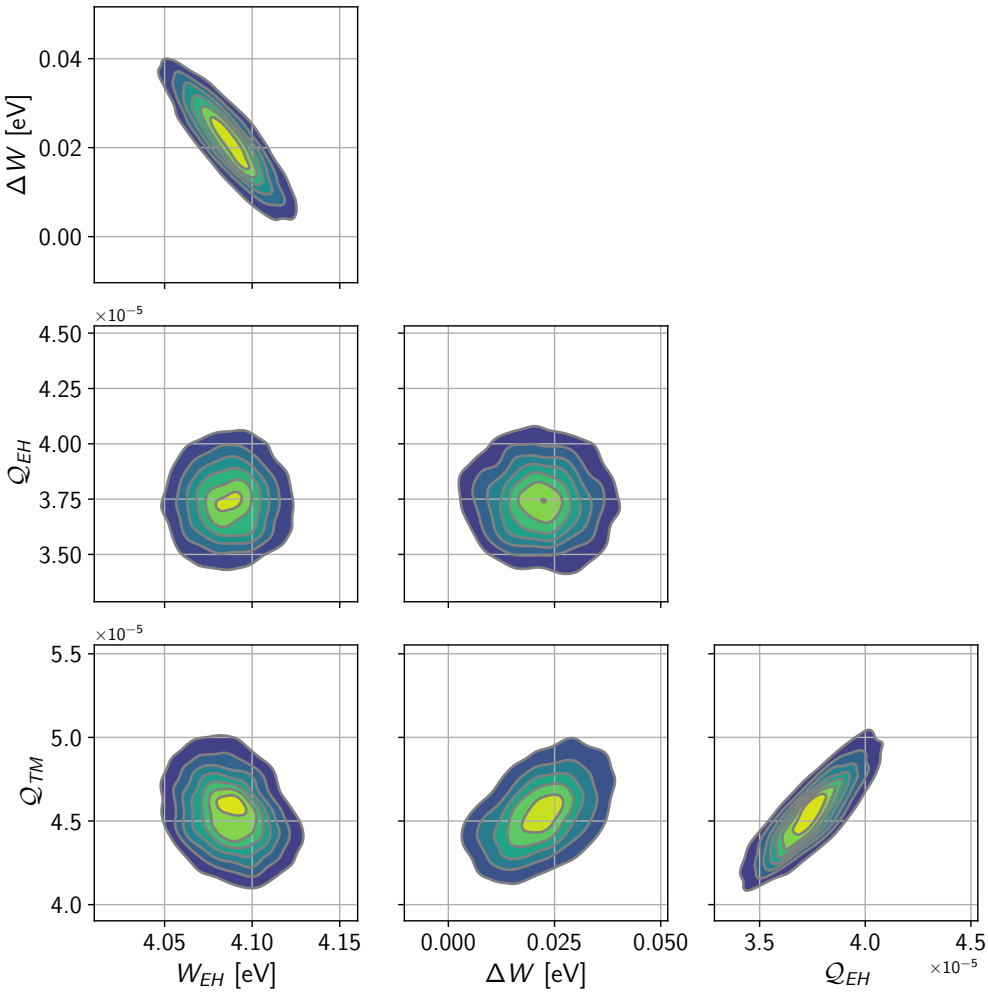

FIGURE 4.19: Pair plot of the MCMC samples of selected model parameters for the data in Figure 4.17.

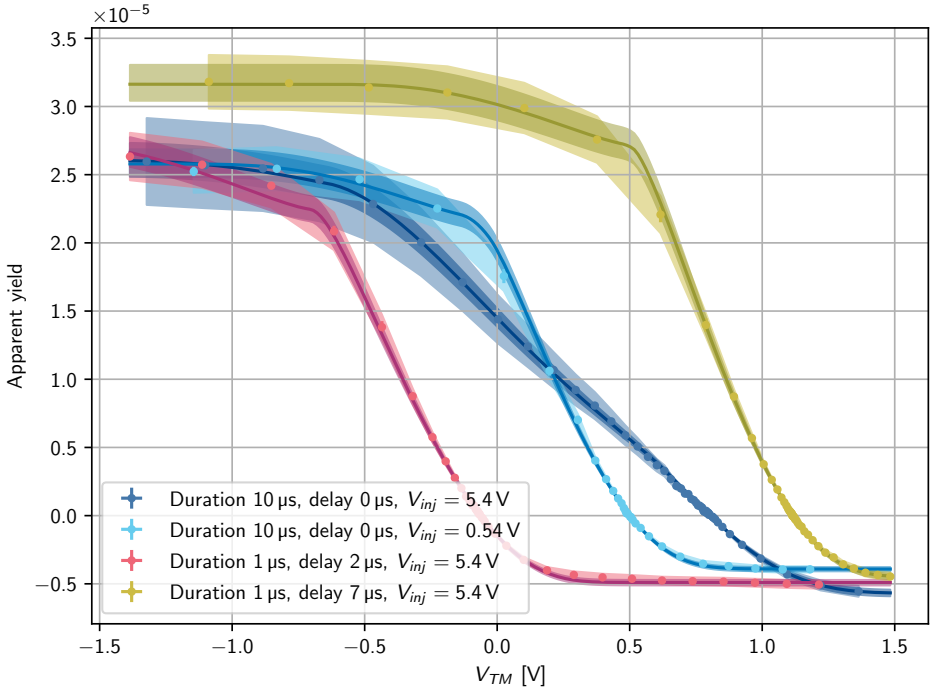

(A) Comparison between experimental data and fit (median with $\pm 1\sigma$-confidence intervals)

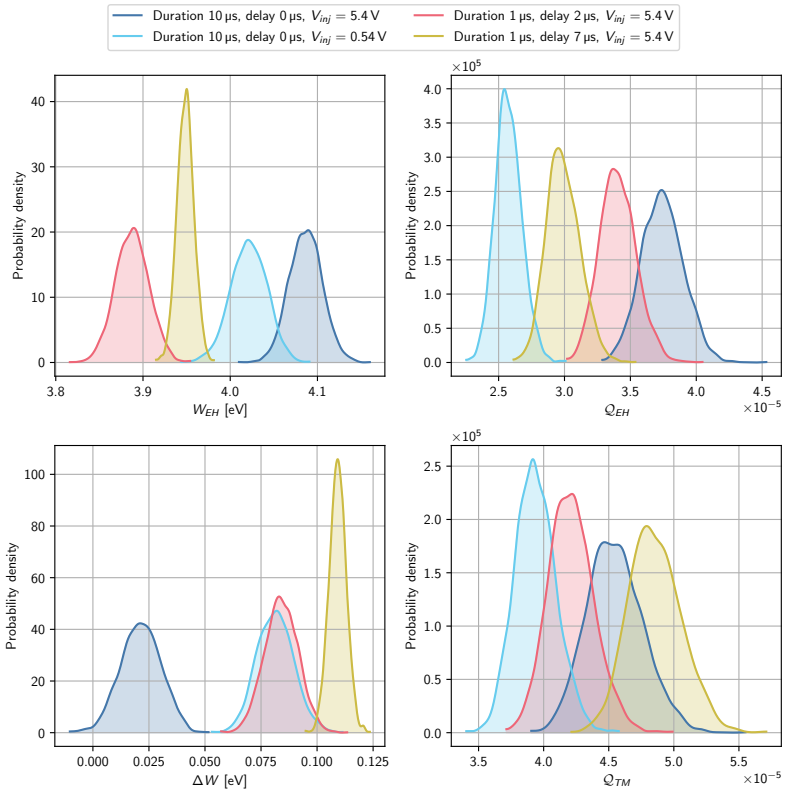

(B) Posterior distributions for a selection of the model parameters

FIGURE 4.20: Crystal 250 apparent yield data for TM illumination.

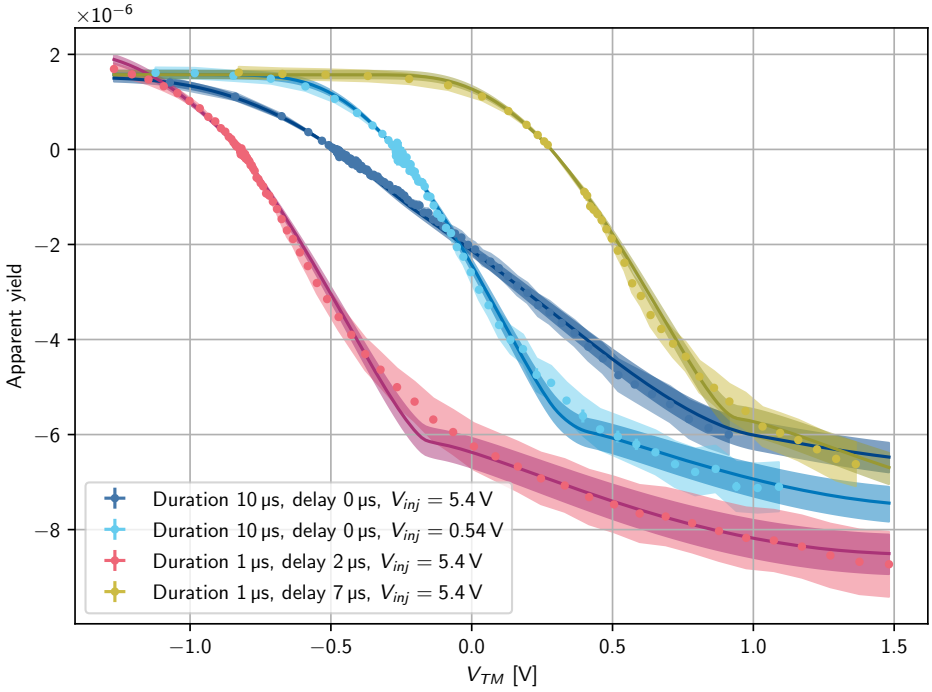

(A) Comparison between experimental data and fit (median with $\pm 1\sigma$-confidence intervals)

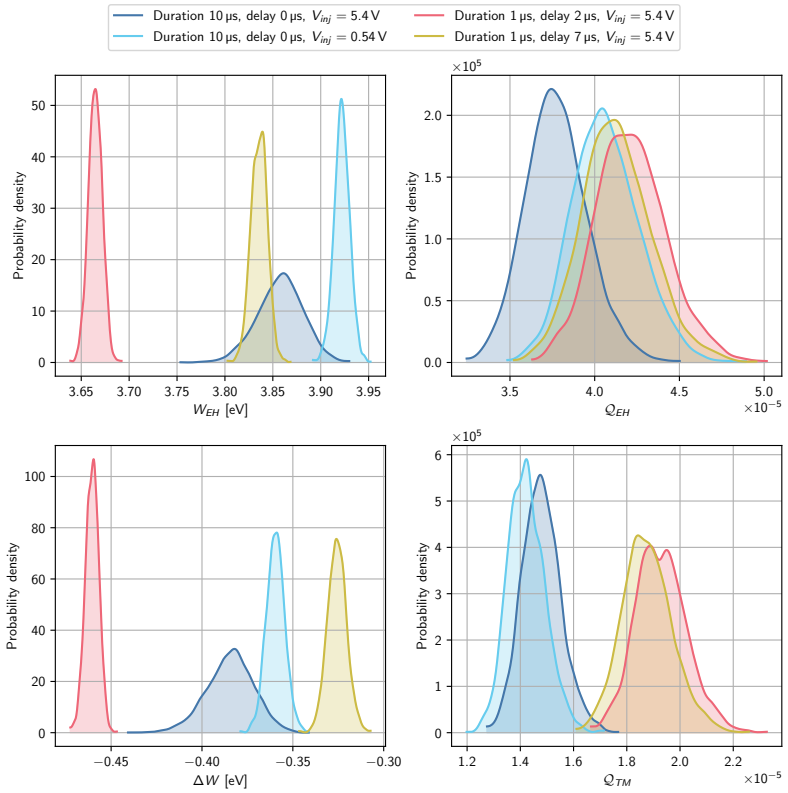

(B) Posterior distributions for a selection of the model parameters

FIGURE 4.21: Crystal 250 apparent yield data for EH illumination.

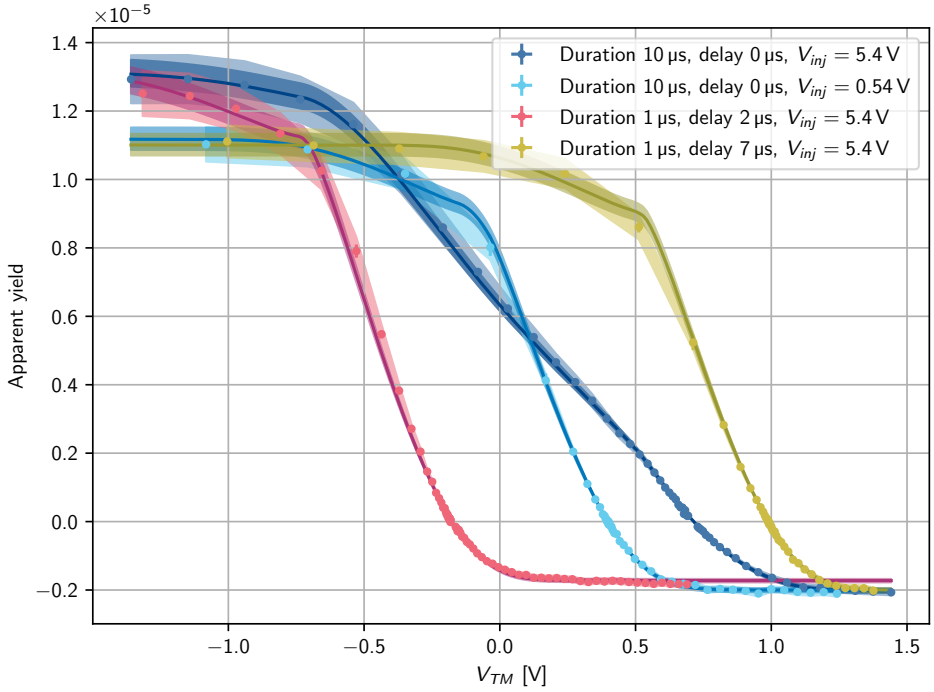

(A) Comparison between experimental data and fit (median with $\pm 1\sigma$-confidence intervals)

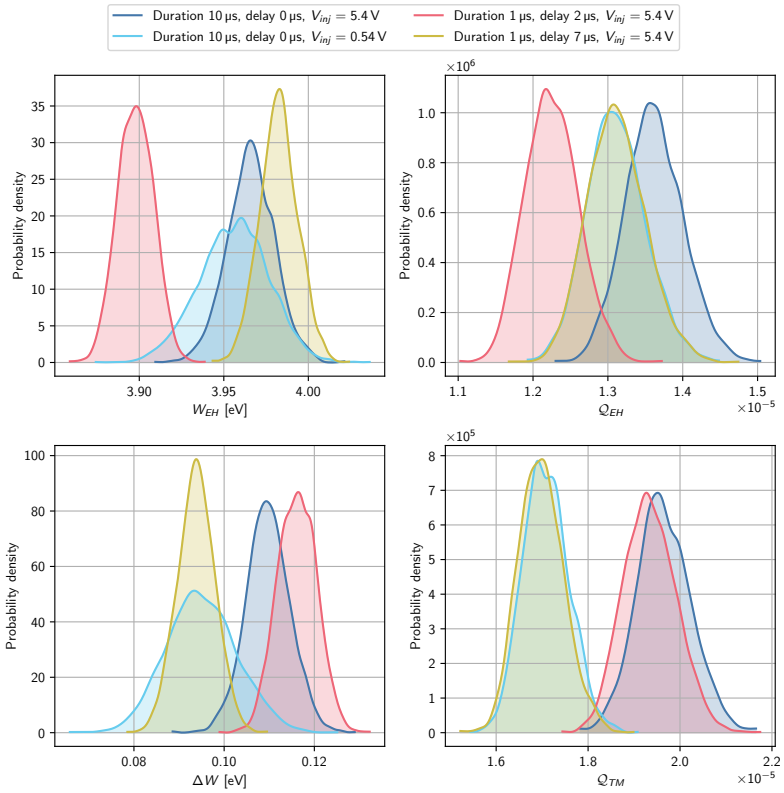

(B) Posterior distributions for a selection of the model parameters

FIGURE 4.22: SETi 255 apparent yield data for TM illumination.

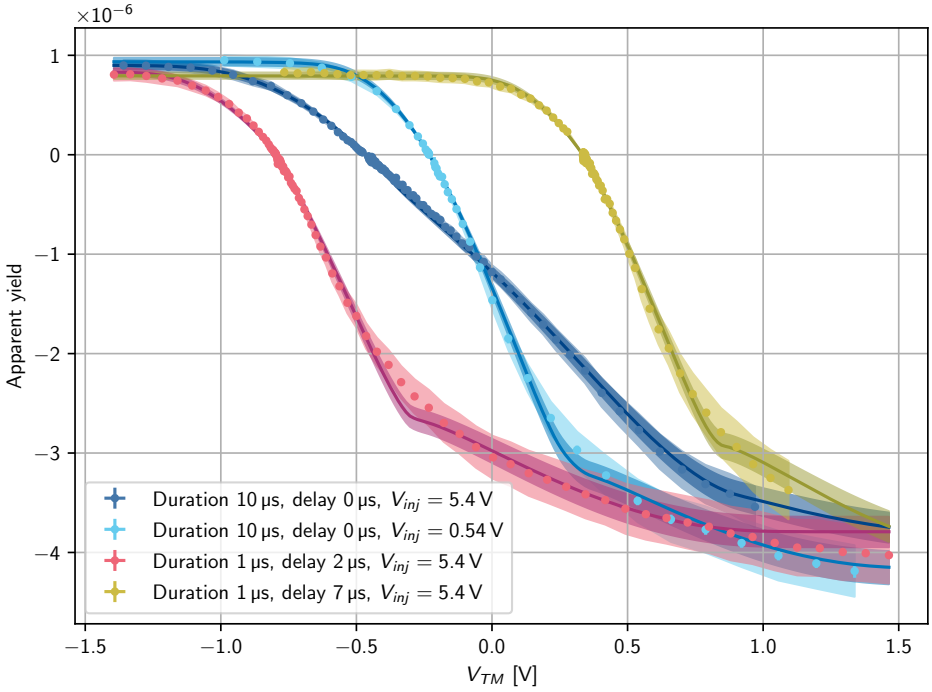

(A) Comparison between experimental data and fit (median with $\pm 1\sigma$-confidence intervals)

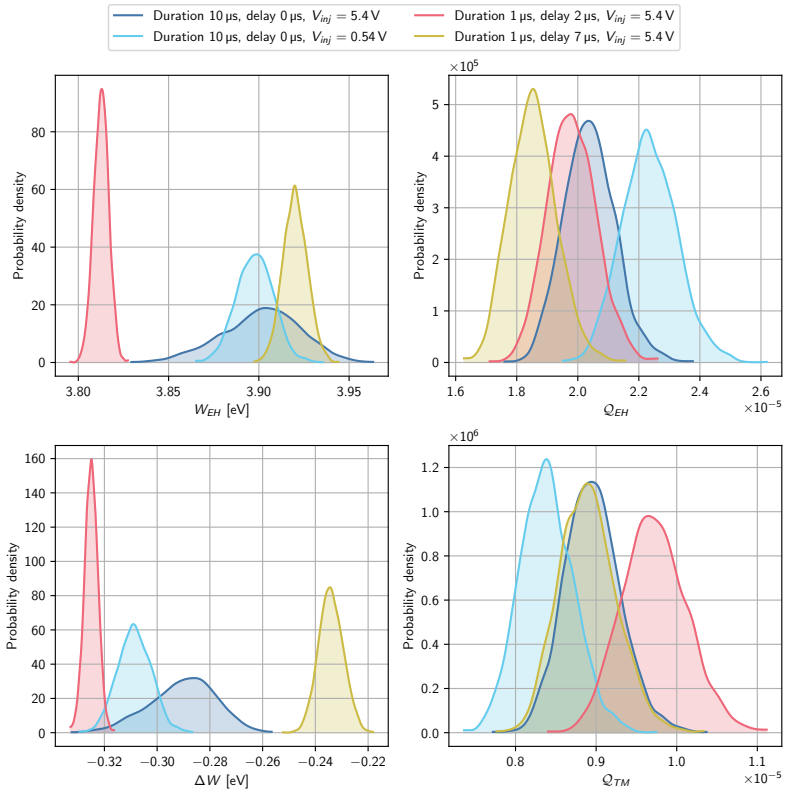

(B) Posterior distributions for a selection of the model parameters

FIGURE 4.23: SETi 255 apparent yield data for EH illumination.

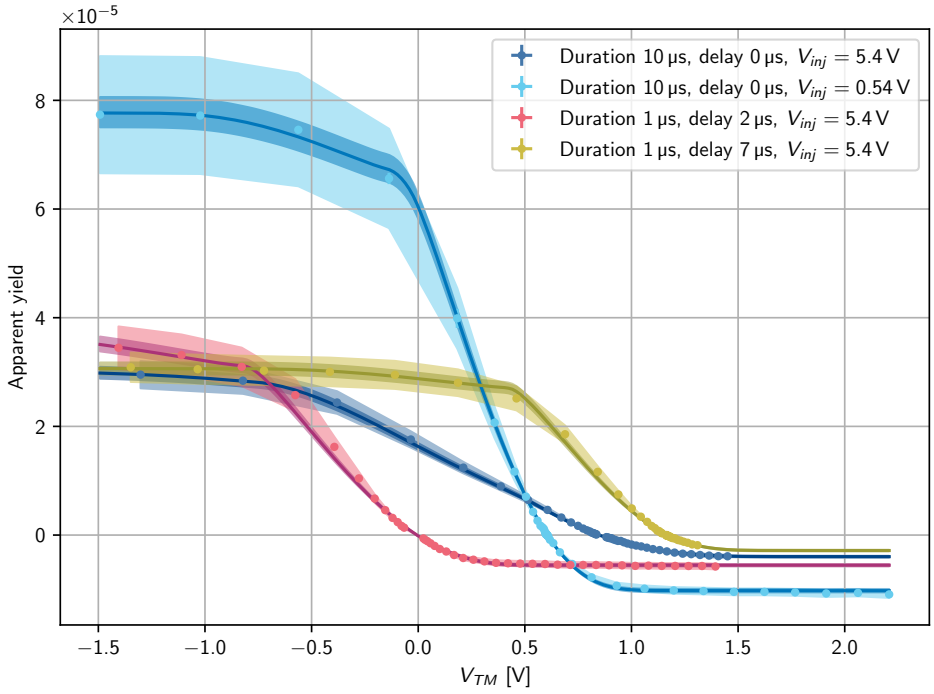

(A) Comparison between experimental data and fit (median with $\pm 1\sigma$-confidence intervals)

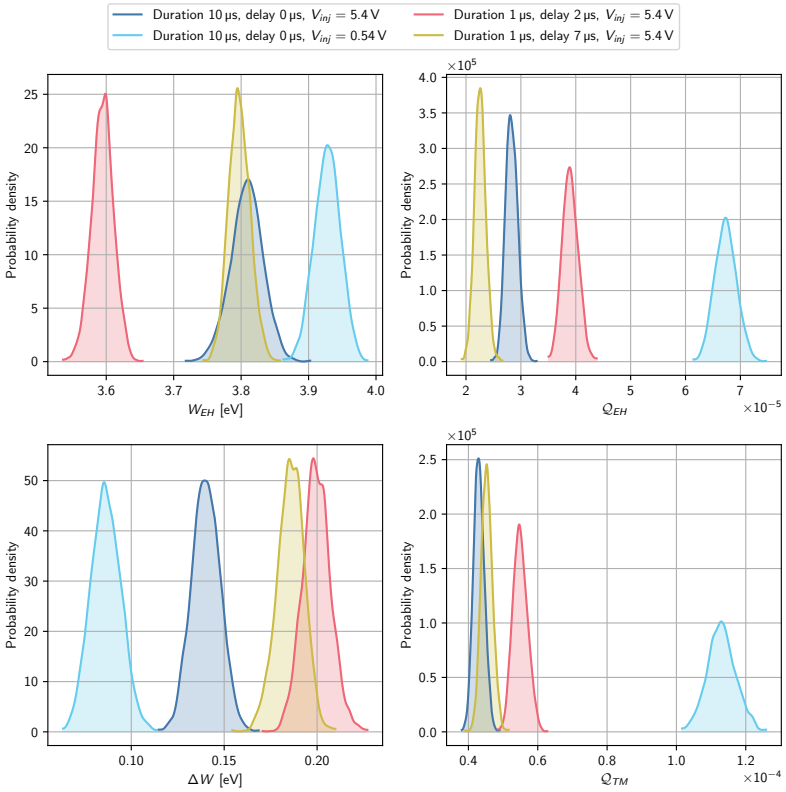

(B) Posterior distributions for a selection of the model parameters

FIGURE 4.24: SETi 240 apparent yield data for TM illumination. The data at 10 µs duration and $V_{inj} = 0.54$ V (*cyan*) were acquired in 2022, hence not directly comparable to the other curves regarding the quantum yield values (see Section 3.4.2).

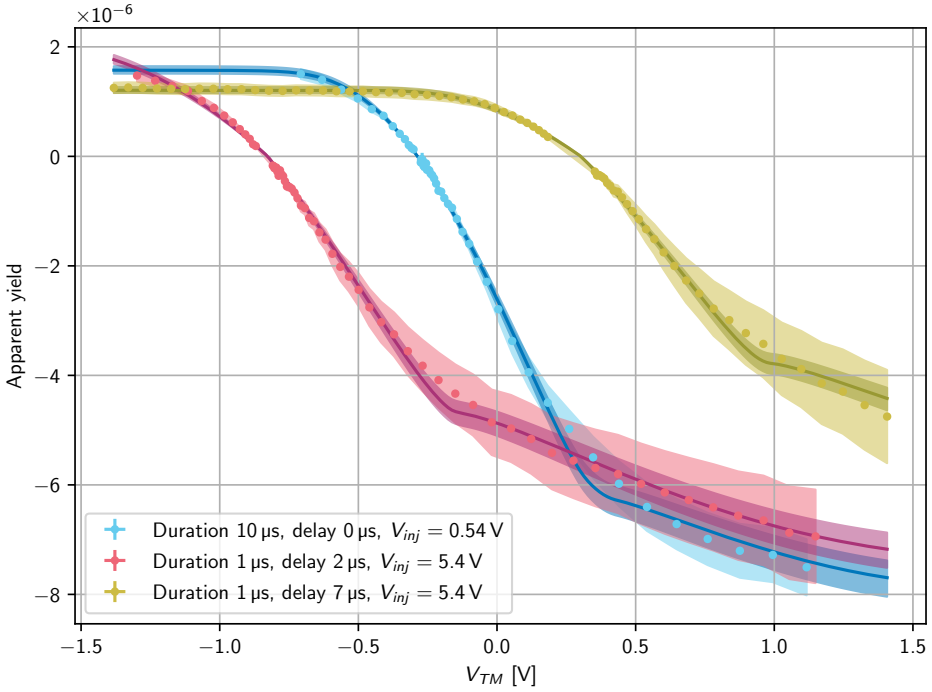

(A) Comparison between experimental data and fit (median with $\pm 1\sigma$-confidence intervals)

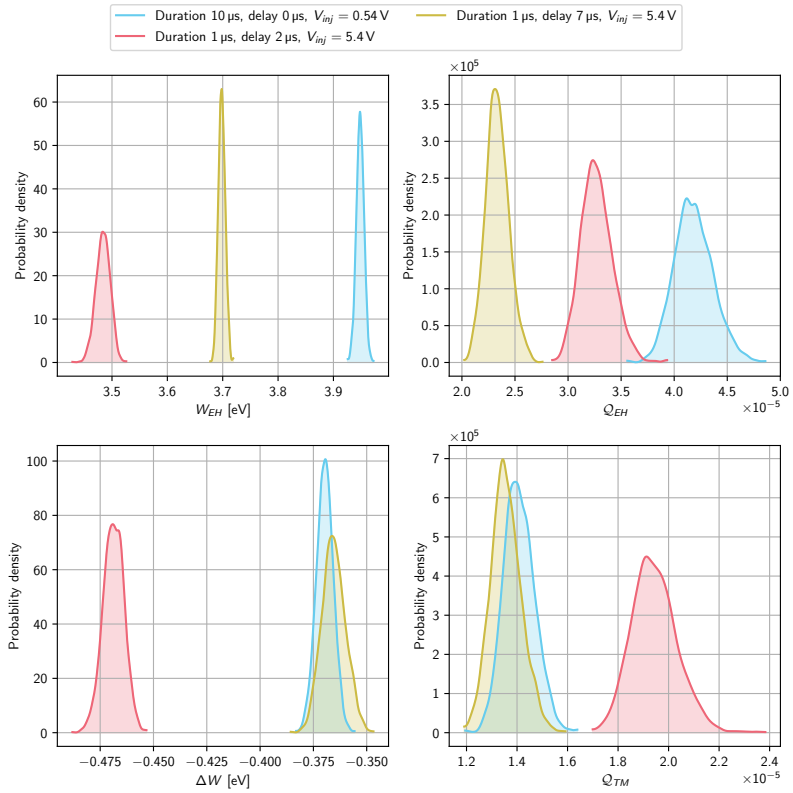

(B) Posterior distributions for a selection of the model parameters

FIGURE 4.25: SETi 240 apparent yield data for EH illumination.

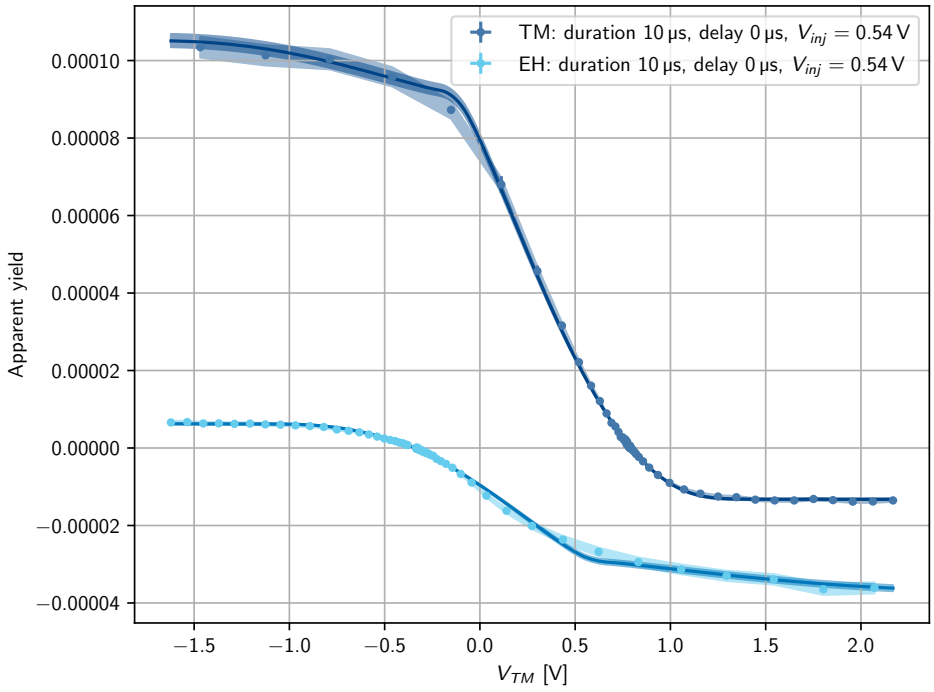

(A) Comparison between experimental data and fit (median with $\pm 1\sigma$-confidence intervals)

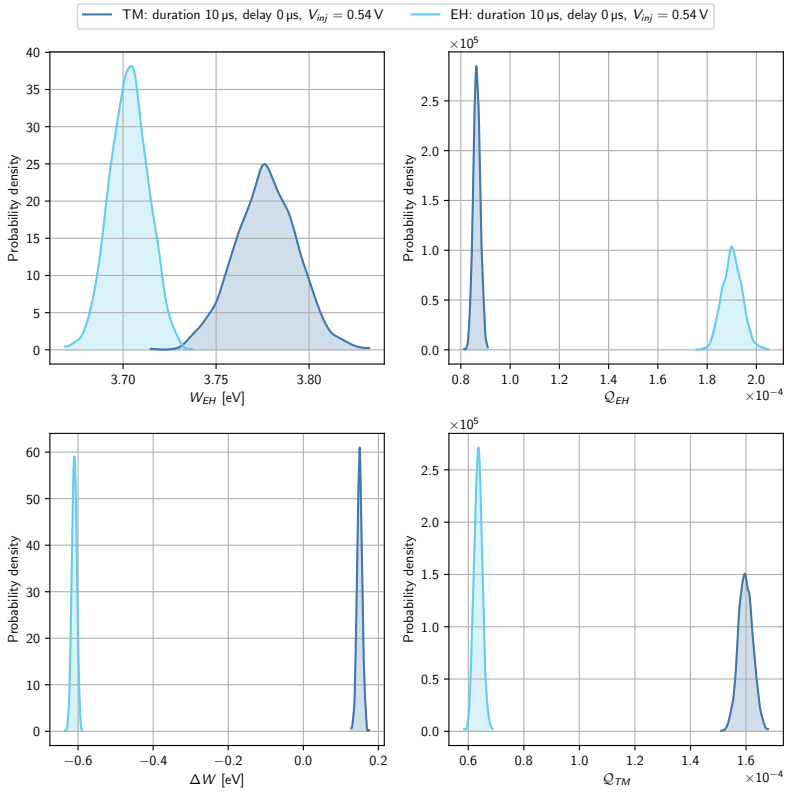

(B) Posterior distributions for a selection of the model parameters

FIGURE 4.26: UVphotonics 230 apparent yield data for TM and EH illumination. The distribution of posterior parameters may look different with respect to previous plots because we are comparing a measurements illuminating different sides of the GRS.

We notice that a few measurements has been taken in 2022 and can not directly compared to the majority of the AY yield measurements (acquired two years previously), because of the systematic increase in the saturation levels described in Section 3.4.2. Such measurements are

- The apparent yield curve with SETi 240 for TM illumination with injection $V_{inj} = 0.54\,\mathrm{V}$ (cyan in Figure 4.24).
- The apparent yield data with UVphotonics 230 (see Figure 4.26).

We suppose that the increase in the apparent yield at saturation is mostly due to a reduction in the transmission coefficient of the optical fibers due to their degradation with use, which makes us underestimate the UV-power injected into the GRS. In the case of the data with the UVphotonics 230, we expect to measure an increase in the quantum yield also because it is the light source that emits the highest-energy photons. We are unable to single out such effect, because it is polluted by the before-mentioned systematic error in the estimate of the UV-power, due to wear of the fibers.

We decided not to re-scale the newer data to match the old ones, because we cannot exclude a change in the emission properties of the surfaces over the years.

DC actuation data

As we can see from Figure 4.27, we were also able to fit reasonably well the data with DC actuation without the need of introducing a specific quantum yield for the actuation electrodes. This fact increases our confidence in the accuracy of the absorption coefficient A_i of the GRS surfaces, as they are completely correlated to the quantum yields $\mathcal{Q}_i$ in the determination of the apparent yield, as evident from (4.66) and (4.70).

In this data set, the only measurements that seems not to be fitted well is the measurement with injection $V_{inj} = 0.54\,\mathrm{V}$ and DC actuation $V_{z-}^{DC} = -5\,\mathrm{V}$ (cyan data in Figure 4.27). In this case the data seem not to saturate completely at negative TM potentials, whereas the fit seem to have reached saturation already at $V_{TM} \lesssim -0.7\,\mathrm{V}$.

AC actuation data

We were not able to fit the data with AC actuation because the evaluation of a more complex model, causes increases dramatically the computational time of the fit. We, therefore, just simulate the predicted apparent yield data for a reasonable choice of the model parameters. This is a nice benchmark to see if our model is also predictive.

During the experimental campaign, we considered only AC actuations in the V_{1z}, V_{2z}, $V_{1\eta}$ and $V_{2\eta}$ patterns, which interest the z-electrodes. The waveform of the single z-electrodes potential can be found from (4.78).

In Figure 4.28 we compare the experimental apparent yield data with the model prediction for EH illumination with SETi 255 when AC actuation is applied on the z-electrodes. In accordance with the experimental data, the model forecasts that there is no significant difference between having just the V_{1z} and V_{2z} AC actuation patterns and adding also the $V_{1\eta}$ and $V_{2\eta}$ waveforms.

In Figure 4.29 we plot a comparison between experimental and predicted apparent yield data for TM and EH illumination with Crystal 250 in the presence of AC actuation.

Overall the agreement between predicted and experimental data is pretty satisfactory, considering that we did not fine tune the model parameters for each measurement, but we considered the same values for all data that share the same source and illumination channel (TM or EH ISUK).

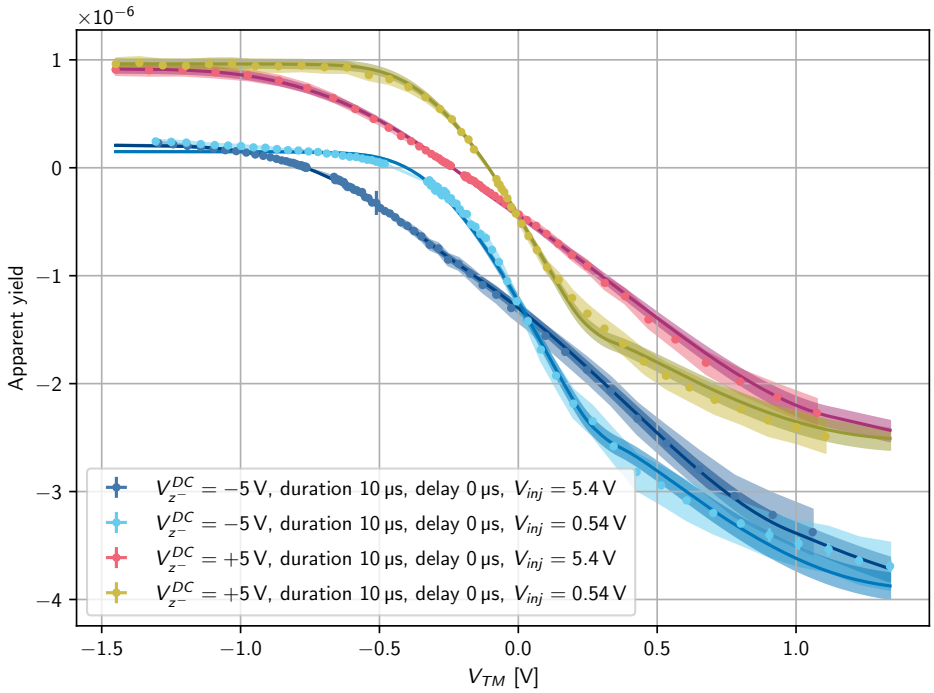

(A) Comparison between experimental data and fit (median with $\pm 1\sigma$-confidence intervals)

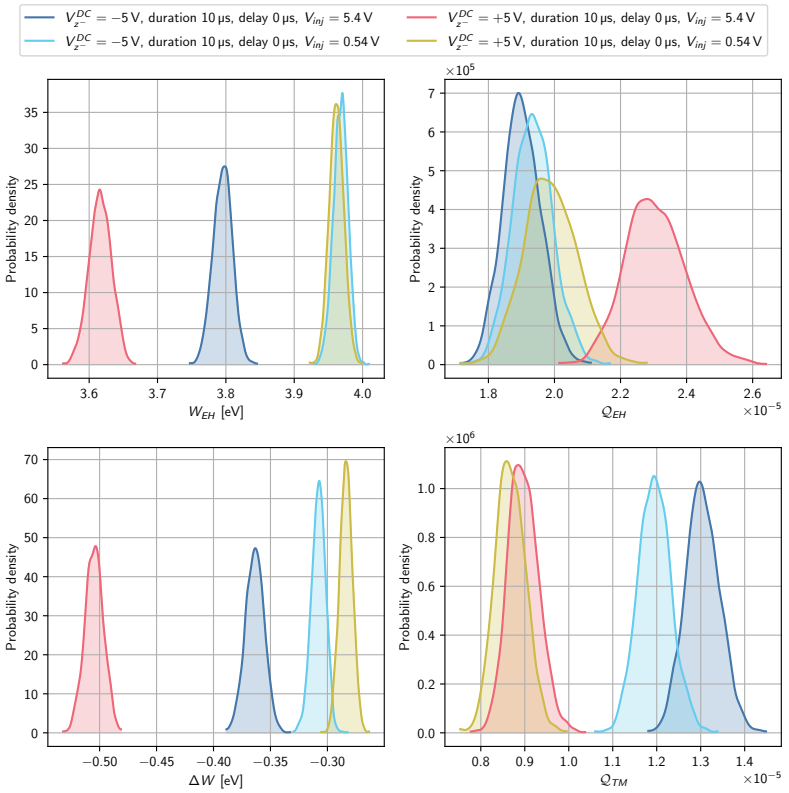

(B) Posterior distributions for a selection of the model parameters

FIGURE 4.27: SETi 255 apparent yield data for EH illumination in the presence of DC actuation on the z-electrodes.

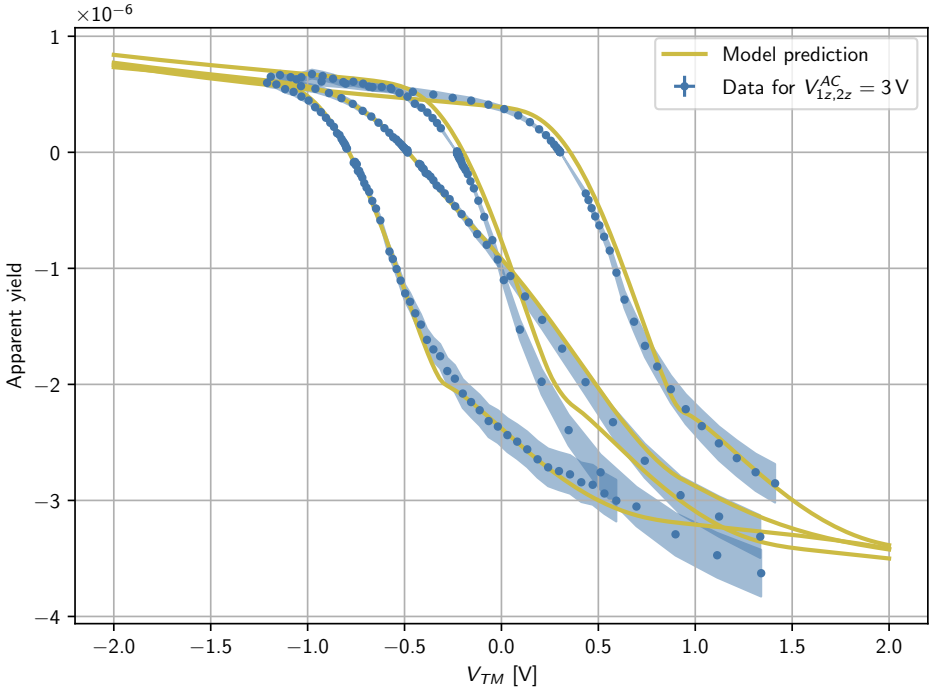

(A) AC actuation pattern $V_{1z} = V_{2z} = 3\,\mathrm{V}$

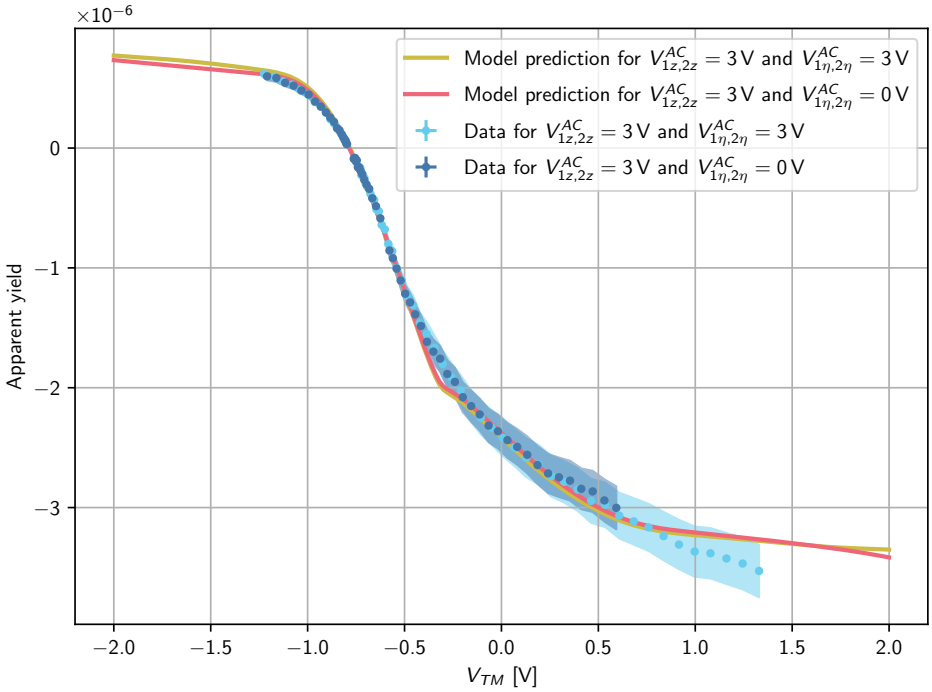

(B) Comparison between apparent yield data with different AC actuation patterns for illumination of duration 1 µs and delay 2 µs

FIGURE 4.28: Comparison between model prediction and experimental apparent yield data for EH illuminations with the SETi 255 in the presence of AC actuation on the z-electrodes. The value of the parameters chosen is $W_{EH} = 4.0\,\mathrm{eV}$, $\Delta W = -0.3\,\mathrm{eV}$, $\mathcal{Q}_{EH} = 2.1 \cdot 10^{-5}$, and $\mathcal{Q}_{TM} = 1.0 \cdot 10^{-5}$.

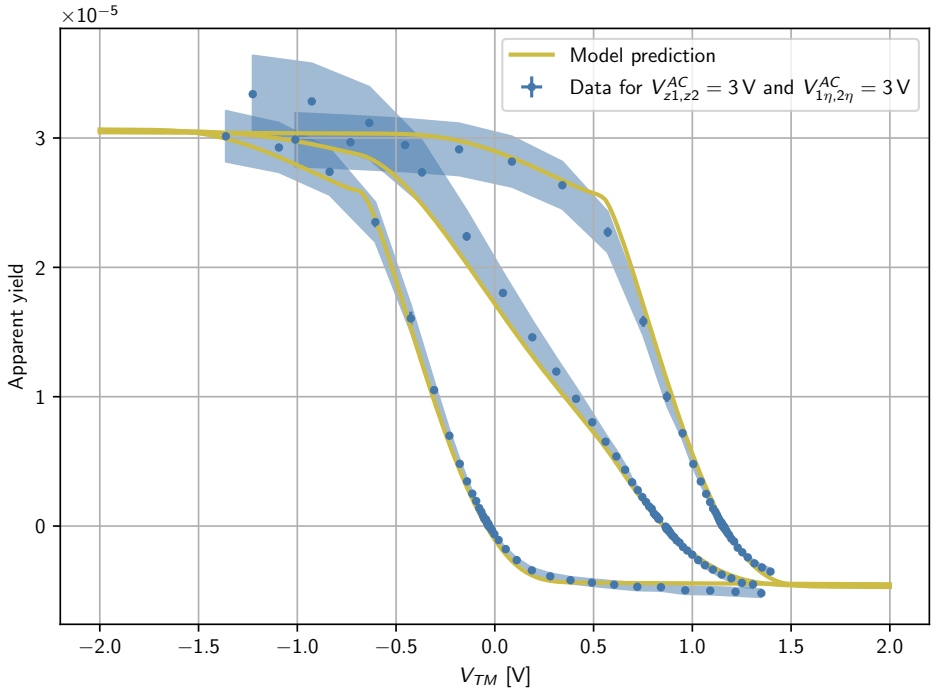

(A) TM illumination with model parameters $W_{EH} = 3.9\,\mathrm{eV}$, $\Delta V = 0.1\,\mathrm{eV}$, $\mathcal{Q}_{EH} = 3.3 \cdot 10^{-5}$, and $\mathcal{Q}_{TM} = 4.7 \cdot 10^{-5}$

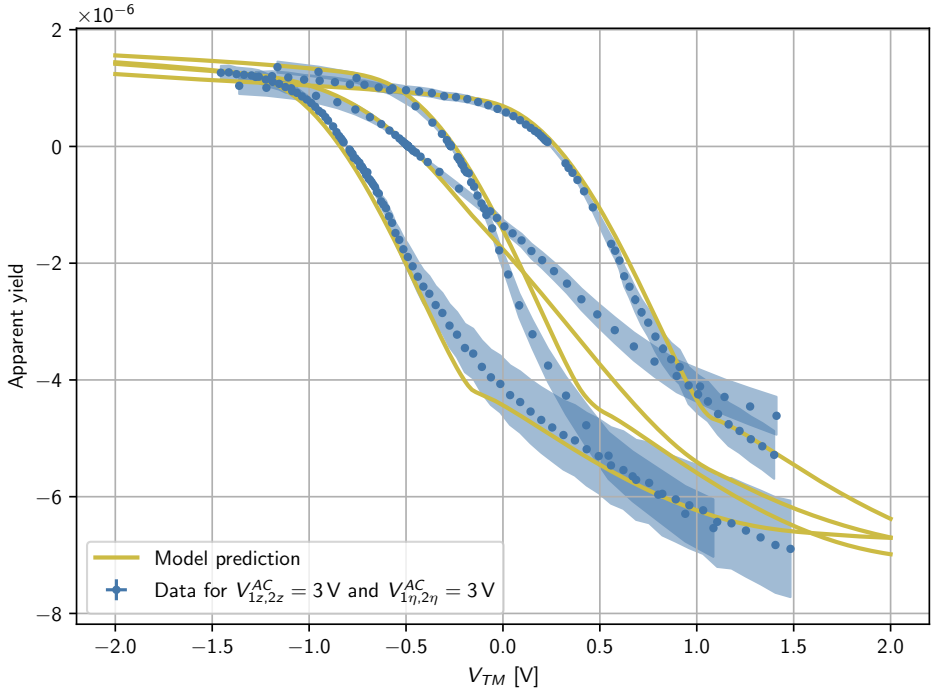

(B) EH illumination with model parameters $W_{EH} = 3.8\,\mathrm{eV}$, $\Delta V = -0.5\,\mathrm{eV}$, $\mathcal{Q}_{EH} = 4.2 \cdot 10^{-5}$, and $\mathcal{Q}_{TM} = 2.0 \cdot 10^{-5}$; the positive branch of the AY curve for pulse duration $10\,\mu\mathrm{s}$ and $V_{inj} = 5.4\,\mathrm{V}$ is not fitted well probably because the UV-power estimate of the specific data series is inaccurate

FIGURE 4.29: Comparison between model prediction and experimental apparent yield data for illuminations with the Crystal 250 in the presence of AC actuation on the z-electrodes.

4.5 Conclusions

Our photoemission model, despite its simplicity, is able to fit the experimental data quite accurately. We are able to extract from the fits, information on the microscopic properties of the surfaces, such as the work function and the quantum yield, which cannot be measured directly.

Regarding the numerical values of the fit parameters we observe:

- Generally the estimated work function is lower than the nominal value for pure gold, which is $W_{\mathrm{Au}} \gtrsim 5.3\,\mathrm{eV}$ [71]. We must notice, however, that the work function depends critically on the status and contamination of the surfaces. Measurement of the workfunction of gold samples exposed to air showed values in the range $3.7 - 4.5\,\mathrm{eV}$ [58], which matches nicely our estimates for W_{EH}.

- The order of magnitude of the estimated quantum yield is consistent with the in-flight measurements of LISA Pathfinder [59], even if a direct comparison is not immediately possible because of the different spectra of the light sources.

- The work function of the EH surfaces is consistently estimated to be within the range $3.6 - 4.0\,\mathrm{eV}$. We find values of the TM work function approximately the same range for TM illumination, but persistently $\sim 0.5\,\mathrm{eV}$ lower for EH illuminations. Such low-values for the TM work function only for EH illuminations are suspect and may indicate that our model is missing some effects, most likely related to the complex 3D geometry of the LISA sensor. Indeed, geometric effect are expected to be particularly significant for EH illumination[28], as evident from the experimental data that seem not to reach complete positive saturation.

- Leaving aside the UVphotonics 230 data, we have that the EH quantum yield values are compatible for both the TM and EH illuminations with the same LED. Instead, the TM apparent yield is larger by approximately a factor two for TM illuminations with respect to EH illuminations. We could explain such difference invoking the fact that, in the case of TM illumination, a large fraction of the light is absorbed by the TM domes, which are not gold-coated (and so they could have different emission properties). A possible alternative explanation is that we assumed the wrong light absorption coefficient A_{TM}.

- The parameters estimated for the SETi 255 in the case of EH illumination with DC actuation are compatible with the ones obtained without actuation: this is an important confirmation of the reliability of our photoemission model.

- Even if we restrict to just the data taken in the same time period (years 2019-2020), the fits suggest that the quantum yield increases, as expected, with the energy of the incident photons. This is evident if we compare the quantum yields of the SETi 255 with the ones of Crystal 250 and SETi 240 (a much smaller difference is found between the latter LEDs, since they have spectra with very close peak energies as we can see from Figure 4.6). We notice that a direct comparison with the UVphotonics 230 data is not possible, as these data series were taken in mid 2022, when we observed a general increase of all saturation levels. We should notice that the determination of the quantum yield is a little tricky because of the problems we had with the UV power measurements (degradation of the optical fibers and uncertainties related to the loose SMA connectors).

[28] The area illuminated with the electrode housing ISUK is geometrically complex because it has groves and holes for the GPRM fingers. Assuming that it can be modeled as infinite plane, as we did in our model, is probably too optimistic.

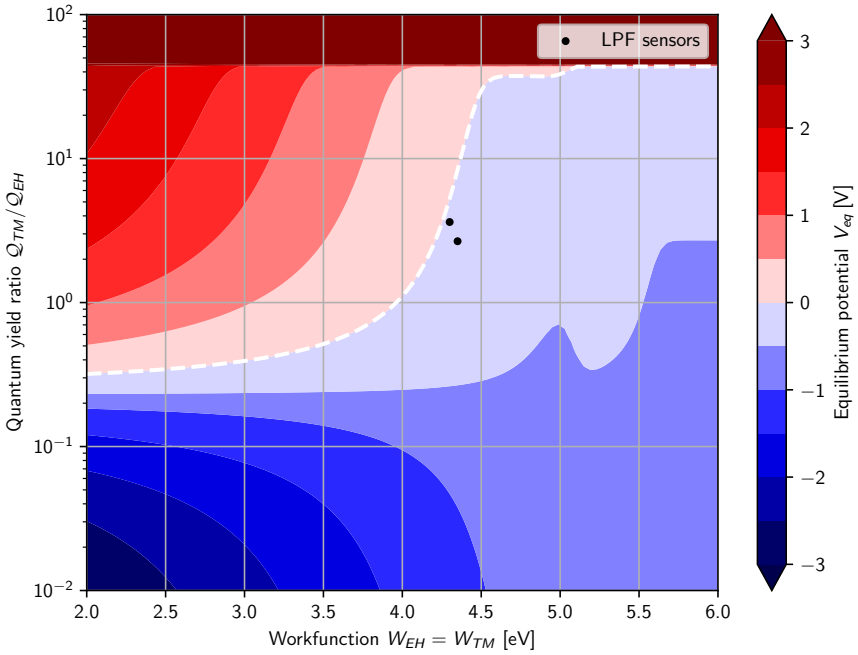

FIGURE 4.30: Simulated equilibrium potentials for the in-phase TM illumination with Crystal 250 (duration 1 µs and delay 2 µs) as a function of the workfunction (assumed equal for TM and EH) and the quantum yield ratio between TM and EH. The dashed white line corresponds to the level $V_{eq} = 0\,\mathrm{V}$. The parameters for LISA Pathfinder inertial sensors have been obtained form [52].

Apart from the success of our simple photoemission model to interpret the apparent yield data, we suggest also developing more advanced 3D models that take into account the complex geometry of the LISA sensor, the photo-electron trajectories, and the precise locations at which photons are absorbed (via ray-tracing simulations). Our hope is that the data produced by such more complex and computationally demanding simulation, would be in accordance with our simple model, so to have an external confirmation of its reliability.

Comment on LISA Pathfinder In LISA Pathfinder, the UV-lamps did not allow the pulsed illumination scheme. Consequently, it was not possible to control the equilibrium potential by adjusting the phase and delay of the light with respect to the injection bias.

As argued in Section 3.5, an interesting application of the model developed in this Chapter is investigating whether we could achieve a negative equilibrium potential (or, equivalently, a net negative photocurrent at neutrality) also for TM illuminations just by controlling the phase and duration of the light pulses also for the emission parameters of the LISA Pathfinder inertial sensors. This is particularly interesting because the LPF apparent yield curves for both LPF sensors, in the case of TM illumination, showed a TM quantum yield ~ 3 times larger than the EH one [52]. In comparison, the GRS installed in our torsion pendulum is more benevolent, as the data generally suggest an apparent yield ratio $\mathcal{Q}_{TM}/\mathcal{Q}_{EH} \simeq 1.3$ for TM illuminations.

The results of the simulation, shown in Figure 4.30, indicate that the pulsed illumination scheme would accomplish a marginally negative equilibrium potential also in the case of TM illumination for both LISA Pathfinder sensors.

Chapter 5

Continuous discharge model and measurements

In this chapter, we will present a model and the experimental results obtained with the 4TM torsion pendulum for the charge noise introduced by the *continuous discharge* strategy to keep the test mass potential under control.

The continuous discharge would be the preferred CMS mode, because it allows to eliminate (or at least reduce) the interruptions in the science observation due to charge management. Indeed, the fast discharge strategy, routinely implemented in LPF, degrades the data quality during the illumination window. The continuous discharge is eased by the use of LEDs as CMS light sources because, by adjusting the phase and the duration of the illumination, it is possible to tune finely the TM equilibrium potential without the need of local DC fields.

Our measurements of the charge noise during continuous discharge mode indicate that the projected acceleration noise on LISA is within the electrostatic budget requirement.

We will also present the spurious effects that limit our sensitivity and a possible way to subtract the dominant one, which is related to the variation of the equilibrium potential with a drift of the TM x-coordinate inside the GRS.

5.1 Linear model for TM charging and discharging processes

The reference for the discharge model presented here is the technical note [72]. The charging rate on test masses can be naïvely modeled as

$$\frac{\mathrm{d}Q_{TM}}{\mathrm{d}t} = \sum_i I_i(Q_{TM}), \tag{5.1}$$

where the summation is intended over all possible charging processes. As the GRS can be interpreted as a capacitor, it is convenient to replace the test mass charge, with the test mass voltage (indeed $C = Q/V$), hence we have

$$\frac{\mathrm{d}V_{TM}}{\mathrm{d}t} = \sum_i \frac{I_i(V_{TM})}{C_{tot}} = \frac{1}{C_{tot}} \left[I_{env}(V_{TM}) + I_{UV}(V_{TM}) \right], \tag{5.2}$$

where in the last passage we highlighted the fact that there are two charging mechanisms acting on the LISA test masses

- The *environmental charging* I_{env}, which is due to mainly cosmic rays and solar energetic particles impinging on the LISA spacecrafts;

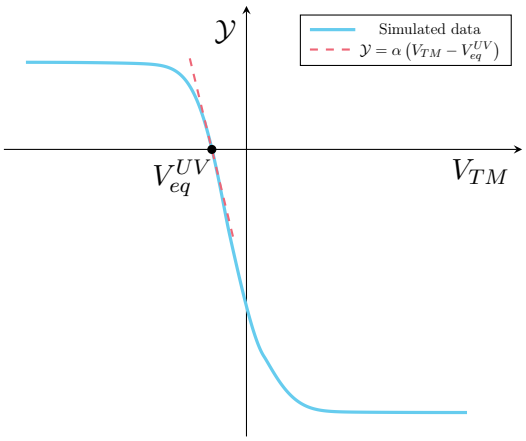

FIGURE 5.1: Linearization of the apparent yield close to the equilibrium voltage.

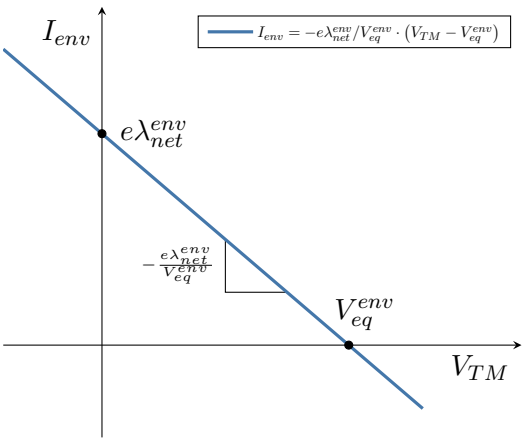

FIGURE 5.2: Extrapolated behavior of the environmental charging current I_{env}.

- The *charging*, or rather, *discharging* I_{UV} due to the Charge Management Device (CMD), which related to the use of UV illumination to counteract the environmental charging and keep the test mass voltage under control.

The current due to UV-illumination can be expressed as

$$I_{UV}(V_{TM}) = \mathcal{Y}(V_{TM}) \cdot eP_{UV}, \tag{5.3}$$

where e is the elementary charge, $\mathcal{Y}$ is the apparent yield[1] of the chosen illumination pattern, and P_{UV} is the UV power[2].

If we suppose that we are close to the equilibrium voltage V_{eq}^{UV} of the illumination, we can linearize the apparent yield curve as (see Figure 5.1)

$$\mathcal{Y}(V_{TM}) \simeq \underbrace{\mathcal{Y}\left(V_{eq}^{UV}\right)}_{0} + \alpha\left(V_{TM} - V_{eq}^{UV}\right) = \alpha(V_{TM} - V_{eq}^{UV}), \tag{5.4}$$

where

$$\alpha = \left.\frac{\mathrm{d}\mathcal{Y}}{\mathrm{d}V_{TM}}\right|_{V_{TM}=V_{eq}^{UV}} \leq 0. \tag{5.5}$$

As evident from the experimental data, the slope α of the apparent yield at the equilibrium is negative. This is an experimental fact and, as we shall see better later, makes the charge management system intrinsically stable.

Of course we must have that the apparent yield vanishes at the equilibrium voltage, i.e. $\mathcal{Y}\left(V_{eq}^{UV}\right) = 0$, otherwise it would not be the equilibrium voltage.

Let us introduce, for reasons that will be clear later, the new quantity τ_{UV} as

$$\tau_{UV} = -\frac{1}{\alpha}\frac{C_{tot}}{eP_{UV}} \geq 0. \tag{5.6}$$

[1] We consider here the apparent yield in units of the net number of elementary charges transferred from TM to EH per unit time and per unit power, i.e. # charges/s/W.

[2] In units W.

The typical scaling for τ_{UV} is

$$\tau_{UV} \simeq 6.3\,\text{hours} \cdot \left(\frac{1\,\text{nW}}{P_{UV}}\right)\left(\frac{10^4\,\text{s}^{-1}\,\text{nW}^{-1}\,\text{V}^{-1}}{-\alpha}\right) \tag{5.7}$$

In this way using the linearization (5.4) and the definition (5.6), we can rephrase equation (5.3), as

$$\begin{aligned} I_{UV}(V_{TM}) &\simeq \alpha\left(V_{TM} - V_{eq}^{UV}\right)\cdot eP_{UV} \\ &\simeq -\frac{1}{\tau_{UV}}\frac{C_{tot}}{P_{UV}}\left(V_{TM} - V_{eq}^{UV}\right)\cdot P_{UV} \\ &\simeq -C_{tot}\frac{V_{TM} - V_{eq}^{UV}}{\tau_{UV}}. \end{aligned} \tag{5.8}$$

The solution of this differential equation is an exponential decay to the equilibrium potential V_{eq}^{UV} with characteristic time τ_{UV}. Note that from (5.6) τ_{UV} is inversely proportional to P_{UV}: the larger is the UV-light power during illumination, the faster will the TM reach the equilibrium potential.

For what regards the cosmic ray charging, LPF observed [36] that the net charging at neutral test mass is approximately $+25\,e/\text{s}$ and that the environmental equilibrium voltage, i.e. the test mass voltage at which the net cosmic ray charging becomes zero, is at about $V_{eq}^{env} = 1\,\text{V}$. As we do not exactly know the functional behavior of the environmental current I_{env} as a function of the test mass voltage, except for the two LPF results just outlined, the safest bet is to assume a linear dependence[3] (see Figure 5.2)

$$I_{env}(V_{TM}) = e\lambda_{net}^{env} - \frac{e\lambda_{net}^{env}}{V_{eq}^{env}}V_{TM} = -\frac{e\lambda_{net}^{env}}{V_{eq}^{env}}\left(V_{TM} - V_{eq}^{env}\right). \tag{5.9}$$

If we define the new quantity τ_{env}, which is the characteristic time of the environmental charging, as

$$\tau_{env} = \frac{V_{eq}^{env}C_{tot}}{e\lambda_{net}^{env}} \geq 0, \tag{5.10}$$

The typical scaling for τ_{env} is

$$\tau_{env} \simeq 100\,\text{days} \cdot \left(\frac{V_{eq}^{env}}{1\,\text{V}}\right)\left(\frac{25\,\text{s}^{-1}}{\lambda_{net}^{env}}\right) \tag{5.11}$$

we can rephrase (5.9) as

$$I_{CR}(V_{TM}) = -C_{tot}\frac{V_{TM} - V_{eq}^{CR}}{\tau_{CR}} \tag{5.12}$$

Putting together the newly found expressions for the UV current due to the illumination (5.8) and for the environmental charging (5.12), we can express the dynamics of the test mass potential (5.2) close to the voltage V_{eq}^{UV} as

$$\begin{aligned} \frac{\mathrm{d}V_{TM}}{\mathrm{d}t} &\simeq -\frac{V_{TM} - V_{eq}^{env}}{\tau_{env}} - \frac{V_{TM} - V_{eq}^{UV}}{\tau_{UV}} \\ &\simeq -\frac{V_{TM} - V_{eq}}{\tau} \end{aligned} \tag{5.13}$$

[3] This behavior seem to be confirmed by the very recent publication [40].

where we defined

$$\tau = \left(\frac{1}{\tau_{env}} + \frac{1}{\tau_{UV}}\right)^{-1} \qquad \text{and} \qquad V_{eq} = \frac{\tau_{env} V_{eq}^{UV} + \tau_{UV} V_{eq}^{env}}{\tau_{env} + \tau_{UV}}. \tag{5.14}$$

We recognize the equation of a simple RC circuit relaxing to the equilibrium voltage V_{eq} with characteristic time $\tau \geq 0$.

Typically we have that $\tau_{UV} \ll \tau_{env}$, hence the previous equations can be simplified to

$$\tau_{UV} \ll \tau_{env} \implies \tau \simeq \tau_{UV} \qquad \text{and} \qquad V_{eq} \simeq V_{eq}^{UV} + \frac{\tau_{UV}}{\tau_{env}} V_{eq}^{env} \tag{5.15}$$

If we define $\Delta V_{eq} = V_{eq} - V_{eq}^{UV}$, we have

$$\tau_{UV} \ll \tau_{env} \implies \Delta V_{eq} \simeq \frac{\tau_{UV}}{\tau_{env}} V_{eq}^{env} = \frac{e\lambda_{net}^{env}}{C_{tot}} \tau_{UV} = -\frac{\lambda_{net}^{env}}{\alpha P_{UV}} \tag{5.16}$$

where we used the definitions (5.10) and (5.6). This last equation tells us that fluctuations in the net environmental charging rate λ_{net}^{env} or in the UV-power during illumination, cause a variation in the equilibrium potential.

Note on stability The differential equation (5.13) represents a *linear time invariant autonomous system.*

A linear autonomous system is a set of differential equations that can be written in the form

$$\frac{\mathrm{d}\boldsymbol{x}}{\mathrm{d}t} = A\boldsymbol{x}, \tag{5.17}$$

where $\boldsymbol{x} = \boldsymbol{x}(t)$ is, in general, a n-dimensional array and A is a $n \times n$ coefficient matrix. A criterion for the stability of a linear autonomous system, known as *Routh–Hurwitz stability criterion*, is that all the eigenvalues of the matrix A have negative real part. Our case is comically trivial as the differential equation (5.13) is one-dimensional: we simply have $A = -\tau^{-1} \leq 0$ and, therefore, the Routh–Hurwitz criterion is met.

The fundamental reason for the stability of the discharge mechanism is to be ascribed to the fact that experimentally the apparent yield curves have a negative slope ($\alpha \leq 0$).

5.1.1 Intrinsic current noise

As the nature of charge transfer is discrete, both the environmental and the UV currents are intrinsically noisy. We can model the noisy part of the currents as extra additive terms in the differential equation (5.13) that defines the system dynamics

$$\frac{\mathrm{d}V_{TM}}{\mathrm{d}t} \simeq -\frac{V_{TM} - V_{eq}}{\tau} + \frac{i_{env}}{C_{tot}} + \frac{i_{UV}}{C_{tot}}, \tag{5.18}$$

where i_{env} and i_{UV} are the noisy part of, respectively, the environmental and CMD currents. At equilibrium they can be treated as zero-mean stochastic processes.

The balance in the number of charges deposited on the LISA test mass due to the various charging processes can be treated as a *counting process.* As the number of charges deposited on the TM due to either environmental charging or UV illumination can be reasonably assumed to be independent Poisson processes, we have that the corresponding currents are the time derivative of Poisson processes, i.e. independent sources of *shot noise.*

The one-sided power spectral density of a shot noise is frequency independent and reads[4]

$$S_{shot}(\omega) = 2j^2\lambda \qquad \text{(one-sided)} \tag{5.19}$$

where λ is the rate parameter of the associated Poisson process and $j \in \mathbb{Z}$ is the *multiplicity*, i.e. the number of unitary increments that characterize the arrival event in the Poisson process.

A property that will be useful later is the *merging* of Poisson process[5] [73], which states that the sum of independent Poisson processes $N_i(t)$, each one with a rate parameter λ_i is a still a Poisson process with rate $\lambda = \sum_i \lambda_i$. Therefore, by comparison with (5.19), the PSD of the shot noise associated with the merging of the independent Poisson processes $\{N_i(t)\}$ is

$$S_{shot}(\omega) = 2\sum_i j_i^2\lambda_i \qquad \text{(one-sided)} \tag{5.20}$$

where j_i is the multiplicity of the ith Poisson process.

Environmental charging noise

The detailed physical models behind the TM charging due to cosmic rays and solar energetic particles are quite complicated. Indeed, as high-energy particles hits the LISA spacecraft a shower of low-energy secondary particles is produced. The role of particles with energy $\lesssim 100\,\text{eV}$ is thought to be relevant. For such reasons, the charging process of the LISA test masses is still being investigated with dedicated numerical simulations [43].

For the sake of our model we can neglect most of the details and assume that the environmental charging is composed of a positive and a negative current. The number of positive and negative charging events per unit time is assumed to follow a Poisson distribution. Hence, the positive and negative photocurrents can be treated as independent sources of shot noise.

Normally the positive current dominates over the negative current, i.e. the net charging rate is positive, but, as anticipated before, at quite large values of the test mass potential ($\sim 1\,\text{V}$), we reach an equilibrium and the two currents balance themselves out.

We repeat the definition of the *net charging rate* and the *effective charging rate*, which are useful quantities to characterize the environmental charging process

$$\lambda_{net}^{env} = \sum_j j\lambda_j \qquad \text{and} \qquad \lambda_{eff}^{env} = \sum_j j^2\lambda_j. \tag{5.21}$$

The index j runs over all integer numbers and represents the *multiplicity*, i.e. the number of elementary charges carried by each charging event. LPF measured (at neutral TM) the values reported in Table 5.1.

From (5.20), the noise power spectra density of the current noise associated with the environmental charging is

$$S_{i_{env}} = 2e^2\sum_j j^2\lambda_j = 2e^2\lambda_{eff}^{env} \qquad \text{(one-sided)} \tag{5.22}$$

[4] See Appendix F for more details.
[5] See Section F.1.7 of Appendix F for the proof.

TABLE 5.1: LPF results for the net and effective environmental charging rates at neutral TM [36].

Quantity	Symbol	TM1	TM2	Units
Net charging rate	λ_{net}^{env}	$+22.9$	$+24.5$	s^{-1}
Effective charging rate	λ_{eff}^{env}	1060 ± 90	1360 ± 130	s^{-1}

The typical scaling of the current noise $S_{i_{env}}$ is

$$S_{i_{env}} \simeq (8.2\,\mathrm{aA})^2 \cdot \left(\frac{\lambda_{eff}^{env}}{1300\,\mathrm{s}^{-1}} \right) \tag{5.23}$$

This is a zero-order approximation as it does not consider that the environmental charging noise is *non-stationary*, as it depends on the test mass potential itself.

Comment on non-stationarity If we consider the potential of the LISA test masses to be nearly constant, the noise properties do not significantly change over time and we can consider the noise as stationary. As stated previously, this is, of course, only an approximation. Here we propose a simple way to take into account the non-stationarity of the environmental charging process.

In the assumption that the charging events deposit on the TM only one elementary charge[6] (that is $j = \pm 1$), we can split the net and effective rate from (5.21), into their positive and negative contributions

$$\lambda_{net}^{env} = \lambda_+ - \lambda_- \qquad \text{and} \qquad \lambda_{eff}^{env} = \lambda_+ + \lambda_- \tag{5.24}$$

Hence

$$\lambda_+ = \frac{\lambda_{net}^{env} + \lambda_{eff}^{env}}{2} \qquad \text{and} \qquad \lambda_- = \frac{\lambda_{eff}^{env} - \lambda_{net}^{env}}{2} \tag{5.25}$$

As we know that the net charging rate vanishes at V_{eq}^{env}, we can assume, coherently with (5.9), that it decreases linearly with the TM potential

$$\lambda_{eff}^{env}(V_{TM}) = \frac{V_{eq}^{env} - V_{TM}}{V_{eq}^{env}} \lambda_{net}^{env}(V_{TM} = 0) \tag{5.26}$$

We do not know the dependence of the effective charging rate from the test mass potential, so we will just assume it to be constant, i.e.

$$\lambda_{eff}^{env}(V_{TM}) = \lambda_{eff}^{env}. \tag{5.27}$$

If we combine these two assumptions into (5.25), we must have

$$\begin{cases} \lambda_+(V_{TM}) = \frac{1}{2}\left[\lambda_{eff}^{env}(V_{TM}=0) + \frac{V_{eq}^{env}-V_{TM}}{V_{eq}^{env}}\lambda_{net}^{env}(V_{TM}=0)\right] \\ \lambda_-(V_{TM}) = \frac{1}{2}\left[\lambda_{eff}^{env}(V_{TM}=0) - \frac{V_{eq}^{env}-V_{TM}}{V_{eq}^{env}}\lambda_{net}^{env}(V_{TM}=0)\right] \end{cases} \tag{5.28}$$

This equations mean that the arrival rate of negative particles λ_- increases linearly with V_{TM}, whereas the arrival rate of positive particles λ_+ decreases linearly with

[6] This assumption may be a little strong. If, on one hand, detailed simulations [41] show that the majority of events carry indeed only one elementary charge, on the other hand, the effective charging rate λ_{eff} grows with the square of the multiplicity, hence rare events that carry a lot of charge could contribute significantly to λ_{eff}.

V_{TM}. Hence, a more realistic expression for the PSD of the noisy environmental current is

$$S_{i_{env}}(V_{TM}) = 2e^2\left[\lambda_+(V_{TM}) + \lambda_-(V_{TM})\right] \qquad \text{(one-sided)} \tag{5.29}$$

These simple observations can be useful to simulate numerically the charge noise on the LISA test mass, without neglecting the dependence of the noise from the test mass voltage itself. We notice that the correction (5.28) is small because $\lambda_{net}^{env} \ll \lambda_{eff}^{env}$ (see Table 5.1).

UV photoelectric charging noise

Also in the case of the charging due to UV illumination, we have two competing currents. As the UV photons are absorbed both from the EH and the TM due to the non-zero reflectivity of the GRS inner surfaces, we will have a photo-electron current coming from the EH and an opposing photoelectron current coming from the TM.

A simple statistical model to describe the processes that generates the photocurrents, or rather their integral in time, i.e. the number of charges deposited on the TM, can be summarized as

1. The number of photons arriving in the GRS per unit time can be assumed as a Poisson process (see Appendix G for some measurements that justify this assumption);
2. The absorption of photons by either the EH or the TM can be modeled as a Bernoulli trial[7];
3. The production of a photo-electron can be also thought as a Bernoulli trial (any absorbed photon may either produce or not a photoelectron).
4. The probability that a photo-electrons emitted by either the TM or the EH reaches the opposing surface can be modeled also as a Bernoulli trial.

Fortunately, the extraction of points in a Poisson process with rate λ according to the outcome of a Bernoulli random variable with success probability η generates a stochastic process which is still Poisson, but characterized by a reduced rate $\lambda' = \lambda\eta$ (see Appendix F.1.6 for more details). Hence, despite the underlying statistical processes, the number of photoelectrons arriving or leaving the TM can be simply modeled as independent Poisson processes with suited rates.

The photocurrents, are the derivative of the number of charges, i.e. of a Poisson process. Hence they can be treated as a shot noise.

5.1.2 Torsion pendulum discharge model

In the 4TM torsion pendulum we do not observe an environmental charging of the test mass (i.e. $\lambda_{net}^{env} = 0$), hence we have $I_{env} = 0$, so the discharge dynamics (5.13) simply reduces to

$$\frac{\mathrm{d}V_{TM}}{\mathrm{d}t} = \underbrace{-\frac{V_{TM} - V_{eq}^{UV}}{\tau_{UV}}}_{\text{deterministic part}} + \underbrace{\frac{i_{shot}}{C_{tot}}}_{\text{noisy part}} \tag{5.30}$$

[7]Success may be interpreted as being absorbed by EH and failure being absorbed by the TM. The reader may rightly think that this means that some correlation may arise between the TM and EH currents. This is actually not true because of the properties of Poisson processes: *splitting* a Poisson process results in two independent Poisson processes (see Appendix F.1.6).

As V_{eq}^{UV} is supposed to be a constant, the previous equation can be equivalently rephrased as

$$\frac{\mathrm{d}\left(V_{TM}-V_{eq}^{UV}\right)}{\mathrm{d}t}=-\frac{V_{TM}-V_{eq}^{UV}}{\tau_{UV}}+\frac{i_{shot}}{C_{tot}} \tag{5.31}$$

Introducing the voltage fluctuations as $\delta V_{TM}=V_{TM}-V_{eq}^{UV}$, we get

$$\frac{\mathrm{d}\delta V_{TM}}{\mathrm{d}t}=-\frac{\delta V_{TM}}{\tau_{UV}}+\frac{i_{shot}}{C_{tot}}. \tag{5.32}$$

If we apply a Fourier transform ot the previous equation, we obtain

$$\mathrm{i}\omega\delta\tilde{V}_{TM}=-\frac{\delta\tilde{V}_{TM}}{\tau_{UV}}+\frac{\tilde{i}_{shot}}{C_{tot}} \tag{5.33}$$

If we solve for $\delta\tilde{V}_{TM}$, we have

$$\delta\tilde{V}_{TM}=\frac{\tilde{i}_{shot}}{C_{tot}\left(\mathrm{i}\omega+\frac{1}{\tau_{UV}}\right)}. \tag{5.34}$$

The transfer function $\delta\tilde{V}_{TM}/\tilde{i}_{shot}$ behaves like an integrator up to a given cutoff frequency, given by $f_c=(2\pi\tau_{UV})^{-1}$.

If we assume that the current driving the system is noisy with power spectral density $S_{i_{shot}}$, we have that the PSD of the test mass voltage noise is

$$S_{V_{TM}}^{shot}(\omega)=\frac{S_{i_{shot}}}{\left|C_{tot}\left(\mathrm{i}\omega+\frac{1}{\tau_{UV}}\right)\right|^2}=\frac{S_{i_{shot}}}{C_{tot}^2\left(\omega^2+\frac{1}{\tau_{UV}^2}\right)} \tag{5.35}$$

We know that the photocurrent can be modeled as *shot noise*, hence its power spectral density is

$$S_{i_{shot}}=2\sum_{j=\pm1,\pm2,\ldots}j^2e^2\lambda_j=2e^2\lambda_{eff}\qquad\text{(one-sided)} \tag{5.36}$$

where $j\in\mathbb{Z}$ is the number of particles or counts per event (multiplicity), e is the elementary charge, and λ_j the rate of the events with multiplicity j. The expression for the characteristic time τ_{UV} was already calculated in (5.6).

Of course, in the case of UV illumination, we actually have two independent currents: one corresponding to the photoelectrons that are extracted from the TM and reach the EH and the opposite one, corresponding to the photoelectrons that travel from the EH towards the TM. For the *merging property* of Poisson processes, their sum is still a Poisson process.

For this reason, from (5.3) the λ_{eff} can be reasonably approximated to be

$$\lambda_{eff}\simeq P_{UV}\left(|\mathcal{Y}_{TM}(V_{eq})|+|\mathcal{Y}_{EH}(V_{eq})|\right), \tag{5.37}$$

where we ignore variations of the apparent yield due to small deviations form the equilibrium[8]. Unfortunately we cannot measure directly $\mathcal{Y}_{TM}(V_{eq})$ or $\mathcal{Y}_{EH}(V_{eq})$, that

[8]This is or course an approximation, but a good one: the observed test mass voltage fluctuations in the continuous discharge measurement are much smaller than the typical scales needed to cause a significant variation of the individual TM or EH currents. In more formal terms, as the rate depends slightly on the test mass voltage, which in turn depends on time, we are dealing with an *in-homogeneous Poisson process*, but we approximate it as an homogeneous one.

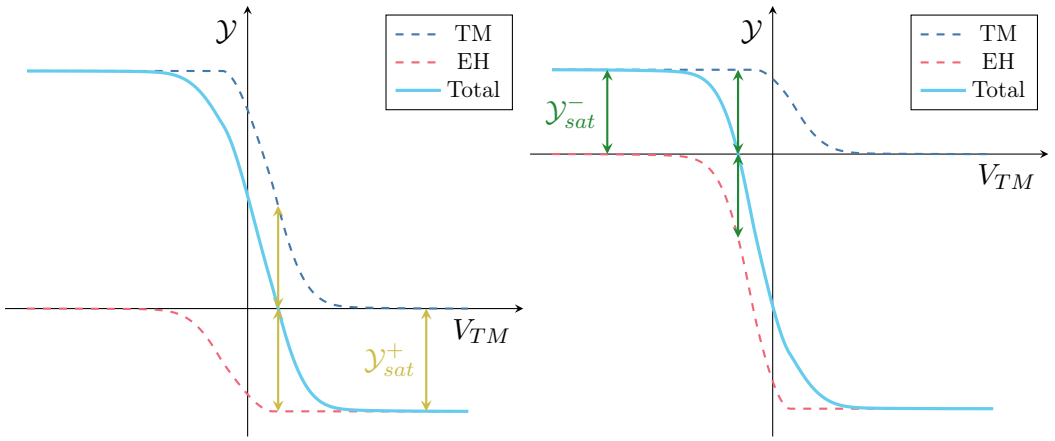

(A) TM illumination (B) EH illumination

FIGURE 5.3: Simulated apparent yield data separated into the TM and EH contributions. At the equilibrium voltage the TM and EH currents must be equal and opposite. More precisely, the magnitude of the current at the equilibrium voltage is very close to the smaller saturation current.

is the TM or EH contributions to the apparent yield at the equilibrium voltage. However, the following observations are certainly true

- Obviously if we are at the equilibrium the test mass potential stays constant: this means that the TM and EH photocurrents and, consequently, the apparent yields must be equal and opposite.

$$|\mathcal{Y}_{TM}(V_{eq})| = |\mathcal{Y}_{EH}(V_{eq})| \tag{5.38}$$

- The values of the TM and EH contributions to the apparent yield at the equilibrium voltage must be smaller than the apparent yield at, respectively, very small and very large test mass potentials (*saturation values*)

$$\begin{cases} |\mathcal{Y}_{TM}(V_{eq})| \leq \lim_{V_{TM}\to-\infty} |\mathcal{Y}(V_{TM})| = \mathcal{Y}^-_{sat} \\ |\mathcal{Y}_{EH}(V_{eq})| \leq \lim_{V_{TM}\to+\infty} |\mathcal{Y}(V_{TM})| = \mathcal{Y}^+_{sat} \end{cases} \tag{5.39}$$

Considering (5.38) and (5.39) we have that a reasonable upper limit the equal and opposite TM and EH apparent yield contributions at the equilibrium voltage is the smaller saturation value

$$|\mathcal{Y}_{TM}(V_{eq})| = |\mathcal{Y}_{EH}(V_{eq})| \lesssim \min\left(\mathcal{Y}^+_{sat}, \mathcal{Y}^-_{sat}\right). \tag{5.40}$$

Simulated data seem to suggest that the true value for the TM or EH contributions to the apparent yield at the equilibrium $|\mathcal{Y}_{TM}(V_{eq})| = |\mathcal{Y}_{EH}(V_{eq})|$ is very close to this upper limit (see Figure 5.3). We put forward two effects that may (slightly) reduce the apparent yield contributions of EH and TM at the equilibrium potential from the proposed upper limit: the *contribution of the injection electrodes*, which may cause a residual slope[9] of the AY curves even at $|V_{TM}| \gtrsim 2\,\mathrm{V}$ (see for example Figure 4.10b)

[9]This effect may be reduced if we consider (as we will, but for another reason) pulsed illuminations centered on the maxima or minima of the injection bias (see Figure 4.11).

and *geometric effects*[10].

From these considerations, we have that a reasonable upper limit for the effective charge rate (5.37) is

$$\lambda_{eff} \lesssim 2P_{UV} \min\left(\mathcal{Y}^{+}_{sat}, \mathcal{Y}^{-}_{sat}\right). \tag{5.41}$$

The positive and negative saturation values can be directly measured from the apparent yield data. If the emission properties of TM and EH are not too different from each other we expect that in the case of EH illumination the negative saturation value of the apparent yield is smaller than the AY value at positive saturation. Vice versa is true for TM illumination. In a formula

$$\begin{cases} \min\left(\mathcal{Y}^{+}_{sat}, \mathcal{Y}^{-}_{sat}\right) = \mathcal{Y}^{-}_{sat} & \text{for EH illumination} \\ \min\left(\mathcal{Y}^{+}_{sat}, \mathcal{Y}^{-}_{sat}\right) = \mathcal{Y}^{+}_{sat} & \text{for TM illumination} \end{cases} \tag{5.42}$$

On the basis of these observations, we have that (5.35) becomes

$$S^{shot}_{V_{TM}}(\omega) \lesssim \frac{4e^2 P_{UV} \min\left(\mathcal{Y}^{+}_{sat}, \mathcal{Y}^{-}_{sat}\right)}{C^2_{tot}\left(\omega^2 + \frac{1}{\tau^2_{UV}}\right)} \qquad \text{(one-sided)} \tag{5.43}$$

From the previous equations, we see that the current shot noise is proportional to the effective rate and hence the UV power ($S_{i_{shot}} \propto \lambda_{eff} \propto P_{UV}$), whereas the characteristic time is inversely proportional to the UV power ($\tau_{UV} \propto 1/P_{UV}$). More precisely, combining the definition of τ_{UV} (5.6) and the expression for λ_{eff} (5.37), we have

$$\lambda_{eff}(\tau_{UV}) \simeq -\frac{C_{tot}}{\alpha e}\frac{|\mathcal{Y}_{TM}(V_{eq})| + |\mathcal{Y}_{EH}(V_{eq})|}{\tau_{UV}} = A \cdot (\tau_{UV})^{-1}, \tag{5.44}$$

where $A \geq 0$ is a positive constant. From the equation (5.43), we see that if we increase the UV power, the shot noise will be larger, but at the same time the response time of the system will be shorter (i.e. the system is more rigid): charge fluctuations that bring the TM farther away from the equilibrium potential will be suppressed. On the other hand, if the UV power is lowered, larger low-frequency charge fluctuations will be permitted, but the overall shot noise level will be smaller.

As the TM potential noise $S_{V_{TM}}$ depends both on the shot noise level and the response time τ_{UV}, one has to chose carefully the UV power to optimize the trade-off between these two quantities.

As we are interested in measuring the charge noise $S_{V_{TM}}$ introduced by the illumination, we have to carefully choose the UV power to enhance the charge noise above the noise floor of the torsion pendulum, while keeping the length of the measurements to an acceptable duration (hence the frequencies available are in the band $10^{-5}\,\text{Hz} \leq f \leq 10^{-3}\,\text{Hz}$).

Of course this is exactly the opposite of what we want to do for LISA. Indeed, during the mission one wants to manage the test mass charge while minimizing the extra noise added by the continuous illumination.

A projection of the expected TM potential noise $S_{V_{TM}}$ as a function of the UV power is showed in Figure 5.4 for TM and EH illuminations with the UV-LED Crystal 250. As one can see the charge noise is generally a factor $2-4$ in amplitude above the instrumental noise floor at 0.1 mHz. The detection limits are quite tight: the expected

[10]For instance if we illuminate with the test mass ISUK, we expect that not all photoelectrons emitted from the EH will ballistically reach the TM at $V_{TM} = V_{eq} \simeq 0\,\text{V}$, but only for $V_{TM} \gg 0\,\text{V} \simeq V_{eq}$. Hence, the absolute value of the apparent yield at positive saturation is expected to be larger than the equilibrium value.

noise start to dominate over the pendulum noise floor only at very low frequencies. This requires to perform very long[11] measurements to have some statistics for the PSD estimation.

5.2 Torsion pendulum measurements

5.2.1 Experimental technique

The experimental method that we applied to measure the noise introduces by the continuous discharge of the test mass is quite simple: we choose an illumination pattern that keeps the TM very close to neutrality (within $\pm 5\,\mathrm{mV}$) and then acquire a long timeseries of the test mass potential (several days). In conjunction with the charge noise measurement, we also estimated the response time τ of the system, as well as the mean UV power during the illumination, to better constrain the model described in the previous section.

The experimental method is summarized in the following checklist

1. Measure the UV power before the illumination;
2. Acquire a charge time-series when shining UV light on either the TM or the EH with the desired illumination pattern;
3. In order to measure the characteristic response time τ_{UV}, we need to displace the TM potential form the equilibrium. We can achieve that by changing the phase of the illumination. Once we reach the desired displacement from the equilibrium voltage, we resume the illumination with the same pattern as the long continuous discharge measurement. We record the time-series of the decay to equilibrium and we estimate τ_{UV} with a fit of the following exponential model

$$V_{TM}(t) = V_1 \cdot \mathrm{e}^{-t/\tau_{UV}} + V_2 \tag{5.45}$$

   In Figure 5.5 we plot an example of such exponential fit on a real data series to estimate the characteristic time τ_{UV}.
4. We check the UV power a second time at the end of the measurement.

We decided to use the Crystal 250 UV-LED as the light source for the continuous discharge measurements.

5.2.2 Extra noise sources

We present in this section further noise sources not directly related to the Poissonian nature of charge transfer that may affect the *continuous discharge* measurements. Such disturbances can be grouped into two categories:

- Disturbances related to the CMD and the light emission:
  - Phase noise of CMD light pulses;
  - Power stability noise of the CMD light;
- Disturbances related to the TM position inside the GRS:

[11] We decided to do measurements of approximately five days in duration. Longer data acquisitions were hard to obtain for practical reasons and by the presence of environmental disturbances (such as earthquakes).

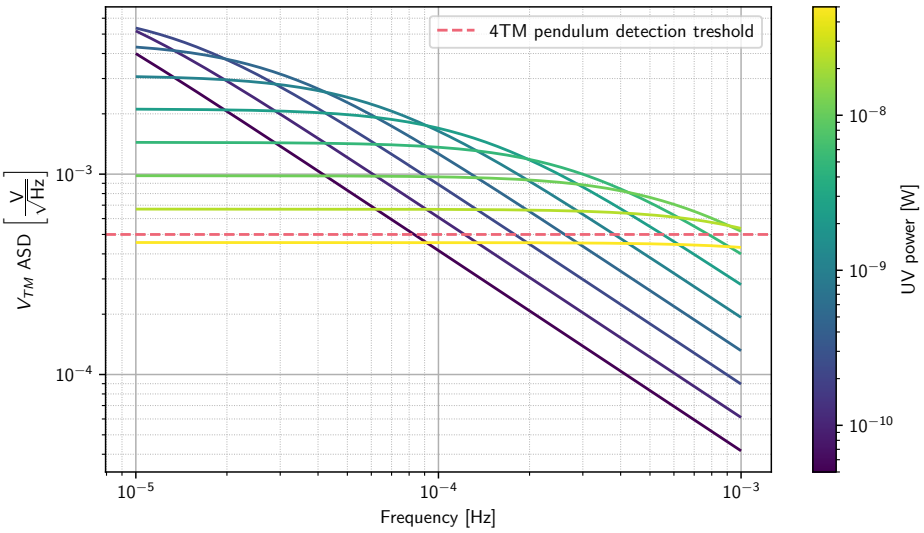

(A) TM illumination

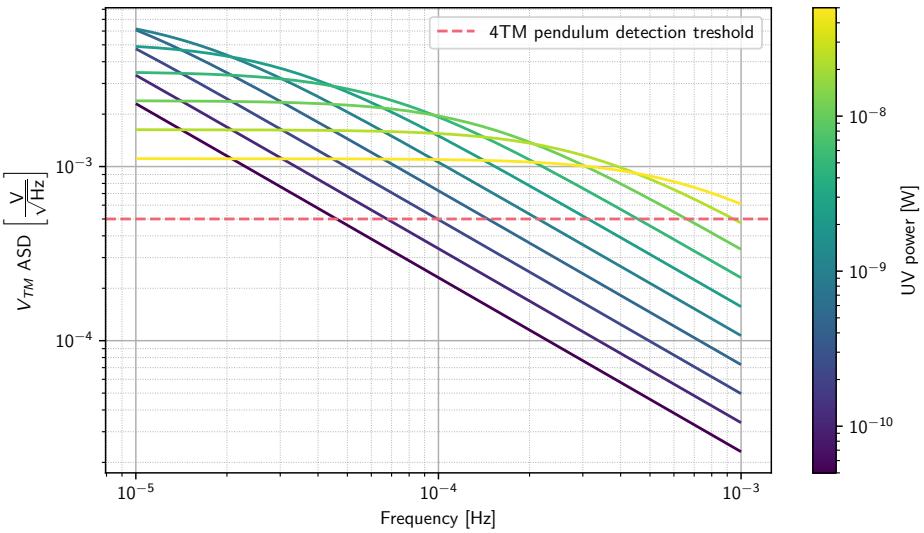

(B) EH illumination

FIGURE 5.4: Estimates of the TM potential noise introduced by the continuous discharge for TM and EH illuminations with Crystal 250 LED as a function of the selected UV power. The dashed line corresponds to the 4TM torsion pendulum force sensitivity at the modulation frequency converted into TM potential.

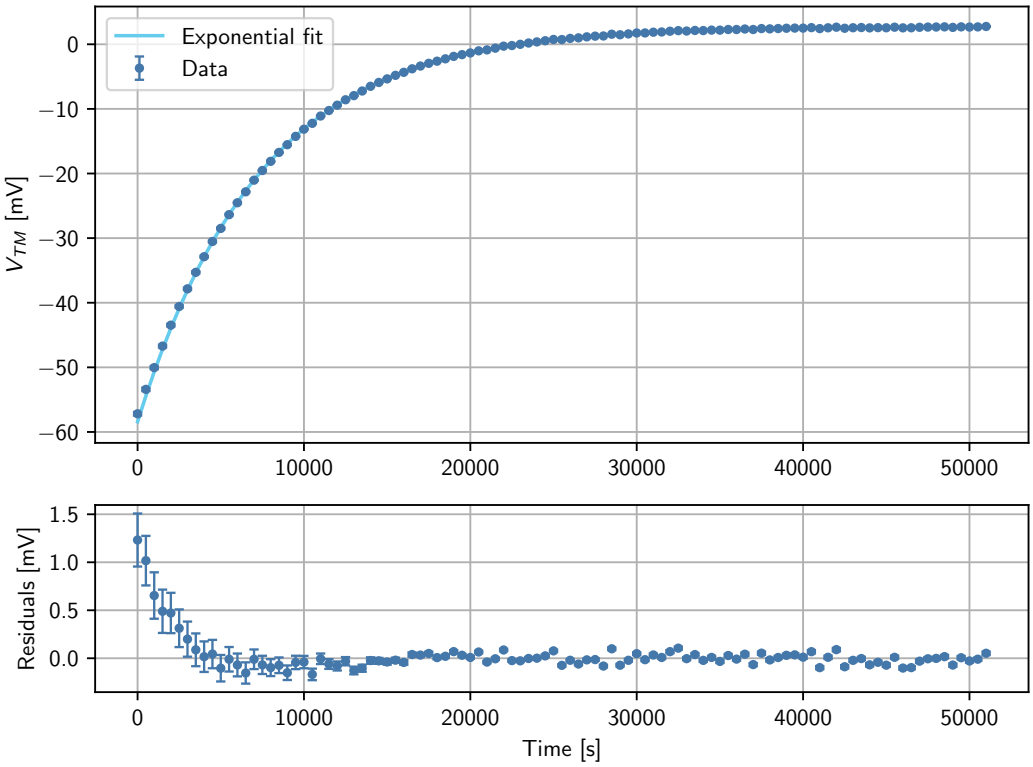

FIGURE 5.5: TM potential time-series for a direct measurement of the characteristic response time τ_{UV}.

– Dependence of the charge measurement on TM position;
– Dependence of equilibrium voltage on TM position;

Phase noise

A fluctuation in the phase of the illumination causes a change in the equilibrium voltage.

The typical dependence of the equilibrium voltage from the phase of the illumination for light pulses of duration 1 µs with the Crystal 250 LED as light source is depicted in Figure 5.6.

As customary, for small variations of the phase with respect to a central value ϕ_0, we can express the dependence of the equilibrium voltage V_{eq} at the linear order as

$$V_{eq}(\phi) \simeq V_{eq}(\phi_0) + \left.\frac{\mathrm{d}V_{eq}}{\mathrm{d}\phi}\right|_{\phi=\phi_0} (\phi - \phi_0) \qquad \text{for} \qquad \phi \ll \phi_0 \tag{5.46}$$

From Figure 5.6, we can observe that if we choose an illumination pattern such that the light pulses are centered around the maxima or minima of the 100 kHz injection bias, we minimize dependence of the equilibrium voltage with the phase of the illumination. In other words, the sensitivity factor $\frac{\mathrm{d}V_{eq}}{\mathrm{d}\phi}$ is minimum if we center the light pulses on the maxima or minima of the injection bias.

It is important to notice that we can still obtain equilibrium potentials close to zero by controlling the *duration* of the illumination: consider for example the case of TM illumination, we can achieve an equilibrium voltage close to neutrality if we

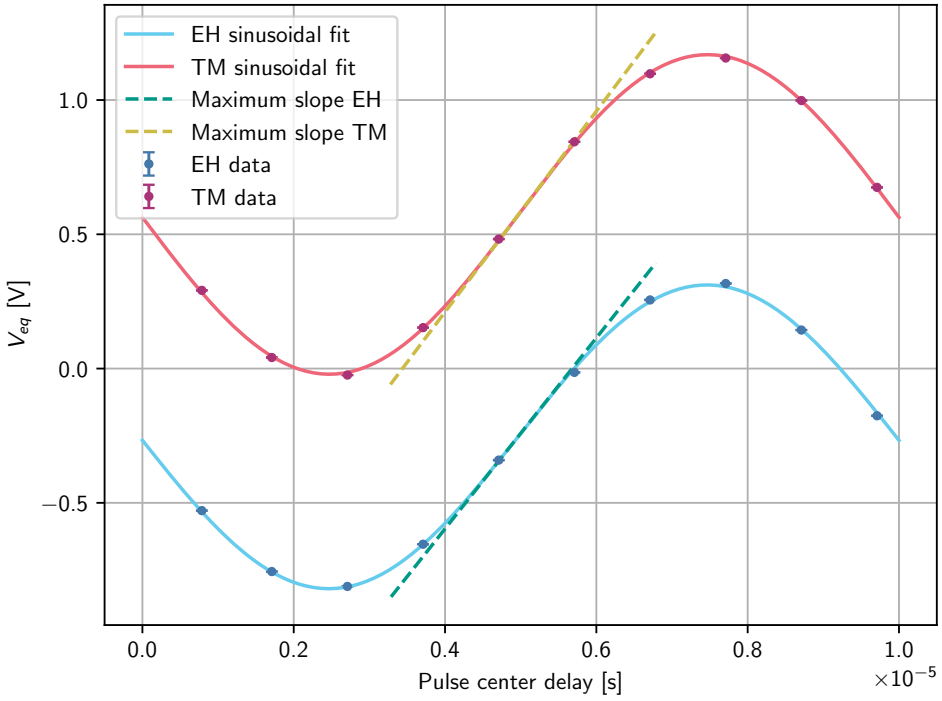

FIGURE 5.6: Dependence of the equilibrium voltage with the delay with respect to the 100 kHz-injection bias in the case of illumination with the Crystal 250 UV-LED. An empirical sinusoidal fit has been performed on the data. The maximum slope has been estimated from such fit computing the derivative at the zero-crossing.

illuminate with light pulses centered around a delay of 2.5 µs with respect to the zero-crossing of the injection bias[12] and increasing gradually the duration of the pulse until the equilibrium potential is sufficiently close to neutrality[13].

The model to convert the phase noise into a test mass voltage noise can be immediately obtained from (5.30). The discharge dynamics, neglecting the noisy Poisson current, can be expressed as

$$\begin{aligned}\frac{\mathrm{d}V_{TM}}{\mathrm{d}t} &= -\frac{V_{TM} - V_{eq}^{UV}(\phi)}{\tau_{UV}} \\ &\simeq -\frac{V_{TM} - \left[V_{eq}(\phi_0) + \left.\frac{\mathrm{d}V_{eq}}{\mathrm{d}\phi}\right|_{\phi=\phi_0}(\phi-\phi_0)\right]}{\tau_{UV}},\end{aligned} \tag{5.47}$$

where we explicitly indicated the dependence of the equilibrium voltage on the phase of the illumination and, in the second passage, we used the linear approximation (5.46). If we now introduce $\delta V_{TM} = V_{TM} - V_{eq}(\phi_0)$ and $\delta\phi = \phi - \phi_0$, we can rephrase[14] the previous equation more conveniently as

$$\frac{\mathrm{d}\delta V_{TM}}{\mathrm{d}t} \simeq -\frac{\delta V_{TM}}{\tau_{UV}} + \frac{1}{\tau_{UV}}\frac{\mathrm{d}V_{eq}}{\mathrm{d}\phi}\cdot\delta\phi \tag{5.48}$$

A quick Fourier transform leads us to

$$\left(\mathrm{i}\omega + \frac{1}{\tau_{UV}}\right)\delta\tilde{V}_{TM} \simeq \frac{1}{\tau_{UV}}\frac{\mathrm{d}V_{eq}}{\mathrm{d}\phi}\cdot\delta\tilde{\phi} \tag{5.49}$$

If we consider that the variations in the phase of the illumination $\delta\phi$ are noisy with PSD $S_{\phi\phi}(\omega)$, we have that the expression of the induced voltage noise on the TM is

$$S_{V_{TM}}^{phase}(\omega) \simeq \frac{\left(\frac{\mathrm{d}V_{eq}}{\mathrm{d}\phi}\right)^2}{|1+\mathrm{i}\omega\tau_{UV}|^2}S_\phi(\omega) = \frac{\left(\frac{\mathrm{d}V_{eq}}{\mathrm{d}\phi}\right)^2}{1+\omega^2\tau_{UV}^2}S_\phi(\omega) \tag{5.50}$$

From the last equation we see that, as expected, the transfer function to convert the *phase noise* into test mass potential noise is just the one of a first order low-pass filter with roll-off frequency $f_c = (2\pi\tau_{UV})^{-1}$ and gain equal to $\frac{\mathrm{d}V_{eq}}{\mathrm{d}\phi}$.

We performed direct measurement of the dependence of the equilibrium potential on the phase of the light pulses for illumination patterns otherwise identical to the continuous discharge measurements presented in Section 5.2.3. Such data allow a precise estimate the factor $\frac{\mathrm{d}V_{eq}}{\mathrm{d}\phi}$ for each measurement. The phase stability measurements are obtained connecting the fast PMT output to a lock-in amplifier Stanford Research Systems SR-830 with reference the 100 kHz injection bias coming from our engineering model of the LISA Pathfinder FEE electronics (ELM-light).

Once a time-series of the in-phase X and quadrature Y components of the lock-in output have been acquired, it is immediate to compute the phase time-series with

[12] In this way we are centered on the minimum of the injection bias.

[13] Similarly, for the case of EH illumination we can repeat the same trick but with the light pulses centered on the maximum of the injection bias (that is with a delay of 7.5 µs) and choosing a suitable duration.

[14] Allow us also to simplify the notation by dropping the explicit indication of the phase at which the derivative is computed, i.e.

$$\left.\frac{\mathrm{d}V_{eq}}{\mathrm{d}\phi}\right|_{\phi=\phi_0} = \frac{\mathrm{d}V_{eq}}{\mathrm{d}\phi}$$

.

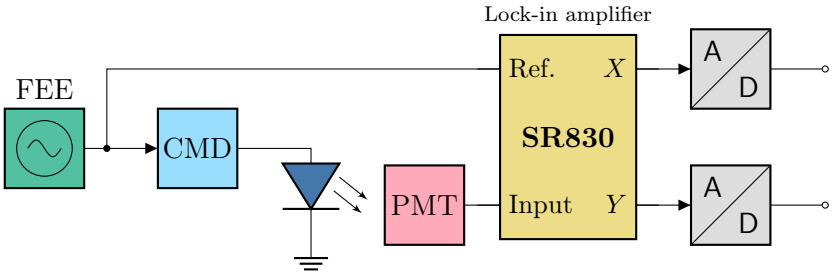

FIGURE 5.7: Scheme for the phase stability measurements. The injection bias produced by the FEE serves as a synchronization signal for the prototype charge management device (CMD) and as the reference for the SR830 DSP lock-in amplifier. After choosing a illumination pattern, the LED output is measured with the calibrated PMT. The PMT signal is the input for the lock-in amplifier. The *in-phase* and *quadrature* components of the signal are then digitized and acquired with our DAQ.

respect to the reference as

$$\phi(t) = \arctan\left[\frac{Y(t)}{X(t)}\right] \tag{5.51}$$

From the time-series $\phi(t)$, we can estimate its power spectral density $S_\phi(\omega)$ with standard techniques (e.g. *Welch's method*). In Figure 5.8 we show a typical spectrum of the phase of the light pulses generated by the CMD prototype provided by INFN/Roma Tor Vergata.

Unfortunately, we were not able to monitor the phase of the light pulses with respect to the injection bias during the illumination, hence a subtraction of the phase noise is impossible. In order to measure the UV-light phase during illumination, we would have needed an optical fiber that splits the light coming from the UV sources into two outputs (one to illuminate the GRS, one for the light-sensitive device). Such hardware is not available at the moment in our laboratory.

We estimate that the extra noise in the continuous discharge measurement due to fluctuations in phase of the illumination is generally small when the light pulses are centered around the maxima or minima of the injection bias (see Section 5.2.3). The phase noise is, however, not negligible if we illuminate with a short pulse centered on the zero-crossing of the injection bias (worst case scenario).

Worst case scenario As we explained previously for the continuous discharge measurement we chose the illumination pattern to suppress the contribution of the phase noise while keeping the equilibrium voltage as close to neutrality as possible. However, during the LISA mission we may have to chose an illumination pattern which does not minimize the dependence of the equilibrium voltage with respect to the phase of the illumination.

From the data of Figure 5.6, we can reasonably obtain a *worst-case* value for the sensitivity factor $\frac{\mathrm{d}V_{eq}}{\mathrm{d}\phi}$, or for $\frac{\mathrm{d}V_{eq}}{\mathrm{d}t_{UV}} = 2\pi f_{inj}\frac{\mathrm{d}V_{eq}}{\mathrm{d}\phi}$, which is the same quantity expressed in terms of the delay of the light pulses with respect to the zero-crossing of the injection voltage instead of the phase, when illuminating with the Crystal 250. Such values for EH and TM illuminations are reported in Table 5.2.

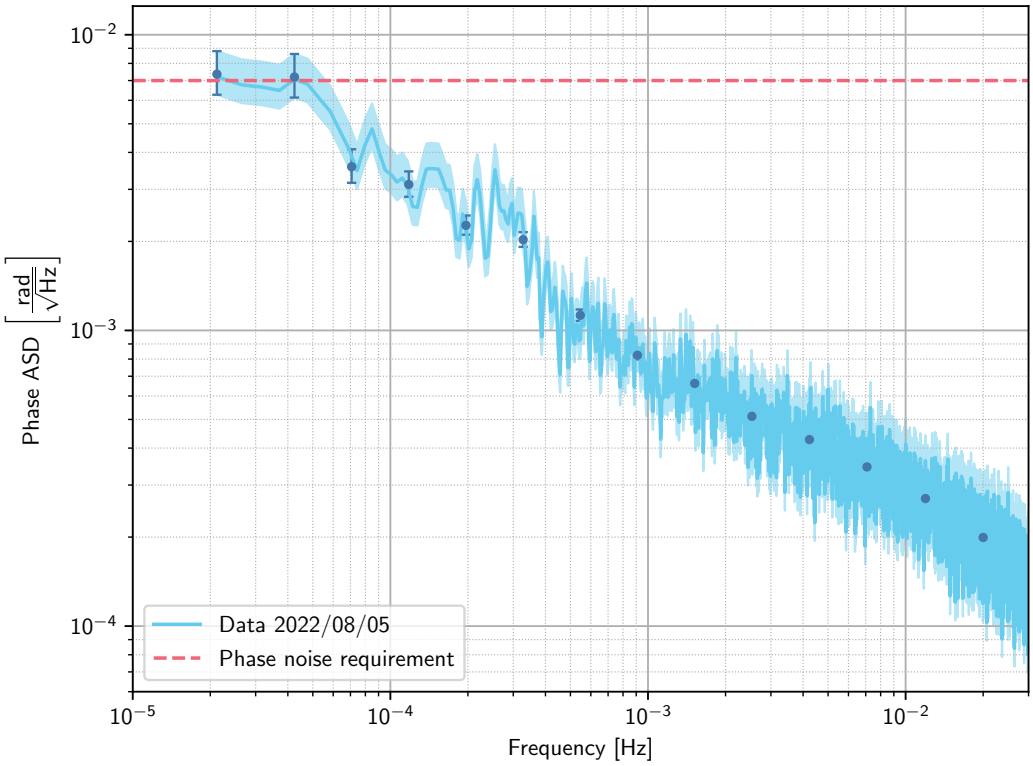

FIGURE 5.8: Amplitude spectral density of the phase timeseries for the CMD prototype provided by INFN/Roma Tor Vergata used in the continuous discharge experimental campaign. The ASD has been computed averaging nine Blackman-Harris windows with 50% overlap. The points with errorbars are Bayesian estimates of the ASD at independent frequencies computed as described in [74]. The phase requirement is set to $7\,\text{mrad}/\sqrt{\text{Hz}}$ [72] and it is marginally violated only at frequencies $\lesssim 5 \cdot 10^{-5}\,\text{Hz}$. During this measurement the temperature in the laboratory hall was not exceptionally stable, so the data could be polluted by temperature induced disturbances.

TABLE 5.2: Reasonable upper limits for the sensitivity factor $\frac{\mathrm{d}V_{eq}}{\mathrm{d}\phi}$, or the equivalent $\frac{\mathrm{d}V_{eq}}{\mathrm{d}t_{UV}}$, in the case of TM or EH illuminations with Crystal 250.

Illumination	$\frac{\mathrm{d}V_{eq}}{\mathrm{d}t_{UV}}$ [V/s]	$\frac{\mathrm{d}V_{eq}}{\mathrm{d}\phi}$ [V/rad]
TM	$(3.74 \pm 0.02) \cdot 10^5$	0.595 ± 0.003
EH	$(3.55 \pm 0.03) \cdot 10^5$	0.566 ± 0.004

UV-power stability

If an environmental charging is present, fluctuations in the UV-power during illumination cause a variation of the equilibrium voltage. Indeed, from (5.13), we have

$$\frac{\mathrm{d}V_{TM}}{\mathrm{d}t} = -\frac{V_{TM} - V_{eq}(P_{UV})}{\tau} \tag{5.52}$$

where P_{UV} is the UV-power during the illumination. If the assume that the UV-power is noisy

$$P_{UV} = \langle P_{UV} \rangle + \delta P_{UV} \tag{5.53}$$

where $\langle \cdot \rangle$ represents the mean operator, we can now expand at linear order the equilibrium potential as

$$\begin{aligned} V_{eq}(P_{UV}) &\simeq V_{eq}(\langle P_{UV} \rangle) + \left.\frac{\mathrm{d}V_{eq}}{\mathrm{d}P_{UV}}\right|_{P_{UV}=\langle P_{UV}\rangle} \delta P_{UV} \\ &\simeq V_{eq}(\langle P_{UV} \rangle) + \frac{\lambda_{net}^{env}}{\alpha \langle P_{UV} \rangle^2} \delta P_{UV} \end{aligned} \tag{5.54}$$

In the last passage we assumed for simplicity $\tau_{UV} \ll \tau_{env}$ so to use (5.16). If we substitute this expression into the differential equation defining the dynamics of the system (5.52), we have

$$\frac{\mathrm{d}V_{TM}}{\mathrm{d}t} \simeq -\frac{V_{TM} - V_{eq}(\langle P_{UV} \rangle) - \frac{\lambda_{net}^{env}}{\alpha \langle P_{UV} \rangle^2} \delta P_{UV}}{\tau} \tag{5.55}$$

At this point we can remember that we just assumed $\tau_{UV} \ll \tau_{env}$, so that $\tau \simeq \tau_{UV}(\langle P_{UV} \rangle)$ hence the previous equation becomes

$$\begin{aligned} \frac{\mathrm{d}V_{TM}}{\mathrm{d}t} &\simeq -\frac{V_{TM} - V_{eq}(\langle P_{UV} \rangle)}{\tau_{UV}(\langle P_{UV} \rangle)} - \frac{\lambda_{net}^{env}}{\alpha \langle P_{UV} \rangle^2 \tau_{UV}(\langle P_{UV} \rangle)} \delta P_{UV} \\ &\simeq -\frac{V_{TM} - V_{eq}(\langle P_{UV} \rangle)}{\tau_{UV}(\langle P_{UV} \rangle)} + \frac{e\lambda_{net}^{env}}{C_{tot}} \frac{\delta P_{UV}}{\langle P_{UV} \rangle} \end{aligned} \tag{5.56}$$

where we used the definition (5.6). If we define $\delta V_{TM} = V_{TM} - V_{eq}(\langle P_{UV} \rangle)$, we have

$$\frac{\mathrm{d}\delta V_{TM}}{\mathrm{d}t} \simeq -\frac{\delta V_{TM}}{\tau_{UV}(\langle P_{UV} \rangle)} + \frac{e\lambda_{net}^{env}}{C_{tot}} \frac{\delta P_{UV}}{\langle P_{UV} \rangle} \tag{5.57}$$

whose Fourier transform is

$$\delta \tilde{V}_{TM} \simeq \frac{e\lambda_{net}^{env} \tau_{UV}}{C_{tot}} \frac{\frac{\delta \tilde{P}_{UV}}{\langle P_{UV} \rangle}}{1 + \mathrm{i}\omega\tau_{UV}} \tag{5.58}$$

where we dropped the dependence of τ_{UV} from the mean power to simplify the notation. In terms power spectral densities

$$S^{power}_{V_{TM}V_{TM}}(\omega) = \left(\frac{e\lambda_{net}^{env}\tau_{UV}}{C_{tot}}\right)^2 \frac{S_{\delta\tilde{P}_{UV}/\langle P_{UV}\rangle}(\omega)}{1 + \omega^2\tau_{UV}^2} \tag{5.59}$$

where $S_{\delta\tilde{P}_{UV}/\langle P_{UV}\rangle}(\omega)$ is the PSD of the relative fluctuations of the UV-power.

The torsion pendulum measurements are not directly affected by fluctuations in the light power emitted by the UV source because on ground the net charging from cosmic

rays and solar energetic particles is zero, i.e. $\lambda_{net}^{env} = 0$. In our setup power fluctuations affect only the statistics of the Poissionian charge transfer and the system response time $\tau_{UV} = \tau_{UV}(P_{UV})$. Unfortunately, we cannot evaluate this effect because we measure the UV power only before and after the continuous discharge measurement. That is why it would be ideal to measure the phase and the power of the UV-light during the illumination with, for example, a splitting fiber.

The noise (5.59) due to fluctuations in the UV-power can be relevant for LISA. The reference [72] places are requirement for the relative UV-power stability of the CMD at $0.1\,\mathrm{Hz}^{-1/2}$.

Measurements of the power stability As in the previous section, we cannot measure the power fluctuations while illuminating the torsion pendulum, but we can perform dedicated stability measurements. From the lock-in amplifier outputs $X(t)$ and $Y(t)$, we can compute the UV power relative amplitude as

$$\frac{\delta P_{UV}(t)}{\langle P_{UV}\rangle} = \frac{\sqrt{X(t)^2 + Y(t)^2}}{\left\langle \sqrt{X(t)^2 + Y(t)^2} \right\rangle} \tag{5.60}$$

In Figure 5.9 we show the ASD of the relative power fluctuations. The data show that the prototype CMD may violate the requirement at frequencies below $4 \cdot 10^{-5}\,\mathrm{Hz}$. We have to point out that the measured relative power noise may have been overestimated at low-frequency due to temperature fluctuations in the laboratory hall.

Dependence of the charge measurement on the TM position

We investigated the dependence of the charge measurement (without UV illumination) on the x-position of the pendulum TM inside the EH.

As shown in Figure 5.10, we noticed a correlation between the measured test mass voltage and ist x-position.

We could change the pendulum x-position by either rotating the round platform on which the GRS flight model replica and the STC are mounted with the dedicated stepper motors, or, alternatively by simply changing manually the equilibrium position of the pendulum with the micro-manipulator that allows rotate the suspension point of the torsion pendulum. From now on we will refer informally to these two methods to alter the TM x-position as *motor* and *manual* rotations.

At first we thought that using the stepper motors was the most convenient procedure to perform such measurements as it allowed for a precise change in the x-position and because it did not require us to access the thermal chamber around the torsion pendulum. We later noticed that the use of the motors caused pretty substantial temperature variations ($\sim 1\,\mathrm{K}$) as measured by the thermometers mounted directly on the GRS: this most likely causes the extra scattering of the data points of Figure 5.10.

We, therefore, switched later to rotating the torsion pendulum *manually* with the micro-manipulator. Such procedure was slower and somewhat burdensome, but it did not induce significant temperature variations in the GRS.

Therefore, we can convert directly the noisy $x(t)$ time-series, into an equivalent readout noise of the test mass potential, as

$$S_{V_{TM}}(\omega) = \left(\frac{\mathrm{d}V_{TM}}{\mathrm{d}x}\right)^2 S_x(\omega) \tag{5.61}$$

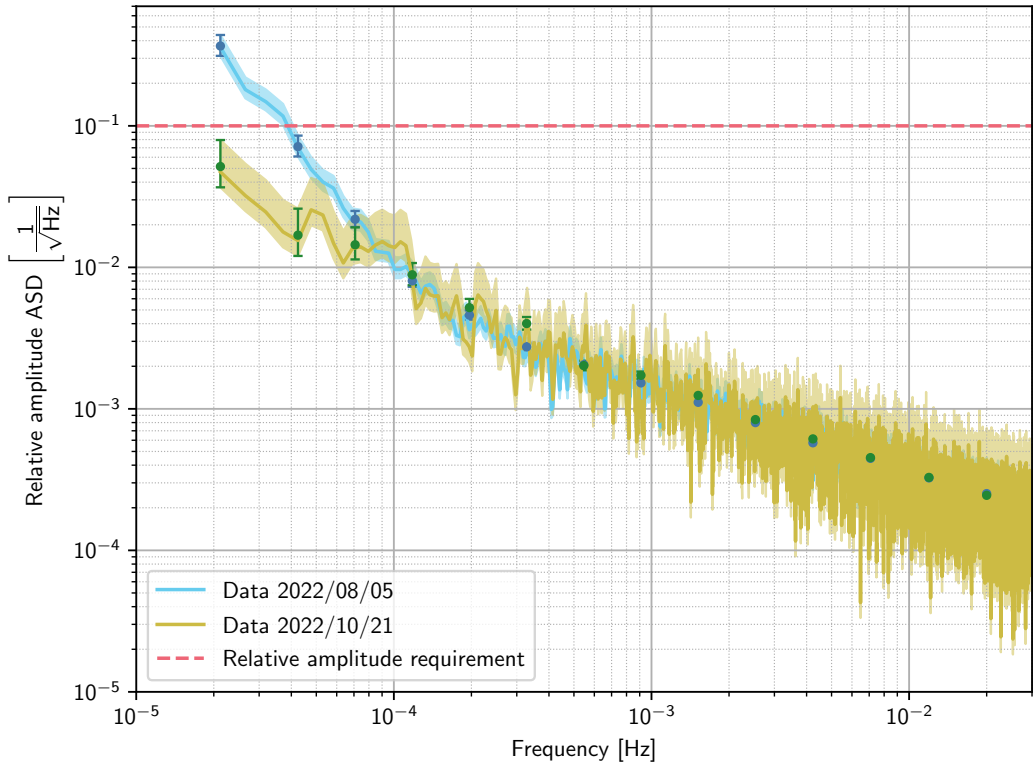

FIGURE 5.9: Amplitude spectral density of the relative power fluctuations of the UV light emitted by the CMD prototype provided by INFN/Roma Tor Vergata used in the continuous discharge experimental campaign. The ASD has been computed averaging nine Blackman-Harris windows with 50% overlap. The points with errorbars are Bayesian estimates of the ASD at independent frequencies computed as described in [74]. The relative amplitude requirement is set to $0.1\,\text{Hz}^{-1/2}$ [72]. During the measurement in August 2022 the temperature in the laboratory hall was not exceptionally stable, so the low-frequency noise may be worse due to temperature induced disturbances. We repeated the measurement in October 2022 (*yellow* data) and we could achieve a relative amplitude noise within the requirements across the whole LISA band.

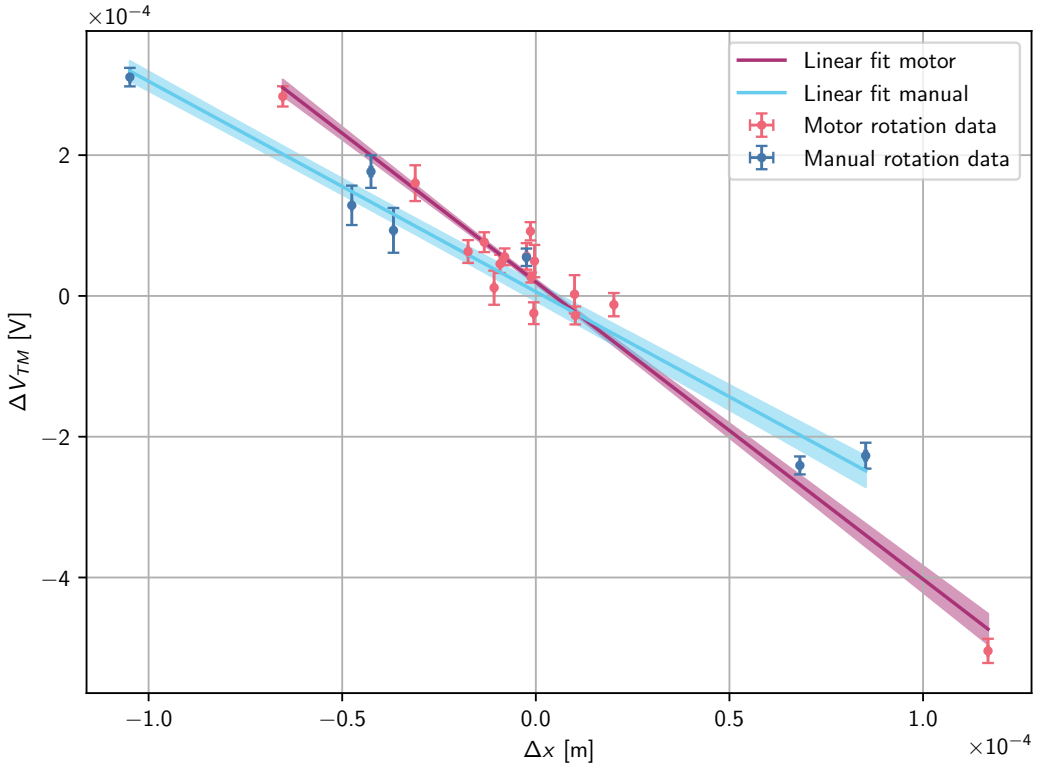

FIGURE 5.10: Dependence of the measured TM charge on its x position in the GRS for the case of no UV illumination (test mass charge is constant). The bands around the fits represent the 1σ-confidence intervals. The *blue* data correspond to changing the TM position by rotating manually the pendulum suspension point, whereas the *red* data are obtained by rotating with the motors the round platform on which the sensor is mounted.

The coupling coefficient is estimated to be $\mathrm{d}V_{TM}/\mathrm{d}x = -2.99 \pm 0.15\,\mathrm{V/m}$. As one will see in Section 5.2.3, the charge noise introduced by this effect is below the torsion pendulum sensitivity and can be neglected.

The origin of the dependence of measured test mass potential on the x-position in the GRS is to ascribe to the presence of stray biases on the x-electrodes. Indeed, in Section 2.3 we have shown that the in-phase force component at the modulation frequency during charge measurement is

$$\begin{aligned} F_{x,I}^{f_{mod}} = -2V_{mod}\Bigg\{\left[\frac{Q_{TM}+C_x(\delta V_1+\delta V_2+\delta V_3+\delta V_4)}{C_{tot}}-\frac{\delta V_3+\delta V_4}{2}\right]\left|\frac{\partial C_x}{\partial x}\right|+ \\ +\frac{\delta V_3+\delta V_4}{2}\left|\frac{\partial C_{x,h}}{\partial x}\right|\Bigg\}+ \\ +V_{mod}\left[\frac{4(\delta V_1-\delta V_2+\delta V_3-\delta V_4)}{C_{tot}}\left|\frac{\partial C_x}{\partial x}\right|^2+\right. \\ \left.+(\delta V_4-\delta V_3)\left(\left|\frac{\partial^2 C_x}{\partial x^2}\right|-\left|\frac{\partial^2 C_{x,h}}{\partial x^2}\right|\right)\right](x-x_0)+ \\ +\mathcal{O}\left[(x-x_0)^2\right] \end{aligned} \tag{5.62}$$

we notice that the term depending on the x-coordinate is

$$\begin{aligned} F_{x,I}^{f_{mod}}(x) = V_{mod}\left[\frac{4(\delta V_1-\delta V_2+\delta V_3-\delta V_4)}{C_{tot}}\left|\frac{\partial C_x}{\partial x}\right|^2+\right. \\ \left.+(\delta V_4-\delta V_3)\left(\left|\frac{\partial^2 C_x}{\partial x^2}\right|-\left|\frac{\partial^2 C_{x,h}}{\partial x^2}\right|\right)\right](x-x_0)+\mathcal{O}\left[(x-x_0)^2\right] \end{aligned} \tag{5.63}$$

As $\frac{1}{C_{tot}}\left|\frac{\partial C_x}{\partial x}\right|^2 \ll \left|\frac{\partial^2 C_x}{\partial x^2}\right|-\left|\frac{\partial^2 C_{x,h}}{\partial x^2}\right|$ and assuming that all stray biases δV_i are the same order of magnitude, we can approximate the previous expression as

$$F_{x,I}^{f_{mod}}(x) \simeq V_{mod}(\delta V_4-\delta V_3)\left(\left|\frac{\partial^2 C_x}{\partial x^2}\right|-\left|\frac{\partial^2 C_{x,h}}{\partial x^2}\right|\right)(x-x_0) \tag{5.64}$$

Hence from equation (2.93), that converts a force into a measure of the TM potential, we have

$$\begin{aligned} \frac{\mathrm{d}V_{TM}}{\mathrm{d}x} &= -\frac{1}{N_{el}V_{mod}\left|\frac{\partial C_x}{\partial x}\right|}\frac{\mathrm{d}F_{x,I}^{f_{mod}}}{\mathrm{d}x} \\ &\simeq -\frac{\delta V_4-\delta V_3}{N_{el}\left|\frac{\partial C_x}{\partial x}\right|}\left(\left|\frac{\partial^2 C_x}{\partial x^2}\right|-\left|\frac{\partial^2 C_{x,h}}{\partial x^2}\right|\right) \end{aligned} \tag{5.65}$$

From the measured $\mathrm{d}V_{TM}/\mathrm{d}x$, we estimate

$$\delta V_4-\delta V_3 = (11.7 \pm 0.6)\,\mathrm{mV} \tag{5.66}$$

The value found is consistent from what we would have expected from the Δ_x measurement with the charge-burst technique (see Section 2.4.2).

Dependence of the equilibrium voltage on the TM position

We subsequently investigated the dependence of the equilibrium voltage of the illumination pattern on the TM x-position. The data are displayed in Figure 5.11. The

TABLE 5.3: Coupling coefficients between measured charge or equilibrium potential during illumination and TM x position.

Illumination	Rotation method	Value	Units
None	Motors	-4.22 ± 0.17	V/m
None	Manual	-2.99 ± 0.15	V/m
TM	Motors	$+93.7 \pm 0.9$	V/m
EH	Motors	-11.3 ± 1.1	V/m

data were acquired keeping the same illumination pattern and by changing the pendulum x-coordinate by rotating the round platform with the motors under the sensor (the same considerations as before for the temperature fluctuations apply also in this case). We found a strong correlation between the x-position and the equilibrium voltage, especially in the case of TM illuminations.

This effect can be explained from the fact that, depending on the TM position, the photon are absorbed and reflected in different locations inside the GRS. This causes a variation of the photon absorption ratios between EH and TM, and in turn of the photo-currents, with respect to the case of a centered TM. This explanation is further supported by the fact that we observe a stronger variation of the equilibrium voltage when we illuminate the TM. Indeed displacements of the test mass produce a more significant effects on the photocurrents when a larger fraction photons are absorbed by the TM. On the other hand, when we illuminate the EH, the relative position of EH and ISUK does not change for variations of the test mass position. In this case the displacement of the TM affects only the absorption location of the reflected photons. We recommend to perform some dedicated simulations with numerical tools, e.g. GEANT4, to check quantitatively the soundness of such observations.

In the 4TM torsion pendulum we cannot avoid a secular drift in the TM position inside the GRS because of the unwinding of the tungsten fiber suspending the pendulum[15]. As the unwinding speed is thought to depend on the temperature, a better thermal stability could help in regularizing this effect.

A dependence of the equilibrium voltage also on the other coordinates of the torsion pendulum is not to be excluded, but both y and z do not suffer of a low frequency drift as much as x for the unwinding. We see only a variation of the y coordinate with temperature due to a thermal expansion of the pendulum neck[16]. However, the main reason that lead us to focus only on x is the fact that we do not have (for now) any measurement correlating cleanly the equilibrium voltage with just variations of the y or z coordinates of the TM.

The model to convert the change of the equilibrium voltage from the variation of the x-coordinate is conceptually equivalent to the one described in the previous section regarding the *phase noise*, provided that one replaces the dependence on the phase of the illumination with the test mass x-position. Substituting ϕ with x into

[15]The 1TM torsion pendulum does not suffer of this problem because it is suspended by a silica fiber.

[16]The "neck" is the elongated upper section of the vacuum chamber of the torsion pendulum that contains the suspending fiber. In order to keep the temperature stable around the torsion pendulum we have a thermal chamber which isolates it from the lab and an active temperature control device (JULABO heating/cooling refrigerator).

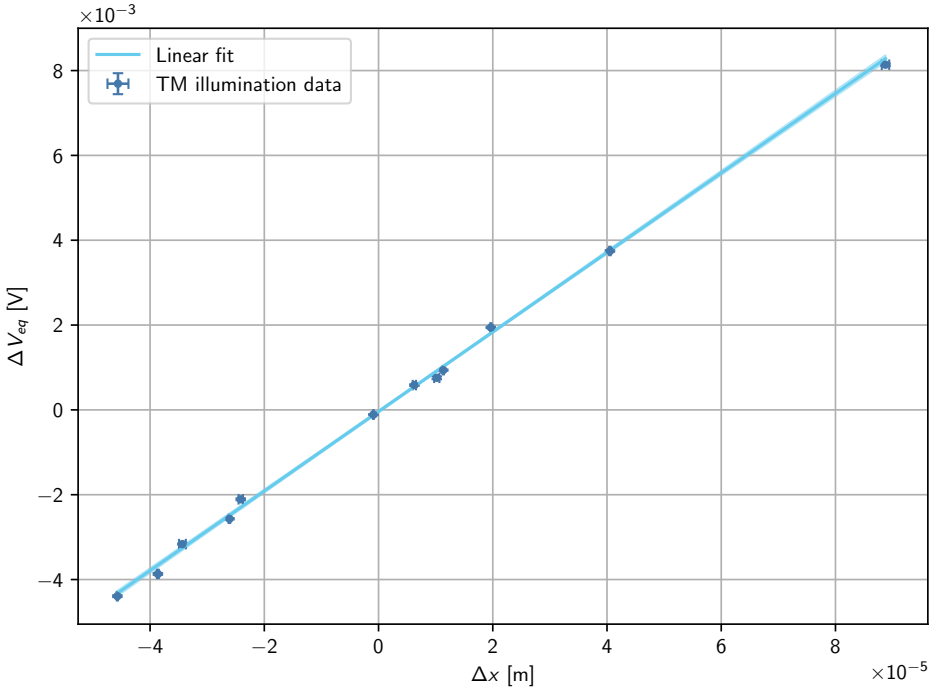

(A) TM illumination

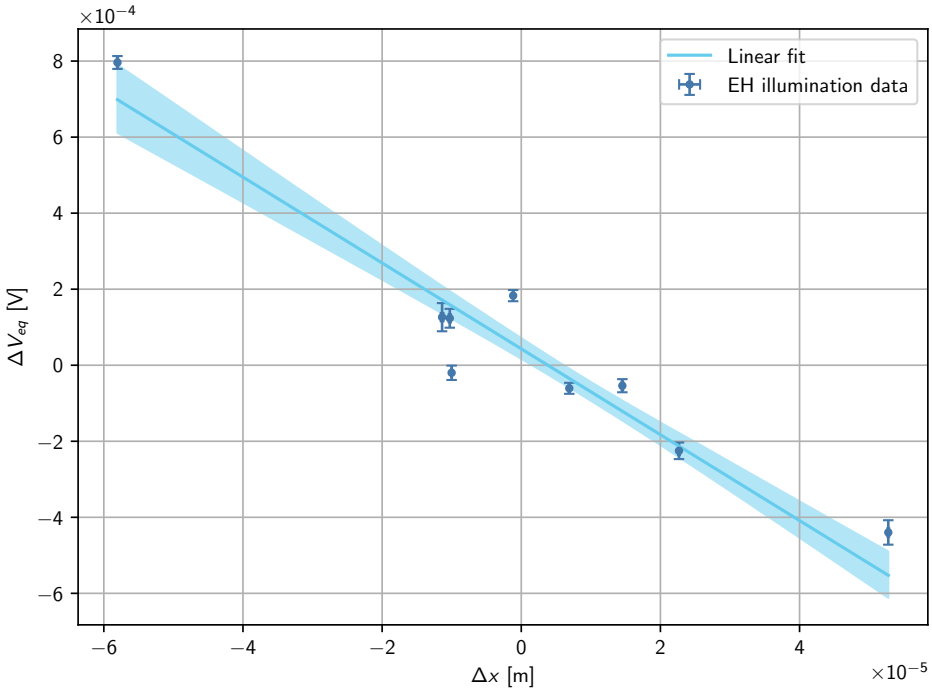

(B) EH illumination

FIGURE 5.11: Dependence of the TM equilibrium potential on the x position for the case of TM and EH illuminations. The band around the fits corresponds to 1σ-confidence.

equation (5.50), we have

$$S_{V_{TM}}^{V_{eq}^{UV}}(\omega) = \frac{\left(\frac{\mathrm{d}V_{eq}^{UV}}{\mathrm{d}x}\right)^2}{1+\omega^2\tau_{UV}^2} S_x(\omega) \tag{5.67}$$

As the time-series of the x-coordinate during the continuous discharge measurement is available, we can try to subtract such effect. A simple method to achieve that is explained hereafter.

Subtraction The data suggest a linear dependence of the TM potential for both TM and EH illuminations, we can try to subtract this effect from the data. Using the observed linear dependence $V_{eq}^{UV} = \beta_1 x + \beta_0$, we can modify equation (5.30) as

$$\begin{aligned} \frac{\mathrm{d}V_{TM}}{\mathrm{d}t} &= -\frac{V_{TM} - V_{eq}^{UV}(x)}{\tau_{UV}} + \frac{i_{shot}}{C_{tot}} \\ &= -\frac{V_{TM} - [\beta_1 x(t) + \beta_0]}{\tau_{UV}} + \frac{i_{shot}}{C_{tot}} \\ &= -\frac{V_{TM}}{\tau_{UV}} + \frac{\beta_1}{\tau_{UV}} x(t) + \frac{\beta_0}{\tau_{UV}} + \frac{i_{shot}}{C_{tot}}, \end{aligned} \tag{5.68}$$

The subtraction can be obtained by least-squares fitting[17] the $x(t)$ time-series plus a constant to the time-series of the discrete derivative[18] of the TM potential $\frac{\mathrm{d}V_{TM}(t)}{\mathrm{d}t}$. The residual time-series after subtraction is

$$\frac{\mathrm{d}V_{TM}^{res}}{\mathrm{d}t} = \frac{\mathrm{d}V_{TM}}{\mathrm{d}t} - \frac{\beta_1}{\tau_{UV}} x(t) - \frac{\beta_0}{\tau_{UV}} \tag{5.69}$$

At this point the time-series of the test mass potential can be reconstructed by numerical integration

$$V_{TM}^{res}(t) = V_{TM}(t=0) + \int_0^t \frac{\mathrm{d}V_{TM}^{res}}{\mathrm{d}t'}\,\mathrm{d}t' \tag{5.70}$$

The subtraction method just presented could be extended immediately to the y- and z-coordinates as well.

We tried also the subtraction method presented in [75]. We preferred the simple least-squares fitting described before because it produces charge time series which are visually more sounded.

Comment for LISA The investigations of the dependence of the charge measurement and of the equilibrium voltages on the x-position of the TM were triggered from the fact that in the 4TM-torsion pendulum there is an unavoidable low-frequency unwinding of the suspending tungsten fiber.

In LISA we may expect that the TM position inside the GRS will be remarkably stable, but still there are some occasions in which a significant test mass motion is possible. One clear example could be the repetition in LISA of the LPF *free-fall experiment* [76], where all actuation voltages on the LPF test masses were set to zero.

[17] As the time derivative of the TM charge have a reasonably white spectrum, it is not terribly wrong to do a least-squares fit in the time domain to attempt a subtraction of this effect.

[18] Obtained with the method of second order accurate central differences.

We must notice that in LISA the control systems keep constant the distance from the TM and the optical bench. Therefore, eventual mechanical relaxations and thermal effect may lead to a change of the test mass position with respect to the GRS (including the ISUKs).

We define the distance along the x-axis of the TM with respect to the optical bench (OB) as $X^{OB}_{TM} = x_{TM} - x_{OB}$ and the distance of the GRS with respect to the optical bench as $X^{OB}_{GRS} = x_{GRS} - x_{OB}$. The noise on such distances has completely different origin: the former is related to imperfections in the performance of the DFACS, the latter to deformations in the MOSA due to thermo-mechanical stress. The LISA performance model [12] states that the current best estimates for the power spectral density of such quantities is

$$S_{X^{OB}_{TM}}(f) = \left(0.95\,\mathrm{nm}/\sqrt{\mathrm{Hz}}\right)^2 \left[1 + \left(\frac{0.2\,\mathrm{mHz}}{f}\right)^2\right] \frac{1 + \left(\frac{f}{0.2\,\mathrm{mHz}}\right)^4}{1 + \left(\frac{f}{8\sqrt{10}\,\mathrm{mHz}}\right)^4} \tag{5.71}$$

and

$$S_{X^{OB}_{GRS}}(f) = \left(0.3\,\mathrm{nm}/\sqrt{\mathrm{Hz}}\right)^2 \left[1 + \left(\frac{1.5\,\mathrm{mHz}}{f}\right)^2\right] \tag{5.72}$$

As the position of the TM with respect to the GRS is given by

$$x = x_{TM} - x_{GRS} = X^{OB}_{TM} - X^{OB}_{GRS}, \tag{5.73}$$

we have that

$$\begin{aligned} S^{LISA}_x &= S_{X^{OB}_{TM}} + S_{X^{OB}_{GRS}} - 2\Re\left[S_{X^{OB}_{TM} X^{OB}_{GRS}}\right] \\ &\leq S_{X^{OB}_{TM}} + S_{X^{OB}_{GRS}} + 2\sqrt{S_{X^{OB}_{TM}} \cdot S_{X^{OB}_{GRS}}} \end{aligned} \tag{5.74}$$

where $\Re\left[S_{X^{OB}_{TM} X^{OB}_{GRS}}\right]$ is the real part of the cross-covariance. The upper limit is true in the unlikely case that the two displacements are fully anti-correlated. From (5.67), we have that

$$S^{LISA}_{V_{TM}}(\omega) = \frac{\left(\frac{\mathrm{d}V^{ill}_{eq}}{\mathrm{d}x}\right)^2}{1 + \omega^2\tau^2_{UV}} S^{LISA}_x(\omega) \leq \left(\frac{\mathrm{d}V^{ill}_{eq}}{\mathrm{d}x}\right)^2 S^{LISA}_x(\omega) \tag{5.75}$$

where we considered the limit of a very strong discharge, i.e. $\tau_{UV} \to 0$. If we convert the test mass voltage noise of equation (5.75) into an acceleration noise due to the presence of an uncompensated DC bias $\Delta_x = 5\,\mathrm{mV}$ using (3.13), we have, as shown in Figure 5.12, a ridiculously small contribution, even in the triple worst case scenario of very fast discharge, TM illumination, and fully-correlated stray displacements.

5.2.3 Experimental data

We present in this section the continuous discharge data we acquired with the 4TM torsion pendulum.

The charge measurements have been performed with the method described in Section 2.3, that is by modulating only the x^+_2 and x^-_2 electrodes with sine voltages of opposite phase at a frequency of $f_{mod} = 2\,\mathrm{mHz}$ and amplitude 5 V. We decided to modulate only the $x^\pm_2$ electrodes because they are far from the point where the ISUKs inject the light into the GRS (only a minor fraction of the light is absorbed

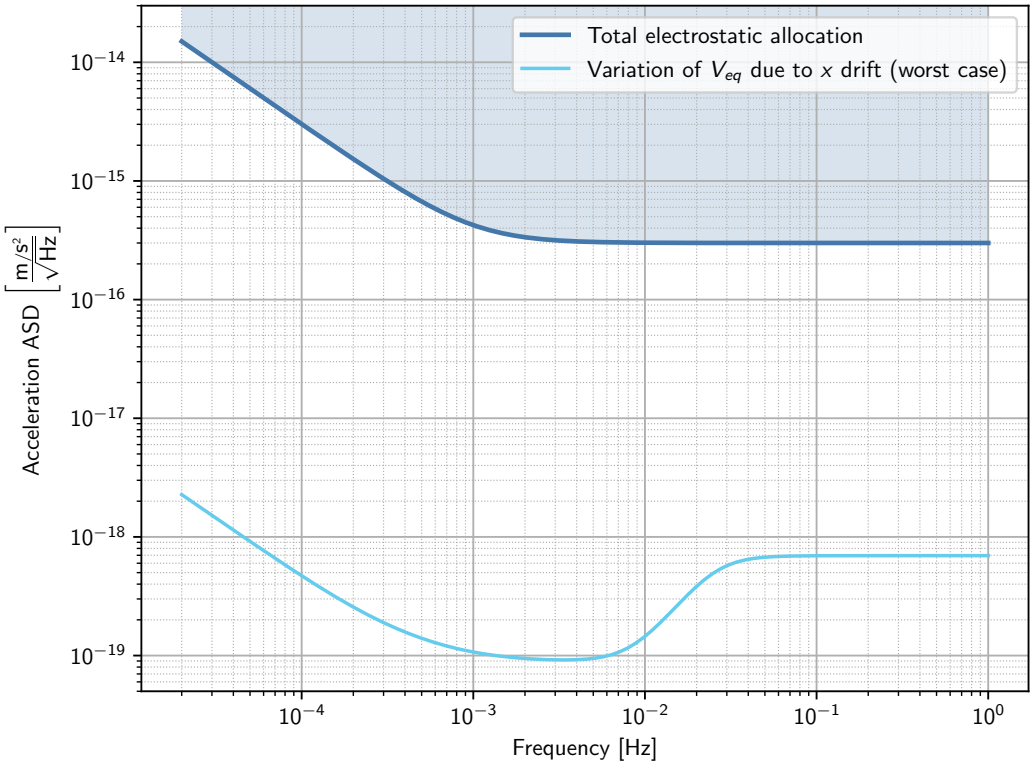

FIGURE 5.12: Worst case estimate for the acceleration noise due to a change in the equilibrium voltage induced by a fluctuation of the x position of the TM inside the GRS for LISA. We considered $\Delta_x = 5\,\mathrm{mV}$ and $\frac{\mathrm{d}V_{eq}^{ill}}{\mathrm{d}x} \simeq 94\,\mathrm{V\,m^{-1}}$ as measured for TM illuminations.

Table 5.4: Experimental settings for the continuous discharge measurement in the case of EH illumination.

Start day	Length [days]	Delay ill. [µs]	Duration ill. [µs]	Decimation [kHz]	τ_{UV} [s]	P_{UV} [nW]
2022-04-15	4.8	4.785	5.425	10.00	6920 ± 30	1.8 ± 0.2
2022-04-24	4.8	4.785	5.425	0.50	95 000 ± 3000	0.089 ± 0.008
2022-04-29	4.6	4.785	5.425	3.03	20 940 ± 40	0.56 ± 0.08
2022-05-12	3.4	4.785	5.425	50.00	1481 ± 3	7.8 ± 0.5
2022-11-09	5.8	4.785	5.425	0.20	210 700 ± 200	0.0408 ± 0.0013
2022-05-20	4.9	5.235	1.000	50.00	6951 ± 13	1.72 ± 0.07

Table 5.5: Experimental settings for the continuous discharge measurement in the case of TM illumination.

Start day	Length [days]	Delay ill. [µs]	Duration ill. [µs]	Decimation [kHz]	τ_{UV} [s]	P_{UV} [nW]
2021-12-24	5.7	1.510	1.925	9.09	5510 ± 50	0.73 ± 0.05
2021-12-30	5.6	1.510	1.925	50.00	1109 ± 9	4.6 ± 0.4
2022-01-14	4.6	1.510	1.925	100.00	583.3 ± 1.6	8.9 ± 1.2
2022-01-21	5.6	1.535	1.875	100.00	600 ± 100	8.1 ± 0.7
2022-02-11	4.5	1.510	1.950	100.00	458.2 ± 1.1	7.6 ± 0.9
2022-10-31	6.6	1.510	1.925	1.00	28 900 ± 400	0.081 ± 0.003

in the region where they are located). Moreover, we took care of placing the torsion pendulum reasonably close to the zero force position x_0 for all measurements (where the $2f_{mod}$ component of the force vanishes).

In Tables 5.4 and 5.5, we present the value of the experimental parameters chosen for the continuous discharge measurements.

The charge time-series before and after the subtraction proposed in Section 5.2.2 are visually presented in Figures 5.13 and 5.14 for EH and TM illuminations, respectively. The residual time series after the subtraction make sense: we observe in the initial part an exponential decay that settles around an equilibrium voltage. On the other hand, the raw time-series show a low-frequency drift of the equilibrium voltage.

In Figures 5.15 and 5.16, we plot the expected contributions of the spurious noise sources described in Section 5.2.2.

We remember that the phase noise has been obtained with a dedicated lock-in measurement and they are not simultaneous with the continuous discharge data. Moreover, as anticipated before, the phase data may be subjected to additional noise sources, among which we list readout noise of PMT, lock-in, or ADC and the temperature dependence of the whole measurement chain (the thermal control in the laboratory hall was not particularly stable during the experimental campaign). The overall contribution of such noise sources is expected to be limited, apart from maybe the temperature fluctuations that may contribute at low-frequencies. Anyhow the projected phase noise is be intended as reasonable upper limit.

The last measurement in the set of EH illuminations (Figure 5.15f) has different settings from the others: we reduced the duration of the illumination to 1 µs and set a delay of 5.235 µs (including systematic delay). This placed the illumination close to the zero crossing of the injection voltage, causing the sensitivity to the phase noise to be much higher than the other measurement where we illuminated centered on the maxima or minima of the injection bias (see Figure 5.6). Indeed the projected phase noise for this measurement is much higher than the other measurements.

The PSD of the TM potential timeseries have been obtained with the Welch method with Blackman-Harris windows and 50% overlap. The number of averages is always three. The bands around the spectra correspond to 1σ-confidence. The points with error-bars are Bayesian estimates of the ASD at independent frequencies computed as described in [74].

The noise floor has been estimated converting the torsion pendulum force ASD at the modulation frequency into an equivalent test mass voltage ASD. It may be a slightly optimistic, i.e. underestimated, limit for the instrumental sensitivity to TM voltage variations.

The spectra can be compared to the model given by (5.35) and the subsequent equations. The numerical values for τ_{UV} have been obtained by a direct measurement right after the each continuous discharge measurement (as explained previously) and for $\mathcal{Y}^{+}_{sat}$ and $\mathcal{Y}^{-}_{sat}$ have been obtained by dedicated apparent yield measurements with same illumination pattern as the continuous discharge measurements[19] and performed in close temporal proximity of the continuous discharge campaign (mid-2022), to avoid systematic errors due to the measured change in the apparent yield with time (see Section 3.4.2).

We observe that not only the EH illuminations produce a shot noise which is generally higher than the TM illuminations, they also are less sensitive to the change

[19] In this way we can estimate directly the numerical parameters relevant for the estimation of the continuous discharge independently from the UV power calibration. There are two possible approaches: relate the apparent yield at saturation with the system response time though the (5.44), or consider an apparent yield normalized by the uncalibrated signal of the PMT or the photodiode.

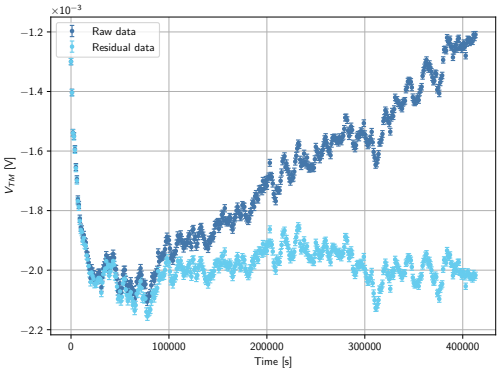

(A) UV power $1.8 \pm 0.2\,\mathrm{nW}$

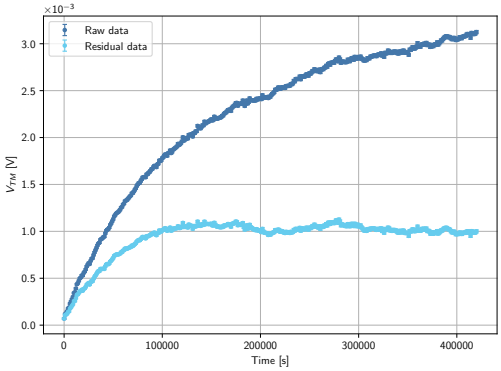

(B) UV power $(8.9 \pm 0.8) \cdot 10^{-2}\,\mathrm{nW}$

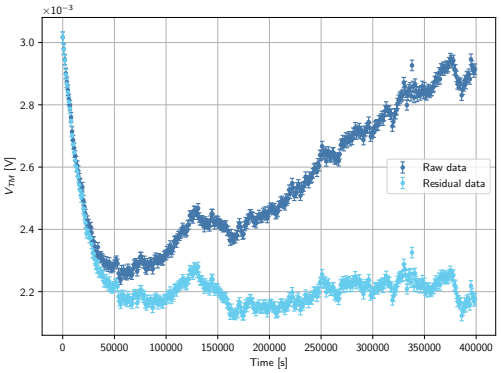

(C) UV power $0.56 \pm 0.08\,\mathrm{nW}$

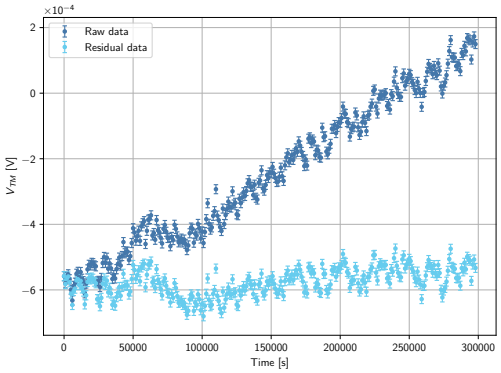

(D) UV power $7.8 \pm 0.5\,\mathrm{nW}$

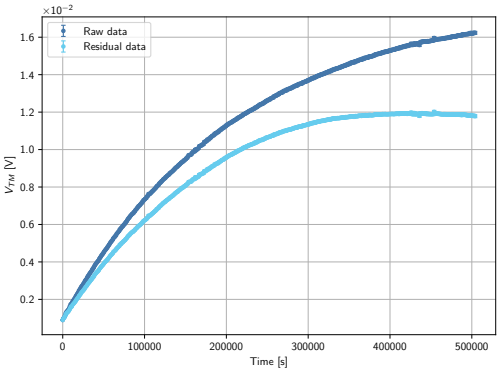

(E) UV power $(4.08 \pm 0.13) \cdot 10^{-2}\,\mathrm{nW}$

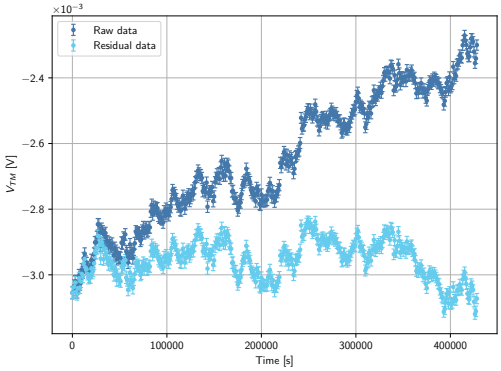

(F) UV power $1.72 \pm 0.07\,\mathrm{nW}$

FIGURE 5.13: Continuous discharge timeseries for EH illumination before and after the subtraction of the change in the equilibrium voltage due to a drift in the pendulum x position. The visual behavior of the residual time series is the one expected: in the first part we see (possibly) an exponential decay that settles around a constant equilibrium voltage.

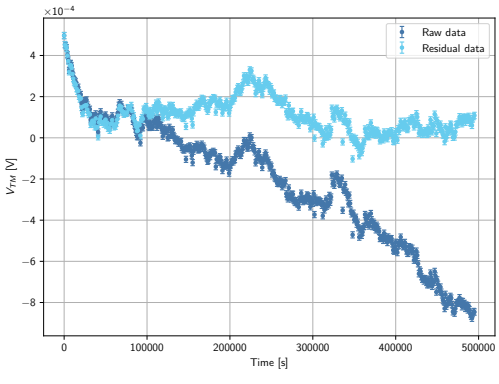

(A) UV power $0.73 \pm 0.05\,\mathrm{nW}$

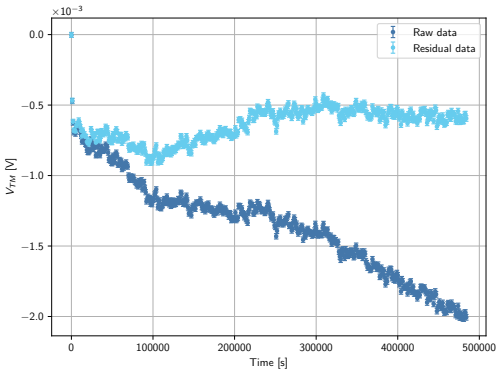

(B) UV power $4.6 \pm 0.4\,\mathrm{nW}$

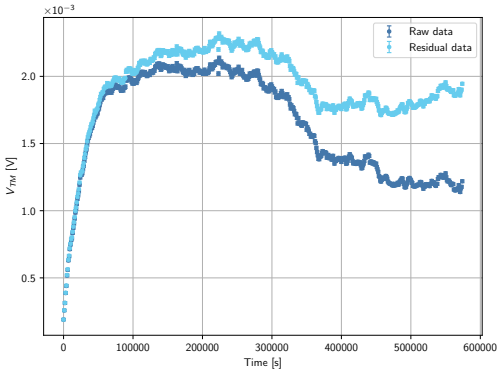

(C) UV power $(8.1 \pm 0.3) \cdot 10^{-2}\,\mathrm{nW}$

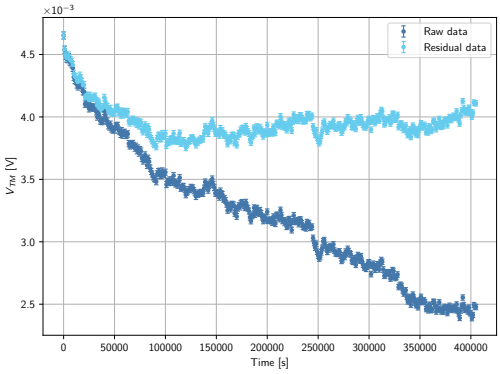

(D) UV power $8.9 \pm 1.2\,\mathrm{nW}$

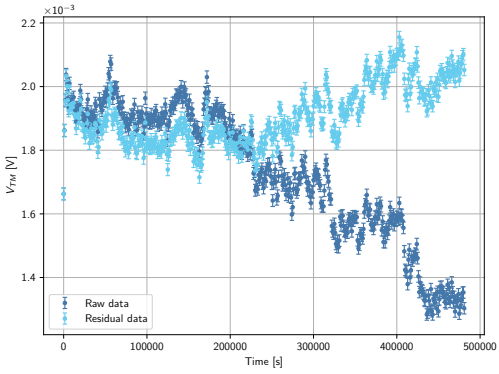

(E) UV power $8.1 \pm 0.7\,\mathrm{nW}$

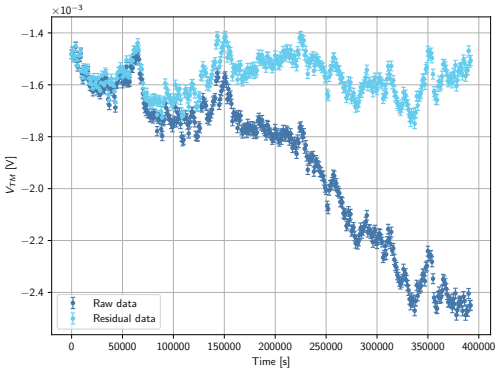

(F) UV power $7.6 \pm 0.9\,\mathrm{nW}$

FIGURE 5.14: Continuous discharge timeseries for TM illumination before and after the subtraction of the change in the equilibrium voltage due to a drift in the pendulum x position. The visual behavior of the residual time series is the one expected: in the first part we see (possibly) an exponential decay that settles around a constant equilibrium voltage.

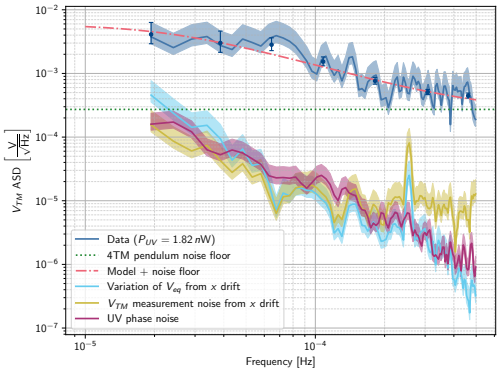

(A) UV power 1.8 ± 0.2 nW

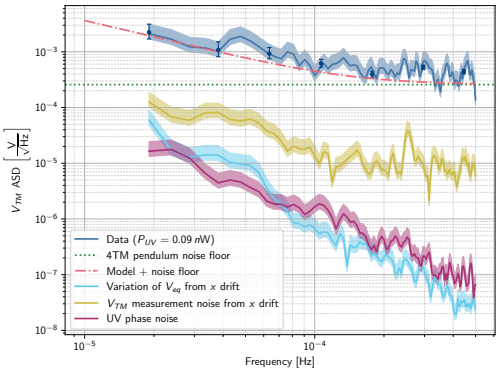

(B) UV power $(8.9 \pm 0.8) \cdot 10^{-2}$ nW

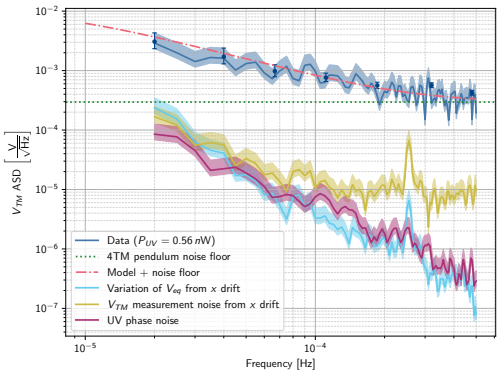

(C) UV power 0.56 ± 0.08 nW

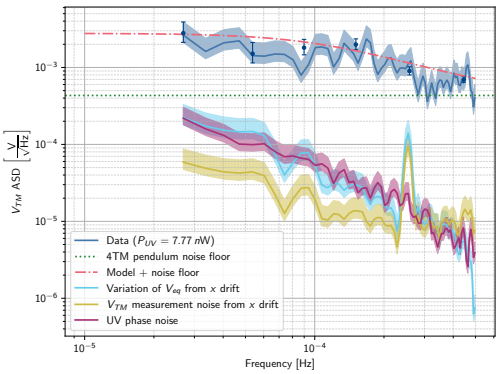

(D) UV power 7.8 ± 0.5 nW

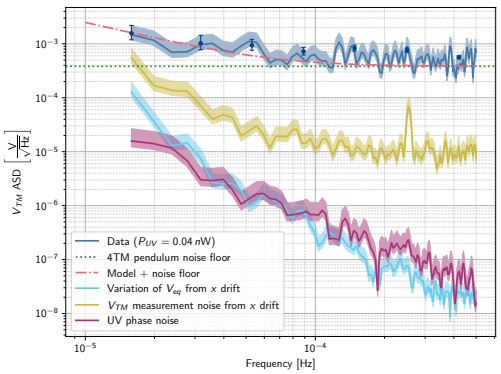

(E) UV power $(4.08 \pm 0.13) \cdot 10^{-2}$ nW

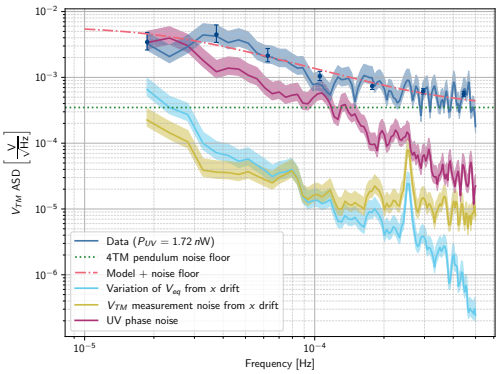

(F) UV power 1.72 ± 0.07 nW

FIGURE 5.15: Amplitude spectral density of the continuous discharge timeseries for EH illumination with projected contributions of the noise sources described in Section 5.2.2.

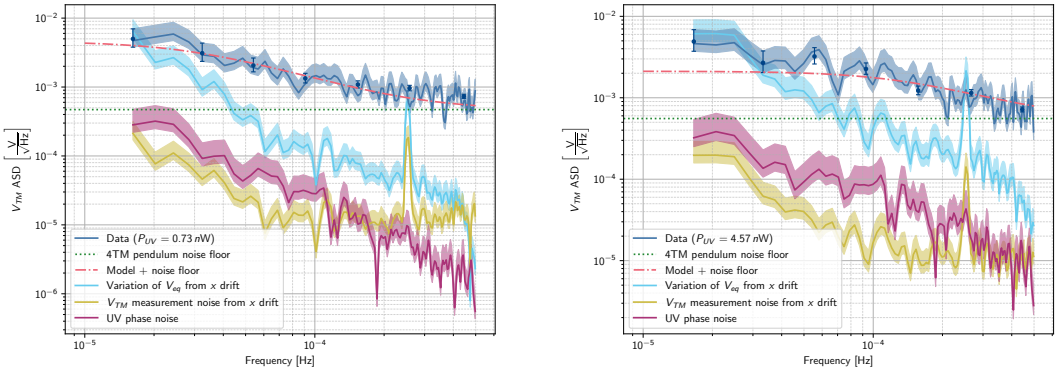

(A) UV power $0.73 \pm 0.05\,\mathrm{nW}$

(B) UV power $4.6 \pm 0.4\,\mathrm{nW}$

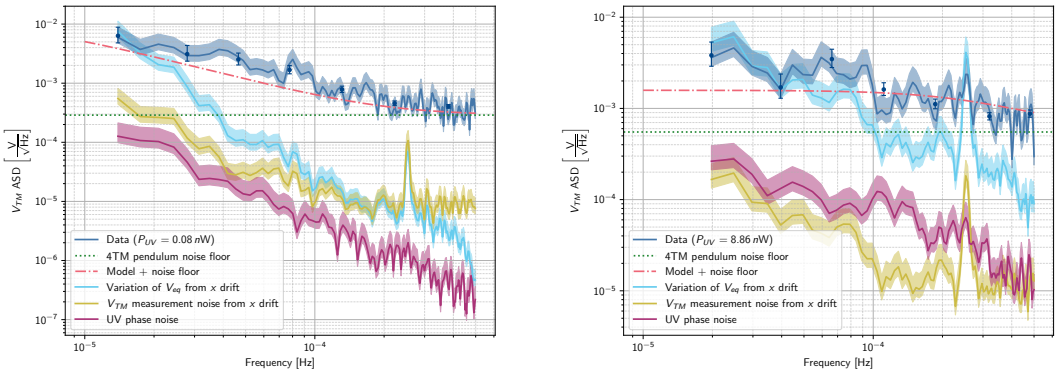

(C) UV power $(8.1 \pm 0.3) \cdot 10^{-2}\,\mathrm{nW}$

(D) UV power $8.9 \pm 1.2\,\mathrm{nW}$

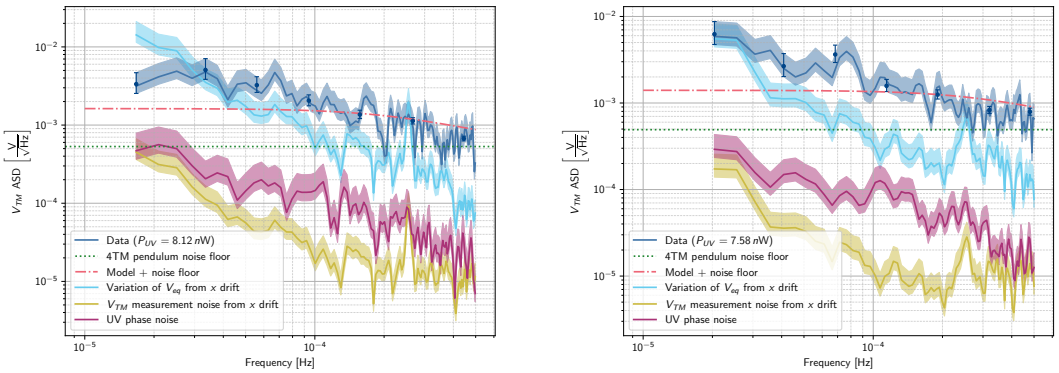

(E) UV power $8.1 \pm 0.7\,\mathrm{nW}$

(F) UV power $7.6 \pm 0.9\,\mathrm{nW}$

FIGURE 5.16: Amplitude spectral density of the continuous discharge timeseries for TM illumination with projected contributions of the noise sources described in Section 5.2.2. Do not worry if the noise due to a change in the equilibrium potential due to a drift of the x-coordinate (*cyan*) may be above the total charge noise, because we subtracted it with the method proposed in the Section 5.2.2.

in the equilibrium voltage due to the low-frequency drift of the x-coordinate. Overall the noise level measured in the case of EH illuminations closely matches the one we expect. On the other hand, TM illuminations seem to be spoiled by an excess noise above the model that we cannot subtract entirely.

Fit of the data

We can try and fit the continuous discharge spectra with the model (5.35) plus a positive constant c to take into account the noise floor of the torsion pendulum

$$\begin{aligned} S^{fit}_{V_{TM}}(\omega;\tau_{UV},\lambda_{eff},c) &= S^{shot}_{V_{TM}}(\omega;\tau_{UV},\lambda_{eff}) + c \\ &= \frac{2e^2\lambda_{eff}}{C^2_{tot}\left(\omega^2+\frac{1}{\tau^2_{UV}}\right)} + c \end{aligned} \tag{5.76}$$

The fit parameters are

- The characteristic time of the illumination τ_{UV};
- The effective charging rate λ_{eff} of the illumination;
- The constant c, that models the instrumental noise floor.

The statistics of the power spectral density tells us that the ratio of the experimental PSD and the true PSD at each frequency is distributed (up to a multiplicative constant) as a chi-squared distribution with number of degrees of freedom equal to two times the number of averaged periodograms N_{avr} used for the spectral estimation (see, for example, the book by M. B. Priestley [77], also known as the bible of spectral estimation). In a formula the previous property translates to

$$q_k = \frac{2N_{avr}\cdot\langle\mathcal{S}_{exp}[k]\rangle}{S^{fit}_{V_{TM}}(\omega_k;\tau_{UV},\lambda_{eff},c)} \sim \chi^2\left(2N_{avr}\right) \tag{5.77}$$

where $S^{fit}_{V_{TM}V_{TM}}$ is our theoretical model for the true PSD, and $\langle\mathcal{S}_{exp}[k]\rangle$ is the experimental PSD from our data at the angular frequency ω_k obtained averaging N_{avr} periodograms. The spectral data $\langle\mathcal{S}_{exp}[k]\rangle$ considered for the fits are the independent Bayesian estimates (i.e. the darker points with error-bar in Figure 5.15 and 5.16). We notice that the numerical recipe [74] followed to estimate the PSD dictates that the number of averaged periodograms increases with the frequency, hence $N_{avr} = N_{avr}[k]$.

From the considerations above, we understand that the log-likelihood of the chi-squared distribution is the correct choice for the fit

$$\begin{aligned} \mathcal{LL}(q_k) = \sum_{k=1,2,\dots}\Bigg\{ &\frac{N_{avr}[k]-2}{2}\log(q_k) - \\ &-\frac{N_{avr}[k]}{2}\log(2) - \log\Gamma\left(\frac{N_{avr}[k]}{2}\right) - \frac{q_k}{2}\Bigg\} \end{aligned} \tag{5.78}$$

where $q_k = q_k(\tau_{UV},\lambda_{eff},c)$ is the quantity defined in (5.77) and $\log\Gamma(\cdot)$ is the logarithm of the Gamma function.

We obtained a Bayesian estimate of the fit parameters by sampling the log-likelihood with the NUTS Hamiltonian Monte Carlo sampler [69] implemented in the PyMC probabilistic programming library for Python [70]. The priors for the fit parameters are

TABLE 5.6: Values of the parameters $\ln(A)$ and B obtained from a linear fit in the log-log space of the data $(\tau_{UV}, \lambda_{eff})$ obtained from continuous discharge measurement sets in the case of EH or TM illumination.

Illumination	$\ln(A)$	B
EH	$+18.1 \pm 0.5$	-0.90 ± 0.06
TM	$+18.4 \pm 1.0$	-0.92 ± 0.14

- For the characteristic time τ_{UV} we used a Gaussian prior with mean and standard deviation equal to the values measured for the specific continuous discharge timeseries under consideration;
- For the pendulum noise floor c we considered an exponential prior with mean equal to the pendulum noise floor for that specific measurement;
- For the effective rate λ_{eff} we opted for a weakly-informative Gaussian prior (i.e. standard deviation $\sim$ mean) centered on the theoretical value from (5.41), but with a large standard deviation to account for the fact that the experimental data may be more noisy than what we may expect from the model.

A comparison between experimental data and fits is presented in Figure 5.17 for EH illuminations and in Figure 5.18 for TM illuminations.

Once the optimal parameters have been obtained from the fit of each measurement, it is interesting to plot the effective rate λ_{eff} as a function of the system response time τ_{UV}, as shown in Figure 5.19. In this way, we can see how the parameters that characterize the continuous discharge noise relate to one another. The expected functional dependence of λ_{eff} on τ_{UV} was derived in (5.44), hence we opted to fit the data with a power-law functional dependence

$$\lambda_{eff}(\tau_{UV}) = A \cdot (\tau_{UV})^B \tag{5.79}$$

We notice that the parameter A depends on the illumination pattern chosen, whereas B is always expected to be -1 if the model developed in Section 5.1.2 is correct.

A linear fit on the logarithm of the data, leads to the results reported in Table 5.6. The fit results for the exponent B gives for both EH and TM illumination a value which is compatible within 2σ with the expected model $\lambda_{eff} \propto 1/\tau_{UV}$.

5.3 Conclusions

We measured experimentally the charge noise introduced by the continuous illumination of either the EH, or the TM.

The experimental data (especially for the set of EH illuminations) are in good agreement with the expectations: we measure charge noise levels that match nicely with the model predictions. We were also able to show that if we illuminate with low power we could achieve an effective UV charging rate below the current LISA requirement. This is remarkable for two reasons:

- The experimental setup of the 4TM torsion pendulum is representative in terms of geometry, readout electronics and CMS hardware, hence the results obtained can be promptly applied to LISA;

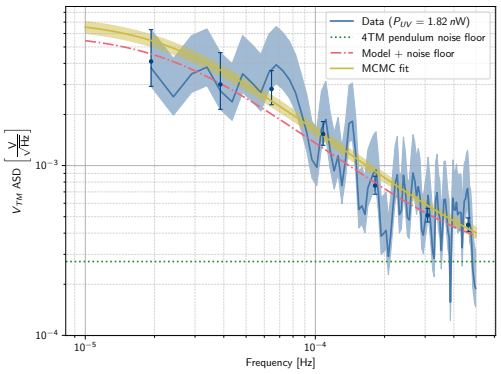

(A) UV power $1.8 \pm 0.2\,\mathrm{nW}$

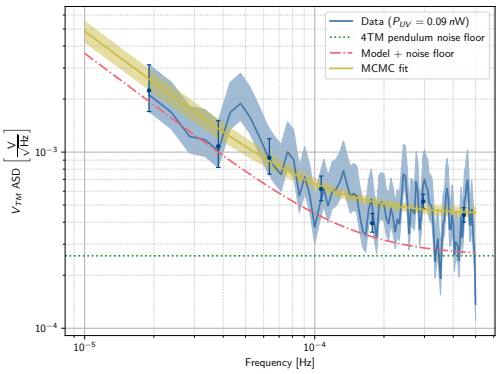

(B) UV power $(8.9 \pm 0.8) \cdot 10^{-2}\,\mathrm{nW}$

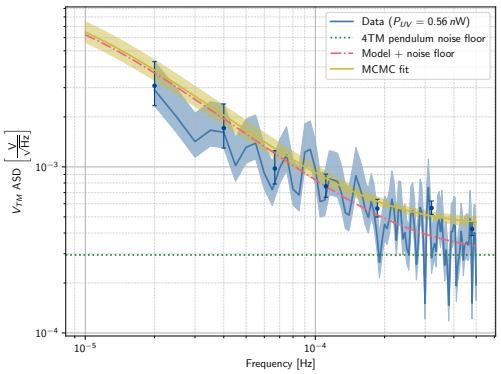

(C) UV power $0.56 \pm 0.08\,\mathrm{nW}$

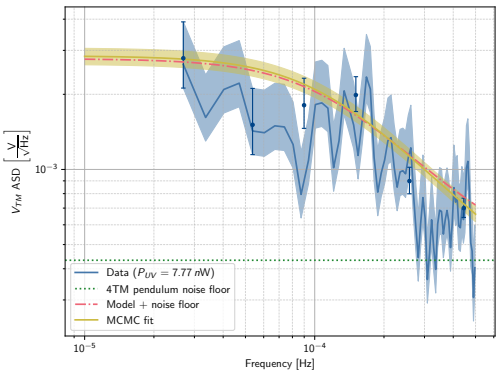

(D) UV power $7.8 \pm 0.5\,\mathrm{nW}$

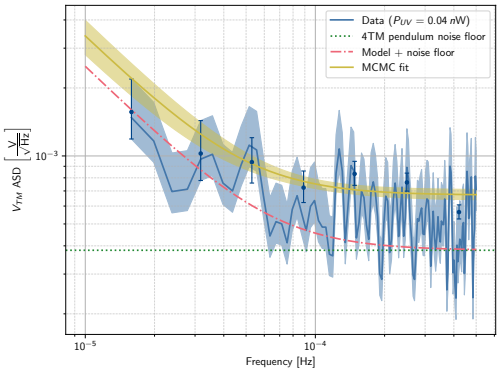

(E) UV power $(4.08 \pm 0.13) \cdot 10^{-2}\,\mathrm{nW}$

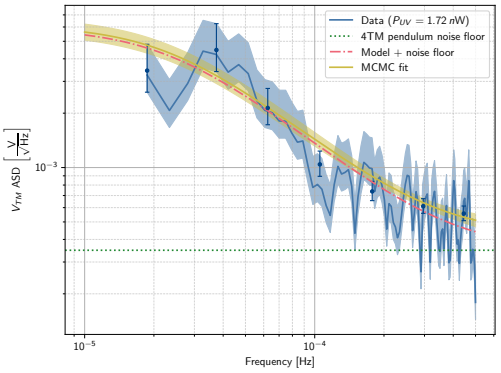

(F) UV power $1.72 \pm 0.07\,\mathrm{nW}$

FIGURE 5.17: Fit of the EH spectra with the correct statistics.

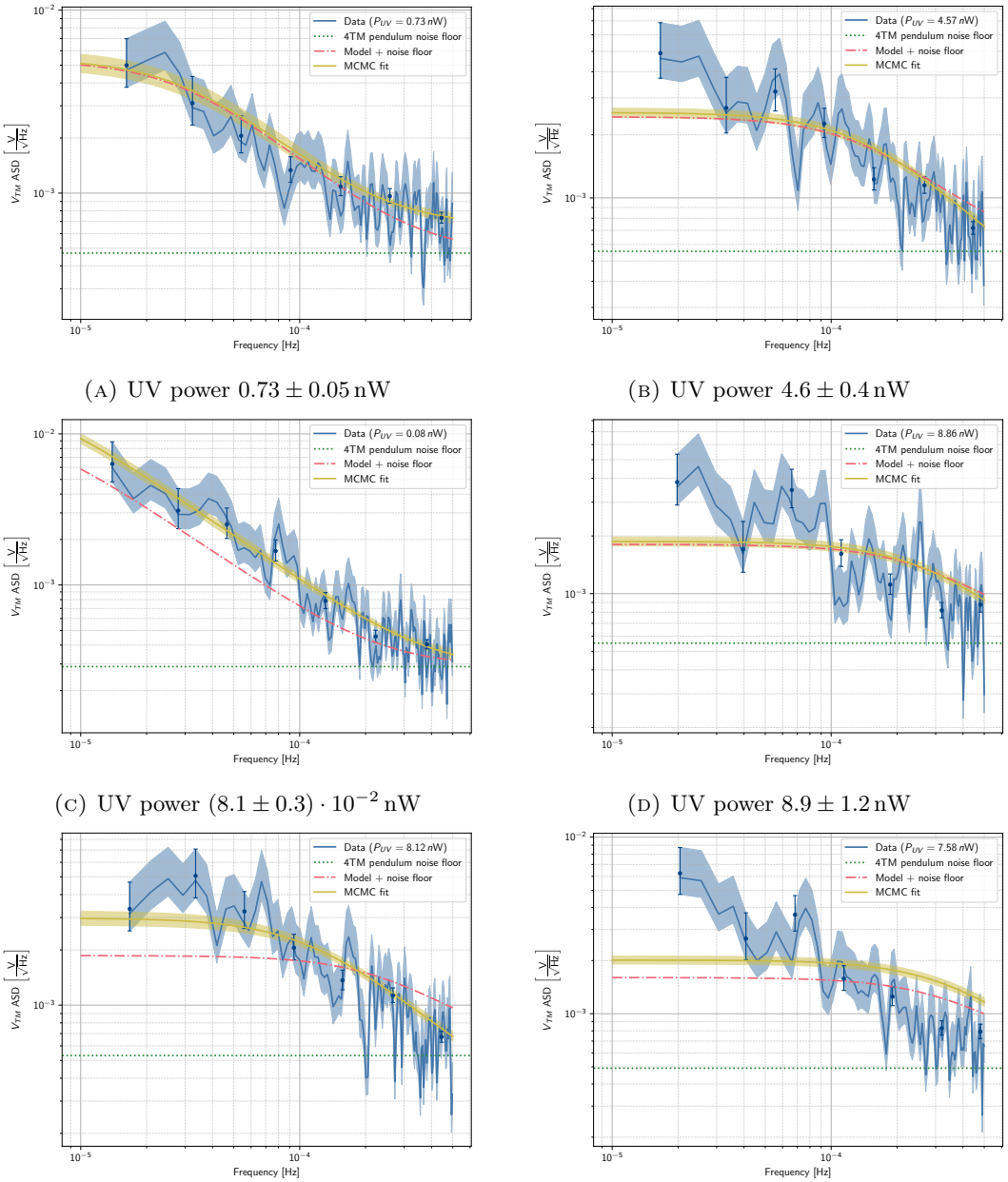

(A) UV power $0.73 \pm 0.05\,\mathrm{nW}$

(B) UV power $4.6 \pm 0.4\,\mathrm{nW}$

(C) UV power $(8.1 \pm 0.3) \cdot 10^{-2}\,\mathrm{nW}$

(D) UV power $8.9 \pm 1.2\,\mathrm{nW}$

(E) UV power $8.1 \pm 0.7\,\mathrm{nW}$

(F) UV power $7.6 \pm 0.9\,\mathrm{nW}$

FIGURE 5.18: Fit of the TM spectra with the correct statistics.

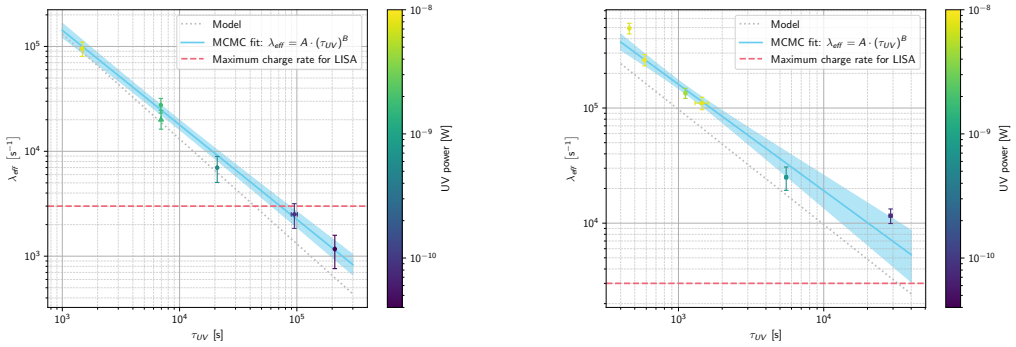

(A) EH illumination (B) TM illumination

FIGURE 5.19: Dependence of the fitted effective charging rate from the characteristic discharge time. The current requirement for the allocated maximum continuous discharge rate for LISA is 3000 elementary charges per second [72]. *Left:* results for EH illuminations. The data point with the triangular marker indicates the measurement with different illumination pattern and has been excluded form the fit. *Right:* results for TM illumination.

- The 4TM torsion pendulum has a lower sensitivity (i.e. more noise) with respect to LISA. Hence, if we proved that we can achieve on ground a continuous discharge of the TM with charge noise within the requirements, it will be, in principle, feasible also in space.

On the other hand, the TM illumination measurements often show excess noise with respect to the model. This is likely due to the fact that for the TM illumination we found a strong coupling between the TM x position and the equilibrium voltage. Although a subtraction method for this spurious effect is proposed, we were probably not able to remove it completely[20].

If we convert the measured charge timeseries for EH illumination at the lowest UV power into an acceleration timeseries, considering the main electrostatic noise sources[21] listed in Section 3.1.1, we have the result presented in Figure 5.20. The projected acceleration noise for LISA during continuous discharge is within the current requirement for the maximum acceleration noise due to electrostatic disturbances. We demonstrated that the continuous discharge procedure can be successfully employed to keep the TM charge under control in LISA without adding excessive acceleration noise.

At the conclusion of our experimental campaign, we need to remember that the equilibrium potential during the continuous discharge remains within the required $\pm 70\,\mathrm{mV}$ from neutrality [72] only if the emission properties of the GRS, the illumination pattern, and the environmental charging do not change dramatically over time. For instance, it is possible that the phase of the CMD light pulses may show a low-frequency drift with respect to the GRS injection bias, or that the quantum yield of either TM or EH diminish with time.

[20] As discussed before, for TM illuminations there may be a strong dependence of the equilibrium voltage not only on the x coordinate, but also on y and z.

[21] Except for the unmodeled extra continuous discharge noise allocation, because at the moment of writing, we have no evidence that there are further noise sources associated with the continuous discharge procedure.

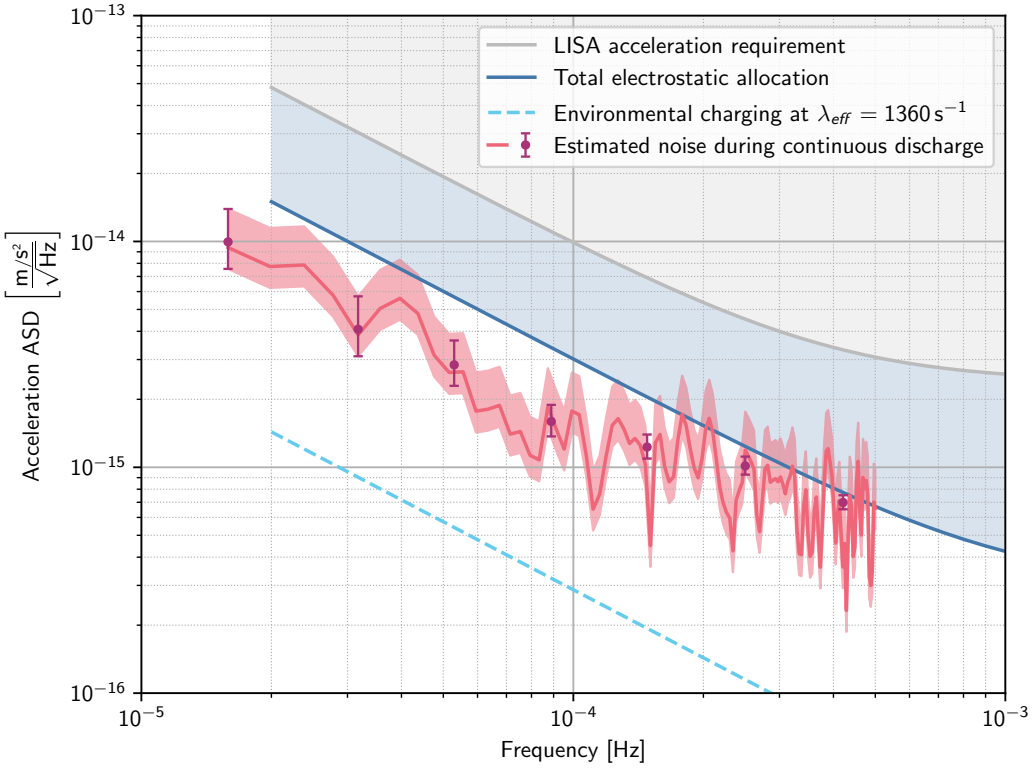

FIGURE 5.20: Estimated acceleration noise due to electrostatic disturbances described in Section 3.1.1 during continuous discharge. The data show a projected noise level within the requirements. To produce the acceleration PSD in this plot we assumed $\Delta_x = 5\,\mathrm{mV}$, a displacement from the zero-force point $x - x_0 = 10\,\mu\mathrm{m}$, noisy stray bias level and single electrodes noise level equal to the requirements in [12], finally the environmental net charging rates considered are $\lambda_{net}^{env} = 24.5\,\mathrm{s}^{-1}$ and $\lambda_{net}^{env} = 1360\,\mathrm{s}^{-1}$.

Fortunately, the LISA Pathfinder data showed that the apparent yield of both sensors did not change significantly (relative variations less than 25%) over the mission lifetime[52], however the limited statistics of just two GRSs may not give the full picture. Moreover, the nominal mission duration of LISA is four years, more than two times the duration of LPF (~ 600 days).

In LISA will, therefore, be necessary to measure the charge of all test masses at regular intervals, to be sure that it remains within the requirements and, eventually, adjust the continuous discharge illumination pattern.

Chapter 6

Lessons learned

6.1 Experimental problems

In this section we will list the main experimental problems encountered during our years-long testing campaign. We will address each problem with a proposed solution in the hope to ease and increase the quality of future measurements.

The main area of improvement for future apparent yield measurements concerns a more accurate measurement of the UV power injected into the GRS. As anticipated, the main problems are:

- The SMA connectors on the LED housings do not fit tightly with the optical fiber connector: detaching the fiber produces changes in the relative transmitted UV power of the order 10%.
- The cleanliness of the environment where the UV fibers are operated is not great. We observe a degradation of their transmittivity over time, indicating that the optical fibers get dirty and are damaged with use.
- The photodiode is not sensitive enough to provide accurate power measurements at low power. Moreover, its calibration may not be so accurate, especially when considering that the source have different emission spectra (introducing systematic errors in the power measurements).
- The transmission coefficients of the optical chain sections inside the vacuum vessel may not be reliable because the measurement performed at integration in 2014 were sloppy.
- The UV-light power is noisy: not only do LEDs degrade over time with use, but also the current produced by the electronics to feed the LEDs may change over time due to the variation of some environmental parameters such as temperature (see Figure 6.1). The measurement in Figure 6.2 is a more direct proof that this effect is not just the readout of our instruments varying with temperature, but the actual UV-light power.

6.2 Proposed improvements

Possible solutions of the problems listed before are:

- Use higher quality SMA connectors on the LED housing, or move to a different type of connector: in fiber optics SMA are generally indicated for high power applications (lasers with $\sim$ mW power), which is not exactly our case. There are other standard connectors that offer better optical coupling for low-power sources.

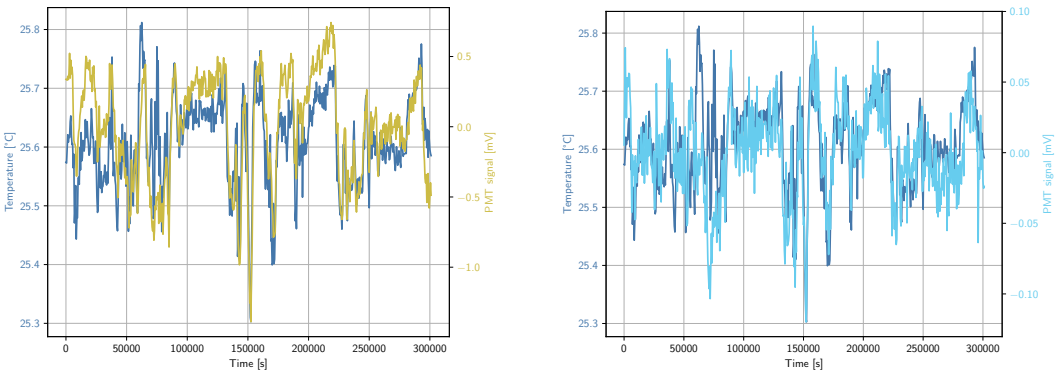

(A) PMT H6780-03 (not-calibrated) (B) PMT R9875U (calibrated)

FIGURE 6.1: Correlation between PMT output signal and laboratory temperature. The PMT signal has been detrended with an second order polynomial.

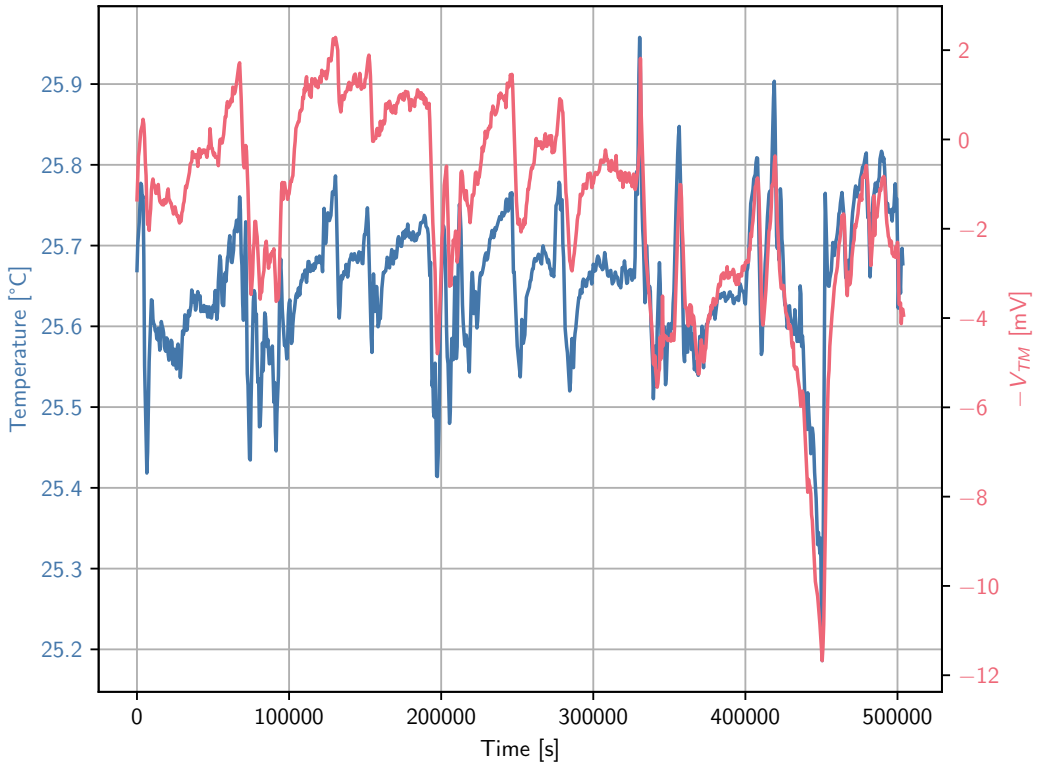

FIGURE 6.2: Anti-correlation between of the TM equilibrium voltage during double illumination and the laboratory temperature: we continuously illuminated both TM and EH ISUKs with two LEDs, setting the light power of the two UV-sources so to have equilibrium voltage close to neutrality. The variations in the equilibrium voltage indicate a dependence of the light-output from the laboratory temperature.

- Keep the optical fibers in a clean environment and avoid stressing them. Future experimenters may consider using of optical switches that allow to divert the light into a specific channel without the need of mechanically removing the fibers.
- Acquire splitting fibers, i.e. optical fibers that have one input and multiple outputs, which would allow to monitor in real time the fluctuations of the UV power (which is relevant especially for the apparent yield measurements) and the the phase of the light pulses (which is relevant for the continuous discharge measurements).
- Characterize better the transmission of the optical chain from UV-source to ISUK, including its possible dependence on wavelength of the light.
- Characterize the emission envelope from the ISUK: this would lead to a better estimation of the locations where the UV-photons are absorbed inside the GRS.
- Always keep an eye on the status of cables and connectors. Unstable lectures on the instruments are often due to flimsy contacts or bad grounding.
- Improve overall the temperature stability of the lab (unfortunately everything depends on temperature).

We also suggest to operate the LEDs at the nominal values for the polarization potential and driving currents: measurements with a broad band spectrometer hint that the LEDs may emit a photons at unexpected wavelengths if the current supplied is outside the optimal design range for the LED under consideration (see Figure 3.13).

Appendix A

Derivation of the quadrupole formula from dimensional analysis

In this appendix we will derive the quadrupole formula for the amplitude of gravitational waves from the principles of dimensional analysis.

Let us assume that the measured amplitude of gravitational waves h depends on

- A nth order time derivative of the mass quadrupole moment I;
- The distance of the observer form the source r;
- The gravitational constant G;
- The speed of light c.

We, therefore, assume for a h generic expression of these quantities

$$h \sim c^a G^b r^m \frac{\partial^n I}{\partial t^n} \tag{A.1}$$

The flux of power[1] from the source (i.e. flux of radiated energy per unit area per unit time) is proportional to the square of the product between wave frequency ν and amplitude h.

$$\text{Flux} \sim \nu^2 h^2 \sim h^2 \tag{A.2}$$

From *conservation of energy*, we must have that the amount of power crossing any surface surrounding the source must be conserved.

$$\text{const.} = \text{Flux} \cdot \text{Area} \sim h^2 \cdot r^2 \qquad \Longrightarrow \qquad h \sim r^{-1} \tag{A.3}$$

Therefore, we can set $m = -1$ from conservation of energy. In this way, equation (A.1) becomes

$$h \sim \frac{c^a G^b}{r} \frac{\partial^n I}{\partial t^n} \tag{A.4}$$

Now we can apply the principle of dimensional analysis to obtain the remaining exponents. The GW amplitude h is dimensionless, because it can be measured as a *strain*, i.e. a ratio of lengths. The gravitational constant G has units of the cube of a length divided by a mass and a time. Converting this in a self-explaining formula

$$[G] = \frac{[L]^3}{[M][T]^2} \tag{A.5}$$

[1] More formally known as *irradiance*.

The quadrupole moment has units of a mass multiplied for the square of a distance.

$$[I] = [M][L]^2 \tag{A.6}$$

Hence its time-derivative of order n will have units

$$\left[\frac{\partial^n I}{\partial t^n}\right] = \frac{[M][L]^2}{[T]^n} \tag{A.7}$$

Finally, the speed of light c has units of distance divided by a time

$$[c] = \frac{[L]}{[T]} \tag{A.8}$$

If we put all together we have the following dimensional equation for the quadrupole formula

$$\underbrace{[L]^0[M]^0[T]^0}_{[h]} = \left(\frac{[L]}{[T]}\right)^a [L]^{-1} \left(\frac{[L]^3}{[M][T]^2}\right)^b \frac{[M][L]^2}{[T]^n} \tag{A.9}$$

which solved for each dimension gives the system

$$\begin{cases} [L]^0 = [L]^{a+3b+1} \\ [M]^0 = [M]^{-b+1} \\ [T]^0 = [T]^{-a-2b-n} \end{cases} \tag{A.10}$$

which has solution $a = -4$, $b = -1$ and $n = 2$. Therefore, from (A.4), we have

$$h \sim \frac{G}{c^4 r} \frac{\partial^2 I}{\partial t^2} \tag{A.11}$$

which is the correct scaling for the quadrupole formula.

Appendix B

4TM pendulum light absorption coefficients

In this appendix we list the UV-light absorption coeffcients considered for our analysis.

The tabulated values are taken by the Astrium technical note *Discharge Model Predictions for the UTN 4Mass Torsion Pendulum* [78]. We decided to use the LPF predictions for the absorption coefficients, because the LPF geometry reflects more realistically the present-day the torsion pendulum setup (the pendulum prediction in the Astrium technical note are based on and outdated geometry and the EH installed currently in our facility is an exact copy of the LPF one, except for the absence of the iridium caging fingers). We also have to point out that in the Astrium technical note the ISUK in the same position as the torsion pendulum are JF01 (*TM illumination*) and JF02 (*EH illumination*), but the latter is modified with the mirror. Therefore, we take the data relative to the third ISUK JF03 (always EH illumination), which is mounted on the opposite corner of the EH with the care of adapting the coordinates, as it were in the position of the JF02 ISUK. Figure B.1 is an useful visual aid to navigate through the difficulties of imagining a 3D geometry.

Results obtained by the ray-tracing method based on the software GEANT4 by Dr. Daniel Hollington [58] give very similar values. As in the work by Daniel Hollington, the light that hits the sides of the electrodes or the groves and holes of the guard rings has been considered lost, because it is assumed to produce photoelectrons that for geometry reasons do not contribute to the photocurrents. Also the fraction of light that is absorbed by the caging fingers is considered lost because of the very low emissivity of iridium [53].

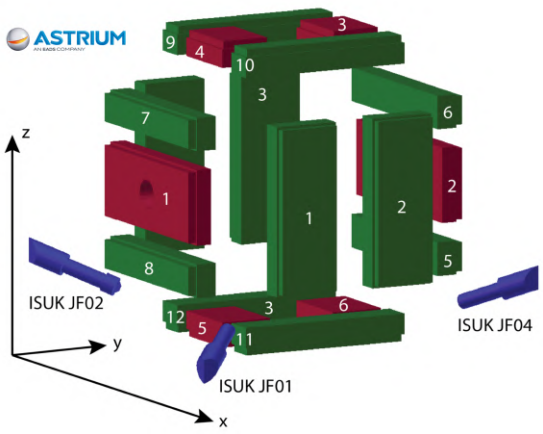

FIGURE B.1: Astrium coordinate system of torsion pendulum model and naming of electrodes [78].

TABLE B.1: Absorption coefficients 4TM torsion pendulum.

Surface	TM illumination [%]	EH illumination [%]
TM injection	0.33	0.78
EH injection	0.45	0.68
TM x_1^- el.	0.00	0.08
TM x_1^+ el.	1.17	0.00
TM x_2^- el.	0.01	0.01
TM x_2^+ el.	0.13	0.01
TM y_1^- el.	1.03	0.04
TM y_1^+ el.	0.01	0.01
TM y_2^- el.	0.00	0.00
TM y_2^+ el.	0.00	0.00
TM z_1^- el.	0.07	0.69
TM z_1^+ el.	0.00	0.00
TM z_2^- el.	1.07	0.13
TM z_2^+ el.	0.00	0.00
EH x_1^- el.	0.00	0.15
EH x_1^+ el.	1.82	0.00
EH x_2^- el.	0.01	0.01
EH x_2^+ el.	0.15	0.01
EH y_1^- el.	1.97	0.10
EH y_1^+ el.	0.01	0.01
EH y_2^- el.	0.01	0.01
EH y_2^+ el.	0.00	0.00
EH z_1^- el.	0.08	5.59
EH z_1^+ el.	0.00	0.00
EH z_2^- el.	0.42	0.14
EH z_2^+ el.	0.00	0.00
TM rest	61.82	9.46
EH rest	10.27	11.62
Lost	19.18	70.47

Appendix C

Solution of the Schrödinger equation for a step potential

The one-dimensional Schrödinger equation for a step potential reads [65]

$$\left[-\frac{\hbar^2}{2m}\frac{\mathrm{d}^2}{\mathrm{d}x^2}+U(x)\right]\psi(x)=E\psi(x) \qquad \text{for} \qquad U(x)=\begin{cases}0, & \text{if } x\leq 0\\ U_0, & \text{if } x>0\end{cases} \tag{C.1}$$

Here we assumed that there is a flux of particles all with same mass m and initial energy E_0 moving along a generic x-axis and impinging on a potentiality step U_0 located in $x=0$.

The solution of this problem depends on the energy E_0 of the of the incoming particle with respect to the height U_0 of the potential step.

Case $E_0 \geq U_0$ As shown in Figure C.1, we can divide the problem in two regions: the first being the space before the barrier ($x \leq 0$) and the second is, of course, the region of the barrier ($x > 0$).

In the first region, where $U(x) = 0$, we have to solve the simple Schrödinger equation

$$-\frac{\hbar^2}{2m}\frac{\mathrm{d}^2\psi_1}{\mathrm{d}x^2}=E_0\psi_1(x) \qquad \text{for} \qquad x\leq 0 \tag{C.2}$$

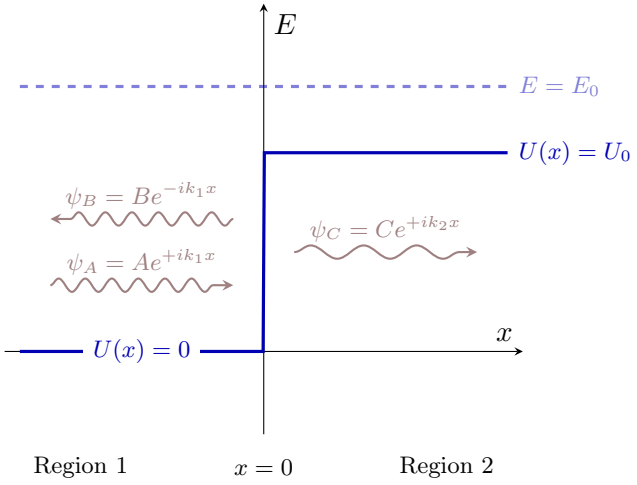

FIGURE C.1: QM potential step problem for $E_0 \geq U_0$.

which can be rephrased more conveniently to

$$\left(\frac{\mathrm{d}^2}{\mathrm{d}x^2} + k_1^2\right)\psi_1(x) = 0 \qquad \text{with} \qquad k_1 = \sqrt{\frac{2m}{\hbar^2}E_0} \tag{C.3}$$

The most general solution is a superposition of an incident and a reflected plane wave

$$\psi_1(x) = \underbrace{Ae^{+\mathrm{i}k_1 x}}_{\psi_A} + \underbrace{Be^{-\mathrm{i}k_1 x}}_{\psi_B} \tag{C.4}$$

In the second region, where $U(x) = U_0$, we have to solve

$$\left[-\frac{\hbar^2}{2m}\frac{\mathrm{d}^2}{\mathrm{d}x^2} + U_0\right]\psi_2(x) = E_0\psi_2(x) \qquad \text{for} \qquad x > 0 \tag{C.5}$$

which, again, can be rearranged as

$$\left(\frac{\mathrm{d}^2}{\mathrm{d}x^2} + k_2^2\right)\psi_2(x) = 0 \qquad \text{with} \qquad k_2 = \sqrt{\frac{2m}{\hbar^2}(E_0 - U_0)} \tag{C.6}$$

As, in this case, the energy of the incoming particle is larger than the potential barrier, the wave vector k_2 is real and positive. The most general solution is once again a superposition of plane waves

$$\psi_2(x) = Ce^{+\mathrm{i}k_2 x} + De^{-\mathrm{i}k_2 x}, \tag{C.7}$$

However in this case we must have $D = 0$ because we assumed that particles are impinging on the barrier only from the negative direction of the x-axis, hence

$$\psi_2(x) = \underbrace{Ce^{+\mathrm{i}k_2 x}}_{\psi_C}. \tag{C.8}$$

Therefore, the complete wave-function is

$$\psi(x) = \begin{cases} \psi_1(x) = Ae^{-\mathrm{i}k_1 x} + Be^{+\mathrm{i}k_1 x}, & \text{if } x \leq 0 \\ \psi_2(x) = Ce^{-\mathrm{i}k_2 x}, & \text{if } x > 0 \end{cases} \tag{C.9}$$

The requirement of the wave-function to be continuous and differentiable in $x = 0$ leads us to

$$\psi_1(x = 0) = \psi_2(x = 0) \qquad \longrightarrow \qquad A + B = C \tag{C.10}$$

and

$$\left.\frac{\mathrm{d}\psi_1}{\mathrm{d}x}\right|_{x=0} = \left.\frac{\mathrm{d}\psi_2}{\mathrm{d}x}\right|_{x=0} \qquad \longrightarrow \qquad k_1(A - B) = k_2 C \tag{C.11}$$

Combining (C.10) and (C.11) gives us

$$A = C\frac{k_1 + k_2}{2k_1} \qquad \text{and} \qquad B = C\frac{k_1 - k_2}{2k_1} \tag{C.12}$$

The transmission coefficient is defined as the ratio of the *probability current density*[1] in the direction normal to the potential step (i.e. along the x-axis) of the transmitted

[1] The probability current density associated with a wavefunction is defined as

$$\boldsymbol{J} = \frac{\hbar}{2m\mathrm{i}}\left(\psi^*\boldsymbol{\nabla}\psi - \psi\boldsymbol{\nabla}\psi^*\right), \tag{C.13}$$

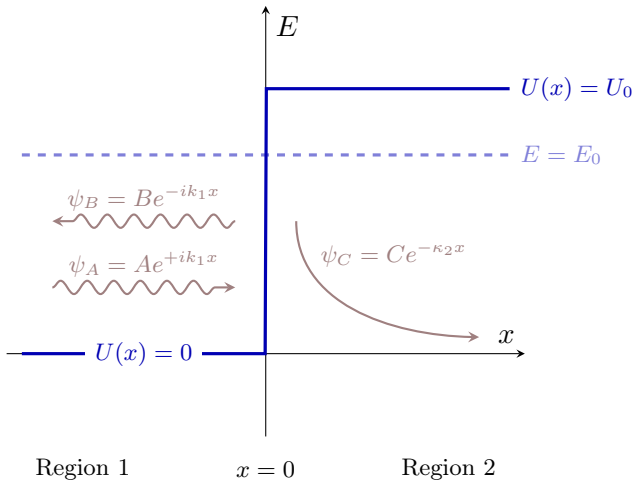

FIGURE C.2: QM potential step problem for $E_0 < U_0$.

wavefunction ψ_C and of the incident wavefunction ψ_A

$$\mathcal{T} = \frac{\boldsymbol{J}_{trans} \cdot \hat{\boldsymbol{x}}}{\boldsymbol{J}_{inc} \cdot \hat{\boldsymbol{x}}} = \frac{J_{trans,x}}{J_{inc,x}} = \frac{\psi_C^* \frac{\mathrm{d}\psi_C}{\mathrm{d}x} - \psi_C \frac{\mathrm{d}\psi_C^*}{\mathrm{d}x}}{\psi_A^* \frac{\mathrm{d}\psi_A}{\mathrm{d}x} - \psi_A \frac{\mathrm{d}\psi_A^*}{\mathrm{d}x}} = \frac{k_2 C^2}{k_1 A^2} = \frac{4k_1 k_2}{(k_2 + k_1)^2}, \tag{C.15}$$

where in the last passage we used the first of (C.12).

In a similar way, we can define the reflection coefficient as the ratio of the probability current density of the reflected wavefunction ψ_B along the negative direction of the x-axis (because the reflected wavefunction is propagating backwards) and of the incident wavefunction ψ_A along the x-axis

$$\mathcal{R} = \frac{\boldsymbol{J}_{refl} \cdot (-\hat{\boldsymbol{x}})}{\boldsymbol{J}_{inc} \cdot \hat{\boldsymbol{x}}} = \frac{-J_{refl,x}}{J_{inc,x}} = \frac{\psi_B \frac{\mathrm{d}\psi_B^*}{\mathrm{d}x} - \psi_B^* \frac{\mathrm{d}\psi_B}{\mathrm{d}x}}{\psi_A^* \frac{\mathrm{d}\psi_A}{\mathrm{d}x} - \psi_A \frac{\mathrm{d}\psi_A^*}{\mathrm{d}x}} = \frac{B^2}{A^2} = \frac{(k_1 - k_2)^2}{(k_2 + k_1)^2}, \tag{C.16}$$

where in the last passage we used (C.12). Naturally $\mathcal{R} + \mathcal{T} = 1$, as expected from the law of total probability (it is certain that the particle will be either transmitted or reflected).

If we substitute the expression for the wave-vectors k_1 and k_2 in the formula for the transmission coefficient, we have

$$\mathcal{T}(E_0, U_0) = \frac{4\sqrt{E_0(E_0 - U_0)}}{\left(\sqrt{E_0} + \sqrt{E_0 - U_0}\right)^2} \qquad \text{for} \qquad E_0 \geq U_0. \tag{C.17}$$

Case $E_0 < U_0$ As we can see in Figure C.2, when the energy of the incoming particle is less than the height of the potential step U_0, the solution in the region $x \leq 0$ remain unchanged. On the other hand, we must find the new solution for the region $x > 0$, where the Schrödinger equation reads

$$\left[-\frac{\hbar^2}{2m}\frac{\mathrm{d}^2}{\mathrm{d}x^2} + U_0\right] \psi_2(x) = E_0 \psi_2(x) \qquad \text{for} \qquad x > 0 \tag{C.18}$$

where ψ^* denotes the complex conjugate of the wavefunction. In our one-dimensional problem, the definition above reduces to

$$\boldsymbol{J} = J_x \, \hat{\boldsymbol{x}} = \frac{\hbar}{2m\mathrm{i}} \left(\psi^* \frac{\mathrm{d}\psi}{\mathrm{d}x} - \psi \frac{\mathrm{d}\psi^*}{\mathrm{d}x}\right) \hat{\boldsymbol{x}} \tag{C.14}$$

which can be rephrased as

$$\left(\frac{\mathrm{d}^2}{\mathrm{d}x^2} - \kappa_2^2\right)\psi_2(x) = 0 \qquad \text{with} \qquad \kappa_2 = \sqrt{\frac{2m}{\hbar^2}(U_0 - E_0)} \tag{C.19}$$

where the wave vector κ_2 is a positive real, as in this case $E_0 < U_0$. The most general solution of the previous equation is

$$\psi_2(x) = Ce^{-\kappa_2 x} + De^{+\kappa_2 x}. \tag{C.20}$$

We must have that $D = 0$, otherwise the wavefunction $\psi_2(x)$ would diverge for $x \to \infty$. The solution in the region $x > 0$, therefore is

$$\psi_2(x) = \underbrace{Ce^{-\kappa_2 x}}_{\psi_C} \tag{C.21}$$

As the solution $\psi_2(x)$ is purely real, the probability current density of the transmitted wavefunction vanishes. Indeed

$$J_{trans,x} = \psi_C^* \frac{\mathrm{d}\psi_C}{\mathrm{d}x} - \psi_C \frac{\mathrm{d}\psi_C^*}{\mathrm{d}x} = \psi_C \frac{\mathrm{d}\psi_C}{\mathrm{d}x} - \psi_C \frac{\mathrm{d}\psi_C}{\mathrm{d}x} = 0 \tag{C.22}$$

where we used the fact that for a real function $\psi^* = \psi$. As the probability current density of the incident wavefunction $J_{inc,x}$ is different from zero (as in the case $E_0 \geq U_0$), we must have the transmission coefficient is null

$$\mathcal{T} = \frac{J_{trans,x}}{J_{inc,x}} = 0 \qquad \text{for} \qquad E_0 < U_0. \tag{C.23}$$

Therefore, if the energy of the incoming particle E_0 is lower that the height of the potential step U_0, the transmission coefficient is zero.

On the other hand, for the law of total probability, we must have

$$\mathcal{R} = 1 \qquad \text{for} \qquad E_0 < U_0, \tag{C.24}$$

as the only possibility for the incoming particles is to be reflected.

Appendix D

Summary tables of the Bayesian fit

In this appendix, we present the tables of the fit parameters relevant for the estimation of the microscopic properties of the TM and EH surfaces. All the values are to be interpreted as the mean of the corresponding posterior distribution with uncertainty given by the standard deviation.

TABLE D.1: Table of the fit posterior parameters for Crystal 250 data.

Measurement	W_{EH} [eV]	ΔW [eV]	$\mathcal{Q}_{EH}$ $\left[\times 10^{-5}\right]$	$\mathcal{Q}_{TM}$ $\left[\times 10^{-5}\right]$
EH ill. duration 10 µs, delay 0 µs, $V_{inj} = 5.4$ V	3.86 ± 0.02	-0.384 ± 0.013	3.8 ± 0.2	1.48 ± 0.07
EH ill. duration 10 µs, delay 0 µs, $V_{inj} = 0.54$ V	3.922 ± 0.008	-0.360 ± 0.005	4.1 ± 0.2	1.42 ± 0.07
EH ill. duration 1 µs, delay 2 µs, $V_{inj} = 5.4$ V	3.665 ± 0.007	-0.460 ± 0.004	4.2 ± 0.2	1.93 ± 0.09
EH ill. duration 1 µs, delay 7 µs, $V_{inj} = 5.4$ V	3.836 ± 0.009	-0.326 ± 0.005	4.1 ± 0.2	1.88 ± 0.09
TM ill. duration 10 µs, delay 0 µs, $V_{inj} = 5.4$ V	4.087 ± 0.019	$+0.021 \pm 0.009$	3.74 ± 0.16	4.5 ± 0.2
TM ill. duration 10 µs, delay 0 µs, $V_{inj} = 0.54$ V	4.02 ± 0.02	$+0.081 \pm 0.008$	2.58 ± 0.10	3.94 ± 0.16
TM ill. duration 1 µs, delay 2 µs, $V_{inj} = 5.4$ V	3.887 ± 0.019	$+0.084 \pm 0.008$	3.41 ± 0.14	4.21 ± 0.18
TM ill. duration 1 µs, delay 7 µs, $V_{inj} = 5.4$ V	3.949 ± 0.010	$+0.109 \pm 0.004$	2.99 ± 0.13	4.9 ± 0.2

TABLE D.2: Table of the fit posterior parameters for SETi 240 data.

Measurement	W_{EH} [eV]	ΔW [eV]	$\mathcal{Q}_{EH}$ $\left[\times 10^{-5}\right]$	$\mathcal{Q}_{TM}$ $\left[\times 10^{-5}\right]$
EH ill. duration 10 µs, delay 0 µs, $V_{inj} = 0.54$ V	3.948 ± 0.007	-0.370 ± 0.004	4.18 ± 0.18	1.41 ± 0.06
EH ill. duration 1 µs, delay 2 µs, $V_{inj} = 5.4$ V	3.484 ± 0.013	-0.469 ± 0.005	3.27 ± 0.15	1.94 ± 0.09
EH ill. duration 1 µs, delay 7 µs, $V_{inj} = 5.4$ V	3.698 ± 0.006	-0.366 ± 0.006	2.33 ± 0.11	1.36 ± 0.06
TM ill. duration 10 µs, delay 0 µs, $V_{inj} = 5.4$ V	3.81 ± 0.02	$+0.140 \pm 0.008$	2.83 ± 0.11	4.30 ± 0.16
TM ill. duration 10 µs, delay 0 µs, $V_{inj} = 0.54$ V	3.928 ± 0.019	$+0.086 \pm 0.008$	6.7 ± 0.2	11.3 ± 0.4
TM ill. duration 1 µs, delay 2 µs, $V_{inj} = 5.4$ V	3.594 ± 0.016	$+0.200 \pm 0.008$	3.90 ± 0.14	5.5 ± 0.2
TM ill. duration 1 µs, delay 7 µs, $V_{inj} = 5.4$ V	3.797 ± 0.016	$+0.186 \pm 0.007$	2.26 ± 0.10	4.53 ± 0.16

Table D.3: Table of the fit posterior parameters for SETi 255 data.

Measurement	W_{EH} [eV]	ΔW [eV]	$\mathcal{Q}_{EH}$ $[\times 10^{-5}]$	$\mathcal{Q}_{TM}$ $[\times 10^{-5}]$
EH ill. duration 10 µs, delay 0 µs, $V_{inj} = 5.4\,\mathrm{V}$	3.90 ± 0.02	-0.290 ± 0.012	2.04 ± 0.08	0.90 ± 0.04
EH ill. duration 10 µs, delay 0 µs, $V_{inj} = 0.54\,\mathrm{V}$	3.898 ± 0.010	-0.309 ± 0.006	2.24 ± 0.09	0.84 ± 0.03
EH ill. duration 1 µs, delay 2 µs, $V_{inj} = 5.4\,\mathrm{V}$	3.813 ± 0.004	-0.325 ± 0.003	1.98 ± 0.08	0.97 ± 0.04
EH ill. duration 1 µs, delay 7 µs, $V_{inj} = 5.4\,\mathrm{V}$	3.920 ± 0.007	-0.234 ± 0.005	1.85 ± 0.08	0.89 ± 0.04
TM ill. duration 10 µs, delay 0 µs, $V_{inj} = 5.4\,\mathrm{V}$	3.966 ± 0.014	$+0.110 \pm 0.005$	1.36 ± 0.04	1.96 ± 0.06
TM ill. duration 10 µs, delay 0 µs, $V_{inj} = 0.54\,\mathrm{V}$	3.96 ± 0.02	$+0.095 \pm 0.008$	1.31 ± 0.04	1.71 ± 0.05
TM ill. duration 1 µs, delay 2 µs, $V_{inj} = 5.4\,\mathrm{V}$	3.898 ± 0.011	$+0.116 \pm 0.004$	1.22 ± 0.04	1.94 ± 0.06
TM ill. duration 1 µs, delay 7 µs, $V_{inj} = 5.4\,\mathrm{V}$	3.982 ± 0.011	$+0.094 \pm 0.004$	1.31 ± 0.04	1.67 ± 0.05
EH ill. $V_{z^-}^{DC} = -5\,\mathrm{V}$, duration 10 µs, $V_{inj} = 5.4\,\mathrm{V}$	3.795 ± 0.014	-0.364 ± 0.008	1.90 ± 0.06	1.30 ± 0.04
EH ill. $V_{z^-}^{DC} = -5\,\mathrm{V}$, duration 10 µs, $V_{inj} = 0.54\,\mathrm{V}$	3.968 ± 0.011	-0.308 ± 0.006	1.94 ± 0.06	1.20 ± 0.04
EH ill. $V_{z^-}^{DC} = +5\,\mathrm{V}$, duration 10 µs, $V_{inj} = 5.4\,\mathrm{V}$	3.616 ± 0.016	-0.505 ± 0.008	2.31 ± 0.09	0.90 ± 0.04
EH ill. $V_{z^-}^{DC} = +5\,\mathrm{V}$, duration 10 µs, $V_{inj} = 0.54\,\mathrm{V}$	3.962 ± 0.011	-0.284 ± 0.006	1.99 ± 0.08	0.87 ± 0.04

Table D.4: Table of the fit posterior parameters for UVphotonics 230 data.

Measurement	W_{EH} [eV]	ΔW [eV]	$\mathcal{Q}_{EH}$ $[\times 10^{-5}]$	$\mathcal{Q}_{TM}$ $[\times 10^{-5}]$
EH ill. duration 10 µs, delay 0 µs, $V_{inj} = 0.54\,\mathrm{V}$	3.703 ± 0.010	-0.610 ± 0.006	19.0 ± 0.4	6.36 ± 0.15
TM ill. duration 10 µs, delay 0 µs, $V_{inj} = 0.54\,\mathrm{V}$	3.777 ± 0.017	$+0.150 \pm 0.007$	8.65 ± 0.14	16.0 ± 0.3

Appendix E

Diagnostic plots for the Bayesian fits

In this appendix, we plot the traces and the pair plots for all apparent yield fits. We also show the comparison between experimental data and median of the posterior predictive checks (with $\pm 1\sigma$-confidence intervals).

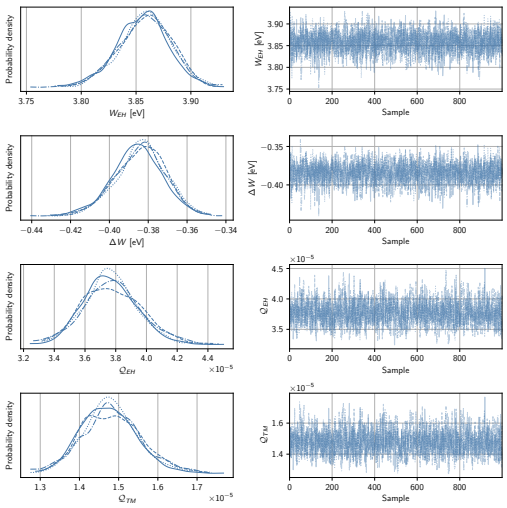

(A) Trace plot

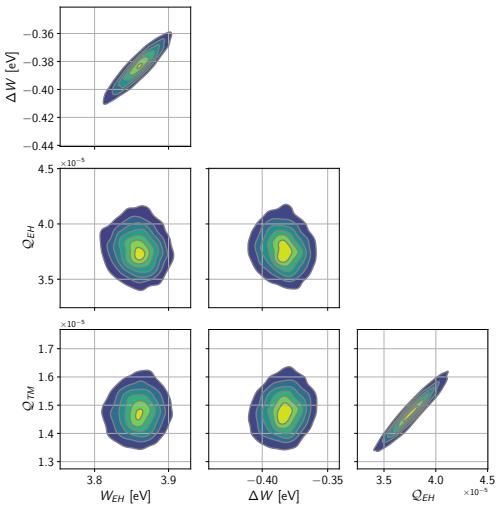

(B) Pair plot

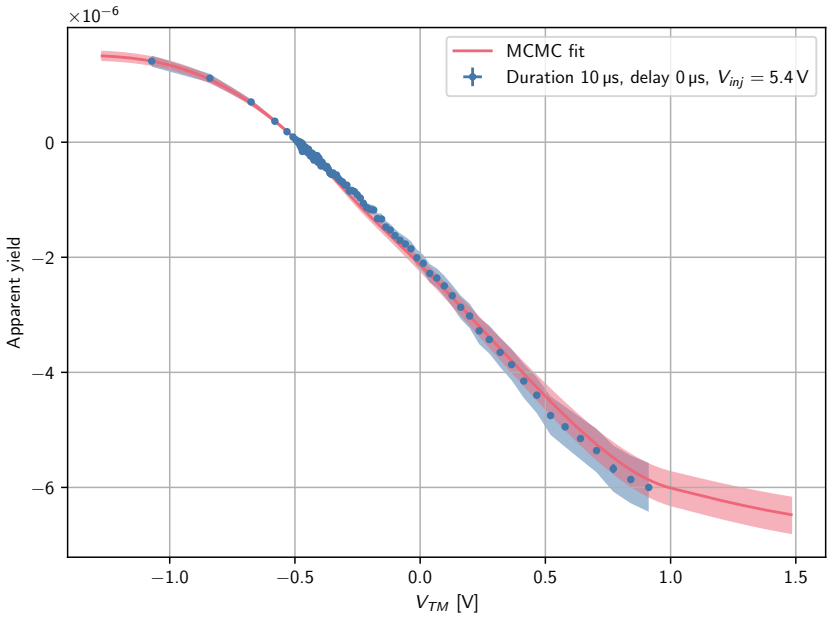

(C) Comparison between data and fit

FIGURE E.1: EH illumination with Crystal 250 (duration 10 µs, delay 0 µs, and $V_{inj} = 5.4$ V).

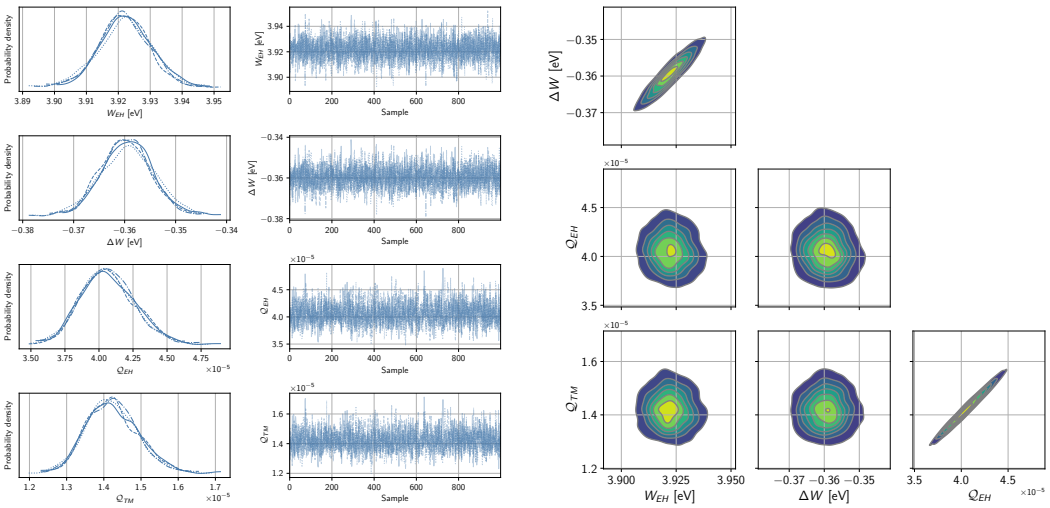

(A) Trace plot

(B) Pair plot

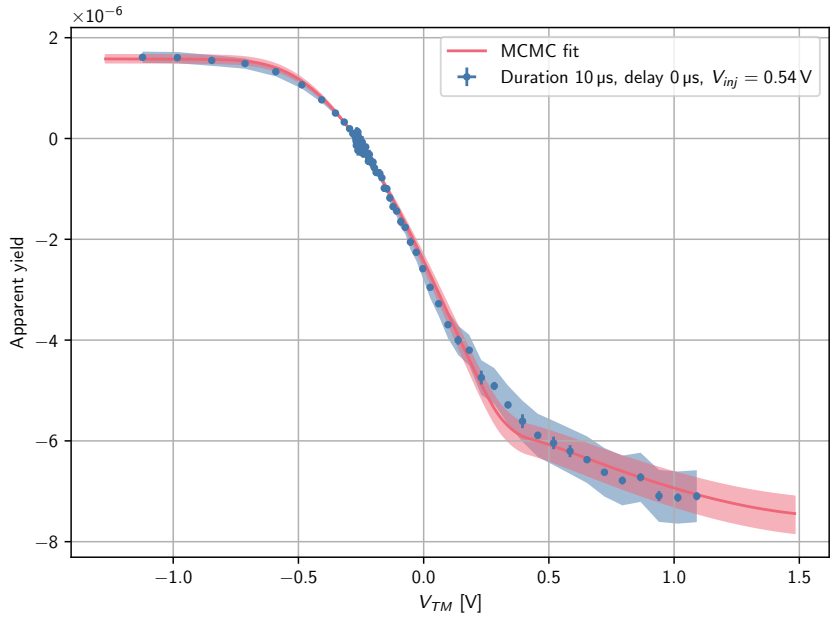

(C) Comparison between data and fit

FIGURE E.2: EH illumination with Crystal 250 (duration 10 µs, delay 0 µs, and $V_{inj} = 0.54$ V).

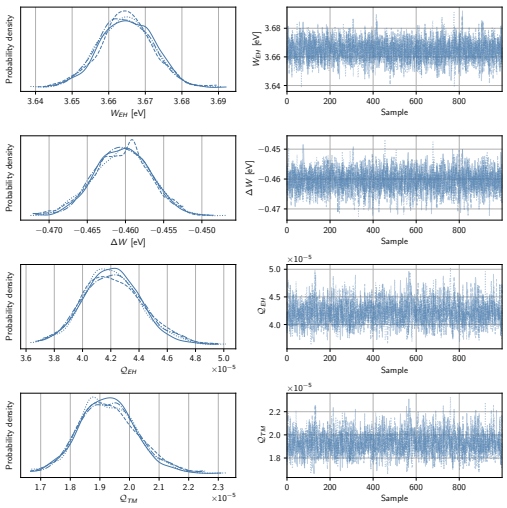

(A) Trace plot

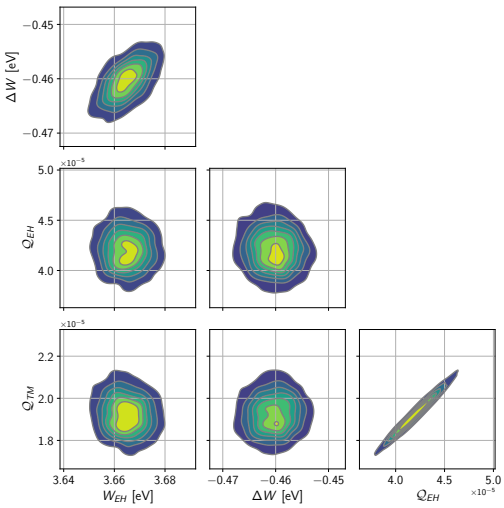

(B) Pair plot

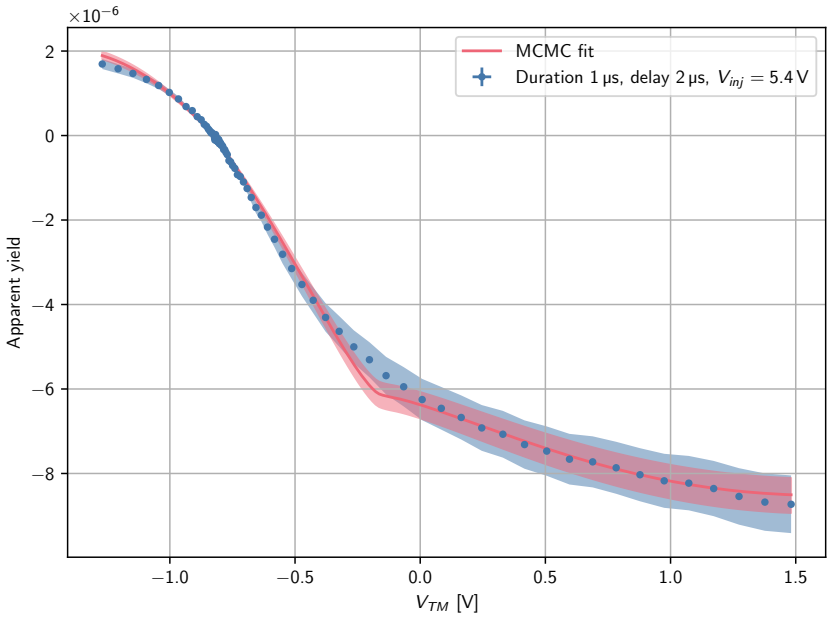

(C) Comparison between data and fit

FIGURE E.3: EH illumination with Crystal 250 (duration 1 µs, delay 2 µs, and $V_{inj} = 5.4$ V).

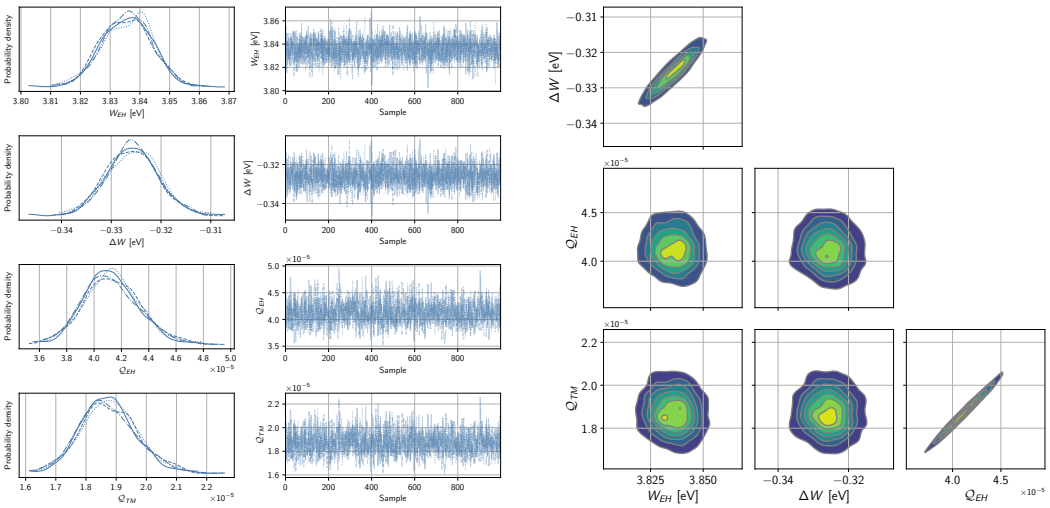

(A) Trace plot

(B) Pair plot

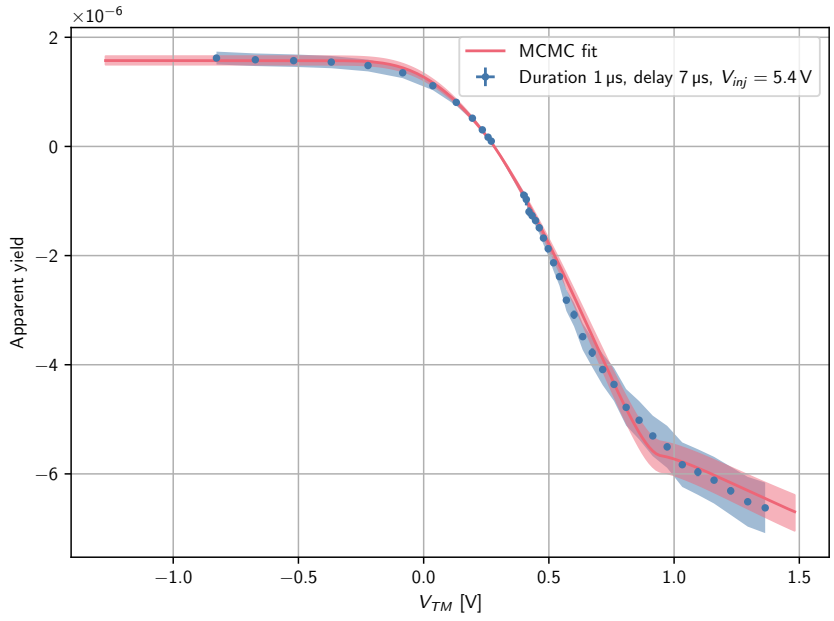

(C) Comparison between data and fit

FIGURE E.4: EH illumination with Crystal 250 (duration 1 µs, delay 7 µs, and $V_{inj} = 5.4$ V).

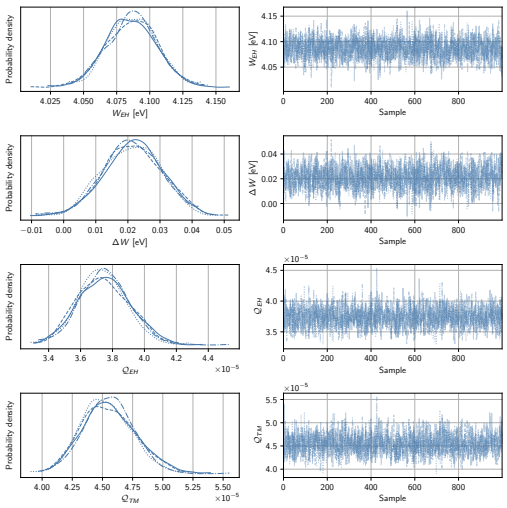

(A) Trace plot

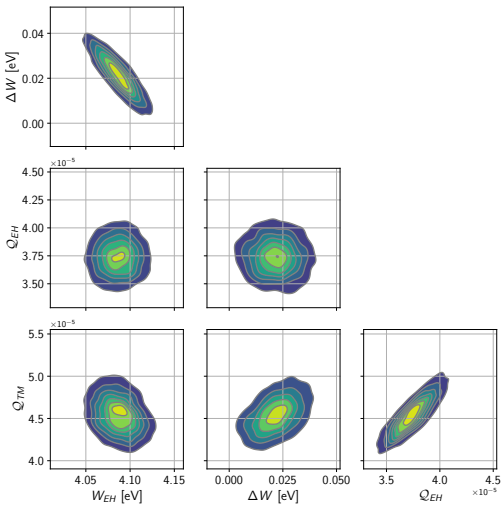

(B) Pair plot

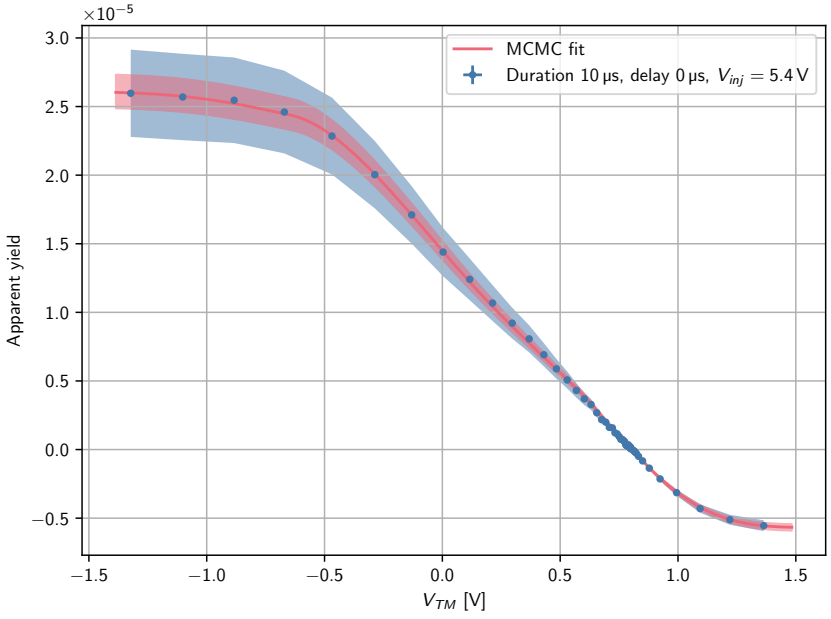

(C) Comparison between data and fit

FIGURE E.5: TM illumination with Crystal 250 (duration 10 µs, delay 0 µs, and $V_{inj} = 5.4$ V).

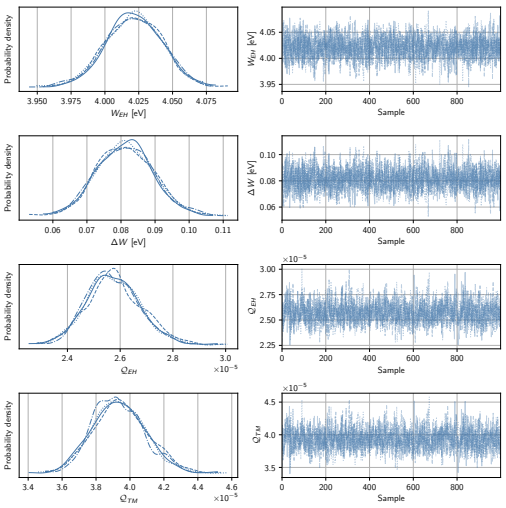

(A) Trace plot

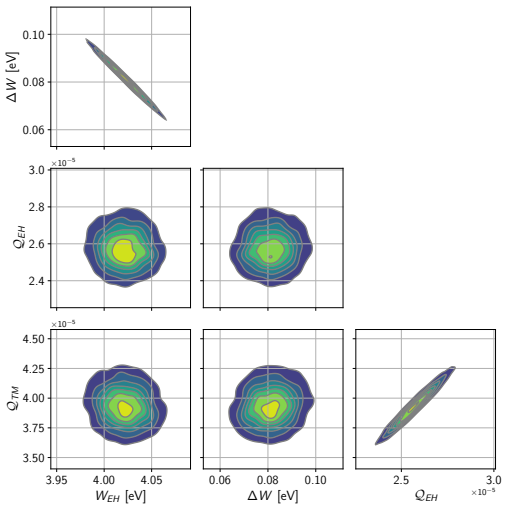

(B) Pair plot

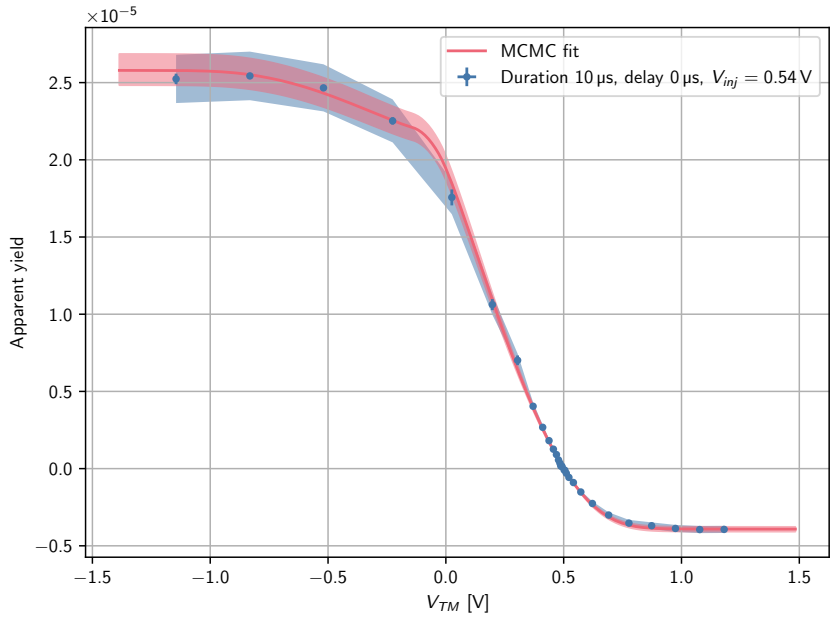

(C) Comparison between data and fit

FIGURE E.6: TM illumination with Crystal 250 (duration 10 µs, delay 0 µs, and $V_{inj} = 0.54$ V).

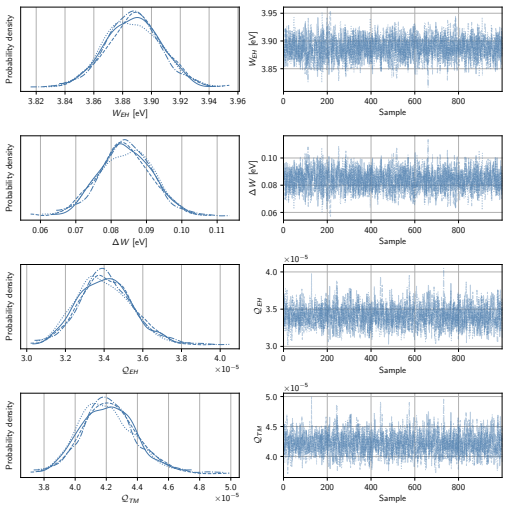

(A) Trace plot

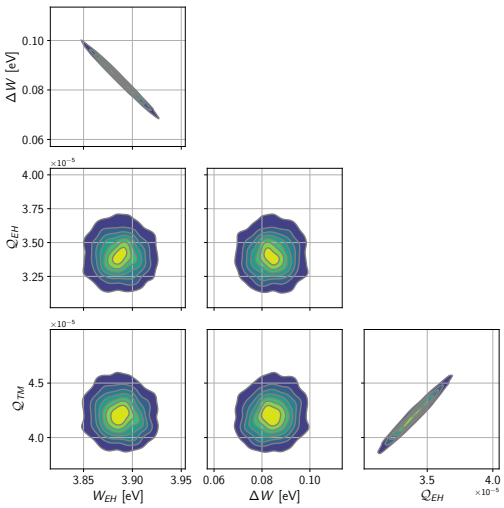

(B) Pair plot

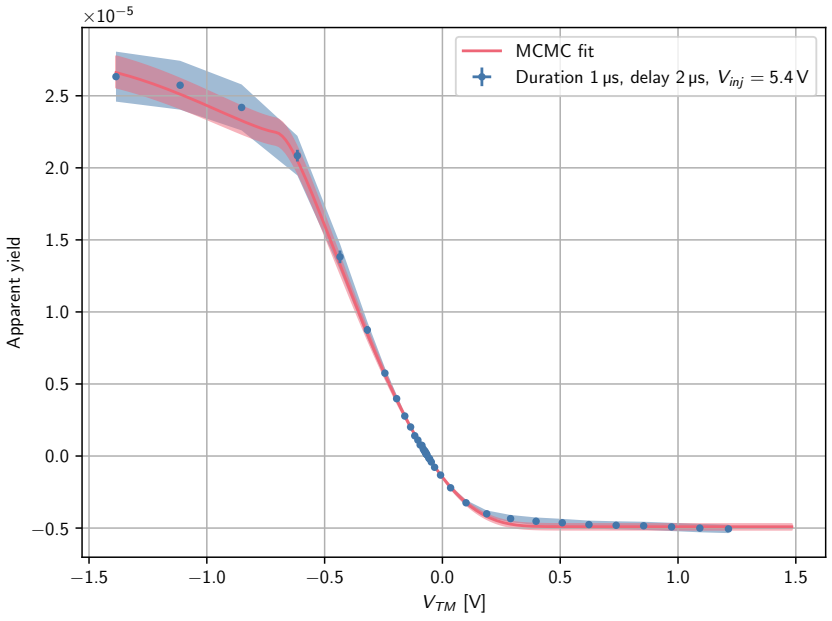

(C) Comparison between data and fit

FIGURE E.7: TM illumination with Crystal 250 (duration 1 µs, delay 2 µs, and $V_{inj} = 5.4$ V).

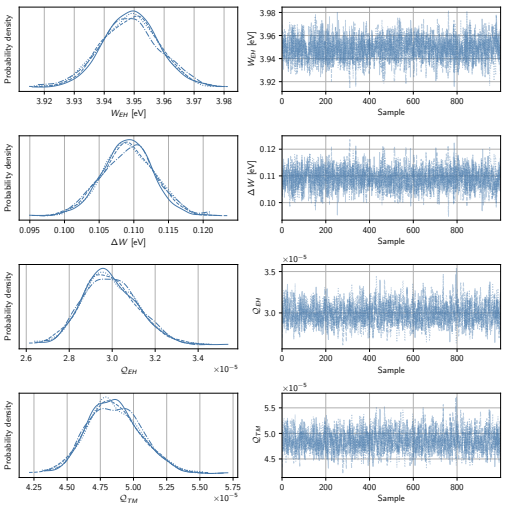

(A) Trace plot

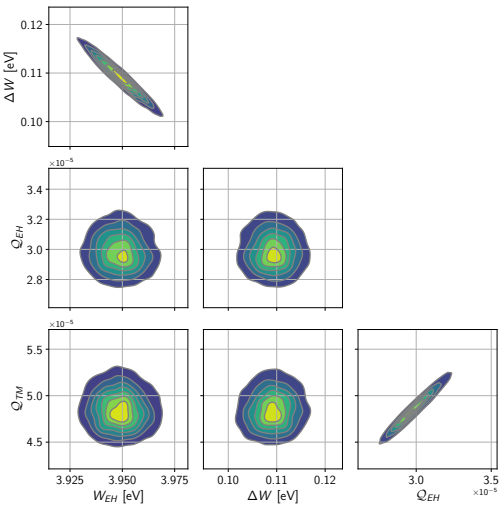

(B) Pair plot

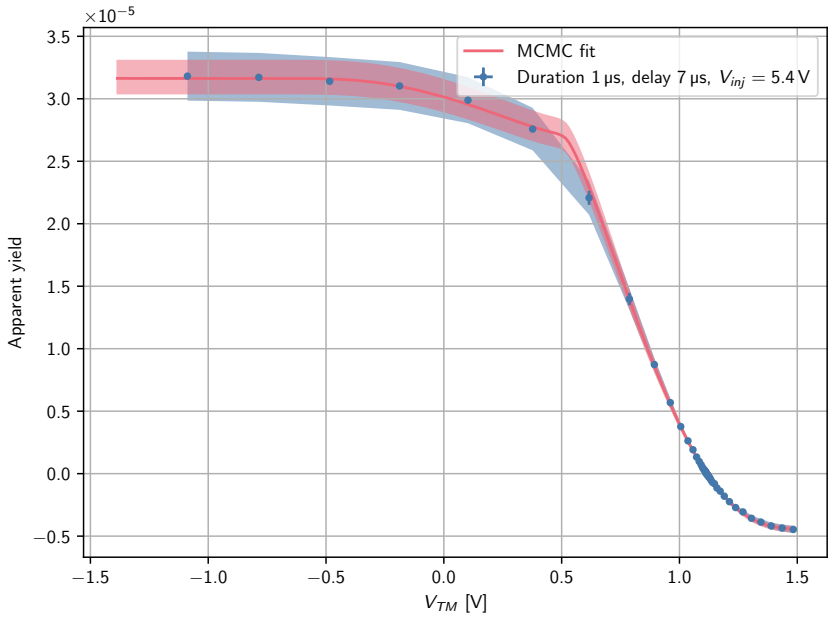

(C) Comparison between data and fit

FIGURE E.8: TM illumination with Crystal 250 (duration 1 µs, delay 7 µs, and $V_{inj} = 5.4$ V).

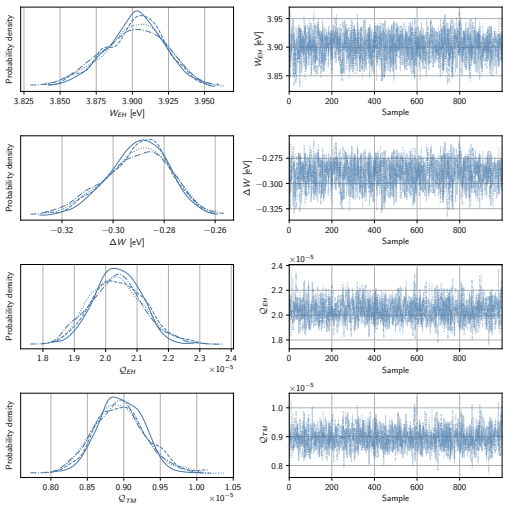

(A) Trace plot

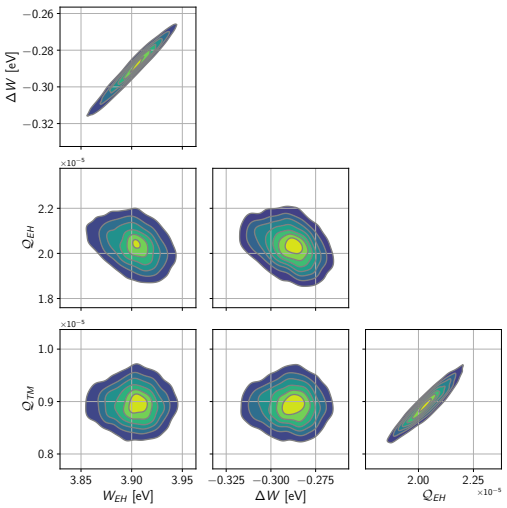

(B) Pair plot

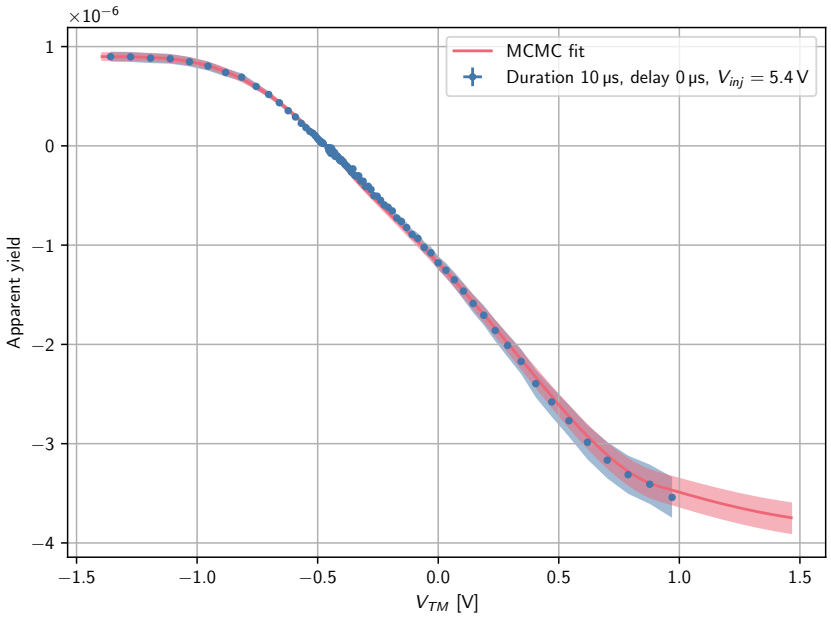

(C) Comparison between data and fit

FIGURE E.9: EH illumination with SETi 255 (duration 10 µs, delay 0 µs, and $V_{inj} = 5.4$ V).

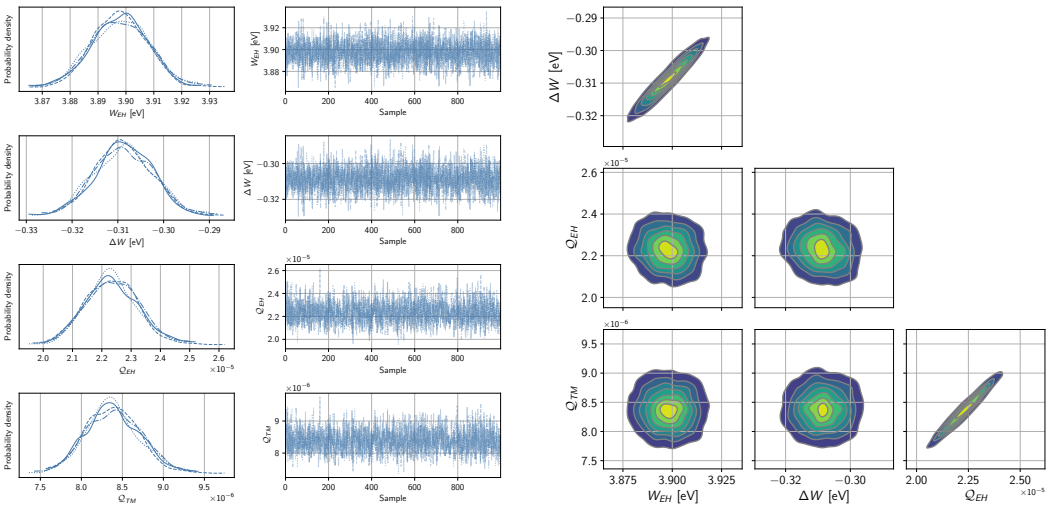

(A) Trace plot

(B) Pair plot

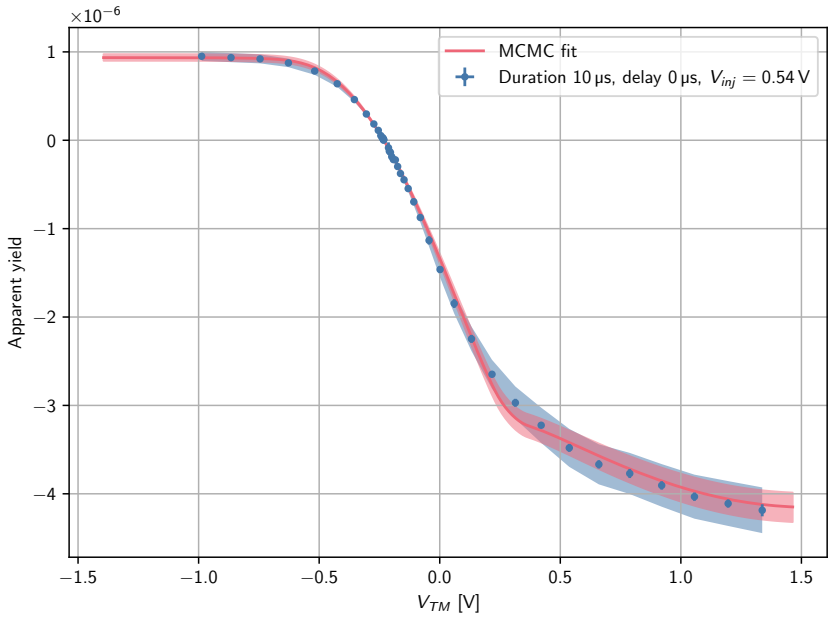

(C) Comparison between data and fit

FIGURE E.10: EH illumination with SETi 255 (duration 10 µs, delay 0 µs, and $V_{inj} = 0.54$ V).

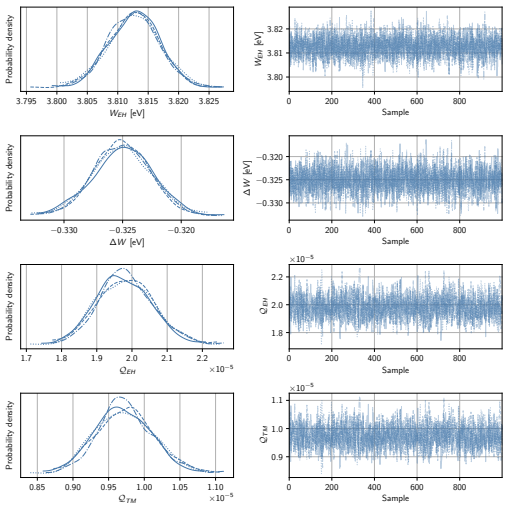

(A) Trace plot

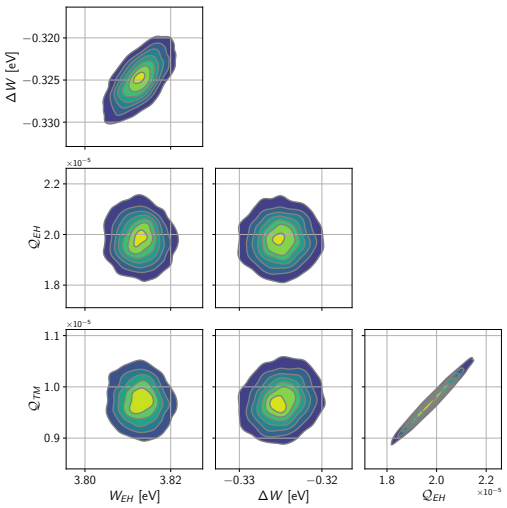

(B) Pair plot

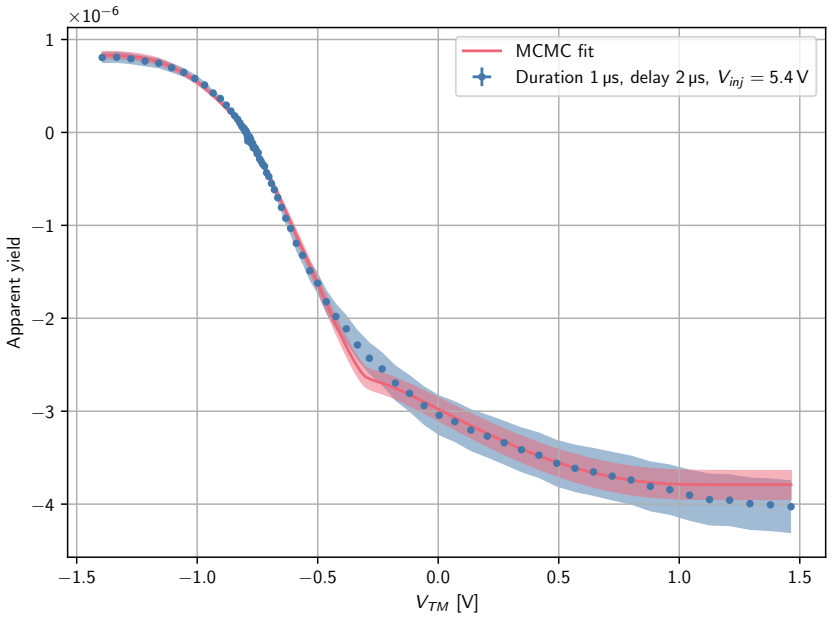

(C) Comparison between data and fit

FIGURE E.11: EH illumination with SETi 255 (duration 1 µs, delay 2 µs, and $V_{inj} = 5.4$ V).

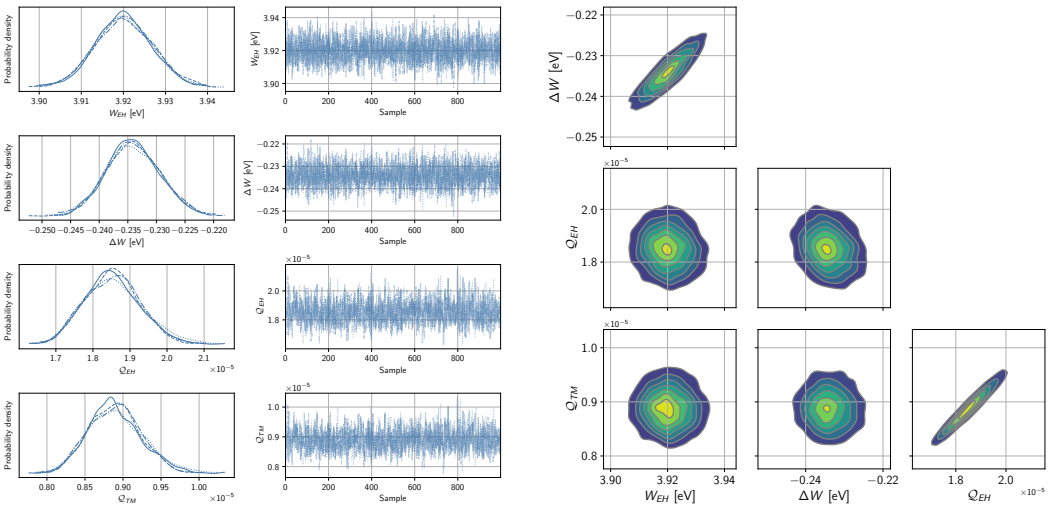

(A) Trace plot

(B) Pair plot

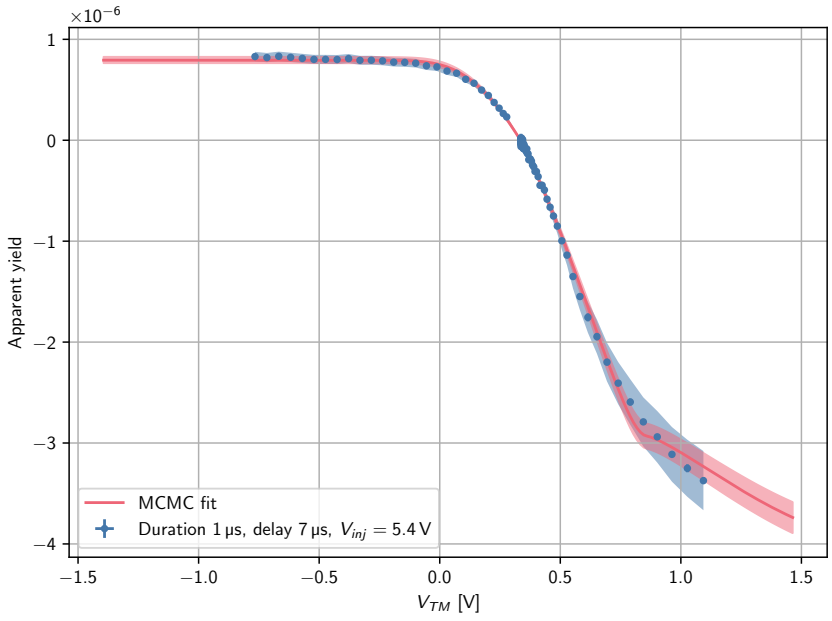

(C) Comparison between data and fit

FIGURE E.12: EH illumination with SETi 255 (duration 1 µs, delay 7 µs, and $V_{inj} = 5.4$ V).

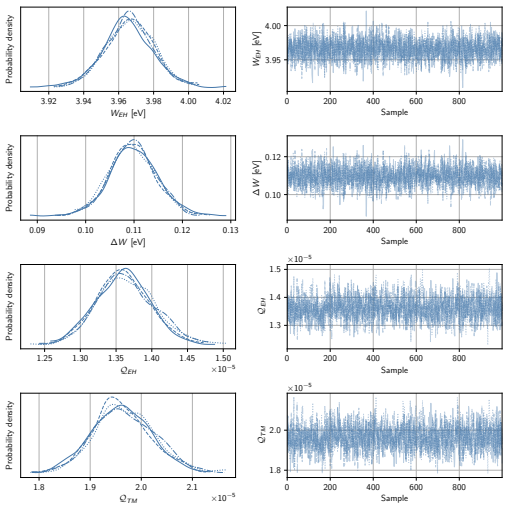

(A) Trace plot

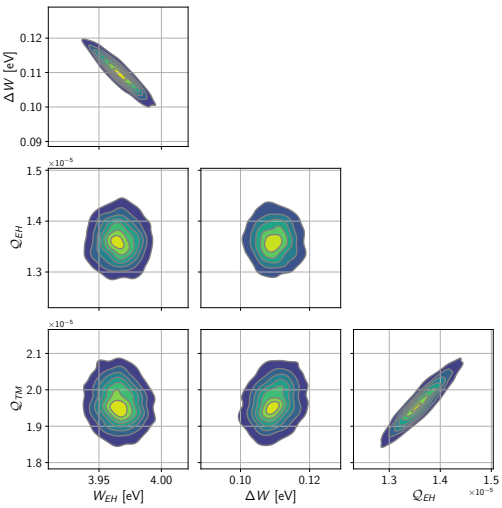

(B) Pair plot

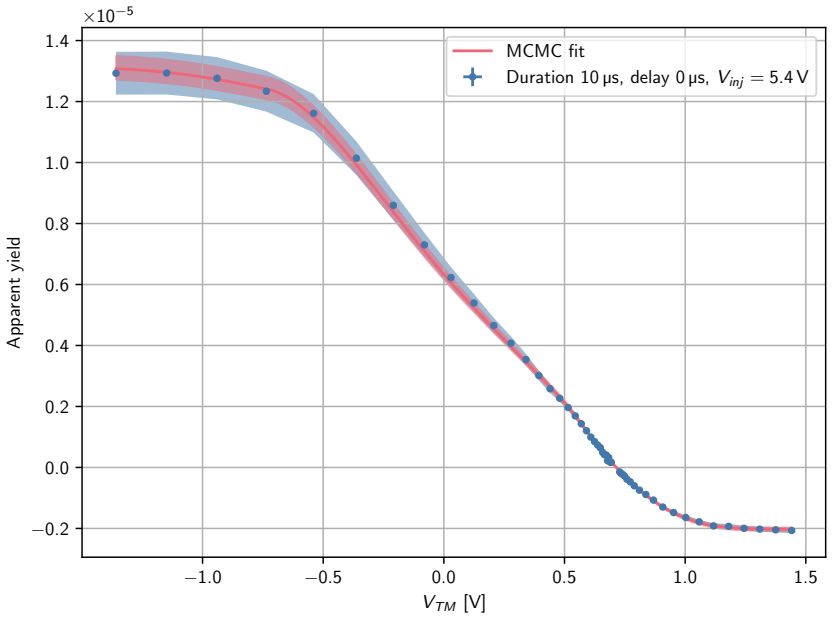

(C) Comparison between data and fit

FIGURE E.13: TM illumination with SETi 255 (duration 10 µs, delay 0 µs, and $V_{inj} = 5.4$ V).

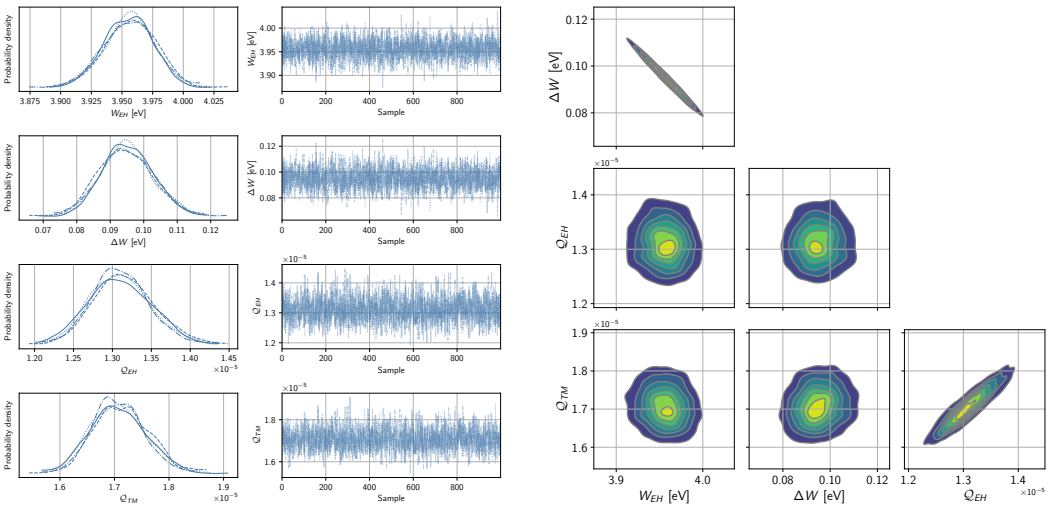

(A) Trace plot

(B) Pair plot

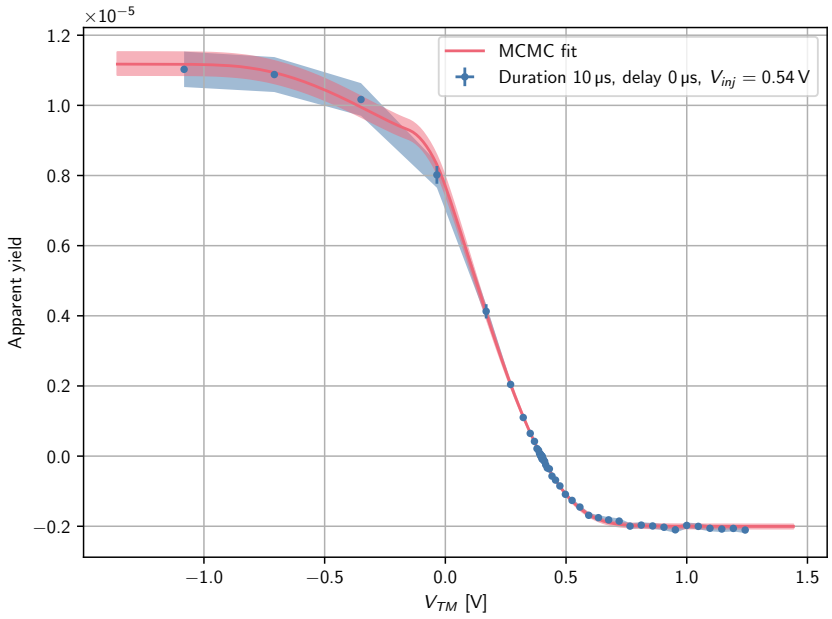

(C) Comparison between data and fit

FIGURE E.14: TM illumination with SETi 255 (duration 10 µs, delay 0 µs, and $V_{inj} = 0.54$ V).

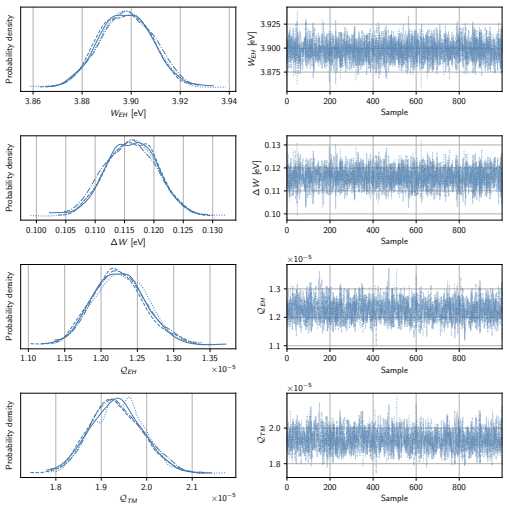

(A) Trace plot

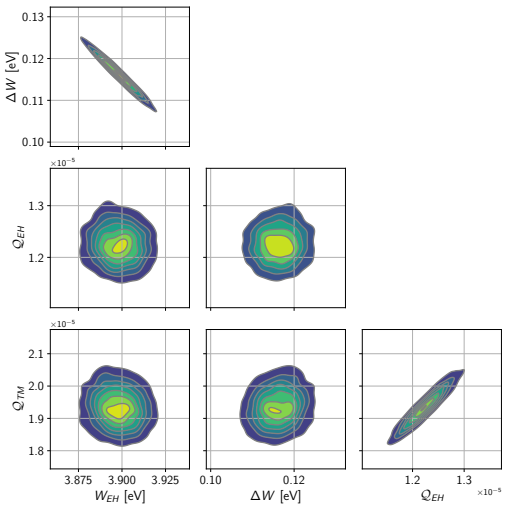

(B) Pair plot

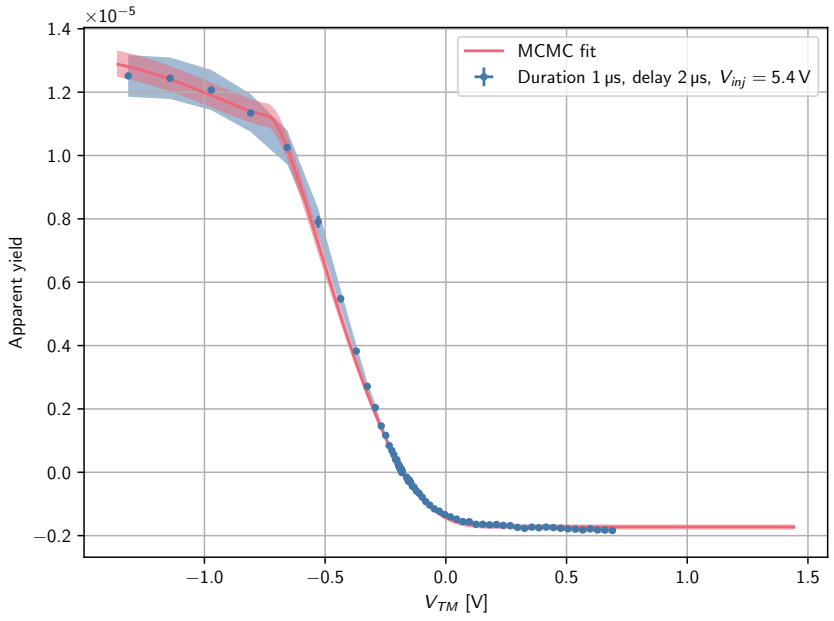

(C) Comparison between data and fit

FIGURE E.15: TM illumination with SETi 255 (duration 1 µs, delay 2 µs, and $V_{inj} = 5.4$ V).

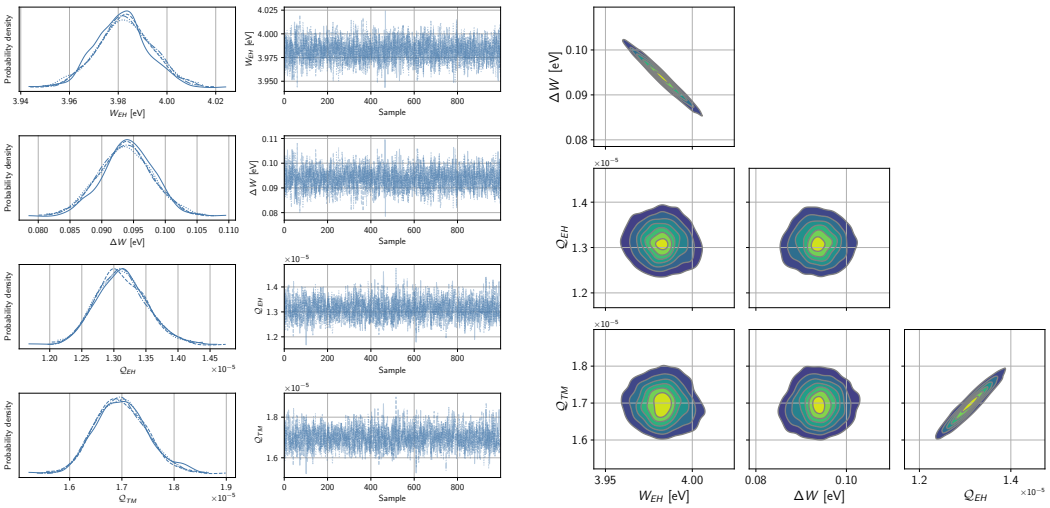

(A) Trace plot

(B) Pair plot

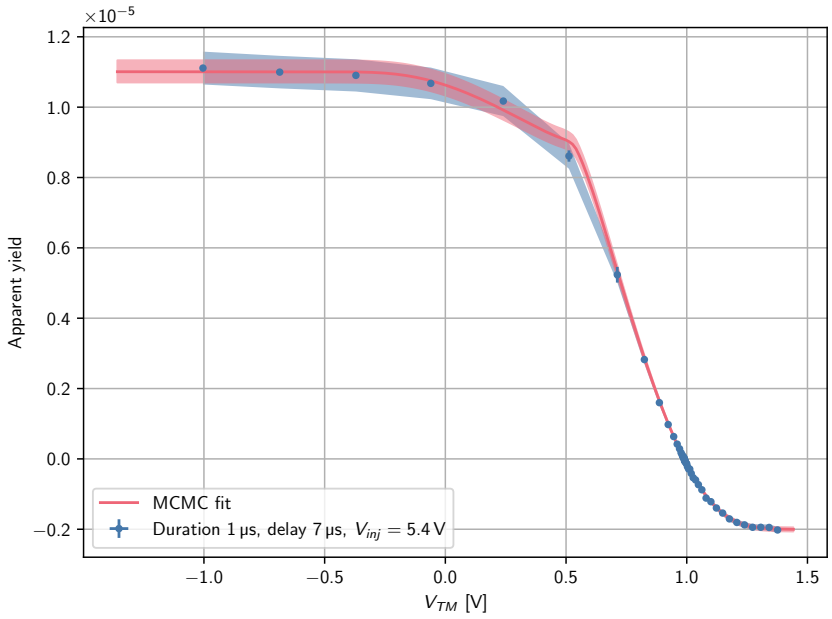

(C) Comparison between data and fit

FIGURE E.16: TM illumination with SETi 255 (duration 1 µs, delay 7 µs, and $V_{inj} = 5.4$ V).

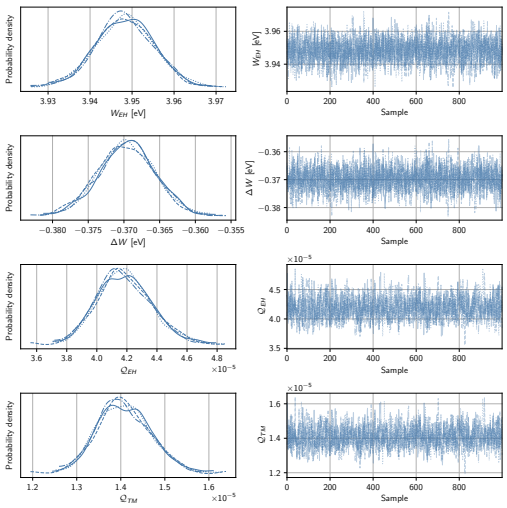

(A) Trace plot

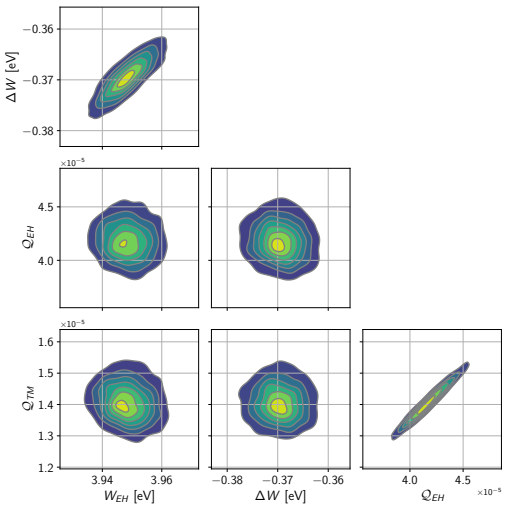

(B) Pair plot

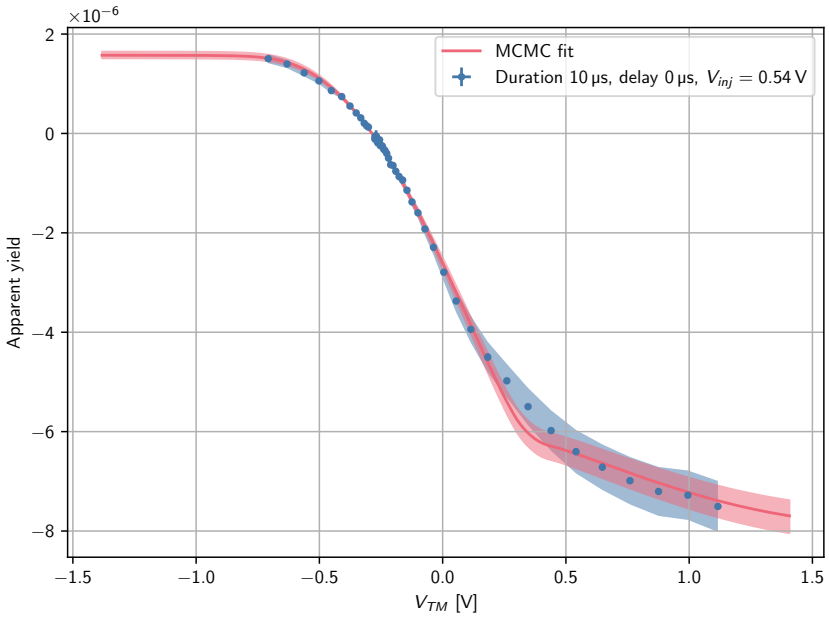

(C) Comparison between data and fit

FIGURE E.17: EH illumination with SETi 240 (duration 10 µs, delay 0 µs, and $V_{inj} = 0.54$ V).

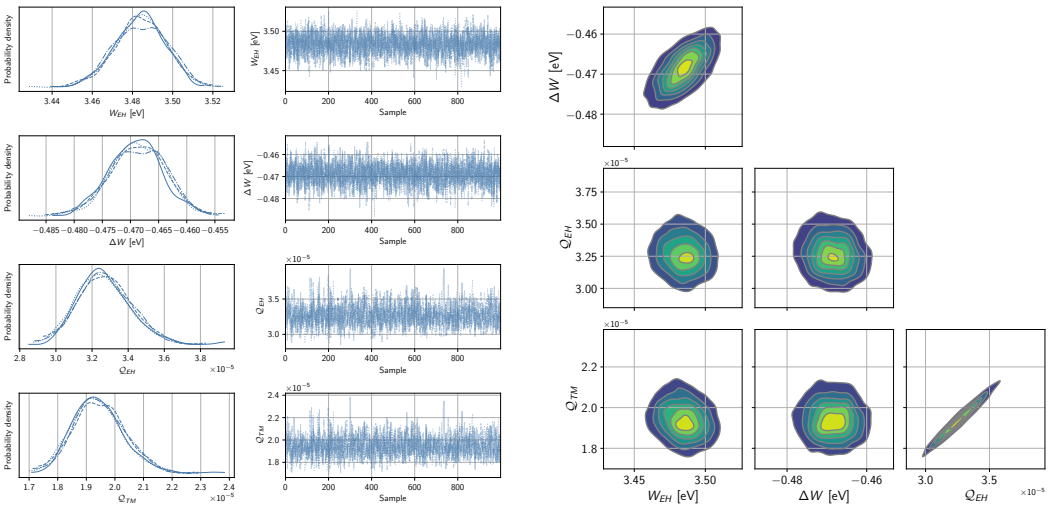

(A) Trace plot

(B) Pair plot

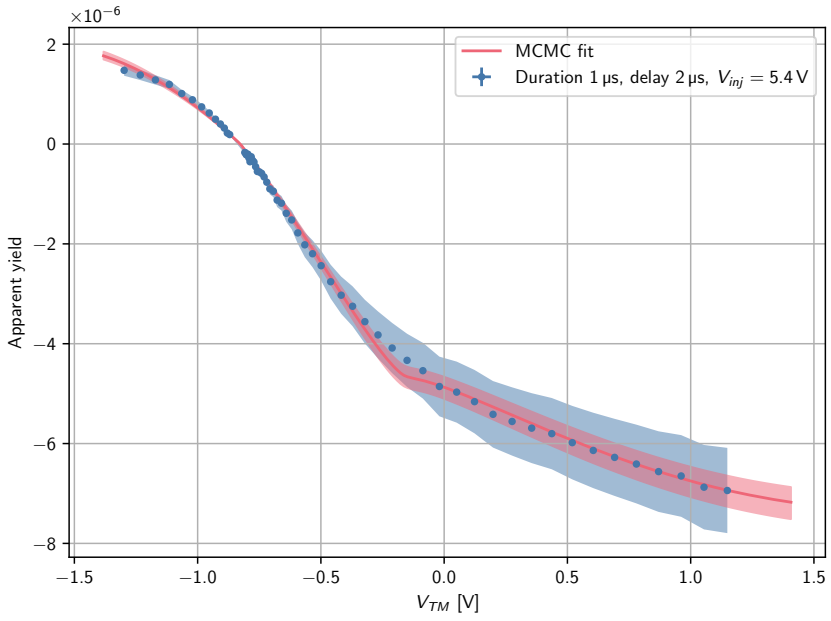

(C) Comparison between data and fit

FIGURE E.18: EH illumination with SETi 240 (duration 1 µs, delay 2 µs, and $V_{inj} = 5.4$ V).

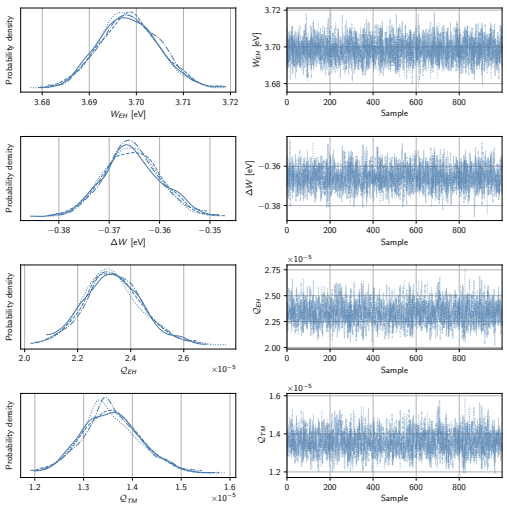

(A) Trace plot

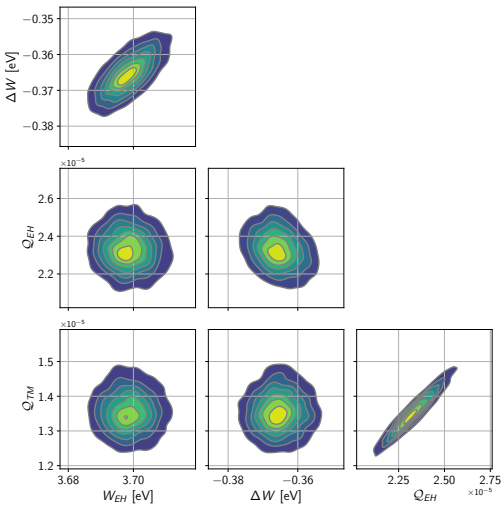

(B) Pair plot

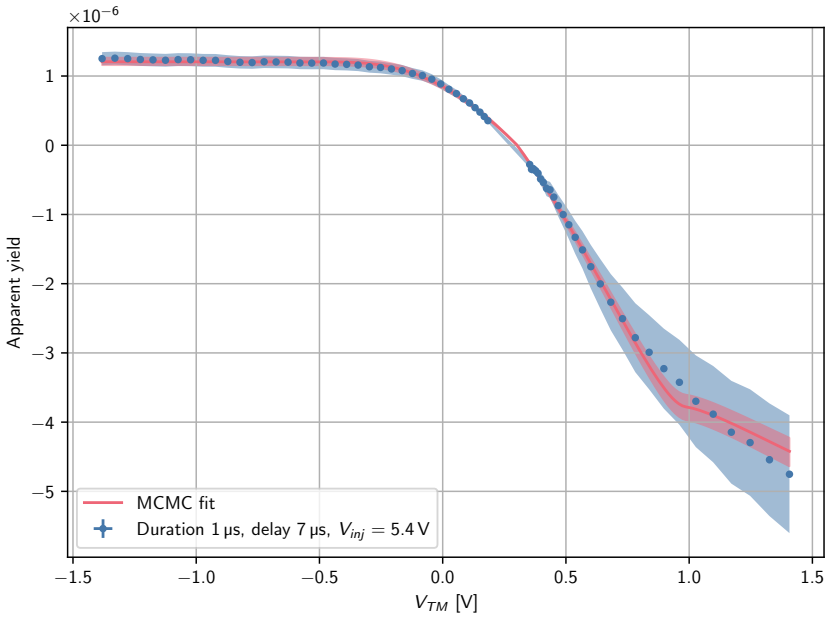

(C) Comparison between data and fit

FIGURE E.19: EH illumination with SETi 240 (duration 1 µs, delay 7 µs, and $V_{inj} = 5.4$ V).

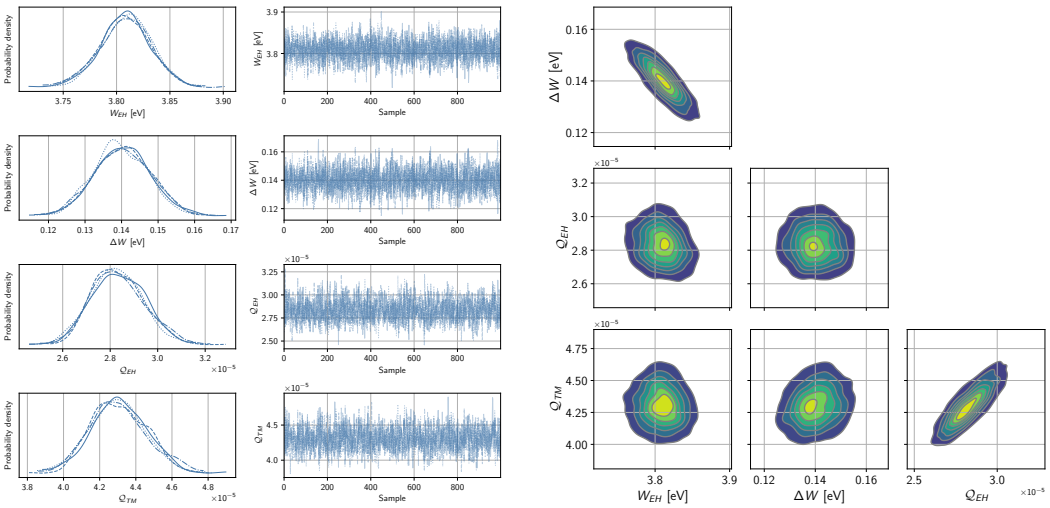

(A) Trace plot

(B) Pair plot

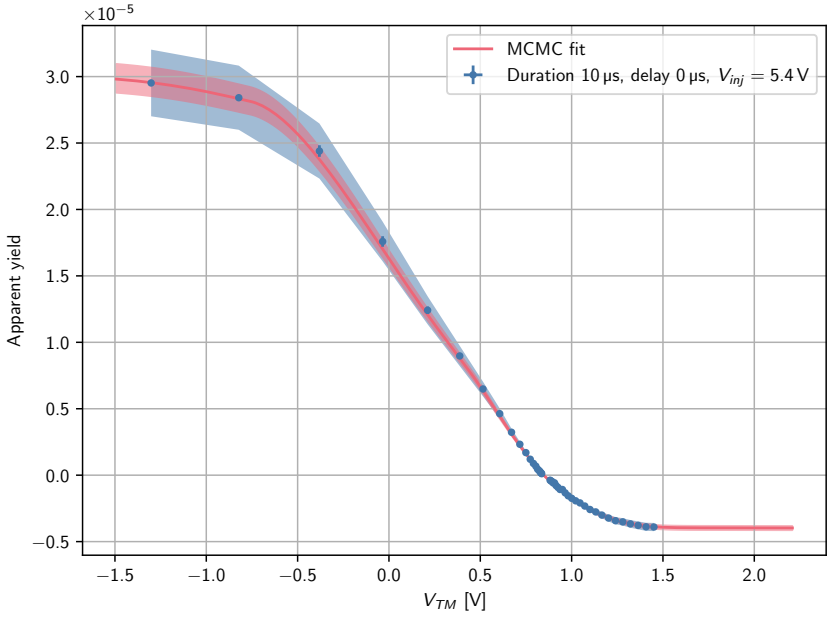

(C) Comparison between data and fit

FIGURE E.20: TM illumination with SETi 240 (duration 10 µs, delay 0 µs, and $V_{inj} = 5.4$ V).

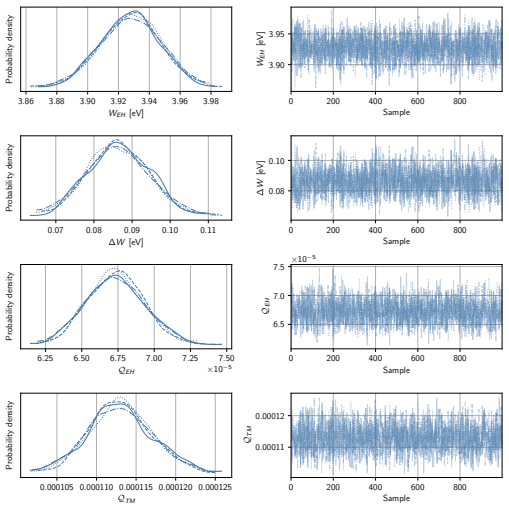

(A) Trace plot

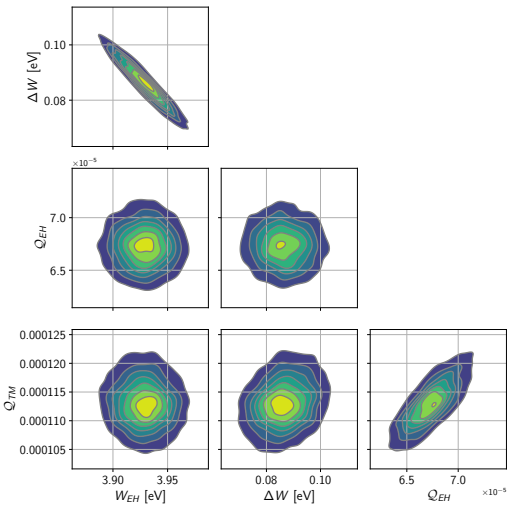

(B) Pair plot

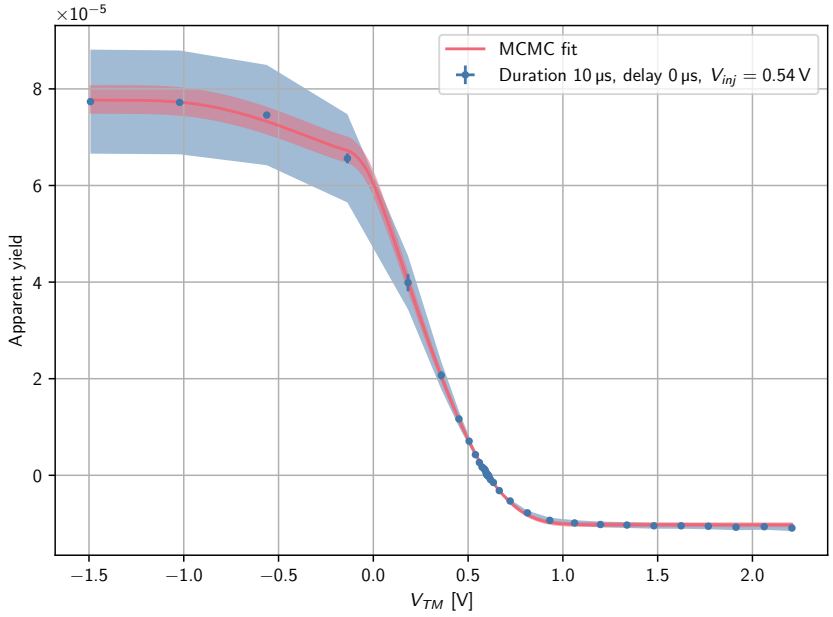

(C) Comparison between data and fit

FIGURE E.21: TM illumination with SETi 240 (duration 10 µs, delay 0 µs, and $V_{inj} = 0.54$ V).

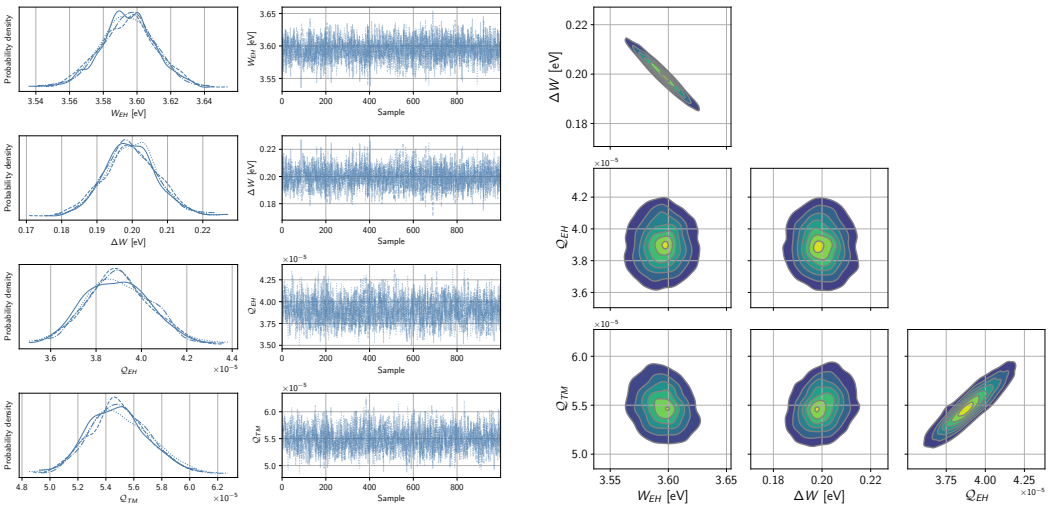

(A) Trace plot

(B) Pair plot

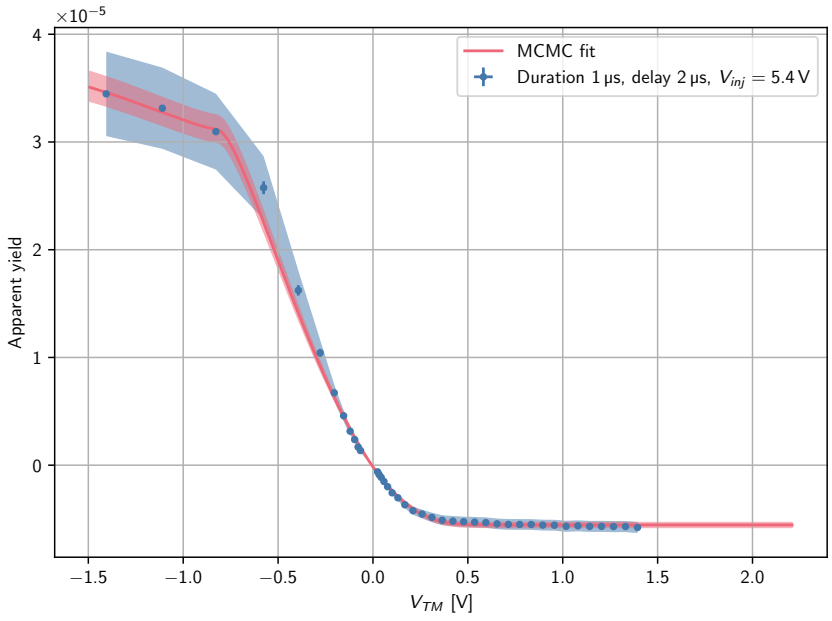

(C) Comparison between data and fit

FIGURE E.22: TM illumination with SETi 240 (duration 1 µs, delay 2 µs, and $V_{inj} = 5.4$ V).

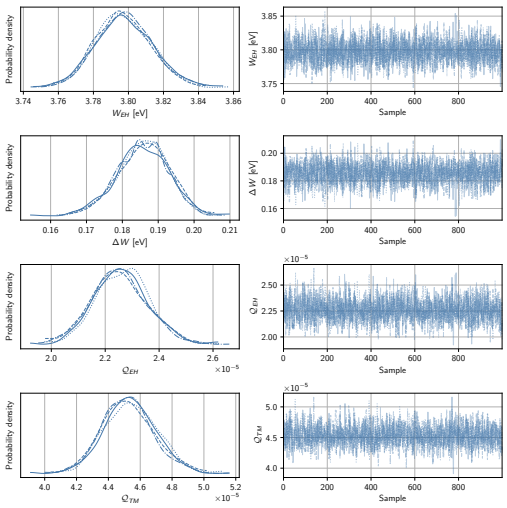

(A) Trace plot

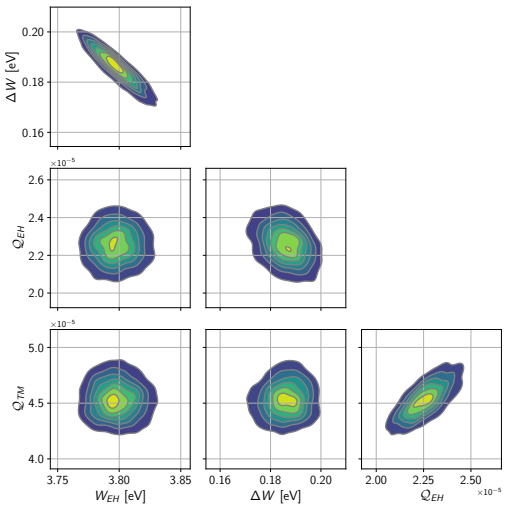

(B) Pair plot

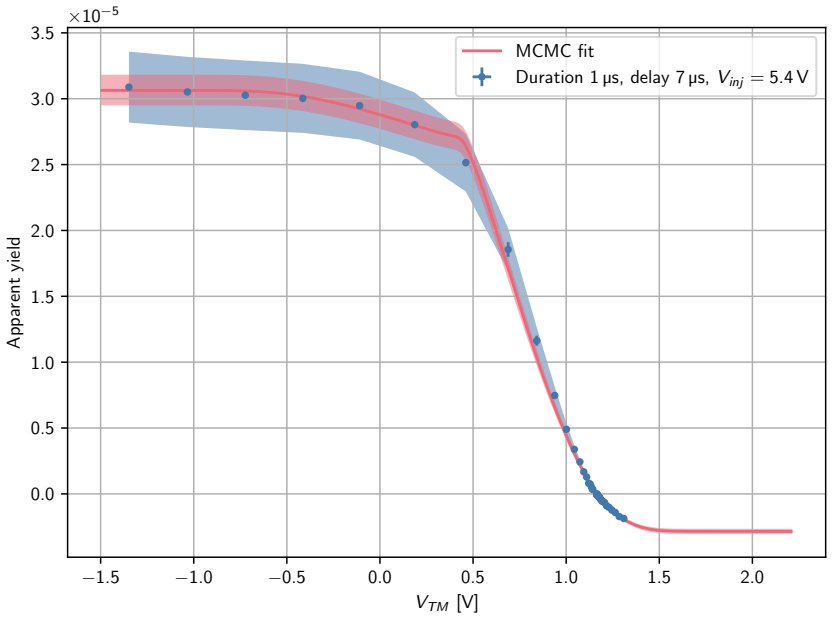

(C) Comparison between data and fit

FIGURE E.23: TM illumination with SETi 240 (duration 1 µs, delay 7 µs, and $V_{inj} = 5.4$ V).

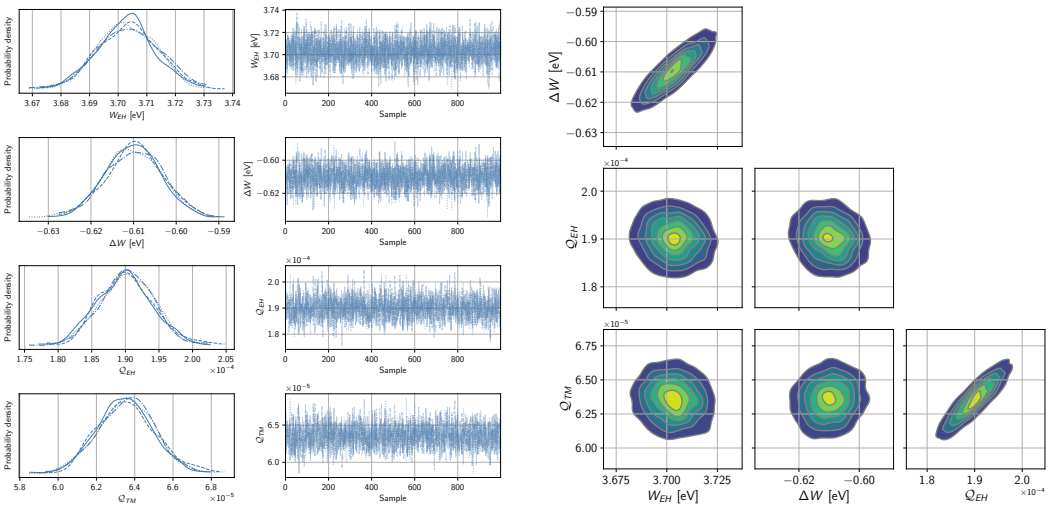

(A) Trace plot

(B) Pair plot

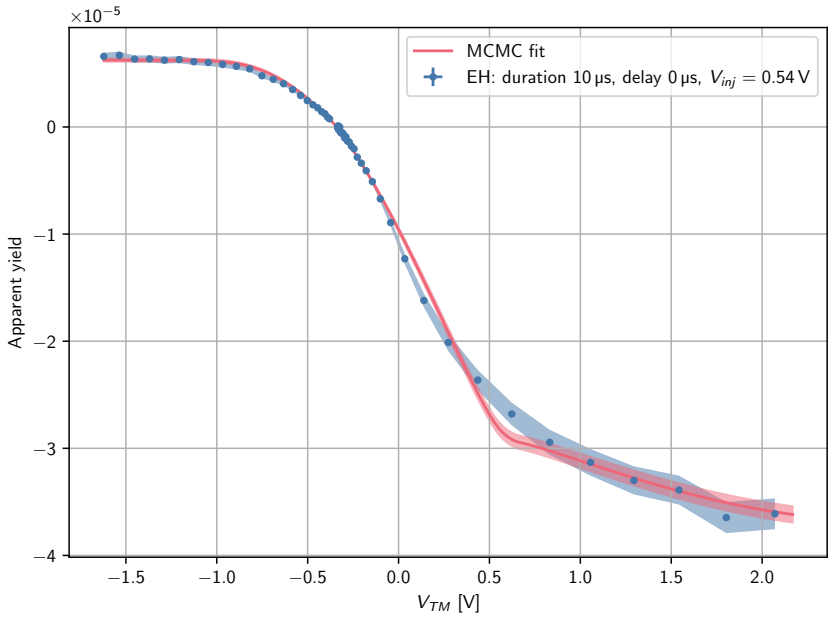

(C) Comparison between data and fit

FIGURE E.24: EH illumination with UVphotonics 230 (duration 10 µs, delay 0 µs, and $V_{inj} = 0.54$ V).

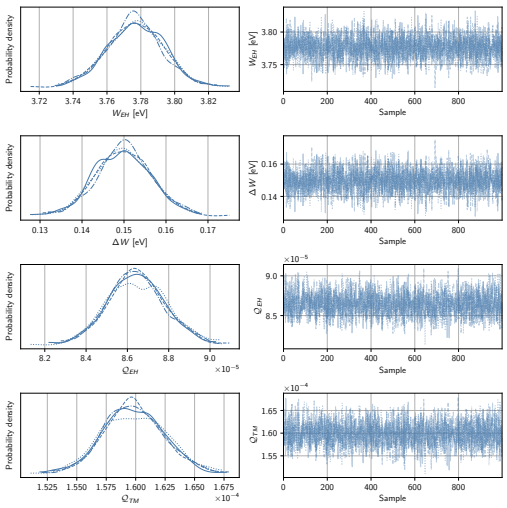

(A) Trace plot

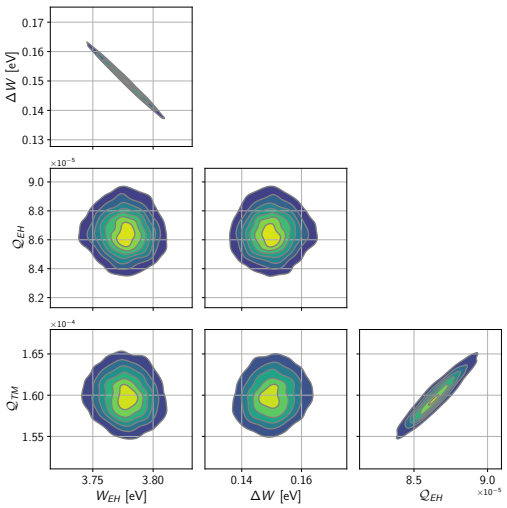

(B) Pair plot

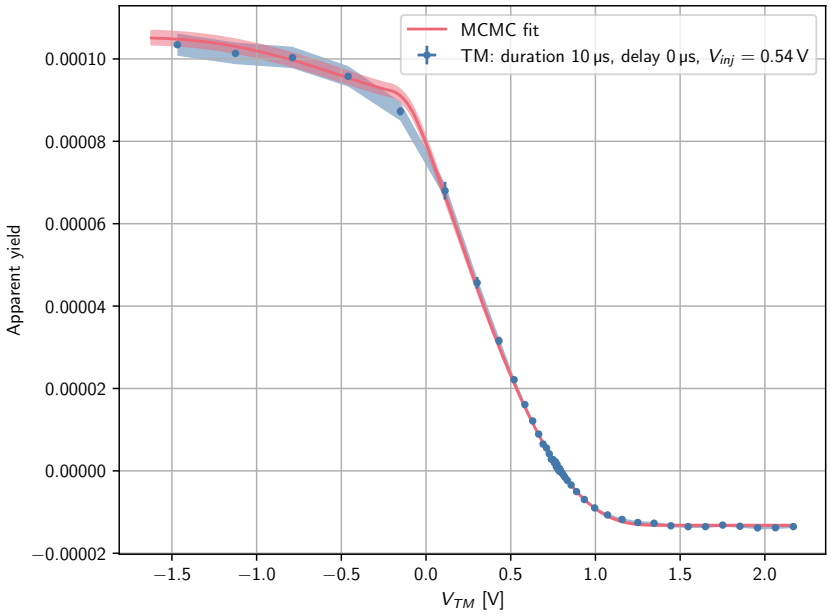

(C) Comparison between data and fit

FIGURE E.25: TM illumination with UVphotonics 230 (duration 10 µs, delay 0 µs, and $V_{inj} = 0.54$ V).

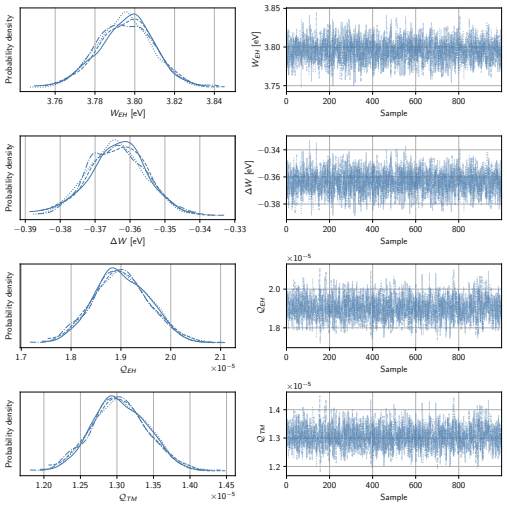

(A) Trace plot

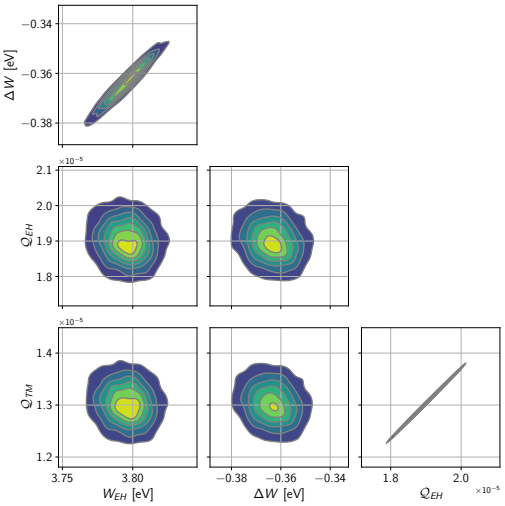

(B) Pair plot

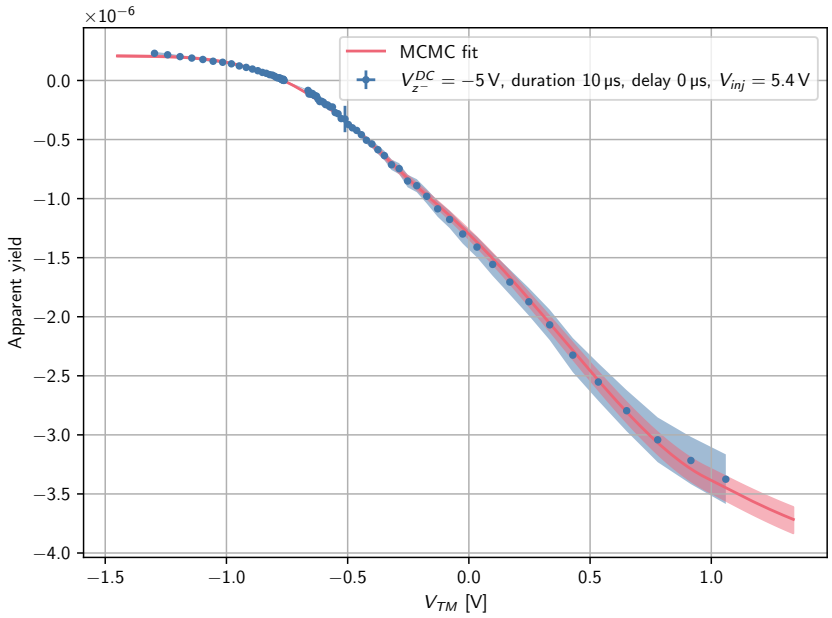

(C) Comparison between data and fit

FIGURE E.26: EH illumination with SETi 255 (duration 10 µs, delay 0 µs, and $V_{inj} = 5.4\,\mathrm{V}$) in the presence of DC actuation $V_{z_1^-} = V_{z_2^-} = -5\,\mathrm{V}$ and $V_{z_1^+} = V_{z_2^+} = +5\,\mathrm{V}$.

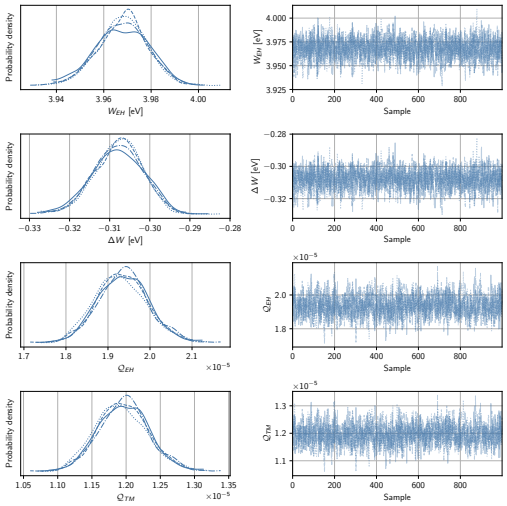

(A) Trace plot

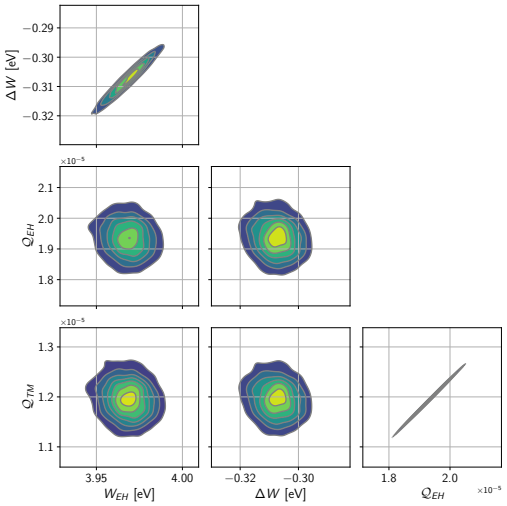

(B) Pair plot

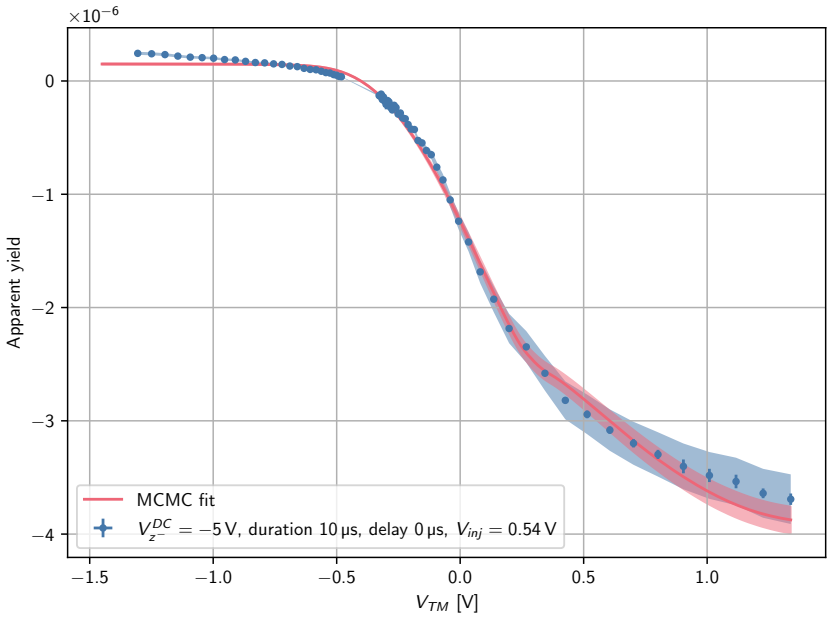

(C) Comparison between data and fit

FIGURE E.27: EH illumination with SETi 255 (duration 10 µs, delay 0 µs, and $V_{inj} = 0.54$ V) in the presence of DC actuation $V_{z_1^-} = V_{z_2^-} = -5$ V and $V_{z_1^+} = V_{z_2^+} = +5$ V..

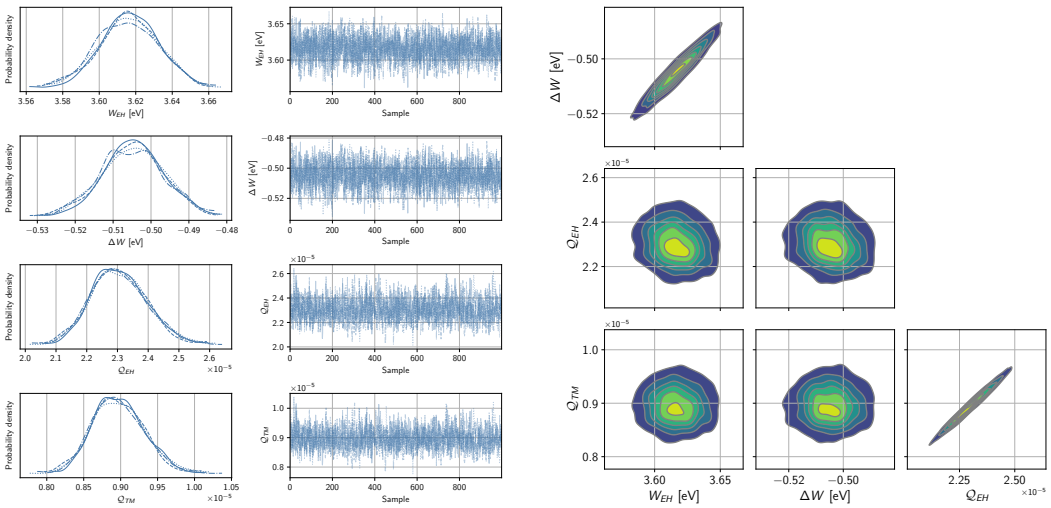

(A) Trace plot

(B) Pair plot

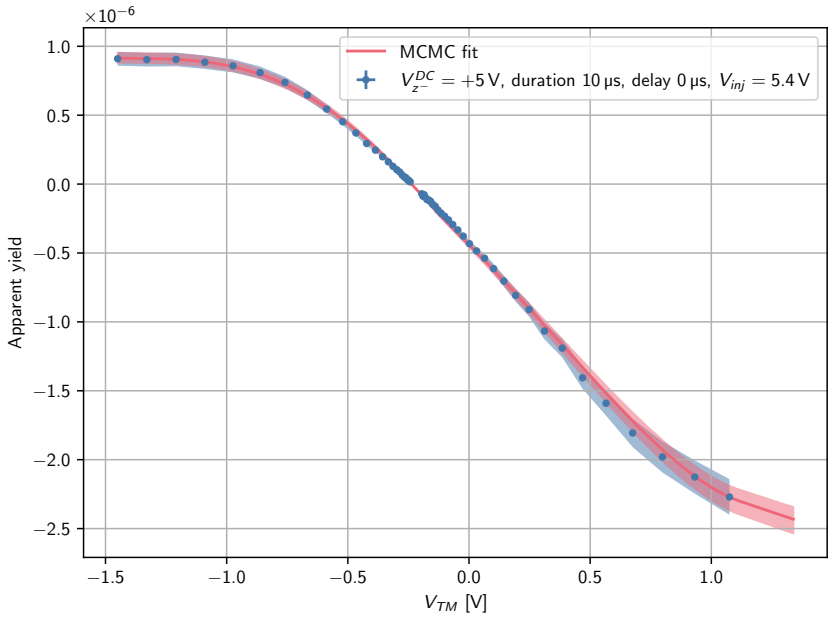

(C) Comparison between data and fit

FIGURE E.28: EH illumination with SETi 255 (duration 10 µs, delay 0 µs, and $V_{inj} = 5.4\,\mathrm{V}$) in the presence of DC actuation $V_{z_1^-} = V_{z_2^-} = +5\,\mathrm{V}$ and $V_{z_1^+} = V_{z_2^+} = -5\,\mathrm{V}$.

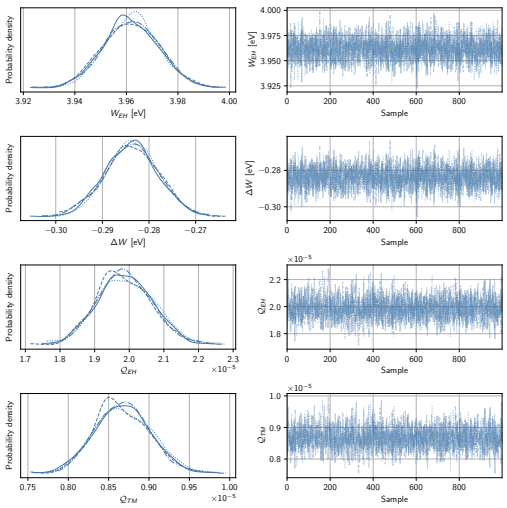

(A) Trace plot

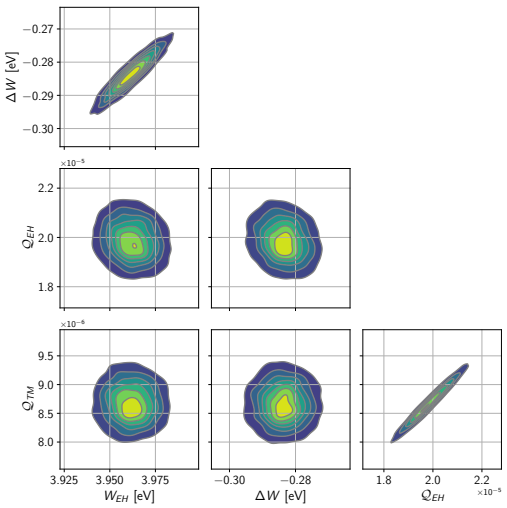

(B) Pair plot

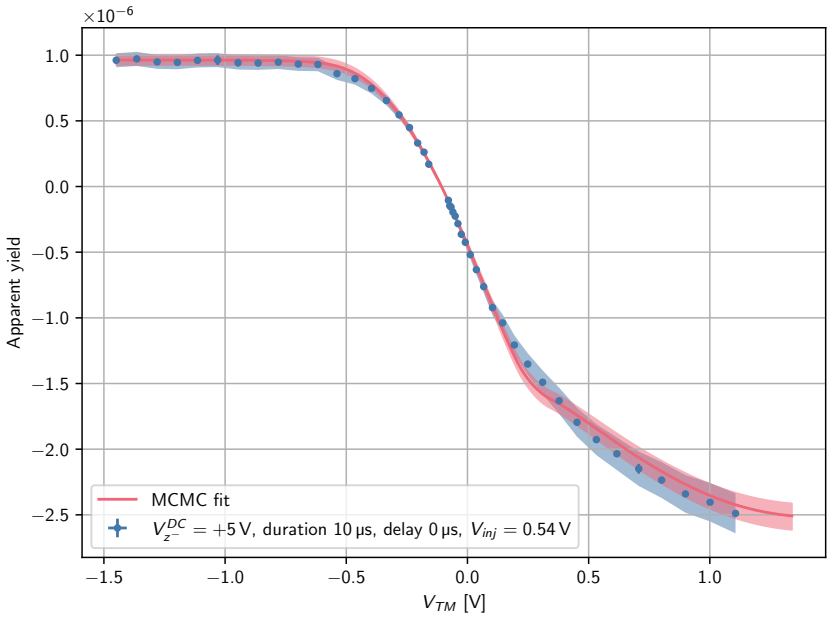

(C) Comparison between data and fit

FIGURE E.29: EH illumination with SETi 255 (duration 10 µs, delay 0 µs, and $V_{inj} = 0.54\,\mathrm{V}$) in the presence of DC actuation $V_{z_1^-} = V_{z_2^-} = +5\,\mathrm{V}$ and $V_{z_1^+} = V_{z_2^+} = -5\,\mathrm{V}$.

Appendix F

Statistical complements

F.1 Poisson processes

In this Section we will present the definition of *Poisson process* and some statistical properties, which have been used in our analyses. The main references for this Appendix are [73, 79]. As common for statistics textbooks, in this appendix we use the symbol $\sim$ with the meaning "distributed as".

F.1.1 Counting processes

A *stochastic*, or *random*, *process* is a collection of random variables indexed by a continuous parameter t, usually time, $\boldsymbol{N} = \{N(t), t \geq 0\}$.

Among all stochastic processes the *counting processes* are particularly important. Indeed, often it is needed to count the occurrences of some type of events which happen at random times, e.g. the number of clients entering in a shop, the number of photons hitting a detector, or the charges deposited on the LISA test masses.

Let us call t_i the time at which the ith occurrence of an event takes place. As the events happen at random times, the sequence $\{t_1, t_2, \ldots, t_n\}$, denoted shortly as $\{t_i\}$, is a random sequence. We assume that the arrival times are non-overlapping (i.e. $t_i \neq t_j$ if $i \neq j$), that is

$$t_0 < t_1 < t_2 \ldots t_n \to \infty \qquad \text{as} \qquad n \to \infty, \tag{F.1}$$

where t_0 is the time from which we start keeping track of the arrival of charges on the TM (we can assume without loss of generality that $t_0 = 0$, although we do not consider t_0 as an arrival time). We shall denote with $N(t)$ the number of arrivals in the interval $(0, t]$. As the arrival times are random, also $N(t)$ is a stochastic variable, which can be represented as

$$N(t) = \sum_{t_i < t} \Theta(t - t_i), \tag{F.2}$$

where $\Theta(\cdot)$ is the *Heaviside step function* (see Figure F.1).

Definition A random process $\{N(t), t \geq 0\}$ is a *counting process* if $N(t)$ is the number of event occurred from the origin of the time axis up to the time t (included). A counting process is characterized by values that are non-negative, integer, and non-decreasing. Hence we can assume

- $N(0) = 0$;
- $N(t) \in \{1, 2, 3, \ldots\}$, for all $t \in [0, +\infty)$;

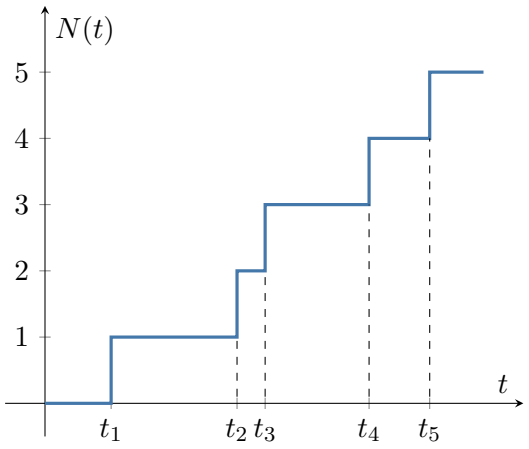

FIGURE F.1: Example of a counting process.

- If $s \leq t$ then $N(s) \leq N(t)$.

An obvious consequence of such definition is that if $0 \leq s < t$ the quantity $N(t) - N(s)$ corresponds to the number of events that occur in the time interval $[s, t)$.

In the following we will simplify the notation and indicate with just $N(t)$ a general counting process.

F.1.2 Definition of Poisson process

Let λ be a positive constant. A counting process $\{N(t), t \geq 0\}$ is called a *Poisson process* with rate λ if

- $N(0) = 0$;
- The increments are *independent*, i.e. the number of arrivals in any non-overlapping (disjoint) intervals are independent random variables;
- The number of events (or points) in any interval of length $\tau > 0$ is a Poisson random variable with parameter $\lambda\tau$.

The last property tells us that in a Poisson process the distribution of the number of arrivals in any interval depends only on its length and not on its exact location on the time axis. This means that Poisson processes are *stationary*, i.e. the random variable $N(t + \tau) - N(t)$ has the same distribution as $N(\tau) - N(0) = N(\tau)$ for any $t \geq 0$ and $\tau > 0$

$$N(t + \tau) - N(t) \sim N(\tau) \sim \text{Poi}(\lambda\tau) \tag{F.3}$$

F.1.3 Expected value and variance

The fact that the number of arrivals $N(t)$ follows a Poisson distribution with parameter λt implies that the expected value and the variance of a Poisson process are equal grow with time

$$N(t) \sim \text{Poi}(\lambda\tau) \quad \Longrightarrow \quad \mathbb{E}\{N(t)\} = \text{Var}\{N(t)\} = \lambda t \tag{F.4}$$

F.1.4 Auto-correlation

We can compute the auto-correlation of a Poisson process from the definition[1]

$$R_{NN}(t,s) = \mathbb{E}\{N(t)\,N(s)\} \tag{F.5}$$

Let us consider the case $t \geq s$ separately from the case $t < s$.

Case $t \geq s$

The definition of auto-correlation can be rewritten as

$$\begin{aligned} R_{NN}(t,s) &= \mathbb{E}\{[N(t) - N(s) + N(s)]\,N(t)\} \\ &= \mathbb{E}\left\{[N(t) - N(s)]\,N(s) + N^2(s)\right\} \end{aligned} \tag{F.6}$$

From the hypothesis of independence, we have that the random variable $N(s)$ is independent from $N(t) - N(s)$, because the time interval $[0, s)$ does not overlap with $[s, t)$. A nice property of independent random variables is that the expected value of their product is equal to the product of their respective expected values, i.e. $\mathbb{E}\{XY\} = \mathbb{E}\{X\}\,\mathbb{E}\{Y\}$ if X and Y are independent[2]

$$\begin{aligned} R_{NN}(t,s) &= \mathbb{E}\{[N(t) - N(s)]\}\,\mathbb{E}\{N(s)\} + \mathbb{E}\left\{N^2(s)\right\} \\ &= \mathbb{E}\{[N(t) - N(s)]\}\,\mathbb{E}\{N(s)\} + \mathbb{E}\{N(s)\}^2 + \mathrm{Var}\{N(s)\} \\ &= \lambda(t-s)\lambda s + \lambda^2 s^2 + \lambda s \\ &= \lambda^2 ts + \lambda s, \end{aligned} \tag{F.8}$$

where we used the definition of variance, i.e. $\mathbb{E}\left\{x^2\right\} = \mathbb{E}\{x\}^2 + \mathrm{Var}\{x\}$.

Case $t < s$

With a similar reasoning we can write the auto-correlation in the case $t < s$ as

$$\begin{aligned} R_{NN}(t,s) &= \mathbb{E}\{N(t)\,[N(s) - N(t) + N(t)]\} \\ &= \mathbb{E}\left\{N(t)\,[N(s) - N(t)] + N^2(t)\right\} \end{aligned} \tag{F.9}$$

In this case we have that the time interval $(t, s]$ does not overlap with $(0, t]$, hence the counts $N(s) - N(t)$ and $N(t)$ are independent. Therefore

$$\begin{aligned} R_{NN}(t,s) &= \mathbb{E}\{N(t)\}\,\mathbb{E}\{[N(s) - N(t)]\} + \mathbb{E}\left\{N^2(t)\right\} \\ &= \mathbb{E}\{N(t)\}\,\mathbb{E}\{[N(s) - N(t)]\} + \mathbb{E}\{N(t)\}^2 + \mathrm{Var}\{N(t)\} \\ &= \lambda t\lambda(s-t) + \lambda^2 t^2 + \lambda t \\ &= \lambda^2 ts + \lambda t \end{aligned} \tag{F.10}$$

[1] The definition of auto-correlation is actually $R_{XX}(t,s) = \mathbb{E}\{X(t)\,X^*(s)\}$, where the star indicates the complex conjugate. However, since we are considering *real* stochastic processes, we can drop the operation of complex conjugation.

[2] This follows immediately from the fact that the joint-probability distribution function of two independent random variables X and Y can be factorized $f_{XY}(x,y) = f_X(x) f_Y(x)$, hence

$$\mathbb{E}\{XY\} = \iint xy f_{XY}(x,y)\,\mathrm{d}x\,\mathrm{d}y = \int x f_X(x)\,\mathrm{d}x \cdot \int y f_Y(y)\,\mathrm{d}y = \mathbb{E}\{X\}\,\mathbb{E}\{Y\}. \tag{F.7}$$

General expression

If we combine (F.8) and (F.10), we can obtain the general expression

$$R_{NN}(t,s) = \lambda^2 ts + \lambda \min(t,s) \tag{F.11}$$

As the expression for the auto-correlation is not invariant for shifts in the origin of the time coordinate, i.e. $R_{NN}(t,s) \neq R_{NN}(t-s)$, we conclude that the Poisson process is not stationary.

F.1.5 Power spectrum of a Poisson process

In a strict mathematical sense, it does not make sense to talk about the power spectrum of a Poisson process, since it is not a *wide-sense stationary* (WSS) process[3]. We can be convinced of the non-stationarity of the Poisson process by simply noticing that its expected value is not constant but it depends on time (F.4).

On the other hand, it makes sense to compute the power spectral density of the time derivative of a Poisson process, which is usually referred to as *shot noise* [80]

$$S(t) = \frac{\mathrm{d}N(t)}{\mathrm{d}t} = \frac{\mathrm{d}}{\mathrm{d}t}\left[\sum_i \Theta(t-t_i)\right] = \sum_i \delta(t-t_i) \tag{F.12}$$

where $\Theta(\cdot)$ is the *Heaviside step function*. In the last passage we used the fact that the derivative of the step function is the Dirac's delta, i.e.

$$\frac{\mathrm{d}\Theta(x)}{\mathrm{d}x} = \delta(x). \tag{F.13}$$

Since the differentiation is a linear operator[4], we can write

$$\mathbb{E}\{S(t)\} = \mathbb{E}\left\{\frac{\mathrm{d}N(t)}{\mathrm{d}t}\right\} = \frac{\mathrm{d}}{\mathrm{d}t}\mathbb{E}\{N(t)\} = \frac{\mathrm{d}(\lambda t)}{\mathrm{d}t} = \lambda \tag{F.15}$$

Analogously for the auto-correlation of the shot noise, we can write

$$\begin{aligned} R_{SS}(t,s) &= \mathbb{E}\{S(t)S(s)\} \\ &= \mathbb{E}\left\{\frac{\mathrm{d}N(t)}{\mathrm{d}t}\frac{\mathrm{d}N(s)}{\mathrm{d}s}\right\} \\ &= \frac{\mathrm{d}}{\mathrm{d}t}\left(\frac{\mathrm{d}}{\mathrm{d}s}\mathbb{E}\{N(t)\,N(s)\}\right) \\ &= \frac{\partial}{\partial t}\frac{\partial R_{NN}(t,s)}{\partial s}, \end{aligned} \tag{F.16}$$

[3] A stochastic process is *strict-sense stationary* (SSS) if all its statistical properties do not change for shifts of the time axis. A stochastic process is *wide-sense stationary* (WSS) if its expected value and auto-correlation do not change for shifts of the time axis. In order to define the power spectrum of a stochastic process it is required to be at least wide-sense stationary.

[4] A fundamental lemma in statistics is that the expected value $\mathbb{E}\{\cdot\}$ commutes with any *linear operator* L, i.e.

$$\mathbb{E}\{L(x)\} = L(\mathbb{E}\{x\}). \tag{F.14}$$

where used the linearity of the differentiation and the expected value. If we remember the expression for the auto-correlation of the Poisson process (F.11), we have

$$\begin{aligned} R_{SS}(t,s) &= \frac{\partial}{\partial t}\frac{\partial}{\partial s}\left[\lambda^2 ts + \lambda \min(t,s)\right] \\ &= \begin{cases} \frac{\partial}{\partial t}\left(\lambda^2 t + \lambda\right), & \text{if } t \geq s \\ \frac{\partial}{\partial t}\left(\lambda^2 t\right), & \text{if } t < s \end{cases} \\ &= \frac{\partial}{\partial t}\left[\lambda^2 t + \lambda\Theta(t-s)\right]. \end{aligned} \tag{F.17}$$

If we now use the fact that the derivative of the step function is the Dirac's delta, equation (F.17) becomes

$$R_{SS}(t,s) = \lambda^2 + \lambda\delta(t-s) \tag{F.18}$$

We conclude that the shot noise $S(t)$ is a wide-sense stationary (WSS) process because its mean does not depend on time and its autocorrelation is independent on shifts of the time axis, i.e. it depends only on the time delay between the temporal points considered $R_{SS}(t,s) = R_{SS}(t-s)$. Therefore, we can compute the two-sided power spectrum of shot noise, which is the Fourier transform of its auto-correlation function

$$\begin{aligned} S_{SS}(\omega) &= \mathcal{F}\left\{R_{SS}(\tau)\right\} \\ &= \int_{-\infty}^{+\infty} R_{SS}(\tau)\, e^{-\mathrm{i}\omega\tau}\,\mathrm{d}\tau \\ &= \int_{-\infty}^{+\infty} \left[\lambda^2 + \lambda\delta(\tau)\right] e^{-\mathrm{i}\omega\tau}\,\mathrm{d}\tau \\ &= 2\pi\lambda^2\delta(\omega) + \lambda \end{aligned} \tag{F.19}$$

The power spectral density of shot noise is white, i.e. independent of frequency, except for a line at zero frequency (inaccessible by real-life experiments).

Although the power spectrum is well defined only for wide-sense stationary stochastic processes, we can still try to obtain an expression for the PSD of Poisson processes.

As a Poisson process is just the integral of shot noise, we can obtain its two-sided power spectral density as[5]

$$S_{NN}(\omega) = \frac{S_{SS}(\omega)}{|\mathrm{i}\omega|^2} = \frac{2\pi\lambda^2\delta(\omega) + \lambda}{\omega^2} \xrightarrow[\omega\neq 0]{} \frac{\lambda}{\omega^2} \qquad \text{(two-sided)} \tag{F.22}$$

In the last passage we neglected the term proportional to the Dirac's delta (relevant only at zero frequency). Despite our quite unorthodox derivation, the expression for the PSD of a Poisson process with rate λ is accurate, as the reader can prove with a numerical simulation.

[5] We use here the fact that the transfer function of an integrator is $H(\omega) = \frac{1}{\mathrm{i}\omega}$. One way to prove this is by observing that the integral of a Dirac's delta is the Heaviside step function, whose respective Fourier transforms are

$$\mathcal{F}\left\{\delta(t)\right\}(\omega) = 1 \qquad \text{and} \qquad \mathcal{F}\left\{\Theta(t)\right\}(\omega) = \pi\delta(\omega) + \frac{1}{\mathrm{i}\omega}. \tag{F.20}$$

The transfer function of the integral operator can be obtained divinding the Fourier transform of the output (the step function) by the Fourier transform of the input (the Dirac's delta), i.e.

$$H(\omega) = \frac{\mathcal{F}\left\{\Theta(t)\right\}(\omega)}{\mathcal{F}\left\{\delta(t)\right\}(\omega)} = \pi\delta(\omega) + \frac{1}{i\omega} \xrightarrow[\omega\neq 0]{} \frac{1}{\mathrm{i}\omega}, \tag{F.21}$$

where, in the last passage, we neglected the term containing the Dirac's delta (relevant only at DC).

Comment for processes with event multiplicity In the derivation above we assumed that each event in the Poisson process carries just an unit increment, but it can be simply generalized to processes with any multiplicity $j \in \mathbb{Z}$. It is just necessary to observe that a Poisson process $N_j(t)$ with event multiplicity j can be interpreted as a Poisson process with unit increments multiplied by the constant j, i.e.

$$N_j(t) = jN(t) \tag{F.23}$$

Hence, the auto-correlation in this case can be written as

$$\begin{aligned} R_{N_j N_j}(t,s) &= \mathbb{E}\left\{N_j(t)\, N_j(s)\right\} \\ &= \mathbb{E}\left\{jN(t)\, jN(s)\right\} \\ &= j^2\mathbb{E}\left\{N(t)\, N(s)\right\} \\ &= j^2 R_{NN}(t,s) \\ &= j^2\left[\lambda^2 ts + \lambda \min(t,s)\right] \end{aligned} \tag{F.24}$$

where we used (F.11). If we repeat the calculation presented previously, we have that the two-sided power spectral density of the associated shot noise is

$$S_{S_j S_j}(\omega) = 2\pi j^2\lambda^2\delta(\omega) + j^2\lambda \qquad \text{(two-sided)} \tag{F.25}$$

whereas the two-sided PSD of the Poisson process with event multiplicity j is

$$S_{N_j N_j}(\omega) = \frac{j^2\lambda}{\omega^2} \qquad \text{(two-sided)} \tag{F.26}$$

F.1.6 Thinning theorem

In this section we will prove that if we select points from a Poisson process according to the outcome of a Bernoulli random variable, we generate a new Poisson process. In other words, the Poisson processes are *closed* to random draws according to a Bernoulli variable.

This is a known result (actually it is a special case of the more general *Thinning theorem*) and we will present it here only for the sake of completeness.

Suppose that we have a Poisson process with rate λ. By definition, the number of events N in any interval of length t is a random variable that follows a Poisson distribution with parameter λt. Therefore, the probability of counting $n \in \mathbb{N}$ events in the time window of duration t is

$$\mathcal{P}_{\mathrm{Poi}(\lambda t)}\left\{N(t) = n\right\} = \frac{(\lambda t)^n}{n!} e^{-\lambda t}. \tag{F.27}$$

Let us consider now the child stochastic process obtained by extracting points from the initial Poisson process according to the outcome of a Bernoulli trial with success probability $\eta \in [0,1]$. The probability of measuring $d \leq n$ events in the time window of length t can be computed as

$$\mathcal{P}\left\{N(t) = d\right\} = \sum_{n=d}^{\infty} \mathcal{P}_{\mathrm{Poi}(\lambda t)}\left\{N(t) = n\right\} \cdot \mathcal{P}_{\mathrm{Bin}(\eta)}\left\{d, n\right\}. \tag{F.28}$$

where we used the fact that the probability of having d successes in n independent Bernoulli trials is the given Binomial distribution $\mathcal{P}_{\mathrm{Bin}(\eta)}\{d, n\}$, which reads

$$\mathcal{P}_{\mathrm{Bin}(\eta)}\{d, n\} = \binom{n}{d}\eta^d(1-\eta)^{n-d} = \frac{n!}{d!(n-d)!}\eta^d(1-\eta)^{n-d} \tag{F.29}$$

which gives the probability of having d successes in n trials each one with success probability equal to η.

If we substitute (F.27) and (F.29) into (F.28), we have

$$\begin{aligned}\mathcal{P}\{N(t) = d\} &= \sum_{n=d}^{\infty} \frac{(\lambda t)^n}{n!}e^{-\lambda t}\frac{n!}{d!(n-d)!}\eta^d(1-\eta)^{n-d} \\ &= \sum_{n=d}^{\infty} \frac{(\lambda\eta t)^n}{d!(n-d)!}\eta^{d-n}(1-\eta)^{n-d}e^{-\lambda t}\end{aligned} \tag{F.30}$$

We can now define $k = n - d$, so that the previous equation becomes

$$\begin{aligned}\mathcal{P}\{N(t) = d\} &= \sum_{k=0}^{\infty} \frac{(\lambda\eta t)^{k+d}}{d!k!}\eta^{-k}(1-\eta)^k e^{-\lambda t} \\ &= \frac{(\lambda\eta t)^d}{d!}e^{-\lambda t}\cdot\sum_{k=0}^{\infty}\left(\frac{1-\eta}{\eta}\right)^k\frac{(\lambda\eta t)^k}{k!} \\ &= \frac{(\lambda\eta t)^d}{d!}e^{-\lambda t}\cdot\sum_{k=0}^{\infty}\frac{(\lambda t - \lambda\eta t)^k}{k!}\end{aligned} \tag{F.31}$$

We notice that the series corresponds to the Taylor expansion of $e^{\lambda t - \lambda\eta t}$, therefore we have

$$\begin{aligned}\mathcal{P}\{N(t) = d\} &= \frac{(\lambda\eta t)^d}{d!}e^{-\lambda t}\cdot e^{\lambda t - \lambda\eta t} \\ &= \frac{(\lambda\eta t)^d}{d!}\cdot e^{-\lambda\eta t} \\ &= \mathcal{P}_{\mathrm{Poi}(\lambda\eta t)}\{N(t) = d\},\end{aligned} \tag{F.32}$$

which is indeed a Poisson process with reduced rate $\lambda\eta$.

This property can be also verified with a simple simulation, as shown in Figure F.2.

F.1.7 Merging of independent Poisson processes

Let $N_1(t)$ and $N_2(t)$ be two independent Poisson processes with rates λ_1 and λ_2 respectively. We can define the process $N(t)$ as

$$N(t) = N_1(t) + N_2(t). \tag{F.33}$$

More precisely, $N(t)$ is the counting process obtained combining the arrivals of $N_1(t)$ and $N_2(t)$. The hypothesis is that $N(t)$ is still a Poisson process with rate $\lambda = \lambda_1 + \lambda_2$.

Proof Let us notice that if $N_1(t)$ and $N_2(t)$ are Poisson processes we have that

$$N(0) = N_1(0) + N_2(0) = 0 + 0 = 0. \tag{F.34}$$

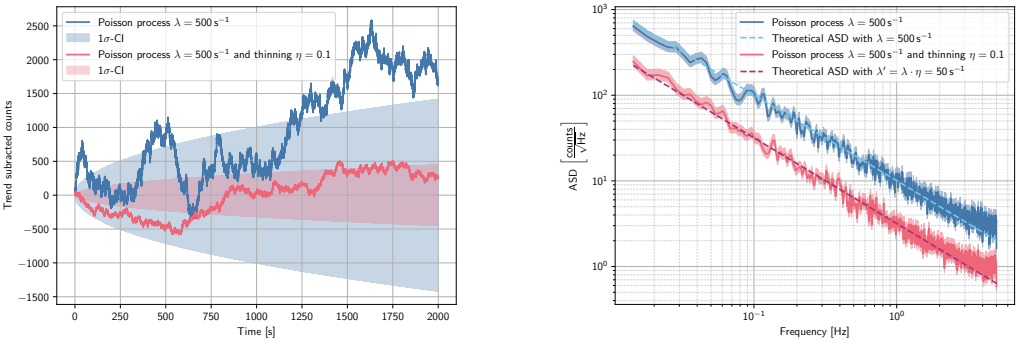

(A) Simulated timeseries after trend subtraction (B) Amplitude spectral density of the timeseries

FIGURE F.2: *Right:* the blue line is a timeseries of a Poisson process with rate λ, whereas the red line is obtained thinning the previous Poisson by extracting points according to the outcome of a Bernoulli random variable with success probability η. In this picture we subtracted for clarity the linear trend from the two timeseries. The colored band correspond to the 1σ-confidence. *Left:* we compute the amplitude spectral density of the simulated timeseries. We see a good agreement between the experimental data an the theoretical spectra (except for some aliasing close to the Nyquist frequency).

Secondly, since $N_1(t)$ and $N_2(t)$ are independent between each other and both have independent increments, we must have that also $N(t)$ has independent increments.

Finally, let us consider a time interval of length τ, such as $I = [t_0, t_0 + \tau)$ for any t_0. The number of arrivals in the interval I associated with the processes $N_1(t)$ and $N_2(t)$ are respectively

$$N_1(t) \sim \text{Poi}(\lambda_1 \tau) \quad \text{and} \quad N_2(t) \sim \text{Poi}(\lambda_2 \tau) \tag{F.35}$$

and they are independent. The number of arrivals in I for the stochastic process $N(t)$ will be

$$N(t) \sim \text{Poi}(\lambda_1 \tau) + \text{Poi}(\lambda_2 \tau) = \text{Poi}(\lambda_1 \tau + \lambda_2 \tau) \tag{F.36}$$

where we used the fact that the sum of independent Poisson random variables is still Poisson with parameter equal to the sum of their respective parameters.

Proof The probability of finding $N(\tau) = n$ is given by

$$\begin{aligned} \mathcal{P}\{N(\tau) = n\} &= \sum_{n_1=0}^{n} \mathcal{P}_{N_1(\tau)N_2(\tau)}\{N_1(\tau) = n_1, N_2(\tau) = n - n_1\} \\ &= \sum_{n_1=0}^{n} \mathcal{P}_{\text{Poi}(\lambda_1\tau)}\{N_1(\tau) = n_1\}\, \mathcal{P}_{\text{Poi}(\lambda_2\tau)}\{N_2(\tau) = n - n_1\} \end{aligned} \tag{F.37}$$

where we immediately used the fact that $N_1(t)$ and $N_2(t)$ are independent Poisson processes. Let us substitute in the previous equation the explicit expression for the

probability mass function of Poisson random variables

$$\begin{aligned}\mathcal{P}\{N(\tau)=n\} &= \sum_{n_1=0}^{n} \frac{e^{-\lambda_1\tau}(\lambda_1\tau)^{n_1}}{n_1!}\frac{e^{-\lambda_2\tau}(\lambda_2\tau)^{n-n_1}}{(n-n_1)!} \\ &= \sum_{n_1=0}^{n} \frac{n!}{n_1!(n-n_1)!}\frac{e^{-\lambda_1\tau}(\lambda_1\tau)^{n_1}e^{-\lambda_2\tau}(\lambda_2\tau)^{n-n_1}}{n!} \\ &= \frac{e^{-(\lambda_1+\lambda_2)\tau}}{n!}\sum_{n_1=0}^{n}\binom{n}{n_1}(\lambda_1\tau)^{n_1}(\lambda_2\tau)^{n-n_1} \\ &= \frac{e^{-(\lambda_1+\lambda_2)\tau}}{n!}[(\lambda_1+\lambda_2)\tau]^n \\ &= \mathcal{P}_{\mathrm{Poi}((\lambda_1+\lambda_2)\tau)}\{N(t)=n\}\end{aligned} \tag{F.38}$$

where we used the definition of binomial coefficient and later the of the binomial formula (in reverse).

We, therefore, proved that the process $N(t)$ respects all properties of Section F.1.2 and hence it is a Poisson process with rate $\lambda = \lambda_1 + \lambda_2$.

Difference of Poisson processes

We observe that the difference of two Poisson processes is not a Poisson process [79]: an informal way to see this is that in a Poisson process we cannot have $N(t) < N(s)$ for $s > t$, but this condition is surely possible if we subtract one Poisson process form another. However, we can compute the power spectral density of the process $N(t) = N_1(t) + N_2(t)$ as

$$\begin{aligned}S_{NN}(\omega) &= S_{N_1N_1}(\omega) + (-1)^2 S_{N_2N_2}(\omega) \\ &= S_{N_1N_1}(\omega) + S_{N_2N_2}(\omega) \\ &= \frac{\lambda_1}{\omega^2} + \frac{\lambda_2}{\omega^2} \\ &= \frac{\lambda_1+\lambda_2}{\omega^2}\end{aligned} \tag{F.39}$$

where we used (F.22). This result can be generalized to any linear combination of independent Poisson processes as

$$N(t) = \sum_i j_i N_i(t) \quad \Longrightarrow \quad S_{NN}(\omega) = \sum_i j_i^2 S_{N_iN_i}(\omega) = \frac{1}{\omega^2}\underbrace{\sum_i j_i^2\lambda_i}_{\lambda_{eff}} \tag{F.40}$$

where we defined the effective rate λ_{eff} consistently with the treatment in Chapter 3.

F.1.8 Splitting of a Poisson process

An interesting consequence of the Thinning theorem is that if we divide the original Poisson process with rate λ into two child processes according to the outcome of Bernoulli trial with success probability η, we obtain two Poisson processes with rates $\eta\lambda$ and $(1-\eta)\lambda$, which are also *independent* from each other.

Let $N(t)$ be a Poisson process and $X(t)$ and $Y(t)$ the child processes obtained splitting each point in the original Poisson process according to the outcome of a Bernoulli variable (with success probability η). We can demonstrate the independence

starting by writing the joint probability mass function of $X(t)$ and $Y(t)$

$$\begin{aligned} f_{X(t)Y(t)}(i,j) &= \mathcal{P}\{X(t)=i, Y(t)=j\} \\ &= \sum_{n=0}^{\infty} \mathcal{P}\{X(t)=i, Y(t)=j \,|N(t)=n\} \cdot \mathcal{P}\{N(t)=n\}, \end{aligned} \tag{F.41}$$

where we used the *law of total probability*. We note that the points of the original Poisson process $N(t)$ can be categorized either in the process $X(t)$ or $Y(t)$, hence we must have $n = i + j$, or, equivalently, $\mathcal{P}\{X(t)=i, Y(t)=j \,|N(t)=n\} = 0$ if $n \neq i+j$. In this way, the previous equation reduces to

$$\begin{aligned} f_{X(t)Y(t)}(i,j) &= \mathcal{P}\{X(t)=i, Y(t)=j \,|N(t)=i+j\} \cdot \mathcal{P}\{N(t)=i+j\} \\ &= \mathcal{P}\{X(t)=i \,|N(t)=i+j\} \cdot \mathcal{P}\{N(t)=i+j\}. \end{aligned} \tag{F.42}$$

The last passage is justified by the fact that if in a time window of length t the original Poisson process $N(t)$ has $i+j$ events and i of them are assigned to the child process $X(t)$, the remainder j events must be necessarily assigned to $Y(t)$. On the other hand, the term $\mathcal{P}\{X(t)=i \,|N(t)=i+j\}$ corresponds to the probability of counting i events in the child process $X(t)$ within a time window of length t provided that the parent process $N(t)$ has $i+j$ events in the same window. As the selection criterion for the point to belong in the $X(t)$ process is the outcome of Bernoulli trial with success probability η, this corresponds to having i successes in $i+j$ independent trials. Hence

$$\mathcal{P}\{X(t)=i \,|N(t)=i+j\} = \mathcal{P}_{\mathrm{Bin}(\eta)}\{i, i+j\} = \binom{i+j}{i}\eta^i(1-\eta)^j. \tag{F.43}$$

Moreover, since we know that $N(t)$ is a Poisson process with rate λ, we have

$$\mathcal{P}\{N(t)=i+j\} = \mathcal{P}_{\mathrm{Poi}(\lambda t)}\{N(t)=i+j\} = \frac{(\lambda t)^{i+j}}{(i+j)!}e^{-\lambda t}. \tag{F.44}$$

If we substitute (F.43) and (F.44) into (F.42), we have that

$$\begin{aligned} f_{X(t)Y(t)}(i,j) &= \binom{i+j}{i}\eta^i(1-\eta)^j \cdot \frac{(\lambda t)^{i+j}}{(i+j)!}e^{-\lambda t} \\ &= \frac{(i+j)!}{i!\,j!}\eta^i(1-\eta)^j \cdot \frac{(\lambda t)^{i+j}}{(i+j)!}e^{-\lambda t} \\ &= \frac{(\lambda t)^i}{i!}e^{-\eta\lambda t} \cdot \frac{[(1-\eta)\lambda t]^j}{j!}e^{-(1-\eta)\lambda t} \\ &= \underbrace{\mathcal{P}_{\mathrm{Poi}(\eta\lambda t)}\{X(t)=i\}}_{f_{X(t)}(i)} \cdot \underbrace{\mathcal{P}_{\mathrm{Poi}((1-\eta)\lambda t)}\{Y(t)=j\}}_{f_{Y(t)}(j)}. \end{aligned} \tag{F.45}$$

As we can write the joint probability mass function as a product, we demonstrated that the child processes $X(t)$ and $Y(t)$ are independent Poisson processes.

F.2 Interrupted Poisson processes

Another complication in our experiment comes from the fact that we are not continuously illuminating, but rather we are using pulses of light at $\sim$ kHz frequency (depending on the decimation chosen for the measurement). Indeed, we would not be able to obtain an equilibrium voltage close to neutrality with DC illuminations.

Hence, the noisy photo-currents is not exactly a shot noise, but rather a shot noise with interruptions, with gaps where photons do not arrive because the illumination is off. Such interruptions violate the hypotheses at the basis of the definition of a Poisson process and could, in principle, change all the statistical properties of the charge noise.

This makes the stochastic process *non-stationary*: its statistical properties depend obviously on time. In the literature such processes are called *evolutionary processes*. A detailed treatment of evolutionary processes is beyond the scope of this thesis (and beyond the mathematical savvy of the PhD candidate writing this thesis).

However, we did a small simulation to investigate this issue from a numerical point of view. We simulated a Poisson process with interruptions. The result is showed in Figure F.3.

As we see from Figure F.3, the spectrum of the interrupted Poisson process resembles the PSD of a normal Poisson process with reduced rate, except for the peaks at frequencies that are integer multiples of the interruptions frequency.

One could expect the presence of those peaks from the Fourier transform of a rectangular wave between 0 and 1 with duty cycle $(T_0 - T_p)/T_0$, that is

$$f(t) = \sum_{n=-\infty}^{+\infty} \Pi\left(\frac{t - nT_0}{T_0 - T_p}\right) \tag{F.46}$$

where $\Pi(t)$ is the rectangular function. The Fourier transform of such square wave is a sum of Dirac's deltas centered at multiples of the fundamental frequency of the interruptions

$$\tilde{f}(\omega) = 2\pi \frac{T_0 - T_p}{T_0} \delta(\omega) + \sum_{\substack{n=-\infty \\ n\neq 0}}^{+\infty} \frac{2}{n} \sin\left(\frac{T_0 - T_p}{T_0} \pi n\right) \delta\left(\omega - \frac{2\pi}{T_0} n\right). \tag{F.47}$$

In our case the period of the light pulses is in the $\sim$ kHz range (depending on the decimation, but the lowest frequency of the light pulses that we chose for the continuous discharge measurements is 500 Hz). Therefore, we conclude that those peaks are way outside the band of the continuous discharge measurement (which is $\lesssim 1$ mHz) and we should only see the smooth part of the noise spectrum $\propto f^{-2}$ (typical of Poisson processes).

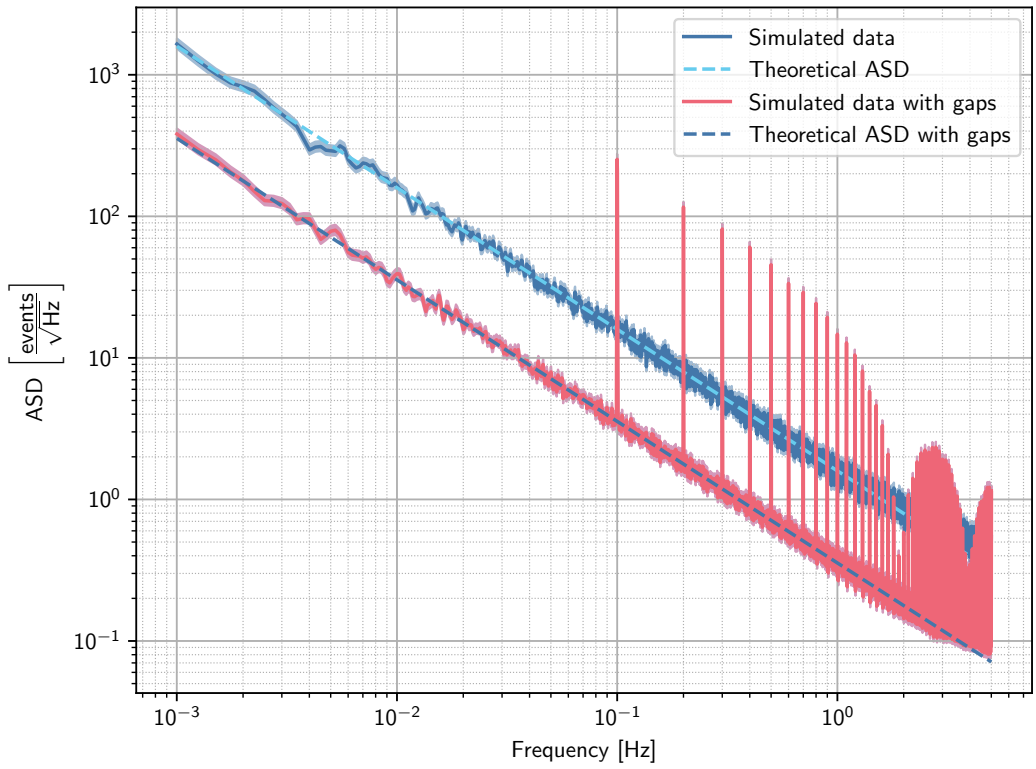

FIGURE F.3: Simulation of a Poisson process with rate $50\,\mathrm{s}^{-1}$ without (blue) and with (red) interruptions. The interruptions last for $T_p = 9.5\,\mathrm{s}$ every $T_0 = 10\,\mathrm{s}$. The peaks are at frequencies multiples of the fundamental one $f_0 = 1/T_0 = 0.1\,\mathrm{Hz}$, below which the spectrum of the data matches the one of the original Poisson process re-scaled by the duty cycle $(T_0 - T_p)/T_0$.

Appendix G

Light source poissonianity

Our PMT setup has the energy resolution to detect the single photon in the UV range.

We decided to conduct some measurements to check the arrival statistics of single photons from our Crystal 250 UV-LED. This may seem a tedious and unnecessarily check, but the reader should be aware that not all light sources are poissonian, there are also sources that produce photons with sub- or super-poissonian statistics.

Poissionian sources are characterized by the fact that, given the event rate λ, in any time window of length t, one expects the variance in of the number of events to be $\sigma_n^2 = \langle n \rangle = \lambda t$. On the other hand for sub-poissonian sources we expect $\sigma_n^2 < \langle n \rangle = \lambda t$ and for super-poissonian sources we have $\sigma_n^2 > \langle n \rangle = \lambda t$.

The idea of the measurement is very easy: we want to record the detection[1] times of the photons from our UV light source and check if they are compatible with a Poisson process. In order to count the single photons, we need to attenuate the light emission from the LED so to have very low chance of two detection overlapping within the time resolution of our PMT system. We acquired a time-series of the PMT output with a fast oscilloscope[2].

The PMT handbook by Hamamatsu Photonics [55] gives an insight on how to correctly choose the photon rate to perform a photon counting experiment.

> The photon counting mode offers excellent linearity over a wide range. The lower limit of the count rate linearity is determined by the number of dark current pulses, and the upper limit by the maximum count rate. The maximum count rate further depends on pulse-pair resolution, which is the minimum time interval at which each pulse can be separated. The reciprocal of this pulse pair resolution would be the maximum count rate. However, since the events in the photon counting region usually occur at random, the counted pulses may possibly overlap. Considering this probability of pulse overlapping (count error caused by pulse overlapping), the actual maximum count rate will be about one tenth of the calculated above. Here, if we let the true count rate be N (in the units s^{-1}), the measured count rate be M (in the units s^{-1}) and time resolution be δt (in the units s), the loss of count rate $N - M$, i.e. the number of missed points per unit time, can also be expressed using the dead time $M \cdot \delta t$ caused by pulse overlapping, as follows:
>
> $$N - M = N \cdot M \cdot \delta t \tag{G.1}$$

[1] Emission rate and detection rate of a photon in our PMT setup are not the same because of the not perfect *quantum efficiency* of our device. The datasheet lists a typical quantum efficiency of 13% and a minimum of 8% at 254 nm wavelength.

[2] We used a Teledyne-Lecroy Wavesurfer oscilloscope (bandwidth up to 1 GHz and sampling rate of 4 GS/s.

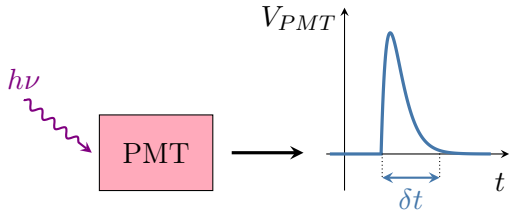

FIGURE G.1: Photon counting experiment.

The calculation by Hamamatsu although reasonable, in our opinion, assumes that the inter-arrival times ΔT_i of the photons, that is the time that passes between a photon arriving on the detector and the subsequent, are *uniformly distributed*. However, in our case we expect the photon emission (and detection) to be Poisson process[3], hence the inter-arrival times are *exponentially distributed*.

$$\Delta T_i \sim N e^{-N \cdot t}, \tag{G.2}$$

where once again N is the true rate of photons. The exponential distribution tells us that small inter-arrival are more likely than long inter-arrival times. This means that in the time window δt where the detector is still blind from the previous pulse statistically it is more likely to have a second photon compared to a time window of the same length at later times.

If the inter-arrival times of the photons are exponentially and not uniformly distributed, the dead time counts proportionally more.

We, therefore, propose to correct the loss counts rate formula (G.1) by Hamamatsu Photonics in the case that the inter-arrival times of the photons are exponentially distributed with the following

$$N - M = N \cdot M \cdot \delta t \, \frac{N\delta t}{1 - e^{-N\delta t}} \quad \xrightarrow{N \to 0} \quad N \cdot M \cdot \delta t \tag{G.3}$$

As showed, in the limit of the rate N going to zero, the exponential distribution tends to an uniform distribution and we recover, as expected, the formula (G.1). In Figure G.2 we show the relative count error $(M - N)/N$ as a function of the true photon rate in units of the pair resolution time δt.

The factor that limits the pulse-pair resolution is the rise time of the amplifier that converts the output current of the PMT into a voltage signal. The typical rise time of the amplifier is $\leq 7\,\text{ns}$, but the data showed that a more realistic value for our experimental setup of $\delta t \simeq 2.5\,\text{ns}$. A conservative upper limit for the photon detection rate in order not to underestimate the rate more than 1% is $N_{max} = 0.01/\delta t \simeq 4\,\text{MHz}$. The lower limit for the photon detection rate is that it has to be significantly larger than the dark count rate, which for our device is pretty low (from the datasheet typically $15\,\text{s}^{-1}$, with a maximum value of $50\,\text{s}^{-1}$ counts per second).

We acquired the signal from the PMT for a few photon rates (always below N_{max} computed before) for the Crystal 250 UV-LED. We employed three checks to investigate the poissonianity of the data.

- We checked if the inter-arrival times between photons follow an exponential distribution;

[3] Or, at least, not to deviate too much from a Poisson process.

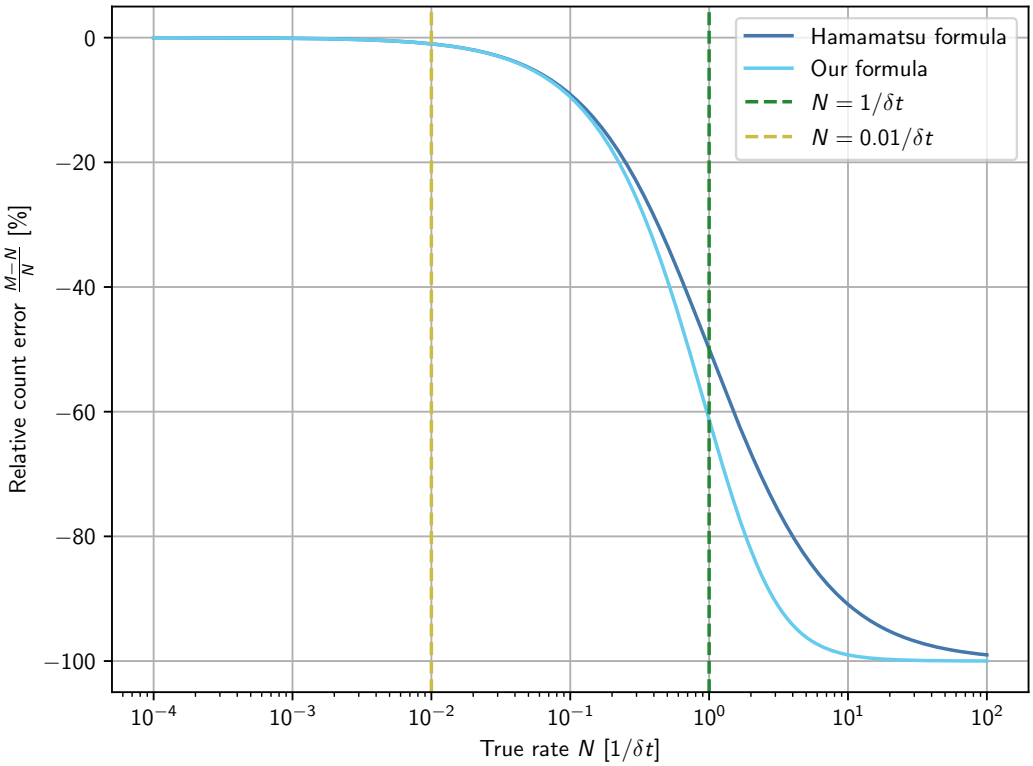

FIGURE G.2: Prevision of the relative count error as a function of the photon detection rate. The blue line correspond to the formula (G.1), whereas the light blue to our correction (G.3), which should be more accurate is the light source is approximately poissonian. As expected the two formulae give the same result for $N\delta \cdot t \ll 1$. If we have a true rate equal to the pair resolution time δt, we underestimate the number of photon detected by $\sim 60\%$. The relative count error drops to less than 1% if we set rates below $0.01/\delta t$.

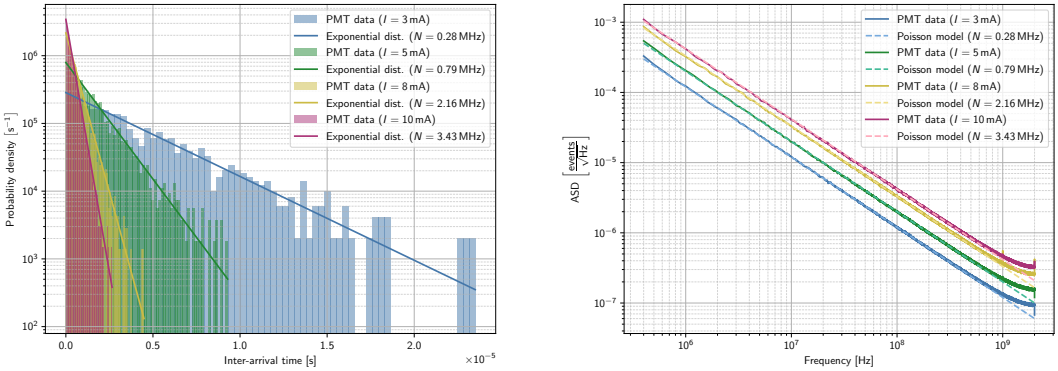

(A) Distribution of the inter-arrival times.

(B) ASD of the cumulative photon count.

FIGURE G.3: Investigation of the poissonian nature of the photons emitted by the Crystal 250 UV-LED.

- We computed the power spectral density of the time-series of the cumulative photon count and checked if it has the expected $\propto f^{-2}$ functional behavior;
- We performed a *Poisson dispersion test*. In a Poisson process with rate λ we have that the number of events in a time window of duration t is a random variable that follows a Poisson distribution with parameter λt. If we chop our experimental PMT time-series into n non-overlapping windows of duration t, we will have a series $(c_1, c_2, \ldots, c_n)$ of counts in each window. The numbers c_i will be random draws from a Poisson distribution with parameter λt. As the mean and variance of a Poission distribution are also equal to λt, the following quantity

$$D = \sum_{i=1}^{n} \frac{(c_i - \langle c \rangle)^2}{\langle c \rangle} \qquad \text{where} \qquad \langle c \rangle = \frac{1}{n} \sum_{i=1}^{n} c_i \tag{G.4}$$

  is expected to follow a chi-squared with $n-1$ degrees of freedom provided that the experimental data are poissonian. Hence, to summarize, we expect

$$D \sim \chi^2(n-1) \qquad \text{if data belong to a Poisson process.} \tag{G.5}$$

We show in Figure G.3 the result for the distribution of the photon inter-arrival times and for the PSD of the time-series obtained from the cumulative photon count. The agreement between data and models is very good. We performed the *Poisson dispersion test* for each data series with several time windows ranging from a duration of 1 μs to 500 μs. At a 2σ-significance level ($\sim 95\%$), the data passed the test the great majority of times, saved for a few outliers that were marginally outside the acceptable interval of the chi-squared distribution.

In general the experimental data obtained with the Crystal 250 LED show no significant deviation from a Poisson process.

Appendix H

LISA Consortium logo contest

During the spring 2020, the Advoreach working group announced a competition to design the LISA Consortium logo open to the whole LISA community.

I took part into the logo contest with my personal design that is depicted in Figure H.1a. With my logo I wanted to convey the ideas of technology, dynamism and space exploration that characterize the LISA mission.

I also desired to include the unique identity of the LISA mission into the design and the perfect opportunity was to replace the letter A in LISA with a triangle representing the three spacecrafts of the constellation connected by laser beams.

I was lucky enough that my logo received the most preferences during the community vote that took place online from the 18th to the 27th of November 2020.

My design was given as a reference to a professional designer that created the final logo shown in Figure H.1b.

The professional version of the logo has a siplified color scheme and replaced the rocket with the Ariane 6.4 (at the request of ESA) which will launch LISA. As the professional design opted for more bold lines, the satellite tracks were removed. This version was adopted as the official LISA Consortium logo in 2021.

(A) My original design

(B) The final LISA Consortium logo

FIGURE H.1: Comparison between my design and the final LISA Consortium logo.

Bibliography

[1] B. P. Abbott et al. "Observation of Gravitational Waves from a Binary Black Hole Merger". In: *Phys. Rev. Lett.* 116 (6 Feb. 2016), p. 061102. DOI: 10.1103/PhysRevLett.116.061102. URL: https://link.aps.org/doi/10.1103/PhysRevLett.116.061102.

[2] B. P. Abbott et al. "GW170817: Observation of Gravitational Waves from a Binary Neutron Star Inspiral". In: *Phys. Rev. Lett.* 119 (16 Oct. 2017), p. 161101. DOI: 10.1103/PhysRevLett.119.161101. URL: https://link.aps.org/doi/10.1103/PhysRevLett.119.161101.

[3] The Event Horizon Telescope Collaboration et al. "First M87 Event Horizon Telescope Results. I. The Shadow of the Supermassive Black Hole". In: *The Astrophysical Journal Letters* 875.1 (Apr. 2019), p. L1. DOI: 10.3847/2041-8213/ab0ec7. URL: https://dx.doi.org/10.3847/2041-8213/ab0ec7.

[4] The Event Horizon Telescope Collaboration. *Press Release (April 10, 2019): Astronomers Capture First Image of a Black Hole*. Accessed: 2023-02-18. URL: https://eventhorizontelescope.org/press-release-april-10-2019-astronomers-capture-first-image-black-hole.

[5] M. P. Hobson, G. P. Efstathiou, and A. N. Lasenby. *General Relativity. An Introduction for Physicists*. Cambridge University Press, 2006. ISBN: 9780521829519.

[6] Bernard Schutz. *A First Course in General Relativity*. 2nd ed. Cambridge University Press, 2009. DOI: 10.1017/9781108610865.

[7] D. V. Martynov et al. "Sensitivity of the Advanced LIGO detectors at the beginning of gravitational wave astronomy". In: *Phys. Rev. D* 93 (11 June 2016), p. 112004. DOI: 10.1103/PhysRevD.93.112004. URL: https://link.aps.org/doi/10.1103/PhysRevD.93.112004.

[8] Pau Amaro-Seoane et al. *Laser Interferometer Space Antenna*. 2017. DOI: 10.48550/ARXIV.1702.00786. URL: https://arxiv.org/abs/1702.00786.

[9] Eleonora Castelli. "LISA Pathfinder noise performance results: disturbances in the sub-mHz frequency band and projection to LISA". University of Trento, Apr. 2020.

[10] Travis Robson, Neil J Cornish, and Chang Liu. "The construction and use of LISA sensitivity curves". In: *Classical and Quantum Gravity* 36.10 (Apr. 2019), p. 105011. DOI: 10.1088/1361-6382/ab1101. URL: https://dx.doi.org/10.1088/1361-6382/ab1101.

[11] T. Kupfer et al. "LISA verification binaries with updated distances from Gaia Data Release 2". In: *Monthly Notices of the Royal Astronomical Society* 480.1 (June 2018), pp. 302–309. ISSN: 0035-8711. DOI: 10.1093/mnras/sty1545. eprint: https://academic.oup.com/mnras/article-pdf/480/1/302/25244351/sty1545.pdf. URL: https://doi.org/10.1093/mnras/sty1545.

[12] Martin Hewitson, Ewan Fitzsimons, and William Joseph Weber. *LISA Performance Model and Error Budget*. LISA-LCST-INST-TN-003 (revision 3). University of Trento and INFN/TIFPA, Oct. 2020.

[13] Paul McNamara and Giuseppe Racca. *Introduction to LISA Pathfinder*. LISA-LPF-RP-0002 (revision 1). European Space Agency, Feb. 2009. URL: https://sci.esa.int/documents/34614/36035/1567257332401-LISA-LPFRP-0002.pdf.

[14] *LISA Pathfinder Multimedia Gallery*. Accessed: 2023-02-18. URL: https://sci.esa.int/web/lisa-pathfinder/multimedia-gallery.

[15] M. Armano et al. "The LISA Pathfinder Mission". In: *Journal of Physics: Conference Series* 610.1 (Apr. 2015), p. 012005. DOI: 10.1088/1742-6596/610/1/012005. URL: https://dx.doi.org/10.1088/1742-6596/610/1/012005.

[16] P. McNamara et al. "LISA Pathfinder". In: *Classical and Quantum Gravity* 25.11 (May 2008), p. 114034. DOI: 10.1088/0264-9381/25/11/114034. URL: https://dx.doi.org/10.1088/0264-9381/25/11/114034.

[17] M. Armano et al. "Beyond the Required LISA Free-Fall Performance: New LISA Pathfinder Results down to 20 μHz". In: *Phys. Rev. Lett.* 120 (6 Feb. 2018), p. 061101. DOI: 10.1103/PhysRevLett.120.061101. URL: https://link.aps.org/doi/10.1103/PhysRevLett.120.061101.

[18] M. Armano et al. "Transient acceleration events in LISA Pathfinder data: Properties and possible physical origin". In: *Phys. Rev. D* 106 (6 Sept. 2022), p. 062001. DOI: 10.1103/PhysRevD.106.062001. URL: https://link.aps.org/doi/10.1103/PhysRevD.106.062001.

[19] Charles-Augustine Coulomb. *Mémoires sur l'électricité et la magnétisme*. Chez Bachelier, libraire, 1789. URL: https://doi.org/10.5479/sil.304245.39088000647479.

[20] Henry Cavendish. "XXI. Experiments to determine the density of the earth". In: *Philosophical Transactions of the Royal Society of London* 88 (1798), pp. 469–526. DOI: 10.1098/rstl.1798.0022. URL: https://royalsocietypublishing.org/doi/abs/10.1098/rstl.1798.0022.

[21] B. E. Clotfelter. "The Cavendish experiment as Cavendish knew it". In: *American Journal of Physics* 55.3 (1987), pp. 210–213. DOI: 10.1119/1.15214. eprint: https://doi.org/10.1119/1.15214. URL: https://doi.org/10.1119/1.15214.

[22] T. A. Wagner et al. "Torsion-balance tests of the weak equivalence principle". In: *Classical and Quantum Gravity* 29.18 (Aug. 2012), p. 184002. DOI: 10.1088/0264-9381/29/18/184002. URL: https://dx.doi.org/10.1088/0264-9381/29/18/184002.

[23] C. D. Hoyle et al. "Submillimeter Test of the Gravitational Inverse-Square Law: A Search for "Large" Extra Dimensions". In: *Phys. Rev. Lett.* 86 (8 Feb. 2001), pp. 1418–1421. DOI: 10.1103/PhysRevLett.86.1418. URL: https://link.aps.org/doi/10.1103/PhysRevLett.86.1418.

[24] Giacomo Ciani et al. "A new torsion pendulum for gravitational reference sensor technology development". In: *Review of Scientific Instruments* 88.6 (2017), p. 064502. DOI: 10.1063/1.4985543. eprint: https://doi.org/10.1063/1.4985543. URL: https://doi.org/10.1063/1.4985543.

[25] Giacomo Ciani. "Free-fall of LISA Test Masses: a new torsion pendulum to test translational acceleration". University of Trento, Feb. 2008.

[26] M. Hueller et al. "Torsion pendulum facility for ground testing of gravitational sensors for LISA". In: *Classical and Quantum Gravity* 19.7 (Mar. 2002), p. 1757. DOI: 10.1088/0264-9381/19/7/372. URL: https://dx.doi.org/10.1088/0264-9381/19/7/372.

[27] Peter R. Saulson. "Thermal noise in mechanical experiments". In: *Phys. Rev. D* 42 (8 Oct. 1990), pp. 2437–2445. DOI: 10.1103/PhysRevD.42.2437. URL: https://link.aps.org/doi/10.1103/PhysRevD.42.2437.

[28] Luigi Ferraioli, Mauro Hueller, and Stefano Vitale. "Discrete derivative estimation in LISA Pathfinder data reduction". In: *Classical and Quantum Gravity* 26.9 (Apr. 2009), p. 094013. DOI: 10.1088/0264-9381/26/9/094013. URL: https://dx.doi.org/10.1088/0264-9381/26/9/094013.

[29] William J. Herrera and Rodolfo A. Diaz. "The geometrical nature and some properties of the capacitance coefficients based on Laplace's equation". In: *American Journal of Physics* 76.1 (2008), pp. 55–59. DOI: 10.1119/1.2800355. eprint: https://doi.org/10.1119/1.2800355. URL: https://doi.org/10.1119/1.2800355.

[30] F. Antonucci et al. "Interaction between Stray Electrostatic Fields and a Charged Free-Falling Test Mass". In: *Phys. Rev. Lett.* 108 (18 Apr. 2012), p. 181101. DOI: 10.1103/PhysRevLett.108.181101. URL: https://link.aps.org/doi/10.1103/PhysRevLett.108.181101.

[31] Richard P. Feynman, Robert B. Leighton, and Matthew Sands. "The Feynman lectures on physics; New millennium edition". In: vol. 2. Basic Books, 2010. Chap. 8. URL: https://www.feynmanlectures.caltech.edu.

[32] Luigi Ferraioli. *GRS Actuation model*. LISA-ETH-INST-TN-006 (version 1.0). ETH Zürich, May 2019.

[33] Nico Brandt and Walter Fichter. "Revised electrostatic model of the LISA Pathfinder inertial sensor". In: *Journal of Physics: Conference Series* 154.1 (Mar. 2009), p. 012008. DOI: 10.1088/1742-6596/154/1/012008. URL: https://dx.doi.org/10.1088/1742-6596/154/1/012008.

[34] Vittorio Chiavegato. "Experimental investigation of Force Noise from Electrostatic Force Actuation in the LISA Gravitational Wave Observatory". University of Trento, 2020.

[35] Wolfram Research Inc. *Mathematica, Version 13.1*. Champaign, IL, 2022. URL: https://www.wolfram.com/mathematica.

[36] M. Armano et al. "Charge-Induced Force Noise on Free-Falling Test Masses: Results from LISA Pathfinder". In: *Phys. Rev. Lett.* 118 (17 Apr. 2017), p. 171101. DOI: 10.1103/PhysRevLett.118.171101. URL: https://link.aps.org/doi/10.1103/PhysRevLett.118.171101.

[37] Saps Buchman et al. "Charge measurement and control for the Gravity Probe B gyroscopes". In: *Review of Scientific Instruments* 66.1 (1995), pp. 120–129. DOI: 10.1063/1.1145276. eprint: https://doi.org/10.1063/1.1145276. URL: https://doi.org/10.1063/1.1145276.

[38] B. Christophe et al. "A new generation of ultra-sensitive electrostatic accelerometers for GRACE Follow-on and towards the next generation gravity missions". In: *Acta Astronautica* 117 (2015), pp. 1–7. ISSN: 0094-5765. DOI: https://doi.org/10.1016/j.actaastro.2015.06.021. URL: https://www.sciencedirect.com/science/article/pii/S0094576515002660.

[39] E. Willemenot and P. Touboul. "On-ground investigation of space accelerometers noise with an electrostatic torsion pendulum". In: *Review of Scientific Instruments* 71.1 (2000), pp. 302–309. DOI: 10.1063/1.1150197. eprint: https://doi.org/10.1063/1.1150197. URL: https://doi.org/10.1063/1.1150197.

[40] M. Armano et al. "Charging of free-falling test masses in orbit due to cosmic rays: Results from LISA Pathfinder". In: *Phys. Rev. D* 107 (6 Mar. 2023), p. 062007. DOI: 10.1103/PhysRevD.107.062007. URL: https://link.aps.org/doi/10.1103/PhysRevD.107.062007.

[41] H. M. Araújo et al. "Detailed calculation of test-mass charging in the LISA mission". In: *Astroparticle Physics* 22.5 (2005), pp. 451–469. ISSN: 0927-6505. DOI: https://doi.org/10.1016/j.astropartphys.2004.09.004. URL: https://www.sciencedirect.com/science/article/pii/S0927650504001604.

[42] Marius S. Potgieter. "Solar Modulation of Cosmic Rays". In: *Living Reviews in Solar Physics* (June 2013). DOI: https://doi.org/10.12942/lrsp-2013-3. URL: 10.12942/lrsp-2013-3.

[43] Grimani, C. et al. "Bridging the gap between Monte Carlo simulations and measurements of the LISA Pathfinder test-mass charging for LISA". In: *A&A* 666 (2022), A38. DOI: 10.1051/0004-6361/202243984. URL: https://doi.org/10.1051/0004-6361/202243984.

[44] Catia Grimani et al. "Low-energy electromagnetic processes affecting free-falling test-mass charging for LISA and future space interferometers". In: *Classical and Quantum Gravity* 38.4 (Dec. 2020), p. 045013. DOI: 10.1088/1361-6382/abd142. URL: https://dx.doi.org/10.1088/1361-6382/abd142.

[45] C. Grimani et al. "LISA Pathfinder test-mass charging during galactic cosmic-ray flux short-term variations". In: *Classical and Quantum Gravity* 32.3 (Jan. 2015), p. 035001. DOI: 10.1088/0264-9381/32/3/035001. URL: https://dx.doi.org/10.1088/0264-9381/32/3/035001.

[46] Benjamin C. Letson et al. "High volume UV LED performance testing". In: *Review of Scientific Instruments* 93.11 (2022), p. 114503. DOI: 10.1063/5.0107372. eprint: https://doi.org/10.1063/5.0107372. URL: https://doi.org/10.1063/5.0107372.

[47] D. Hollington et al. "Lifetime testing UV LEDs for use in the LISA charge management system". In: *Classical and Quantum Gravity* 34.20 (Sept. 2017), p. 205009. DOI: 10.1088/1361-6382/aa87eb. URL: https://dx.doi.org/10.1088/1361-6382/aa87eb.

[48] Ke-Xun Sun et al. "UV LED operation lifetime and radiation hardness qualification for space flights". In: *Journal of Physics: Conference Series* 154.1 (Mar. 2009), p. 012028. DOI: 10.1088/1742-6596/154/1/012028. URL: https://dx.doi.org/10.1088/1742-6596/154/1/012028.

[49] Ke-Xun Sun et al. "LED deep UV source for charge management of gravitational reference sensors". In: *Classical and Quantum Gravity* 23.8 (Mar. 2006), S141. DOI: 10.1088/0264-9381/23/8/S19. URL: https://dx.doi.org/10.1088/0264-9381/23/8/S19.

[50] Tobias Ziegler et al. *Modeling and Performance of Contact-Free Discharge Systems for Space Inertial Sensors*. 2012. arXiv: 1207.0394 [physics.ins-det]. URL: https://doi.org/10.48550/arXiv.1207.0394.

[51] D. Hollington et al. "Characterising and testing deep UV LEDs for use in space applications". In: *Classical and Quantum Gravity* 32.23 (Nov. 2015), p. 235020. DOI: 10.1088/0264-9381/32/23/235020. URL: https://dx.doi.org/10.1088/0264-9381/32/23/235020.

[52] M. Armano et al. "Precision charge control for isolated free-falling test masses: LISA pathfinder results". In: *Phys. Rev. D* 98 (6 Sept. 2018), p. 062001. DOI: 10.1103/PhysRevD.98.062001. URL: https://link.aps.org/doi/10.1103/PhysRevD.98.062001.

[53] Stefano Nannarone. *Measurement of quantum yield and UV photoemission from Ir samples (semi-cylinders)*. Tech. rep. University of Modena, July 2010.

[54] Samantha Parry Kenyon et al. "A Charge Management System for Gravitational Reference Sensors – Design and Instrument Testing". In: *2021 IEEE Aerospace Conference (50100)*. 2021, pp. 1–9. DOI: 10.1109/AERO50100.2021.9438339.

[55] Hamamatsu Photonics. *Photomultipliers Tubes. Basics and Applications*. 2007. URL: https://www.hamamatsu.com/content/dam/hamamatsu-photonics/sites/documents/99_SALES_LIBRARY/etd/PMT_handbook_v3aE.pdf.

[56] MathWorks Inc. *polyfit*. Accessed: 2023-04-06. URL: https://it.mathworks.com/help/matlab/ref/polyfit.html.

[57] Taiwo Olatunde et al. "Characterisation of Au surface properties relevant for UV photoemission-based charge control for space inertial sensors". In: *Classical and Quantum Gravity* 37.19 (Sept. 2020), p. 195009. DOI: 10.1088/1361-6382/aba588. URL: https://dx.doi.org/10.1088/1361-6382/aba588.

[58] Daniel Hollington. "The Charge Management System for LISA and LISA Pathfinder". PhD thesis. Imperial College London, Nov. 2011. DOI: https://doi.org/10.25560/9083. URL: http://hdl.handle.net/10044/1/9083.

[59] M. Armano et al. "Precision charge control for isolated free-falling test masses: LISA Pathfinder results". In: *Phys. Rev. D* 98 (6 Sept. 2018), p. 062001. DOI: 10.1103/PhysRevD.98.062001. URL: https://link.aps.org/doi/10.1103/PhysRevD.98.062001.

[60] Gerald Hechenblaikner et al. "Energy distribution and quantum yield for photoemission from air-contaminated gold surfaces under ultraviolet illumination close to the threshold". In: *Journal of Applied Physics* 111.12 (2012), p. 124914. DOI: 10.1063/1.4730638. eprint: https://doi.org/10.1063/1.4730638. URL: https://doi.org/10.1063/1.4730638.

[61] Neil W. Ashcroft and Nathaniel D. Mermin. *Solid State Physics*. Harcourt College Publishers, 1976.

[62] Mark E. Tuckerman. *Statistical Mechanics: Theory and Molecular Simulation*. Oxford University Press, 2010.

[63] R. H. Fowler. "The Analysis of Photoelectric Sensitivity Curves for Clean Metals at Various Temperatures". In: *Phys. Rev.* 38 (1 July 1931), pp. 45–56. DOI: 10.1103/PhysRev.38.45. URL: https://link.aps.org/doi/10.1103/PhysRev.38.45.

[64] Lee A. DuBridge. "Theory of the Energy Distribution of Photoelectrons". In: *Phys. Rev.* 43 (9 May 1933), pp. 727–741. DOI: 10.1103/PhysRev.43.727. URL: https://link.aps.org/doi/10.1103/PhysRev.43.727.

[65] Claude Cohen-Tannoudji, Bernard Diu, and Franck Laloë. *Quantum Mechanics*. Wiley VCH, 1977.

[66] David Wood. *The Computation of Polylogarithms*. Tech. rep. 15-92*. University of Kent, Canterbury, UK: University of Kent, Computing Laboratory, June 1992, pp. 182–196. URL: http://www.cs.kent.ac.uk/pubs/1992/110.

[67] David H. Dowell and John F. Schmerge. "Quantum efficiency and thermal emittance of metal photocathodes". In: *Phys. Rev. ST Accel. Beams* 12 (7 July 2009), p. 074201. DOI: 10.1103/PhysRevSTAB.12.074201. URL: https://link.aps.org/doi/10.1103/PhysRevSTAB.12.074201.

[68] H. Inchauspé et al. "Numerical modeling and experimental demonstration of pulsed charge control for the space inertial sensor used in LISA". In: *Phys. Rev. D* 102 (4 Aug. 2020), p. 042002. DOI: 10.1103/PhysRevD.102.042002. URL: https://link.aps.org/doi/10.1103/PhysRevD.102.042002.

[69] Matthew D. Hoffman and Andrew Gelman. *The No-U-Turn Sampler: Adaptively Setting Path Lengths in Hamiltonian Monte Carlo*. 2011. DOI: 10.48550/ARXIV.1111.4246. URL: https://arxiv.org/abs/1111.4246.

[70] John Salvatier, Thomas V. Wiecki, and Christopher Fonnesbeck. "Probabilistic programming in Python using PyMC3". In: *PeerJ Computer Science* 2 (Apr. 2016), e55. DOI: 10.7717/peerj-cs.55. URL: https://doi.org/10.7717/peerj-cs.55.

[71] W.M.H. Sachtler, G.J.H. Dorgelo, and A.A. Holscher. "The work function of gold". In: *Surface Science* 5.2 (1966), pp. 221–229. ISSN: 0039-6028. DOI: https://doi.org/10.1016/0039-6028(66)90083-5. URL: https://www.sciencedirect.com/science/article/pii/0039602866900835.

[72] William Joseph Weber. *Analysis of LISA Electrostatic Force and Charge Management Requirements*. LISA-UTN-INST-TN-014 (version 0.99). University of Trento and INFN/TIFPA, Jan. 2021.

[73] Hossein Pishro-Nik. *Introduction to Probability. Statistics and Random Processes*. 1st ed. Kappa Research LLC, 2014. ISBN: 9780990637202. URL: https://www.probabilitycourse.com.

[74] Stefano Vitale, Eleonora Castelli, and Lorenzo Sala. *Minimum-error, low-correlation, power spectral density estimation with proper error statistics*. S2-UTN-TN-3130 (version 2.0). University of Trento and INFN/TIFPA, Feb. 2021.

[75] Stefano Vitale et al. "Data series subtraction with unknown and unmodeled background noise". In: *Phys. Rev. D* 90 (4 Aug. 2014), p. 042003. DOI: 10.1103/PhysRevD.90.042003. URL: https://link.aps.org/doi/10.1103/PhysRevD.90.042003.

[76] Roberta Giusteri et al. "The free-fall mode experiment on LISA Pathfinder: first results". In: *Journal of Physics: Conference Series* 840 (May 2017), p. 012005. DOI: 10.1088/1742-6596/840/1/012005. URL: https://doi.org/10.1088/1742-6596/840/1/012005.

[77] Maurice B. Priestley. *Spectral Analysis and Time Series*. 1st ed. Academic Press, Oct. 1982. ISBN: 9780125649223.

[78] P. Bergner, T. Ziegler, and D. Kolbe. *Discharge Model Predictions for the UTN 4Mass Torsion Pendulum*. Tech. rep. S2-ASD-TN-3198. Astrium, Jan. 2013.

[79] Athanasios Papoulis and S. Unnikrishna Pillai. *Probability, Random Variables and Stochastic Processes*. 4th ed. McGraw-Hill, 2002. ISBN: 0071122567.

[80] Zoran Nenadic. *Counting Process*. Accessed: 2023-04-06. URL: http://robotics.caltech.edu/~zoran/Research/poisson/node1.html.